TECHNISCHE UNIVERSITÄT ILMENAU

COMMUNICATIONS RESEARCH LABORATORY

CRL

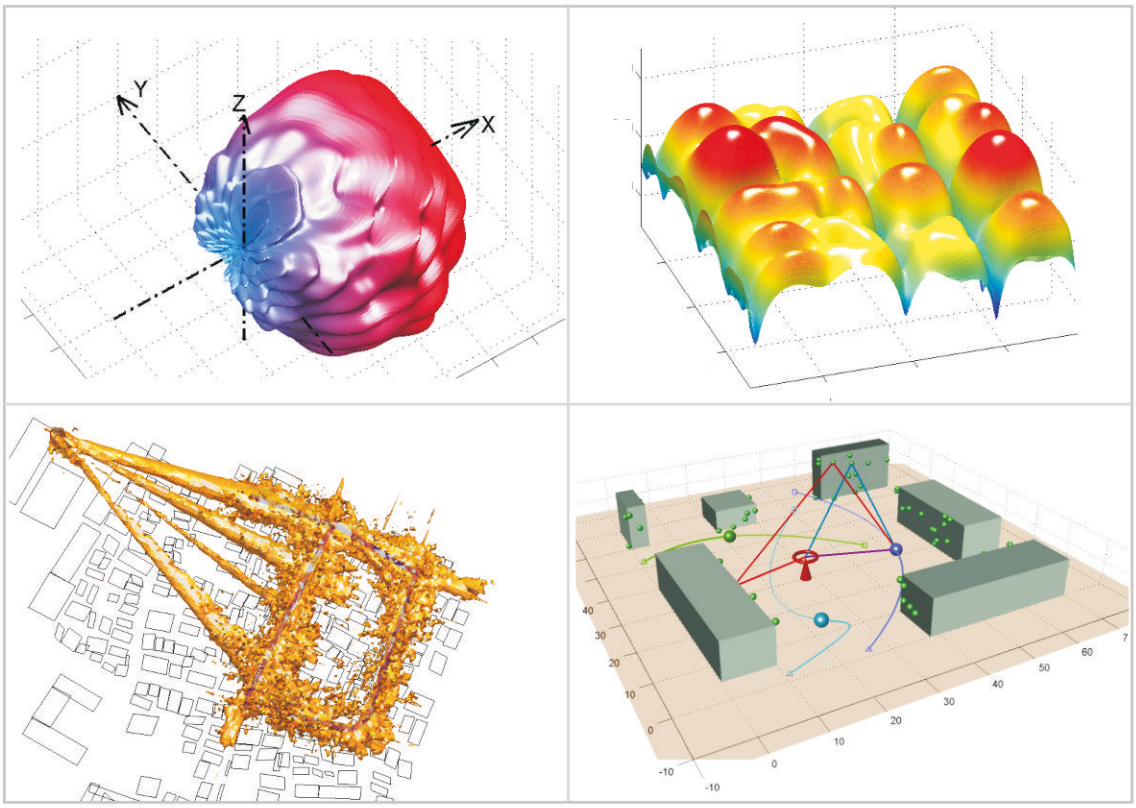


# Geometry-based Channel Modeling for Multi-User MIMO Systems and Applications

Giovanni Del Galdo

**Reports from the Communications Research Laboratory at Ilmenau University of Technology**
Editor: Univ.-Prof. Dr.-Ing. Martin Haardt
Ilmenau, Germany, 2007

Research Reports from the Communications Research Laboratory
at Ilmenau University of Technology

*Giovanni Del Galdo*

# Geometry-based Channel Modeling for Multi-User MIMO Systems and Applications

2007

**Bibliografische Information Der Deutschen Bibliothek**
Die Deutsche Bibliothek verzeichnet diese Publikation in der Deutschen Nationalbibliografie; detaillierte bibliografische Daten sind im Internet über http://dnb.ddb.de abrufbar.

ISBN 978-3-938843-27-7



Verlag ISLE, Betriebsstätte des ISLE e.V. ,
Werner-von-Siemens-Str. 16, 98693 Ilmenau

Printed in Germany

TECHNISCHE UNIVERSITÄT ILMENAU

Fakultät für Elektrotechnik und Informationstechnik
der Technischen Universität Ilmenau

# Geometry-based Channel Modeling for Multi-User MIMO Systems and Applications

*Giovanni Del Galdo*

Dissertation zur Erlangung des
akademischen Grades Doktor-Ingenieur (Dr.-Ing)

| | |
|---|---|
| Anfertigung im: | Fachgebiet Nachrichtentechnik<br>Institut für Informationstechnik<br>Fakultät für Elektrotechnik und Informationstechnik |
| Gutachter: | Univ.-Prof. Dr.-Ing. Martin Haardt<br>Univ.-Prof. Dr.-Ing. habil. Reiner S. Thomä<br>o.Univ.Prof. i.R. Dipl.-Ing. Dr.techn. Ernst Bonek |
| Vorgelegt am: | 09.02.07 |
| Verteidigt am: | 31.05.07 |

urn:nbn:de:gbv:ilm1-2007000136

# PREFACE

Welcome to the first volume of the Research Reports from the Communications Research Laboratory at Ilmenau University of Technology.

It is the doctoral dissertation of Giovanni Del Galdo, entitled "Geometry-Based Channel Modeling for Multi-User MIMO Systems and Applications". In this thesis, Giovanni Del Galdo deals with geometry-based and analytical channel modeling concepts for multi-user MIMO systems and their applications to evaluate the performance of advanced signal processing algorithms in wireless communications.

Multi-user MIMO systems are a key component of wireless communication systems beyond the third generation, e.g., the fourth generation, to increase their spectral efficiency and to enable higher data rates with a reduced cost per bit as compared to third generation mobile communication systems. Realistic models of the wireless channel are essential to predict and evaluate the performance of advanced signal processing schemes.

In this volume, Giovanni Del Galdo solves a variety of challenging tasks that are highly relevant for the design of future wireless communication systems in an elegant way. These tasks are at the intersection of several scientific disciplines including channel modeling, signal processing, communications, linear algebra, antennas, propagation, and electromagnetic theory. The results of this thesis represent a significant contribution to the field of wireless channel modeling and, therefore, have an important impact on the design and realistic evaluation of multi-user MIMO systems.

Ilmenau, June 2007 Martin Haardt

# ACKNOWLEDGEMENTS

Many people deserve my gratitude. First of all my tutor and mentor Prof. Martin Haardt, from whom I have learned most of what I know in the fields of linear algebra and multi-sensor techniques, the fine art of critical thinking, as well as the importance of expressing my ideas and results in a comprehensive and precise way. The time spent working with him shaped greatly my professional identity and effectively made me the researcher I am today. For this, I will be eternally grateful.

I had the pleasure to meet and discuss with several key members of the research community. I'm particularly grateful for the time they dedicated to me, which always had a great impact on my personal and professional life. Among them, I would like to mention Prof. Reiner Thomä, Prof. Ernst Bonek, Prof. Bernard Fleury, Prof. Christoph Mecklenbräuker, Prof. Umberto Spagnolini, Prof. Alex Gershman, Prof. Tadashi Matsumoto, Prof. Alister Burr, Prof. Pertti Vainikainen, Prof. Visa Koivunen, and Prof. Lars Rasmussen.

A longer list of fellow researchers deserves my gratitude for the successful collaborations and interesting discussions: Nicolai Czink, Dr. Osvaldo Simeone, Dr. Thomas Zemen, Dr. Jari Salo, Dr. Fabio Belloni, Dr. Xuefeng Yin, Dr. Alexander Ihlow, Daniel Baum, and Pekka Kyösti. A special thanks goes to the researchers of the Ilmenau University of Technology, in particular Martin Fuchs, Veljko Stankovic, Markus Landmann, Gerd Sommerkorn, Dr. Wim Kotterman, Vadim Algeier, Christian Schneider, Marko Milojevic, Marko Hennöfer, Florian Römer, Jörn Weber, Nuan Song, Dr. Mike Wolf, Ulrike Korger, and Christian Käs. Especially I would like to thank those who have spent time reading early versions of my thesis, always giving constructive feedback.

I would like to thank the National Institute of Information and Communications Technology (NICT) and FUJITSU for the support and provision of the measurement equipment for the measurements presented in Section 5.3.5. Furthermore, I would like to thank the members of the Takada Laboratory of Tokyo Institute of Technology for the support during the measurements and Markus Landmann, for the carrying out the parameter-estimation step and for his valuable support in analyzing the parameters estimates.

I would like to thank the Fraunhofer Institute, in particular Albert Heuberger, for the fruitful collaboration on the satellite to indoor scenario presented in Section 5.2.3.

I would also like to thank the students whom I coached during their Master theses and student projects who had an impact on this work. In particular Jörg Lotze, for the long successful collaboration on the IlmProp and on the antenna radiation pattern modeling, and for his support with my LaTeX difficulties. He has been an irreplaceable help. Martin Weis, for the tensor appendix and his contributions to the correlation tensor channel model, and Alejandro Braun, for the long time spent on Mathematica deriving the asymmetric pencil beam PDF and for finding efficient ways to compute it numerically.

A huge thanks to my parents, for teaching me the importance of integrity, commitment, ambition, and self confidence. These principles motivate me every day in striving to become a better researcher.

An even bigger thanks to my wife, especially for staying up late with me to proofread this work, and for feeding me during the long working hours of the last months.

I feel a special gratitude for Prof. Thomä, for his interest in my research and for sharing his deep understanding of the MIMO world in long interesting discussions.

I'm very grateful to Prof. Bonek for the fruitful comments and discussions, and especially for accepting to be a reviewer of my work.

*My biggest gratitude goes indeed to modern medicine, which, through the hands of skilled surgeons of the Zentralklinik Bad Berka, not only saved my life, but effectively granted me a wonderful new one.*

Ilmenau, May 2007 Giovanni Del Galdo

# ABSTRACT

This thesis deals with channel modeling of wireless time variant frequency selective multi-user Multiple Input Multiple Output (MIMO) systems. By defining a multi-dimensional tensor-based extension of the Bello system equations, we emphasize how the channel displays dispersion in the delay, Doppler, and angular domains. The origin of this phenomenon lies in the multi-path nature of the radio channel. In the transformed domains, namely frequency, time, and space, the channel shows selectivity, i.e., the random fading of the channel power along these dimensions. By introducing a less conventional notation, we are able to show the strong analogy between all domain pairs.

We present and categorize some of the most relevant channel modeling approaches, underlining their drawbacks and benefits.

For geometry-based channel models it is crucial to model accurately and efficiently the far-field antenna radiation patterns. To do so, we develop a novel descriptor based on the Discrete Vector Spherical Fourier Transform (DVSFT). This method allows us to describe these complex vector functions with higher accuracy than other known methods, as the DVSFT represents the natural Fourier domain for spherical problems. The proposed method leads to several novel applications: a lossless rotation of the pattern, measurement noise reduction, SNR estimation, the optimization of the calibration process, a rotation-invariant power spectrum, the concept of level bandwith, and the accurate computation of the antenna efficiency.

We then present the major contribution of this work: the IlmProp. The IlmProp is a geometry-based channel modeling framework. It fills the gap between conventional directional channel models and ray-tracers. The IlmProp allows multiple users to coexist in the same environment. It models the Multi-Path Components (MPCs) explicitly by means of point-like Interacting Objects (IOs) placed in the three-dimensional space. In this manner, the correlation in time, frequency, space, and between users evolves realistically in time.

The IlmProp model parameters can be set arbitrarily or derived from high-resolution parameter estimates. In the former case, the IlmProp can be used to test a variety of transmit and receive schemes, as well as scheduling algorithms. Moreover, we can compare and evaluate different antenna arrays and array configurations under realistic conditions. In order to obtain the IlmProp parameters from high-resolution parameter estimates, we propose a novel algorithm which localizes the Interacting Objects (IOs) by following a classical Bayesian inversion theory approach. The method allows us to reconstruct the trajectory of each propagation path from the mere information on the Direction Of Arrival, Direction Of Departure, and

Time Delay Of Arrival. This gives a powerful visualization tool to validate the channel measurements and the parameter estimator, as well as to gain a deeper understanding of the propagation conditions of the environment under study.

We then review the so-called Measurement-Based Parametric Channel Model (MBPCM) concept. The latter allows us to obtain realistic synthetic channels for antenna arrays, mobile trajectories, and frequency bandwidths other than the ones used during the measurement. This is possible thanks to an antenna independent double directional channel description. With the knowledge of the position of the IOs we can improve the MBPCM concept by exploiting the more accurate information on the paths' trajectories.

The localization algorithm and the improved IlmProp MBPCM concept are tested on synthetic and measured scenarios. The results show the correctness and applicability of the methods.

# KURZFASSUNG

Im Rahmen dieser Dissertation wird die Kanalmodellierung von zeitvarianten, frequenzselektiven Mehrnutzer Multiple Input Multiple Output (MIMO) Kanälen für die Funkübertragung behandelt. Durch eine Erweiterung der Bello Funktionen auf mehrere Dimensionen mit Hilfe von Tensoren wird die Dispersion des Funkkanals, hervorgerufen durch Mehrwegeausbreitung, in Abhängigkeit von Verzögerung, Dopplerverschiebung und Einfallswinkel dargestellt. Der Kanal weist Selektivität auf, d.h. durch Fading verursachte zufällige Schwankungen der Signalleistung, entlang der Frequenz-, Zeit- und Raumachse. Die eingeführte unkonventionelle Notation ermöglicht den starken Zusammenhang zwischen den unterschiedlichen Darstellungsbereichen aufzuzeigen. Es werden einige der wichtigsten Ansätze zur Kanalmodellierung vorgestellt, klassifiziert und jeweils die Vor– und Nachteile herausgearbeitet. Für geometrische Kanalmodelle ist es entscheidend die Richtcharakteristika der Antennen im Fernfeld genau und effizient zu beschreiben. Zu diesem Zweck wird ein neues Beschreibungsverfahren entwickelt, das auf der Discrete Vector Spherical Fourier Transform (DVSFT) basiert. Dadurch ist es möglich, komplexe Vektorfunktionen auf der Kugel mit höherer Genauigkeit als bisher zu beschreiben, da die DVSFT auf sphärische Problemstellungen zugeschnitten ist. Die vorgeschlagene Methode führt zu einer Reihe von neuen Anwendungsmöglichkeiten. So ist eine verlustlose Rotation der Richtcharakteristik ebenso möglich wie die Reduktion von Rauschen, SNR Schätzungen, die Optimierung des Kalibrierungsprozesses, ein rotationsinvariantes Leistungsdichtespektrum, die Einführung einer sphärischen Bandbreite und die genaue Berechnung der Antenneneffizienz. Der Schwerpunkt dieser Dissertation ist IlmProp; ein Geometrie-basiertes Framework zur Kanalmodellierung. Es füllt die Lücke zwischen konventionellen direktionalen Kanalmodellen und so genannten "Ray-Tracer"Kanalmodellen. IlmProp ermöglicht es gleichzeitig mehrere Nutzer in der selben Umgebung zu simulieren. Mehrwege-Komponenten werden an Hand von punktförmigen Wechselwirkungsobjekten, so genannten Interaction Objects (IOs), im dreidimensionalen Raum modelliert. Dadurch wird die zeitliche Variation der Korrelation in Zeit, Frequenz, Raum und zwischen den Nutzern realitätsnah modelliert. Die Parameter des IlmProp Kanalmodells können willkürlich gesetzt oder aus hochauflösenden Parameterschätzverfahren gewonnen werden. Im ersten Fall kann IlmProp dazu genutzt werden, verschiedene Sende–, Empfangs– und Scheduling–Algorithmen zu testen. Darüber hinaus können unterschiedliche Antennenarrays und Arraykonfigurationen unter realistischen Bedingungen evaluiert werden. Um aus hochauflösenden Parameterschätzungen die IlmProp–Parameter zu gewinnen, wurde ein neuartiger Algorithmus entwickelt, der die Interaction Objects (IOs) lokalisiert. Er basiert auf dem klassischen Ansatz der Bayes'schen Inversionstheorie. Diese Methode erlaubt es, jeden einzelnen Ausbreitungs-

pfad lediglich aus Einfallswinkel, Austrittswinkel und der Ausbreitungszeit zu rekonstruieren. Dies macht IlmProp zu einem leistungsfähigen Visualisierungswerkzeug, um Kanalmessungen und Parameterschätzverfahren zu validieren. Des Weiteren ist ein tieferer Einblick in die Ausbreitungsbedingungen des untersuchten Szenarios möglich. Im weiteren Verlauf der Arbeit wird das Konzept des messungsbasierten parametrischen Kanalmodells, des so genannten Measurement-Based Parametric Channel Model (MBPCM), vorgestellt. Es ermöglicht durch eine antennenunabhängige, doppelt-direktionale Kanalbeschreibung, aus vorhandenen Kanalmessungen zusätzliche realitätsnahe, synthetische Kanalrealisierungen zu erzeugen. Die Lokalisierung der IOs ermöglicht eine weitere Verbesserung des MBPCM-Konzepts durch die daraus resultierende genauere Kenntnis der Ausbreitungspfade. Der Lokalisierungs-Algorithmus und das verbesserte IlmProp MBPCM-Konzept wurden sowohl in künstlichen als auch gemessenen Szenarios getestet. Die Ergebnisse bestätigen die Validität und Anwendbarkeit der vorgestellten Methoden.

# CONTENTS

# LIST OF FIGURES

# LIST OF TABLES

# 1. INTRODUCTION

A shot fired by a rifle in 1895 marked the beginning of a new era dominated by wireless communications. It was fired by Guglielmo Marconi's butler as he received the morse code for the letter "S", one hundred meters away from the transmitter operated by his master. In more than one century the technology of radio communications has developed greatly, although staying true to its original aim, i.e., transport information.

While the third generation of mobile communications slowly substitutes the second one, governments and companies around the globe finance research for the fourth generation, which promises ubiquitous coverage with data rates up to 1 Gbit/s and more.

The most likely method to achieve such ambitious goals is the exploitation of the spatial dimension, which can be accessed by the use of Multiple Input Multiple Output (MIMO) technologies, namely employing antenna arrays at both link-ends.

In order to carry out deployment planning, algorithm design, and system simulations, a profound knowledge of the underlying physical channel is necessary. Therefore, it is fundamental to develop channel models which give particular attention to those aspects of the channel which have an impact on the system.

In the case of single antenna narrowband systems, large measurement campaigns have been carried out over several decades, resulting in standardized models such as the COST 207 [74].

On the contrary, MIMO channel measurements and the understanding of the true potentials of MIMO systems started only in the late 1990's.

One of the first models proposed was the so-called flat-fading *white channel*, also reported in [172]. The channel matrix contains i.i.d.[1] Zero Mean Circular Symmetric Complex Gaussian (ZMCSCG) random numbers. Assuming this channel, theoretical results could be derived in [206, 81, 42], promising tremendous capacity gains with respect to single antenna systems. Moreover, space-time codes [204, 205] promised a practical way of coming reasonably close to such gains. These investigations brought much interest to MIMO techniques and basically opened a new research topic. Physically, the white channel can be achieved in a very rich scattering environment, where a large number of propagation paths leave the transmitter and reach the receiver from all directions.

Pioneering measurements to investigate the directional properties of the wireless channel started in the mid 1990s, such as the one reported in [122], by means of rudimental rotating

[1] The acronym i.i.d. stands for *independent identically distributed*.

directive antennas at one side of the link only. They showed how the energy was actually concentrated within small angular spreads, especially in rural and suburban environments. These preferred directions violate the assumptions of the white channel and, with much unhappiness of the MIMO enthusiasts, it also implied lower capacities.

In [134], two-dimensional Direction Of Arrival (DOA) measurements were carried out. The data was processed by the 2D Unitary ESPRIT algorithm [93], which delivered DOA (azimuth and elevation) and Time Delay Of Arrival (TDOA) information on the propagation paths. The results confirmed once more the directional nature of the radio channel. One of the first measurements employing a MIMO *channel sounder*, i.e., the instrument to measure the channel, was carried out at Ilmenau University of Technology in 1999 [199]. This measurement permitted to investigate both spatial domains (i.e., at the receiver and at the transmitter), as well as the frequency domain, sampled on a bandwidth of 120 MHz. The results showed that significant gains over single antenna systems could be indeed achieved with MIMO techniques under realistic circumstances. Most importantly, these measurements showed the need of investigating the multi-path nature of the radio propagation further.

From this milestone, in the years, many achievements have been obtained. Larger antenna arrays and more sophisticated channel sounders have been employed. This led to the possibility of estimating larger numbers of paths with higher accuracy, also thanks to improved parameter estimation techniques [133, 94, 77, 208]. Moreover, the introduction of dual polarized antennas was crucial, as one of the most important parameters of an ElectroMagnetic (EM) wave is indeed its polarization status. Nonetheless, the hardware necessary to carry out state-of-the-art MIMO measurements is nowadays still very expensive and the required know-how to perform reliable measurement campaigns is possessed only by few institutions and companies in the world. There exist several commercial channel sounders, however they are all based on modified products manufactured by two companies, the Finnish Elektrobit Oy [212] and the German MEDAV GmbH [155].

Channel models were developed in conjunction with the results of the channel measurement campaigns. As more insight in the MIMO channel was obtained, more realistic channel models could be designed.

Two main approaches to channel modeling can be identified: one focuses on modeling the physical mechanisms ruling the propagation, the other models the channel coefficients directly, treating the multi-dimensional channel as a stochastic process.

The main categories of channel models following the physical approach are deterministic models and directional channel models. The deterministic models aim at solving Maxwell's equations directly, in order to predict the propagation for a given environment. To reduce the computational complexity, approximations based on the Geometrical Theory of Diffraction (GTD) [117, 152] can be applied. The most relevant models following the GTD are the *ray-tracers*, as the GTD approximates planar EM waves with *rays*. The main drawback of these models when used for system planning or system simulations, is that they require precise information on the environment, i.e., the EM properties and geometrical information

of every object present in the scenario. This information, usually called *data base*, is extremely expensive to gather. Therefore, for larger scale simulations they become practically unfeasible.

So-called *directional channel models*, on the other hand, were developed to carry out large scale statistical analyses. They are based on the double-directional representation [198, 200]. This approach sees a number of propagation paths, geometrically characterized by a DOA, a Direction Of Departure (DOD), and a TDOA, which link the transmitter to the receiver. The main model parameters are drawn from stochastic processes, whose characterization is derived from measurements. For this reasons, these models are also called Geometry-based Stochastic Channel Models (GSCM). The main advantage of these models is the possibility to generate a large quantity of channels by simply drawing new random parameters. Many of such models have been proposed. The main differences lie in the number of bounces allowed, in the way the trajectories of the paths are determined, and in the use of clusters. The main drawback is that the individual links, i.e, the channel between one base station and one mobile, are modeled independently. Moreover, channel parameters which vary slowly in time, such as the path-loss, the shadow-fading, and the average directions of arrival and departure, are normally kept fixed within one channel realization, usually called *drop*. This has the effect that the correlation in time, frequency, and space does not evolve in time, and only stationary channels can be modeled.

In order to test adaptive algorithms which are sensible to time, frequency, and spatial correlation, we need models which are capable of representing these correlations and most importantly, their evolution in time. A similar problem arises when considering algorithms for multi-user systems, for which it is of great importance to model the correlation between different users and its temporal evolution.

As these issues are very difficult to model in a statistical framework, directional channel models cannot cope with them. On the contrary, deterministic channel models do not suffer from this drawback. However, as already mentioned, they require a prohibitive modeling effort.

In this work we focus primarily on these open problems, proposing a channel model which fills the gap between ray-tracers and GSCMs.

When performing MIMO channel measurements, in order to achieve better angular resolution of the propagation paths, it is necessary to employ antenna arrays with a larger number of sensors. This issue has the drawback, that the measured channels can be used only for parameter estimation purposes, and cannot be employed to simulate practical transmission systems. In fact, it is extremely unlikely that a wireless mobile terminal would employ such large and expensive arrays. This represents a significant difference with respect to the channel sounding of single antenna systems, where the antenna used for the measurement can be the very same antenna used for the planned application. To cope with this problem, [209] proposes the so-called Measurement-Based Parametric Channel Model (MBPCM) concept. The latter allows us to obtain realistic synthetic channels for antenna arrays, mobile trajectories,

and frequency bandwidths other than the ones used during the measurement. This is possible, once more, thanks to an antenna independent double directional channel description. However, this method does not consider the entire trajectory of the propagation paths, but merely the DOAs, DODs, and TDOAs. Therefore, the full potential of the method is not exploited.

This work deals in detail with these aspects, proposing solutions to improve the MBPCM concept.

Another important aspect to be considered with any geometry-based channel model is the accurate modeling of the polarimetric antenna radiation patterns. In fact, the double-directional representation is independent on the antennas employed and simply determines the propagation paths which virtually link one point in space to another. To compute the MIMO channel, it is then crucial to consider the radiation patterns, as these complex vector functions describe how the signals are sent and received by an antenna with respect to the DOD and DOA, respectively. Known modeling methods include the straight-forward representation of the sampled radiation patterns in angle domain, as well as more sophisticated methods based on a two-dimensional (2D) Discrete Fourier Transform (DFT) transform, such as the Effective Aperture Distribution Function (EADF) [137, 138].

These methods do not consider correctly the spherical symmetry exhibited by the problem, as well as its vector nature. In fact, they consider each polarization vector component separately and treat the radiation patterns as 2D signals. This problem can be solved only by using a descriptor based on the Vector Spherical Harmonics (VSHs), as addressed in detail in the work.

The following section illustrates the outline of the work.

## Overview and Contributions

**Chapter 2** reviews in a didactic fashion well known fundamentals of MIMO systems. It also introduces both the deterministic as well as the stochastic description of the time variant frequency selective MIMO channel. The Bello channel characterization [47] has been extended to the spatial domain by several authors. However, by introducing a less conventional notation we show the strong analogy between all domain pairs, in that the 2D angular domain (azimuth and elevation) is transformed by a multi-dimensional Fourier transform to obtain the 3D spatial domain, normalized to the wavelength. This fact allows us to show that if the channel experiences *dispersion* in the angle domain, its representation in space will exhibit *selectivity*. Although these results have been presented in one way or another in other publications, the homogenous notation introduced well emphasizes the similarities of the different dimensions.

**Chapter 3** introduces the channel modeling topic, with its motivations, possible approaches, and main applications in detail. It presents some exemplary well known channel models and channel modeling principles, underlining their qualities and drawbacks. The author's contributions to some of the topics dealt in this chapter have been published in [1, 24, 28].

**Chapter 4** deals in detail with the crucial problem of efficiently and accurately modeling the polarimetric antenna array response. At first, we summarize basic concepts and definitions of antenna theory. Then, we review the EADF [137, 138]. As already mentioned, it is a method based on a 2D DFT applied on the radiation pattern expressed in azimuth and elevation. Both the EADF as well as a straightforward description in the angular domain do not consider correctly the spherical symmetries exhibited by the problem, as they are based on a 2D representation of the signals.

This drawback is overcome by the novel descriptor of the polarimetric radiation patterns based on the Discrete Vector Spherical Fourier Transform (DVSFT), which represents one of the major contributions of the work. It provides a higher accuracy than the EADF, however at a higher computational complexity.

By using the DVSFT, we propose several novel applications:

- Lossless rotation of a pattern in the spectral domain, so that the radiation pattern can be measured on any convenient coordinate system and then rotated without loss of information. The latter is not possible with known 2D approaches.
- Measurement noise reduction. We achieve higher SNR by employing a Wiener-like filter to suppress the noise introduced during the antenna measurement in the anechoic chamber.
- Introduction of rotation-invariant descriptors. Known 2D descriptors change significantly as we measure the very same antenna with different coordinate systems. This is not the case for the DVSFT, which allows us to define a rotation-invariant *level power spectrum* and a *level bandwidth*. The latter tells us the number of spectral coefficients needed to describe a certain antenna.
- Use different sampling grids to optimize the measurement process. The DVSFT allows us to gather the same information sampling the sphere with less points. This reduces the measurement time, or alternatively, improves the measurement SNR. In addition, the DVSFT allows us to formulate a sampling theorem on the sphere, so that we can predict the minimum number of sampling points required for an arbitrary antenna.
- Compute the antenna efficiency. The latter accounts for the total losses of the antenna. By means of the DVSFT we can estimate it with higher precision in the spectral domain.

All these benefits come from the fact that the representation by means of the DVSFT is the most natural, compact, and precise descriptor for radiation patterns.

We propose a processing scheme which combines the EADF with the DVSFT descriptor. It relies on a first preprocessing step based on the DVSFT and then on the computation

of the EADF under optimal conditions. In fact, in the first step we can take advantage of the benefits of the DVSFT mentioned above, while in the second we can employ the EADF which represents the best trade-off between accuracy and computational complexity for the geometry-based channel modeling needs. Parts of the material dealt in this chapter have been published in [12, 22, 30, 31, 33].

**Chapter 5** introduces the *IlmProp*, a geometry-based channel modeling framework, which constitutes one of the main contributions of this work. The IlmProp is capable of dealing with multi-user time variant frequency selective scenarios. Similarly to the directional channel models previously discussed, the IlmProp approximates the propagation as a sum of rays. However, it models the physical environment more in depth by defining explicitly the complete trajectories of the Multi-Path Components (MPCs), and, most importantly, their evolution in time as the users move. At the link-ends, arbitrary antenna arrays can be considered. The three-dimensional (3D) polarimetric antenna radiation patterns are modeled accurately. A general description and a validation of the IlmProp have been published in [11, 8, 14].

Although the geometrical information of the modeled scenario is represented more accurately than in a directional channel model, the IlmProp does not go into the details required by a ray-tracer, i.e., defining the EM properties of all physical objects present in the environment. In fact, the multi-path trajectories are simply defined by point like Interacting Objects (IOs).

Due to the modeling principle assumed by the IlmProp, the synthetic channels exhibit time, frequency, and spatial correlation which evolves realistically in time. Several different signal processing algorithms as well as measured antenna arrays can be investigated with the IlmProp. Examples of these studies are summarized in Section 5.2, and are published in [9, 10, 13, 15, 16, 17, 18, 19, 20, 21, 23, 25, 27, 32, 26, 34].

In Section 5.3 we show how the IlmProp can be used to improve the so-called Measurement-Based Parametric Channel Model (MBPCM) concept [209]. We present a novel IOs localization algorithm based on the classical Bayesian inversion theory. The algorithm is completely automatic and does not require any cumbersome tracking of the IOs. To apply this method, reliable parameter estimates as well as accurate information on the position and orientation of the antenna arrays are required.

When this information is available it is possible to obtain an IlmProp geometry, i.e., the explicit geometrical description of the propagation paths. It is then possible to compute new synthetic channels by changing different model parameters, such as the antenna arrays, the trajectories of the arrays, and the frequency bandwidth. This method allows us to measure the environment once and, in a post-processing step, obtain realistic synthetic channels for different antenna arrays, mobile trajectories and so on. The localization algorithm, besides serving to the MBPCM aim, provides also a novel visualization tool very helpful in giving a physical interpretation to the parameter estimates, in that we can understand how the propagation took place. In particular, the results of the parameter estimation carried out on

several measurement runs can be visualized at once. Finally, the algorithm also represents a validation for the channel measurement and the whole processing chain.

The localization algorithm and the improved IlmProp MBPCM concept are tested on one synthetic and two measured scenarios. The results show the robustness and applicability of the proposed method and allow us to gain a deeper insight in the propagation mechanisms of the investigated scenarios. Parts of the results proposed in this section are published in [3, 4, 5, 6, 7].

**Chapter 6** summarizes the key issues covered in this work, emphasizing their impact on the international scientific community.

An online version of this doctoral dissertation, as .pdf file, can be downloaded from http://www.delgaldo.com. On this site, you can also find up-to-date information on the author and on his research activities.

# 2. MIMO SYSTEMS AND CHANNEL CHARACTERIZATION

This chapter deals with introductory issues of multiple antenna systems as well as with the deterministic and stochastic representations of the channel.

Section 2.1 introduces Multiple Input Multiple Output (MIMO) systems and briefly summarizes their main advantages over single antenna systems.

Section 2.2 deals with the deterministic description of the MIMO channel. After explaining the well known Bello system functions in Section 2.2.1 for Single Input Single Output (SISO) systems, we extend them to the spatial domain at the receiver in Section 2.2.2. Section 2.2.3 presents the full polarimetric channel description for MIMO systems, thus extending the Bello functions to the spatial domain at both link-ends. Section 2.2.4 introduces the notation for the sampled MIMO channel, achieved by means of tensors, explained in detail in Appendix D.

Section 2.3 presents the representation of the channel when interpreted as a stochastic process. In Section 2.3.1 we first review the fundamentals for continuous stochastic processes, including vector-valued and multi-dimensional processes. In Section 2.3.2 we introduce the stochastic description for MIMO channels, deriving power profiles in delay, Doppler, and angle domains, as well as autocorrelation functions for the frequency, time, and spatial domains. Sections 2.3.3 presents the stochastic representations for sampled MIMO channels, including the correlation tensor and the equivalent two-dimensional (2D) correlation matrix. The tensor notation used is described in detail in Appendix D.

## 2.1 Definition and Advantages of MIMO systems

The acronym MIMO stands for Multiple Input Multiple Output and in the case of a communication system it refers to the use of antenna arrays at both link ends. Antenna arrays are fixed structures consisting of more than one antenna, often referred to as *sensors* or *elements*. Figure 2.1 shows an exemplary antenna array employed for channel measurements. It is an $8 \times 8$ element Uniform Rectangular Patch Array (URPA). The array actually mounts $14 \times 14$ patch antennas, as the outer ones serve as passive elements. This is often done, as passive elements help in obtaining similar radiation patterns for all antennas by reducing border effects.

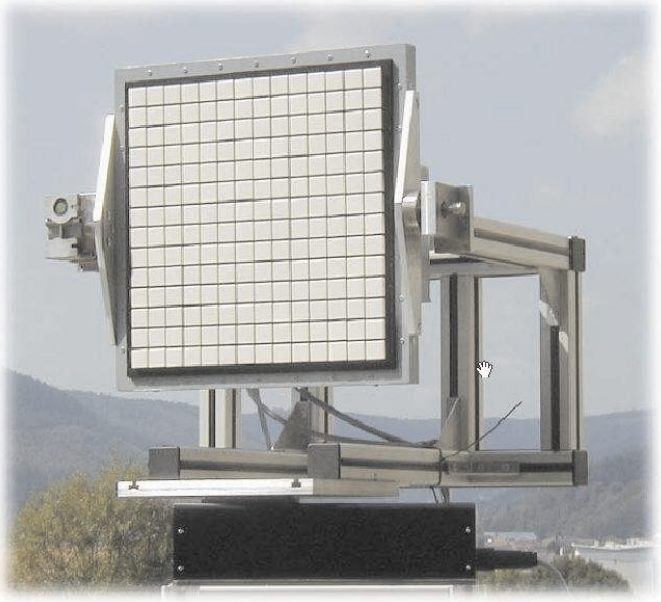

Fig. 2.1: An $8 \times 8$-element Uniform Rectangular Patch Array (URPA) employed in MIMO channel measurements, also known as channel sounding campaigns.
(source: Institute of Information Technology, Ilmenau University of Technology)

A traditional communication system has only one antenna for both transmitter and receiver. Such a system is called SISO, which stands for Single Input Single Output. When only the transmitter employs an antenna array we speak of a Multiple Input Single Output (MISO) system. When the smart antenna is deployed at the receiver we deal with a Single Input Multiple Output (SIMO) system.

### 2.1.1 MIMO for Wireless Communication Systems

In SISO systems it is possible to exploit only two physical dimensions of the radio channel, namely time and frequency. With the advent of MIMO we gain the possibility of accessing the spatial dimension as well. This fact alone leads to a multitude of advantages over simple SISO systems. At the same time, new challenges arise in the channel modeling task, as discussed in Chapter 3.

### 2.1.2 Spatial Filtering

The simplest way of accessing the spatial dimension is given by the so-called *vector modulation-demodulation* schemes, or *spatial filtering* techniques. A simple example of such a system is given in Figure 2.2.

The transmit signal is processed by a spatial filter $\boldsymbol{w} = [w_1,\ w_2,\ \ldots,\ w_{M_\mathrm{T}}]^\mathrm{T} \in \mathbb{C}^{M_\mathrm{T} \times 1}$, where $M_\mathrm{T}$ is the number of sensors at the transmit side (Tx). On the receiver side (Rx), on the other hand, the received signals coming from the $M_\mathrm{R}$ antennas are filtered with $\boldsymbol{u} = [u_1,\ u_2,\ \ldots,\ w_{M_\mathrm{r}}]^\mathrm{T} \in \mathbb{C}^{M_\mathrm{R} \times 1}$. The vectors $\boldsymbol{w}$ and $\boldsymbol{u}$ are also referred to as *weight vectors*. For

simplicity, in the following we restrict ourselves to a narrowband system, so that the channel can be assumed flat-fading.

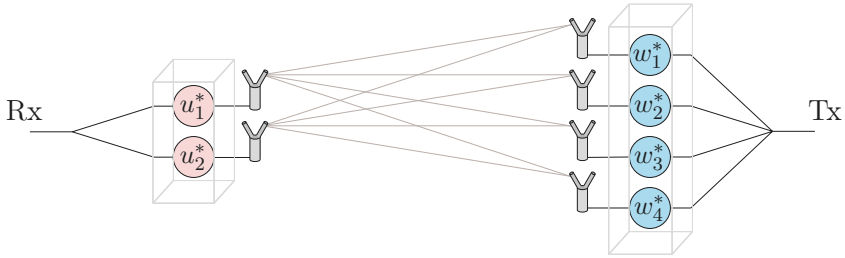


Fig. 2.2: Simple $4 \times 2$ MIMO system. The transmit signal is processed by the spatial filter $\boldsymbol{w} = [w_1,\ w_2,\ w_2,\ w_4]^{\mathrm{T}}$. At the receiver, the received signals are filtered with $\boldsymbol{u} = [u_1,\ u_2]^{\mathrm{T}}$.

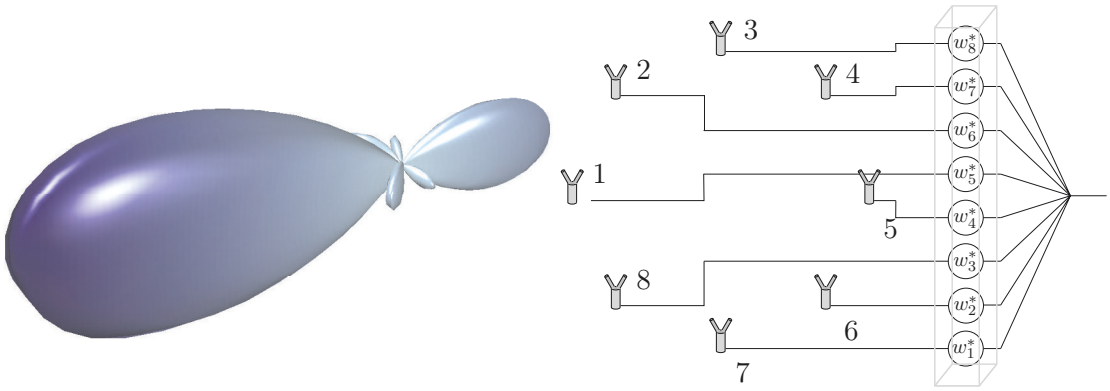


Fig. 2.3: Schematics of the *beamforming* principle. The transmit signal is multiplied with complex weights $w_i^*$ and fed to the 8 antennas (in this case Hertzian dipoles). By setting proper coefficients it is possible to modify the beam pattern at will.

By properly selecting the elements of the complex weight vectors, we can achieve a variety of goals. Most of them can be well described by interpreting $\boldsymbol{w}$ and $\boldsymbol{u}$ as *beamforming* vectors, as through them it is possible to modify at will the effective radiation pattern[1] of the antenna array. An example for the transmit side is given in Figure 2.3, where 8 antennas lying on a circle are fed with the same signal pre-multiplied with a proper weight. The result is that the transmit power is enhanced in certain directions while it is reduced, or even suppressed, in others. Since antennas obey the reciprocity theorem[2], we have a similar interpretation at the receiver side.

[1] The *radiation pattern* or *beam pattern* of an antenna describes how the power density propagates to different directions. See Section 4.1.4.

[2] The reciprocity theorem, also called Lorentz reciprocity theorem, states that the relationship between an oscillating current and the resulting electric field is unchanged if one interchanges the points where the current is placed and where the field is measured. Applied to antennas, it implies that the radiation pattern of an transmit antenna does not change when used as a receiver [121, Ch. IV.21].

In a multi-user scenario, the benefits of multiple antenna systems are:

- spatial multiplexing of data streams
- Spatial Division Multiple Access (SDMA)
- improving the SNR at the receiver
- interference reduction

Figure 2.4 shows a multi-user MIMO system employing both spatial multiplexing and SDMA.

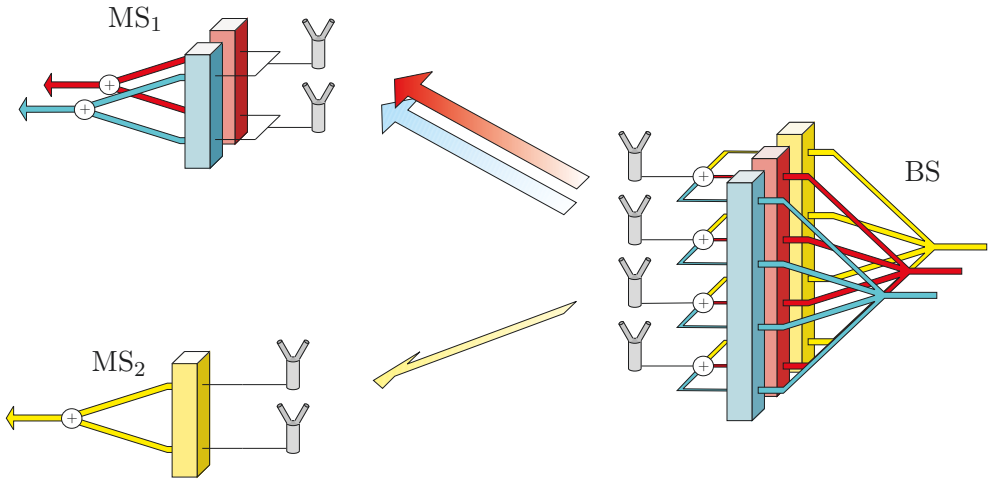


Fig. 2.4: A multi-user MIMO system employing spatial multiplexing and SDMA. At the Base Station (BS), two data streams are sent to the first Mobile Station ($MS_1$). A third data stream is sent to $MS_2$.

Two parallel data streams are sent to the first Mobile Station ($MS_1$) (spatial multiplexing), while a third data stream is sent to $MS_2$ (SDMA). In general, the transmit weight vector has an effect on both SNR and Signal to Interference and Noise Ratio SINR of each user. When we want to send one data stream to one user only and maximize its SNR, we achieve the so-called *antenna array gain*. The antenna array gain is at most equal to the number of elements of the array, e.g., for a 2 elements array we can achieve 3 dB. Obviously, this gain is obtained regardless of the interference caused to other users. Other schemes which consider interference aim at maximizing the SINR. Techniques which force the interference to be zero are called *Zero Forcing* (ZF) methods. One of such methods is the Block Diagonalization (BD) [193, 194].

Most beamforming techniques require some sort of Channel State Information (CSI), which can consist of the channel coefficients themselves, or of some statistical description, such as the spatial correlation matrix. Techniques which do not require any CSI are called *blind*.

Exhaustive overviews as well as a complete literature review of the signal processing techniques for multiple antenna systems can be found in many wireless communications textbooks, such as [49, 86, 172, 158]. The concepts illustrated in this section can be extended to a broadband system, where the fading cannot be assumed flat any longer.

### 2.1.3 Space-Time Processing

When the processing is carried out in a multiple antenna system which operates both in the time as well as in the space dimension jointly, we deal with a so-called *space-time* transmission scheme. Examples of these techniques are space-time codes, such as the Alamouti code, which does not require CSI at the transmitter. Once more we refer the reader to these textbooks [49, 86, 172, 158] for a more insightful overview and a complete literature review.

## 2.2 The Deterministic Description of the MIMO Radio Channel

Any description of the time variant frequency selective MIMO channel currently in use finds its roots in the seminal paper published by Bello in the early 60's [47]. Bello's original work is introduced in Section 2.2.1, while 2.2.2 presents the channel representation recently proposed by Fleury in [75], which extends Bello's ideas to the spatial dimension. Fleury's description, although rather comprehensive, does not obtain an antenna de-embedding[3], and considers the spatial dimension at the receiver side only. For these reasons, we extend Fleury's work to obtain a full MIMO, antenna de-embedded description in Section 2.2.3. For its simplicity and comprehensiveness we will adopt the latter throughout this work.

Table 2.1 summarizes the notation used for the functions, vectors, and matrices introduced in this part. It can be helpful while reading the following sections.

### 2.2.1 The Bello System Functions

Bello proposed in [47] a framework for the characterization of a linear time variant system by defining four equivalent descriptions. Let $s(t)$ and $x(t)$ be the input and output of a linear system, respectively, as shown in Figure 2.5. The behavior of the system can be described

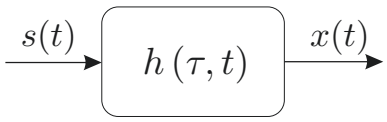


Fig. 2.5: A simple schematic representation of a time variant Single Input Single Output (SISO) system.

by the function $h(\tau, t)$ in delay time $\tau$ and time $t$, which we will refer to as Channel Impulse Response (CIR), or informally as *channel*. The output signal can then be computed as

$$x(t) = \int_{\mathbb{R}} h(\tau, t)\ s(t-\tau)\ \mathrm{d}\tau, \tag{2.1}$$

an expression which is also known as the *system equation*. By a simple change of variables, and carrying out Fourier transforms on both the input signal $s(t)$ and on the channel $h(\tau, t)$,

[3] The term *antenna de-embedding* indicates that the antenna radiation pattern is not treated explicitly in the description (see Section 3.1.4 for more details).

| Symbol | Description |
|---|---|
| $t$ | time |
| $f$ | frequency |
| $\tau$ | delay time |
| $\nu$ | Doppler frequency |
| $\varphi$ | azimuth |
| $\theta$ | elevation |
| $\Omega$ | a direction in the three-dimensional (3D) space defined by the azimuth elevation pair $\{\varphi,\ \theta\}$ |
| $\Omega_{\mathrm{R}}$ | Direction Of Arrival (DOA) |
| $\Omega_{\mathrm{T}}$ | Direction Of Departure (DOD) |
| $\boldsymbol{\Omega}_{\mathrm{R}}$ | unit vector representing the DOA, so that $-\boldsymbol{\Omega}_{\mathrm{R}}$ points towards the direction $\Omega_{\mathrm{R}}$ |
| $\boldsymbol{\Omega}_{\mathrm{T}}$ | unit vector representing the DOD, so that $\boldsymbol{\Omega}_{\mathrm{T}}$ points towards the direction $\Omega_{\mathrm{R}}$ |
| $\boldsymbol{p}_{\mathrm{O}}$ | origin of the coordinate system. Also referred to as the *origin of phases*, it is equal to $\mathbf{0} = [0,\ 0,\ 0]^{\mathrm{T}}$ |
| $\boldsymbol{p}_{\mathrm{T}}$ | position vector of the transmitter w.r.t. $\boldsymbol{p}_{\mathrm{O}}$ |
| $\boldsymbol{p}_{\mathrm{R}}$ | position vector of the receiver w.r.t. $\boldsymbol{p}_{\mathrm{O}}$ |
| $\boldsymbol{q}_{\mathrm{T}}$ | normalized position vector of the transmitter w.r.t. $\boldsymbol{p}_{\mathrm{O}}$ |
| $\boldsymbol{q}_{\mathrm{R}}$ | normalized position vector of the receiver w.r.t. $\boldsymbol{p}_{\mathrm{O}}$ |
| $h(\cdots)$ | channel function. The arguments define in which domains it is represented |

Tab. 2.1: Notation used in this chapter. A comprehensive list of symbols is given on page 249.

we obtain

$$x(t) = \int_{\mathbb{R}} h(f,t)\ S(f)\ \mathrm{e}^{-j2\pi ft}\ \mathrm{d}f, \tag{2.2}$$

where

$$\begin{aligned} h(f,t) &= \int_{\mathbb{R}} h(\tau,t)\ \mathrm{e}^{-j2\pi f\tau}\ \mathrm{d}\tau \\ S(f) &= \int_{\mathbb{R}} s(\tau)\ \mathrm{e}^{-j2\pi f\tau}\ \mathrm{d}\tau. \end{aligned} \tag{2.3}$$

We would like to remark that we denote any function describing the system as $h(\cdots)$, where its arguments specify unambiguously in which domains it is represented. For instance, $h(f,t)$, appearing in equation (2.2), is a function which describes the system in frequency and time, whereas $h(\tau,t)$, used in (2.1), is another function which represents it in delay time and time. This might seem inappropriate, as one would expect different notations for different functions. Due to the large number of possible system representations, and the length of the formulas, we feel forced to simplify the notation at the expense of a less rigorous derivation.

The interpretation of $h(f,t)$ is straightforward in the case of a quasi-static system: the spectrum of the input signal, i.e., $S(f)$, is multiplied with the current transfer function of the system, that is the transfer function for the current time instant $t$.

In case of a Linear Time Invariant (LTI) system, $h(\tau, t)$ becomes $h(\tau)$, as there is no dependence on time. Equation (2.1) becomes the very well known convolution integral

$$x(t) = \int_{\mathbb{R}} h(\tau)\ s(t-\tau)\ \mathrm{d}\tau = \int_{\mathbb{R}} h(t-\tau)\ s(\tau)\ \mathrm{d}\tau. \tag{2.4}$$

By transforming $h(f, t)$ along the temporal dimension, we obtain $h(f, \nu)$, a channel description in frequency $f$ and Doppler frequency $\nu$

$$h(f, \nu) = \int_{\mathbb{R}} h(f, t)\ \mathrm{e}^{-j2\pi\nu t}\ \mathrm{d}t. \tag{2.5}$$

Equation (2.1) can be transformed into

$$X(f) = \int_{\mathbb{R}} h(f-\nu, \nu)\ S(f-\nu)\ \mathrm{d}\nu. \tag{2.6}$$

allowing us to compute $X(f)$, i.e., the Fourier transform of $x(t)$. Thus, $x(t)$ can be computed as

$$x(t) = \iint_{\mathbb{R}\,\mathbb{R}} h(f-\nu, \nu)\ S(f-\nu)\ \mathrm{e}^{j2\pi f\tau}\ \mathrm{d}\nu\ \mathrm{d}f. \tag{2.7}$$

In a similar way we can write the system equation with respect to the channel expressed in delay time $\tau$ and Doppler frequency $\nu$

$$x(t) = \iint_{\mathbb{R}\,\mathbb{R}} h(\tau, \nu)\ s(t-\tau)\ \mathrm{e}^{j2\pi\nu t}\ \mathrm{d}\tau\ \mathrm{d}\nu. \tag{2.8}$$

The four channel descriptions, namely $h(\tau, \nu)$, $h(f, t)$, $h(\tau, t)$, and $h(f, \nu)$, are called *Bello*

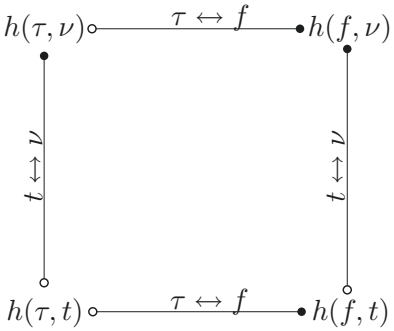


Fig. 2.6: Fourier relationships between the four Bello channel descriptions

*functions*, or *first set of Bello functions* [47]. Figure 2.6 shows the mutual relationships between the four channel descriptions.

The function $h(\tau, t)$ can be interpreted as a time varying CIR. For this reason, when expressing the channel in delay time $\tau$, it is possible to consider the *dispersion* suffered by the transmit signal. The origin of dispersion lies in the multi-path nature of the radio channel. In

fact, the signal traveling through different paths reaches the receiver at different delay times. In the frequency domain $f$, on the other hand, we can observe the *selectivity* caused by the channel, i.e., how the different frequency components of the transmit signal are affected by the channel. Bello's merit is to have observed that dispersion and selectivity are dual expressions in different domains of the very same phenomenon. The link between the two is evidently given by the Fourier transform. This can be observed also in time $t$ and Doppler frequency $\nu$, where time shows selectivity and Doppler frequency displays dispersion. The origin of dispersion in Doppler is the fact that different propagation paths experience different radial velocities, yielding different Doppler shifts.

### 2.2.2 Extension of the Bello System Functions to the Spatial Domain

Time variant frequency selective MIMO channels cannot be fully described by the Bello system functions introduced in Section 2.2.1, as they require one more dimension: space. Several books and articles deal explicitly with this issue, such as [172, 158, 177]; nonetheless we feel that Fleury in his recent work [75] captured Bello's spirit best in extending his vision to the new dimension. To include the spatial dimension, he introduces two vectors: $\boldsymbol{p}$ and $\boldsymbol{\Omega}$, to identify the position of the receiver and the Direction Of Arrival (DOA) of the impinging wave, respectively. Figure 2.7 depicts the coordinate system used. The Cartesian coordinates of the position of the receiver are stored in the vector $\boldsymbol{p}$ as $\boldsymbol{p} = [p_x,\ p_y,\ p_z]^{\mathrm{T}}$. The DOA is defined either by the azimuth and elevation pair $\Omega = \{\varphi,\ \theta\}$, or by the vector $\boldsymbol{\Omega}$ so that $-\boldsymbol{\Omega}$ is a unit vector pointing in the direction $\{\varphi, \theta\}$, which is a vector with the same direction as the wave vector $\boldsymbol{k}$ but with norm 1. Alternatively, the vector $\boldsymbol{\Omega}$ can be obtained from $\Omega = \{\varphi,\ \theta\}$ as

$$\boldsymbol{\Omega} = -\left[\cos(\theta)\cdot\cos(\varphi),\ \cos(\theta)\cdot\sin(\varphi),\ \sin(\theta)\right]^{\mathrm{T}}. \tag{2.9}$$

Note that a generic function of the direction of arrival $g(\Omega)$ can be equivalently expressed as $g(\boldsymbol{\Omega})$ or as $g(\varphi, \theta)$ by means of equation (2.9). The vector $\boldsymbol{\Omega} \in \mathcal{S}^2$, so that $\mathcal{S}^2 \subset \mathbb{R}^3$ is the set of points $\{x,\ y,\ z\}$ in $\mathbb{R}^3$ which satisfy $x^2 + y^2 + z^2 = 1$, i.e., all points on the surface of the unit sphere [102]. An integral of the function $g(\Omega)$ over $\mathcal{S}^2$ is denoted by $\int_{\mathcal{S}^2} g(\Omega)\ \mathrm{d}\Omega$. Equivalently, we can express it with respect to $\boldsymbol{\Omega}$ and to the more conventional azimuth $\varphi$ and elevation $\theta$ as

$$\int_{\mathcal{S}^2} g(\Omega)\ \mathrm{d}\Omega = \int_{\mathcal{S}^2} g(\Omega)\ \mathrm{d}\boldsymbol{\Omega} = \int_{-\pi}^{\pi}\int_{-\frac{\pi}{2}}^{\frac{\pi}{2}} g(\Omega)\ \sin(\theta)\ \mathrm{d}\theta\ \mathrm{d}\varphi. \tag{2.10}$$

The integral $\int \mathrm{d}\Omega$ corresponds to the integral of the solid angle over the whole surface of the sphere. It is equal to

$$\int_{\mathcal{S}^2} \mathrm{d}\Omega = 4\pi. \tag{2.11}$$

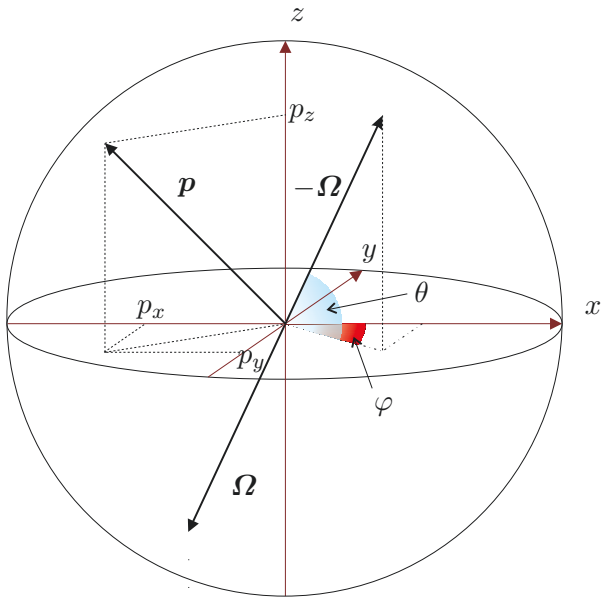


Fig. 2.7: The vector $\boldsymbol{p}$ corresponds to the position of the receiver, while $\Omega$ defines the Direction Of Arrival (DOA), also described by $\varphi$ and $\theta$, azimuth and elevation, respectively

Let $\boldsymbol{p}_{\mathrm{O}} = \mathbf{0} = [0,\ 0,\ 0]^{\mathrm{T}}$ define the origin of the coordinate system of Figure 2.7. Let us now assume a single ideal uniform planar wave[4] – the received signal at an arbitrary position $\boldsymbol{p}$ will differ with respect to the one at $\boldsymbol{p}_{\mathrm{O}}$ only by a phase term [215]: $\exp(-jk\ \boldsymbol{\Omega}^{\mathrm{T}} \cdot \boldsymbol{p})$, where $k$ is the phase constant $\frac{2\pi}{\lambda}$ and $\lambda$ is the wavelength. Since the product $\boldsymbol{\Omega}^{\mathrm{T}} \cdot \boldsymbol{p}_{\mathrm{O}}$ is equal to zero for all DOAs, the origin of the coordinate system is also referred to as the *center of phases* or the *phase reference*.

Equation (2.8), computed at the receiver location $\boldsymbol{p}$, becomes then

$$x(t;\boldsymbol{p}) = \int_{\mathbb{R}}\int_{\mathbb{R}}\int_{\mathcal{S}^2} h(\tau,\nu,\Omega)\ s(t-\tau)\ \mathrm{e}^{-\left(jk\ \boldsymbol{\Omega}^{\mathrm{T}}\cdot\boldsymbol{p}\right)}\ \mathrm{e}^{j2\pi\nu t}\ \mathrm{d}\Omega\ \mathrm{d}\tau\ \mathrm{d}\nu. \tag{2.12}$$

The channel's behavior is represented by $h(\tau,\nu,\Omega)$, which is a function of delay time $\tau$, Doppler frequency $\nu$, and angle $\Omega$. To simulate a SIMO transmission, it is simply necessary to compute $M_{\mathrm{R}}$ times the system equation (2.12) for the $M_{\mathrm{R}}$ positions of the receive antennas. To simulate a $M_{\mathrm{R}} \times M_{\mathrm{T}}$ MIMO system, on the other hand, for each of the $M_{\mathrm{R}}$ receive positions we need to compute the received signal for all $M_{\mathrm{T}}$ positions at the transmit side.

When the propagation is characterized by a discrete number $K$ of rays only, the channel $h(\tau,\nu,\Omega)$ takes the following form

$$h(\tau,\nu,\Omega) = \sum_{k=1}^{K} \alpha_k \cdot \delta(\tau-\tau_k) \cdot \delta(\nu-\nu_k) \cdot \delta(\Omega-\Omega_k), \tag{2.13}$$

[4] An ideal uniform planar wave propagating in a lossless medium is characterized by planar wavefronts and a unique wavelength. Furthermore, the sources of the field are assumed to be at an infinite distance from the region of observation [171, p. 348].

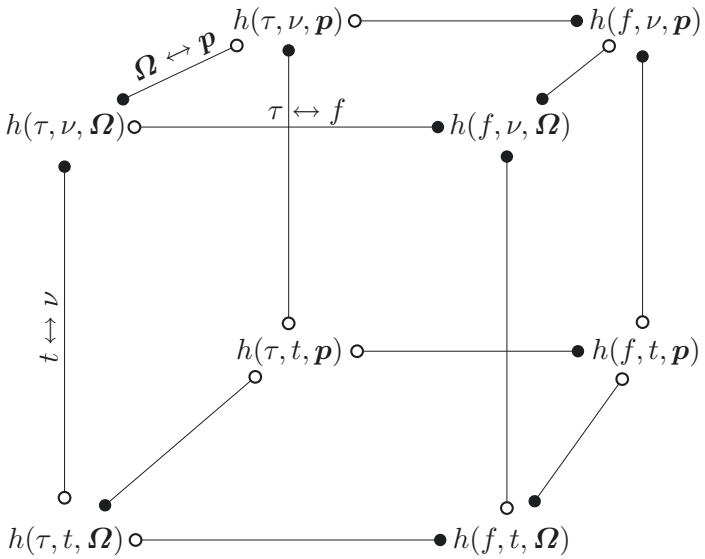


Fig. 2.8: Fourier relationships between the eight Spreading Functions (SFs) of the radio channel. A similar diagram has appeared in [210] and [114]. However, in these papers, the authors have simplified the spatial dimension to a 1-dimensional domain which they call *aperture*.

where the $k$-th path is characterized by a path strength $\alpha_k$, a Time Delay Of Arrival (TDOA) $\tau_k$, a Doppler shift $\nu_k$, and a DOA $\Omega_k$. However, the system integral equation (2.12) is capable of coping with diffuse models as well. In this case $h(\tau, \nu, \Omega)$ will simply be a continuous function in the parameter space. The Dirac $\delta$-function $\delta(\Omega) : \mathcal{S}^2 \to \mathbb{R}$ is a straightforward extension of its $\mathbb{R} \to \mathbb{R}$ representation. It is defined by

$$\begin{aligned} \delta(\Omega - \Omega_k) &= \begin{cases} \infty & \text{for } \Omega = \Omega_k \\ 0 & \text{otherwise} \end{cases} \\ \int_{\mathcal{S}^2} \delta(\Omega - \Omega_k)\, \mathrm{d}\Omega &= 1. \end{aligned}$$

Similarly to the Bello system functions, we obtain equivalent descriptions of the channel $h(\tau, \nu, \Omega)$ by applying a Fourier transform along one or more dimensions. Note that the transformation along the angle domain requires a multi-dimensional Fourier transform [197], properly modified because of the additional term $\lambda$ in the kernel

$$\begin{aligned} h(\tau, \nu, \boldsymbol{p}) &= \int_{\mathcal{S}^2} h(\tau, \nu, \Omega)\, \mathrm{e}^{\left(-j\frac{2\pi}{\lambda}\, \boldsymbol{\Omega}^{\mathrm{T}} \cdot \boldsymbol{p}\right)}\, \mathrm{d}\Omega. \\ h(\tau, \nu, \Omega) &= \frac{1}{\lambda} \int_{\mathbb{R}^3} h(\tau, \nu, \boldsymbol{p})\, \mathrm{e}^{\left(j\frac{2\pi}{\lambda}\, \boldsymbol{\Omega}^{\mathrm{T}} \cdot \boldsymbol{p}\right)}\, \mathrm{d}\boldsymbol{p}. \end{aligned} \tag{2.14}$$

For its similarity we will refer to it as the *modified Fourier transform* along the angle domain. The proof for equation (2.14) is given in Theorem 2.2.1.

Figure 2.8 shows the eight equivalent channel representations which describe the radio

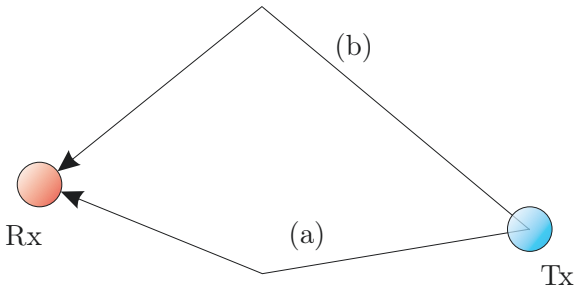


Fig. 2.9: A simple 2 ray model. The receiver is reached by two rays, (a) and (b).

channel in the three domains and their counterparts. The representations are obtained by applying the modified Fourier transform along the angle domain from the four original Bello system functions shown in Figure 2.6. As mentioned before, the function $h(\tau, \nu, \Omega)$ describes the dispersion, and therefore we refer to it as the *Spreading Function* (SF) of the radio channel. On the other hand, its counterpart $h(f, t, \boldsymbol{p})$ represents the selectivity.

We now interpret physically the dispersion expressed by $h(\tau, \nu, \Omega)$ by considering the simple 2 ray model in Figure 2.9. In this case, considering (2.13), $h(\tau, \nu, \Omega)$ takes the simpler form

$$h(\tau, \nu, \Omega) = h_{(a)}(\tau, \nu, \Omega) + h_{(b)}(\tau, \nu, \Omega), \tag{2.15}$$

where

$$\begin{aligned} h_{(a)}(\tau, \nu, \Omega) = &\quad \alpha_{(a)} \cdot \delta(\tau - \tau_{(a)}) \cdot \delta(\nu - \nu_{(a)}) \cdot \delta(\Omega - \Omega_{(a)}) \\ h_{(b)}(\tau, \nu, \Omega) = &\quad \alpha_{(b)} \cdot \delta(\tau - \tau_{(b)}) \cdot \delta(\nu - \nu_{(b)}) \cdot \delta(\Omega - \Omega_{(b)}). \end{aligned} \tag{2.16}$$

The first path, marked with $(a)$, is characterized by $\tau_{(a)}$, $\nu_{(a)}$, and $\Omega_{(a)}$, i.e., TDOA, Doppler shift, and DOA, respectively. Assuming that the second path (b) possesses different parameters, we will observe dispersion in all three domains, namely $\tau$, $\nu$, and $\Omega$. Unfortunately, a four dimensional function is difficult to visualize. Therefore, we derive the *marginal SFs*, defined as $h(\tau)$, $h(\nu)$, and $h(\Omega)$, and we compute them as

$$\begin{aligned} h(\tau) &= \int_{\mathbb{R}} \iint_{\mathcal{S}^2} h(\tau, \nu, \Omega)\ \mathrm{d}\Omega\ \mathrm{d}\nu \quad &= h(\tau, t, \boldsymbol{p})\,|_{t=0,\ \boldsymbol{p}=\mathbf{0}} \\ h(\nu) &= \int_{\mathbb{R}} \iint_{\mathcal{S}^2} h(\tau, \nu, \Omega)\ \mathrm{d}\Omega\ \mathrm{d}\tau \quad &= h(f, \nu, \boldsymbol{p})\,|_{f=0,\ \boldsymbol{p}=\mathbf{0}} \\ h(\Omega) &= \int_{\mathbb{R}} \int_{\mathbb{R}} h(\tau, \nu, \Omega)\ \mathrm{d}\tau\ \mathrm{d}\nu \quad &= h(f, t, \Omega)\,|_{f=0,\ t=0}\ , \end{aligned} \tag{2.17}$$

where the vector $\mathbf{0} = \boldsymbol{p}_{\mathrm{O}} = [0,\ 0,\ 0]^{\mathrm{T}}$. Figure 2.10 shows the marginal SFs for the 2 ray model of Figure 2.9. In each domain, as expected, the rays appear as two distinct Dirac impulses. An ideal channel, i.e., without any dispersion, would appear as a single Dirac impulse.

On the other hand, in the transformed domains, namely frequency $f$, time $t$, and position

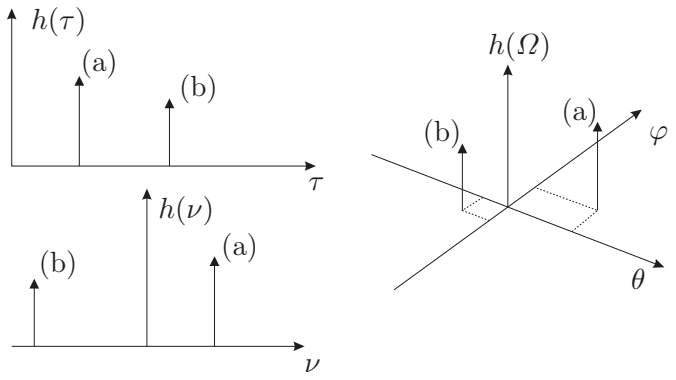


Fig. 2.10: Marginal Spreading Functions (SFs) for the 2 ray model shown in Figure 2.9.

$\boldsymbol{p}$, the channel exhibits selectivity, which presents itself as the variability of the channel coefficients with respect to different frequencies, time instants, and positions.

**Theorem 2.2.1.** *Let*

$$h(\tau,\nu,\boldsymbol{p}) = \int_{\mathcal{S}^2} h(\tau,\nu,\boldsymbol{\Omega})\ \mathrm{e}^{\left(-j\frac{2\pi}{\lambda}\ \boldsymbol{\Omega}^{\mathrm{T}}\cdot\boldsymbol{p}\right)}\ \mathrm{d}\Omega, \tag{2.18}$$

*then*

$$h(\tau,\nu,\boldsymbol{\Omega}) = \frac{1}{\lambda}\ \int_{\mathbb{R}^3} h(\tau,\nu,\boldsymbol{p})\ \mathrm{e}^{\left(j\frac{2\pi}{\lambda}\ \boldsymbol{\Omega}^{\mathrm{T}}\cdot\boldsymbol{p}\right)}\ \mathrm{d}\boldsymbol{p}. \tag{2.19}$$

*Proof.* Let $F(\boldsymbol{x})$ and $f(\boldsymbol{k})$ be 3D functions of the vectors $\boldsymbol{x}$ and $\boldsymbol{k} \in \mathbb{R}^3$, respectively. We assume that they are a Fourier pair, so that

$$\begin{aligned} F(\boldsymbol{x}) &= \int_{\mathbb{R}^3} f(\boldsymbol{k})\ \mathrm{e}^{-j2\pi\langle\boldsymbol{x},\boldsymbol{k}\rangle}\ \mathrm{d}\boldsymbol{k} \\ f(\boldsymbol{k}) &= \int_{\mathbb{R}^3} F(\boldsymbol{x})\ \mathrm{e}^{j2\pi\langle\boldsymbol{x},\boldsymbol{k}\rangle}\ \mathrm{d}\boldsymbol{x}, \end{aligned} \tag{2.20}$$

where $\langle\cdot,\cdot\rangle$ indicates the inner product[5]. Let

$$h(\tau,\nu,\boldsymbol{p}) = \int_{\mathcal{S}^2} h(\tau,\nu,\boldsymbol{\Omega})\ \mathrm{e}^{\left(-j\frac{2\pi}{\lambda}\ \boldsymbol{\Omega}^{\mathrm{T}}\cdot\boldsymbol{p}\right)}\ \mathrm{d}\Omega, \tag{2.21}$$

which can be rewritten as

$$h(\tau,\nu,\boldsymbol{p}) = \int_{\mathbb{R}^3} h(\tau,\nu,\boldsymbol{\Omega})\ \mathrm{e}^{\left(-j\frac{2\pi}{\lambda}\ \boldsymbol{\Omega}^{\mathrm{T}}\cdot\boldsymbol{p}\right)}\ \mathrm{d}\boldsymbol{\Omega}, \tag{2.22}$$

assuming that $h(\tau,\nu,\boldsymbol{\Omega})$ is non zero only for $\boldsymbol{\Omega} \in \mathcal{S}^2$. We now set

$$\begin{aligned} \boldsymbol{k} &= \boldsymbol{\Omega} \\ \boldsymbol{x} &= \frac{\boldsymbol{p}}{\lambda} \end{aligned} \tag{2.23}$$

[5] The inner product $\langle\boldsymbol{x},\boldsymbol{y}\rangle$ between the vectors of same size $\boldsymbol{x}$ and $\boldsymbol{y}$ is defined as $\langle\boldsymbol{x},\boldsymbol{y}\rangle = \boldsymbol{y}^{\mathrm{H}}\cdot\boldsymbol{x}$, where the superscript $(\cdot)^{\mathrm{H}}$ indicates the Hermitian transpose, i.e., conjugate transpose.

so that

$$h(\tau, \nu, \boldsymbol{p}) = F(\boldsymbol{x}) = \int_{\mathbb{R}^3} f(\boldsymbol{k})\ \mathrm{e}^{-j2\pi\langle \boldsymbol{x},\boldsymbol{k}\rangle}\ \mathrm{d}\boldsymbol{k}, \tag{2.24}$$

with

$$h(\tau, \nu, \boldsymbol{\Omega}) = f(\boldsymbol{k}). \tag{2.25}$$

we can now compute $h(\tau, \nu, \boldsymbol{\Omega})$ as

$$h(\tau, \nu, \boldsymbol{\Omega}) = f(\boldsymbol{k}) = \int_{\mathbb{R}^3} F(\boldsymbol{x})\ \mathrm{e}^{j2\pi\langle \boldsymbol{x},\boldsymbol{k}\rangle}\ \mathrm{d}\boldsymbol{x} = \frac{1}{\lambda} \int_{\mathbb{R}^3} h(\tau, \nu, \boldsymbol{p})\ \mathrm{e}^{-j\frac{2\pi}{\lambda}\langle \boldsymbol{\Omega},\boldsymbol{p}\rangle}\ \mathrm{d}\boldsymbol{p}. \tag{2.26}$$

□

#### 2.2.2.1 Polarization

The extension of the system equation (2.12) to dual-polarized antennas is straightforward. This expression needs merely to be quadruplicated in order to obtain such an input–output relationship for each co- and crosspolarization radio channel [75]. A similar derivation is carried out in the next section for the full MIMO channel representation.

### 2.2.3 The Full Channel Representation

The channel description given in [75] and explained in Section 2.2.2 shows two drawbacks: it describes the spatial dimension at the receiver side only, and it treats the antenna beam patterns implicitly. The first issue is undesirable as the MIMO channel, having multiple antennas at the transmit side also, should treat the spatial dimension of the transmitter explicitly. The second problem, also known as antenna de-embedding (see Section 3.1.4), implies a description which already takes into account the specific antennas employed at the receiver. This is unfortunate, as we would like to characterize the MIMO channel independently from the antennas which are employed. To overcome these issues in this section we extend the channel description proposed by Fleury. To do so we assume, as in the previous sections, that the system is linear and that the propagation can be approximated by a sum of planar waves.

Let $\boldsymbol{p}_\mathrm{R}$ and $\boldsymbol{p}_\mathrm{T}$ correspond to the position of the receiver and transmitter, respectively, as depicted in Figure 2.11. The Direction Of Departure (DOD) and the Direction Of Arrival (DOA) are defined by the unit vectors $\boldsymbol{\Omega}_\mathrm{T}$ and $\boldsymbol{\Omega}_\mathrm{R}$, or, equivalently, by the azimuth and elevation pairs $\{\varphi_\mathrm{T},\ \theta_\mathrm{T}\}$ and $\{\varphi_\mathrm{R},\ \theta_\mathrm{R}\}$, so that

$$\boldsymbol{\Omega}_\mathrm{R} = \ - \ [\cos(\theta_\mathrm{R}) \cdot \cos(\varphi_\mathrm{R}),\ \cos(\theta_\mathrm{R}) \cdot \sin(\varphi_\mathrm{R}),\ \sin(\theta_\mathrm{R})]^\mathrm{T} \tag{2.27}$$

$$\boldsymbol{\Omega}_\mathrm{T} = \ \ [\cos(\theta_\mathrm{T}) \cdot \cos(\varphi_\mathrm{T}),\ \cos(\theta_\mathrm{T}) \cdot \sin(\varphi_\mathrm{T}),\ \sin(\theta_\mathrm{T})]^\mathrm{T}. \tag{2.28}$$

Let us now consider the radiation patterns of the antennas. First we take into account

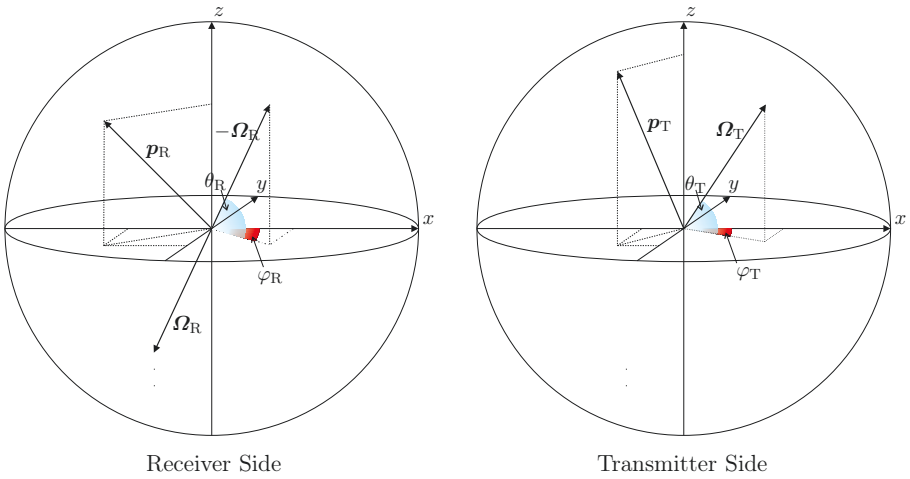


Fig. 2.11: The vectors $\boldsymbol{p}_{\mathrm{R}}$ and $\boldsymbol{p}_{\mathrm{T}}$ correspond to the position of the receiver and transmitter, while the unit vectors $\boldsymbol{\Omega}_{\mathrm{R}}$ and $\boldsymbol{\Omega}_{\mathrm{T}}$ define the Direction Of Arrival (DOA), and Direction Of Departure (DOD), respectively

one polarization only by defining the antenna response function $a\left(\varphi,\theta\right)$ as

$$a\left(\varphi,\theta\right)=\sqrt{4\pi}\cdot b\left(\varphi,\theta\right),$$

where the function $b\left(\varphi,\theta\right)$ is the radiation pattern of one polarization. The radiation pattern is treated in detail in Section 4.1.4. This function determines how the antenna radiates in the direction specified by $\varphi$, and $\theta$. Please notice that omitting one polarization is in general only possible when the antennas radiate (and receive) in one polarization only. This is the case of ideal electric or magnetic dipoles. In fact, the polarization status, as treated in Section 4.1.4, is a characteristic inherent to ElectroMagnetic (EM) waves, so that we cannot avoid considering it. Most of the time, in order to simplify the equations, we can assume a certain linear polarization status.

The received signal at the location $\boldsymbol{p}_{\mathrm{R}}$, given a transmitter in $\boldsymbol{p}_{\mathrm{T}}$, can be computed with a straightforward extension of the system equation (2.12) as

$$\begin{aligned}x(t;\boldsymbol{p}_{\mathrm{T}},\boldsymbol{p}_{\mathrm{R}})=&\int_{\mathbb{R}}\int_{\mathbb{R}}\int_{\mathcal{S}^2}\int_{\mathcal{S}^2}a_{\mathrm{T}}\left(\varphi_{\mathrm{T}},\theta_{\mathrm{T}}\right)\cdot a_{\mathrm{R}}\left(\varphi_{\mathrm{R}},\theta_{\mathrm{R}}\right)\cdot h(\tau,\nu,\Omega_{\mathrm{T}},\Omega_{\mathrm{R}})\cdot\\&\cdot s(t-\tau)\cdot\mathrm{e}^{-jk\ \boldsymbol{\Omega}_{\mathrm{T}}^{\mathrm{T}}\cdot\boldsymbol{p}_{\mathrm{T}}}\cdot\mathrm{e}^{-jk\ \boldsymbol{\Omega}_{\mathrm{R}}^{\mathrm{T}}\cdot\boldsymbol{p}_{\mathrm{R}}}\cdot\mathrm{e}^{j2\pi\nu t}\ \mathrm{d}\Omega_{\mathrm{T}}\ \mathrm{d}\Omega_{\mathrm{R}}\ \mathrm{d}\tau\ \mathrm{d}\nu,\end{aligned}\tag{2.29}$$

where the subscripts $(\cdot)_{\mathrm{R}}$ and $(\cdot)_{\mathrm{T}}$ specify the receiver and transmitter side, respectively. This expression, as (2.12), requires modified multi-dimensional Fourier transforms along the angles $\Omega_{\mathrm{R}}$ and $\Omega_{\mathrm{T}}$. In order to generalize this equation even further, thus using only traditional Fourier transforms, we introduce the vectors $\boldsymbol{q}_{\mathrm{T}}$ and $\boldsymbol{q}_{\mathrm{R}}$ so that they represent the position of the transmitter and receiver, respectively, normalized to the wavelength. Notice that the phase shifts introduced by the displacements from the centers of phases depend not only on the displacement vectors $p_{\mathrm{T}}$ and $p_{\mathrm{R}}$, but also on the wavelength $\lambda$. Therefore, the normalized

vectors $\boldsymbol{q}_{\mathrm{T}}$ and $\boldsymbol{q}_{\mathrm{R}}$ change as well with the wavelength $\lambda$.

$$\begin{aligned} \boldsymbol{q}_{\mathrm{R}} &= \frac{\boldsymbol{p}_{\mathrm{R}}}{\lambda} \\ \boldsymbol{q}_{\mathrm{T}} &= \frac{\boldsymbol{p}_{\mathrm{T}}}{\lambda}. \end{aligned} \tag{2.30}$$

Equation (2.29) becomes

$$\begin{aligned} x(t;\boldsymbol{q}_{\mathrm{T}},\boldsymbol{q}_{\mathrm{R}}) = \int_{\mathbb{R}}\int_{\mathbb{R}}\int_{\mathcal{S}^2}\int_{\mathcal{S}^2} & a_{\mathrm{T}}\left(\Omega_{\mathrm{t}}\right)\cdot a_{\mathrm{R}}\left(\Omega_{\mathrm{R}}\right)\cdot h(\tau,\nu,\Omega_{\mathrm{T}},\Omega_{\mathrm{R}})\cdot \\ & \cdot s(t-\tau)\cdot \mathrm{e}^{-j2\pi\ \langle \boldsymbol{\Omega}_{\mathrm{T}},\boldsymbol{q}_{\mathrm{T}}\rangle}\cdot \mathrm{e}^{-j2\pi\ \langle \boldsymbol{\Omega}_{\mathrm{R}},\boldsymbol{q}_{\mathrm{R}}\rangle}\cdot \mathrm{e}^{j2\pi\nu t}\ \ \mathrm{d}\Omega_{\mathrm{T}}\ \mathrm{d}\Omega_{\mathrm{R}}\ \mathrm{d}\tau\ \mathrm{d}\nu, \end{aligned} \tag{2.31}$$

where $\langle\cdot,\cdot\rangle$ indicates the inner product, and $\mathrm{e}^{-j2\pi\ \langle \boldsymbol{\Omega}_{\mathrm{T}},\boldsymbol{q}_{\mathrm{T}}\rangle}$ is the kernel of the multi-dimensional Fourier transform [197]

$$\begin{aligned} h(\tau,\nu,\Omega_{\mathrm{T}},\boldsymbol{q}_{\mathrm{R}}) &= \int_{\mathcal{S}^2} h(\tau,\nu,\Omega_{\mathrm{T}},\Omega_{\mathrm{R}})\ \mathrm{e}^{-j2\pi\ \langle \boldsymbol{\Omega}_{\mathrm{R}},\boldsymbol{q}_{\mathrm{R}}\rangle}\ \mathrm{d}\Omega_{\mathrm{R}}. \\ h(\tau,\nu,\Omega_{\mathrm{T}},\Omega_{\mathrm{R}}) &= \int_{\mathbb{R}^3} h(\tau,\nu,\Omega_{\mathrm{T}},\boldsymbol{q}_{\mathrm{R}})\ \mathrm{e}^{j2\pi\ \langle \boldsymbol{\Omega}_{\mathrm{R}},\boldsymbol{q}_{\mathrm{R}}\rangle}\ \mathrm{d}\boldsymbol{q}_{\mathrm{R}}. \end{aligned} \tag{2.32}$$

Note that Molisch in [158] proposes a similar channel description. However, he condenses the term $k\cdot\boldsymbol{\Omega}$ into $\boldsymbol{k}$, i.e., the *wave vector*. In doing so, he obtains a term $\exp(-j\ \langle \boldsymbol{k},\boldsymbol{p}\rangle)$ which, although the kernel of a multi-dimensional Fourier transform, is not consistent with the other Fourier transforms, as we use frequency $f$ instead of the angular frequency $\omega$, where $\omega = 2\pi f$.

By applying Fourier transforms along one or more dimensions we obtain a total of 16 equivalent channel descriptions. Figure 2.8, which was derived for the spatial dimension at the receiver only, needs to be extended to include the transmit side as well. Unfortunately, to do so we would need a fourth dimension, to obtain an hyper-cube with 16 vertices.

The Spreading Function (SF) $h(\tau,\nu,\Omega_{\mathrm{T}},\Omega_{\mathrm{R}})$ describes the propagation phenomenon in delay time $\tau$, Doppler shift $\nu$, direction of departure $\Omega_{\mathrm{T}}$, and direction of arrival $\Omega_{\mathrm{R}}$, independent on where the receiver and transmitter are and on which antennas are employed. It expresses the dispersion that the signal experiences in the four domains. The dispersion in the angle domain at the transmitter implies that the signal will propagate towards more than one direction. Similarly, the spread at the receiver implies that the transmitted signal reaches the receiver from different directions. Similarly to what was shown in the previous section,

we can derive the four marginal spreading functions as

$$
\begin{aligned}
h(\tau) = &\int_{\mathbb{R}}\int_{\mathcal{S}^2}\int_{\mathcal{S}^2} h(\tau,\nu,\Omega_\mathrm{T},\Omega_\mathrm{R})\,\mathrm{d}\Omega_\mathrm{R}\,\mathrm{d}\Omega_\mathrm{T}\,\mathrm{d}\nu &&= h(\tau,t,\boldsymbol{p}_\mathrm{T},\boldsymbol{p}_\mathrm{R})\,|_{t=0,\ \boldsymbol{p}_\mathrm{T}=\mathbf{0},\ \boldsymbol{p}_\mathrm{R}=\mathbf{0}}\\
h(\nu) = &\int_{\mathbb{R}}\int_{\mathcal{S}^2}\int_{\mathcal{S}^2} h(\tau,\nu,\Omega_\mathrm{T},\Omega_\mathrm{R})\,\mathrm{d}\Omega_\mathrm{R}\,\mathrm{d}\Omega_\mathrm{T}\,\mathrm{d}\tau &&= h(f,\nu,\boldsymbol{p}_\mathrm{T},\boldsymbol{p}_\mathrm{R})\,|_{f=0,\ \boldsymbol{p}_\mathrm{T}=\mathbf{0},\ \boldsymbol{p}_\mathrm{R}=\mathbf{0}}\\
h(\Omega_\mathrm{R}) = &\int_{\mathbb{R}}\int_{\mathbb{R}}\int_{\mathcal{S}^2} h(\tau,\nu,\Omega_\mathrm{T},\Omega_\mathrm{R})\,\mathrm{d}\Omega_\mathrm{T}\,\mathrm{d}\tau\,\mathrm{d}\nu &&= h(f,t,\boldsymbol{p}_\mathrm{T},\Omega_\mathrm{R})\,|_{f=0,\ t=0,\ \boldsymbol{p}_\mathrm{T}=\mathbf{0}}\\
h(\Omega_\mathrm{T}) = &\int_{\mathbb{R}}\int_{\mathbb{R}}\int_{\mathcal{S}^2} h(\tau,\nu,\Omega_\mathrm{T},\Omega_\mathrm{R})\,\mathrm{d}\Omega_\mathrm{R}\,\mathrm{d}\tau\,\mathrm{d}\nu &&= h(f,t,\Omega_\mathrm{T},\boldsymbol{p}_\mathrm{R})\,|_{f=0,\ t=0,\ \boldsymbol{p}_\mathrm{R}=\mathbf{0}}\ ,
\end{aligned}
$$

where the vector $\mathbf{0} = \boldsymbol{p}_\mathrm{O} = [0,\ 0,\ 0]^\mathrm{T}$.

Figure 2.12 shows a marginal SF, namely $h(\tau,t)$, which is obtained from $h(\tau,t,\boldsymbol{p}_\mathrm{T},\boldsymbol{p}_\mathrm{R})$ for $\boldsymbol{p}_\mathrm{T} = \boldsymbol{p}_\mathrm{R} = \mathbf{0}$.

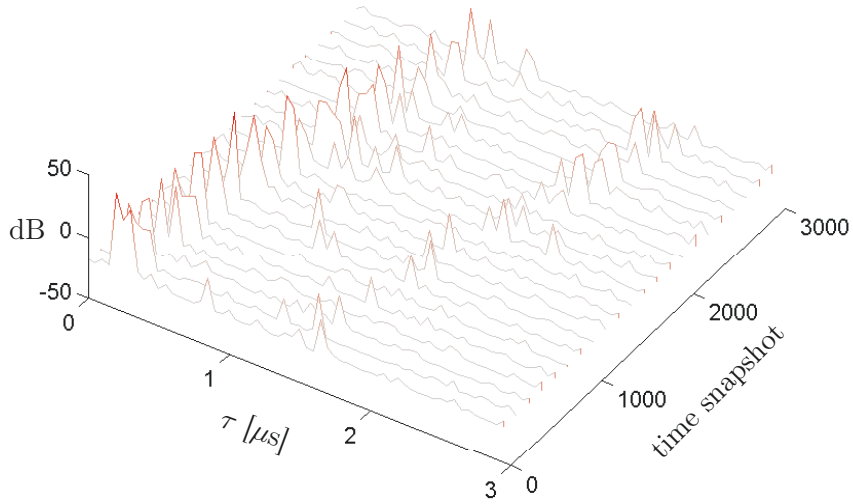


Fig. 2.12: Plot of a marginal SF $h(\tau,t)$, obtained from $h(\tau,t,\boldsymbol{p}_\mathrm{T},\boldsymbol{p}_\mathrm{R})$ for $\boldsymbol{p}_\mathrm{T} = \boldsymbol{p}_\mathrm{R} = \mathbf{0}$.
(source: channel measurements in a hotspot scenario)

The independence from the Rx and Tx position of the directional channel representation, namely $h(\ldots,\Omega_\mathrm{T},\Omega_\mathrm{R})$, is a consequence of the assumption that the electromagnetic field can be interpreted as a sum of planar waves, so that the DOD and DOA are an exhaustive geometrical description of a wave. In practical applications, this is a rather good approximation in the vicinity of the phase references. However, as we move further away from the centers of phases, i.e., from the origins of the coordinate systems shown in Figure 2.11, this assumption becomes more coarse. Figure 2.13 shows a simple LOS case. If the receive position $\boldsymbol{p}_\mathrm{O} = \mathbf{0}$ is the center of phases, the receiver position $\boldsymbol{p}_1$ will see path (c) instead of (b), when assuming planar wavefronts. For this reason, at large distances from the phase references, i.e., for vectors $\boldsymbol{q}_\mathrm{T}$ and $\boldsymbol{q}_\mathrm{R}$ with larger norms, it would be advisable to obtain a new SF for closer

centers of phases. The planar wavefront approximation becomes exact only when the ray sources, i.e., the transmitter or the last Interacting Object (IO) are at infinite distance from the observation point.

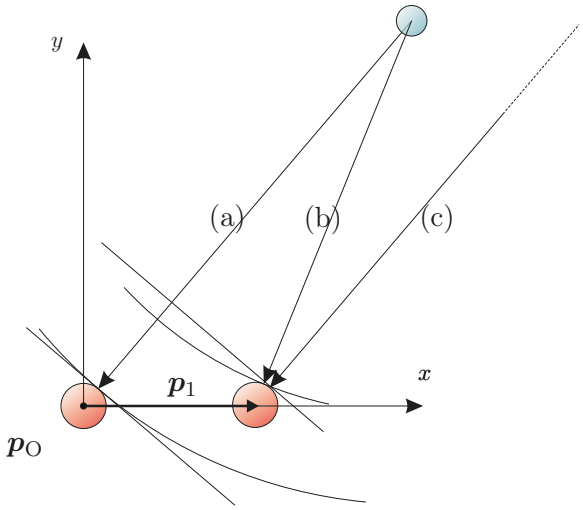


Fig. 2.13: This figure shows the effect of the planar wavefront approximation. Let the receive position $\boldsymbol{p}_\mathrm{O}$ lie in the *center of phases*. It is connected to the transmitter via a LOS path (a). At $\boldsymbol{p}_1$ the receiver sees the LOS path (b). However, when planar wavefronts are assumed, path (b) is approximated with (c).

#### 2.2.3.1 Polarization

As already mentioned the polarization status is one of the most important characteristic of EM waves. For a detailed physical interpretation of polarization, please refer to Section 4.1.4. The extension of the full MIMO antenna independent system equation (2.31) to a full polarimetric description is straightforward. Let $a_\theta(\Omega)$ and $a_\varphi(\Omega)$ be the antenna response for the vertical and horizontal polarization, respectively. They give the complex response to a planar wave impinging from the direction indicated by $\Omega$. Figure 2.14 depicts the coordinate systems used. The vertical polarization determines the component of the electric field directed as $\boldsymbol{e}_\vartheta$, whereas the horizontal towards $\boldsymbol{e}_\varphi$. The basis unit vectors $\boldsymbol{e}_\vartheta$ and $\boldsymbol{e}_\varphi$ are defined locally. They are treated in detail in Appendix E.2. Assuming that $s(t)$ is the signal fed to the transmit antenna, we can compute the received signal $x(t; \boldsymbol{q}_\mathrm{T}, \boldsymbol{q}_\mathrm{R})$ for the receive position $\boldsymbol{p}_\mathrm{R} = \lambda \cdot \boldsymbol{q}_\mathrm{R}$,

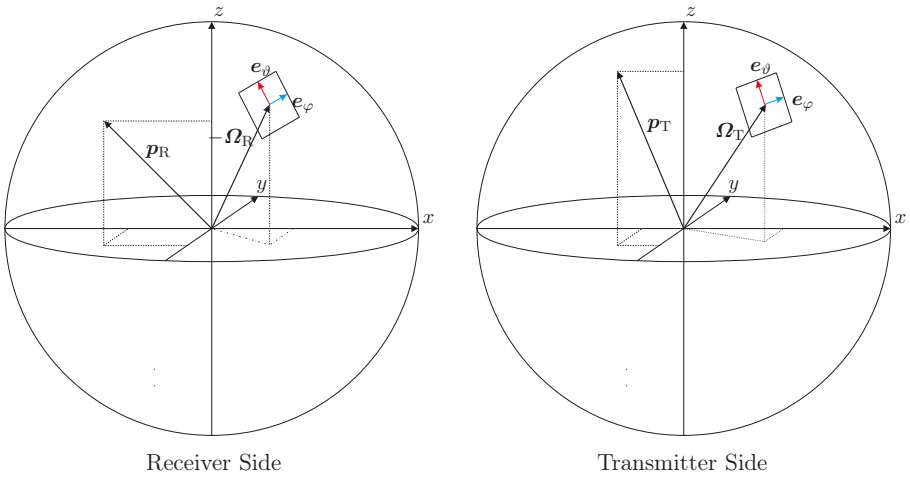


Fig. 2.14: The vectors $\boldsymbol{p}_\mathrm{R}$ and $\boldsymbol{p}_\mathrm{T}$ correspond to the position of the receiver and transmitter, while $\Omega_\mathrm{R}$ and $\Omega_\mathrm{T}$ define the Direction Of Arrival (DOA), and Direction Of Departure (DOD), respectively. The basis vectors $\boldsymbol{e}_\vartheta$ and $\boldsymbol{e}_\varphi$ are defined locally. They are treated in Appendix E.2.

the transmit position $\boldsymbol{p}_\mathrm{T} = \lambda \cdot \boldsymbol{q}_\mathrm{T}$ as

$$\begin{aligned} x_\theta(t; \boldsymbol{q}_\mathrm{T}, \boldsymbol{q}_\mathrm{R}) = \int_\mathbb{R}\int_\mathbb{R}\int_{\mathcal{S}^2}\int_{\mathcal{S}^2} \Big( & a_{\mathrm{v,T}}\left(\Omega_\mathrm{T}\right) \cdot h_{\mathrm{v}\to\mathrm{v}} \cdot a_{\mathrm{v,R}}\left(\Omega_\mathrm{R}\right) \\ & + a_{\mathrm{v,T}}\left(\Omega_\mathrm{T}\right) \cdot h_{\mathrm{v}\to\mathrm{h}} \cdot a_{\mathrm{h,R}}\left(\Omega_\mathrm{R}\right) \\ & + a_{\mathrm{h,T}}\left(\Omega_\mathrm{T}\right) \cdot h_{\mathrm{h}\to\mathrm{v}} \cdot a_{\mathrm{v,R}}\left(\Omega_\mathrm{R}\right) \\ & + a_{\mathrm{h,T}}\left(\Omega_\mathrm{T}\right) \cdot h_{\mathrm{h}\to\mathrm{h}} \cdot a_{\mathrm{h,R}}\left(\Omega_\mathrm{R}\right) \Big) \\ \cdot \mathrm{e}^{-j2\pi\ \langle \boldsymbol{\Omega}_\mathrm{R}, \boldsymbol{q}_\mathrm{R}\rangle} \cdot \mathrm{e}^{-j2\pi\ \langle \boldsymbol{\Omega}_\mathrm{T}, \boldsymbol{q}_\mathrm{T}\rangle} \cdot \mathrm{e}^{j2\pi\nu t}\ & \mathrm{d}\Omega_\mathrm{T}\ \mathrm{d}\Omega_\mathrm{R}\ \mathrm{d}\tau\ \mathrm{d}\nu. \end{aligned} \tag{2.33}$$

The equation above can be expressed in matrix products as

$$\begin{aligned} x_\theta(t; \boldsymbol{q}_\mathrm{T}, \boldsymbol{q}_\mathrm{R}) = \int_\mathbb{R}\int_\mathbb{R}\int_{\mathcal{S}^2}\int_{\mathcal{S}^2} & \begin{bmatrix} a_{\mathrm{v,R}}\left(\Omega_\mathrm{R}\right) & a_{\mathrm{h,R}}\left(\Omega_\mathrm{R}\right) \end{bmatrix} \cdot \begin{bmatrix} h_{\mathrm{v}\to\mathrm{v}} & h_{\mathrm{h}\to\mathrm{v}} \\ h_{\mathrm{v}\to\mathrm{h}} & h_{\mathrm{h}\to\mathrm{h}} \end{bmatrix} \cdot \begin{bmatrix} a_{\mathrm{v,T}}\left(\Omega_\mathrm{T}\right) \\ a_{\mathrm{h,T}}\left(\Omega_\mathrm{T}\right) \end{bmatrix} \\ & \cdot \mathrm{e}^{-j2\pi\ \langle \boldsymbol{\Omega}_\mathrm{T}, \boldsymbol{q}_\mathrm{T}\rangle} \cdot \mathrm{e}^{-j2\pi\ \langle \boldsymbol{\Omega}_\mathrm{T}, \boldsymbol{q}_\mathrm{T}\rangle} \cdot \mathrm{e}^{j2\pi\nu t}\ \mathrm{d}\Omega_\mathrm{T}\ \mathrm{d}\Omega_\mathrm{R}\ \mathrm{d}\tau\ \mathrm{d}\nu. \end{aligned} \tag{2.34}$$

The antenna de-embedded channel is now represented by four functions, namely $h_{\mathrm{v}\to\mathrm{v}}$, $h_{\mathrm{h}\to\mathrm{v}}$, $h_{\mathrm{v}\to\mathrm{h}}$ and $h_{\mathrm{h}\to\mathrm{h}}$, which depend on TDOA $\tau$, Doppler frequency $\nu$, DOA $\Omega_\mathrm{R}$, and DOD $\Omega_\mathrm{T}$. They define how the transmitter is linked to the receiver with respect to the two polarizations.

### 2.2.4 The Sampled MIMO Channel

In this subsection we introduce the issues and notation for the deterministic representations of a sampled MIMO channel. In practical applications, the sampled MIMO channel $h(\cdots)$ of equation (2.31) is often expressed in the domains which display selectivity, namely frequency $f$, time $t$, and positions $\boldsymbol{p}_{\mathrm{R}}$ and $\boldsymbol{p}_{\mathrm{T}}$. Space is sampled so that there are $M_{\mathrm{R}}$ receive and $M_{\mathrm{T}}$ transmit antennas, respectively. On the other hand, frequency and time are sampled with $M_f$ and $M_t$ samples, respectively. The terms $\Delta f$ and $\Delta t$ are the sampling intervals, and $B_f$ is the bandwidth spanned by the sampled channel, so that $B_f = M_f \cdot \Delta f$. Thus, the channel is represented by $M_{\mathrm{R}} \cdot M_{\mathrm{T}} \cdot M_t \cdot M_f$ samples, which are conveniently stored in form of the four dimensional tensor $\boldsymbol{\mathcal{H}}$, as

$$\boldsymbol{\mathcal{H}} \in \mathbb{C}^{M_{\mathrm{R}} \times M_{\mathrm{T}} \times M_t \times M_f}. \tag{2.35}$$

The MIMO channel at a certain frequency $f$ and time $t$ is a matrix, and is denoted as

$$\boldsymbol{H}(t, f) \in \mathbb{C}^{M_{\mathrm{R}} \times M_{\mathrm{T}}}. \tag{2.36}$$

The channel for the $n$-th transmit antenna at frequency $f$ and time $t$ is a vector, denoted as

$$\boldsymbol{h}(n, t, f) \in \mathbb{C}^{M_{\mathrm{R}}}. \tag{2.37}$$

Aliasing issues when sampling the MIMO channel are similar to the ones encountered in 1-dimensional signals, as the sampling theorem applies separately to the different dimensions. Note that it would be practically unfeasible to sample the spatial dimension with enough points so that it was possible to operate the multi-dimensional Fourier transform along the spatial dimension as in equation (2.32) without introducing aliasing. For this reason, the estimation of the DOA and DOD is normally done with parametric rather than periodogram-like techniques.

## 2.3 Stochastic Characterization

In this section we extend the deterministic description of the channel presented in Section 2.2 to obtain a stochastic representation. Section 2.3.1 briefly reviews the basic statistics theory which will be needed in the rest of the work, whereas Section 2.3.2 introduces the statistical description of radio channels.

### 2.3.1 Principles of Stochastic Processes

In this subsection we review the basic theory of the characterization of stochastic processes [168].

#### 2.3.1.1 Continuous processes

Let $f(t)$ and $g(t)$, $t \in T$, be a complex-valued random process with finite moments of the second order.

**Definition 2.3.1.** The term $\mu_f(t)$ is called the ***mean value*** or the *first moment* of $f(t)$. It is defined as

$$\mu_f(t) = \mathrm{E}\left[f(t)\right]. \tag{2.38}$$

**Definition 2.3.2.** The term $\sigma_f^2(t)$ is called the ***variance*** of $f(t)$. It is defined as

$$\sigma_f^2(t) = \mathrm{E}\left[|f(t) - \mu_f(t)|^2\right] = \mathrm{E}\left[|f(t)|^2\right] - |\mu_f(t)|^2. \tag{2.39}$$

**Definition 2.3.3.** The term $C_{f,g}(t,t')$ is called the ***covariance function*** of $f(t)$ and $g(t)$. It is defined as

$$C_{f,g}(t,t') = \mathrm{E}\left[(f(t) - \mu_f(t))^* \cdot (g(t') - \mu_g(t'))\right], \tag{2.40}$$

where the superscript $(\cdot)^*$ denotes the conjugate. The term $C_{f,f}(t,t')$ is the ***autocovariance function*** of $f(t)$. The autocovariance function has an important probabilistic interpretation – it defines the linear dependence which exists between the values of a random process at two time instants, namely $t$ and $t'$. The autocovariance function $C_{f,f}(t,t')$ in $t = t' = 0$ constitutes the *second moment* of $f(t)$.

**Definition 2.3.4.** The term $R_{f,g}(t,t')$ is called the ***correlation function*** of $f(t)$ and $g(t)$. It is defined as

$$R_{f,g}(t,t') = \mathrm{E}\left[f^*(t) \cdot g(t')\right]. \tag{2.41}$$

The term $R_{f,f}(t,t')$ is the ***autocorrelation function*** of $f(t)$. Note that the autocovariance function of $f(t)$ is the autocorrelation function of the process $f(t) - \mu_f(t)$. The correlation function possesses the following properties:

- $R_{f,f}(0,0) \geq 0$
- $R_{f,g}(t,t') = R^*_{g,f}(t',t)$.

**Definition 2.3.5.** We say that a random process $f(t)$ is ***stationary in a strict sense*** when all its statistical properties are invariant to a shift of the origin. In other words, the process $f(t)$ and $f(t+\Delta t)$ have the same statistics. When this happens, its first and second moments can be greatly simplified, so that the variance and mean are constant and the autocorrelation

and the autocovariance functions are dependent only on the time difference $\Delta t = t' - t$, as

$$\begin{aligned} \mu_f(t) &= \mu_f \\ \sigma_f^2(t) &= \sigma_f^2 \\ C_{f,f}(t,t') = C_{f,f}(\Delta t) &= \mathrm{E}\left[(f(t) - \mu_f(t))^* \cdot (f(t+\Delta t) - \mu_f(t+\Delta t))\right] \\ R_{f,f}(t,t') = R_{f,f}(\Delta t) &= \mathrm{E}\left[f^*(t) \cdot f(t+\Delta t)\right]. \end{aligned} \tag{2.42}$$

Note that fulfilling the properties in equation (2.42) is not sufficient to guarantee the strict sense stationarity. A more rigorous definition of strict sense stationarity can be given according to [168, pp. 219-220] as follows. Let $f_{t_i}$ and $f_{t_i+\Delta t}$ be random variables obtained by sampling the random process $f$ at $t = t_i$ and $t = t_i + \Delta t$, respectively. We now take $N \in \mathbb{N}$ random variables $f_{t_1},\ f_{t_2},\ \ldots,\ f_{t_N}$. If the process is stationary in a strict sense, then for its $N$-th order joint Probability Density Function (PDF), denoted by $p(\cdot)$, it must hold that

$$p\left(f_{t_1},\ f_{t_2},\ \ldots,\ f_{t_N}\right) = p\left(f_{t_1+\Delta t},\ f_{t_2+\Delta t},\ \ldots,\ f_{t_N+\Delta t}\right), \tag{2.43}$$

for every $N,\ t_1,\ t_2,\ \ldots,\ t_N$, and $\Delta t$.

**Definition 2.3.6.** In many practical applications we encounter random processes for which the first and second moments are a sufficient statistical description. In this case, when the properties in (2.42) hold, we say that the process is ***stationary in a wide sense*** [168, p. 220].

**Definition 2.3.7.** Let $f_{\mathrm{WSS}}(t)$ be a complex-valued zero mean Wide Sense Stationary (WSS) random process, characterized by finite moments of the second order. By Khinchin's theorem [120, 185, 85], the autocovariance function $C_{f_{\mathrm{WSS}},f_{\mathrm{WSS}}}(\Delta t)$ of $f_{\mathrm{WSS}}(t)$ can be expressed as

$$C_{f_{\mathrm{WSS}},f_{\mathrm{WSS}}}(\Delta t) = \int_{\mathbb{R}} P(\omega)\ \mathrm{e}^{j\omega\Delta t}\ \mathrm{d}\omega, \tag{2.44}$$

which is a Fourier integral and is called the *Wiener-Khinchin relationship*. The function $P(\omega)$ is the ***Power Spectral Density function (PSD)*** of the process. However, depending on the physical interpretation of $\omega$, the function assumes different names, as discussed in Section 2.3.2.

If we apply a Fourier transform on the process itself we obtain

$$f_{\mathrm{WSS}}(t) = \int_{\mathbb{R}} F_{\mathrm{OSM}}(\omega)\ \mathrm{e}^{j\omega t}\ \mathrm{d}\omega. \tag{2.45}$$

The random process $F_{\mathrm{OSM}}(\omega)$ possesses uncorrelated increments, so that

$$\begin{aligned} \mathrm{E}\left[F(\omega_1) \cdot F^*(\omega_2)\right] &= \quad 0, \quad \text{for } \ \omega_1 \neq \omega_2 \\ \mathrm{E}\left[F(\omega) \cdot F^*(\omega)\right] &= \ \mathrm{E}\left[|F(\omega)|^2\right] = P(\omega). \end{aligned} \tag{2.46}$$

The latter expression yields

$$P(\omega) \geq 0, \quad \forall\, \omega. \tag{2.47}$$

The properties of $F_{\mathrm{OSM}}(\omega)$ allow us to consider any zero-mean WSS process $f_{\mathrm{WSS}}(t)$ as a superposition of a set of uncorrelated harmonic oscillations with random amplitudes and phases. The PSD defines the distribution of the average power among the different harmonics which constitute $f_{\mathrm{WSS}}(t)$. The subscript OSM stands for ***Orthogonal Stochastic Measure*** [85], which is the Fourier counterpart of a WSS process. Note that the kernels of the integral in expressions (2.44) and (2.45) can have sign $\pm$, so that a WSS process is connected to an OSM via both a direct and an inverse Fourier transform.

**Definition 2.3.8.** A random process is ***ergodic*** with respect to one statistical description when one realization of such process would be sufficient to obtain this statistical property. For instance, signals for which the mean and autocorrelation function can be obtained from one realization are ergodic with respect to these functions [168, pp. 245-246].

#### 2.3.1.2 Continuous vector-valued processes

Let $f(\boldsymbol{\Omega})$ be a complex-valued random process of the unit vector $\boldsymbol{\Omega} \in \mathbb{S}^2 \subset \mathbb{R}^3$ with finite moments of the second order. While the definitions of first and second order moments is straightforward, the interpretation of WSS and OSM is not, and is dealt in detail in the following.

**Definition 2.3.9.** The process $f_{\mathrm{OSM}}(\boldsymbol{\Omega})$ is an ***Orthogonal Stochastic Measure*** when its multi-dimensional Fourier transform $f_{\mathrm{WSS}}(\boldsymbol{q})$ (either direct or inverse) is a WSS process

$$f_{\mathrm{WSS}}(\boldsymbol{q}) = \int_{\mathcal{S}^2} f_{\mathrm{OSM}}(\boldsymbol{\Omega})\ \mathrm{e}^{\pm j2\pi\langle \boldsymbol{\Omega}, \boldsymbol{q}\rangle}\ \mathrm{d}\Omega. \tag{2.48}$$

A vector-based ***Wide Sense Stationary*** process is WSS along all dimensions of the vector. This implies the following

$$\begin{aligned} \mathrm{E}\left[f(\boldsymbol{\Omega}) \cdot f^*(\boldsymbol{\Omega}')\right] &= \ 0, \quad \text{for } \ \boldsymbol{\Omega} \neq \boldsymbol{\Omega}' \\ \mathrm{E}\left[f(\boldsymbol{\Omega}) \cdot f^*(\boldsymbol{\Omega})\right] &= \quad \mathrm{E}\left[|F(\boldsymbol{\Omega})|^2\right]. \end{aligned} \tag{2.49}$$

#### 2.3.1.3 Continuous multi-dimensional processes

We now review the statistical definitions proposed in the previous subsections for multi-dimensional continuous signals.

Let $f(t_1, t_2, \ldots t_N)$ and $g(t_1, t_2, \ldots t_N)$, $t_i \in T_i \in \mathbb{R}$, be complex-valued $\mathbb{R}^N \to \mathbb{R}$ random process with finite moments of the second order. To simplify the notation, we introduce the

sets $\mathcal{T}$ and $\mathcal{T}'$ of indices

$$\begin{aligned} \mathcal{T} = &\quad \{t_1,\ t_2,\ \ldots,\ t_N\} \in \mathbb{R}^N \\ \mathcal{T}' = &\quad \left\{t'_1,\ t'_2,\ \ldots,\ t'_N\right\} \in \mathbb{R}^N, \end{aligned} \tag{2.50}$$

and the sets $\mathcal{T}_n^-$ and $\mathcal{T}_n'^-$

$$\begin{aligned} \mathcal{T}_n^- = &\quad \{t_1,\ \ldots,\ t_{n-1},\ t_{n+1},\ \ldots,\ t_N\} \in \mathbb{R}^{N-1} \\ \mathcal{T}_n'^- = &\quad \left\{t'_1,\ \ldots,\ t'_{n-1},\ t'_{n+1},\ \ldots,\ t'_N\right\} \in \mathbb{R}^{N-1}, \end{aligned} \tag{2.51}$$

which are the indices $\mathcal{T}$ and $\mathcal{T}'$ deprived of the $n$-th dimension.

**Definition 2.3.10.** The term $\mu_f(\mathcal{T})$ is called the ***mean value*** or the *first moment* of $f(\mathcal{T})$. It is defined as

$$\mu_f(\mathcal{T}) = \mathrm{E}\left[f(\mathcal{T})\right]. \tag{2.52}$$

**Definition 2.3.11.** The term $\sigma_f^2(\mathcal{T})$ is called the ***variance*** of $f(\mathcal{T})$. It is defined as

$$\sigma_f^2(\mathcal{T}) = \mathrm{E}\left[|f(\mathcal{T}) - \mu_f(\mathcal{T})|^2\right] = \mathrm{E}\left[|f(\mathcal{T})|^2\right] - \mu_f^2(\mathcal{T}). \tag{2.53}$$

**Definition 2.3.12.** The term $C_{f,g}(\mathcal{T},\mathcal{T}')$ is called the ***covariance function*** of $f(\mathcal{T})$ and $g(\mathcal{T})$. It is defined as

$$C_{f,g}(\mathcal{T},\mathcal{T}') = \mathrm{E}\left[(f(\mathcal{T}) - \mu_f(\mathcal{T}))^* \cdot (g(\mathcal{T}') - \mu_g(\mathcal{T}'))\right], \tag{2.54}$$

where the superscript $(\cdot)^*$ denotes the conjugate. The term $C_{f,f}(\mathcal{T},\mathcal{T}')$ is the ***autocovariance function*** of $f(\mathcal{T})$. Note that the function $C_{f,f}(\mathcal{T},\mathcal{T}')$ is $\mathbb{R}^{2N} \to \mathbb{R}$. The autocovariance function has an important probabilistic interpretation – it defines the linear dependence which exists between the values of a random process at two points in the $N$-dimensional space, namely in $\mathcal{T}$ and $\mathcal{T}'$.

**Definition 2.3.13.** The term $R_{f,g}(\mathcal{T},\mathcal{T}')$ is called the ***correlation function*** of $f(\mathcal{T})$ and $g(\mathcal{T})$. It is defined as

$$R_{f,g}(\mathcal{T},\mathcal{T}') = \mathrm{E}\left[f^*(\mathcal{T}) \cdot g(\mathcal{T}')\right]. \tag{2.55}$$

The term $R_{f,f}(\mathcal{T},\mathcal{T}')$ is the *autocorrelation function* of $f(\mathcal{T})$. Note that the autocovariance function of $f(\mathcal{T})$ is the autocorrelation function of the process $f(\mathcal{T}) - \mu_f(\mathcal{T})$.

**Definition 2.3.14.** ***Wide Sense Stationarity (WSS)*** for the $N$-dimensional process $f(\mathcal{T})$ is defined independently for each dimension. For instance, the process is wide sense stationary

for the $n$-th dimension if

$$\begin{aligned} \mu_f(\mathcal{T}) &= \mu_f(\mathcal{T}_n^-) \\ \sigma_f^2(\mathcal{T}) &= \sigma_f^2(\mathcal{T}_n^-) \\ C_{f,f}(\mathcal{T},\mathcal{T}') &= C_{f,f}(\mathcal{T}_n^-, \Delta t_n, \mathcal{T}_n'^-) \\ R_{f,f}(\mathcal{T},\mathcal{T}') &= R_{f,f}(\mathcal{T}_n^-, \Delta t_n, \mathcal{T}_n'^-). \end{aligned} \tag{2.56}$$

We say that a multi-dimensional random process $f(\mathcal{T})$ is ***stationary in a strict sense*** with respect to the $n$-th dimension when all its statistical properties are independent of $t_n$.

**Definition 2.3.15.** A multi-dimensional random process $f(\mathcal{T})$ is an ***Orthogonal Stochastic Measure*** with respect to the $n$-th dimension when its Fourier transform (either direct or inverse) along that dimension is a WSS for $t_n$. For instance, let $f(\mathcal{T}_n^-, \omega_n)$ be the Fourier transform of $f(\mathcal{T})$ along $n$, as

$$f(\mathcal{T}_n^-, \omega_n) = \int_{\mathbb{R}} f(\mathcal{T})\ \mathrm{e}^{-j\omega t_n}\ \mathrm{d}t_n. \tag{2.57}$$

If the process $f$ is WSS along $n$, then its Fourier transform is an OSM along this dimension, so that

$$\mathrm{E}\left[f(\mathcal{T}_n^-, \omega_n) \cdot f^*(\mathcal{T}_n'^-, \omega_n')\right] = 0, \quad \text{for } \omega_n \neq \omega_n'. \tag{2.58}$$

We can apply Khinchin's theorem [120, 185, 85] to the multi-dimensional case similarly to equation (2.44), so that

$$C_{f,f}(\mathcal{T}_n^-, \Delta t_n) = \int_{\mathbb{R}} P(\mathcal{T}_n^-, \omega_n)\ \mathrm{e}^{j\omega_n \Delta t_n}\ \mathrm{d}\omega_n, \tag{2.59}$$

The multi-dimensional random process $f(\mathcal{T})$ is ***Wide Sense Omni-Stationary (WSOS)*** when along all its dimensions the process is either WSS or OSM. If the process is WSS along all dimensions we have

$$\begin{aligned} \mu_f(\mathcal{T}) &= \mu_f \\ \sigma_f^2(\mathcal{T}) &= \sigma_f^2 \\ C_{f,f}(\mathcal{T},\mathcal{T}') &= C_{f,f}(\Delta t_1, \ldots, \Delta t_N) \\ R_{f,f}(\mathcal{T},\mathcal{T}') &= R_{f,f}(\Delta t_1, \ldots, \Delta t_N). \end{aligned} \tag{2.60}$$

**Definition 2.3.16.** A multi-dimensional random process $f(\mathcal{T})$ is ***ergodic*** with respect to one statistical property and along the $n$-th dimension when one realization of such process is sufficient to obtain this statistical property. For instance, signals for which the mean and autocorrelation function along $t_n$ can be obtained from one realization, are ergodic with respect to these functions.

### 2.3.2 Stochastic Description of the full MIMO Radio Channel

This subsection presents the statistical descriptions of the MIMO radio channel. Table 2.2 together with Table 2.1 summarizes the notation used for the functions, vectors, and matrices introduced in the following.

| Symbol | Description |
|---|---|
| $R(\cdots)$ | correlation function. The arguments define in which domains it is represented |
| $P(\cdot)$ | power profile. The argument defines the domain in which it is represented |
| $\tilde{P}(\cdot)$ | normalized power profile. The argument defines the domain in which it is represented |
| $\rho(\cdot)$ | autocorrelation function. The argument defines the domain in which it is represented |
| $P_{\mathrm{m}}$ | total received average power |
| $\mu_{\cdot}$ | mean value |
| $\sigma_{\cdot}^2$ | variance |
| $\Delta f_{\mathrm{coe}}$ | coherence bandwidth |
| $\Delta t_{\mathrm{coe}}$ | coherence time |
| $\boldsymbol{\Delta q}_{\mathrm{coe}}$ | coherence distance |
| $\sigma_\tau(\tau)$ | RMS delay spread |
| $\sigma_\nu(\nu)$ | RMS Doppler spread |
| $\sigma_\Omega(\Omega)$ | RMS angle spread |
| WSS | Wide Sense Stationary |
| OSM | Orthogonal Stochastic Measure |

Tab. 2.2: Notation used in this chapter. A comprehensive list of symbols is given on page 249.

As seen in Section 2.2.3 the channel $h(\cdots)$ can be represented in delay time $\tau$, Doppler frequency $\nu$, angle of arrival $\Omega_{\mathrm{R}}$, and angle of departure $\Omega_{\mathrm{T}}$. Alternatively, it can be transformed along any dimension via either a direct or an inverse (one- or multi-dimensional) Fourier transform to obtain an equivalent representation. This leads to $2^4 = 16$ equivalent channel descriptions.

We now treat the multi-dimensional function $h(\cdots)$ as a stochastic random process. In a domain in which we observe selectivity the process can be Wide Sense Stationary (WSS) and, consequently, in the transformed domain (i.e., where the channel displays dispersion) the process can be an Orthogonal Stochastic Measure (OSM). Table 2.3 summarizes the domain pairs, their relationship, and their possible statistical properties, namely WSS or OSM.

Let us now assume a zero-mean Wide Sense Omni-Stationary (WSOS) channel $h(\ldots)$. Its correlation function is the 8-dimensional function

$$R(\tau, \nu, \Omega_{\mathrm{T}}, \Omega_{\mathrm{R}}, \tau', \nu', \Omega'_{\mathrm{T}}, \Omega'_{\mathrm{R}}) = \mathrm{E}\left[h^*(\tau, \nu, \Omega_{\mathrm{T}}, \Omega_{\mathrm{R}}) \cdot h(\tau', \nu', \Omega'_{\mathrm{T}}, \Omega'_{\mathrm{R}})\right], \tag{2.61}$$

| Domains for the description of the channel $h(\dots)$ | | | | | | |
|---|---|---|---|---|---|---|
| delay time | $\tau$ | OSM | $\xrightarrow{\mathcal{F}\{\cdot\}}$ | WSS | $f$ | frequency |
| Doppler frequency | $\nu$ | OSM | $\xleftarrow{\mathcal{F}\{\cdot\}}$ | WSS | $t$ | time |
| Angle of Arrival | $\Omega_\mathrm{R}$ | OSM | $\xrightarrow{\mathcal{F}\{\cdot\}}$ | WSS | $\boldsymbol{q}_\mathrm{R}$ | Rx position |
| Angle of Departure | $\Omega_\mathrm{T}$ | OSM | $\xrightarrow{\mathcal{F}\{\cdot\}}$ | WSS | $\boldsymbol{q}_\mathrm{T}$ | Tx position |

Tab. 2.3: This table summarizes the domain pairs in which the channel can be represented, and their relationship. The channel, seen as a stochastic process along each dimension, can be either Wide Sense Stationary (WSS) or an Orthogonal Stochastic Measure (OSM).

| Domains for the description of the correlation $R(\dots)$ | | | | | | |
|---|---|---|---|---|---|---|
| delay time | $\tau$ | OSM | $\xrightarrow{\mathcal{F}\{\cdot\}}$ | WSS | $\Delta f$ | frequency offset |
| Doppler frequency | $\nu$ | OSM | $\xleftarrow{\mathcal{F}\{\cdot\}}$ | WSS | $\Delta t$ | time lag |
| Angle of Arrival | $\Omega_\mathrm{R}$ | OSM | $\xrightarrow{\mathcal{F}\{\cdot\}}$ | WSS | $\boldsymbol{\Delta q}_\mathrm{R}$ | Rx position offset |
| Angle of Departure | $\Omega_\mathrm{T}$ | OSM | $\xrightarrow{\mathcal{F}\{\cdot\}}$ | WSS | $\boldsymbol{\Delta q}_\mathrm{T}$ | Tx position offset |

Tab. 2.4: This table summarizes the domain pairs in which the channel correlation can be represented, and their relationship. For the WSS domains, the function depends only on a lag.

which, as the process $h(\dots)$ itself, can be transformed in one or more domains by one- or multi-dimensional Fourier transforms, to obtain a total of 16 equivalent statistical descriptions. Note that we refer to these functions always with the notation $R(\dots)$, where the arguments in the brackets specify unequivocally in which domains they are computed. Table 2.4 shows the four domain pairs. In those in which the channel is WSS we have dependency on a lag. For instance, for frequency $f$ we have $R(\dots, f, \dots, f', \dots) = R(\dots, \Delta f, \dots)$, where $\Delta f = f - f'$. For OSM dimensions we have that the correlation is non zero only between a point and the point itself. For instance, in delay time $\tau$ we have $R(\dots, \tau, \dots, \tau', \dots) = R(\dots, \tau, \dots)\delta(\tau - \tau')$.

Special cases are represented by the correlation function $R(\dots)$ in all WSS domains

$$R(\tau, \nu, \Omega_\mathrm{T}, \Omega_\mathrm{R}) = \mathrm{E}\left[|h(\tau, \nu, \Omega_\mathrm{T}, \Omega_\mathrm{R})|^2\right], \tag{2.62}$$

and the one in all OSM domains

$$R(\Delta f, \Delta t, \boldsymbol{\Delta q}_\mathrm{T}, \boldsymbol{\Delta q}_\mathrm{R}) = \mathrm{E}\left[h^*(f, t, \boldsymbol{q}_\mathrm{T}, \boldsymbol{q}_\mathrm{R}) \cdot h(f + \Delta f, t + \Delta t, \boldsymbol{q}_\mathrm{T} + \boldsymbol{\Delta q}_\mathrm{T}, \boldsymbol{q}_\mathrm{R} + \boldsymbol{\Delta q}_\mathrm{R})\right].$$

Figure 2.15 shows the function $R(\tau, \nu)$ for a Single Input Single Output (SISO) link.

Considering Table 2.4, any of the 16 correlation functions $R(\dots)$ can be computed either by solving an expectation operator similar to the one in equation (2.61), or by transforming an already known $R(\dots)$ function via Fourier. The latter is useful when dealing with sampled

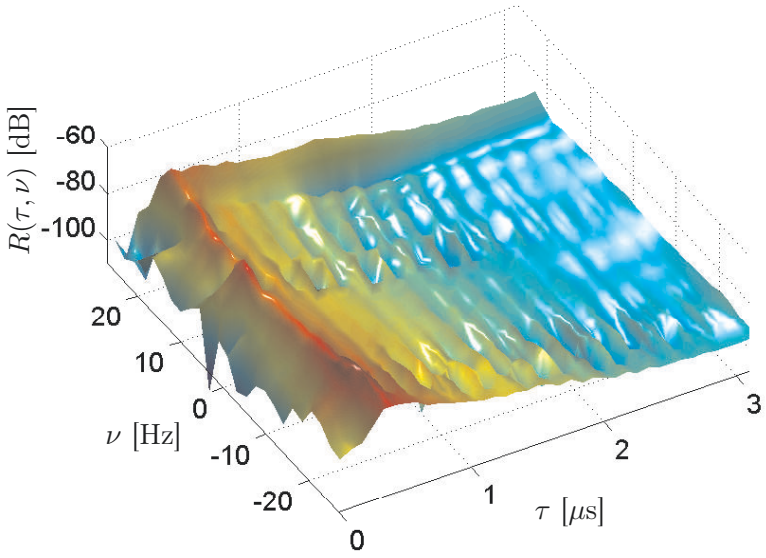


Fig. 2.15: Scattering function $R(\tau, \nu)$ for a SISO link. The function, expressed in dB, gives the average power displayed by the channel for the TDOA $\tau$ and Doppler frequency $\nu$.
(source: channel measurements in a hotspot scenario)

channels, as discussed in the following subsection.

From the most general correlation function $R(\ldots)$ it is possible to derive marginal statistical representations by integrating along all OSM domains and by setting all lags to zero, except for one dimension. Therefore, there are four marginal representations for the WSS domains, and four for the OSM. The following sections present these functions in detail. The ones defined in the OSM domains represent average powers and are therefore termed "power profiles" and are denoted as $P(\cdot)$. The functions defined in the WSS domains, on the other hand, are denoted as $\rho(\cdot)$ and are autocorrelation functions.

#### 2.3.2.1 Power Delay Profile

By condensing all domains but delay $\tau$ we obtain the ***power delay profile*** $P(\tau)$, which indicates the average power of the channel with respect to the different taps. It is defined as

$$P(\tau) = \mathrm{E}\left[|h(\tau)|^2\right]. \tag{2.63}$$

It can be computed from any correlation function $R(\tau, \ldots)$ by setting the lags to zero and by integrating over the OSM domains. For instance,

$$P(\tau) = \int_{\mathbb{R}} \int_{\mathcal{S}^2} R(\tau, \nu, \boldsymbol{\Delta q}_\mathrm{T}, \Omega_\mathrm{R})|_{\boldsymbol{\Delta q}_\mathrm{T}=\mathbf{0}} \, \mathrm{d}\Omega_\mathrm{R} \, \mathrm{d}\nu. \tag{2.64}$$

To compact the statistical description even further we derive the following parameters. Let $P_\mathrm{m}$ be the *average received power*, defined as

$$P_\mathrm{m} = \int_{\mathbb{R}} P(\tau)\ \mathrm{d}\tau = \mathrm{E}\left[|h(\tau)|^2\right], \tag{2.65}$$

and $\tilde{P}(\tau)$ the *normalized power delay profile*, defined as

$$\tilde{P}(\tau) = \frac{P(\tau)}{P_\mathrm{m}}. \tag{2.66}$$

The *mean delay* $\mu_\tau$ is defined as the mean of the normalized power delay profile

$$\mu_\tau = \int_{\mathbb{R}} \tilde{P}(\tau)\tau\ \mathrm{d}\tau = \mathrm{E}\left[\tilde{P}(\tau)\right]. \tag{2.67}$$

The normalized second-order central moment is known as the *Root Mean Square (RMS) delay spread* $\sigma_\tau$, it is defined as

$$\sigma_\tau = \sqrt{\int_{\mathbb{R}} \tilde{P}(\tau)\ \tau^2\ \mathrm{d}\tau - P_\mathrm{m}^2} \tag{2.68}$$

The RMS delay spread has grown particularly importance as it was shown that under specific conditions there exist a proportionality with the bit error rate [158]. The reason of its popularity is however given by its simplicity, as it makes it possible to describe a channel's characteristics in delay domain with one number only. Obviously, this is a rather coarse description. Figure 2.16 shows an exemplary power delay profile $P(\tau)$ and its corresponding mean delay $\mu_\tau$ and the Root Mean Square (RMS) delay spread $\sigma_\tau$.

#### 2.3.2.2 Autocorrelation Function in Frequency Domain

By condensing all domains but the frequency offset $\Delta f$ we obtain the ***autocorrelation function in frequency domain*** $\rho(\Delta f)$. It is defined as

$$\rho(\Delta f) = \mathrm{E}\left[h(f) \cdot h^*(f + \Delta f)\right]. \tag{2.69}$$

It can be computed from any correlation function $R(\Delta f, \ldots)$ by setting the lags to zero and by integrating over the OSM domains. For instance,

$$\rho(\Delta f) = \int_{\mathbb{R}} \int_{\mathcal{S}^2} R(\Delta f, \nu, \boldsymbol{\Delta q}_\mathrm{T}, \Omega_\mathrm{R})|_{\boldsymbol{\Delta q}_\mathrm{T}=\mathbf{0}}\ \mathrm{d}\Omega_\mathrm{R}\ \mathrm{d}\nu. \tag{2.70}$$

To compact this statistical representation even further we define the *coherence bandwidth* $\Delta f_\mathrm{coe}$, which can be interpreted as the bandwidth in which the channel can reasonably be considered flat fading. It is defined as the bandwidth for which the autocorrelation function has fallen below 70 % of its maximum. This empirical approach led to different definitions. For instance, [158] defines $\Delta f_\mathrm{coe}$ at 50%. Note that the delay power profile and the autocorre-

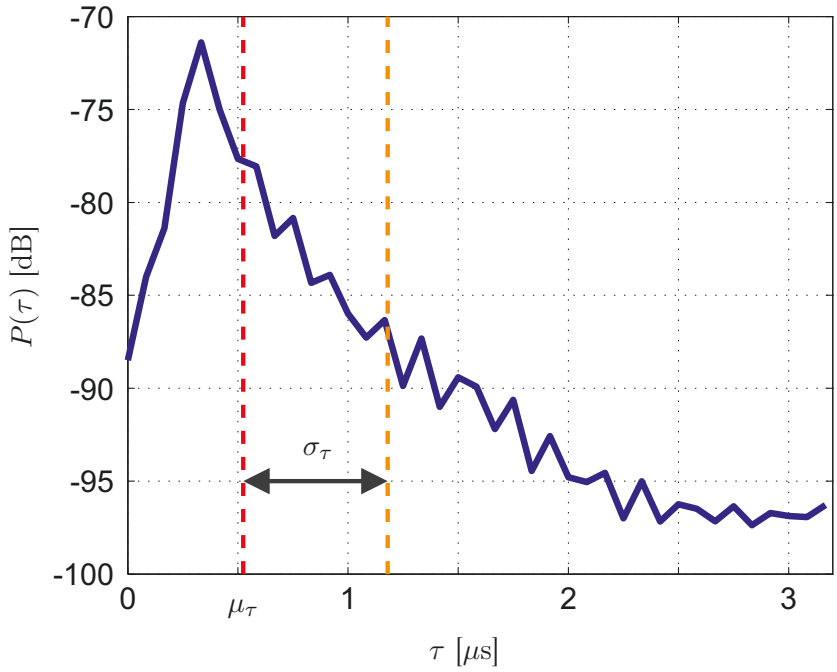


Fig. 2.16: Power delay profile $P(\tau)$ for a SISO link. The function, expressed in dB, gives the average power displayed by the channel for the TDOA $\tau$. The mean delay $\mu_\tau$ and the Root Mean Square (RMS) delay spread $\sigma_\tau$ are also displayed.
(source: channel measurements in a hotspot scenario)

lation function in frequency domain make a Fourier pair because of the relationship given in Table 2.4. For the same reason, the coherence bandwidth displays an inverse proportionality with respect to the RMS delay spread.

Figure 2.17 shows the autocorrelation function in frequency domain $\rho(\Delta f)$ and the coherence bandwidth $\Delta f_{\text{coe}}$ computed at 50% of the maximum value. Please note that the autocorrelation function has been scaled so that its maximum equals 1.

#### 2.3.2.3 Power Doppler Profile

By condensing all domains but Doppler frequency $\nu$ we obtain the ***power Doppler profile*** $P(\nu)$ , which indicates the average power of the channel with respect to different Doppler frequencies. It is defined as

$$P(\nu) = \mathrm{E}\left[|h(\nu)|^2\right]. \tag{2.71}$$

It can be computed from any correlation function $R(\nu, \ldots)$ by setting the lags to zero and by integrating over the OSM domains. For instance,

$$P(\nu) = \int_{\mathbb{R}} \int_{\mathcal{S}^2} R(\tau, \nu, \boldsymbol{\Delta q}_{\mathrm{T}}, \Omega_{\mathrm{R}})|_{\boldsymbol{\Delta q}_{\mathrm{T}}=\mathbf{0}} \, \mathrm{d}\Omega_{\mathrm{R}} \, \mathrm{d}\tau. \tag{2.72}$$

Similarly to what is done in delay domain, to compact the statistical description we derive the following parameters. Assuming that $P_{\mathrm{m}}$ is the *average received power*, which alternatively to

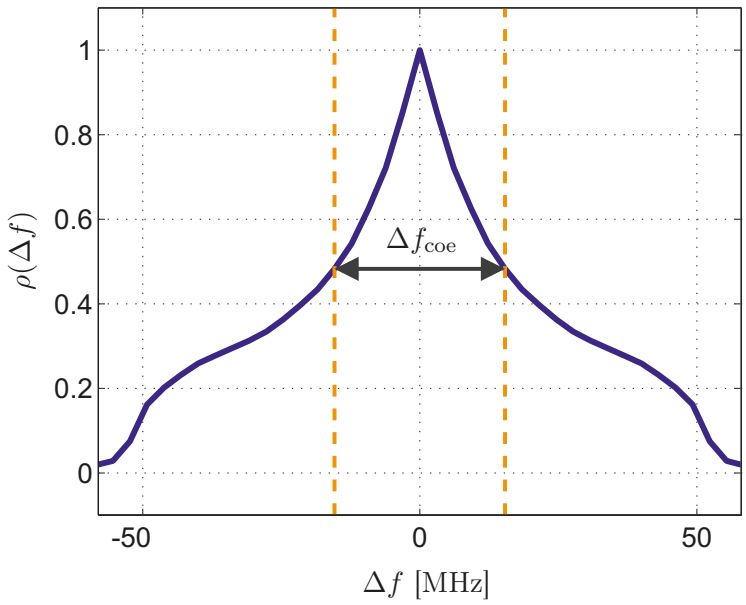


Fig. 2.17: The autocorrelation function in frequency domain $\rho(\Delta f)$ and the coherence bandwidth $\Delta f_{\text{coe}}$ computed at 50% of the maximum value. Please note that the autocorrelation function has been scaled so that its maximum equals 1.
`(source: channel measurements in a hotspot scenario)`

equation (2.65) can be computed as

$$P_{\text{m}} = \int_{\mathbb{R}} P(\nu)\ \mathrm{d}\nu, \tag{2.73}$$

and $\tilde{P}(\nu)$ is the *normalized power Doppler profile*, defined as

$$\tilde{P}(\nu) = \frac{P(\nu)}{P_{\text{m}}}. \tag{2.74}$$

The *mean Doppler shift* $\mu_\nu$ is defined as the mean of the normalized power Doppler profile

$$\mu_\nu = \int_{\mathbb{R}} \tilde{P}(\nu)\nu\ \mathrm{d}\nu = \mathrm{E}\left[\tilde{P}(\nu)\right]. \tag{2.75}$$

The normalized second-order central moment is known as the *Root Mean Square (RMS) Doppler spread* $\sigma_\nu$, it is defined as

$$\sigma_\nu(\nu) = \sqrt{\int_{\mathbb{R}} \tilde{P}(\nu)\ \nu^2\ \mathrm{d}\nu - P_{\text{m}}^2}. \tag{2.76}$$

The remarks given for the RMS delay spread are valid also for the RMS Doppler spread, which with one number indicates the dispersion behavior of the channel with respect to Doppler. Figure 2.18 shows an exemplary power delay profile $P(\tau)$ and its corresponding mean Doppler shift $\mu_\nu$ and the Root Mean Square (RMS) Doppler spread $\sigma_\nu$.

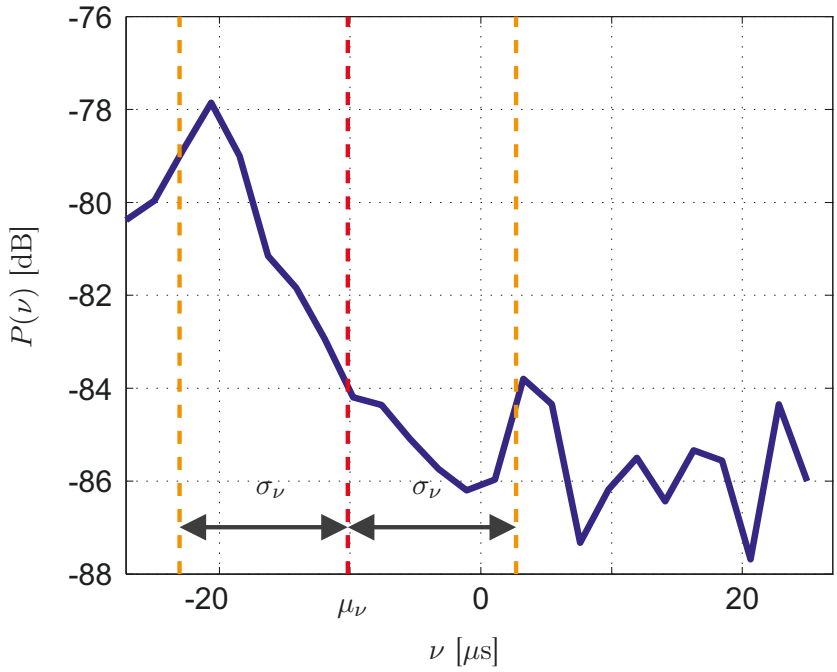


Fig. 2.18: Power Doppler profile $P(\nu)$ for a SISO link. The function, expressed in dB, gives the average power displayed by the channel for the Doppler frequency $\nu$. The mean Doppler shift $\mu_\nu$ and the Root Mean Square (RMS) Doppler spread $\sigma_\nu$ are also displayed.
(source: channel measurements in a hotspot scenario)

#### 2.3.2.4 Autocorrelation Function in Time Domain

By condensing all domains but the time interval $\Delta t$ we obtain the ***autocorrelation function in time domain*** $\rho(\Delta t)$. It is defined as

$$\rho(\Delta t) = \mathrm{E}\left[h(t) \cdot h^*(t + \Delta t)\right]. \tag{2.77}$$

It can be computed from any correlation function $R(\Delta t, \ldots)$ by setting the lags to zero and by integrating over the OSM domains. For instance,

$$\rho(\Delta t) = \int_{\mathbb{R}} \int_{\mathcal{S}^2} R(\tau, \Delta t, \boldsymbol{\Delta q}_\mathrm{T}, \Omega_\mathrm{R})|_{\boldsymbol{\Delta q}_\mathrm{T}=\mathbf{0}} \, \mathrm{d}\Omega_\mathrm{R} \, \mathrm{d}\tau. \tag{2.78}$$

To compact this statistical representation even further we define the *coherence time* $\Delta t_\mathrm{coe}$, which can be interpreted as the time interval in which the channel can reasonably be considered time invariant. It is defined as the time interval for which the autocorrelation function has fallen below 70 % of its maximum. Similarly to the frequency and delay time pair, the Doppler power profile and the autocorrelation function in time domain are a Fourier pair due to the relationship given in Table 2.4. For the same reason, the coherence time displays an inverse proportionality with respect to the RMS Doppler spread.

Figure 2.19 shows the autocorrelation function in time domain $\rho(\Delta t)$ and the coherence

time $\Delta t_{\text{coe}}$ computed at 50% of the maximum value. Please note that the autocorrelation function has been scaled so that its maximum equals 1.

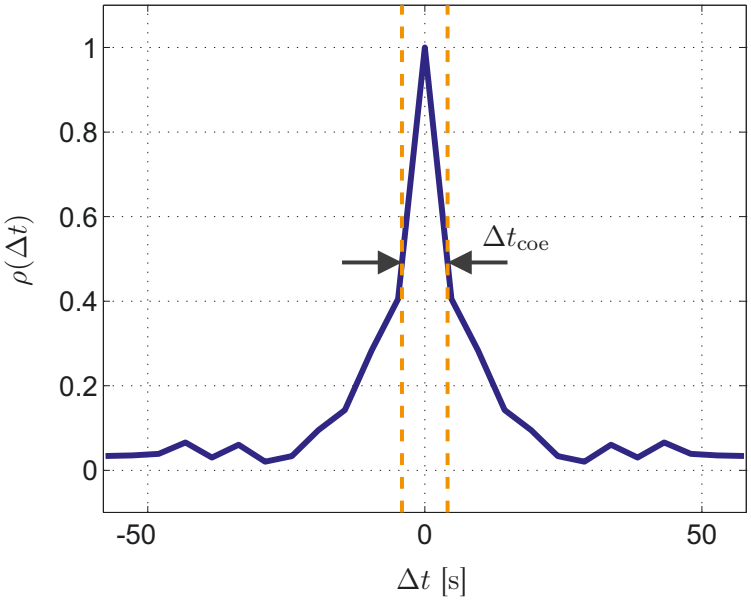


Fig. 2.19: The autocorrelation function in time domain $\rho(\Delta t)$ and the coherence time $\Delta f_{\text{coe}}$ computed at 50% of the maximum value. Please note that the autocorrelation function has been scaled so that its maximum equals 1.
(source: channel measurements in a hotspot scenario)

#### 2.3.2.5 Power Angular Profile

We now derive the definitions for the statistical description in the angular domain $\Omega_{\text{T}}$. Note that all formulas and definitions apply also for $\Omega_{\text{R}}$.

By condensing all domains but the DOD $\Omega_{\text{T}}$, we obtain the ***power angular profile*** $P(\Omega_{\text{T}})$, which indicates the average power of the channel with respect to different Doppler frequencies. It is defined as

$$P(\Omega_{\text{T}}) = \text{E}\left[|h(\Omega_{\text{T}})|^2\right]. \tag{2.79}$$

It can be computed from any correlation function $P(\Omega_{\text{T}}, \dots)$ by setting the lags to zero and by integrating over the OSM domains. For instance,

$$P(\Omega_{\text{T}}) = \int_{\mathbb{R}} \int_{\mathbb{R}} R(\tau, \nu, \Omega_{\text{T}}, \boldsymbol{\Delta q}_{\text{R}})|_{\boldsymbol{\Delta q}_{\text{R}}=\mathbf{0}} \, \text{d}\nu \, \text{d}\tau. \tag{2.80}$$

The angular domain, due to its inherit bi-dimensional geometry, makes it harder to derive more compact statistical descriptions, similarly to the delay and Doppler domains. In fact, the direction of departure $\Omega_{\text{T}}$ actually consists of two variables, namely azimuth $\varphi_{\text{T}}$ and elevation $\theta_{\text{T}}$. Consequently, the vector $\boldsymbol{\Omega}_{\text{T}}$, defined as in equation (2.28), is bound to lie on the unit

sphere $\mathcal{S}^2$. As in the other domains, let $P_\mathrm{m}$ be the *average received power*, which alternatively to equation (2.65) and (2.73) can be computed as

$$P_\mathrm{m} = \int_{\mathcal{S}^2} P(\Omega_\mathrm{T})\ \mathrm{d}\Omega_\mathrm{T}. \tag{2.81}$$

From the power angular profile it is possible to derive the *power azimuthal profile* $P(\varphi_\mathrm{T})$ and the *power elevation profile* $P(\theta_\mathrm{T})$ as follows

$$\begin{aligned} P(\varphi_\mathrm{T}) &= \int_{-\frac{\pi}{2}}^{\frac{\pi}{2}} P(\varphi_\mathrm{T}, \theta_\mathrm{T})\ \sin(\theta_\mathrm{T})\ \mathrm{d}\theta_\mathrm{T} \\ P(\theta_\mathrm{T}) &= \int_{0}^{2\pi} P(\varphi_\mathrm{T}, \theta_\mathrm{T})\ \mathrm{d}\theta_\mathrm{T}. \end{aligned} \tag{2.82}$$

We now normalize these functions to obtain

$$\begin{aligned} \tilde{P}(\Omega_\mathrm{T}) &= \frac{P(\Omega_\mathrm{T})}{P_\mathrm{m}} \\ \tilde{P}(\varphi_\mathrm{T}) &= \frac{P(\varphi_\mathrm{T})}{P_\mathrm{m}} \\ \tilde{P}(\theta_\mathrm{T}) &= \frac{P(\theta_\mathrm{T})}{P_\mathrm{m}}. \end{aligned} \tag{2.83}$$

The *mean angle* $\mu_{\Omega_\mathrm{T}} = \{\mu_{\varphi_\mathrm{T}}, \mu_{\theta_\mathrm{T}}\}$ represents the mean direction of departure. Similarly to the center of mass, it is computed as

$$\begin{aligned} \mu_{\varphi_\mathrm{T}} &= \int_{-\frac{\pi}{2}}^{\frac{\pi}{2}} \tilde{P}(\varphi_\mathrm{T})\ \mathrm{d}\varphi_\mathrm{T} \\ \mu_{\theta_\mathrm{T}} &= \int_{0}^{2\pi} \tilde{P}(\theta_\mathrm{T})\ \mathrm{d}\theta_\mathrm{T} \end{aligned} \tag{2.84}$$

To derive a normalized second-order central moment for the angular domain the common approach is to apply equation (2.39) to the azimuth alone. The main reason being the difficulty in treating a bi-dimensional signal defined on the sphere. In most cases, as noticed by Fleury in [75], the periodicity of the azimuthal angle is even ignored. To include elevation and consider the spherical geometry of the problem we propose an alternative definition of the *Root Mean Square (RMS) angular spread* $\sigma_{\Omega_\mathrm{T}}(\Omega_\mathrm{T})$. It is measured in degrees and is defined as

$$\sigma_{\Omega_\mathrm{T}} = \sqrt{\int_{\mathcal{S}^2} \tilde{P}(\Omega_\mathrm{T})\ \left(\cos^{-1}\left(\langle \boldsymbol{\Omega}_\mathrm{T}, \bar{\boldsymbol{\Omega}}_\mathrm{T}\rangle\right)\right)^2\ \mathrm{d}\Omega_\mathrm{T}}, \tag{2.85}$$

where $\boldsymbol{\Omega}_\mathrm{T}$ and $\bar{\boldsymbol{\Omega}}_\mathrm{T}$ are the vectors pointing towards the mean angle $\mu_{\Omega_\mathrm{T}}$ and the integration angle $\Omega_\mathrm{T}$, respectively. Their inner product $\langle \boldsymbol{\Omega}_\mathrm{T}, \bar{\boldsymbol{\Omega}}_\mathrm{T}\rangle$ gives the cosine of the angle between the two directions. The RMS angular spread gives an indication of the mean dispersion around the mean angle.

The plots in Figure 2.20 show the marginal angular power profiles $P(\varphi_\mathrm{T})$ and $P(\theta_\mathrm{T})$. The

mean angles $\mu_{\varphi_\mathrm{T}}$ and $\mu_{\theta_\mathrm{T}}$ and the Root Mean Square (RMS) angular spread $\sigma_{\Omega_\mathrm{T}}$ computed as mentioned above are also shown.

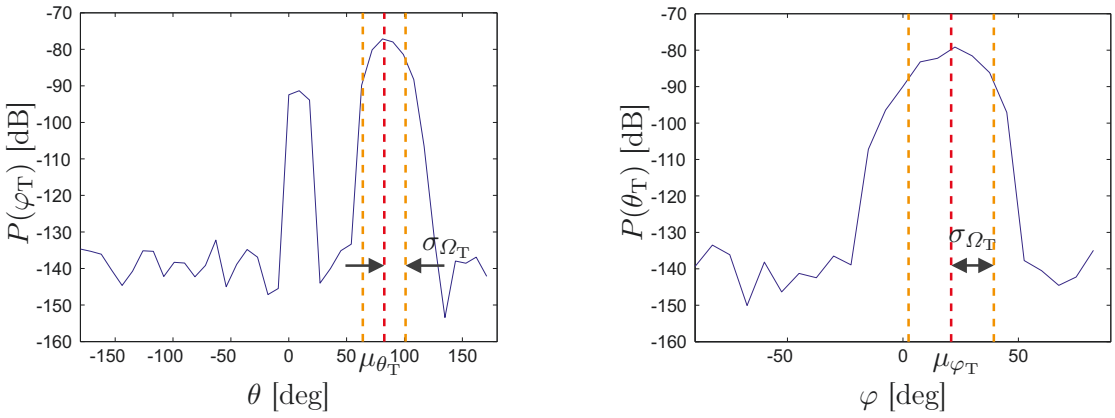


(a) Power azimuthal profile

(b) Power elevation profile

Fig. 2.20: The two marginal angular power profiles: (a) power azimuthal profile $P(\varphi_\mathrm{T})$; (b) power elevation profile $P(\theta_\mathrm{T})$. The mean angles $\mu_{\varphi_\mathrm{T}}$ and $\mu_{\theta_\mathrm{T}}$ as well as the Root Mean Square (RMS) angular spread $\sigma_{\Omega_\mathrm{T}}$ are shown. This explanatory figures are obtained from a synthetic channel computed with the IlmProp.

Figure 2.21 shows the power angular profile $P(\Omega_\mathrm{T})$. The dashed line marks the mean angle $\mu_{\Omega_\mathrm{T}}$ whereas the cylinder has a radius equal to the RMS angular spread $\sigma_{\Omega_\mathrm{T}}$.

#### 2.3.2.6 Joint Power Angular Profiles

In some cases it is interesting to investigate the directional properties of a channel at the Rx and Tx jointly. This is possible thanks to the ***joint power angular profile*** $P(\Omega_\mathrm{T}, \Omega_\mathrm{R})$. It is defined as

$$P(\Omega_\mathrm{T}, \Omega_\mathrm{R}) = \mathrm{E}\left[|h(\Omega_\mathrm{T}, \Omega_\mathrm{R})|^2\right]. \tag{2.86}$$

Due to the difficulty in treating a four dimensional function, it is often computed the *joint power azimuthal profile*, $P(\varphi_\mathrm{T}, \varphi_\mathrm{R})$, which denotes the average power transfer between the azimuth $\varphi_\mathrm{T}$ at the transmitter and $\varphi_\mathrm{R}$ at the receiver.

#### 2.3.2.7 Autocorrelation Function in Spatial Domain

We now derive the statistical descriptions in the spatial domain at the transmitter. Note that all formulas apply to the spatial dimension at the receiver as well. By condensing all domains but the position offset $\boldsymbol{\Delta q}_\mathrm{T}$ we obtain the ***autocorrelation function in spatial domain at the transmitter*** $\rho(\boldsymbol{\Delta q}_\mathrm{T})$. It is defined as

$$\rho(\boldsymbol{\Delta q}_\mathrm{T}) = \mathrm{E}\left[h(\boldsymbol{q}_\mathrm{T}) \cdot h^*(\boldsymbol{q}_\mathrm{T} + \boldsymbol{\Delta q}_\mathrm{T})\right]. \tag{2.87}$$

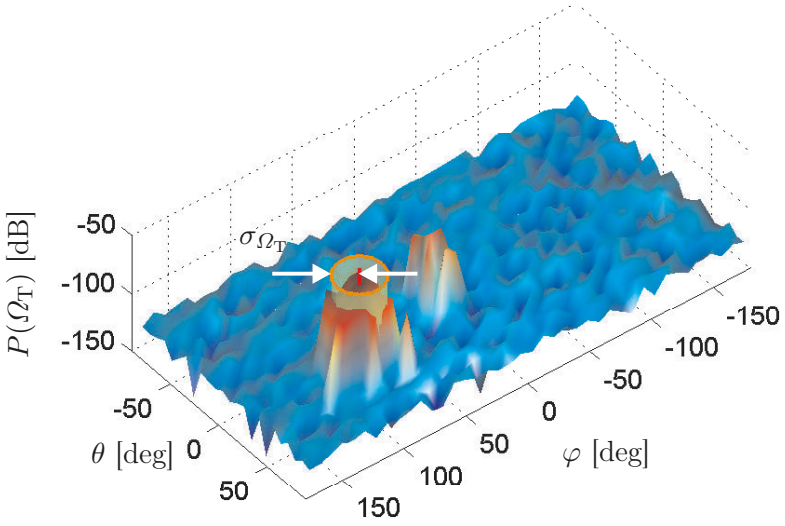


Fig. 2.21: Power angular profile $P(\Omega_T)$. The dashed line marks the mean angle $\mu_{\Omega_T}$ whereas the cylinder has a radius equal to the RMS angular spread $\sigma_{\Omega_T}$. This explanatory figure is obtained from a synthetic channel computed with the IlmProp.

It can be computed from any correlation function $R(\boldsymbol{\Delta q}_T, \ldots)$ by setting the lags to zero and by integrating over the OSM domains. For instance,

$$\rho(\boldsymbol{\Delta q}_T) = \int_{\mathbb{R}} \int_{\mathcal{S}^2} R(\tau, \nu, \boldsymbol{\Delta q}_T, \boldsymbol{\Delta q}_R)|_{\boldsymbol{\Delta q}_R = \mathbf{0}} \, \mathrm{d}\nu \, \mathrm{d}\tau. \tag{2.88}$$

Similarly to the angle domain, the dimensionality of space, namely $\mathbb{R}^3$ complicates the derivation of more compact statistical representations. In [75] a *coherence distance* $\Delta d_{\mathrm{coe}}$ is obtained by choosing the smallest *directional coherence distance* $\Delta d_{\mathrm{coe},\boldsymbol{\Omega}}$, as

$$\Delta d_{\mathrm{coe}} = \min_{\Omega} \left( \Delta d_{\mathrm{coe},\boldsymbol{\Omega}} \right), \tag{2.89}$$

where $\Delta d_{\mathrm{coe},\boldsymbol{\Omega}}$ is the spatial offset in the direction $\Omega$ for which the autocorrelation function falls below 70 % of its maximum. The coherence distance is an important parameter as it tells us that within a spatial offset smaller than $\Delta d_{\mathrm{coe}}$ the channel can be considered constant.

### 2.3.3 The Sampled Correlation Function

When we deal with measured channels just as well as with synthetic channels obtained from channel models, we cannot apply directly the formulas derived in the previous section as the channels will be sampled and bandlimited in all domains. To compute the correlation functions $R(\ldots)$ we can follow standard non-parametric estimation techniques, as in [226, 178]

- autocorrelation estimation for the WSS domains
- periodogram for the OSM domains,

working independently on the different dimensions. As already mentioned, the correlation function $R(\ldots)$ will be sampled, so that we can conveniently store it in form of a tensor.

As in equation (2.35), let the channel coefficients in space, time, and frequency be denoted by the tensor $\boldsymbol{\mathcal{H}}$, so that

$$\boldsymbol{\mathcal{H}} \in \mathbb{C}^{M_{\mathrm{R}} \times M_{\mathrm{T}} \times M_t \times M_f}, \tag{2.90}$$

where $M_{\mathrm{R}}$, $M_{\mathrm{T}}$, $M_t$, and $M_f$ are the number of samples taken in space at the receiver and at the transmitter, and in time $t$ and frequency $f$, respectively. Notice that the order in which we store the dimensions is irrelevant. The sampled correlation function $R(\boldsymbol{q}_{\mathrm{R}}, \boldsymbol{q}_{\mathrm{T}}, t, f, \boldsymbol{q}'_{\mathrm{R}}, \boldsymbol{q}'_{\mathrm{T}}, t', f')$, introduced in Section 2.3.2, is stored in the eight-dimensional tensor $\boldsymbol{\mathcal{R}}$, which we refer to as the *correlation tensor*, so that

$$\boldsymbol{\mathcal{R}} \in \mathbb{C}^{M_{\mathrm{R}} \times M_{\mathrm{T}} \times M_t \times M_f \times M_{\mathrm{R}} \times M_{\mathrm{T}} \times M_t \times M_f}. \tag{2.91}$$

The generic element of the tensor $\boldsymbol{\mathcal{R}}$ can be written as

$$(\boldsymbol{\mathcal{R}})_{m_{\mathrm{R}}, m_{\mathrm{T}}, t, f, m'_{\mathrm{R}}, m'_{\mathrm{T}}, t', f'} = \mathrm{E}\left[h(m_{\mathrm{R}}, m_{\mathrm{T}}, t, f) \cdot h^*(m'_{\mathrm{R}}, m'_{\mathrm{T}}, t', f')\right]. \tag{2.92}$$

Alternatively, the correlation tensor can be expressed as

$$\boldsymbol{\mathcal{R}} = \mathrm{E}\left[\boldsymbol{\mathcal{H}} \circ \boldsymbol{\mathcal{H}}^*\right], \tag{2.93}$$

where the symbol $\circ$ is the tensor outer product defined in equation (D.13). This straightforward extension to tensors has been suggested independently in [27] and [60].

To compute numerically the expectation operator in equation (2.93) we need more realizations of the channel tensor $\boldsymbol{\mathcal{H}}$. As this is in general not possible, we use of the dimensions to perform the average. Along this dimension we implicitly assume that the process is stationary with respect to all other dimensions. Stationarity for multi-dimensional processes is given in Definition 2.3.14.

An application of the computation of the correlation tensor is given in Section 5.2.6 for a novel subspace-based channel model.

#### 2.3.3.1 Bidimensional Correlation Matrix for N-dimensional Problems

If we have a narrowband SIMO system, namely multiple antennas at the receiver side only, the channel at time $t$ takes the form of the vector

$$\boldsymbol{h}(t) \in \mathbb{C}^{M_{\mathrm{R}} \times 1}, \tag{2.94}$$

where $M_{\mathrm{R}}$ is the number of receive antennas. If we assume that the channel is WSS with respect to the spatial domain along time, the correlation matrix $\boldsymbol{R}$ does not depend on time and is defined as

$$\boldsymbol{R} = \mathrm{E}\left[\boldsymbol{h}(t) \cdot \boldsymbol{h}^{\mathrm{H}}(t)\right] \in \mathbb{C}^{M_{\mathrm{R}} \times M_{\mathrm{R}}}, \tag{2.95}$$

where the superscript $(\cdot)^{\mathrm{H}}$ indicates the Hermitian transpose.

For a more complicated system, when the channel comprises $N$ dimensions, such as time, frequency, and antennas at both sides, we can describe the correlation between any pair of channel coefficients by means of the correlation tensor $\boldsymbol{\mathcal{R}}$, as described in the previous section, namely

$$\begin{aligned} \boldsymbol{\mathcal{H}} &\in \mathbb{C}^{I_1 \times \ldots \times I_N} \\ \boldsymbol{\mathcal{R}} &= \mathrm{E}\left[\boldsymbol{\mathcal{H}} \circ \boldsymbol{\mathcal{H}}^*\right] \in \mathbb{C}^{I_1 \times \ldots \times I_N \times I_1 \times \ldots \times I_N}, \end{aligned} \tag{2.96}$$

where $I_1$, $I_2$, …, $I_N$ denote the number of samples in the $N$ different dimensions. Notice that the correlation tensor $\boldsymbol{\mathcal{R}}$ does not depend on any of the variables, implicitly meaning that the muldi-dimensional process is Wide Sense Omni-Stationary (WSOS)[6].

Alternatively, we can store the very same information in form of a bi-dimensional descriptor by stacking all elements of the channel tensor $\boldsymbol{\mathcal{H}}$ into a column vector, and then compute a correlation matrix $\boldsymbol{R}$ as in equation (2.95), so that

$$\begin{aligned} \boldsymbol{h} &= \boldsymbol{\mathcal{H}}_{[N+1]}^{\mathrm{T}} = \mathrm{vec}\left\{\boldsymbol{\mathcal{H}}\right\} \in \mathbb{C}^{I_1 \cdot \ldots \cdot I_N \times 1} \\ \boldsymbol{R} &= \mathrm{E}\left[\boldsymbol{h} \cdot \boldsymbol{h}^{\mathrm{H}}\right] \in \mathbb{C}^{I_1 \cdot \ldots \cdot I_N \times I_1 \cdot \ldots \cdot I_N}. \end{aligned} \tag{2.97}$$

The fact that the tensor $\boldsymbol{\mathcal{R}}$ and the matrix $\boldsymbol{R}$ contain the very same information can be conveniently expressed using the MATLAB-like matrix unfolding described in Appendix D.2.2 as

$$\boldsymbol{r} = \boldsymbol{\mathcal{R}}_{[2N+1]}^{\mathrm{T}} = \boldsymbol{R}_{[3]}^{\mathrm{T}} = \mathrm{vec}\left\{\boldsymbol{\mathcal{R}}\right\} = \mathrm{vec}\left\{\boldsymbol{R}\right\} \in \mathbb{C}^{I_1 \cdot \ldots \cdot I_N \cdot I_1 \cdot \ldots \cdot I_N \times 1}. \tag{2.98}$$

This notation will be useful in Section 5.2.6 for the correlation tensor-based channel model.

[6] See equation (2.60) for more details on the Wide Sense Omni-Stationary (WSOS) assumption.

# 3. MODELING APPROACHES OF THE MIMO CHANNEL

This chapter deals with the issue of channel modeling, its motivation and applications. It also introduces some exemplary well known channel models and channel modeling principles, underlining their qualities and drawbacks.

In Section 3.1 we motivate and categorize different modeling approaches. We present three different classifications. Two with respect to the application of the channel model and one with respect to the modeling principle. We then introduce key concepts in channel modeling, such as propagation scenarios (Section 3.1.3), antenna dependency (Section 3.1.4), and validation (Section 3.1.5).

Following the categorization with respect to the modeling principle we deal more in detail with analytical, deterministic, and hybrid channel models in Sections 3.2, 3.3, and 3.4, respectively.

The concepts presented in this chapter are useful to understand the differences of the IlmProp from other channel models, the motivation for its being, and where it is located in the panorama of channel modeling. These issues are covered in Chapter 5.

## 3.1 Motivation and Classification of Channel Models

The term *channel modeling* denotes in a strict sense the modeling of the Channel Impulse Responses[1] (CIR).

In this work we focus mainly on single and multi-user time variant frequency selective wideband MIMO channels. In other words, one or more users are moving in a multi-path environment, where each link-end can employ multiple antennas.

To predict the performance of a narrowband Single Input Single Output (SISO) system it is sufficient to consider the received power and the time varying amplitude distribution of the channel, namely the statistics of the *fading*. A channel model capable of generating such features is quite simple and the channels it produces are, with respect to these characteristics, very realistic. Note that the level of detail reached by a channel model cannot be measured on an absolute scale, but must be evaluated with respect to the system which will be tested on the

[1] In a broader sense, some researchers refer to it also as the modeling of specific features of the channels, such as their path-loss, time variance, delay spread, SNR, and so on.

synthetic channels. Unfortunately, this is often forgotten and researchers constantly propose improvements of well established channel models simply by claiming a better accuracy, yet without showing how this might affect the results of a system simulation.

Molisch in [158] well expressed the goal which should be kept in mind when developing new channel models: *"More than accuracy in a general sense, we need to model more realistically those features which have an impact on the system".*

Mainly there are two motivations for the development of a new channel model:

- to model a certain feature of the channel previously neglected
- to model more realistically the channels when new and more sophisticated channel measurements are available.

In order to assess the performance of a MIMO wideband system in a practical scenario it is crucial to consider realistic channels. As mentioned above, SISO systems can be accurately studied simply by considering power level distributions and Doppler shifts. On the other hand, MIMO systems take advantage of the spatial dimension, whose modeling requires to incorporate additional concepts such as angles of arrival and departure, and arbitrary antenna geometries. Furthermore, as more advanced channel measurements are being carried out, we gather a better understanding of the MIMO channel, allowing us to develop more sophisticated channel models.

Categorizing channel models is not an easy task. In fact there exist an enormous number of channel models, among which most of them are based on the very same modeling principle, and differ only by smaller details. Additionally, channel models can correspond to a very complex simulation chain, implemented in hundreds of code lines, which hardly can be exhaustively described in a few pages. For this reason, putting some order in the channel modeling jungle is challenging, to say the least. The complexity of most models makes it also very hard to determine who first proposed a certain modeling approach. In fact, it has happened many times that researchers re-invented old ideas presenting them inadvertently as original and novel. Most classifications are based either on the modeling principle followed, or by the applications of the synthetic channels. If we follow the latter approach, we can identify three main applications for the channels generated by a channel model:

- *system deployment*
- *system design*
- *system performance evaluation.*

**System deployment** applications consist in predicting the propagation conditions in a certain scenario with high accuracy. For instance, the channels obtained are then useful to decide where to locate a base station, or what coverage a certain access point will have. For this reason system deployment channel models are very *site specific*, and are normally

based on physical models. For instance, the Winprop channel model [35] also discussed in Section 5.2.3 is one of such models, as its aim is to predict the propagation conditions for both outdoor and indoor scenarios.

**System design** applications require a large number of channels which are typical for the areas where a certain system under study will operate. By the analysis of these channels it is then possible to devise the system parameters so that the system will operate optimally. For instance by the analysis of typical channels for a high data-rate cellular network, OFDM presents itself as a good solution to combat frequency selectivity. System design is clearly *site independent*. A system design oriented channel model must then be capable of generating efficiently numerous channels for a variety of different scenarios. In some cases the system design can be carried out without the knowledge of the channel coefficients, but only considering specific metrics which characterize the environment. For instance, in [38], the WINNER channel model, presented in Section 3.4.2, is applied in order to decide which beamforming technique to use.

**System performance evaluation** consists in evaluating the system performance (characterized by some standard metric) in realistic operating conditions. A system can be evaluated on a larger scale, for instance during a system design phase, or on a smaller scale, in which a specific scenario is taken and a particular aspect of the system is tested. An example for a small scale system performance evaluation is the investigation of the behavior of a scheduler in a multi-user scenario. An example for a system performance evaluation model is the 802.11n model [108], developed to investigate a MIMO WLAN system in indoor environments, or the COST207 model [74] used to evaluate the GSM standard.

Obviously system design and system performance evaluation are very much related. The former analyzes the channels in order to determine the best matching system which fulfills the requirements. The latter, on the other hand, uses the channels to simulate a transmission in order to compute some performance metric.

An alternative categorization, still based on the channel modeling applications, is:

- *link level channel modeling*
- *system level channel modeling.*

**Link level** channel models aim to model realistically a single link only, i.e., the channel between one transmitter and one receiver.

**System level** channel models, on the other hand, consider more than one link and need to take into account also long term changing parameters, such as path-loss and shadow fading. The channels generated by a system level channel model are usually fed into a large scale system simulation. Therefore, the implementation of these models need to be very efficient since they are asked to compute thousands of time samples for hundreds of links.

If we now categorize channel models with respect to their modeling principle we can identify three different approaches:

- *stochastic channel models*, also known as *analytical channel models*
- *deterministic channel models*, also known as *geometry-based channel models*
- *hybrid channel models*, also known as *directional channel models*

The **analytical channel modeling** approach ignores all physical mechanisms which rule the propagation phenomenon and limit themselves to studying the channel coefficients as random variables. The modeling effort then focuses on describing these random processes properly.

**Deterministic channel modeling**, on the other hand, focuses on solving Maxwell's equations. Most deterministic channel models are based on the approximation of an electromagnetic wave as a ray, and are therefore also referred to as *ray-based* channel models.

**Hybrid channel models** are, as the name indicates, a mixture of the previous two approaches. They are established on some form of deterministic ray-based mechanism whereas several parameters are modeled statistically.

According to this last classification, Sections 3.2, 3.3, and 3.4 present the pros and cons of the three modeling approaches by giving examples of well established channel models.

The following publications contain surveys of MIMO channel models: [235, 150, 100, 73, 24, 158]. In particular, [24] deals in details with the 802.11n, the 3GPP SCM, and METRA models. In [73], the authors present some exemplary channel models to illustrate different modeling approaches for micro and macrocellular outdoor scenarios. They divide the channel models into: general statistically based models, more site-specific models based on measurement data, and entirely site-specific models. In [150] and [100], the authors focus on Directional Channel Models (DCMs), presenting in detail the channel model developed at the Technische Universiteit Eindhoven (TU/e). Molisch, in [158], covers most aspects of channel modeling, focusing on DCMs as well as deterministic channel modeling (ray-tracing). In [235], Yu and Ottersten divide channel models into physical and non-physical ones. Among the non-physical models they review the METRA and IST SATURN models. Among the physical ones they discuss the COST 259, the modified Saleh Valenzuela, and the one and two ring models.

### 3.1.1 Theoretical Investigations

Besides the applications stated in the previous section, there is one more purpose to channel modeling. When a very simple analytical channel model is proposed, occasionally it is possible to derive theoretical bounds for significant system parameters. For instance, the simplest channel model is the so-called *white channel*, usually denoted by the symbol $\boldsymbol{H}_{\mathrm{w}}$, which is characterized by channel coefficients that are i.i.d.[2] Zero Mean Circular Symmetric Complex Gaussian (ZMCSCG) [172]. This simple mathematical model allows researchers to derive theoretical results, such as the ergodic capacity in [81]. For more complicated channel models

[2] The acronym i.i.d. stands for *independent identically distributed*.

the derivation of theoretical results is either much more challenging or not possible at all (as in the case of ray-tracers for instance). For this reason, there exist many channel models whose realism is questionable but for which deriving analytical results is still feasible. Examples are the one-ring [192] and two-ring [191] models for which analytical forms of the covariance matrix and channel capacity can be derived.

### 3.1.2 Choosing the Right Channel Model

The choice of the channel model strongly influences the performance of the system under study. For instance, when trying to prove that the extension to MIMO is worth the costs, it is desirable to have channels very rich in multi path components. In fact, in this case the capacity grows linearly with the number of antennas used, while it grows only logarithmically with the transmit power applied, making a great argument in favor of MIMO techniques. On the other hand, if the channels are characterized by a Line of Sight (LOS) only, the MIMO advantage will be reduced to an antenna gain. In a similar way, the choice of the channel model can decide the fate of a specific transmit strategy with respect to other competitors. For this reason, the selection of the channel model, which should be driven only by scientific reasoning, might suffer also from political pressures.

### 3.1.3 Propagation Scenarios

In this section we have already mentioned the concept of *site dependency*. When a channel model is site dependent it means that the channels obtained from it are characteristic of a specific environment only. Clearly, for a system level analysis it is desirable to dispose of a channel model capable of generating typical channels for the scenarios in which the system under study will operate. Such a property is referred to as *site independence*, to stress that the channels generated by such a channel model are typical for a certain environment *kind*, and yet they are not specific to any particular location. Since the propagation conditions of a time variant frequency selective MIMO channel vary so much depending on the environment type, the first step in proposing a system level channel model is always the definition of *propagation scenarios*. The definition of scenarios is not trivial, and aims at identifying environments in which the propagation conditions are similar. Typical criteria used to distinguish among different scenarios are

- outdoor or indoor
- LOS regime
- maximum distance between receiver and transmitter, i.e., cell size
- user mobility
- base station height
- richness of multi path components
- maximum delay and angle spreads

Exemplary scenarios can be seen in Table 3.1 for the COST 259 channel model.

When the definition of the scenarios is complete, several measurements for each scenario need to be carried out, so that it is then possible to derive statistical descriptions of the main channel model parameters.

### 3.1.4 Antenna Dependency

Another important topic for channel modeling is the so-called *antenna dependency* or *antenna embedding*. When dealing with physical models it is possible to propose channel models which define the propagation phenomenon without considering the antennas. For instance, a ray-tracer models the propagation with a number of rays leaving the transmitter and reaching the receiver after several interacting points. Such a description is antenna independent, as the antenna characteristics are not considered yet. However, when computing the CIR, it is then obvious that the antenna responses need to be taken into account. In the ray-tracer example mentioned above, the path strengths of the rays are summed at the receiver after multiplying them with the antenna gains in the corresponding Direction Of Arrivals (DOAs). When the antenna beam patterns can be arbitrarily de-embedded from the propagation description, we have antenna independence. Geometry-based channel models can usually achieve a complete antenna de-embedding, while analytical models normally cannot.

### 3.1.5 Validation

The validation step of a new channel model is a particularly important phase of its development as it guarantees its validity and consequently its applicability. However, depending on the different nature of the channel model, this term denotes quite dissimilar procedures.

Deployment channel models are usually designed for certain classes of scenarios, such as indoor or outdoor. Within these limits, they need to prove to be capable of *predicting* the channels for an arbitrary environment. In this case, the validation is carried out by performing one or more channel measurements in different scenarios compatible with the capabilities of the channel model. Then, these specific environments are fed to the channel model which generates the synthetic channels. The measured and synthetic channels can then be compared directly. For instance, such a validation has been performed in [83], where a ray-tracer was used to model a scenario which was also measured.

In the case of channel models whose parameters are drawn from stochastic processes, such as the ones discussed in Section 3.4, the validation step requires a significant effort. In fact, these channel models are always *site independent*, meaning that they are capable of generating channels which are representative for a certain propagation scenario (for instance suburban), nevertheless are different from any particular channel measurement carried out in such a scenario, e.g., the town center of Ilmenau. In this case, the model cannot be compared directly to the measurements. The validation needs to be performed considering numerous

measured and synthetic channels, choosing a proper metric which analyzes the channels from a statistical point of view. A proper validation requires that the measurements used for the validation should not be he same used to derive the statistics of the model parameters. Since the effort for such procedure is not negligible, often the validation step consists in simply testing the correctness of the implementation. Such a validation has been carried out for the WINNER Phase I channel model in [46], also reviewed in Section 3.4.4.

Other channel models require their parameters to be obtained from one specific measurement. Then, they are capable of generating new channel realizations, statistically independent, yet which exhibit similar features, for instance the same spatial correlation, or the same fading statistics. This is the case of the channel models presented in Section 3.2. In this case, the validation consists in gathering the model parameters and then assess the *fitting* of the synthetic channels with respect to the measured ones for a proper metric. Such a validation has been carried out in [166] for the Kronecker, Weichselberger, and the virtual channel representation. The latter has been proposed by Sayeed in [189], whereas the other two are discussed in detail in Sections 3.2.2 and 3.2.3, respectively. The IlmProp channel model, proposed in Chapter 5 belongs to this third category. Its validation is discussed in Section 5.1.8.

Typical metrics used for validation are the fitting of spatial correlation matrices, power angular profiles, bit error rate curves, ergodic mutual information, outage capacity, diversity order, etc. Although the validation step delivers quantitative results, the choice of which metric to use and determining when the fitting is "good enough" is quite arbitrary. In addition, determining to which measured channels the synthetic ones should be compared to, influences greatly the results of the validation. As Prof. Jørgen Bach Andersen once said: "*you can always find an environment which fits your model*!". Eventually, the final validation for a channel model is carried out by the scientific community itself, in that the model's success is determined by the number of researchers who employ it.

## 3.2 Analytical Channel Models

Analytical channel models require generally less computational power than physical ones. They aim at modeling the channel coefficients themselves, while their parametrization is straightforward. Most analytical channel models which cope with MIMO systems are limited to frequency-flat time-invariant channels, as in [222, 118, 189]. When they do consider temporal variation and frequency selectivity they normally treat them separately from the spatial domain, such as in [54, 84, 173, 161]. In doing so, the joint statistics in time, frequency, and space are not preserved. More sophisticated ways of incorporating the joint statistics result in *hybrid models* (dealt in Section 3.4), such as [59, 231]. Note that Section 5.2.6 proposes a new tensor based fully analytical channel model which can generate realistic time variant frequency selective channels.

In this section we concentrate only on pure analytical channel models which aim at modeling the correlation between the antennas of a MIMO system. The following sections present

the most well known mechanisms in reproducing spatial correlation.

### 3.2.1 Full Spatial Correlation Matrix Channel Model

Let us assume a stationary, zero-mean, time invariant, and flat-fading MIMO channel. Under these assumptions it is possible to fully characterize it with second-order statistics. Let $M_{\mathrm{R}}$ and $M_{\mathrm{T}}$ represent the number of antennas at the receiver and transmitter, respectively. The most general way of achieving a channel realization $\boldsymbol{H} \in \mathbb{C}^{M_{\mathrm{R}} \times M_{\mathrm{T}}}$ is by

$$\mathrm{vec}\left\{\boldsymbol{H}\right\} = \boldsymbol{R}_{\mathrm{full}}^{\frac{1}{2}} \cdot \mathrm{vec}\left\{\boldsymbol{H}_{\mathrm{w}}\right\}, \tag{3.1}$$

where the matrix $\boldsymbol{H}_{\mathrm{w}} \in \mathbb{C}^{M_{\mathrm{R}} \times M_{\mathrm{T}}}$, also referred to as the white channel [172], contains i.i.d. ZMCSCG random numbers with zero mean and unit variance. The matrix $\boldsymbol{R}_{\mathrm{full}}^{\frac{1}{2}}$ is computed as

$$\boldsymbol{R}_{\mathrm{full}}^{\frac{1}{2}} = \boldsymbol{U} \cdot \boldsymbol{\Sigma}^{\frac{1}{2}} \cdot \boldsymbol{U}^{\mathrm{H}} \tag{3.2}$$

by carrying out an EigenValue Decomposition (EVD) on $\boldsymbol{R}_{\mathrm{full}}$, as

$$\boldsymbol{R}_{\mathrm{full}} = \boldsymbol{U} \cdot \boldsymbol{\Sigma} \cdot \boldsymbol{U}^{\mathrm{H}} \tag{3.3}$$

and $\boldsymbol{\Sigma}^{\frac{1}{2}}$ is obtained by applying the square root on the elements of the diagonal of $\boldsymbol{\Sigma}$. The vec$\{\cdot\}$ operator stacks all the columns of the matrices as one column vector of size $M_{\mathrm{R}} \cdot M_{\mathrm{T}} \times 1$. The square matrix $\boldsymbol{R}_{\mathrm{full}} \in \mathbb{C}^{M_{\mathrm{R}} \cdot M_{\mathrm{T}} \times M_{\mathrm{R}} \cdot M_{\mathrm{T}}}$ is the *full spatial correlation matrix* and exhaustively characterizes the channel by defining the correlation between any two antennas present in the system. The full correlation matrix can be written as

$$\boldsymbol{R}_{\mathrm{full}} = \mathrm{E}\left[\mathrm{vec}\left\{\boldsymbol{H}\right\} \cdot \mathrm{vec}\left\{\boldsymbol{H}\right\}^{\mathrm{H}}\right], \tag{3.4}$$

where the superscript $\{\cdot\}^{\mathrm{H}}$ is the Hermitian transpose, i.e., conjugate transpose. The matrix $\boldsymbol{R}_{\mathrm{full}}$, being a correlation matrix, is by definition Hermitian, and therefore only close to half of its elements can be chosen independently. More precisely the elements of the diagonal and the ones of one of the two triangular matrices (strictly upper or lower triangular). Furthermore, if we assume that the channel is Wide Sense Stationary (WSS) in space, the full spatial correlation matrix becomes Toeplitz. An extension to this approach to more than two dimensions is discussed in Section 5.2.6.

### 3.2.2 The Kronecker Channel Model

The well known Kronecker channel model [55] assumes independent spatial correlations at the receiver and transmitter ends. This implies that the full spatial correlation matrix in equation (3.4) can be factored into a Kronecker product

$$\boldsymbol{R}_{\mathrm{full}} = \boldsymbol{R}_{\mathrm{T}}^{*} \otimes \boldsymbol{R}_{\mathrm{R}}, \tag{3.5}$$

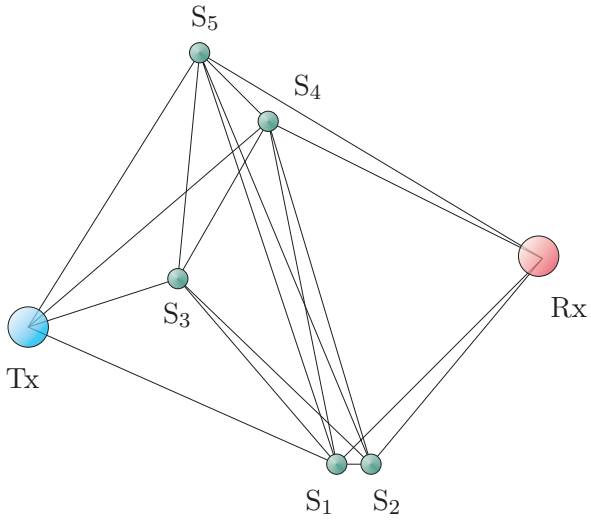


Fig. 3.1: The figure shows a simple propagation model for which the Kronecker approximation holds. All scatterers seen by the transmitter, namely $S_1$, $S_3$, $S_4$, and $S_5$ are connected to all scatterers seen by the receiver: $S_1$, $S_2$, $S_4$, and $S_5$.

where $\otimes$ denotes the Kronecker product[3], and the matrices $\boldsymbol{R}_{\mathrm{R}} \in \mathbb{C}^{M_{\mathrm{R}} \times M_{\mathrm{R}}}$ and $\boldsymbol{R}_{\mathrm{T}} \in \mathbb{C}^{M_{\mathrm{T}} \times M_{\mathrm{T}}}$ are defined as

$$\begin{aligned} \boldsymbol{R}_{\mathrm{R}} &= \frac{1}{\sqrt{P}} \, \mathrm{E}\left[\boldsymbol{H} \cdot \boldsymbol{H}^{\mathrm{H}}\right] \\ \boldsymbol{R}_{\mathrm{T}} &= \frac{1}{\sqrt{P}} \, \mathrm{E}\left[\boldsymbol{H}^{\mathrm{H}} \cdot \boldsymbol{H}\right], \end{aligned} \tag{3.6}$$

where the power $P$ is computed as the expectation of the Frobenius norm of the channel matrix, namely

$$P = \mathrm{E}\left[\|\boldsymbol{H}\|_{\mathrm{F}}^2\right]. \tag{3.7}$$

Even though several measurements proved its validity [118, 153, 234], others have shown its deficiencies [167, 78, 222]. It has been observed that the Kronecker approximation holds in real channels when all scatterers illuminated by the transmitter are interconnected with all scatterers which radiate towards the receiver. Such a scenario is depicted in Figure 3.1. All scatterers seen by the transmitter, namely $S_1$, $S_3$, $S_4$, and $S_5$ are connected to all scatterers which are connected to the receiver, i.e., $S_1$, $S_2$, $S_4$, and $S_5$.

Another consequence of the Kronecker assumption is that the joint power azimuthal profile $P(\varphi_{\mathrm{R}}, \varphi_{\mathrm{T}})$, introduced on page 42, becomes a separable function, so that:

$$P_{\mathrm{joint}}(\varphi_{\mathrm{R}}, \varphi_{\mathrm{T}}) = P_{\mathrm{R}}(\varphi_{\mathrm{R}}) \cdot P_{\mathrm{T}}(\varphi_{\mathrm{T}}), \tag{3.8}$$

where $P_{\mathrm{R}}(\varphi_{\mathrm{R}})$ and $P_{\mathrm{T}}(\varphi_{\mathrm{T}})$ are the marginal power angular profiles at the receiver and transmitter, respectively. Figure 3.2 shows these functions for a simple propagation model, similar to the one depicted in Figure 3.1, where the Kronecker assumption holds.

In order to generate synthetic channels with the correlation properties described by $\boldsymbol{R}_{\mathrm{R}}$

[3] the Kronecker product is also called the *matrix direct product* [190].

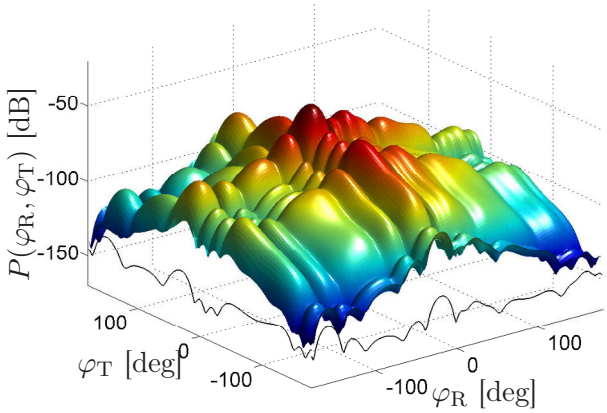


Fig. 3.2: Joint power azimuthal profile $P(\varphi_R, \varphi_T)$ for a simple synthetic propagation model. The curves represent the marginal power azimuthal profiles for the receiver $P_R(\varphi_R)$ and transmitter $P_T(\varphi_T)$.

and $\boldsymbol{R}_T$, we use equation (3.1), which, thanks to the Kronecker structure, can be written as

$$\boldsymbol{H} = \boldsymbol{R}_R^{\frac{1}{2}} \cdot \boldsymbol{H}_w \cdot (\boldsymbol{R}_T^{\frac{1}{2}})^H. \tag{3.9}$$

The main advantages in employing the Kronecker model with respect to the full spatial correlation matrix channel model are

- the spatial correlation properties of the channel can be estimated separately at the link-ends.
- the number of parameters needed is reduced
- the synthesis of channel matrices is cheaper.

Despite the advantages, the Kronecker simplification destroys completely any dependence of the Direction Of Departures (DODs) with the DOAs. This, among other effects, leads to channels with a lower ergodic capacity [222].

### 3.2.3 The Weichselberger Channel Model

The Weichselberger model [222] exploits both the simplicity of the Kronecker model [118], as well as the advantages of the *virtual channel representation* proposed by Sayeed [189]. The idea behind the Weichselberger model lies in the decomposition of the eigenstructure of the full spatial correlation matrix into receiver and transmit side, rather than the correlation matrix itself. By applying an EigenValue Decompostion (EVD) of the full spatial correlation matrix $\boldsymbol{R}_{full}$, we have

$$\boldsymbol{R}_{full} = \boldsymbol{U}_{full}\ \boldsymbol{\Lambda}_{full}\ \boldsymbol{U}_{full}^H, \tag{3.10}$$

and with two more EVD's carried out on the matrices $\boldsymbol{R}_{\mathrm{R}}$ and $\boldsymbol{R}_{\mathrm{T}}$ we obtain

$$\begin{aligned} \boldsymbol{R}_{\mathrm{R}} &= \boldsymbol{U}_{\mathrm{R}}\ \boldsymbol{\Lambda}_{\mathrm{R}}\ \boldsymbol{U}_{\mathrm{R}}^{\mathrm{H}} \\ \boldsymbol{R}_{\mathrm{T}} &= \boldsymbol{U}_{\mathrm{T}}\ \boldsymbol{\Lambda}_{\mathrm{T}}\ \boldsymbol{U}_{\mathrm{T}}^{\mathrm{H}}. \end{aligned} \tag{3.11}$$

The Weichselberger model proposes to decompose in a Kronecker way the eigenspace of $\boldsymbol{R}_{\mathrm{full}}$, assuming that

$$\boldsymbol{U}_{\mathrm{full}} \approx \boldsymbol{U}_{\mathrm{T}} \otimes \boldsymbol{U}_{\mathrm{R}}. \tag{3.12}$$

The synthesis of new channel realizations is obtained by

$$\boldsymbol{H} = \boldsymbol{U}_{\mathrm{R}}\ \left(\boldsymbol{\Omega}^{\frac{1}{2}} \odot \boldsymbol{H}_{\mathrm{w}}\right)\ \boldsymbol{U}_{\mathrm{T}}^{\mathrm{T}}, \tag{3.13}$$

where the white channel $\boldsymbol{H}_{\mathrm{w}}$ has size $M_{\mathrm{R}} \times M_{\mathrm{T}}$, the symbol $\odot$ indicates the Schur element-wise product, and the matrix $\boldsymbol{\Omega}$ is the *coupling matrix*, computed as

$$\boldsymbol{\Omega} = \mathrm{E}\left[\left(\boldsymbol{U}_{\mathrm{R}}^{\mathrm{H}}\ \boldsymbol{H}\ \boldsymbol{U}_{\mathrm{T}}^{*}\right) \odot \left(\boldsymbol{U}_{\mathrm{R}}^{\mathrm{T}}\ \boldsymbol{H}^{*}\ \boldsymbol{U}_{\mathrm{T}}\right)\right], \tag{3.14}$$

where the superscripts $(\cdot)^{T}$,$(\cdot)^{H}$, and $(\cdot)^{*}$ denote transpose, Hermitian transpose, and conjugate, respectively. The coupling matrix $\boldsymbol{\Omega} \in \mathbb{C}^{M_{\mathrm{R}} \times M_{\mathrm{T}}}$ contains the eigenvalues of the full spatial correlation matrix and represents the average power coupling between each receive eigenmode with each transmit eigenmode. The Weichselberger model is a good compromise between simplicity of the model (thus yielding a lower computational complexity) and the correct description of the correlation between all antennas in the MIMO system [222].

In a recent publication [60], a tensor extension of the Weichselberger model has been proposed. A more general approach to analytical channel modeling based on tensors is discussed in Section 5.2.6.

## 3.3 Deterministic Channel Models

*Deterministic* or *physical models* use the physical laws which describe the wireless propagation phenomenon to model the channel. For this aim, they require a detailed description of the environment around the antennas, which, in most cases, is obtained with a significant effort. This modeling approach is obviously *site dependent*, as only by defining meticulously a scenario it is possible to simulate the actual physical wave propagation process which would take place in it.

The propagation of ElectroMagnetic (EM) waves and their interaction with objects can be modeled following two main approaches

- the full-wave approach
- the Geometrical Theory of Diffraction (GTD) approach.

which we explain in detail in the following sections.

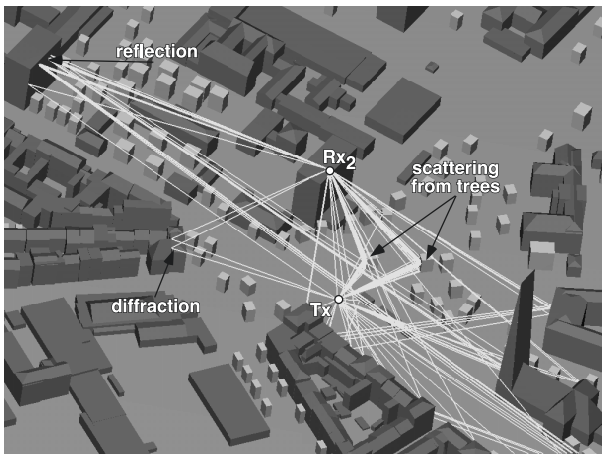


Fig. 3.3: The figure shows the digital representation of the city of Karlsruhe, Germany. The rays were computed with the ray-tracer from Prof. Wiesbeck's group [83].

### 3.3.1 Full-Wave Approach

The so-called *full-wave approach* consists is applying Maxwell's equations directly, either in integral or in differential form. The integral equations are particularly suited to describe the propagation in the vicinity of inhomogeneous objects in an infinite homogeneous medium. The most common numerical method used to solve these equations is the Method of Moments (MoM).

Differential equations, on the other hand, exist in different forms and are solved by discretizing the computational domain on a lattice. The two most used methods are the Finite Difference in Time Domain method (FDTD) and the Finite Element Method (FEM). Although very accurate, the full-wave approach is rather expensive from a computational complexity point of view. Additionally, as already mentioned, detailed information on the geometry and electromagnetic properties of all the objects in the environment is needed. Therefore, when applied to wireless channel modeling, rough approximations need to be taken to decrease the computational complexity, such as in [107], where the surfaces are assumed magnetically perfectly conducting (soft surfaces), with no transverse variations, and no back scattering. These methods find larger consent in other applications, such as predicting the beam pattern of an antenna [106].

### 3.3.2 GTD Approach

The *GTD approach*, as in Geometrical Theory of Diffraction [117, 152], approximates planar electromagnetic waves with *rays*. Therefore, GTD based models are also called *ray-tracers*. The accuracy of GTD grows for higher frequencies and for objects much larger than the wavelength. These models are also referred to as *asymptotic methods*, as they become exact for the frequency going to infinity. Further research led to the Uniform geometrical Theory of Diffraction (UTD) [132], and to the Uniform Asymptotic Theory of diffraction (UAT) [40, 148].

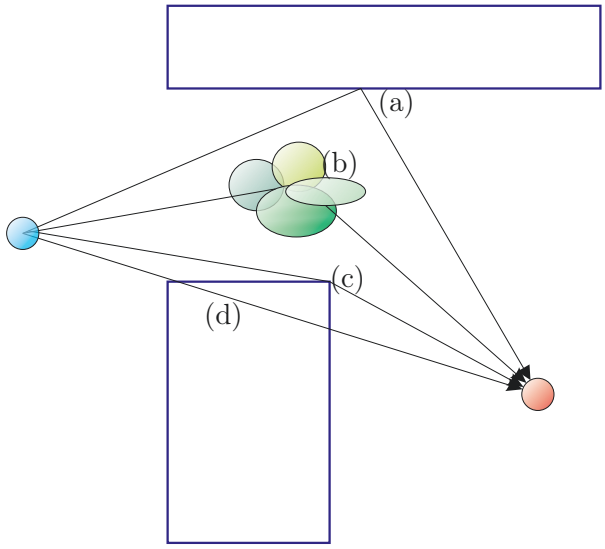


Fig. 3.4: The figure shows four possible propagation mechanisms experienced by rays: (a) reflection, (b) scattering or diffuse reflection, (c) edge diffraction, and (d) transmission or penetration.

Note that UTD and UAT are better models in the transition regions around the object boundaries, while they reduce to GTD outside these regions. An exemplary outdoor model based on UTD is the one developed by van Dooren in his doctoral dissertation [214], or the one by Jong de and Herben [112], or the one proposed by Prof. Wiesbeck's group [83]. Figure 3.3 depicts an exemplary scenario for the latter channel model. Ray-tracers have been developed also for indoor scenarios, such as the one proposed by Valenzuela [213]. Most ray-tracing channel models can cope with four kinds of interactions:

- reflection
- transmission
- diffraction
- scattering

Figure 3.4 shows an example of these four propagation mechanisms. Reflections, transmissions, and diffraction can be described by Geometrical Optics (GO) and UTD or UAT. On the other hand, scattering, which is the dispersion of radio waves due to an interaction with objects with irregular structure of surfaces (such as trees or complicated buildings' facades), is more complex to describe and more empirical approaches are taken [150, 100].

## 3.4 Hybrid Channel Models

As seen in Section 3.3, deterministic channel models can be applied neither when dealing with large scale system simulations, nor with site independent system performance evaluations. In fact, although very accurate, they require a detailed description of the scenario, which makes

them site dependent; furthermore they are highly computational complex, making the effort of computing the CIR for numerous users prohibitive.

Analytical channel models would be better suited as they can be site independent and can generate channels for a considerable number of users at a very low computational cost. However, as underlined in Section 3.2, they cannot cope well with time variant frequency selective channels.

Hybrid channel models were proposed to solve the drawbacks of both analytical and deterministic channel models when applied to system level simulations and to system performance evaluations. They are based on both deterministic and stochastic modeling approaches. Most hybrid channels are based on the *directional channel modeling* (DCM) concept. The channel coefficients are computed as a sum of rays, just like a ray-tracer would do, however the Direction Of Departure (DOD), Time Delay Of Arrival (TDOA), path-strength and other parameters of each ray are realizations of random processes. Note that the assumption that the electromagnetic field in space can be computed as a superposition of plane waves was introduced in the 70's, where the reference publication on the matter is [110] by Jakes.

The following subsections present well established DCM based channel models: the COST 259 SCM, the 3GPP SCM, the WINNER SCME and the WINNER WIM.

### 3.4.1 COST 259 Geometry-based Stochastic Channel Model (GSCM)

The COST 259 Spatial Channel Model [59] represents the first significant choral work based on the Directional Channel Model (DCM) concept. The model is based on the Double Directional Channel Impulse Response (DDCIR) approach

$$h(n, m, \boldsymbol{r}, \tau, \theta^{\mathrm{R}}, \theta^{\mathrm{T}}) = \sum_{l=1}^{L(\boldsymbol{r})} h_l(n, m, \boldsymbol{r}, \tau, \theta^{\mathrm{R}}, \theta^{\mathrm{T}}), \tag{3.15}$$

where $n$ and $m$ are the indices identifying the $n$-th receiver and $m$-th transmit antennas, respectively. The vector $\boldsymbol{r}$ contains the relative position of the receiver with respect to the transmitter, $\tau$ is delay time, while $\theta^{\mathrm{R}}$, and $\theta^{\mathrm{T}}$ are the Angles of Arrival (AoA) and Angle of Departure (AoD), respectively. The term $h_l(\boldsymbol{r}, \tau, \theta^{\mathrm{R}}, \theta^{\mathrm{T}})$ is the channel response for the $l$-th impinging wave out of a total of $L(\boldsymbol{r})$ rays. The model parametrization relies greatly on previous projects: COST 231 [64], COST 207 [74], TSUNAMI-II [157], Magic Wand [99], and METAMORP [227].

The COST 259 modeling framework consists of three levels, depicted in Figure 3.5. The first level sees three different *cell types*: macro, micro, and pico. As the names suggest, they differ in the possible distances between mobiles and the Base Station (BS). For each cell type there exist several *Radio Environments* (RE's), which characterize different scenarios. The acronyms of the RE's are reported in Table 3.1. Within one RE, the propagation conditions encountered are characterized by proper parameters, also called *Global Parameters* (GP's). The GP's are defined statistically by Probability Density Functions (PDFs) or by moments.

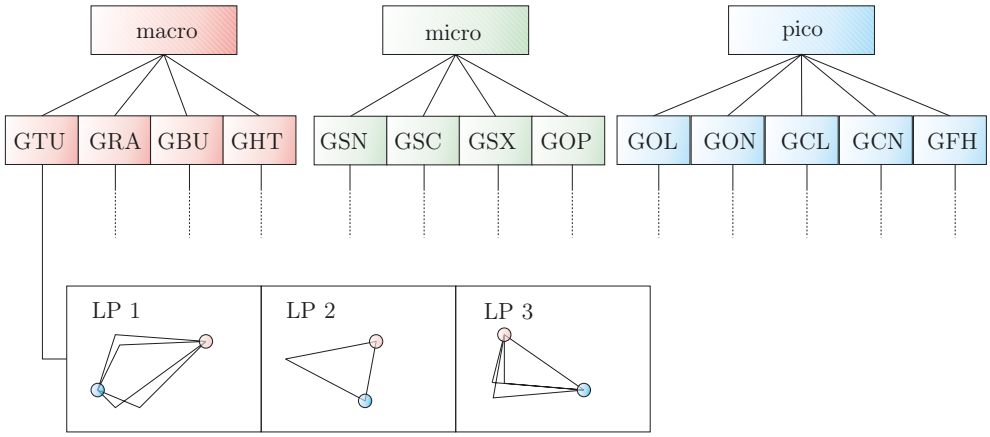


Fig. 3.5: The COST 259 three level modeling framework. The acronyms are given in Table 3.1.

| Symbol | Acronym | Symbol | Acronym |
|---|---|---|---|
| GTU | General Typical Urban | GOP | General Open Place |
| GRA | General Rural Area | GOL | General Office LOS |
| GBU | General Bad Urban | GON | General Office NLOS |
| GHT | General Hilly Terrain | GCL | General Corridor LOS |
| GSN | General Street NLOS | GCN | General Corridor NLOS |
| GSC | General Street Canyon | GFH | General Factory or Hall |
| GSX | General Street Crossing | | |

Tab. 3.1: Acronyms for the Global Parameters (GP) of the COST 259 Channel Model depicted in Figure 3.5

The third level is constituted by the propagation scenarios themselves, which are obtained by generating realizations of the GP's for a specific RE. The random instances are called *Local Parameters* (LP's).

Small-scale variations originate from the fact that different Multi-Path Components (MPCs) sum at the receiver with different phases as the mobile moves. On the other hand, large-scale fluctuations are modeled by letting some LP's drift, and by a birth-death mechanism of the MPCs. Furthermore, the MPCs are organized as clusters, so that several rays share similar parameters (i.e., DOA, delay, and so on). The large-scale behavior of different clusters is independent while it is the same for all MPCs which belong to the same cluster.

### 3.4.2 3GPP Spatial Channel Model (SCM)

The groups 802.11 and 3GPP, in order to answer to the need of reliable MIMO channel models, proposed the 3GPP Spatial Channel Model (SCM) [72, 39]. The model defines three environments (Suburban Macro, Urban Macro, and Urban Micro) where the latter is

differentiated in Line Of Sight (LOS) and Non-LOS (NLOS) propagation. There is a fixed number of 6 *paths* in every scenario, each represented by a Dirac function in delay domain, but made up of 20 spatially separated *sub-paths* according to the sum of sinusoids method. The 20 sub-paths form a Zero Delay Spread Cluster (ZDSC), as they all arrive in the same Time Delay Of Arrival (TDOA). Path powers, path delays, and angular properties for both sides of the link are modeled as random variables defined through PDFs and cross correlation functions. All parameters, except for fast-fading, are drawn independently in time, in what is termed *drops*. In other words, for every drop all long term parameters are independently generated from stochastic processes. Within a drop, the fast-fading is obtained by summing the different sub-paths, each having a slightly different Doppler shift.

The *drop* approach constitutes both the advantage and disadvantage of this channel model. With this simplification, in fact, the generation of a significant number of channels is extremely efficient, as the computation of the long term parameters is cheap, and the subsequent generation of a time snapshot is the well known sum of sinusoid method, whose implementation can be highly optimized. An efficient MATLAB® implementation has been presented in [28]. It is available under a public license in [29]. Although very computationally efficient, the drop method does not model realistically the long term time variations of the channel. In fact, each drop can be considered as a totally independent scenario in which all parameters are randomly drawn. To solve this problem and improve other issues, an extension to the 3GPP SCM was proposed within the EU project WINNER. The next subsection presents this model.

### 3.4.3 WINNER Spatial Channel Model Extended (SCME)

Within the WINNER project, the channel modeling work package (WP5) developed an extension to the 3GPP SCM model presented in the previous section. The model is called *Interim Channel Model for Beyond-3G Systems* and denoted SCME, as Spatial Channel Model Extended. The model was presented in [1] and a public implementation is available at [45]. The SCM is defined for a 5 MHz bandwidth CDMA system in the 2 GHz band, whereas the WINNER system parameters are 100 MHz in both 2 and 5 GHz frequency range. Other issues which constituted a drawback for the WINNER goals were the drop based concept, i.e., no short-term system-level time-variability in the model, the lack of Ricean K-factor models (LOS support) for macro scenarios, and the lack of a rural scenario.

To obtain a larger bandwidth, the 20 sub-paths of the original SCM are divided into *mid-paths*, so that each mid-path has a slightly different TDOA. This introduces an intra-cluster delay spread, which was already proposed by Saleh and Valenzuela [187] for indoor and by the COST 259 [59] for outdoor propagation.

To obtain a more realistic time variant channel the SCME implements the drifting of the TDOAs and of the Angles of Arrival (AoA's) and Angles of Departure (AoD's), as well as a drifting of the shadow fading. More details can be found in [1].

### 3.4.4 WINNER Phase I Channel Model (WIM)

The channel modeling work package (WP5) of the WINNER project proposed a channel model in [46]. This model is the outcome of the first two year long phase of the EU funded project. The model has been defined for seven specific scenarios and takes a similar approach as the 3GPP SCM described in Section 3.4.2. A large set of long term varying parameters, called *bulk parameters*, are defined for each scenario. For each *channel segment*, i.e., drop as in the SCM nomenclature, the bulk parameters are drawn from random processes. The channel is computed as a sum of rays organized in a number of ZDSCs. Their delays and directional properties are generated from statistical distributions (different for each scenario), which are obtained from measurement results or from the literature. The number of ZDSCs varies from one scenario to another. The number of rays within one ZDSC is set to 10, so that they all possess the same delays and powers and may differ only in angles of departure or arrival. The WINNER model is antenna independent, as different antenna configurations can be simulated. The WINNER Phase I channel model does not include any temporal variability of the bulk parameters, and is therefore limited to the drop approach already proposed in the 3GPP SCM.

# 4. POLARIMETRIC ANTENNA RESPONSE MODELING

This chapter presents the modeling approaches for the polarimetric antenna response, i.e., the description on how the ElectroMagnetic (EM) wave propagates from an antenna into the far-field.

In Section 4.1 we introduce the major principles of antenna theory, including the definitions of the Poynting vector (Section 4.1.1), the antenna gain and directivity functions (Section 4.1.2), the link budget and path-loss (Section 4.1.3), and the polarimetric radiation pattern (Section 4.1.4). In Section 4.1.5, we define the polarimetric antenna array response, which describes all array sensors at once. In Section 4.1.6, we show typical antenna arrays used in practice to perform channel sounding, i.e., channel measurements.

The polarimetric radiation patterns defined in Section 4.1.4 give the most accurate description of the behavior of an antenna. Furthermore, this information is crucial in a geometry-based channel model like the IlmProp, as discussed in Chapter 5.

In Sections 4.2, 4.3, and 4.4 we describe three modeling approaches for these functions, namely the angular domain representation, the Effective Aperture Distribution Function (EADF), and the Discrete Vector Spherical Fourier Transform (DVSFT)-based model, respectively. The first two methods do not consider the spherical symmetries correctly as they are based on a two-dimensional (2D) representation of the signals. The novel DVSFT-based model, on the other hand, operates in the natural Fourier domain for complex vector functions defined on the sphere. The latter method leads to novel applications which include accurate interpolation, measurement noise reduction, SNR estimation, and improvements of the measurement process. Nonetheless, the EADF represents the most efficient solution for the accuracy required by a geometry-based channel model. In order to take advantage of the benefits brought by the DVSFT-based model, in Section 4.5, we combine the two methods in a two-steps processing scheme which represents the optimal choice for the IlmProp.

Notice that in this chapter a few vectors will be denoted by bold capital letters, such as the electric field or the Poynting vector. We do this to be consistent with the notation used in most physics books.

## 4.1 Antennas and The Polarimetric Radiation Patterns

Antennas are the devices, essential for wireless communications, through which we are able to send and receive ElectroMagnetic (EM) waves. EM waves in the *far-field region*[1] are transversal in nature, i.e., both electric and magnetic fields are orthogonal to the direction of propagation. While near the transmitting antenna the EM fields assume quite complicated forms, in the far-field they can be described by simple equations. They are given, in one form or the other, in all antenna theory books, such as [105, 70]. However, we feel that Paraboni in [169, pp. 2-4] presents the most appropriate for our aims. The fields assume the following expressions

$$\begin{aligned} \boldsymbol{E}(\vartheta,\varphi,r,t) &= \Re\left\{\sqrt{\eta_0}\ \frac{\mathrm{e}^{-j(kr-\omega t)}}{r}\left[b_\vartheta(\vartheta,\varphi)\,\boldsymbol{e}_\vartheta + b_\varphi(\vartheta,\varphi)\,\boldsymbol{e}_\varphi\right]\right\} \\ \boldsymbol{H}(\vartheta,\varphi,r,t) &= \Re\left\{\frac{1}{\sqrt{\eta_0}}\ \frac{\mathrm{e}^{-j(kr-\omega t)}}{r}\left[-b_\vartheta(\vartheta,\varphi)\,\boldsymbol{e}_\vartheta + b_\varphi(\vartheta,\varphi)\,\boldsymbol{e}_\varphi\right]\right\}, \end{aligned} \tag{4.1}$$

where $r$, $\vartheta$ and $\varphi$ are the radius, co-elevation and azimuth, respectively, as defined in Appendix E, and depicted in Figure E.2. The real vectors $\boldsymbol{E}$ and $\boldsymbol{H}$ represent the electric and magnetic fields, respectively, so that their norm is the intensity and their direction specifies how the fields are oriented. They depend on the point where they are observed, and at any given instant they are orthogonal with respect to each other and to the radial direction. The unit vectors $\boldsymbol{e}_\vartheta$ and $\boldsymbol{e}_\varphi$, directed towards positive azimuth and co-elevation angles, are defined in Appendix E. The intrinsic impedance of free space is $\eta_0$. If $\mu_0$ and $\epsilon_0$ are the vacuum permeability and permittivity, respectively, then

$$\eta_0 = \sqrt{\frac{\mu_0}{\epsilon_0}}. \tag{4.2}$$

The term $k$ is the *phase constant* also known as *wave number*[2]:

$$k = \frac{2\pi}{\lambda}, \tag{4.3}$$

where $\lambda$ is the wavelength. The functions $b_\vartheta(\vartheta,\varphi)$ and $b_\varphi(\vartheta,\varphi)$ are the *polarimetric antenna radiation patterns*, which are specific to each antenna and can be normally measured in the antenna's calibration stage. They will be covered in detail in Section 4.1.4. The term $\omega$ is the *angular frequency*, so that if $c$ is the wave's velocity, then $\omega = k \cdot c$.

Equation (4.1) shows how the electric field radiated by an antenna is a time variant vector field. The amplitude of the field decreases with the distance from the antenna $r$ as $r^{-1}$. The complex exponential $\mathrm{e}^{-j(kr-\omega t)}$ describes the field's evolution in time $t$ at a certain radius

[1] The *far-field* or *Fraunhofer region* is defined as that region, where "the relative angular distribution of the [radiated] field becomes essentially independent of distance" [37]. For an antenna of overall dimension $D > \lambda$, this region is obtained at distances greater than $2D^2/\lambda$, where $\lambda$ is the wavelength.

[2] The vector $\boldsymbol{k} = k \cdot \boldsymbol{e}_\mathrm{d}$, also introduced in Section 2.2.2, is usually called *wave vector* [51]. The unit vector $\boldsymbol{e}_\mathrm{d}$ points towards the direction of propagation.

$r$. The complex functions $b_\vartheta(\vartheta,\varphi)$ and $b_\varphi(\vartheta,\varphi)$, on the other hand, describe the angular variation of the field, and determine the direction towards which $\boldsymbol{E}$ is oriented.

### 4.1.1 The Poynting Vector

Defining the instantaneous electromagnetic power which enters an antenna, normally through a coaxial line, is straightforward, being the product of voltage and electrical current at the antenna port. Much more complicated is defining the power which exits the antenna in form of propagating electromagnetic waves. We now define the Poynting vector $\boldsymbol{S}$ as

$$\boldsymbol{S} = \boldsymbol{E} \times \boldsymbol{H}^\star, \tag{4.4}$$

where $\boldsymbol{E}$ and $\boldsymbol{H}$ are the electric and magnetic fields, respectively, and the superscript $(\cdot)^\star$ indicates the complex conjugate. The spatio-temporal dependencies, namely from $\vartheta$, $\varphi$, $r$, and $t$, have been omitted for simplicity. The symbol $\times$ indicates the cross product (see Section B.2). Thus, the Poynting vector is parallel to the direction of propagation. Since the ratio between $\|\boldsymbol{E}\|$ and $\|\boldsymbol{H}\|$ is constant, we can also write

$$\boldsymbol{S} = \frac{\|\boldsymbol{E}\|^2}{\eta_0}\,\boldsymbol{e}_r, \tag{4.5}$$

where $\boldsymbol{e}_r$ is the radial unit basis vector[3] and $\eta_0 = \sqrt{\frac{\mu_0}{\epsilon_0}} = 377\,\Omega$ is the free space intrinsic impedance. The norm of the Poynting vector, denoted by $\|\boldsymbol{S}\|$, is expressed in $\mathrm{W/m^2}$, and it can be interpreted as a local power flow. This definition, however, has to be taken carefully, since we could set up a permanent magnet to create a static magnetic field, and a pair of charged metallic plates to induce a static electric field. Even though a non-zero Poynting vector exists, there is evidently no power dissipation in the system. To avoid such misunderstandings, the Poynting vector must be integrated on a closed surface in the three-dimensional space. In practical cases, however, the Poynting vector, when originated from a radiating antenna, is used also locally, i.e., by integrating it on an open surface.

### 4.1.2 Antenna Gain, Directivity Functions, and Efficiency

The norm of the Poynting vector denoted by $S(\vartheta,\varphi) = \|\boldsymbol{S}(\vartheta,\varphi)\|$ expresses the *power density of radiation* since its integral on a surface gives a power. This quantity is usually compared to the intensity of radiation $S_i$ of an ideal lossless isotropic radiator, which can be easily computed as

$$S_i = \frac{P_\mathrm{T}}{4\pi r^2}, \tag{4.6}$$

where $P_\mathrm{T}$ is the transmit power at the antenna port, and $r$ is the radius at which $S_i$ is computed. We can now express any intensity of radiation $S(\vartheta,\varphi)$ with the help of the so-

[3] See Appendix E.2 for the polar coordinate system.

called *directivity function* $d(\vartheta, \varphi)$, as

$$S(\vartheta, \varphi) = S_i \cdot d(\vartheta, \varphi). \tag{4.7}$$

The maximum of the directivity function $d_{\max}$, usually referred to as the *antenna directivity*, expresses the maximum intensity of radiation normalized to the average intensity.

The following equation holds for the directivity function

$$\int_{\mathcal{S}^2} d(\vartheta, \varphi)\ \mathrm{d}\Omega = 4\pi, \tag{4.8}$$

where the integral is carried out over the solid angle $\Omega$ on the entire surface of the unit sphere, denoted by $\mathcal{S}^2$.

We now introduce the *antenna gain function* $g(\vartheta, \varphi)$, defined as the ratio between the power actually transmitted in the direction of $\vartheta$ and $\varphi$, to the one which would be radiated by an isotropic antenna.

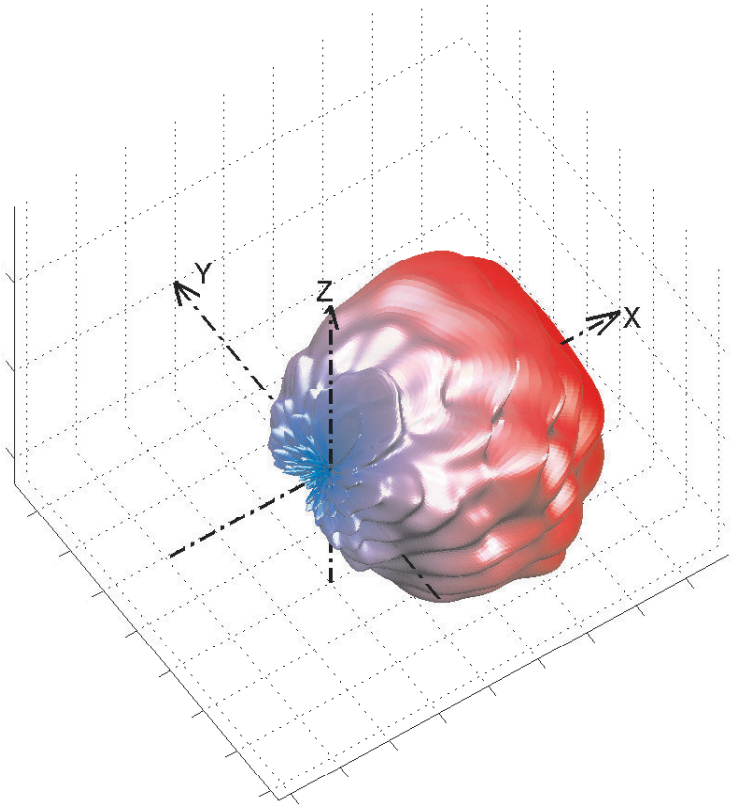


Fig. 4.1: The measured antenna gain function $g(\vartheta, \varphi)$ of an element of a Stacked Polarimetric Uniform Circular Patch Array (SPUCPA) having 192 elements in total, disposed on four rings.

Figure 4.1 shows the gain function $g(\vartheta, \varphi)$ of one element of a Stacked Polarimetric Uniform Circular Patch Array (SPUCPA) having 192 elements in total. A picture of the antenna array

can be seen in Figure 4.5 on page 75.

Let $\xi$ be the *antenna efficiency*, defined as

$$\xi = \frac{g(\vartheta, \varphi)}{d(\vartheta, \varphi)}. \tag{4.9}$$

The antenna efficiency expresses the losses of the antenna. The *antenna gain* is the maximum value assumed by the antenna gain function, which we denote by $g_{\max}$. In a lossless antenna we have $\xi = 1$, and thus $g_{\max} = d_{\max}$.

The power fed to the antenna $P_{\mathrm{T}}$ can then be expressed as

$$P_{\mathrm{T}} = \frac{1}{\xi} \int_{\mathcal{S}^2} S(\vartheta, \varphi) \, \mathrm{d}\Omega. \tag{4.10}$$

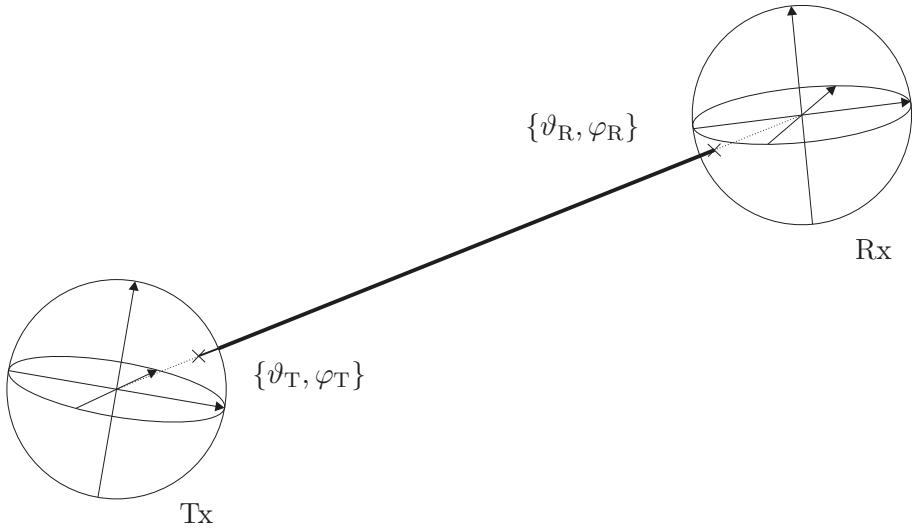


Fig. 4.2: A direct LOS link between two antennas. The angles of arrival and departure in the corresponding coordinate systems are indicated.

Let us assume a direct link, as shown in Figure 4.2, between a receiving (Rx) and a transmitting (Tx) antenna. The figure shows the angles of arrival and departure, expressed by $\{\vartheta_{\mathrm{R}}, \varphi_{\mathrm{R}}\}$ and $\{\vartheta_{\mathrm{T}}, \varphi_{\mathrm{T}}\}$, respectively. Notice that the co-elevation and azimuth angles are expressed with respect to a local coordinate system.

The receiving properties of an antenna are usually characterized by the so-called *effective area* $A(\vartheta, \varphi)$, a function of the receiving direction, so that the received power $P_{\mathrm{R}}$ can be computed as

$$P_{\mathrm{R}} = A(\vartheta_{\mathrm{R}}, \varphi_{\mathrm{R}}) \cdot S(\vartheta_{\mathrm{T}}, \varphi_{\mathrm{T}}). \tag{4.11}$$

### 4.1.3 Link Budget and Path-loss

A major result of antenna theory is that we can express the effective area as a function of the antenna directivity with the following formula

$$A(\vartheta, \varphi) = d(\vartheta, \varphi) \cdot \frac{\lambda^2}{4\pi}. \tag{4.12}$$

This leads to the well known link budget formula, also known as *Friis' formula* [82]

$$\frac{P_{\mathrm{R}}}{P_{\mathrm{T}}} = g_{\mathrm{R}}(\vartheta_{\mathrm{R}}, \varphi_{\mathrm{R}}) \cdot \left(\frac{\lambda}{4\pi d}\right)^2 \cdot g_{\mathrm{T}}(\vartheta_{\mathrm{T}}, \varphi_{\mathrm{T}}), \tag{4.13}$$

which determines the power transfer between two antennas. Please note that the dependency on frequency of the antenna gain functions has been omitted for simplicity.

The inverse of the term $\left(\frac{\lambda}{4\pi d}\right)^2$ is called *path-loss*. However, equation (4.13) only considers the power transmission and is therefore not intended to treat multi-path propagation. Additionally, equation (4.13) does not consider explicitly polarization.

### 4.1.4 Polarimetric Antenna Radiation Pattern

Even though both the directivity function and the gain function are useful descriptors of the antenna characteristics, they contain information neither on the polarization state of the radiated field nor on its time dependency. This information, as discussed in Sections 2.2.3 and 3.1.4, is crucial for an antenna independent channel description and modeling. Furthermore, most parameter estimation techniques [133] which retrieve Direction Of Arrivals (DOAs) and Direction Of Departures (DODs), require the so-called *array manifold*, which is the array response to a planar wavefront impinging from different directions. The array manifold, although expressed in different terms, is an equivalent description of the antenna radiation patterns including the coupling effects and the phase shifts introduced by the relative displacement of the array elements.

Describing the polarization of a spherical wave in a certain direction means describing how the electric field oscillates on the plane transverse to the propagation, ignoring the transmitted power and considering only the relative relationships between the components of the field's vector. In fact, as mentioned above, the electric field at a given co-elevation $\vartheta$, azimuth $\varphi$, and distance $r$, assuming far-field conditions, lies always in the plane whose normal matches the direction of propagation. Furthermore, it can be observed that the electric field at $\vartheta$, $\varphi$, and $r$, as time evolves, moves on an ellipse, as the one shown in Figure 4.3.

In order to describe efficiently this phenomenon, we decompose the field into two linearly

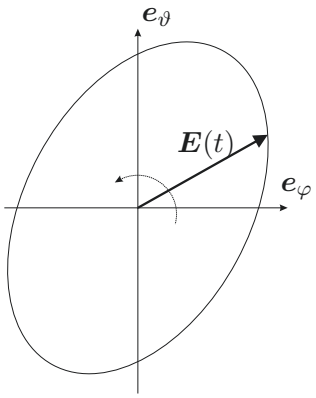


Fig. 4.3: At at a given co-elevation $\vartheta$, azimuth $\varphi$, and distance $r$, the electric field $\boldsymbol{E}(t)$ moves on an ellipse which lies on the transversal plane, i.e., the plane orthogonal to the propagation.

polarized waves as follows

$$\begin{aligned}
\boldsymbol{E}(\vartheta,\varphi,r,t) &= E_\vartheta(\vartheta,\varphi,r,t)\ \boldsymbol{e}_\vartheta + E_\varphi(\vartheta,\varphi,r,t)\ \boldsymbol{e}_\varphi \\
E_\vartheta(\vartheta,\varphi,r,t) &= \Re\left\{\sqrt{\eta_0}\ \frac{\mathrm{e}^{-j(kr-\omega t)}}{r}\cdot b_\vartheta(\vartheta,\varphi)\right\} \\
E_\varphi(\vartheta,\varphi,r,t) &= \Re\left\{\sqrt{\eta_0}\ \frac{\mathrm{e}^{-j(kr-\omega t)}}{r}\cdot b_\varphi(\vartheta,\varphi)\right\}.
\end{aligned} \tag{4.14}$$

The amplitude and phase difference between the complex functions $b_\vartheta(\vartheta,\varphi)$ and $b_\varphi(\vartheta,\varphi)$ determine the shape of the ellipse for each direction $\{\vartheta,\varphi\}$. When the amplitudes are equal and the phase difference is $\pi/2$ we have a circularly polarized wave, whereas for in-phase components we have linear polarizations. As the expressions in (4.14) clearly show, the knowledge of the polarimetric radiation patterns, namely $b_\vartheta(\vartheta,\varphi)$ and $b_\varphi(\vartheta,\varphi)$, the phase constant $k$, and the wave's velocity $c$ are sufficient to exhaustively describe the field at the space–time coordinates $\{\vartheta,\varphi,r,t\}$, once more, assuming that we are in the antenna's far-field.

Alternatively, we can decompose the field into two orthogonal circularly polarized waves. Using the helicity vectors described in Appendix E.3, we can write

$$\begin{aligned}
\boldsymbol{E}(\vartheta,\varphi,r,t) &= E_+(\vartheta,\varphi,r,t)\ \boldsymbol{e}_+ + E_-(\vartheta,\varphi,r,t)\ \boldsymbol{e}_- \\
E_+(\vartheta,\varphi,r,t) &= \Re\left\{\sqrt{\eta_0}\ \frac{\mathrm{e}^{-j(kr-\omega t)}}{r}\cdot b_+(\vartheta,\varphi)\right\} \\
E_-(\vartheta,\varphi,r,t) &= \Re\left\{\sqrt{\eta_0}\ \frac{\mathrm{e}^{-j(kr-\omega t)}}{r}\cdot b_-(\vartheta,\varphi)\right\}.
\end{aligned} \tag{4.15}$$

This will be particularly helpful when dealing with the pattern descriptor based on the Vector Spherical Harmonics (VSHs) in Section 4.4.

For convenience we define the polarimetric antenna radiation pattern vector $\boldsymbol{b}(\vartheta,\varphi)$, whose components represent the two polarizations. It can be expanded into polar basis vectors[4], i.e.,

into linearly polarized components, as

$$\boldsymbol{b}(\vartheta,\varphi) = b_{\vartheta}\left(\vartheta,\varphi\right)\boldsymbol{e}_{\vartheta} \;+\; b_{\varphi}\left(\vartheta,\varphi\right)\,\boldsymbol{e}_{\varphi}, \tag{4.16}$$

or, equivalently, into helicity basis vectors[4], i.e., into circular polarized components, as

$$\boldsymbol{b}(\vartheta,\varphi) = b_{+}\left(\vartheta,\varphi\right)\boldsymbol{e}_{+} \;+\; b_{-}\left(\vartheta,\varphi\right)\,\boldsymbol{e}_{-}. \tag{4.17}$$

The relationship between the radiation patterns and the radiation intensity introduced in Section 4.1.2 is given in the following

$$d\left(\vartheta,\varphi\right)\cdot S_i\left(\vartheta,\varphi\right) = d\left(\vartheta,\varphi\right)\cdot\frac{P_{\mathrm{T}}}{4\pi r^2} = \frac{1}{r^2}\left\|\boldsymbol{b}\left(\vartheta,\varphi\right)\right\|^2, \tag{4.18}$$

so that

$$d\left(\vartheta,\varphi\right) = 4\pi\left\|\boldsymbol{b}\left(\vartheta,\varphi\right)\right\|^2, \tag{4.19}$$

and

$$g\left(\vartheta,\varphi\right) = 4\pi\;\xi\;\left\|\boldsymbol{b}\left(\vartheta,\varphi\right)\right\|^2. \tag{4.20}$$

The latter leads to the following normalization condition which the radiation pattern needs to fulfill

$$\int_{\mathcal{S}^2}\left\|\boldsymbol{b}\left(\vartheta,\varphi\right)\right\|^2\,\mathrm{d}\Omega = 1. \tag{4.21}$$

Omnidirectional antennas, although physically impossible to build, are often assumed in many investigations on wireless systems. According to equation (4.21), the radiation pattern characterizing an omnidirectional antenna, namely $\boldsymbol{b}_{\mathrm{omni}}\left(\vartheta,\varphi\right)$, assumes the following expression

$$\left\|\boldsymbol{b}_{\mathrm{omni}}\left(\vartheta,\varphi\right)\right\|^2 = \frac{1}{4\pi}.$$

### 4.1.5 The Polarimetric Antenna Array Response

In channel modeling applications, we need to consider the antenna radiation patterns while computing the Channel Impulse Response (CIR) of a Single Input Single Output (SISO) wireless link. For this reason, rather than computing the electric field in an arbitrary point in space, we are interested in the ratio between the electric fields at the antenna ports. In fact, this ratio computed at a particular frequency and time constitutes the channel. More details on this are given in Section 5.1.

We introduce the *antenna response* for the vertical polarization $a_{\vartheta}(\vartheta,\varphi)$ as

$$a_{\vartheta}(\vartheta,\varphi) = \sqrt{4\pi\xi}\cdot b_{\vartheta}(\vartheta,\varphi), \tag{4.22}$$

where $\xi$ is the antenna efficiency, presented in Section 4.1.2, and $b_{\vartheta}(\vartheta,\varphi)$ is the radiation

[4] See Appendices E.2 and E.3 for the polar and helicity coordinate systems, respectively.

pattern introduced in the previous section. We define the *polarimetric antenna response* $\boldsymbol{a}(\vartheta, \varphi)$ as

$$\boldsymbol{a}(\vartheta, \varphi) = \sqrt{4\pi\xi} \cdot \boldsymbol{b}(\vartheta, \varphi) = \sqrt{4\pi\xi} \cdot \begin{bmatrix} b_\vartheta(\vartheta, \varphi) \\ b_\varphi(\vartheta, \varphi) \end{bmatrix}. \tag{4.23}$$

Notice that the norm squared of the polarimetric antenna response is simply the gain function

$$g(\vartheta, \varphi) = \|\boldsymbol{a}(\vartheta, \varphi)\|^2. \tag{4.24}$$

For convenience, we introduce the *polarimetric antenna array response* $\boldsymbol{A}(\vartheta, \varphi)$. Assuming planar wave-fronts, for an $M$-element array, it is defined as

$$\boldsymbol{A}(\vartheta, \varphi) = \sqrt{4\pi\xi} \cdot \begin{bmatrix} \boldsymbol{b}_1(\vartheta, \varphi) & \boldsymbol{b}_2(\vartheta, \varphi) & \dots & \boldsymbol{b}_M(\vartheta, \varphi) \end{bmatrix}^{\mathrm{T}} \in \mathbb{C}^{M \times 2}, \tag{4.25}$$

where $\boldsymbol{b}_i(\vartheta, \varphi)$ is the polarimetric radiation pattern of the $i$-th element

$$\boldsymbol{b}_i(\vartheta, \varphi) = b_{\vartheta,i}(\vartheta, \varphi)\, \boldsymbol{e}_\vartheta \; + \; b_{\varphi,i}(\vartheta, \varphi)\; \boldsymbol{e}_\varphi.$$

Alternatively, we can write the *antenna array response* for each polarization separately. Then we have

$$\begin{aligned} \boldsymbol{a}_\vartheta &= \sqrt{4\pi\xi} \cdot \begin{bmatrix} b_{\vartheta,1}(\vartheta, \varphi) & b_{\vartheta,2}(\vartheta, \varphi) & \dots & b_{\vartheta,M}(\vartheta, \varphi) \end{bmatrix}^{\mathrm{T}} \in \mathbb{C}^{M \times 1} \\ \boldsymbol{a}_\varphi &= \sqrt{4\pi\xi} \cdot \begin{bmatrix} b_{\varphi,1}(\vartheta, \varphi) & b_{\varphi,2}(\vartheta, \varphi) & \dots & b_{\varphi,M}(\vartheta, \varphi) \end{bmatrix}^{\mathrm{T}} \in \mathbb{C}^{M \times 1}, \end{aligned} \tag{4.26}$$

so that

$$\boldsymbol{A}(\vartheta, \varphi) = \begin{bmatrix} \boldsymbol{a}_\vartheta(\vartheta, \varphi) & \boldsymbol{a}_\varphi(\vartheta, \varphi) \end{bmatrix} = \begin{bmatrix} \boldsymbol{a}_1^{\mathrm{T}}(\vartheta, \varphi) \\ \boldsymbol{a}_2^{\mathrm{T}}(\vartheta, \varphi) \\ \vdots \\ \boldsymbol{a}_M^{\mathrm{T}}(\vartheta, \varphi) \end{bmatrix} \in \mathbb{C}^{M \times 2}. \tag{4.27}$$

As a special case, let us consider a Uniform Linear Array (ULA) consisting of $M$ sensors such as the one displayed in Figure 4.4, where $M = 6$. Let us further assume that the radiation pattern of all antennas is non-zero only for the vertical polarization and that the gain function is omnidirectional. In this case, the antenna response assumes the very simple expression of a *Vandermonde* vector [215, pp. 1368–1369], as follows

$$\boldsymbol{a}_\vartheta = \begin{bmatrix} 1 & \mathrm{e}^{-j\frac{2\pi}{\lambda}\Delta\sin(\psi)} & \mathrm{e}^{-j\frac{2\pi}{\lambda}2\Delta\sin(\psi)} & \dots & \mathrm{e}^{-j\frac{2\pi}{\lambda}M\Delta\sin(\psi)} \end{bmatrix}^{\mathrm{T}}, \tag{4.28}$$

where the angle $\psi$ is depicted in Figure 4.4. The horizontal component, namely $\boldsymbol{a}_\varphi$ is zero for all sensors and all angles. As equation (4.28) shows, there is no dependency on elevation.

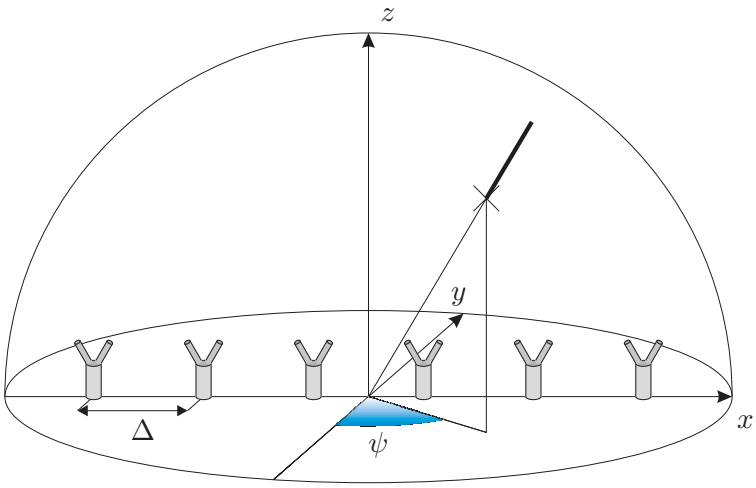


Fig. 4.4: Simplified coordinate system for a ULA and an impinging planar wavefront.

### 4.1.6 Typical Antenna Arrays

Antenna arrays differ greatly with respect to the number of sensors, their relative position, and the type of antenna used. Following the nomenclature used by the INIT[5], we distinguish between ULA, Uniform Circular Array (UCA), and Uniform Rectangular Array (URA), which distribute antennas uniformly on a line, on a circle, and on the surface of a rectangle, respectively. The number of sensors used in practice for channel sounding aimed at high-resolution parameter estimation is normally less than 100. This number is mostly limited by cost factors, as the more sensors we employ the higher resolution we can achieve. The types of antenna employed are usually either electric dipoles or patch antennas. The latter are particularly interesting because they can have two ports, one for each polarization, allowing a full polarimetric measurements.

Figure 4.5 shows a Stacked Polarimetric Uniform Circular Patch Array (SPUCPA) and a Uniform Circular Array (UCA). The SPUCPA possesses four rings of 24 patch antennas each. The Uniform Circular Array (UCA), on the other hand, has 16 vertical dipoles uniformly distributed on a circle. Figure 4.6 shows a Polarimetric Uniform Linear Patch Array (PULPA) and a Uniform Rectangular Patch Array (URPA). The 8 elements of the PULPA are not visible, as they are covered with a *radome*[6] for outdoor employment. The Uniform Rectangular Patch Array (URPA), on the other hand, mounts $8 \times 8$ elements, as well as a series of passive elements to reduce boundary effects.

[5] The INIT is the Institute of Information Technology at Ilmenau University of Technology .
[6] The radome, term originally used in aeronautics, is a plastic housing sheltering the antenna assembly.

(a) SPUCPA

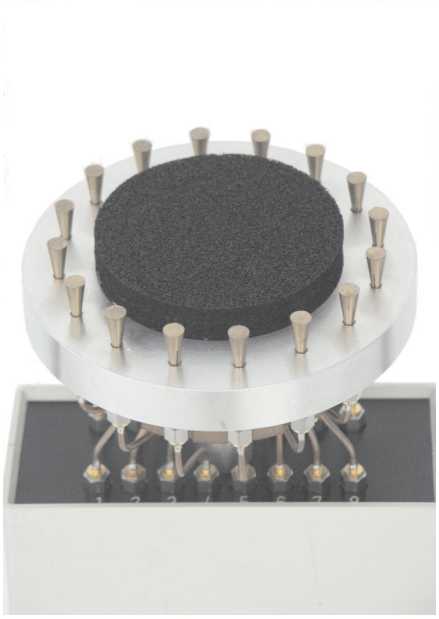

(b) UCA

Fig. 4.5: The Stacked Polarimetric Uniform Circular Patch Array (SPUCPA) possesses four rings of 24 patch antennas each. The Uniform Circular Array (UCA), on the other hand, has 16 vertical dipoles uniformly distributed on a circle
(source: Institute of Information Technology, Ilmenau University of Technology)

(a) PULPA

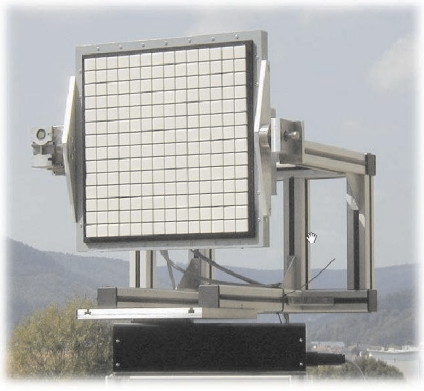

(b) URPA

Fig. 4.6: A Polarimetric Uniform Linear Patch Array (PULPA) and a Uniform Rectangular Patch Array (URPA). The 8 elements of the PULPA are covered by a radome for outdoor employment. The Uniform Rectangular Patch Array (URPA), on the other hand, mounts $8 \times 8$ elements, as well as a series of passive elements to reduce boundary effects.
(source: Institute of Information Technology, Ilmenau University of Technology)

### 4.1.7 Measuring and Storing the Polarimetric Radiation Patterns

Traditionally, the radiation pattern for each polarization is stored in form of a matrix obtained by sampling the pattern on a regular grid on the sphere, namely a grid obtained by uniformly sampling azimuth and elevation. This is a straightforward representation which is normally used to measure an antenna array, a procedure which is referred to as *antenna calibration*. In case of an antenna array consisting of $M$ elements, for each point in azimuth and elevation the response of each sensor to each polarization is measured. With this approach the coupling between the $M$ sensors is included.

Physically, the radiation pattern is measured as depicted in Figure 4.7: a probe antenna, acting as transmitter, is mounted on a robotic arm which can move at any arbitrary elevation and azimuth with respect to the center of the coordinate system, where the antenna under study is placed. Alternatively, the probe antenna can be kept fixed, while the antenna under study is rotated. The probe antenna is a carefully calibrated well known antenna, usually a dipole or a horn antenna. This set-up is shown in Figure 4.8, where the array under study, a 16-element UCA, is mounted on a robotic arm in the anechoic chamber at Ilmenau University of Technology.

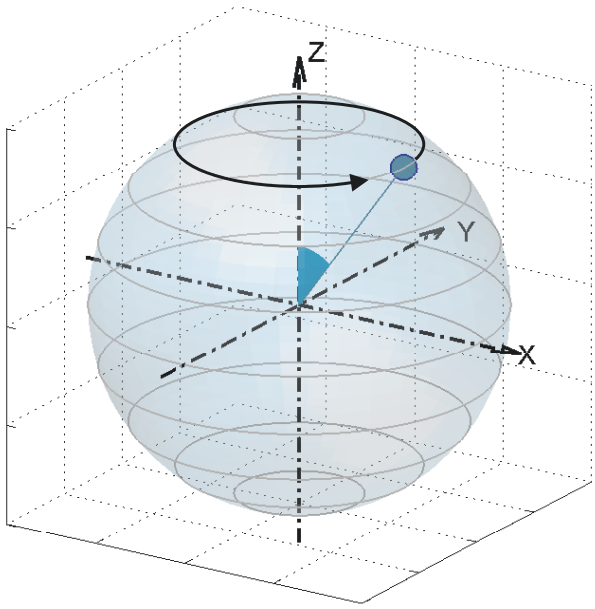


Fig. 4.7: Measurement set-up to measure the radiation pattern of an antenna. A known transmit antenna is put at a specific co-elevation and rotated for all azimuths. The antenna under study is placed in the origin of the coordinate system.

The antenna calibration is performed in an anechoic chamber, in order to suppress all echoes which would corrupt the measurement.

Once the measurements have been carried out, the data gathered needs to be processed and stored. Requiring the knowledge of the radiation pattern means, in practice, that the values

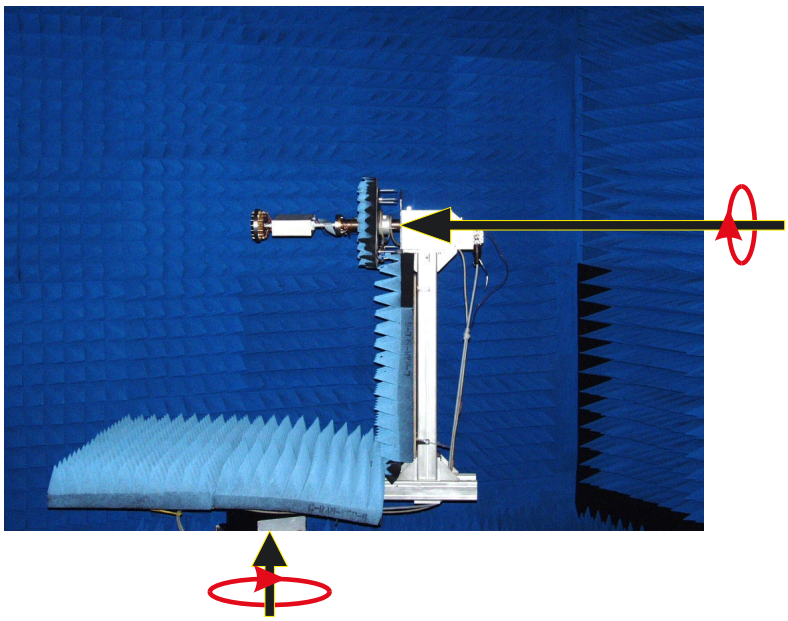

Fig. 4.8: Measurement set-up to measure the radiation patterns of an antenna array. The array under study, a 16-element UCA, is mounted on a robotic arm in the anechoic chamber at Ilmenau University of Technology. The arrows identify the two axes of rotation. The probe antenna, not visible, is kept fixed.
(source: Institute of Information Technology, Ilmenau University of Technology)

of the radiation pattern functions for both polarizations are needed for arbitrary directions. This is obtained by an interpolation of the information stored during the calibration process.

One approach is to store and process the data in the domain in which it was measured, namely in the angle domain. This is addressed in Section 4.2. Alternatively, when the measuring grid was equi-angle spaced, the information can be treated as a traditional two-dimensional (2D) discrete signal, so that spectral analysis tools can be used. This principle sets the basis for the Effective Aperture Distribution Function (EADF) presented in Section 4.3. The EADF implements a 2D Fast Fourier Transform (FFT) applied on a periodified version of the radiation pattern. In the spectral domain it is possible to store the information more efficiently, to perform noise filtering as well as to carry out interpolation in the transformed domain.

The EADF achieves a good accuracy with a very low computational complexity. Nonetheless, the antenna radiation pattern descriptor based on the VSHs, dealt in Section 4.4, obtains higher precision additionally allowing us to process the patterns for other applications.

## 4.2 The Radiation Pattern Description in the Angle Domain

When the radiation patterns are measured on a grid whose points are taken by sampling uniformly in azimuth and elevation, we can then store the information simply in matrix form, treating each polarization component separately. At this point, the information can be

treated as a traditional 2D discrete signal so that conventional interpolation techniques can be used, such as 2D cubic splines. However, such an approach is computationally unattractive due to the large number of complex values to be stored. This is discussed on page 103 in Section 4.4.4.2, where the interpolation accuracy and its computational cost is compared to the other two radiation pattern models dealt with in this work, namely the Effective Aperture Distribution Function (EADF) and the Discrete Vector Spherical Fourier Transform (DVSFT)-based representation.

## 4.3 The Effective Aperture Distribution Function (EADF)

This section introduces an efficient representation of the polarimetric antenna response, which we refer to as the Effective Aperture Distribution Function. The EADF has been first proposed in [137, 138]. Later, its usefulness for channel modeling applications has been recognized and its merits were stressed in [22]. The EADF achieves a high data compression, allowing us to reduce the number of samples needed to fully describe an antenna. Furthermore, it provides an efficient way of interpolation.

Section 4.3.1 introduces the data model and the basic idea behind the EADF. Sections 4.3.2 and 4.3.3 illustrate its use in channel modeling and in high-resolution parameter estimation, respectively. Section 4.3.4 deals with the limitations introduced by the spherical coordinate system. Later, on page 103 in Section 4.4.4.2 we compare the interpolation accuracy and efficiency of the EADF with the other two radiation pattern models dealt in with this work, namely the angular and the DVSFT-based representations.

### 4.3.1 The Data Model and the Basic Idea

Let $\vartheta \in [0, \pi]$ and $\varphi \in [0, 2\pi)$ be the co-elevation and azimuth, respectively, as described in Appendix E.2. The narrowband radiation pattern $b(\vartheta, \varphi)$ corresponding to each polarization component can be either measured or generated synthetically, and is then stored in form of the matrix $\boldsymbol{B} \in \mathbb{C}^{N_1 \times N_2}$, sampling both coordinates uniformly.

Let $\Delta\vartheta$ and $\Delta\varphi$ be the sampling intervals for the azimuth and co-elevation, respectively, defined as

$$\begin{aligned} \Delta\vartheta &= \frac{\pi}{N_1 - 1} \\ \Delta\varphi &= \frac{2\pi}{N_2}, \end{aligned} \tag{4.29}$$

so that the matrix $\boldsymbol{B}$ is sampled at

$$\begin{aligned} \boldsymbol{\vartheta} &= \begin{bmatrix} 0 & \Delta\vartheta & 2\Delta\vartheta & \dots & \pi \end{bmatrix}^{\mathrm{T}} \in \mathbb{C}^{N_1 \times 1} \\ \boldsymbol{\varphi} &= \begin{bmatrix} 0 & \Delta\varphi & 2\Delta\varphi & \dots & 2\pi - \Delta\varphi \end{bmatrix}^{\mathrm{T}} \in \mathbb{C}^{N_2 \times 1}. \end{aligned} \tag{4.30}$$

The radiation patterns are measured as described in Section 4.1.4, so that for each polarization, each row in the matrix $\boldsymbol{B}$ corresponds to the signal received as the arm set to a specific elevation is rotated for the whole 360° azimuth. This is illustrated in Figure 4.9.

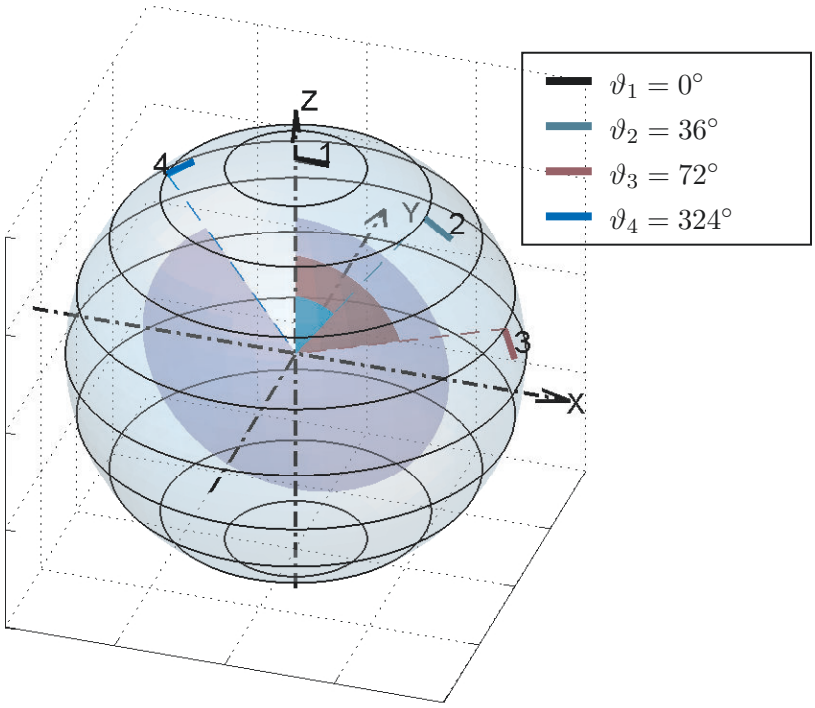


Fig. 4.9: Measurement set-up to measure the radiation pattern of an antenna. A known transmit antenna is put at a specific co-elevation and rotated for all azimuths. The antenna under study is placed in the origin of the coordinate system.

The radiation pattern described in this way is periodic only with respect to the azimuthal coordinate. In order to make it periodic across co-elevation, the radiation pattern description can be simply extended for co-elevations larger than $\pi$, i.e., starting from $\pi + \Delta\vartheta$, up to $\vartheta = 2\pi - \Delta\vartheta$. For instance, the fourth position depicted in Figure 4.9 shows the orientation of the transmit antenna for a co-elevation of $\vartheta_4 = 324°$. At this particular point, the measured radiation pattern will be the negated version of what was measured at $\vartheta_2 = 36°$ for an azimuth of 180°.

Let $\boldsymbol{\vartheta}'$ be the vector containing the co-elevations at which the periodic radiation pattern is sampled. It is defined as

$$\boldsymbol{\vartheta}' = \begin{bmatrix} 0 & \Delta\vartheta & 2\Delta\vartheta & \dots & (2\pi - \Delta\vartheta) \end{bmatrix}^{\mathrm{T}} = \begin{bmatrix} \boldsymbol{\vartheta}^{\mathrm{T}}, & \boldsymbol{\vartheta}_{\mathrm{r}}^{\mathrm{T}} \end{bmatrix}^{\mathrm{T}} \in \mathbb{C}^{N_1' \times 1},$$

where $N_1' = 2N_1 - 2$. Notice that $\boldsymbol{\vartheta}_{\mathrm{r}}$ contains two samples less than $\boldsymbol{\vartheta}$, as it includes neither the south nor the north pole. The resulting sampled radiation pattern is stored in the matrix $\boldsymbol{B}_{\mathrm{p}}$ defined on $\boldsymbol{\varphi}$ and $\boldsymbol{\vartheta}'$, so that

$$\boldsymbol{B}_{\mathrm{p}} \in \mathbb{C}^{N_1' \times N_2}. \tag{4.31}$$

Let $\boldsymbol{B}_\mathrm{r}$ contain the data sampled at $\boldsymbol{\varphi}$ and $\boldsymbol{\vartheta}_\mathrm{r}$. Then, the periodic radiation pattern $\boldsymbol{B}_\mathrm{p}$ can be interpreted as the stacking of the matrices $\boldsymbol{B}$ and $\boldsymbol{B}_\mathrm{r}$, as

$$\boldsymbol{B}_\mathrm{p} = \begin{bmatrix} \boldsymbol{B} \\ \boldsymbol{B}_\mathrm{r} \end{bmatrix}. \tag{4.32}$$

When the number of samples along azimuth, namely $N_2$, is even, then the matrix $\boldsymbol{B}_\mathrm{r}$ comprises the same information also contained in $\boldsymbol{B}$. This can be observed in the exemplary grids shown in Figure 4.10. The red dots mark the samples for $\boldsymbol{B}$ while the blue squares the ones for $\boldsymbol{B}_\mathrm{r}$. Plot (a) assumes $N_2 = 13$, whereas for (b) we have $N_2 = 12$. Both grids feature $N_1' = 16$. In Plot (b), for an even $N_2$, the sampling points of $\boldsymbol{B}_\mathrm{r}$ coincide with the ones gathered for $\boldsymbol{B}$. In this case it is possible to compute $\boldsymbol{B}_\mathrm{p}$ by simply measuring $\boldsymbol{B}$. On the other hand, for an odd $N_2$, it is required to measure new points in order to obtain $\boldsymbol{B}_\mathrm{r}$.

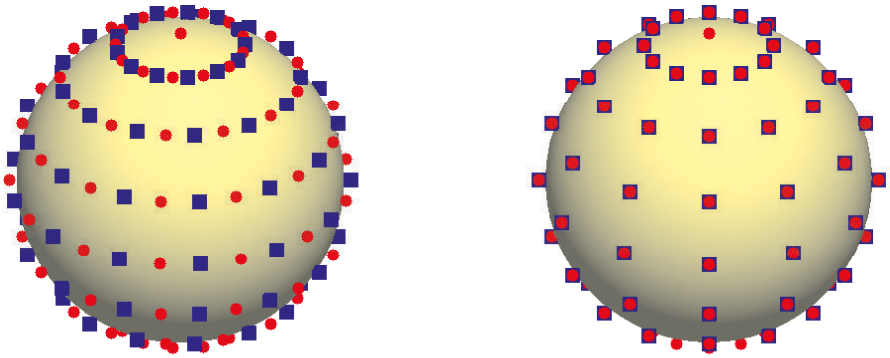

(a) (b)

Fig. 4.10: Sampling grid to compute the 2D DFT for the EADF . Both grids have $N_1 = 9$ samples in elevation, so that $N_1' = 16$. Plot (a) assumes $N_2 = 13$, whereas for (b) we have $N_2 = 12$. The red dots mark the samples for $\boldsymbol{B}$ while the blue squares for $\boldsymbol{B}_\mathrm{r}$.

The periodic radiation pattern $\boldsymbol{B}_\mathrm{p}$ can then be transformed via a two-dimensional DFT

$$\boldsymbol{G}_\mathrm{tot} = \mathcal{DFT}\left\{\boldsymbol{B}_\mathrm{p}\right\}. \tag{4.33}$$

For instance, the element of $\boldsymbol{G}_\mathrm{tot}$ corresponding to the spatial frequencies $\mu_1$ and $\mu_2$, denoted by $g_\mathrm{tot}(\mu_1, \mu_2)$, is computed as

$$g_\mathrm{tot}(\mu_1, \mu_2) = \frac{1}{N_1' \cdot N_2} \cdot \left(\mathrm{e}^{-j\boldsymbol{\vartheta}\mu_1}\right)^\mathrm{T} \cdot \boldsymbol{B}_\mathrm{p} \cdot \mathrm{e}^{-j\boldsymbol{\varphi}\mu_2}$$

The resulting complex matrix $\boldsymbol{G}_\mathrm{tot}$ has size $N_1' \times N_2$.

Figure 4.11 shows a measured radiation pattern $\boldsymbol{B}$ for both polarizations separately. On the right it shows the absolute value of the corresponding matrix $\boldsymbol{G}_\mathrm{tot}$ in dB.

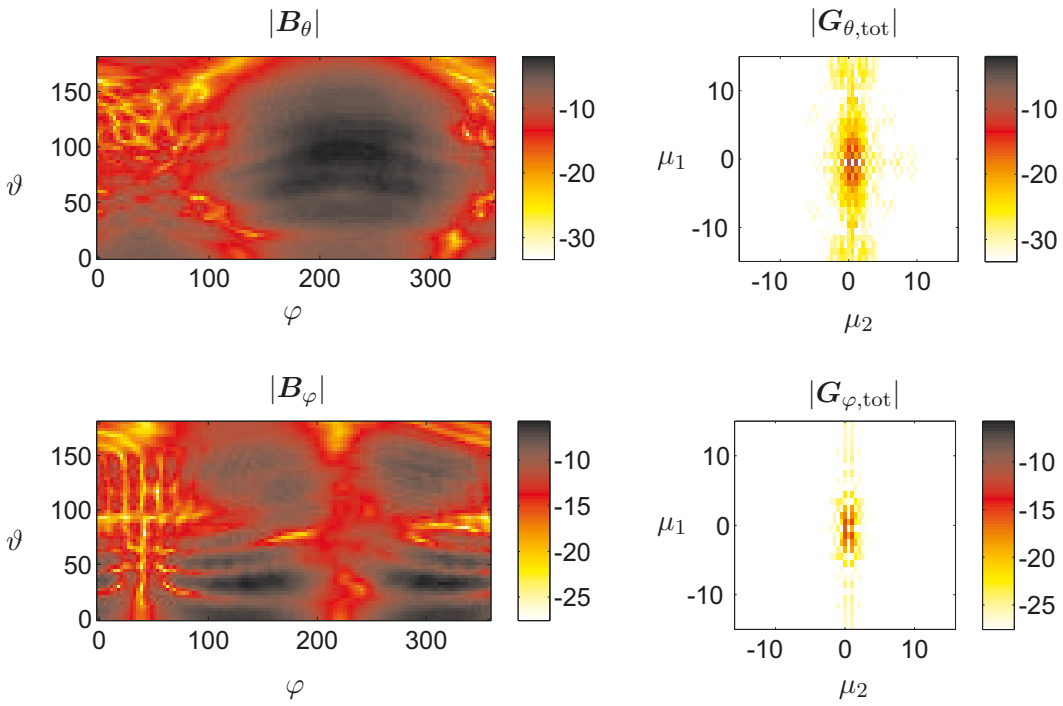


Fig. 4.11: Sampled radiation patterns $\boldsymbol{B}_\theta$ and $\boldsymbol{B}_\varphi$, for the vertical and horizontal polarization, respectively. On the right, the 2D DFT of the corresponding periodified versions. The values are given in dB. The measured antenna is the same as the one shown in Figure 4.1. The supports of $\boldsymbol{G}_{\theta,\mathrm{tot}}$ with energy is the EADF.

In case of an oversampling of the radiation pattern in the angular domain[7], this transformation can be used to achieve a data compression. In other words, only a subset of the elements of the matrix $\boldsymbol{G}_{\mathrm{tot}}$ are significant and are taken into account for further processing. These coefficients are stored in the matrix $\boldsymbol{G} \in \mathbb{C}^{L_1 \times L_2}$ which we call the Effective Aperture Distribution Function (EADF) of the radiation pattern. The parameters $L_1$ and $L_2$ are always odd numbers. In fact, the finite support of $\boldsymbol{G}$ is obtained by considering $(L-1)/2$ samples in the positive as well as in the negative frequencies, plus the direct component.

The complex radiation pattern $b(\varphi, \vartheta)$ for one polarization, sampled at an arbitrary azimuth $\varphi$ and co-elevation $\vartheta$, can be efficiently calculated as

$$b(\varphi, \vartheta) \approx \boldsymbol{d}_{\mathrm{b1}}^{\mathrm{T}}(\vartheta) \cdot \boldsymbol{G} \cdot \boldsymbol{d}_{\mathrm{b2}}(\varphi), \tag{4.34}$$

where

$$\begin{aligned} \boldsymbol{d}_{\mathrm{b1}}(\vartheta) &= \mathrm{e}^{j\vartheta\boldsymbol{\mu}_1} \in \mathbb{C}^{L_1 \times 1} \\ \boldsymbol{d}_{\mathrm{b2}}(\varphi) &= \mathrm{e}^{j\varphi\boldsymbol{\mu}_2} \in \mathbb{C}^{L_2 \times 1}, \end{aligned} \tag{4.35}$$

[7] With oversampling we indicate that a sampling frequency higher than the minimum required has been used.

and

$$\begin{aligned}\boldsymbol{\mu}_1 &= \left[\tfrac{-(L_1-1)}{2} \quad \tfrac{-(L_1-3)}{2} \quad \dots \quad \tfrac{(L_1-1)}{2}\right]^{\mathrm{T}} \in \mathbb{Z}^{L_1\times 1} \\ \boldsymbol{\mu}_2 &= \left[\tfrac{-(L_2-1)}{2} \quad \tfrac{-(L_1-3)}{2} \quad \dots \quad \tfrac{(L_2-1)}{2}\right]^{\mathrm{T}} \in \mathbb{Z}^{L_2\times 1}.\end{aligned} \tag{4.36}$$

Notice that the expression in equation (4.34) is basically an Inverse Discrete Fourier Transform (IDFT). The MATLAB-like notation used in equation (4.35) indicates that the $i$-th element of the vector $\boldsymbol{d}_{\mathrm{b1}}$ is equal to the exponent of the $i$-th element of the vector $\boldsymbol{\mu}_1$.

In Section 4.3.2, equation (4.34) leads to a very efficient interpolation technique as well as the possibility to obtain analytical expressions for the radiation pattern derivatives.

### 4.3.2 The EADF in Channel Modeling

In order to improve the realism of an antenna independent[8] channel model it is important to accurately model the antenna elements of the arrays, namely considering their radiation patterns and behavior with respect to polarization. This includes the necessity to efficiently store the information regarding each antenna element and, more importantly, the possibility to retrieve quickly the antenna array response for an impinging wave coming from arbitrary directions. The EADF can be successfully employed to solve both issues. The data compression allows us to store as little data as possible, while the interpolation seen in equation (4.34) can be extended to multiple antennas as follows.

Let $\boldsymbol{G}_m$ be the EADF of the $m$-th antenna of an array with $M$ sensors. Assuming that the EADFs of all elements have the same size, namely $L_1 \times L_2$, we can construct a tensor $\boldsymbol{\mathcal{G}}$ by stacking in the third dimension the different EADFs, as

$$\boldsymbol{\mathcal{G}} = \left[\boldsymbol{G}_1 \quad \underset{3}{\smile} \quad \boldsymbol{G}_1 \quad \underset{3}{\smile} \quad \dots \quad \underset{3}{\smile} \quad \boldsymbol{G}_M\right] \in \mathbb{C}^{L_1\times L_2\times M}. \tag{4.37}$$

where the symbol $\underset{n}{\smile}$ denotes the concatenation operation in the $n$-th dimension, as explained in Section D.3.1. If we now consider both polarizations, we can construct in the way just mentioned one tensor $\boldsymbol{\mathcal{G}}$ for each polarization, which we denote with $\boldsymbol{\mathcal{G}}_\vartheta$ and $\boldsymbol{\mathcal{G}}_\varphi$ for the vertical and horizontal polarization, respectively. Assuming that all EADFs are expressed in the same coordinate system, we can compute the antenna array responses $\boldsymbol{a}_\vartheta(\vartheta,\varphi)$ and $\boldsymbol{a}_\varphi(\vartheta,\varphi)$, introduced in Section 4.1.5. These vectors contain the antenna response of each array element with respect to a planar wave impinging from an arbitrary azimuth $\varphi$ and co-elevation $\vartheta$

$$\begin{aligned}\boldsymbol{a}_\vartheta &= \mathrm{vec}\left\{\boldsymbol{\mathcal{G}}_\vartheta \times_1 \boldsymbol{d}_{\mathrm{b1}}^{\mathrm{T}} \times_2 \boldsymbol{d}_{\mathrm{b2}}^{\mathrm{T}}\right\} \\ \boldsymbol{a}_\varphi &= \mathrm{vec}\left\{\boldsymbol{\mathcal{G}}_\varphi \times_1 \boldsymbol{d}_{\mathrm{b1}}^{\mathrm{T}} \times_2 \boldsymbol{d}_{\mathrm{b2}}^{\mathrm{T}}\right\},\end{aligned} \tag{4.38}$$

where the $\mathrm{vec}\{\cdot\}$ operator, defined in Appendix D.2.2, in this case, simply rearranges the tensor of size $1\times 1\times M$ into a column vector. The $n$-mode product, denoted by $\times_n$ is defined in Appendix D.3.3.

[8] See Chapter 3.

### 4.3.3 The EADF in Parameter Estimation

The EADF finds several important applications in the field of parameter estimation as well.

Most parameter estimation algorithms, such as [76, 95, 182, 208, 93], are based on the description of the channel through a data model. One of the most commonly used is the base-band double directional model which approximates the narrowband radio channel by the superposition of a finite number of propagation paths [236]. Every path is parameterized by 14 real values, namely the real and imaginary part of the four polarimetric complex path weights, the DOD, the Time Delay Of Arrival (TDOA), the Doppler-shift, and the DOA. The use of the EADF in such a data model allows us to carry out a 2D DFT along the angular domains at both link-ends, so that each path being described by a Dirac $\delta$-function in angular domain $\{\vartheta, \varphi\}$, we obtain a 2D complex exponential in the $\{\mu_1, \mu_2\}$ domain. The latter allows us to compute derivatives with respect to $\mu_1$ and $\mu_2$ with ease. As a consequence, the EADF becomes also helpful in those algorithms which rely on gradient based methods [181]. In this cases, the derivatives of the observations with respect to the channel parameters are needed. They can be computed as follows

$$\begin{aligned} \frac{\partial b(\varphi,\vartheta)}{\partial \varphi} &= j \cdot \boldsymbol{d}_{b1}^{\mathrm{T}}(\vartheta) \cdot \boldsymbol{G} \cdot (\boldsymbol{d}_{b2}(\varphi) \odot \boldsymbol{\mu}_2) \\ \frac{\partial b(\varphi,\vartheta)}{\partial \vartheta} &= j \cdot (\boldsymbol{d}_{b1}(\vartheta) \odot \boldsymbol{\mu}_1)^{\mathrm{T}} \cdot \boldsymbol{G} \cdot \boldsymbol{d}_{b2}(\varphi), \end{aligned} \tag{4.39}$$

where $\odot$ denotes the Schur element-wise product.

Moreover, the continuous derivatives can also be applied in the evaluation of antenna arrays for channel parameter estimation [138, 139], via the calculation of the Fisher Information Matrix (FIM), leading to the Cramér-Rao Lower Bound (CRLB), as also discussed in Section 5.3.2.

### 4.3.4 Limits of the Spherical Coordinate System

Unfortunately, the transformation from the spherical coordinate system to a 2D representation, such as the EADF, is strongly non-linear (in the three-dimensional (3D) Euclidean geometry). In the new representation, the samples are treated as if they were uniformly spaced from one another, which in the original coordinate system is evidently not true. Furthermore, the particular periodicity existing in the spherical system is lost. The EADF partly solves the periodicity issue by considering an elevation angle which is defined for a 360° range. By doing this, the radiation pattern description is periodic along elevation as well, at the expense of introducing redundancy. Nonetheless, the strong non-linearity of the transformation is impossible to overcome. The possible loss in accuracy due to this non-linearity is partly compensated by the fact that the sampling grid is much denser where the non-linearity is stronger, i.e., in the regions near the poles. A deeper investigation on these issues is given in [136].

As mentioned before, the very same radiation pattern has different EADFs depending on the coordinate system chosen. For instance, let $\boldsymbol{B}^{(1)}$ and $\boldsymbol{B}^{(2)}$ be the radiation patterns measured from the same antenna with two different coordinate systems. If the axes which connect the poles of both systems do not perfectly overlap, then there exists no linear transformation which can transform $\boldsymbol{B}^{(1)}$ into $\boldsymbol{B}^{(2)}$.

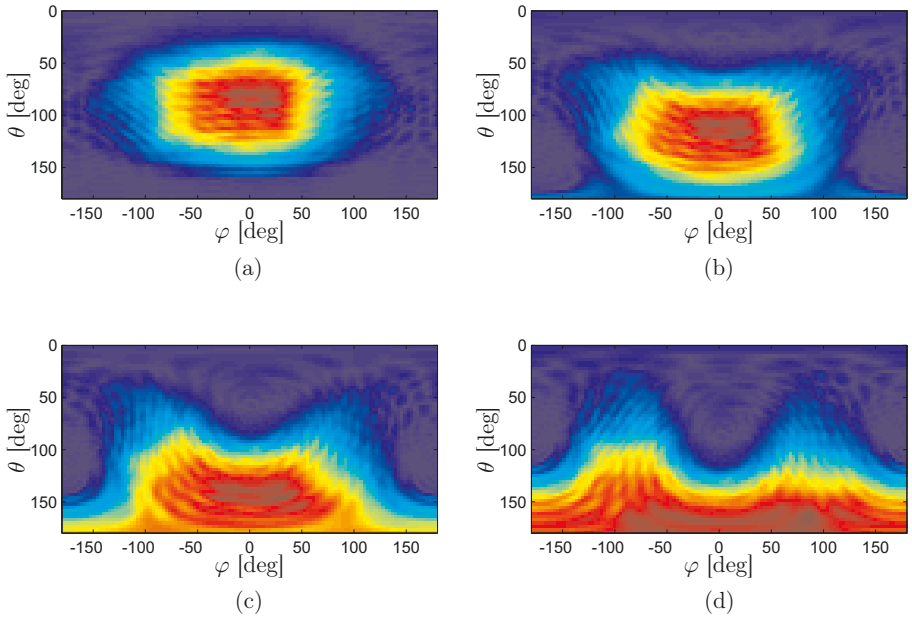


Fig. 4.12: The radiation pattern expressed in azimuth and elevation for the very same antenna rotated so that the main lobe is oriented towards four different elevations (a), (b), (c), and (d), for $\Delta\theta = 0°, 30°, 60°$ and $90°$, respectively.

Figure 4.12 shows the radiation pattern of the very same antenna rotated so that its main lobe is oriented towards four different elevations. Although the shape of the 3D radiation pattern does not change with the rotation, the 2D function stored in the matrix $\boldsymbol{B}$ varies significantly. As a consequence, $\boldsymbol{B}_\mathrm{p}$ will change and the EADF, being the 2D Fourier transform of $\boldsymbol{B}_\mathrm{p}$, will vary as well. Thus, the EADF is not a rotation-invariant descriptor of the radiation pattern. Note that if the radiation pattern is rotated about the main axis of the coordinate system, i.e., along azimuth, then the values in the matrix $\boldsymbol{B}$ will simply shift in one direction. In other words, the shape of the radiation pattern is simply shifted and the EADF remains unaltered except for a linear phase introduced across $\mu_2$.

## 4.4 The Descriptor Based on the Vector Spherical Harmonics

This section is dedicated to one of the major contribution of this work: the modeling of radiation patterns via Vector Spherical Harmonic (VSH). As already mentioned in the previous sections, the radiation pattern is traditionally represented either in the angular domain (see Section 4.2), where it is measured, or in a transformed domain by means of a 2D Discrete Fourier Transform (DFT). The latter approach is followed by the EADF, presented in Section 4.3. These methods implicitly apply a non-linear transformation on the radiation pattern, so that the samples are treated as if they were uniformly spaced from one another, which in the original 3D coordinate system is evidently not true. As direct consequences, the particular periodicity existing on the sphere is lost and the representations are not rotation-invariant. In other words, when we choose a different coordinate system the 2D functions describing the radiation pattern change significantly. Furthermore, these methods treat the two polarizations separately, thus ignoring the true nature of the radiation pattern, i.e., a complex vector field on the 2-sphere.

The natural domain to treat such functions is represented by the series expansion of VSHs, also called the Vector Spherical Fourier Transform (VSFT). In Section 4.4.2 we introduce the mathematical fundamentals of the continuous Vector Spherical Fourier Transform (VSFT), including its main properties. Section 4.4.3 introduces the Discrete Vector Spherical Fourier Transform (DVSFT) and the numerous non trivial issues concerning its practical use on sampled radiation patterns. Section 4.4.4 presents several interesting applications of the DVSFT for radiation pattern modeling and manipulation. Section 4.4.5 deals with the practical challenges arising in the calibration process of an antenna array, i.e., the measurement of the elements' radiation patterns.

Section 4.5 deals with the proposed antenna radiation pattern model for the IlmProp channel model. It consists of two steps. In a first phase the DVSFT-based descriptor is used to optimize the measurement process and denoise the measurement data. In a second step, we compute the EADF under optimal conditions. This processing scheme gives as an optimal trade-off between computational cost and accuracy.

In the following section we present a literature survey on the VSHs. This section stresses the differences with respect to related work, emphasizing the novelty of the proposed methods.

### 4.4.1 Distinction from Related Work

Spherical Harmonics (SHs) and Vector Spherical Harmonics (VSHs) are well known in numerous fields of science. Mostly, in those disciplines in which the problems dealt show spherical symmetries. This is the case of meteorology [184, 195, 68], chemistry [218], image processing [115], acoustics [207, 156], and physics [88, 50]. Scalar SHs were presumably proposed first in 1935 in [97]. In particular, the most comprehensive books dealing with the VSHs and SHs have been published in the field of quantum mechanics, such as [216, 135, 69, 61, 53, 160]. We feel that the latter are essential in order to gain a deeper understanding of the VSFT.

Similar to the proposed methods are the expansion series known as Spherical Wave Expansion (SWE) [96] or Spherical Mode Expansion (SME)[9] [202, 98, 109], which are quite well known in antenna theory. Both are expansions of the propagating EM wave into a series of orthogonal spherical wave functions. However, they describe the propagating wave in the full 3D space, and not only the transverse polarimetric radiation pattern on a sphere in the far-field. In fact, these methods are commonly applied to compute the far-field radiation pattern from near-field measurements [96].

A statistical analysis of the inverse problem, i.e., estimating the near-field or current distribution of the antenna from far-field measurements, was undertaken by Nordebo *et al.* in [163, 165]. Recently, Nordebo *et al.* derived the Cramér-Rao Lower Bound (CRLB) for arbitrary antennas for DOA estimation [164]. Furthermore, Gustafsson and Nordebo investigated the spectral efficiency of antennas given their diameters from a signal processing point of view in [90], and they analyzed the quality factor of antennas in [91]. The same laboratory used spherical vector waves to characterize the correlation loss of synthetic MIMO antennas in [92]. All mentioned publications from Gustafsson and Nordebo use the spherical vector wave expansion to characterize arbitrary antennas and analyze signal processing issues. However, none of the above publications deals with the modeling of polarimetric antenna radiation patterns for the applications discussed in this work, among which interpolation, noise reduction, SNR estimation, and improvements of the measurement process. Additionally, only theoretical results are derived and measured radiation patterns are never used. In fact, the expansion coefficients, similar to the VSHs coefficients, are never computed numerically from measured or simulated radiation patterns, and only analytical expressions for theoretical antennas are used. To apply the results of the above publications in praxis, it is crucial to develop methods to compute the expansion coefficients numerically. This is a challenging step which is dealt in detail in Section 4.4.3. Furthermore, the problems occurring during antenna measurements, such as displacements, phase shifts, and influence of the equipment, discussed in Section 4.4.5, are also not considered. Therefore, the applications and problems addressed in this work are not covered by the mentioned publications of Nordebo and Gustafsson [90, 91, 92, 163, 165, 164].

A research group at the VTT Technical Research Centre of Finland investigates antenna radiation patterns using the SWE. In [129], Koivisto proposes an algorithm for noise reduction in measured antenna radiation patterns by finding the optimal truncation level of the spherical mode spectrum. However, in Section 4.4.4.4 we derive a more efficient noise reduction method based on Wiener filtering. In [127], Koivisto investigates the capabilities of the SWE to reduce reflection errors occurring during measurements, and in [130] the author shows the impact of incomplete measurement data on the SWE. Although the mentioned publications show interesting results and give suggestions for future research and practical tests, the actual computation of the SWE is rather different from the VSFT proposed in this work. The SWE expansion coefficients are obtained via a simple least squares fitting method,

[9] Sometimes the SME is also called 'multipole expansion'.

while we use a direct Fourier method to compute the VSFT. This method, termed the orthonormality approach, and its benefits are explained in detail in Section 4.4.3. Moreover, besides noise reduction, none of the applications proposed in Section 4.4.4 are included in any of the mentioned publications.

Allard and Werner propose an interpolation method of antenna radiation patterns using SHs in [41], which is similar to the VSFT-based interpolation method proposed in Section 4.4.4.2. However, their method allows them to interpolate the radiation pattern along elevation only and it was tested on a theoretical vertical dipole. In this case, the radiation pattern can be represented by a scalar function rather than by a vector field. However, arbitrary polarimetric radiation patterns cannot in general be represented by a scalar spherical harmonic expansion, assumption without which their method would not work.

In [125, 126, 124, 123], Klemp *et al.* (Universität Hannover) use the SME to compute the correlation between different antennas in an antenna array for Multiple Input Multiple Output (MIMO) capacity analysis, antenna coupling investigation, and diversity applications. The SME coefficients are computed via a simple numerical least squares method. We propose the computation of the VSFT using a direct Fourier method, which, although mathematically demanding, possesses several advantages. These are explained in detail in Section 4.4.3. The applications of the SME proposed in the above publications were not investigated here, although they open interesting research topics for for future work.

The methods developed for this work, applied on the scalar SHs led to interesting applications in the field of acoustics. In [31] and [30] the sound field is measured by a virtual microphone array on the surface of a sphere. By computing the SH coefficients it is possible to extract valuable information on the room acoustics. In particular, the decomposition in SH allows the reconstruction of the intensity flux of the sound field, which can be used in assessing the psychological impact of early reflections from the walls of a room, or for studying how different materials diffuse sound waves.

### 4.4.2 The Continuous Vector Spherical Fourier Transform

The VSFT is based on a generalized Fourier series[10] of vector functions on the sphere. It is the spherical complement of the conventional Fourier Series (FS) in one dimension and shares several of its properties. Some of them are summarized in Table 4.1.

The kernel of the VSFT are the *Vector Spherical Harmonics* (VSHs), which we denote with $\boldsymbol{Y}_{lm}^{(\nu)}(\vartheta, \varphi)$. They are mutually orthogonal harmonic vector functions on the 2-sphere[11] $\mathcal{S}^2$. A countable infinite number of VSHs exists. The ranges for the *level* $l$, *mode* $m$, and *component* $\nu$ are

$$l, m, \nu \in \mathbb{Z} \ , \quad l \geq 0 \ , \quad |m| \leq l \ , \quad \nu \in \{-1, 0, 1\} \ . \tag{4.40}$$

[10] Eric W. Weisstein [223] defines the *generalized Fourier series* as "[...] a series expansion of a function based on the special properties of a complete orthogonal system of functions".

[11] The 2 sphere comprises all points on the surface of the unit sphere [102].

Thus, for each level $l$ there are $2l+1$ modes $m$. Since we deal with radiation patterns in the far-field, we expect the radial component of the field to be always zero. For this reason we can drop one component of the VSH as well, namely $\nu = -1$, which in fact represents the radial component only [216], so that for $\nu = \{0, 1\}$ the VSHs are transverse.

Varshalovich *et al.* [216] give an explicit definition of $\mathbf{Y}_{lm}^{(\nu)}(\vartheta, \varphi)$ in terms of the polar basis vectors[12] $\boldsymbol{e}_\vartheta$ and $\boldsymbol{e}_\varphi$ as

$$\begin{aligned} \mathbf{Y}_{lm}^{(0)}(\vartheta,\varphi) &= \frac{j}{\sqrt{l(l+1)}} \left[ \boldsymbol{e}_\vartheta \, \frac{1}{\sin\vartheta} \, \frac{\partial}{\partial\varphi} Y_{lm}(\vartheta,\varphi) - \boldsymbol{e}_\varphi \, \frac{\partial}{\partial\vartheta} Y_{lm}(\vartheta,\varphi) \right] \\ \mathbf{Y}_{lm}^{(1)}(\vartheta,\varphi) &= \frac{1}{\sqrt{l(l+1)}} \left[ \boldsymbol{e}_\vartheta \, \frac{\partial}{\partial\vartheta} Y_{lm}(\vartheta,\varphi) + \boldsymbol{e}_\varphi \, \frac{1}{\sin\vartheta} \, \frac{\partial}{\partial\varphi} Y_{lm}(\vartheta,\varphi) \right] , \end{aligned} \tag{4.41}$$

where $Y_{lm}(\vartheta, \varphi)$ are scalar SHs. Although it seems convenient to write the VSHs in terms of SHs, this introduces problems at the poles (i.e., for co-elevation $\vartheta = 0, \pi$) when they are implemented numerically. In fact, the term $\frac{1}{\sin\vartheta}$ in (4.41) goes to infinity at the poles. Expressing $\mathbf{Y}_{lm}^{(\nu)}(\vartheta, \varphi)$ in terms of the helicity basis vectors[12] $\boldsymbol{e}_+$ and $\boldsymbol{e}_-$ shows better behavior at the poles

$$\begin{aligned} \mathbf{Y}_{lm}^{(0)}(\vartheta,\varphi) &= \sqrt{\tfrac{2l+1}{8\pi}} \left[ -\boldsymbol{e}_+ \, D^l_{-1,-m}(0,\vartheta,\varphi) \; + \boldsymbol{e}_- \, D^l_{1,-m}(0,\vartheta,\varphi) \right] \\ \mathbf{Y}_{lm}^{(1)}(\vartheta,\varphi) &= \sqrt{\tfrac{2l+1}{8\pi}} \left[ \boldsymbol{e}_+ \, D^l_{-1,-m}(0,\vartheta,\varphi) \; + \boldsymbol{e}_- \, D^l_{1,-m}(0,\vartheta,\varphi) \right] , \end{aligned} \tag{4.42}$$

where $D^l_{mm'}(\alpha, \beta, \gamma)$ are the Wigner $D$-functions, discussed on page 90.

The VSHs can be interpreted as the spherical complement to the complex exponentials $\exp(j\,2\pi\mu f_0)$ in the conventional one-dimensional FS, where $\mu \in \mathbb{Z}^+$ and $\mu f_0$ identifies the harmonic frequency. For the VSHs, the role of $\mu$ is played by the level $l$. Figure 4.13 shows the magnitude of the VSHs on the $x$–$z$ plane for the first levels and modes. It can be observed that the variation along elevation increases with the level. The magnitude of the VSHs does not vary with azimuth $\varphi$ and is the identical for $\nu = 0, 1$ and both vector components $\boldsymbol{e}_+$, $\boldsymbol{e}_-$. The level $l = 0$ corresponds to the Direct Current (DC) component, similarly to $\mu = 0$ for the FS. Transverse vector functions cannot have a DC component [216], we have that

$$\mathbf{Y}_{0m}^{(0)}(\vartheta,\varphi) = \mathbf{Y}_{0m}^{(1)}(\vartheta,\varphi) = \mathbf{0} \; . \tag{4.43}$$

Notice that this fact implies that omnidirectional antennas are physically impossible.

From Figure 4.13 it can also be observed that only the modes $m = \pm 1$ have power directed towards the poles. Symbolically, this can be expressed as [216]

$$\mathbf{Y}_{lm}^{(0)}(0,\varphi) = (-1)^l \, \mathbf{Y}_{lm}^{(0)}(\pi,\varphi) = \begin{cases} -m\sqrt{\frac{2l+1}{8\pi}} \, \boldsymbol{e}_+ & m = +1 \\ -m\sqrt{\frac{2l+1}{8\pi}} \, \boldsymbol{e}_- & m = -1 \\ 0 & \text{otherwise} \; , \end{cases} \tag{4.44}$$

[12] For a definition of the polar basis vectors see Appendix E.2.

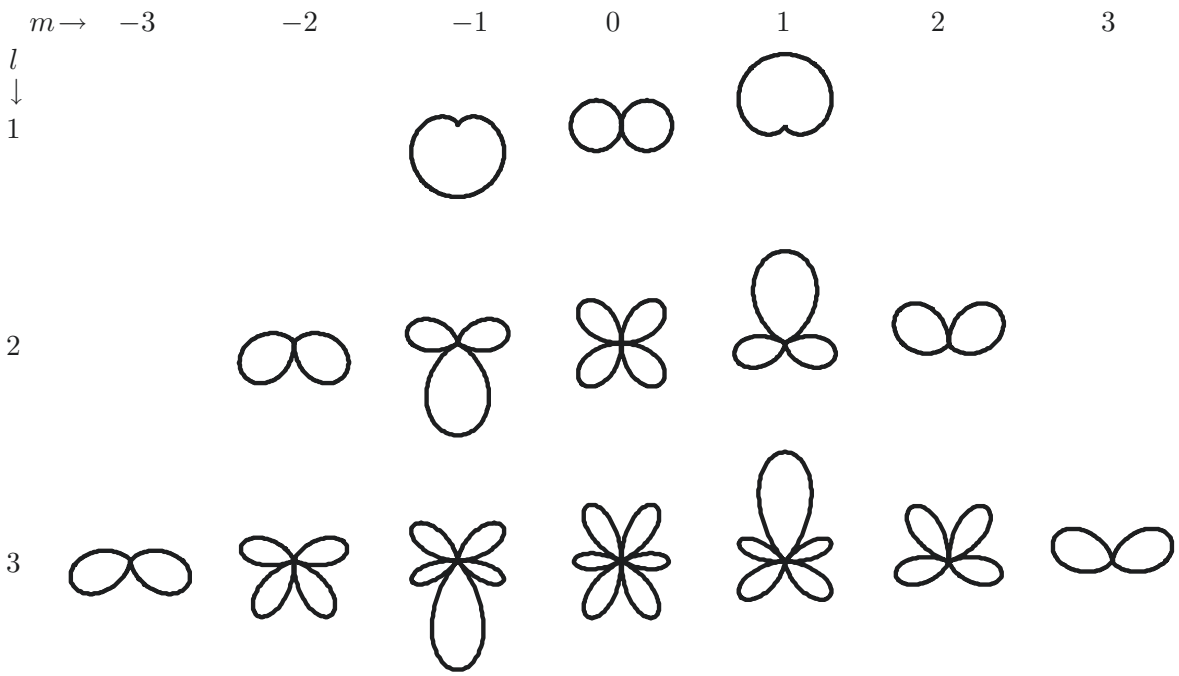


Fig. 4.13: Magnitude of the VSHs against co-elevation $\vartheta$ at a fixed azimuth $\varphi = 0, \pi$ ($x$–$z$ plane). The diagrams are oriented so that the north pole points towards the top of the page.

and

$$\boldsymbol{Y}_{lm}^{(1)}(0,\varphi) = (-1)^{l-1}\,\boldsymbol{Y}_{lm}^{(1)}(\pi,\varphi) = \begin{cases} \sqrt{\frac{2l+1}{8\pi}}\,\boldsymbol{e}_+ & \text{if } m = +1 \\ \sqrt{\frac{2l+1}{8\pi}}\,\boldsymbol{e}_- & \text{if } m = -1 \\ 0 & \text{otherwise .} \end{cases} \tag{4.45}$$

As already mentioned, the set of VSHs form an orthonormal system

$$\left\langle \boldsymbol{Y}_{lm}^{(\nu)}(\vartheta,\varphi), \boldsymbol{Y}_{l'm'}^{(\nu')}(\vartheta,\varphi) \right\rangle = \delta_{l,l'}\,\delta_{m,m'}\,\delta_{\nu,\nu'}\ , \tag{4.46}$$

which is complete for transverse vector functions on the sphere. The function $\delta_{a,b}$ is the *Kronecker delta symbol*, defined in Appendix B.3, which is 1 for $a = b$ and zero otherwise. The inner product between two vector functions $\boldsymbol{a}(\vartheta,\varphi)$ and $\boldsymbol{b}(\vartheta,\varphi)$, denoted as $\langle \boldsymbol{a}(\vartheta,\varphi), \boldsymbol{b}(\vartheta,\varphi)\rangle$, is defined as

$$\langle \boldsymbol{a}(\vartheta,\varphi), \boldsymbol{b}(\vartheta,\varphi)\rangle = \int_{\mathcal{S}^2} \boldsymbol{b}^{\mathrm{H}}(\vartheta,\varphi)\cdot\boldsymbol{a}(\vartheta,\varphi)\ \mathrm{d}\Omega, \tag{4.47}$$

where the superscript $(\cdot)^{\mathrm{H}}$ is the Hermitian transpose, i.e., conjugate transpose, and $\Omega$ is the solid angle, already introduced in Chapter 2. The inner product is then a surface integral on the 2-sphere.

We can now write the VSFT of the vector function $\boldsymbol{f}(\vartheta,\varphi)$ and its inverse as

$$F_{lm}^{(\nu)} = \left\langle \mathbf{Y}_{lm}^{(\nu)}(\vartheta,\varphi), \boldsymbol{f}(\vartheta,\varphi) \right\rangle \tag{4.48}$$

$$\boldsymbol{f}(\vartheta,\varphi) = \sum_{\nu=0}^{1} \sum_{l=0}^{\infty} \sum_{m=-l}^{l} F_{lm}^{(\nu)}\, \mathbf{Y}_{lm}^{(\nu)}(\vartheta,\varphi). \tag{4.49}$$

In the following we will denote the coefficients of the VSHs $F_{lm}^{(\nu)}$ as the VSFT of the function $\boldsymbol{f}(\vartheta,\varphi)$. For convenience, we abbreviate the direct transform in equation (4.48) as

$$F_{lm}^{(\nu)} = \mathcal{VSFT}\left\{\boldsymbol{f}(\vartheta,\varphi)\right\} \ , \qquad \boldsymbol{f}(\vartheta,\varphi) \overset{\mathcal{VSFT}}{\longrightarrow} F_{lm}^{(\nu)} \ , \tag{4.50}$$

whereas the Inverse Vector Spherical Fourier Transform (IVSFT) in equation (4.49) is abbreviated as

$$\boldsymbol{f}(\vartheta,\varphi) = \mathcal{IVSFT}\left\{F_{lm}^{(\nu)}\right\} \ , \qquad F_{lm}^{(\nu)} \overset{\mathcal{VSFT}}{\longleftarrow} \boldsymbol{f}(\vartheta,\varphi) \ . \tag{4.51}$$

Furthermore, we always denote the transformed version of a function with the corresponding capital letter.

Let us now introduce the Wigner $D$-functions. They are given explicitly in [216] as

$$D_{mm'}^{l}(\alpha,\beta,\gamma) = \mathrm{e}^{-j\,m\alpha} \cdot d_{mm'}^{l}(\beta) \cdot \mathrm{e}^{-j\,m'\gamma} \ , \tag{4.52}$$

Many different explicit expressions for $d_{mm'}^{l}(\beta)$ can be found in the literature, most of them are reported in [216]. One of them, involving simple trigonometric functions, is

$$\begin{aligned} d_{mm'}^{l}(\beta) = (-1)^{l-m'} \sqrt{(l+m)!(l-m)!(l+m')!(l-m')!} \\ \cdot \sum_{k} (-1)^{k} \frac{\left(\cos\frac{\beta}{2}\right)^{m+m'+2k} \left(\sin\frac{\beta}{2}\right)^{2l-m-m'-2k}}{k!(l-m-k)!(l-m'-k)!(m+m'+k)!} \ , \end{aligned} \tag{4.53}$$

where $k$ runs for all integer values for which the factorials exist, thus,

$$k \in \mathbb{Z}, \quad \max\left\{0,\ -(m+m')\right\} \leq k \leq \min\left\{l-m,\ l-m'\right\} \ . \tag{4.54}$$

Notice that $d_{mm'}^{l}(\beta)$ is real-valued. Considering the equations above and the expressions in (4.42), it can be observed that the VSHs can be expressed as a product of two functions, each dependent on only one variable, as

$$\mathbf{Y}_{lm}^{(\nu)}(\vartheta,\varphi) = \boldsymbol{g}_{lm}^{(\nu)}(\vartheta) \cdot \mathrm{e}^{jm\varphi} \tag{4.55}$$

where

$$\boldsymbol{g}_{lm}^{(0)}(\vartheta) = \frac{j}{\sqrt{l(l+1)}}\left[-\boldsymbol{e}_{+}\, d_{-1-m}^{l}(\vartheta) + \boldsymbol{e}_{-}\, d_{1-m}^{l}(\vartheta)\right] \tag{4.56}$$

$$\boldsymbol{g}_{lm}^{(1)}(\vartheta) = \frac{j}{\sqrt{l(l+1)}}\left[\boldsymbol{e}_{+}\, d_{-1-m}^{l}(\vartheta) + \boldsymbol{e}_{-}\, d_{1-m}^{l}(\vartheta)\right] \ . \tag{4.57}$$

This separability with respect to $\vartheta$ and $\varphi$ can be exploited in order to reduce the computational complexity, as discussed in Section 4.4.4.2. Additionally, the Wigner $D$-functions play an important role in the rotation of vector functions in the spectral domain, as discussed in Section 4.4.2.2.

**Property 4.4.1.** *The VSFT is linear, therefore we have that*

$$\mathcal{VSFT}\left\{a\cdot\boldsymbol{f}(\vartheta,\varphi)+b\cdot\boldsymbol{g}(\vartheta,\varphi)\right\} = a\cdot\mathcal{VSFT}\left\{\boldsymbol{f}(\vartheta,\varphi)\right\}+b\cdot\mathcal{VSFT}\left\{\boldsymbol{g}(\vartheta,\varphi)\right\} \ , \tag{4.58}$$

*where* $a, b \in \mathbb{C}$.

**Property 4.4.2.** *When transforming a vector function via the VSFT the energy is preserved. This property is valid for any generalized Fourier series and is known as the Parseval theorem [224]*

$$\int_{\mathcal{S}^2} \left\|\boldsymbol{f}(\vartheta,\varphi)\right\|^2 \mathrm{d}\Omega = \sum_{\nu=0}^{1}\sum_{l=0}^{\infty}\sum_{m=-l}^{l}\left|F_{lm}^{(\nu)}\right|^2 \ . \tag{4.59}$$

#### 4.4.2.1 The Level Power Spectrum

As proposed in [12], we introduce the Level Power Spectrum (LPS) $\Gamma_l^{(\nu)}$ of an antenna radiation pattern $\boldsymbol{b}(\vartheta,\varphi)$ as

$$\Gamma_l^{(\nu)} = \frac{1}{2l+1}\sum_{m=-l}^{l}\left|B_{lm}^{(\nu)}\right|^2 \ , \tag{4.60}$$

where $B_{lm}^{(\nu)}$ is the VSFT spectrum of the pattern $\boldsymbol{b}(\vartheta,\varphi)$. The level power spectrum represents the mean power for each level $l$ of the spectrum.

#### 4.4.2.2 Rotation of the Coordinate System

When we translate a one-dimensional (1D) period function in time, the coefficients of its Fourier Series maintain the same energy and are simply rotated by a certain phase shift which depends on the lag. On the sphere, in a similar fashion, a rotation of the vector function $\boldsymbol{f}(\vartheta,\varphi)$ corresponds to a modification of the coefficients of the vector spherical Fourier coefficients $F_{lm}^{(\nu)}$, so that the energy within one level and component stays constant, while phase and energy of the coefficients for different modes changes in a predictable way, as described in the following.

Let us first define formally an arbitrary rotation in the 3D space by means of the *Euler angles* $\alpha$, $\beta$, and $\gamma$. The Euler theorem states that any rotation can be described exhaustively by three angles about three known axes. Vashalovich *et al.* give an explanation of the Euler angles [216, Sec. 1.4], while Devanathan fully derives the rotation operator in different coordinate systems in [69, Ch. 4–5].

Any rotation can be interpreted as a rotation of the function while keeping the coordinate system fixed, or vice versa, by rotation the coordinate system while maintaining the function fixed. Following the latter interpretation, we can describe the Euler rotation with three steps

1. rotation about the $z$-axis by $\alpha$ $(0 \leq \alpha \leq 2\pi)$,
2. rotation about the rotated $y$-axis by $\beta$ $(0 \leq \beta \leq \pi)$,
3. rotation about the new $z$-axis (obtained after step 2) by $\gamma$ $(0 \leq \gamma \leq 2\pi)$.

Different interpretations are given in [216, Sec. 1.4].

For simplicity, we introduce the rotation operator $\widehat{D}_{\alpha,\beta,\gamma}\{\cdot\}$ [216], which rotates a vector or a vector function by the Euler angles $\alpha$, $\beta$, and $\gamma$. For instance, the rotation of the vector $\boldsymbol{a}$ results in the vector $\breve{\boldsymbol{a}}$, which can be written as

$$\breve{\boldsymbol{a}} = \widehat{D}_{\alpha,\beta,\gamma}\{\boldsymbol{a}\}. \tag{4.61}$$

**Property 4.4.3.** *If* $\boldsymbol{f}(\vartheta,\varphi) \overset{\mathcal{VSFT}}{\longrightarrow} F_{lm}^{(\nu)}$ *and* $\widehat{D}_{\alpha,\beta,\gamma}\{\cdot\}$ *is the rotation operator for the Euler angles* $\alpha$*,* $\beta$*, and* $\gamma$*, then*

$$\widehat{D}_{\alpha,\beta,\gamma}\{\boldsymbol{f}(\vartheta,\varphi)\} \overset{\mathcal{VSFT}}{\longrightarrow} \sum_{m=-l}^{l} D_{mm'}^{l}(\alpha,\beta,\gamma)\cdot F_{lm}^{(\nu)}\,, \tag{4.62}$$

*where* $D_{mm'}^{l}(\alpha,\beta,\gamma)$ *are the Wigner D-functions.*

As already mentioned, the rotation implies a different distribution of energy among the modes in each level and component, whereas the total energy in each level and component does not change.

This implies that the LPS, introduced in equation (4.60), is a rotation-invariant descriptor. Notice that this important property of the VSHs allows us to define bandlimited functions in Definition 4.4.4.

Using a convenient matrix notation, we can write equation (4.62) as

$$\breve{\boldsymbol{F}}_l^{(\nu)} = \begin{bmatrix} \breve{F}_{l,-l}^{(\nu)} \\ \vdots \\ \breve{F}_{l,l}^{(\nu)} \end{bmatrix} = \boldsymbol{D}^{l}(\alpha,\beta,\gamma)\cdot\boldsymbol{F}_l^{(\nu)} = \begin{bmatrix} D_{-l,-l}^{l}(\alpha,\beta,\gamma) & \dots & D_{l,-l'}^{l}(\alpha,\beta,\gamma) \\ \vdots & \vdots & \vdots \\ D_{-l,l}^{l}(\alpha,\beta,\gamma) & \dots & D_{l,l}^{l}(\alpha,\beta,\gamma) \end{bmatrix} \cdot \begin{bmatrix} F_{l,-l}^{(\nu)} \\ \vdots \\ F_{l,l}^{(\nu)} \end{bmatrix},$$

where $\boldsymbol{D}^{l}(\alpha,\beta,\gamma)$ is a square matrix with $2l+1$ rows and columns, and $\boldsymbol{F}_l^{(\nu)}$ and $\breve{\boldsymbol{F}}_l^{(\nu)}$ are vectors containing the coefficients of the original and rotated function, respectively, for the

$l$-th level, so that $\boldsymbol{F}_l^{(\nu)} \in \mathbb{C}^{2l+1\times 1}$. This equation shows once more how a rotation operates on different levels separately.

In general, an infinite number of coefficients is needed to exactly represent arbitrary transversal vector functions on the sphere using the VSFT. However, if we want to integrate numerically we have to truncate the series at a certain level. This restricts the functions that can be described exactly to bandlimited transversal spherical vector functions.

**Definition 4.4.4** (bandlimit)**.** A piecewise-continuous transverse spherical vector function $\boldsymbol{f}(\vartheta,\varphi)$ with VSFT coefficients $F_{lm}^{(\nu)}$ is called *bandlimited* with bandlimit $L$ if

$$F_{lm}^{(\nu)} = 0 \quad \text{for } l > L \ .$$

In other words, the spherical coefficients of the function $\boldsymbol{f}(\vartheta,\varphi)$ possess energy only at the first $L+1$ levels, namely for $0 \leq l \leq L$.

By applying the property that the LPS is a rotation-invariant function, we can state the following

**Theorem 4.4.5** (bandlimit theorem)**.** *If a piecewise-continuous transverse spherical vector function $\boldsymbol{f}(\vartheta,\varphi)$ is bandlimited with bandlimit $L$, then $\forall\ \alpha,\beta,\gamma$, $\widehat{D}_{\alpha,\beta,\gamma}\{\boldsymbol{f}(\vartheta,\varphi)\}$ is bandlimited with bandlimit $L$.*

In other words, a rotated version of a bandlimited function $\boldsymbol{f}(\vartheta,\varphi)$, here expressed mathematically by means of the rotation operator $\widehat{D}_{\alpha,\beta,\gamma}\{\cdot\}$ introduced in equation (4.61), is characterized by the very same bandlimit.

This important property of the VSFT is shared neither by the direct angular domain model nor by the EADF. This means, that both the angular representation and the EADF descriptors change when we rotate the antenna, or, equivalently, when we choose a different coordinate system.

#### 4.4.2.3 Transform of White Noise

Of particular interest is the representation in the spherical spectral domain of white Gaussian noise. We denote white Gaussian noise on the surface of the 2-sphere with $\boldsymbol{n}(\vartheta,\varphi)$ so that

$$\boldsymbol{n}(\vartheta,\varphi) = n_+(\vartheta,\varphi)\cdot\boldsymbol{e}_+ + n_-(\vartheta,\varphi)\cdot\boldsymbol{e}_-, \tag{4.63}$$

where the scalar functions $n_+(\vartheta,\varphi)$ and $n_-(\vartheta,\varphi)$ are Zero Mean Circular Symmetric Complex Gaussian (ZMCSCG) processes with variance $\sigma_n^2$, so that for two points on the sphere $\{\vartheta,\varphi\}$ and $\{\vartheta',\varphi'\}$,

$$\mathrm{E}\left[\boldsymbol{n}(\vartheta,\varphi)\boldsymbol{n}^{\mathrm{H}}(\vartheta',\varphi')\right] = \sigma_n^2\,\boldsymbol{I}_2\,\delta_{\vartheta,\vartheta'}\,\delta_{\varphi,\varphi'} \tag{4.64}$$

where $\boldsymbol{I}_2$ is the identity matrix of size $2\times 2$, and $\delta_{a,b}$ is the Kronecker delta symbol, defined in Appendix B.3.

Let $N_{lm}^{(\nu)}$ be the spherical Fourier coefficients of $\boldsymbol{n}(\vartheta,\varphi)$, so that

$$\boldsymbol{n}(\vartheta,\varphi) \overset{\mathcal{VSFT}}{\longrightarrow} N_{lm}^{(\nu)}. \tag{4.65}$$

The correlation between the VSH coefficients can be written as

$$\mathrm{E}\left[N_{lm}^{(\nu)} N_{l'm'}^{(\nu')*}\right] = \int_{\mathcal{S}^2}\int_{\mathcal{S}^2} \left[\boldsymbol{Y}_{lm}^{(\nu)}(\vartheta,\varphi)\right]^{\mathrm{H}} \mathrm{E}\left[\boldsymbol{n}(\vartheta,\varphi)\,\boldsymbol{n}^{\mathrm{H}}(\vartheta',\varphi')\right] \boldsymbol{Y}_{l'm'}^{(\nu')}(\vartheta',\varphi')\mathrm{d}\Omega\mathrm{d}\Omega', \tag{4.66}$$

where the expectation operator $\mathrm{E}[\cdot]$ has been moved inside the integrals considering that the $\boldsymbol{Y}_{lm}^{(\nu)}(\vartheta,\varphi)$ are deterministic. Substituting equation (4.64) in (4.66) we have

$$\mathrm{E}\left[N_{lm}^{(\nu)} N_{l'm'}^{(\nu')*}\right] = \int_{\mathcal{S}^2}\int_{\mathcal{S}^2} \left[\boldsymbol{Y}_{lm}^{(\nu)}(\vartheta,\varphi)\right]^{\mathrm{H}} \sigma_n^2\,\delta_{\vartheta,\vartheta'}\,\delta_{\varphi,\varphi'}\boldsymbol{Y}_{l'm'}^{(\nu')}(\vartheta',\varphi')\mathrm{d}\Omega\mathrm{d}\Omega'\ . \tag{4.67}$$

Due to the Kronecker delta symbols involved, the above integral does not vanish only for $\vartheta=\vartheta'$ and $\varphi=\varphi'$, or equivalently, for $\Omega=\Omega'$. Using the orthonormality property of the VSHs we obtain the following result

$$\mathrm{E}\left[N_{lm}^{(\nu)} N_{l'm'}^{(\nu')*}\right] = \sigma_n^2\,\delta_{\nu,\nu'}\,\delta_{l,l'}\,\delta_{m,m'}\ . \tag{4.68}$$

Additionally, we can say that the VSH coefficients $N_{lm}^{(\nu)}$ are Gaussian distributed, due to the linearity of the operations carried out in the derivation above. Therefore, we can state that the VSFT transform of ZMCSCG white noise in angular domain gives VSH coefficients $N_{lm}^{(\nu)}$ which are as well ZMCSCG with variance $\sigma_n^2$.

Tab. 4.1: Properties of the VSFT and FS in comparison.

| **Property** | **VSFT** | **FS** |
|---|---|---|
| **Linearity** | $\mathcal{VSFT}\left\{a\cdot\boldsymbol{f}(\vartheta,\varphi)+b\cdot\boldsymbol{g}(\vartheta,\varphi)\right\}$ $=a\cdot\mathcal{VSFT}\left\{\boldsymbol{f}(\vartheta,\varphi)\right\}$ $+b\cdot\mathcal{VSFT}\left\{\boldsymbol{g}(\vartheta,\varphi)\right\}$ | $\mathcal{FS}\left\{a\cdot f(t)+b\cdot g(t)\right\}$ $=a\cdot\mathcal{FS}\left\{f(t)\right\}$ $+b\cdot\mathcal{FS}\left\{g(t)\right\}$ |
| **Parseval** | $\int\limits_{\mathcal{S}^2}\left\|\boldsymbol{f}(\vartheta,\varphi)\right\|^2\mathrm{d}\Omega$ $=\sum\limits_{\nu lm}\left\|F_{lm}^{(\nu)}\right\|^2$ | $\lim\limits_{T\to\infty}\frac{1}{T}\int\limits_{T}\left\|f(t)\right\|^2\mathrm{d}t$ $=\sum\limits_{\mu}\left\|F_{\mu}\right\|^2$ |
| **Shifting** | $\widehat{D}_{\alpha,\beta,\gamma}\left\{\boldsymbol{f}(\vartheta,\varphi)\right\}$ $\Big\downarrow\mathcal{VSFT}$ $\sum\limits_{m}D^{l}_{mm'}(\alpha,\beta,\gamma)F_{lm}^{(\nu)}$ | $f(t-t_0)$ $\Big\downarrow\mathcal{FS}$ $F_{\mu}\mathrm{e}^{-j2\pi\mu f_0 t_0}$ |
| **Filtering** | multiply in spectral domain | multiply in spectral domain or convolve in time |
| **White Noise** | $\boldsymbol{n}(\vartheta,\varphi)\sim\mathcal{ZMCSCG}(\sigma_n^2)$ $\Big\downarrow\mathcal{VSFT}$ $N_{lm}^{(\nu)}\sim\mathcal{ZMCSCG}(\sigma_n^2)$ | $n(t)\sim\mathcal{ZMCSCG}(\sigma_n^2)$ $\Big\downarrow\mathcal{FS}$ $N_{\mu}\sim\mathcal{ZMCSCG}(\frac{\sigma_n^2}{2})$ |

### 4.4.3 The Discrete Vector Spherical Fourier Transform

In order to use the VSFT introduced in the previous section on measured radiation patterns, we need to introduce numerical methods to compute the VSH coefficients.

In general, there exist two approaches to compute coefficients of a generalized Fourier series, such as the VSFT, from sampled functions, namely

- least squares approach
- orthonormality approach.

The least squares approach consists first in determining the number of coefficients, i.e., levels to be computed. In a second step, the coefficients are estimated so that the reconstructed function is optimal in a least square sense. In other words, the samples are approximated with a series of VSHs by minimizing the mean squared error. In [125, 126, 124, 123, 129, 130], this approach is followed for the similar SME also known as the SWE. In [233], a least squares approximation of the coefficients of the scalar Spherical Fourier Transform (SFT) is derived.

To follow the *orthonormality approach*, we need a numerical method to compute the continuous integrals in equation (4.48). This problem is known in science as *quadrature* or *cubature*, and is dealt in detail in Appendix C. This method is often used for the scalar SFT, e.g., in [12, 195, 176, 116].

Section C.2 presents three quadratures which allow us to integrate functions on the 2-sphere exactly, under certain conditions. They are the Chebyshev, the Gauss-Legendre, and the Lebedev quadratures.

For the scalar case, the integral to be solved and its corresponding numerical computation can be expressed as

$$\int_{\mathcal{S}^2} f(\vartheta,\varphi)\,\mathrm{d}\Omega \approx \sum_{s=0}^{N_s-1} f(\vartheta_s,\varphi_s)\,w_s\ , \tag{4.69}$$

where the function $f$ is known at the $N_s$ quadrature points given by $\vartheta_s$ and $\varphi_s$, and $w_s$ are the corresponding quadrature weights.

The major advantage of the least squares approach is that no particular sampling grid is needed. However, it is difficult to decide how many parameters (i.e., VSHs coefficients) should be estimated and whether the sampling grid is sufficient to represent a given angular function, i.e., no exact sampling theorem can be given. Blais and Soofi investigated the accuracy and complexity of both methods empirically in [48], with the result that the accuracy is comparable while the Fourier method is computationally more efficient. Nevertheless, the data was provided on the same grid for both experiments. Thus, the number of parameters to be estimated by the least squares method was known and it was guaranteed that aliasing could not occur. On the contrary, when the data is provided on a grid which might be insufficient to represent the continuous function, the accuracy of the least squares spectral approximation decreases. The major advantage of the orthonormality method is its accuracy

and the possibility to give an explicit sampling theorem, as we see below. Furthermore, an efficient noise reduction method can be derived.

In some applications, such as in geophysics [50] and meteorology [184], it is either not possible or very costly to sample the sphere at desired quadrature grid points. Therefore, a least squares approximation of the VSFT or SFT coefficients is the only possibility. This is not the case for radiation patterns, which can be sampled at will in the anechoic chamber, as discussed in Section 4.1.7 on page 76.

#### 4.4.3.1 The Orthonormality Approach for Computing the DVSFT

Following the orthonormality principle already discussed above, we require to compute inner products as in equation (4.48) by means of solving integrals as in (4.47), namely

$$F_{lm}^{(\nu)} = \int_{\mathcal{S}^2} \boldsymbol{f}^{\mathrm{H}}(\vartheta,\varphi) \cdot \mathbf{Y}_{lm}^{(\nu)}(\vartheta,\varphi)\ \mathrm{d}\Omega, \tag{4.70}$$

where $\boldsymbol{f}(\vartheta,\varphi)$ is the function under study, i.e., the polarimetric radiation pattern, and $F_{lm}^{(\nu)}$ is the corresponding desired VSH coefficient for level $l$, mode $m$, and component $\nu$. By substituting (4.49) in the above equation we obtain

$$\begin{aligned} F_{lm}^{(\nu)} &= \int_{\mathcal{S}^2} \left[\mathbf{Y}_{lm}^{(\nu)}(\vartheta,\varphi)\right]^{\mathrm{H}} \sum_{\nu'=0}^{1} \sum_{l'=0}^{L} \sum_{m'=-l}^{l} F_{l'm'}^{(\nu')} \mathbf{Y}_{l'm'}^{(\nu')}(\vartheta,\varphi)\, \mathrm{d}\Omega \\ &= \sum_{\nu'=0}^{1} \sum_{l'=0}^{L} \sum_{m'=-l}^{l} F_{l'm'}^{(\nu')} \int_{\mathcal{S}^2} \left[\mathbf{Y}_{lm}^{(\nu)}(\vartheta,\varphi)\right]^{\mathrm{H}} \mathbf{Y}_{l'm'}^{(\nu')}(\vartheta,\varphi)\, \mathrm{d}\Omega\ . \end{aligned} \tag{4.71}$$

From this equation we can see that the desired VSH coefficient $F_{lm}^{(\nu)}$ is a sum of all coefficients multiplied with integrals of the products of VSHs. Now, if we could integrate all VSHs exactly, the integrals would all vanish but the one for $l = l'$, $m = m'$, and $\nu = \nu'$, thanks to the orthonormality property given in equation (4.46). Unfortunately, this is not the case for sampled VSHs, which, depending on the chosen quadrature, can be integrated exactly only until a certain level $l_{\max}$, as discussed in detail in Appendix C.2. We overcome this problem by assuming that the function to be analyzed is bandlimited with bandlimit $L = l_{\max}$. In this case, the integrals of the VSHs vanish for $l \leq L$, while the coefficients themselves are 0 for $l > L$. As a consequence of this assumptions we have that by computing numerically the right hand side of equation (4.71), we obtain the correct VSHs coefficients for all levels $l$.

We can now write the DVSFT as

$$F_{lm}^{(\nu)} = \int_{\mathcal{S}^2} \left[\mathbf{Y}_{lm}^{(\nu)}(\vartheta,\varphi)\right]^{\mathrm{H}} \boldsymbol{f}(\vartheta,\varphi)\, \mathrm{d}\Omega \approx \sum_{s=0}^{N_s-1} w_s \left[\mathbf{Y}_{lm}^{(\nu)}(\vartheta_s,\varphi_s)\right]^{\mathrm{H}} \boldsymbol{f}(\vartheta_s,\varphi_s)\ , \tag{4.72}$$

where $\{\vartheta_s,\varphi_s\}$ are the quadrature points of one of the three quadratures introduced in Ap-

pendix C.2, and $w_s$ are their corresponding weights. The quadratures presented in Appendix C.2 are defined with respect to the maximum order $M$ of the polynomials which they can correctly integrate over the 2-sphere.

For functions with bandlimit $L$, the product of VSHs gives origin to polynomials up to level $2L$. This leads to the following sampling theorem for the DVSFT

**Theorem 4.4.6** (sampling theorem)**.** *If a piecewise-continuous transverse spherical vector function $\boldsymbol{f}(\vartheta, \varphi)$ is bandlimited with bandlimit $L$, quadrature grids with $M \geq 2L$ are required to compute the VSHs coefficients exactly with the DVSFT.*

If the sampling theorem is not fulfilled, i.e., if the function is not bandlimited, or if the quadrature grid has not enough sampling points for the bandlimit, then we can not exactly compute the VSHs coefficients with the DVSFT. In this case, products involving higher levels of VSHs might result in polynomials higher than the degree for which we can compute exactly. Then, the last integral in (4.71), when computed numerically, does not vanish if the indices do not match (i.e., the discrete VSHs are not orthonormal). In this case, power will leak from higher to lower levels. This effect, although originating from a different mechanism, is similar to the aliasing phenomenon seen for the DFT.

If the functions are bandlimited with bandlimit $L$ and the sampling points are on a quadrature grid with $M \geq 2L$, the approximation of the integral in (4.72) using the quadrature rule becomes an equality. Table 4.2 shows the required number of samples in order to correctly compute the DVSFT coefficients for $l \leq L$. A table including more values for $L$ can be found

Tab. 4.2: Number of required samples to exactly compute the DVSFT coefficients from a function with bandlimit $L$ with the Chebyshev, Gauss-Legendre, and Lebedev quadratures

| $L$ | $M$ | $N_{\mathrm{Ch}}$ | $N_{\mathrm{GL}}$ | $N_{\mathrm{Lb}}$ |
|---|---|---|---|---|
| 2 | 5 | 20 | 12 | 14 |
| 7 | 15 | 210 | 112 | 68 |
| 15 | 31 | 930 | 480 | 350 |
| 29 | 59 | 3422 | 1740 | 1202 |
| 65 | 131 | 17030 | 8580 | 5810 |

for reference on page 225.

Notice that we define the DVSFT merely as an approximation of the VSFT. For this reason, the Inverse Discrete Vector Spherical Fourier Transform (IDVSFT) is identical to the IVSFT with the exception that the levels considered are limited, namely

$$\boldsymbol{f}(\vartheta, \varphi) \approx \sum_{\nu=0}^{1} \sum_{l=0}^{L} \sum_{m=-l}^{l} F_{lm}^{(\nu)} \, \boldsymbol{Y}_{lm}^{(\nu)}(\vartheta, \varphi) \ . \tag{4.73}$$

This equation reveals the interpolation capabilities of the IDVSFT. Not only can the function be computed on the original sampling grid, but additionally at any point on the sphere $\{\vartheta, \varphi\}$.

Note that in a noiseless case, a bandlimited function properly sampled and transformed can be interpolated exactly over the whole sphere using the IDVSFT.

#### 4.4.3.2 Numerical Stability and Computational Complexity

The implementation of the DVSFT presents non trivial challenges. The basis functions given in equation (4.42) require the computation of the Wigner $D$-functions. Let us recall these functions

$$D^l_{mm'}(\alpha,\beta,\gamma) = \mathrm{e}^{-j\,m\alpha} d^l_{mm'}(\beta) \mathrm{e}^{-j\,m'\gamma}, \tag{4.74}$$

where

$$d^l_{mm'}(\beta) = (-1)^{l-m'} \sqrt{(l+m)!(l-m)!(l+m')!(l-m')!} \cdot \sum_i (-1)^i \frac{\left(\cos\frac{\beta}{2}\right)^{m+m'+2i} \left(\sin\frac{\beta}{2}\right)^{2l-m-m'-2i}}{i!(l-m-i)!(l-m'-i)!(m+m'+i)!}\,.$$

The factorials in $d^l_{mm'}(\beta)$ for higher levels assume extremely large values, which imply a substantial computational effort. However, the main problem is caused by numerical instability introduced by the multiplication of large numbers with very small ones due to the finite precision in floating point numerical computations. For instance, if we want to compute $d^{30}_{1,-30}(\beta)$, some of the factorials reach values of $60! \approx 10^{82}$, while others are small integer numbers. Lotze in [149, pp. 55-60] proposes an efficient and stable implementation of the DVSFT. The numerical stability is achieved with a recursive method based on the three-term recurrence to compute $d^l_{mm'}$ from $d^{l-1}_{mm'}$ and $d^{l-2}_{mm'}$ [131]. A better efficiency is obtained by exploiting the symmetries displayed by the VSHs and by applying a FFT along azimuth, in case of the Chebyshev or Gauss-Legendre grids.

Figure 4.14 compares the computation time for different maximum levels $L$ of the DVSFT using the different optimizations just mentioned. Notice that the range of $L$ between 5 and 50 is adequate for the application of the DVSFT for radiation patterns of antennas used in wireless communications. We compare a straightforward implementation, marked with "not optimized", a more efficient version denoted by "no optimization", which implements the optimizations proposed in [149, pp. 55-60], and an optimized version which additionally includes a FFT along azimuth. As already mentioned, the latter is possible only for the Chebyshev and Gauss-Legendre grids. All curves are computed using the numerically stable implementation based on the three-term recurrence. The number of grid points for all quadratures is chosen to be the smallest possible which avoids aliasing. The comparison is carried out with respect to the mean computation time in seconds, averaged over 100 random transformations. The DVSFTs are computed on an AMD 64 bit X2 4400+ processor with 1 GB DDR2 RAM using MATLAB® R2006a under Windows XP.

The Gauss-Legendre quadrature in combination with the FFT achieves the best performance. This is in spite of the fact that this grid requires more points than the Lebedev grid.

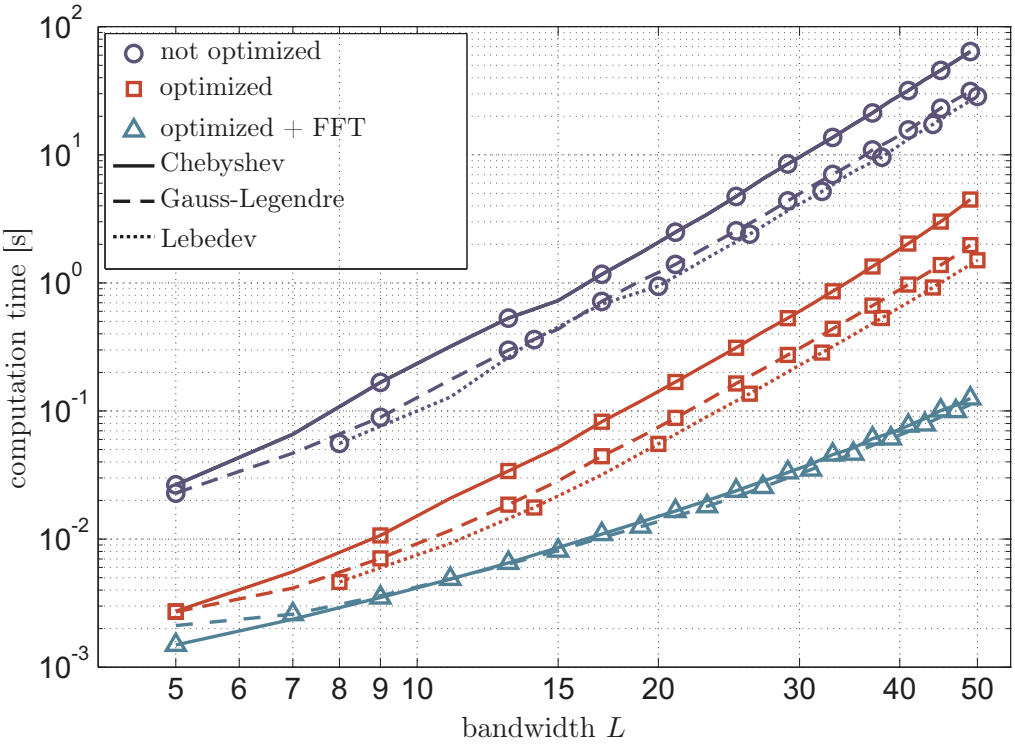


Fig. 4.14: Average computation time for one DVSFT for different bandlimits $L$ with different optimizations and quadratures.

The speed and accuracy of the IDVSFT for interpolation compared with traditional antenna radiation pattern models is discussed in the next section.

### 4.4.4 Application of the DVSFT on Polarimetric Radiation Patterns

In this section we address the numerous applications of the DVSFT in the modeling and manipulation of antenna polarimetric radiation patterns, namely

- compression of information
- interpolation in the angle domain
- noise reduction
- SNR estimation
- computation of the antenna efficiency
- improvement of the antenna measurements

In order to use the DVSFT for any of these applications, as already mentioned in the previous section, it is necessary that the functions in the angle domain, i.e., the radiation patterns, are bandlimited. In fact, if this assumption did not hold, we could not compute the spherical Fourier coefficients via the orthonormality method given in equation (4.72).

#### 4.4.4.1 Bandlimits of Polarimetric Radiation Patterns

The radiation of EM waves from an antenna into the 3D space can be interpreted as taking place in a spherical waveguide, as suggested in [98, pp. 264 ff.] and in [96, 202]. In contrast to conventional waveguides, the cross-section increases with distance. However, properties such as the orthogonality of the modes, the cut-off frequencies, the evanescence phenomenon, known from conventional waveguides, hold also in this case.

Let the smallest possible radius of a spherical surface fully enclosing the antenna (*minimum sphere*) be denoted by $r_0$. Every cross-section of the waveguide has a finite area, and thus, only a finite number of modes can propagate. The propagation modes are represented by the very same VSHs introduced in Section 4.4.2, as they are the solutions to the Laplace's equation in spherical coordinates. With larger cross-sections, higher order of VSHs represent candidate modes for the propagation. The transition from evanescence to propagation of a mode $m$ of level $l$ occurs around a radius $r_t = l/k$, where $k$ is the free-space wave number $2\pi/\lambda$ [96]. In other words, at a radius $r \ll r_t$ the mode is evanescent, while for $r \gg r_t$ the mode propagates with a decay proportional to $r^{-1}$. As a direct consequence, we have that the dominant modes for the propagation are characterized by $l \leq kr_0$, as the higher modes are heavily attenuated in the range between $r_0$ and the corresponding transition regions $r_t$, from where they can start propagating.

Therefore, the radiation pattern of a finite antenna has always a spherical low pass character, i.e., with decaying power when $l$ increases. This result is particularly interesting as it guarantees that any physical antenna possesses a radiation pattern which can be well approximated as a bandlimited spherical signal (see Definition 4.4.4). The maximum level $L$ at which we can truncate the expansion series depends directly on the antenna's size and on the excitation frequency. For practical purposes, the truncation level $L$ is given by the empirical rule [96]

$$L = \lceil kr_0 \rceil + \iota \ , \tag{4.75}$$

where $\lceil kr_0 \rceil$ indicates the smallest integer number larger than or equal to $kr_0$, and the term $\iota$ is a positive integer depending on the required accuracy. Choosing $\iota$ as large as 10 is enough for all practical purposes. Hansen carries out further investigations on the choice of $\iota$ in [96], and other authors, such as Koivisto in [128], address the issue in more detail. However, for our applications the rule given in 4.75 is sufficient. Typical values for $kr_0$ with antennas used in mobile communications are between 5 and 15, thus, we expect to compute no more than $L = 30$ levels.

#### 4.4.4.2 Compression and Interpolation

Assuming that a polarimetric radiation pattern has bandlimit $L$, we can represent it via a VSFT by computing $N_{\text{VSFT}}$ spherical Fourier coefficients, so that

$$N_{\text{VSFT}} = 2(L+1)^2 - 2. \tag{4.76}$$

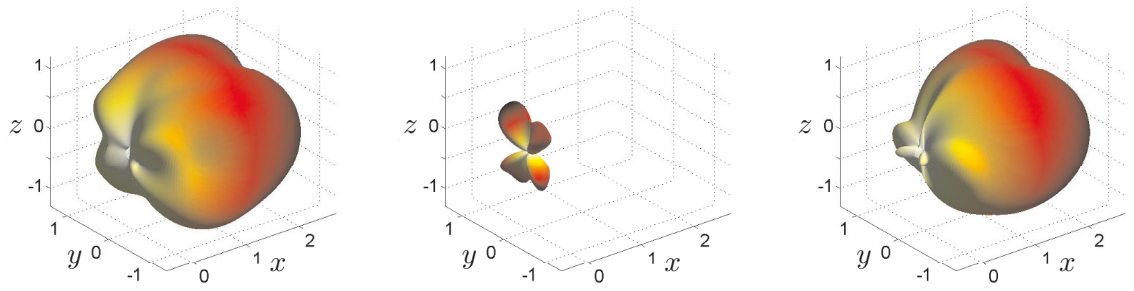


(a) directivity (b) vertical pattern (c) horizontal pattern

Fig. 4.15: Radiation pattern of a synthetic patch antenna.

For the direct angular representation, also discussed in Section 4.2, assuming the traditional Chebyshev grid (see Appendix C.2.1.1) we need at least $2L + 1$ samples along elevation and $4L$ along azimuth. Considering the two polarizations, the total number of required sampling points, denoted by $N_{\text{angular}}$ is

$$N_{\text{angular}} = 2(2L + 1) \times 4L \approx 16L^2 \ . \tag{4.77}$$

The ratio between $N_{\text{angular}}$ and $N_{\text{VSFT}}$ gives the information compression factor, approximately equal to

$$\frac{N_{\text{angular}}}{N_{\text{VSFT}}} \approx 8 \ . \tag{4.78}$$

In practice, this compression factor can be increased even further when a required accuracy for the interpolation is given, as described below.

If the radiation pattern is bandlimited and sampled on an appropriate sampling grid, the DVSFT coefficients represent an exhaustive descriptor, so that an exact interpolation can be carried out. In reality, because of non-idealities of the antenna and of the measurement system, no radiation pattern is strictly bandlimited. However, after a certain spherical level the power of the VSHs coefficients is so small that we can neglect them without significant errors.

We now analyze the truncation error using an exemplary radiation pattern obtained from an EM simulation of a patch antenna. The pattern is originally computed in the angular domain for an equiangular grid with 3° separation in both elevation and azimuth. Figure 4.15(a) shows the directivity function, and Figures 4.15(b) and 4.15(c) show the squared magnitudes of $b_\vartheta(\vartheta, \varphi)$ and $b_\varphi(\vartheta, \varphi)$, respectively, which represent the vertical and horizontal antenna radiation patterns introduced in Section 4.1.4.

Figure 4.16 shows the number of coefficients needed to achieve a certain interpolation accuracy. The latter is measured in terms of the Normalized Mean Squared Error (NMSE),

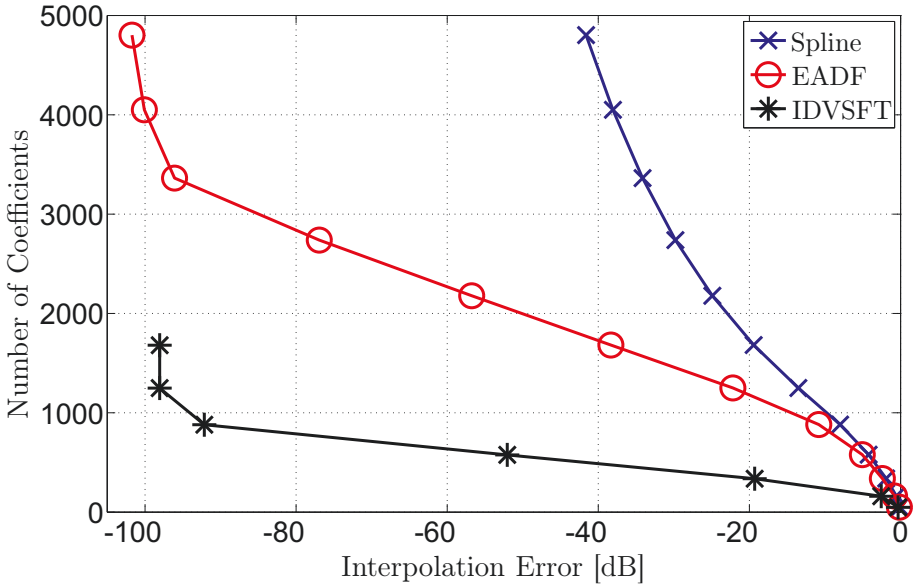


Fig. 4.16: Comparison of the required number of coefficients against interpolation accuracy of IDVSFT, EADF, and spline-based interpolation. The synthetic patch antenna radiation pattern shown in Figure 4.15 was used.

computed as

$$\mathrm{NMSE} = \frac{\mathrm{E}\left[\left\|\boldsymbol{b}(\vartheta_u, \varphi_v) - \boldsymbol{b}_{\mathrm{I}}(\vartheta_u, \varphi_v)\right\|^2\right]}{\mathrm{E}\left[\left\|\boldsymbol{b}(\vartheta_u, \varphi_v)\right\|^2\right]}, \tag{4.79}$$

where the interpolated radiation pattern at point $\{\vartheta_u, \varphi_v\}$ is denoted by $\boldsymbol{b}_{\mathrm{I}}(\vartheta_u, \varphi_v)$. In the figure we compare the three interpolation methods considered in this work, namely the spline-based approach for the angular representation (Section 4.2), the EADF-based approach for the 2D DFT representation (Section 4.3.2), and the IDVSFT-based approach introduced in this section.

In order to reduce the number of coefficients, i.e., samples in the angular domain we simply perform a decimation. For the EADF we reduce the size of the limited support, namely the number of Fourier coefficients considered. Similarly, for the IDVSFT we consider the VSH coefficients up to a desired level. For all three cases, we interpolate the pattern on the original grid on which it was simulated, so that we can compare it with $\boldsymbol{b}(\vartheta_u, \varphi_v)$. It can be seen that the IDVSFT can achieve very low interpolation errors even with a low number of coefficients. In comparison, the spline approach shows a rather poor performance. The figure shows, as expected, that the VSFT gives the most compact and accurate description of the radiation pattern. However, for interpolation purposes, another important aspect is the computational complexity required.

To investigate this aspect we express the computational complexity in terms of the average processing time. A more rigorous approach, namely counting the number of additions and multiplications required, is particularly complicated to follow, as further optimizations and approximations should be considered. An indicative comparison is given in Figure 4.17. The

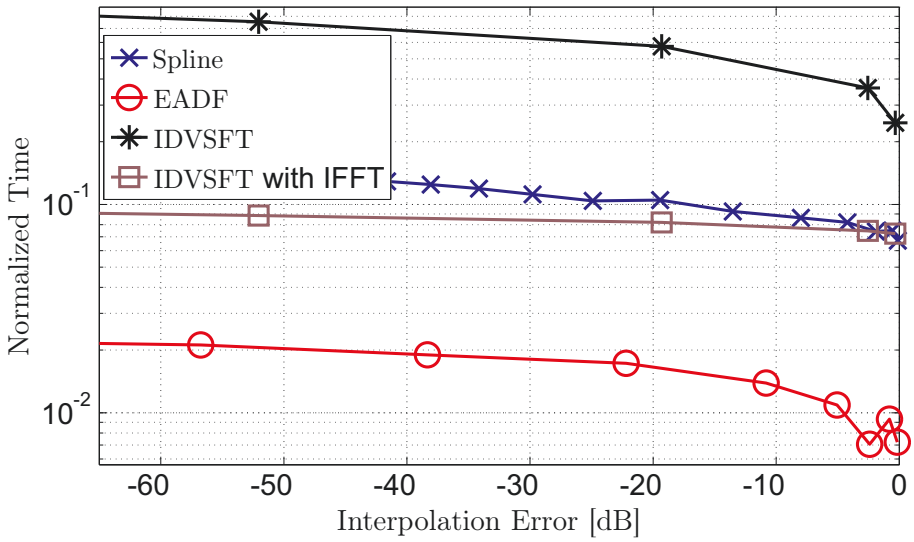


Fig. 4.17: Comparison of the computation time of IDVSFT-based interpolation with EADF and spline interpolation. The IDVSFT was computed with and without using the IFFT. A synthetic patch antenna radiation pattern was used. The time is normalized to the time required to compute the IDVSFT with an interpolation error of -95 dB (not shown in the figure).

figure shows the normalized average computation time to interpolate the radiation pattern at a random point on the sphere. The normalization is such that the time required to interpolate via the IDVSFT with an accuracy of -95 dB is set to 1. A MATLAB® version of the IDVSFT has been used, while the curve for the EADF is obtained via a C implementation provided by M. Landmann. For the spline interpolation we use standard MATLAB® commands. For sure the IDVSFT could be optimized further, however it is very unlikely that it will ever be as fast as the EADF due to the much more complicated mathematics involved.

Therefore, in an application where an accuracy of -40 dB or less is sufficient and the computational effort plays an important role, the EADF represents without doubt the optimal solution. This is the case of a geometry-based channel model such as the IlmProp, as discussed in Section 5.1.1. In order to take advantage of the benefits offered by the DVSFT, we combine the two methods in a processing scheme presented in Section 4.5.

#### 4.4.4.3 SNR Estimation

In equation (4.68) we have seen that the application of a VSFT on ZMCSCG noise implied VSHs coefficients with the very same distribution. With the DVSFT, on the other hand, this result does not hold, as white noise is not bandlimited.

In [149, pp. 66-69], a detailed investigation on the effects of the aliasing on the spectrum of white noise is carried out. The results show, as expected, that the distribution of power among modes and levels is not homogenous. Furthermore, the distribution changes depending on the grid chosen. However, the variation in power is always below 3 dB. Considering that the dynamic range of the values of the spherical coefficients varies between 30 and 50 dB, we

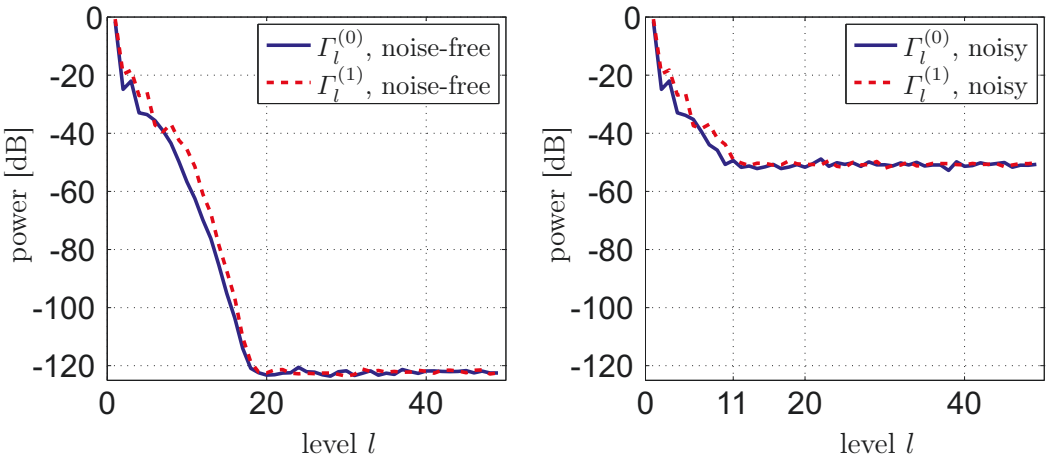


Fig. 4.18: Level power spectra of a simulated patch antenna radiation pattern. Left: noise-free, right: with additive white Gaussian noise of 10 dB SNR. The term $l_c$ represents the cut-off level, picked manually, after which the noise dominates over the signal.

can still consider the VSHs coefficients obtained from a DVSFT applied on the sampled white noise to be white, so that all coefficients possess the same power.

Due to the spherical low pass character of a radiation pattern, we expect that its noiseless LPS decays with the level $l$. On the other hand, the LPS of the noise is assumed to remain constant.

In case of a well sampled measured radiation pattern, by identifying the levels which contain the signal, and those dominated by the noise, we can estimate the Signal to Noise Ratio (SNR) and develop a strategy to reduce the noise.

Figure 4.18 shows the LPS of the simulated antenna radiation pattern shown in Figure 4.15. The LPS of the noise-free radiation pattern is plotted on the left hand side. The remaining noise floor at around -120 dB is caused by numerical quantization noise of the simulator and of the DVSFT itself. The plot on the right hand side shows the LPS of the same radiation pattern after adding complex white Gaussian noise with an average SNR of 10 dB in the angular domain.

When we transform the VSFT spectrum back in angular domain, and we compare it to the noise-less radiation pattern we can compute an average SNR of 21 dB. This is due to the fact that the noise cannot be represented exhaustively by the computable number of spectral coefficients, while the signal part can. In other words, some power of the noise is implicitly cut off when the DVSFT and IDVSFT are applied.

In a practical application, we can estimate the SNR by first choosing a cut-off level $l_c$ (also shown in Figure 4.18). The cut-off level is reached when the noise starts dominating over the signal. We pick $l_c$ manually, as an elbow marking this point is always easily recognizable, also in measured patterns.

The noise power $\sigma_n^2$ can be estimated by averaging the power of the coefficients which have a level $l \geq l_c$. In the same way, for $l < l_c$, we can estimate the sum $(P_b + \sigma_n^2)$, where $P_b$ is the power of the radiation pattern and $\sigma_n^2$ the power of the noise. The SNR estimate can

then be computed as

$$\mathrm{SNR} = \frac{P_b}{\sigma_n^2} = \frac{P_b + \sigma_n^2}{\sigma_n^2} - 1 \ . \tag{4.80}$$

#### 4.4.4.4 Noise Reduction via the Spherical Wiener Filter

Once we have identified the cut-off level $l_\mathrm{c}$, we can simply disregard the coefficients for $l > l_\mathrm{c}$ to obtain a noise reduction. However, this method is not optimal and requires user intervention in the choice of $l_\mathrm{c}$. The optimal spectral filter for this purpose is represented by the *spherical Wiener filter*.

The derivation of this filter, as the name suggests, is a straightforward extension of the well known Wiener filter in signal processing applied on our problem. Additionally, we require the filter to be real valued and constant with respect to the modes of the same level and component. Let the function $G_l^{(\nu)}$ denote the filter, and $\Gamma_l^{(\nu)}$ the LPS of the noisy radiation pattern. We can compute the filter as

$$G_l^{(\nu)} = \frac{\Gamma_l^{(\nu)} - \sigma_n^2}{\Gamma_l^{(\nu)}} \ , \tag{4.81}$$

where $\sigma_n^2$ is the power of the noise and $\Gamma_l^{(\nu)}$ is the power signal plus noise at the level $l$ and component $\nu$. In practical cases, a good estimate of $\sigma_n^2$ can be obtained simply by considering the last level computed for the DVSFT, denoted by $l_\mathrm{max}$, as

$$\sigma_n^2 \approx \frac{1}{2}\left(\Gamma_{l_\mathrm{max}}^{(0)} + \Gamma_{l_\mathrm{max}}^{(1)}\right), \tag{4.82}$$

so that substituting in equation (4.81) we obtain

$$G_l^{(\nu)} \approx \frac{\Gamma_l^{(\nu)} - \frac{1}{2}\left(\Gamma_{l_\mathrm{max}}^{(0)} + \Gamma_{l_\mathrm{max}}^{(1)}\right)}{\Gamma_l^{(\nu)}} \ . \tag{4.83}$$

For a more detailed derivation we refer the reader to [149].

As an example, we use the synthetic radiation pattern from Section 4.4.4.4, once more with white noise added at each sampling point in the angular domain with an average SNR of 10 dB. Figure 4.19 shows the LPS and the estimated Wiener filter using equation (4.83). It can be seen that the filter approximately follows the signal and goes to zero when the noise becomes dominant. After applying the Wiener filter in the spectral domain, and transforming back into angular domain we obtain an SNR of 34.4 dB, thus, with a gain of 24.4 dB. Clearly, the gain varies depending on the oversampling in angular domain and on the spectrum of the pattern.

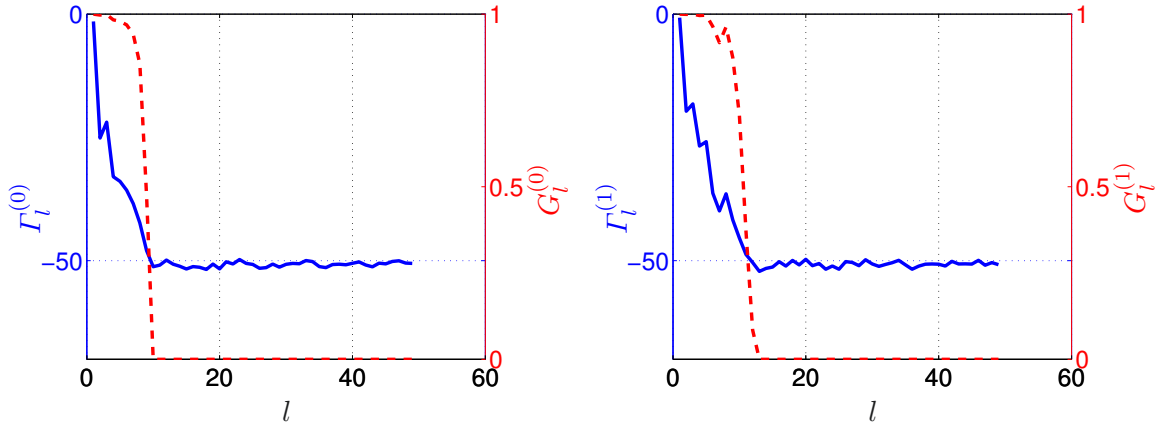


Fig. 4.19: Level power spectrum $\Gamma_l^{(\nu)}$ of a synthetic patch antenna radiation pattern (solid blue curves) and the corresponding estimated Wiener filter (dashed red curves). Left: $\nu = 0$, right: $\nu = 1$

#### 4.4.4.5 Computing the Antenna Efficiency for Measured Radiation Patterns

The quadrature rules introduced in Appendix C.2 and the DVSFT introduced in Section 4.4.3 are particularly useful in computing the antenna efficiency $\xi$ introduced in Section 4.1.2. The antenna efficiency is defined as the ratio of the radiated power to the power fed into the antenna port. Thus, it accounts for the total losses of the antenna. An alternative definition in terms of the directivity function $d(\vartheta, \varphi)$ and gain function[13] $g(\vartheta, \varphi)$ is

$$\xi = \frac{g(\vartheta, \varphi)}{d(\vartheta, \varphi)}. \tag{4.84}$$

We now take advantage of the fact that the surface integral over the 2-sphere $\mathcal{S}^2$ of the directivity function is equal to $4\pi$, as shown in equation (4.8). The antenna efficiency $\xi$ can then be computed as

$$\xi = \frac{\int_{\mathcal{S}^2} g(\vartheta, \varphi)\ \mathrm{d}\Omega}{\int_{\mathcal{S}^2} d(\vartheta, \varphi)\ \mathrm{d}\Omega} = \frac{\int_{\mathcal{S}^2} g(\vartheta, \varphi)\ \mathrm{d}\Omega}{4\pi}. \tag{4.85}$$

When the antenna is studied in an anechoic chamber, as discussed in Section 4.1.7, we can measure a sampled noisy version of the polarimetric antenna response $\boldsymbol{a}(\vartheta, \varphi)$ (discussed in Section 4.1.5), which we denote as $\widehat{\boldsymbol{a}}(\vartheta, \varphi)$.

If the measurement system is properly calibrated, the values of the measured response are correct in an absolute scale. Please notice that if this were not the case, we could not compute the efficiency with the method here described.

Assuming that the antenna response is a properly sampled bandlimited function, we can apply the quadrature rule given in equation (4.69), and considering that

$$g(\vartheta, \varphi) = \|\boldsymbol{a}(\vartheta, \varphi)\|^2 \tag{4.86}$$

[13] also presented in Section 4.1.2

we can compute the efficiency $\xi$ as

$$\xi = \frac{\int_{\mathcal{S}^2} \|\boldsymbol{a}(\vartheta,\varphi)\|^2 \, \mathrm{d}\Omega}{4\pi} = \frac{1}{4\pi} \sum_{i=0}^{N-1} \|\boldsymbol{a}(\vartheta_i,\varphi_i)\|^2 \, w_i, \tag{4.87}$$

where $N$ is the number of sampling points, $w_i$ is the weight corresponding to the quadrature point $\{\vartheta_i, \varphi_i\}$, and $i = 0,\ 1,\ \ldots,\ N-1$. By using the noisy estimate $\widehat{\boldsymbol{a}}(\vartheta,\varphi)$ we have

$$\xi \approx \sum_{i=0}^{N-1} \|\widehat{\boldsymbol{a}}(\vartheta,\varphi)\|^2 \, w_i. \tag{4.88}$$

Alternatively, we can carry out a DVSFT on $\widehat{\boldsymbol{a}}(\vartheta,\varphi)$ to obtain the VSHs coefficients $\widehat{A}_{lm}^{(\nu)}$. In the spectral domain we can carry out the noise reduction as explained in the previous section, and then, considering the Parseval's theorem for the VSH given in equation (4.59), we can compute

$$\xi \approx \sum_{\nu=0}^{1} \sum_{l=0}^{l_{\max}} \sum_{m=-l}^{l} \left| G_l^{(\nu)} \cdot \widehat{A}_{lm}^{(\nu)} \right|^2, \tag{4.89}$$

where $G_l^{(\nu)}$ is the spherical Wiener filter given in equation (4.83) and $l_{\max}$ is the number of levels which are computed by the DVSFT.

This method has been applied to compute the efficiency of measured antenna arrays in [33]. The major results of this investigation are reported in Section 5.2.4.

#### 4.4.4.6 Efficient Antenna Measurements

As discussed at the beginning of Section 4.4.4, the physics behind the propagation of EM waves guarantees that radiation patterns are bandlimited functions in the VSFT domain. Furthermore, with equation (4.75) we can predict the bandlimit $L$ by knowing the physical dimensions of the antenna. Once a certain quadrature on the sphere has been chosen, i.e., the grid of sampling points on the sphere[14], we can determine the minimum of sampling points required to avoid aliasing. Notice that this important theoretical result (summarized in the Theorem 4.4.6) can be achieved only by using the proposed VSHs representation.

If the choice of quadrature is not bound to the measurement equipment, we can think of using a more efficient quadrature, i.e., with less points.

Let us now consider the three quadratures given in Appendix C.2, namely the Chebyshev, the Gauss-Legendre, and the Lebedev quadrature and the corresponding minimum numbers of sampling points required, $N_{\mathrm{Ch}}$, $N_{\mathrm{GL}}$, and $N_{\mathrm{Lb}}$. We can write the relation between them as

$$N_{\mathrm{Ch}} \approx 2N_{\mathrm{GL}} \approx 3N_{\mathrm{Lb}} \ . \tag{4.90}$$

The above equation tells us that we could obtain the same information with approximately

[14] See Appendix C.2.

one third of the measurement points if we used the Lebedev grid instead of the Chebyshev one.

However, the noise level in the spectral domain increases if we measure on less quadrature points, so that an oversampling could be desirable. As a trade-off solution, we can measure the same sampling point many times, and average the results to improve the SNR. Since the movement of the robotic arm holding the test antenna is usually much slower than the actual measurement of one sampling point, it is likely that using less sampling points measured with higher accuracy represents a better solution.

The optimal solution to this trade-off clearly depends on the measurement equipment and software employed, so that no general solution can be given here.

### 4.4.5 Practical Challenges During Measurements

During the measurements of antenna radiation patterns in an anechoic chamber, several problems arise which might result in an inaccurate DVSFT based descriptor. Focussing on antennas designed for wireless communications and measured in anechoic chambers, [149] and [136] deal with the issues discussed in this section more in detail.

The problems involve

- the misalignment of the antenna in the measurement coordinate system
- the inaccuracy of the step motor
- phase shifts introduced by the cables
- influences of the positioner in the near-field
- missing samples at one of the poles.

In the following sections we discuss each issue more in detail.

#### 4.4.5.1 Misplacement and Misalignment of the Antenna Under Study

As mentioned in Section 4.1.7 on page 76, in order to measure the radiation pattern in the anechoic chamber, the antenna under study is rotated by a positioner. Ideally, the center of the antenna would be placed in the center of rotation. Unfortunately, this is practically not possible when more antennas mounted on an array are measured at the same time. An example is given in Figure 4.20, which shows a Stacked Polarimetric Uniform Circular Patch Array (SPUCPA), used at the Ilmenau University of Technology for channel sounding. The positioner rotates the antenna around the $z$-axis to measure the different azimuth angles $\varphi$. The marked antenna under study finds itself displaced from the axis of rotation. This virtually enlarges the radius of the minimum sphere enclosing the antenna, which increases the number of DVSFT levels required (see equation (4.75)).

We can model the far-field polarimetric radiation pattern of the displaced antenna as

$$\boldsymbol{b}_{\text{disp}}(\vartheta,\varphi) = \boldsymbol{b}(\vartheta,\varphi)\,\mathrm{e}^{jk\boldsymbol{u}^{\mathrm{T}}(\vartheta,\varphi)\boldsymbol{d}}\,, \tag{4.91}$$

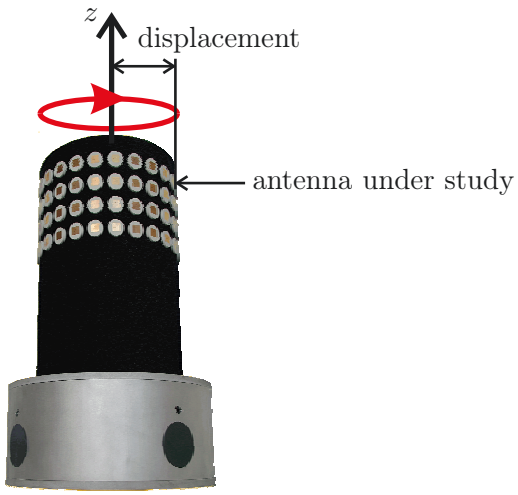


Fig. 4.20: Stacked Polarimetric Uniform Circular Patch Array (SPUCPA). The antenna under study is displaced with respect to the center of rotation. The SPUCPA consists of 96 patch antennas with 2 polarization ports each.
(source: Institute of Information Technology, Ilmenau University of Technology)

where $k$ is the wave number, equal to $2\pi/\lambda$, $\boldsymbol{d}$ is the *displacement vector* pointing towards the position of the probe antenna with respect to the center of the coordinate system, as depicted in Figure 4.21. The functions $\boldsymbol{b}(\vartheta, \varphi)$ and $\boldsymbol{b}_{\text{disp}}(\vartheta, \varphi)$ are the true antenna radiation pattern

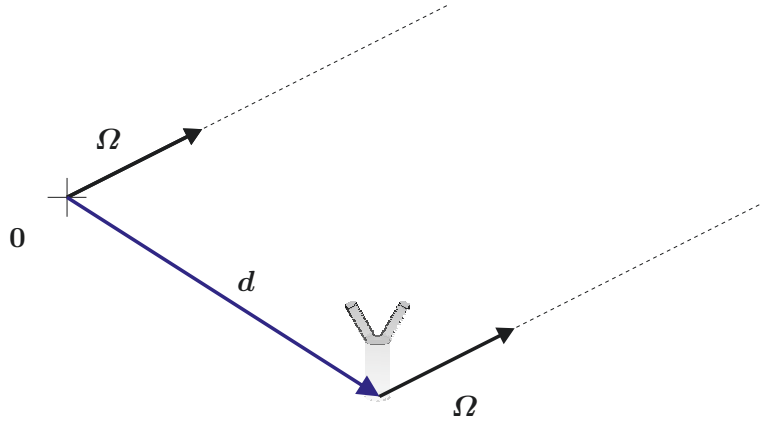


Fig. 4.21: Visualization of the displacement problem. The antenna under study is not in the origin of the coordinate system, denoted by $\mathbf{0}$. The radiation pattern is observed at a point far from $\mathbf{0}$, in the direction indicated by $\boldsymbol{\Omega}$.

and the measured one, respectively. The vector $\boldsymbol{\Omega}$, is the unit vector pointing towards the point of observation. It is defined as

$$\boldsymbol{\Omega} = [\cos(\theta) \cdot \cos(\varphi),\ \cos(\theta) \cdot \sin(\varphi),\ \sin(\theta)]^{\mathrm{T}}\,. \tag{4.92}$$

By estimating the position of the antenna $\boldsymbol{d}$ we can correct the radiation pattern $\boldsymbol{b}_{\text{disp}}(\vartheta, \varphi)$ by multiplying $\mathrm{e}^{-jk\boldsymbol{\Omega}^{\mathrm{T}}\widehat{\boldsymbol{d}}}$.

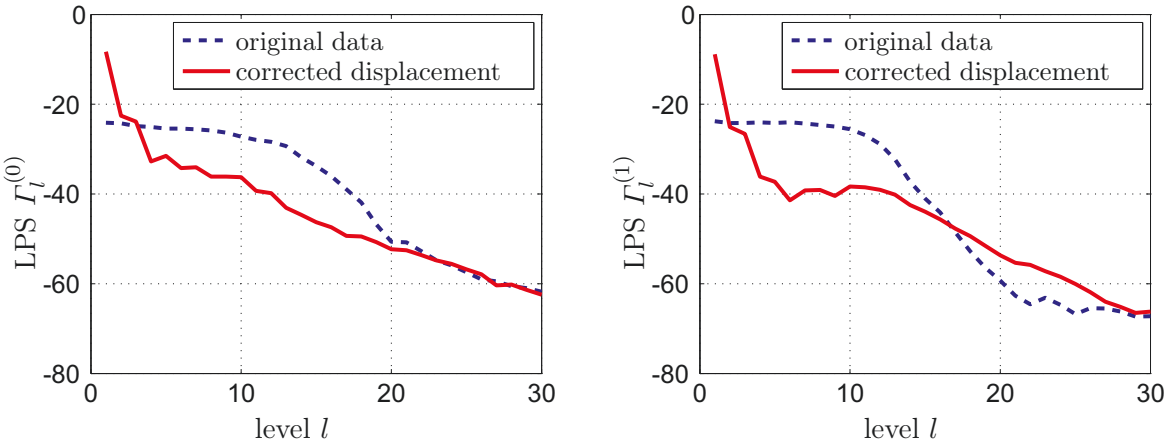


Fig. 4.22: LPS of one measured element of the SPUCPA, with and without antenna displacement correction. It can be seen, that the LPS changes significantly.

If exact positioning is technically possible, the vector $\widehat{\boldsymbol{d}}$ can be obtained directly from the antenna array specifications. If not, we can estimate $\widehat{\boldsymbol{d}}$ with a method proposed in [149, pp. 82-84], which is similar to the one developed in [141] for the EADF. As equation (4.91) shows, the displacement does not change the power in the radiaion pattern, as only the phase is affected. However, as already stated, the number of significant spherical levels is increased. We can deduce that the power in the spherical spectrum will be spread across more levels, in comparison to the centered antenna. For this reason, we can find the estimate of the displacement vector, namely $\widehat{\boldsymbol{d}}$, by searching for the most compact spectrum. This is implicitly achieved by maximizing the power in the very first level. To solve this problem, a numerical optimization method is proposed in [149].

To test the algorithm we apply it to a measured radiation pattern of one element of the SPUCPA shown in Figure 4.20. The results are depicted in Figure 4.22. The blue dashed curve shows the LPS of the measured antenna radiation pattern. After estimating the displacement, and correcting it, we obtain the LPS indicated by the red solid curve. It can be seen that the power at the lower levels increases significantly, although the total power is unchanged. Noise reduction and pattern interpolation can be performed more efficiently on the spectrum of the corrected pattern, and potential aliasing is prevented.

#### 4.4.5.2 Finite Resolution of the Step Motor

The positioner of the antenna under study is controlled by a step motor. The latter possesses a finite resolution, so that we cannot position the array at any arbitrary azimuth and elevation.

For instance, the positioner used in the anechoic chamber at the Ilmenau University of Technology has a minimum step size of $\frac{0.9^\circ}{188} \approx 0.00479^\circ$ in azimuth and $\frac{0.9^\circ}{100} = 0.009^\circ$ in elevation. Notice that these steps are very small compared to the typical spacing between the sampling points.

The effects of this non-ideality is studied in [149], where it is proven that the errors are so low that they can be neglected. Obviously, when a less precise step motor was used, we would need to reconsider the issue more carefully.

#### 4.4.5.3 Phase Shifts Introduced by Cables

To gather full polarimetric radiation patterns a dual-polarized probe antenna is used during the antenna measurements. A dual-polarized antenna possesses two ports, one for each polarization, so that the vertical and horizontal polarization components, namely $b_\vartheta(\vartheta, \varphi)$ and $b_\varphi(\vartheta, \varphi)$, respectively, are measured separately. It is unavoidable, that the cables connected to the two ports have slightly different lengths, which results in a constant phase shift between the two polarization components. The absolute value of the circular polarized components, i.e., the magnitude of the helicity radiation pattern components (see Section E.3), must be constant at the poles ($\vartheta = 0, \pi$) for all $\varphi$, since their derivatives with respect to $\varphi$ is zero. When a constant phase shift is added to one of the polar components of the radiation pattern, this condition is not fulfilled, which results in an erroneous DVSFT description.

The impact of the constant phase shift between the polarization components on the reconstruction error is analyzed in [149]. The investigations demonstrate the necessity to correct this phase before applying the DVSFT. To do so, the phase shift between the two polarization components is estimated from measurement data gathered at one of the poles. When the Gauss-Legendre or Lebedev grid are used, more sampling points at one of the poles need to be measured in order to perform the estimation.

#### 4.4.5.4 Other Measurement Distortions

Every metal object which is in the near-field of the antenna strongly influences the radiation pattern, so that it can almost be considered part of the antenna itself. This creates the biggest problem while calibrating an unknown antenna, as we cannot avoid having some rigid support to hold it. Correcting the effects of the positioner in the measured data is very complicated and represents a broad and challenging topic for future research.

In some anechoic chambers due to the limited movement capabilities of the positioner, it is not possible to measure over the whole sphere around the antenna under study. In this case there will be a "blind area", meaning that several points of the sampling grid miss completely. Missing values represent a difficulty for methods based on transformations such as the DVSFT and the EADF. On the other hand the descriptor in angular domain (see Section 4.2) would not suffer much from it, with the exception that we cannot interpolate in the blind area. The investigations in [149] show that the IDVSFT-based interpolation still performs well in such a case. However, a more detailed analysis considering the least squares approach to compute the VSHs coefficients should be carried out.

Other issues represent sources for possible errors in the measurement process. The walls of the anechoic chamber are never capable of fully suppressing the echoes. The dual polarized

probe antenna cannot measure the two polarization components with an ideal decoupling, so that a certain cross talk between polarizations always occurs.

## 4.5 Antenna Radiation Pattern Model for the IlmProp

In Section 4.4.4.2 we showed, that the EADF is the best choice for applications requiring fast and fairly accurate interpolation of polarimetric antenna radiation patterns, such as for channel modeling. On the other hand, the DVSFT is a precious tool to plan and optimize the antenna measurements, as well as to reduce measurement noise and to interpolate with the highest accuracy. With this in mind, we propose the processing scheme depicted in Figure 4.23. The measurement is carried out on one of the quadrature grids introduced in Appendix C.2. The number of quadrature points is chosen considering the sampling theorem 4.4.6 and the physical bandlimit obtained from equation (4.75), and maximizing the SNR while keeping the measurement time within desired values. The measured antenna response $\widehat{\boldsymbol{a}}(\vartheta_i, \varphi_i)$ is then transformed by means of the DVSFT to obtain the VSHs coefficients $\widehat{A}_{lm}^{(\nu)}$. The latter are filtered with the spherical Wiener filter $G_l^{(\nu)}$ introduced in Section 4.4.4.4. The denoised spherical spectrum is transformed back in angular domain into a proper periodic Chebyshev grid, so that the EADF can be computed.

Figure 4.24 compares the interpolation error of the EADF with and without noise reduction with the DVSFT.

White noise with an average SNR of 10 dB was added to the synthetic polarimetric radiation pattern shown in Figure 4.15. The NMSE of the interpolation versus the size of the square support of the EADF is shown (blue dashed curve). The green solid curve shows the interpolation error of the EADF computed after noise reduction with the spherical Wiener

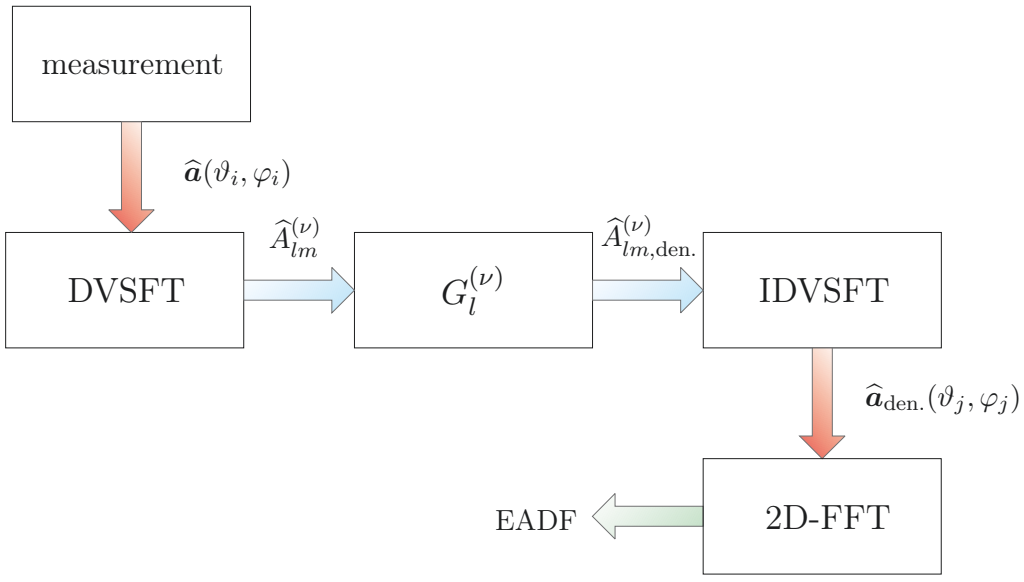


Fig. 4.23: Scheme to apply the DVSFT as a preprocessing step before computing the EADF.

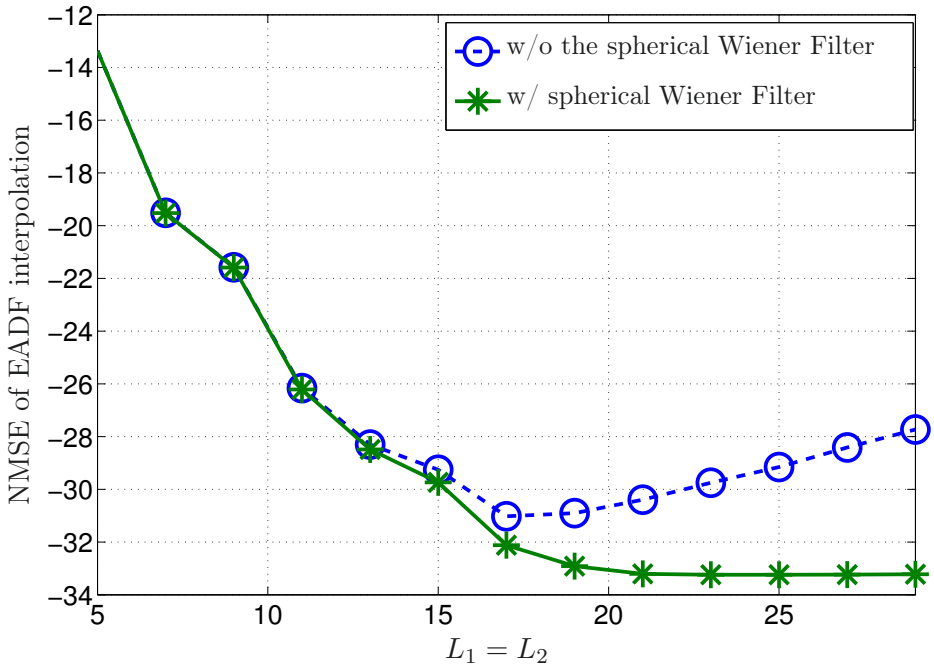


Fig. 4.24: Interpolation error of the EADF with and without spherical Wiener filter. Significantly lower errors can be achieved when the noise of the radiation pattern is reduced by applying a Wiener filter on the DVSFT spectrum before computing the EADF. The error of the EADF increases for $L_1 = L_2 > 17$ as the noise becomes dominating.

filter (Section 4.4.4.4). As the figure shows, the EADF-based descriptor can be improved significantly using the DVSFT and spherical Wiener filtering.

# 5. THE ILMPROP CHANNEL MODEL

This chapter presents the main achievement of this work: the IlmProp. It is a geometry-based channel model for multi-user time variant frequency selective Multiple Input Multiple Output (MIMO) systems.

The IlmProp fills the gap between directional channel models and ray-tracers. Similarly to the directional channel models discussed in Section 3.3, the IlmProp approximates the propagation as a sum of rays. However, the IlmProp models the physical environment more in depth by defining explicitly the complete trajectories of the Multi-Path Components (MPCs), i.e., the propagation paths, as well as by accurately modeling the three-dimensional (3D) polarimetric antenna radiation patterns. Yet, the IlmProp does not go into the details required by a ray-tracer, i.e., defining the ElectroMagnetic (EM) properties of all physical objects present in the environment.

The modeling principles and the key concepts characterizing the IlmProp are explained in detail in Section 5.1.

The IlmProp can be used following two very different strategies:

- Non measurements-based approach
- Measurements-based approach.

The difference lies in the way in which the model parameters are defined. In the non measurements-based approach, explained in Section 5.2, the parameters are set by the user arbitrarily, whereas in the measurements-based approach, discussed in Section 5.3, these are obtained from high-resolution parameter estimates.

When the IlmProp is used following the first approach, it serves a variety of aims

- compare different precoding schemes as carried out for the Block Diagonalization (BD) and Successive Optimization (SO) zero-forcing methods in Section 5.2.1
- investigate the behavior of scheduling algorithms as discussed in Section 5.2.2 for the *ProSched* algorithm, a scheduler for Space-Division Multiple Access (SDMA) schemes
- investigate different receiver strategies in Section 5.2.3 we compare different array configurations in a satellite to indoor scenario. The investigations considered single antennas, linearly and circularly polarized, as well as 2-element arrays with different polarizations and offsets

- evaluate the performance of different antenna arrays as investigated in Section 5.2.4 for a 3-element array with and without a Decoupling and Matching Network (DMN). The performance evaluation is carried out by means of comparing the antenna correlation and efficiency, as well as computing the channel capacity and BER curves for different IlmProp scenarios

- investigate the behavior of parameter estimation techniques as performed in Section 5.2.5 for the ISIS estimator [77].

- test analytical channel models as done in Section 5.2.6 for a novel subspace-based channel model which characterizes the multi-dimensional channel by means of the correlation tensor.

Other minor applications are mentioned in Section 5.2.7.

The measurement-based applications follow the Measurement-Based Parametric Channel Model (MBPCM) concept, proposed by Thomä *et al.* in [209]. This method requires MIMO channel measurements in which precise information on the position and orientation of the antenna arrays has been gathered. Moreover, the algorithm requires the parameter estimates obtained from a high-resolution parameter estimation technique. From this information, thanks to the novel localization algorithm proposed in Section 5.3.1, it is possible to obtain an IlmProp geometry, i.e., the explicit geometrical description of the propagation paths. It is then possible to compute new synthetic channels by changing different model parameters, such as the antenna arrays, the trajectories of the arrays, the number of users, and the frequency bandwidth. This method allows us to measure the environment once and, in a post-processing step, obtain realistic synthetic channels for different antenna arrays, mobile trajectories and so on.

The localization algorithm consists of two steps, the probability map inversion and the scatterers identification, dealt in Sections 5.3.1.1 and 5.3.1.2, respectively. Validations for the first step are given in Section 5.3.3 for synthetic data and in Section 5.3.4 for two-dimensional (2D) channel measurements. A validation for the whole processing chain on full polarimetric 3D measurements is presented in Section 5.3.5.

In 2006 the IlmProp MATLAB® implementation was made public by posting part of the code on the Internet. This boosted the attention that the IlmProp was able to capture so that several students and researchers contributed to its development, as discussed in Section 5.4.

## 5.1 Modeling Principle

The IlmProp is a flexible geometry-based multi-user Multiple Input Multiple Output (MIMO) channel modeling tool, capable of dealing with time variant frequency selective scenarios. Its main scope is the generation of Channel Impulse Responses (CIRs) as a sum of propagation

rays. One or more Mobile Stations (MSs) are modeled in the three-dimensional (3D) space by storing their Cartesian coordinates at all time snapshots considered. One Base Station (BS), which can also be moved in space, represents the other side of the link. Figure 5.1 illustrates

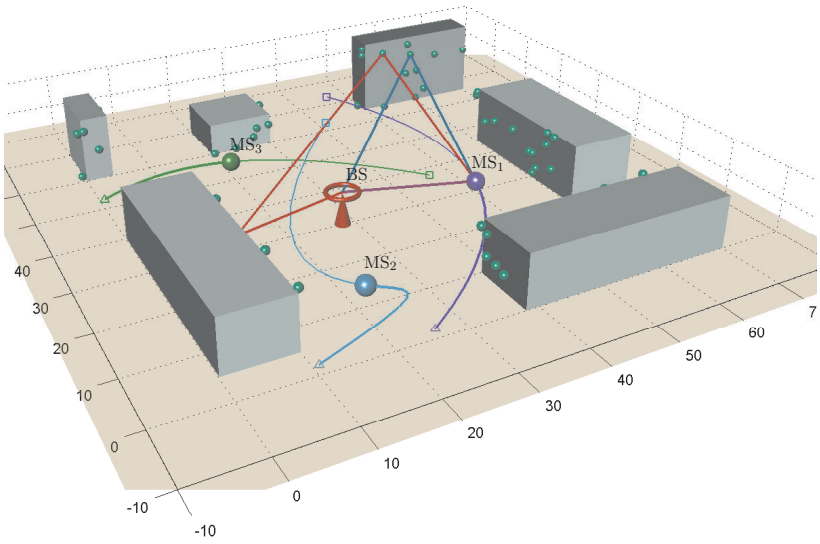


Fig. 5.1: Sample scenario generated with the IlmProp to illustrate the capabilities of the channel model. The LOS and two NLOS paths are visible.

an exemplary IlmProp scenario. Three MSs ($MS_1$, $MS_2$, and $MS_3$) move around the BS. Their curvilinear trajectories are shown. The BS and mobile terminals can employ any number of antennas arranged in an array with an arbitrary geometry. More details on the antenna arrays are given in Section 4.1.6.

Note that the IlmProp assumes an uplink channel. Therefore, often the base station is referred to as the receiver (Rx), and the mobiles as transmitters (Tx). This is only a matter of convenience since the reciprocity of the wireless link[1] allows us to use the computed CIRs for the downlink as well.

The propagation is modeled as a sum of ray-like paths which link the MSs to the BS. The LOS is the path which connects directly the MS to the BS. The NLOS components, on the other hand, are modeled by defining a series of point-like Interacting Objects (IOs) through which the path propagates.

The IOs model any interaction of the planar wave with a physical object, such as a reflection or a diffraction[2]. Since an IO does not specify the type of interaction, we refer to it simply as *scatterer*. To each scatterer, a time variant *scattering coefficient* is assigned. The scattering coefficient determines the percentage of power scattered by the IO towards the next IO or, in case of the last scatterer of a path, towards the receiver. The scattering coefficient

[1] The reciprocity theorem, also called *Lorentz reciprocity theorem*, states that the relationship between an oscillating current and the resulting electric field is unchanged if one interchanges the points where the current is placed and where the field is measured. Applied to wireless systems, it implies that the uplink channel is identical to the downlink channel for the same time and frequency [121, Ch. IV.21].

[2] More details on the interactions are given in Section 3.3.2.

$\rho \in \mathbb{C}$ is expressed as a ratio of voltages and is in general complex to allow the modeling of a phase shift introduced by the scatterer.

The IlmProp, as most geometry-based channel models, assumes that the propagation of ElectroMagnetic (EM) waves can be well described by rays. This is the basic axiom of the Geometrical Theory of Diffraction (GTD), already introduced in Section 3.3.2.

In the scenario depicted in Figure 5.1, the scatterers are placed randomly on the surfaces of some buildings, and are represented by green dots. The figure shows also two paths linking the first MS to the BS. One passes through one scatterer only, and therefore represents a single-bounce path. The other is a double-bounce. The number of paths, and which scatterers they travel through are arbitrary and can change at any time instant. This information, for the $p$-th path and time instant $t$, is stored in the index set $\mathcal{K}_\mathrm{p}(t)$. For instance, $\mathcal{K}_2(t_0) = [3\ 4\ 1]$ indicates that the second path at time instant $t = t_0$ is a path traveling through the third, fourth, and then first scatterer before reaching the BS.

The CIRs are generated by sampling both the time and frequency domain with $M_t$ and $M_f$ samples, respectively. After setting up the geometry of the scenario and defining the range and sampling intervals for time and frequency, assuming one MS only, the IlmProp calculates the channel coefficients as a superposition of the LOS path and $M_\mathrm{P}(t)$ NLOS paths in the time-frequency domain. For each time snapshot $t$, frequency $f$, and path $p$, the complex path weight $\gamma_p$, path length $d_p$, Direction Of Departure (DOD) $\{\varphi_{p,\mathrm{T}}, \theta_{p,\mathrm{T}}\}$, and Direction Of Arrival (DOA) $\{\varphi_{p,\mathrm{R}}, \theta_{p,\mathrm{R}}\}$ are determined. We first assume that the antennas receive and transmit on the vertical polarization only. The coefficients are stored in the matrix $\boldsymbol{H}(t,f) \in \mathbb{C}^{M_\mathrm{R} \times M_\mathrm{T}}$, where $M_\mathrm{T}$ and $M_\mathrm{R}$ are the numbers of transmitting and receiving antennas, respectively. It is calculated as

$$\boldsymbol{H}(t,f) = \sum_{p=0}^{M_\mathrm{P}} \gamma_p \ \mathrm{e}^{-j2\pi f d_p/c} \ \boldsymbol{a}_{\theta,R}(\varphi_{p,\mathrm{R}}, \theta_{p,\mathrm{R}}) \cdot \boldsymbol{a}^\mathrm{H}_{\theta,T}(\varphi_{p,\mathrm{T}}, \theta_{p,\mathrm{T}}), \tag{5.1}$$

where $c$ is the speed of light and $\boldsymbol{a}_{\theta,T}(\cdot) \in \mathbb{C}^{M_\mathrm{T} \times 1}$ and $\boldsymbol{a}_{\theta,R}(\cdot) \in \mathbb{C}^{M_\mathrm{R} \times 1}$ are the transmitting and receiving array response vectors for the vertical polarization[3] for the plane wave impinging from the azimuth $\varphi$ and the elevation $\theta$ specified in their arguments. The distance $d_p$ is computed with respect to the centers of the arrays. The additional phase shifts due to the antenna displacements are included in the array response vectors. The superscript $(\cdot)^\mathrm{H}$ denotes the Hermitian transpose operator. The dependency from time $t$ is omitted for simplicity for $\gamma_p$, $M_\mathrm{P}$, and $d_p$, as well as for the DODs and the DOAs. The calculation above has to be repeated for every time and frequency sample in order to obtain the four dimensional tensor $\boldsymbol{\mathcal{H}} \in \mathbb{C}^{M_\mathrm{R} \times M_\mathrm{T} \times M_t \times M_f}$ containing the channel coefficients for a certain MS.

[3] The antenna array response vector $\boldsymbol{a}_\theta(\varphi, \theta)$ is introduced in Section 4.1.5.

The complex path weight $\gamma_p$ can be expressed as

$$\begin{aligned} \gamma_p &= \omega_p \, \varsigma_p \, \frac{c}{4\pi f d_p} \\ \varsigma_p &= \prod_{i \in \mathcal{K}_\mathrm{p}(t)} \rho_i, \end{aligned} \tag{5.2}$$

where $\varsigma_p$ is the product of the scattering coefficients along the $p$-th path, which is defined by the index set $\mathcal{K}_\mathrm{p}(t)$. The term $\omega_p$ is a boolean variable which is set to zero if an obstacle is obstructing the path and to one otherwise. For the LOS component (i.e., for $p = 0$), $\varsigma_0 = 1$ and the term $d_0$ is simply the distance between the Tx and Rx antenna arrays. Note that the terms $\omega_p$, $\varsigma_p$, and $d_p$ are time variant.

### 5.1.1 Full Polarimetric Channel Modeling

When polarimetric antenna radiation patterns are used, we need to consider polarization explicitly. The scattering coefficient $\rho$ becomes then a *scattering coefficient matrix*, denoted by $\boldsymbol{\rho} \in \mathbb{C}^{2\times 2}$. The scattering coefficient matrix determines how the scatterer reflects or diffracts energy with respect to the different polarizations, namely vertical and horizontal. The scattering coefficient matrix, for one scatterer, is defined as

$$\boldsymbol{\rho} = \begin{bmatrix} \rho_{\mathrm{v}\to\mathrm{v}} & \rho_{\mathrm{h}\to\mathrm{v}} \\ \rho_{\mathrm{v}\to\mathrm{h}} & \rho_{\mathrm{h}\to\mathrm{h}}, \end{bmatrix} \tag{5.3}$$

where $\rho_{\mathrm{h}\to\mathrm{v}}$ determines the power transfer between the horizontal polarization (seen at the transmitter) to the vertical polarization (seen at the receiver). Similarly to the scalar scattering coefficient $\rho$, the elements of $\boldsymbol{\rho}$ are expressed as ratios of voltages and can be complex, in order to model possible phase shifts introduced by the scatterer with respect to the different polarizations.

As in equation (5.1), the channel coefficient $h(m_\mathrm{R}, m_\mathrm{T}, t, f)$ for the $m_\mathrm{R}$-th receive and $m_\mathrm{T}$-th transmit antenna, is computed as

$$h(m_\mathrm{R}, m_\mathrm{T}, t, f) = \sum_{p=0}^{M_\mathrm{P}} \mathrm{e}^{-j2\pi f d_p/c} \, \boldsymbol{a}^\mathrm{T}_{m_\mathrm{R},\mathrm{R}}(\varphi_{p,\mathrm{R}}, \theta_{p,\mathrm{R}}) \cdot \boldsymbol{\gamma}_p \cdot \boldsymbol{a}^*_{m_\mathrm{T},\mathrm{T}}(\varphi_{p,\mathrm{T}}, \theta_{p,\mathrm{T}}), \tag{5.4}$$

where the superscript $(\cdot)^*$ indicates complex conjugate. The polarimetric antenna response vectors $\boldsymbol{a}_{m_\mathrm{R},\mathrm{R}}(\varphi_{p,\mathrm{R}}, \theta_{p,\mathrm{R}})$ and $\boldsymbol{a}_{m_\mathrm{T},\mathrm{T}}(\varphi_{p,\mathrm{T}}, \theta_{p,\mathrm{T}})$ of size $2\times 1$ comprise the antenna responses for the two polarizations. These vector functions, as introduced in Section 4.1.5, can be obtained by the polarimetric radiation pattern $\boldsymbol{b}$ and the antenna efficiency $\xi$ defined in Sections 4.1.4 and 4.1.2, respectively, as

$$\boldsymbol{a}(\varphi, \theta) = \sqrt{4\pi\xi} \cdot \boldsymbol{b}(\varphi, \theta), \tag{5.5}$$

so that the norm squared of $\boldsymbol{a}(\varphi, \theta)$ is equal to the gain function $g(\varphi, \theta)$

$$g(\varphi, \theta) = \|\boldsymbol{a}(\varphi, \theta)\|^2 . \tag{5.6}$$

The polarimetric radiation patterns are stored in form of their Effective Aperture Distribution Function (EADF), computed as explained in Section 4.3. The EADF, first introduced in [137, 138], represents the best trade-off between accuracy and computational complexity for channel modeling applications, as discussed in Section 4.4.4.2.

The polarimetric complex path weight matrix $\boldsymbol{\gamma}_p$ for the $p$-th path is defined as

$$\begin{aligned} \boldsymbol{\gamma}_p &= \omega_p \frac{c}{4\pi f d_p} \cdot \boldsymbol{\varsigma}_\mathrm{p} \\ \boldsymbol{\varsigma}_p &= \bigodot_{i \in \mathcal{K}_\mathrm{p}(t)} \boldsymbol{\rho}_i . \end{aligned} \tag{5.7}$$

The matrix $\boldsymbol{\varsigma}_p$ is obtained by multiplying via Schur products[4] the scattering coefficient matrices indicated by the index set $\mathcal{K}_\mathrm{p}(t)$.

To obtain a more compact form of equation (5.4), we can use the polarimetric antenna array response matrix $\boldsymbol{A}(\theta, \varphi)$ introduced in Section 4.1.5. The matrix $\boldsymbol{A}(\theta, \varphi) \in \mathbb{C}^{M \times 2}$ contains the responses of the $M$ antennas for both polarizations. The entire channel matrix $\boldsymbol{H}(t, f) \in \mathbb{C}^{M_\mathrm{R} \times M_\mathrm{T}}$ at time $t$ and frequency $f$ is computed as

$$\boldsymbol{H}(t, f) = \sum_{p=0}^{M_\mathrm{P}} \mathrm{e}^{-j2\pi f d_p / c} \, \boldsymbol{A}_\mathrm{R}(\varphi_{p,\mathrm{R}}, \theta_{p,\mathrm{R}}) \cdot \boldsymbol{\gamma}_p \cdot \boldsymbol{A}_\mathrm{T}^\mathrm{H}(\varphi_{p,\mathrm{T}}, \theta_{p,\mathrm{T}}). \tag{5.8}$$

Without loss of generality, the antennas which possess multiple ports are modeled simply as co-located multiple antennas, each having one port only.

### 5.1.2 The Multi-User Case

In the multi-user case, the MIMO channel matrix is computed for each MS separately, using the same environment. The resulting dimensions of the channel coefficient tensor are $M_\mathrm{R} \times M_\mathrm{T} \times M_t \times M_f \times M_\mathrm{U}$, where $M_\mathrm{U}$ is the number of users. The information through which scatterers the paths are linked can be different for each user.

### 5.1.3 Obstacles

Figure 5.2 shows a simple scenario with an obstructed LOS and three clusters of scatterers which are connected by single and double reflected rays.

[4] The Schur product is the element-wise product, denoted by the symbol $\odot$, so that $\bigodot_{n=1}^{N} a_n = a_1 \odot a_2 \odot \ldots \odot a_N$.

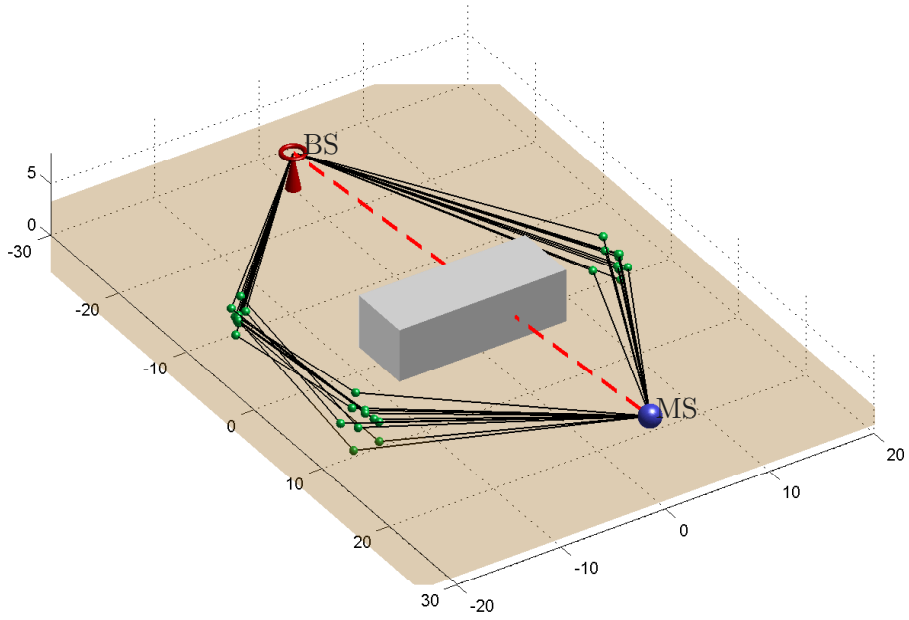


Fig. 5.2: Simple IlmProp scenario showing multiple reflections and an obstructed LOS.

The obstacles, representing buildings or other physical objects, do not cause any reflections or diffractions per se. The IlmProp simply determines whether each path is obstructed by them or not, namely determining the value of the boolean variable $\omega_p$ in equations (5.2) and (5.7).

Such obstacles are ideal to obtain birth-death events of the Multi-Path Components (MPCs) with little modeling effort. To drastically reduce the computational complexity, the obstacles can only have the shape of a parallelepiped and must be oriented as the $x$, $y$, and $z$ axes. Except for these restrictions, the obstacle may have any size. The following section describes the ray-tracing algorithm which is responsible to determine whether there exists an object in the propagation course of a given path.

#### 5.1.3.1 Fast Ray-Tracing Engine

Figure 5.3 shows the problem of detecting an obstruction by an object for the propagation path connecting two points, namely $\boldsymbol{p}_\mathrm{A}$ and $\boldsymbol{p}_\mathrm{B}$ defined by their coordinates $\boldsymbol{p}_\mathrm{A} = [x_A, y_A, z_A]^\mathrm{T}$ and $\boldsymbol{p}_\mathrm{B} = [x_B, y_B, z_B]^\mathrm{T}$. Let the points $\boldsymbol{p}_L = [x_L, y_L, z_L]^\mathrm{T}$ and $\boldsymbol{p}_R = [x_R, y_R, z_R]^\mathrm{T}$ be two vertices of the parallelepiped, so that

$$\begin{aligned} x_L &< x_R \\ y_L &< y_R \\ z_L &< z_R. \end{aligned}$$

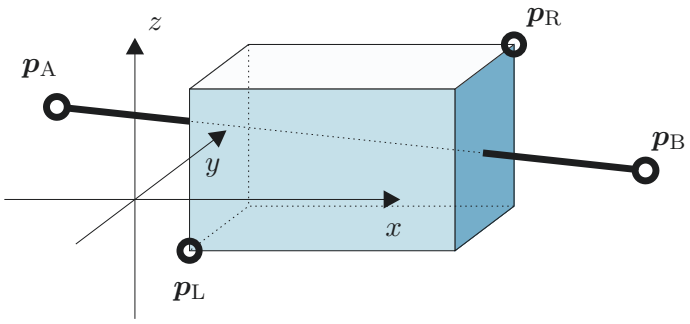


Fig. 5.3: An obstacle oriented as $x$, $y$, and $z$ is a parallelepiped. The ray-tracing problem is to find whether the path between $\boldsymbol{p}_\mathrm{A}$ and $\boldsymbol{p}_\mathrm{B}$ is obstructed.

We now define a linear operator $\mathcal{T}\{\boldsymbol{p}\}$ which transforms the Cartesian coordinates of the

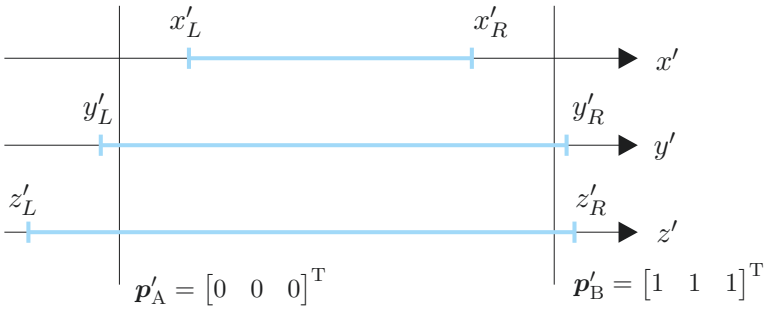


Fig. 5.4: Transformed domain for the problem given in Figure 5.3.

3D point $\boldsymbol{p}$ in such a way that $\mathcal{T}\{\boldsymbol{p}_\mathrm{A}\} = \begin{bmatrix}0 & 0 & 0\end{bmatrix}^\mathrm{T}$ and $\mathcal{T}\{\boldsymbol{p}_\mathrm{B}\} = \begin{bmatrix}1 & 1 & 1\end{bmatrix}^\mathrm{T}$. Figure 5.4 shows the three transformed coordinates. If $\boldsymbol{p} = [x, y, z]^\mathrm{T}$ and $\boldsymbol{p}' = [x', y', z']^\mathrm{T} = \mathcal{T}\{\boldsymbol{p}\}$ we have that the transformation for the first coordinate is

$$x' = \frac{x - x_A}{x_B - x_A}, \tag{5.9}$$

and is similar for the other two coordinates. The space occupied by the obstacles can be represented as segments on each coordinate. It is obtained using the transformation $\mathcal{T}\{\cdot\}$ on the coordinates of $\boldsymbol{p}_\mathrm{L}$ and $\boldsymbol{p}_\mathrm{R}$. If the segments overlap on at least one point between 0 and 1 it means that for those coordinates the corresponding point on the line between $\boldsymbol{p}_\mathrm{A}$ and $\boldsymbol{p}_\mathrm{B}$ lies inside the obstacle, and therefore the path is obstructed by it. Note that this transformation is only possible if obstacles are parallelepipeds.

The computational complexity can be further reduced if the search for obstruction is carried out in a clever way. In general, NLOS propagation paths consist of more than 1 segment. For instance, a double reflection possesses 3 segments. The fact that the user moves slowly in the environment allows us to track the obstructions, so that if a the $i$-th path was obstructed by the $k$-th object, which intersects its $n$-th segment, it is advisable in the next time snapshot to start checking for obstructions right from the $k$-th object and the $n$-th segment, before moving onto other segments and obstacles.

### 5.1.4 Correlation and Time Variance in the IlmProp

The time variance in the channel is introduced in the model implicitly, as it is a consequence of the time variance of the parameters, i.e., the position and orientation of the antenna arrays, and possibly the position of the IOs, as well as their scattering coefficients. This means that no extra modeling effort is spent to obtain time variance and that no particular Doppler spectrum can be input as a parameter. The Doppler spectrum obtained, on the other hand, will be a result of the geometry itself. The fact that multiple users can coexist in the same environment simplifies greatly the modeling effort in generating correlated users, as they can be simply placed close one another. Similarly, to obtain a gradual "decorrelation" between two users, we can make them move away from each other.

### 5.1.5 The Applications of the IlmProp

The IlmProp, seen as a modeling tool, allows the generation of a variety of channels – in principle all which can be modeled as a sum of rays. Obviously, the parameters which describe the paths are crucial. In the IlmProp, they can be either retrieved from measurements via high-resolution parameter estimation techniques (see Section 5.3), or defined manually (see Section 5.2). These sections deal with the two approaches, in particular specifying the applications for which they are intended.

### 5.1.6 The Diffuse Multipath Component

Recent publications [183, 140] have shown that state-of-the-art parameter estimators are incapable of distinguishing enough rays to make up for the whole power present in the channel. The residual, i.e., the part of the channel not modeled by the discrete Multi-Path Components (MPCs) can reach significant percentages of power. According to the measurements presented in [140], in the NLOS regions the power of the Diffuse Multi-path Component (DMC) ranges between 37 and 47 % of the total power, whereas in the obstructed LOS it goes from 10 % to 37 %. In [183], the DMC power is about 20 % in the LOS case and ranges between 40 and 90 % in the remaining regions.

These values clearly indicate that the DMC cannot be ignored while modeling the channel. It is reasonable to believe that if we applied larger antenna arrays we could identify a larger number of discrete MPCs, thus accounting for a larger portion of the power. However, this can be investigated only with channel measurements. In [180], Richter proposes to characterize the DMC as a multi-dimensional Zero Mean Circular Symmetric Complex Gaussian (ZMCSCG) random noise properly filtered so that its power delay profile[5] decays exponentially.

This description has been recently confirmed by Andersen *et al.* in [43]. In the latter, the authors apply Sabine's reverberation formula [186] (commonly used in room acoustics) to the

[5] The power delay profile is discussed in Section 2.3.2.1.

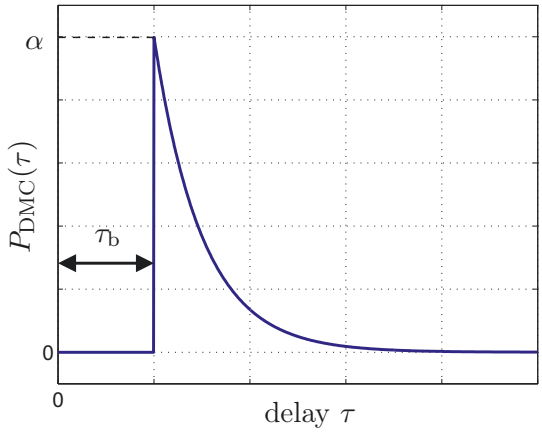


Fig. 5.5: Power delay profile $P_{\mathrm{DMC}}(\tau)$ of the DMC component modeled as proposed in [180].

propagation of EM waves in an indoor scenario. By doing so, they obtain a similar decaying exponential model for the power delay profile.

Other research groups are considering the DMC in their channel models as well. For instance, Pedersen *et al.* propose a novel modeling approach based on directed graphs [174, 175]. The vertices of a graph represent scatterers while the edges model the wave propagation between them. The synthetic impulse responses exhibit an exponentially decaying power delay profile as a result of the recursive scattering structure.

The DMC component, as modeled in [180], can be easily added to the IlmProp channels in a post-processing step. This has been carried out, for instance, in [18], where the parameters of the diffuse component have been derived directly from the IlmProp geometry. Figure 5.5 depicts the power delay profile $P_{\mathrm{DMC}}(\tau)$ modeled as a decaying complex exponential. It can be expressed as

$$P_{\mathrm{DMC}}(\tau) = \begin{cases} 0 & \tau < \tau_{\mathrm{b}} \\ \frac{1}{2}\,\alpha & \tau = \tau_{\mathrm{b}} \\ \alpha \cdot \mathrm{e}^{-(\tau-\tau_{\mathrm{b}})\cdot B} & \tau > \tau_{\mathrm{b}} \end{cases} \tag{5.10}$$

The parameter $\tau_{\mathrm{b}}$ is the *base delay* at which the DMC first appears. The term $B$ is the coherence bandwidth of the random process, and in practice determines the slope of the decaying exponential, while the power at $\tau_{\mathrm{b}}$ is equal to $\alpha$.

We now define these parameters for each time snapshot. The time variant parameters $\tau_{\mathrm{b}}(t)$, $\alpha(t)$, $B(t)$ are chosen so that $\tau_{\mathrm{b}}$ is set equal to the shortest Time Delay Of Arrival (TDOA) of the discrete MPCs. The power $\alpha$ is determined so that the power of the DMC component equals a certain percentage $q$ of the total power of the channel. The slope of the complex exponential, defined by the parameter $B(t)$, is computed so that the power profile assumes a certain value $\eta \cdot \alpha$ for the delay corresponding to the last arrival. By setting the parameters $q$ and $\eta$ we can influence the general behavior of the DMC, whereas its time evolution is derived automatically from the IlmProp geometry. An example is given in Figure 5.6, where we depict the scattering function $R_{\mathrm{DMC}}(\tau, t)$. The latter shows how the power delay profile

of the DMC component for different time snapshots follows the trend of the first arrival.

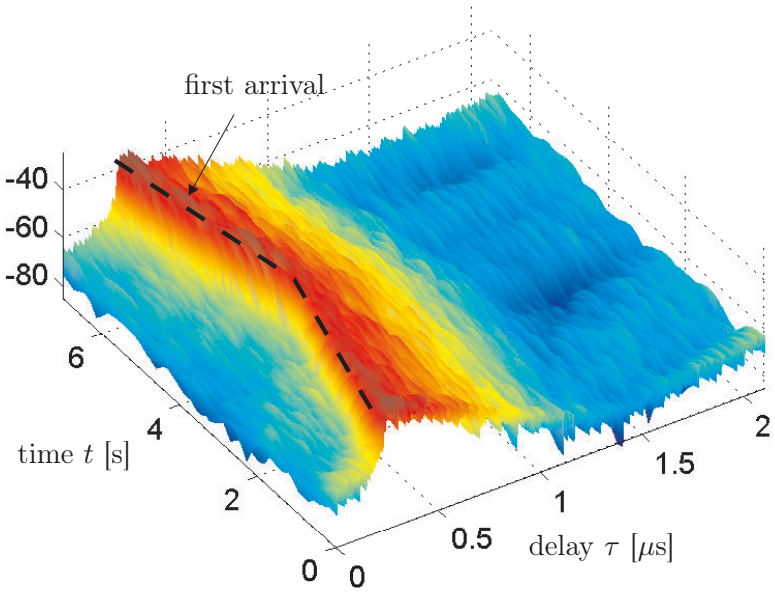


Fig. 5.6: Scattering function $R_{\mathrm{DMC}}(\tau, t)$ of the DMC component for an exemplary IlmProp geometry. Notice how the power delay profile for each time snapshot follows the trend set by the first arrival.

In this section we merely propose a method to combine the results from [180] to the IlmProp model. However, to carry out a rigorous validation and to develop an algorithm to determine the parameters $q$ and $\eta$ goes beyond the scope of this work, and is therefore left to future work. Moreover, the model proposed in [180] only considers a characterization in delay time, so that the random process is implicitly assumed white along the angle and time dimensions. This, of course, needs to be further investigated with appropriate channel measurements. In [183], the authors have computed the capacity for the discrete MPCs and for the DMC considered separately. In the NLOS region, the contribution from the DMC is significant. An interesting research topic for future work is assessing how much of the capacity from the DMC can be actually achieved by a realistic system. In fact, it is reasonable to expect Channel State Information (CSI) on the DMC is much harder to obtain. Such investigations can be well carried out with a geometry-based channel model as the IlmProp.

### 5.1.7 Fitting the Scattering Coefficients to Known Path-Loss Models

Although in the IlmProp the paths can be set arbitrarily, i.e., by placing the scatterers in space and assigning to them scattering coefficients at will, we can obtain more realistic channels by estimating the scattering coefficients using existing path-loss models. In other words, given an IlmProp scenario, the coefficients are chosen so that the resulting path-loss fits an arbitrary predefined path-loss model.

This idea has been developed by Jörg Lotze in a Studienarbeit[6] and the results have been published in [23].

Path-loss models describe the mean received power for given distances [188]. The basic principle of the algorithm is to adjust the IlmProp scattering coefficients in order to obtain the same mean received power as given by the path-loss model. We define as cost function the Mean Squared Error (MSE) between the IlmProp path-loss and the loss defined by the chosen model. Via a multi-dimensional optimization we find the values of the scattering coefficients which minimize the MSE. More details on the algorithm can be found in [23]

In reality, scattering coefficients are generally time-variant, due to object movement or changes of temperature and sunlight, and depend on the angle of incidence [217, pp. 93-98, 123-142]. However, we assume constant scattering coefficients independent on the angle of incidence to reduce the degrees of freedom and the computational complexity of the estimation algorithm.

Since no physical information about the objects is given, the phases of the scattering coefficients are assumed to be independent random variables which do not influence the mean received power. Only the magnitudes are estimated, the phases are assumed random variables uniformly distributed between 0 and $2\pi$.

In the following we show the fitting results for a NLOS urban microcell scenario.

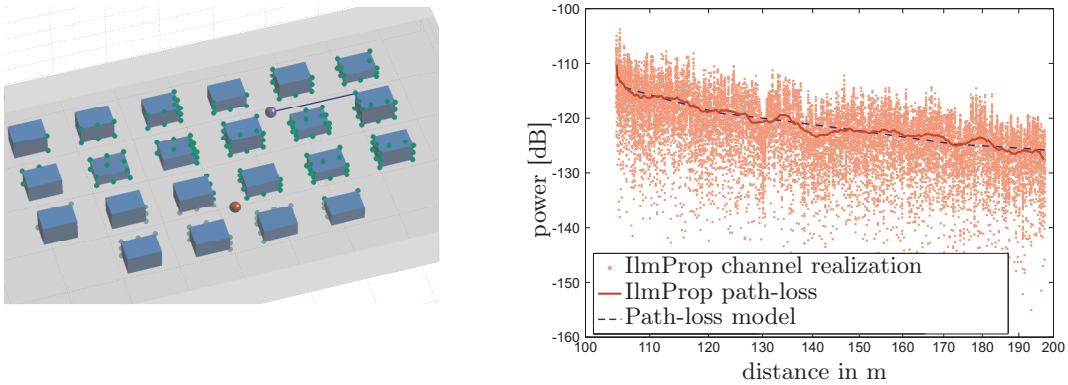


(a) NLOS urban microcell scenario: BS (red), MS (blue) moving along a transversal street, buildings (blue), and scatterers (green).

(b) Coefficient estimation result: IlmProp path-loss (solid red) compared to the COST231-WI NLOS path-loss model (dashed blue).

Fig. 5.7: NLOS urban microcell with the COST 231 Walfisch-Ikegami path-loss model [64, pp. 135-140].

Figure 5.7 depicts a typical urban microcell with a rectangular grid of streets and buildings modeled in the IlmProp. The buildings have different heights, between 12 m and 21 m, the scatterers are attached to the building surfaces. The user moves along a transversal street having no LOS connection to the base station within a distance of 100 m to 200 m. Numerous paths, single, double, and triple reflections, connect the MS (2 m above ground) with the BS (10 m above ground). The scenario spans an area of approximately 350 m $\times$ 200 m. The carrier frequency was chosen to be 2 GHz.

[6] The German equivalent of a student project.

The path-loss model applied here was the COST 231 Walfish-Ikegami NLOS path-loss model [64, pp. 135-140], which is well suited for this kind of urban scenarios. The result can be seen in Figure 5.7(b). The algorithm performs very well for this scenario, since the path-loss model (dashed blue curve) matches almost exactly the IlmProp path-loss curve (solid red). The Root Mean Squared Error (RMSE) of 5.94 dB can be interpreted as the standard deviation of the shadow fading which is a typical value for urban microcells.

The coefficient estimation algorithm shows very good results when used with the COST 231 Walfish-Ikegami model in this urban microcell scenario.

### 5.1.8 IlmProp Validation

As discussed in Section 3.1.5, the validation of a channel model is an important phase of its development. Since the IlmProp does not generate its parameters from random processes, the validation can be carried out by assessing the fitting of the synthetic channels to the measured ones.

As explained in Section 5.1.5, the IlmProp model parameters can be obtained either from high-resolution parameter estimates or from manual input. For the former method, the IlmProp constructs the synthetic channels according to the DOAs, DODs, TDOAs, and path weights computed by the parameter estimator. Therefore, when the high-resolution parameter estimation technique delivers reliable parameters, the IlmProp channel reconstruction will be consequently accurate. To obtain the IlmProp geometry from the parameter estimates we develop a IOs localization algorithm. The latter is introduced in Section 5.3.1. A validation for this algorithm is represented by verifying that the estimated scatterers match the positions of physical objects. This has been carried out in Section 5.3.5.

When parameter estimates are not available, a rough positioning of the scatterers is often enough to recreate the main features which characterize the measured channel. Such an approach is shown by Xiao and Burr in [229]. The authors compare three models with respect to the extended Correlation Matrix Distance (CMD). The CMD measures the similarity of spatial correlation matrices, [101]. The models investigated were the IlmProp, a 3GPP SCM-based extension [230], and the WINNER SCM, discussed in Section 3.4.4.

With respect to the extended CMD, the results show a good agreement with the measurement, so that

> *"the IlmProp channel model can well reflect the multi-path structure of the time variant channels, and is capable of predicting the short-term time variation of the frequency selective channels in outdoor scenarios mainly including single-bounce reflections."* [229]

Another validation has been carried out in [14], [11], and [8]. Also in this case, the position of the scatterers was chosen by visual inspection of the scenario, as no parameter estimates were available.

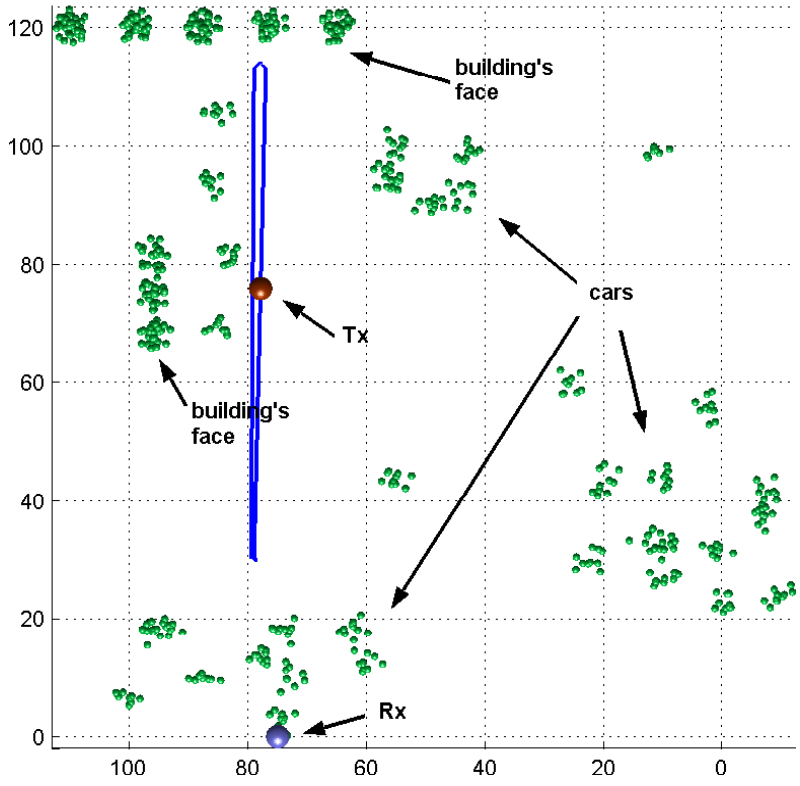


Fig. 5.8: Bird's eye view of the synthetic reconstruction of the scenario in which MIMO channel measurements were carried out.

Figure 5.8 shows the bird's eye view of the reconstructed scenario. The receiver was a $4 \times 8$ Uniform Rectangular Patch Array (URPA) mounted by a window on the second floor of a building. The transmitter was a single 2 GHz vertical dipole mounted on a wheeled cart pulled by hand up a road in the direction of a second building. In its proximity, the cart was turned around and pulled in the opposite direction (towards the receiver), approximately on the same path. The measurement device employed was the broadband real-time channel sounder RUSK from MEDAV [155].

Cars, buildings, light poles, and trash bins have been identified as the probable sources of scattering.

Figure 5.9 shows the marginal Spreading Functions (SFs) in time $t$ and delay time $\tau$ for the measured (a) and synthetic (b) channels.

The synthetic channel shows good agreement with the measured one. The LOS is clearly visible and, as expected, its delay lag grows as the transmitter moves further away from the receiver. When the cart is turned around and pulled back towards the receiver, the TDOA decreases. Many echoes are visible as well. Note that as the transmitter moves, most echoes arrive earlier, meaning that their path length becomes smaller. The strong echo labeled *double-bounce* has the same trend as the LOS, just delayed by approximately $0.8\,\mu$s, which corresponds to 240 m, the distance between the top and bottom buildings doubled. For this

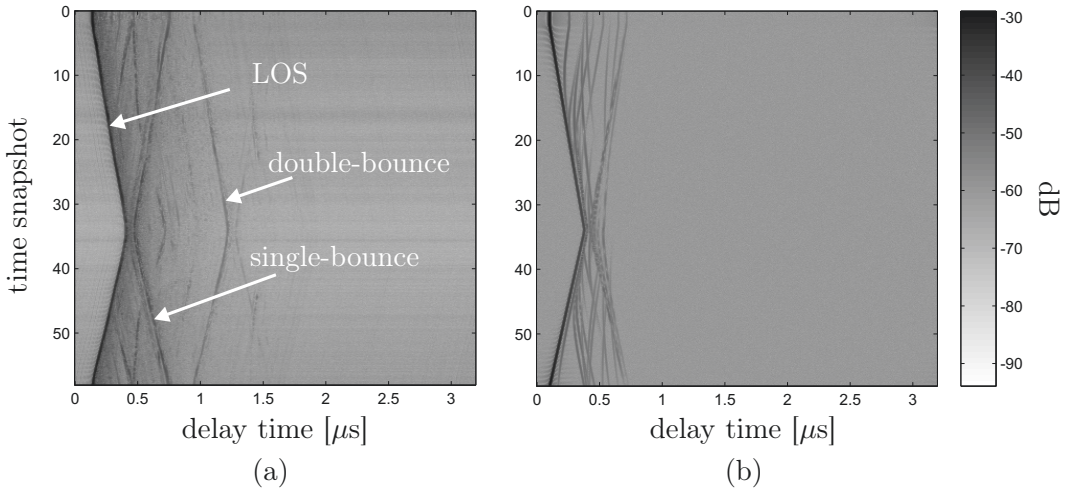


Fig. 5.9: Absolute value of the measured (a) and synthetic (b) marginal SF $h(\tau, t)$. The LOS, single-bounce, and far double-bounce paths are clearly visible and are marked with the arrows.

reason it is very likely that this arrival corresponds to the signal reflected by the bottom building first, and then by the top building, thus a double-bounce echo. Since the IlmProp contained only single-bounce paths, the double-bounce is not reproduced in the synthetic channel.

Moreover, in [14] the power profiles and autocorrelation functions introduced in Section 2.3.2 have been computed, showing good agreement with the measurement.

### 5.1.9 Coordinate Systems and Transformation Matrices

The IlmProp models the wireless channel by considering a simplified reconstruction of the environment's geometry. As explained in detail in Section 5.1, the BS and MSs move freely in a common three-dimensional space. Scatterers are set in the very same space and the propagation rays are computed with a simple Geometric Optics (GO) engine. In order to simplify the understanding of the geometry, as well as the computations required, an efficient coordinate system is needed.

The IlmProp employs three different Cartesian coordinate systems: global system, antenna array system and antenna system.

- the GLobal System (GLS) is the reference system in which the position of all scatterers, obstacles and antenna arrays is defined.
- the Antenna Array System (AAS), on the other hand, is solidly bound to the antenna array. The position and orientation of the single elements constituting the antenna array are defined in the AAS. There exist one AAS for the BS and one for each of the MSs.
- the ANtenna System (ANS) is introduced since the polarimetric antenna radiation functions are normally expressed with respect to a single antenna element. The ANS moves

solidly with each array element. There exist as many ANS as antenna elements present in the environment.

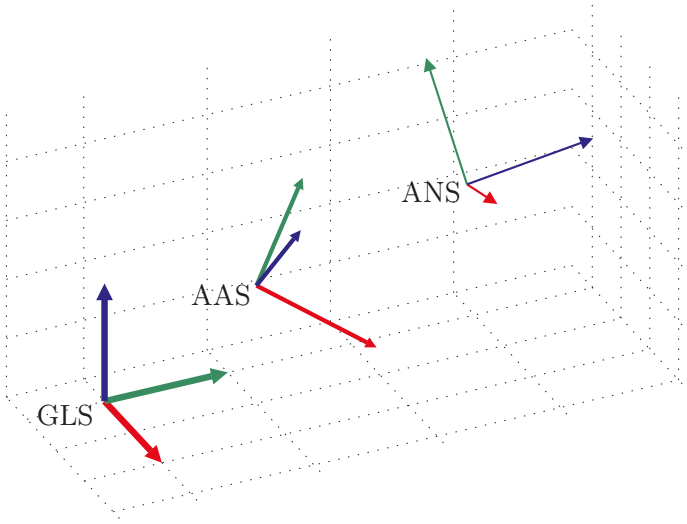


Fig. 5.10: Orthonormal coordinate systems used in the IlmProp. GLobal System (GLS), Antenna Array System (AAS), and ANtenna System (ANS).

Figure 5.10 shows the three coordinate systems. In order to uniquely define the position and orientation of an orthonormal basis in space we define six independent parameters, namely three rotation angles: $\alpha_{x_{\mathrm{AAS}}}$, $\alpha_{y_{\mathrm{AAS}}}$, and $\alpha_{z_{\mathrm{AAS}}}$, and three Cartesian coordinates: $x_{\mathrm{AAS}}, y_{\mathrm{AAS}}$, and $z_{\mathrm{AAS}}$. The orientation of the AAS is obtained by rotating a basis at first identical to the GLS according to the angles $\alpha_{x_{\mathrm{AAS}}}$, $\alpha_{y_{\mathrm{AAS}}}$, and $\alpha_{z_{\mathrm{AAS}}}$. First we carry out a rotation about the axis $x_{\mathrm{GLS}}$ by $\alpha_{x_{\mathrm{AAS}}}$, and then, similarly, by $\alpha_{y_{\mathrm{AAS}}}$ about $y_{\mathrm{GLS}}$, and finally, by $\alpha_{z_{\mathrm{AAS}}}$ about $z_{\mathrm{GLS}}$. The order of the rotations is not commutative. The direction of rotation is indicated in Figure 5.11. The rotated axis is then translated in the position defined by $x_{\mathrm{AAS}}, y_{\mathrm{AAS}}$, and

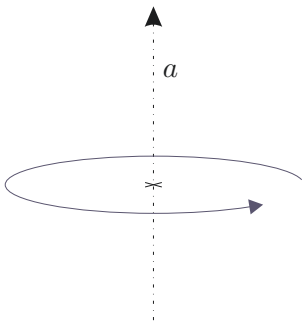


Fig. 5.11: Convention on the direction of rotation used in the IlmProp. The rotation is carried out about the oriented axis $a$ by a positive angle.

$z_{\mathrm{AAS}}$.

In a similar fashion, the axes of an ANS are defined by six parameters in the corresponding AAS.

In order to greatly simplify the coordinate transformations from one system to another, homogeneous coordinates can be employed.

#### 5.1.9.1 Homogeneous Coordinates and Transformation Matrices

In Euclidean geometry, a rotation about an axis can be conveniently expressed by a matrix-vector product. Let $\boldsymbol{p} = [x, y, z]^{\mathrm{T}}$ be a point to be rotated and $\boldsymbol{p}' = [x', y', z']^{\mathrm{T}}$ the same point after the rotation. The rotation can be carried out by a properly constructed $3 \times 3$ matrix $\boldsymbol{R}$ as follows:

$$\boldsymbol{p}' = \boldsymbol{R} \cdot \boldsymbol{p} \tag{5.11}$$

This notation is particularly convenient because several rotations can be compacted in a single matrix. For instance let $\boldsymbol{R}_1$ and $\boldsymbol{R}_2 \in \mathbb{R}^{3\times3}$ correspond to two rotations about different axes. The matrix $\boldsymbol{R}_{1,2} = \boldsymbol{R}_2 \cdot \boldsymbol{R}_1$ conveniently combines both:

$$\begin{aligned} \boldsymbol{p}' &= \boldsymbol{R}_2 \cdot \boldsymbol{R}_1 \cdot \boldsymbol{p} \\ \boldsymbol{p}' &= \boldsymbol{R}_{1,2} \cdot \boldsymbol{p}. \end{aligned} \tag{5.12}$$

Another frequently required transformation is the translation, which can be interpreted as the addition of a constant vector to the point $\boldsymbol{p}$. As a consequence, it is not possible to write such a transformation in the form of a matrix vector product. In order to overcome this problem, we employ homogeneous coordinates [89, pp. 29–49] in place of the common Cartesian ones.

Homogeneous coordinates have a natural application to Computer Graphics (CG). They form a basis for the projective geometry used extensively to project a three-dimensional scene onto a two-dimensional image plane. They also unify the treatment of common graphical transformations and operations.

The homogeneous finite point $\boldsymbol{p}_{\mathrm{hom}}$ is simply $[x, y, z, 1]^{\mathrm{T}}$. The rotation matrix $\boldsymbol{R}$ expressed in homogeneous coordinates becomes $\boldsymbol{R}_{\mathrm{hom}}$ such that

$$\boldsymbol{R}_{\mathrm{hom}} = \begin{bmatrix} & & & 0 \\ & \boldsymbol{R} & & 0 \\ & & & 0 \\ 0 & 0 & 0 & 1 \end{bmatrix}. \tag{5.13}$$

A translation of a vector $\boldsymbol{v} = [v_{\mathrm{x}} v_{\mathrm{y}} v_{\mathrm{z}}]$ can now be expressed in form of the matrix $\boldsymbol{T}_{\mathrm{hom}}$

defined as

$$\boldsymbol{T}_{\text{hom}} = \begin{bmatrix} 1 & 0 & 0 & 0 \\ 0 & 1 & 0 & 0 \\ 0 & 0 & 1 & 0 \\ v_{\text{x}} & v_{\text{y}} & v_{\text{z}} & 1 \end{bmatrix}. \tag{5.14}$$

The homogeneous coordinates allow us to combine rotations and translations into one 4-by-4 matrix. This is particularly convenient when defining transformations between different coordinate systems. For instance, in order to obtain the coordinates in the GLS denoted by $\boldsymbol{p}^{(GLS)}$ of a point $\boldsymbol{p}^{(AAS)}$ defined in the AAS, we need to rotate it first about $x_{\text{AAS}}$, then about $y_{\text{AAS}}$, and finally about $z_{\text{AAS}}$. The angles for the rotation are defined by $\alpha_{x_{\text{AAS}}}$, $\alpha_{y_{\text{AAS}}}$, and $\alpha_{z_{\text{AAS}}}$. Subsequently, we translate by $x_{\text{AAS}}$, $y_{\text{AAS}}$, and $z_{\text{AAS}}$. All this transformations can be performed by a single 4-by-4 matrix $\boldsymbol{Q}$ , as follows

$$\boldsymbol{p}^{(GLS)} = \boldsymbol{Q} \cdot \boldsymbol{p}^{(AAS)}, \tag{5.15}$$

where

$$\boldsymbol{Q} = \boldsymbol{T} \cdot \boldsymbol{R}_{\text{z}} \cdot \boldsymbol{R}_{\text{y}} \cdot \boldsymbol{R}_{\text{x}} \tag{5.16}$$

$$\boldsymbol{T} = \begin{bmatrix} 1 & 0 & 0 & 0 \\ 0 & 1 & 0 & 0 \\ 0 & 0 & 1 & 0 \\ x_{\text{AAS}} & y_{\text{AAS}} & z_{\text{AAS}} & 1 \end{bmatrix}, \tag{5.17}$$

and

$$\boldsymbol{R}_x = \begin{bmatrix} 1 & 0 & 0 & 0 \\ 0 & \cos(\alpha_{x_{\text{AAS}}}) & -\sin(\alpha_{x_{\text{AAS}}}) & 0 \\ 0 & \sin(\alpha_{x_{\text{AAS}}}) & \cos(\alpha_{x_{\text{AAS}}}) & 0 \\ 0 & 0 & 0 & 1 \end{bmatrix} \tag{5.18}$$

$$\boldsymbol{R}_y = \begin{bmatrix} \cos(\alpha_{y_{\text{AAS}}}) & 0 & \sin(\alpha_{y_{\text{AAS}}}) & 0 \\ 0 & 1 & 0 & 0 \\ -\sin(\alpha_{y_{\text{AAS}}}) & 0 & \cos(\alpha_{y_{\text{AAS}}}) & 0 \\ 0 & 0 & 0 & 1 \end{bmatrix} \tag{5.19}$$

$$\boldsymbol{R}_z = \begin{bmatrix} \cos(\alpha_{z_{\text{AAS}}}) & -\sin(\alpha_{z_{\text{AAS}}}) & 0 & 0 \\ \sin(\alpha_{z_{\text{AAS}}}) & \cos(\alpha_{z_{\text{AAS}}}) & 0 & 0 \\ 0 & 0 & 1 & 0 \\ 0 & 0 & 0 & 1 \end{bmatrix}. \tag{5.20}$$

The inverse transformation, namely

$$\boldsymbol{p}^{(GLS)} = \boldsymbol{Q}^{-1} \cdot \boldsymbol{p}^{(AAS)}, \tag{5.21}$$

requires the computation of $\boldsymbol{Q}^{-1}$, which can be obtained simply by

$$\boldsymbol{Q}^{-1} = \boldsymbol{R}_{\mathrm{x}}^{\mathrm{T}} \cdot \boldsymbol{R}_{\mathrm{y}}^{\mathrm{T}} \cdot \boldsymbol{R}_{\mathrm{z}}^{\mathrm{T}} \cdot \boldsymbol{T}^{-1}, \tag{5.22}$$

where

$$\boldsymbol{T}^{-1} = \begin{bmatrix} 1 & 0 & 0 & 0 \\ 0 & 1 & 0 & 0 \\ 0 & 0 & 1 & 0 \\ -x_{\mathrm{AAS}} & -y_{\mathrm{AAS}} & -z_{\mathrm{AAS}} & 1 \end{bmatrix}. \tag{5.23}$$

Another advantage of this description is that the matrix $\boldsymbol{Q}$ can be computed once and stored for future use.

## 5.2 Non Measurement-based Applications

As described in Section 5.1, the IlmProp models the propagation as a sum of paths, which are described in terms of their trajectory and path-strength for each time snapshot. This information can be defined manually, so that the user is required to specify the positions and the scattering coefficients of all Interacting Objects (IOs) present in the environment. A more extensive list of parameters is given in Table 5.1.

| **Parameter** | **Description** |
|---|---|
| center frequency | frequency at which the system operates |
| frequency sampling | defines the frequency bins at which the channel will be computed |
| time sampling | defines the time instants at which the channel will be computed |
| position and orientation of Tx and Rx | describes the position and orientation of the transmitter and receiver for every time snapshot |
| obstacles | defines the position and size of objects (such as buildings) which obstruct the paths |
| scatterers | the position and scattering coefficient of each IO present in the environment |
| paths | defines how the scatterers are linked to form paths which connect the transmitters to the receiver |

Tab. 5.1: IlmProp basic parameters which can be input by the user to define a scenario.

Assuming that the user inputs a realistic propagation scenario, the IlmProp will model realistically the correlation in time, frequency and space, as they are inherent to the geometry.

In other applications, the user might want to model realistically only specific features of the channels in order to test the performance of an algorithm in such a context.

For instance, to test an algorithm sensible to spatial correlation between MSs, one can develop an IlmProp scenario in which the users are close to one another. Furthermore, by letting one user move away from another, it is possible to investigate the behavior of the algorithm with respect to a progressive spatial decorrelation of the channels. Other adaptive algorithms can be tested in a similar way, as all path parameters, namely DOA, DOD, TDOA, and path-strength vary according to the geometry in a natural way.

In the following sections we present the results proposed in several publications which follow this approach. They are focused on different algorithms which are tested on IlmProp channels. As an explanatory example, we treat in detail the comparison of Zero Forcing (ZF) methods in Section 5.2.1. Several other publications concentrate on the use of the IlmProp to test a variety of algorithms. In Sections 5.2.2 to 5.2.7 we summarize the most significant, stressing the role of the channel model in the investigations. These examples are particularly useful in understanding the modeling philosophy behind the IlmProp.

### 5.2.1 The IlmProp to Compare Zero-Forcing Methods

This section presents an example on how the IlmProp can be useful to investigate the behavior of ZF precoding algorithms. It is based on [9].

The use of Space-Division Multiple Access (SDMA) in the downlink of a multi-user MIMO wireless communication system can offer a substantial gain in system throughput. In this section we compare the throughput achieved by employing two recently developed algorithms for transmit beamforming in multi-user MIMO systems: the Block Diagonalization (BD) and the Successive Optimization (SO). These algorithms are briefly reviewed in Appendix F and can be found in [193, 194]. Both algorithms aim to maximize the overall capacity subject to zero multi-user interference constraints. In order to study the performance of these algorithms in correlated channels as time evolves, we construct several synthetic channels generated with the IlmProp.

#### 5.2.1.1 Uncorrelated channels

The first scenario that we illustrate is a weakly correlated channel, which represents a Non Line Of Sight (NLOS) link in a very rich scattering environment. Such a scenario is shown in Figure 5.12. Notice that the LOS component is artificially suppressed.

This IlmProp geometry emulates the totally uncorrelated channel, often denoted in the literature as the *white channel* [172, p. 39], already mentioned in Section 3.1.1. This channel is usually taken as benchmark to test all sorts of beamforming algorithms, partly due to its simplicity. We assume that both MSs employ the same number of antennas. As we are looking

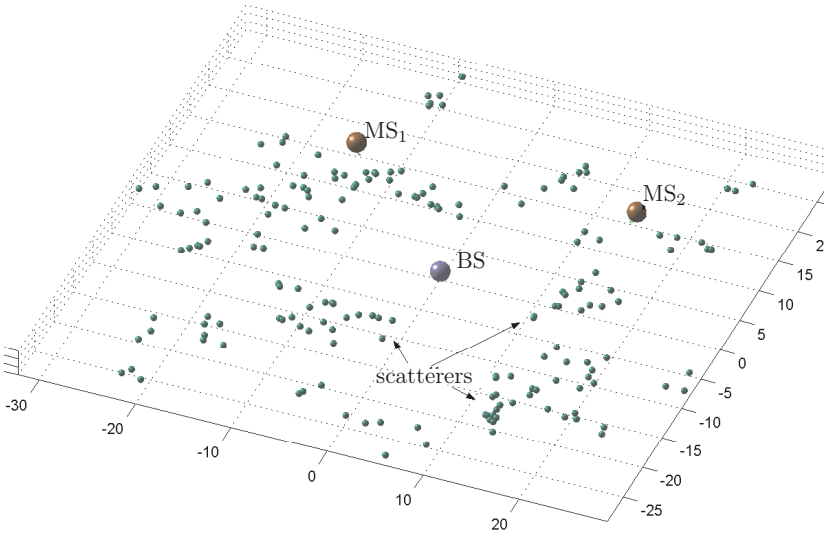


Fig. 5.12: A weakly correlated scenario generated with the IlmProp. The LOS component is suppressed. All scatterers are linked with single-bounce paths.

at the downlink the BS acts as the transmitter. The IlmProp flat-fading channel coefficients are stored in the tensor $\boldsymbol{\mathcal{H}}_{\text{IlmProp}} \in \mathbb{C}^{M_{\text{R}} \times M_{\text{T}} \times M_t \times 2}$.

Let us now assume a white channel for both users in the MIMO system under study. The downlink flat-fading channel coefficients are stored in a tensor $\boldsymbol{\mathcal{H}}_{\text{w}}$ of size $M_{\text{R}} \times M_{\text{T}} \times M_t \times 2$ whose elements are independent Zero Mean Circular Symmetric Complex Gaussian (ZMCSCG) random numbers with unit variance.

In Figure 5.13, the BD algorithm is compared with the blind beamformer and the channel inversion solution on both the $\boldsymbol{\mathcal{H}}_{\text{w}}$ channel and the IlmProp channel $\boldsymbol{\mathcal{H}}_{\text{IlmProp}}$.

The latter is normalized in order to compare the capacity curves with the ones derived from the white channel. The normalization is performed so that the total power present in the IlmProp channel matches the one in $\boldsymbol{\mathcal{H}}_{\text{w}}$. The channel tensor must be scaled so that

$$\|\boldsymbol{\mathcal{H}}_{\text{w}}\|_{\text{H}}^2 = \|\boldsymbol{\mathcal{H}}_{\text{IlmProp}}\|_{\text{H}}^2 \tag{5.24}$$

where $\|\cdot\|_{\text{H}}$ indicates the higher order norm as defined in equation (D.19). Exploiting the statistical properties of the elements of $\boldsymbol{\mathcal{H}}_{\text{w}}$, it is possible to express equation (5.24) as

$$\text{E}\left[\|\boldsymbol{\mathcal{H}}_{\text{w}}\|_{\text{H}}^2\right] = M_{\text{R}} \cdot M_{\text{T}} \cdot M_t \cdot 2. \tag{5.25}$$

For the blind beamforming, the modulation matrix $\boldsymbol{M}_i$ is set equal to a scaled identity matrix, so that the total power sent is $P$, under the assumption that only one user is served at a time.

For the channel inversion solution the modulation matrix $\boldsymbol{M}_{\text{S}}$ at each time snapshot is

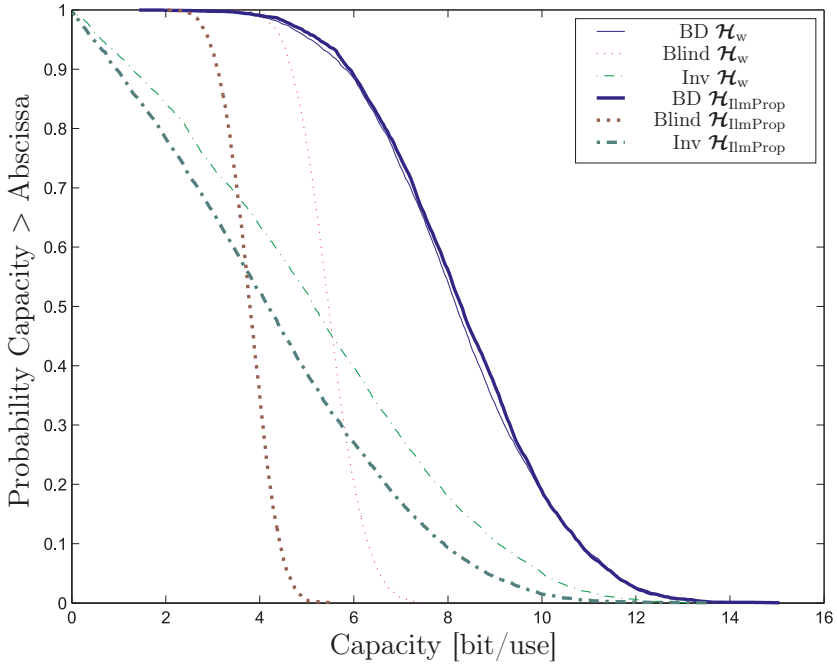


Fig. 5.13: Complementary Cumulative Distribution Functions (CCDF) of the system's sum capacity for two mobiles with $M_{\mathrm{R}} = 2$ antennas each at 10 dB SNR. The BS has $M_{\mathrm{T}} = 4$ antennas.

derived from the Moore-Penrose pseudo-inverse of $\boldsymbol{H}_S$ so that $\boldsymbol{M}_{\mathrm{S}} = \boldsymbol{H}_S^{+}$ where

$$\begin{aligned} \boldsymbol{M}_{\mathrm{S}} &= [\boldsymbol{M}_1 \;\; \boldsymbol{M}_2] \\ \boldsymbol{H}_S &= \left[\boldsymbol{H}_1^{\mathrm{T}} \;\; \boldsymbol{H}_2^{\mathrm{T}}\right]^{\mathrm{T}}. \end{aligned}$$

The matrices $\boldsymbol{H}_1$ and $\boldsymbol{H}_1$ contain the channel coefficients for the two users at the time snapshot under study, similarly $\boldsymbol{M}_1$ and $\boldsymbol{M}_2$ are the corresponding modulation matrices.

Due to the intrinsic geometric nature of the model, the channel appears to be vaguely more correlated than $\boldsymbol{\mathcal{H}}_{\mathrm{w}}$, leading to worse performance for both the pseudo-inverse and the blind beamforming. On the other hand, the performance of the BD beamformer does not change. For this reason, the gain of BD compared to the blind beamforming is significantly larger in the weakly correlated scenario.

#### 5.2.1.2 Correlated channels

Figure 5.14 shows a model which corresponds to a correlated channel. Two users $\mathrm{MS}_1$ and $\mathrm{MS}_2$ move in a space rich of scatterers in the proximity of a fixed BS. Each mobile has $M_{\mathrm{R}} = 2$ antennas while the base station has $M_{\mathrm{T}} = 4$ antennas. All antenna arrays are Uniform Linear Arrays (ULAs). The trajectories of the two users are also visible. The first user moves on an elliptical trajectory and eventually crosses the path traveled by $\mathrm{MS}_2$. At one instant in time, the two users occupy the same space. This is of course physically not possible, but the model lets us experience the behavior of the algorithms for two fully correlated channels.

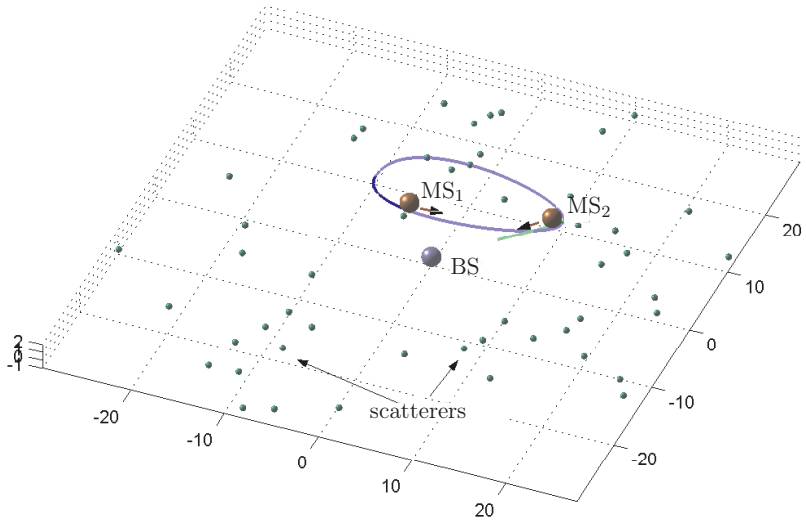


Fig. 5.14: A spatially correlated scenario generated with the IlmProp.

The geometrical representation intrinsically gives a realistic time variance to the channel letting us investigate the performance of the algorithms as a function of time.

The upper plot of Figure 5.15 shows the user rates, while the bottom one shows the Rician $K$-factors[7]. The user rate $r_i$ of the $i$-th user is calculated as in equation (F.3) for both algorithms. The scattering coefficients have been kept constant for the whole duration of the simulation. The trends for the Rician $K$-factors are thus a result of the changing path-losses deriving simply from the movement of the mobiles. The BD algorithm, as expected, allows better transfer rates to the mobile which has a better channel, in order to maximize the sum capacity of the system. Between 15 and 25 s we see a significant drop in the user rates. This is due to the fact that the two channels are perfectly correlated since the mobiles are at the same position. In this case, the BD algorithm chooses modulation matrices which give no power for both user as interference cannot be avoided. The Successive Optimization algorithm performs better than BD when calculated for the first user first. In this case the modulation matrix of the first user is calculated independently from the second user. For this reason the user rate does not drop to zero as for BD. However, the second modulation matrix is chosen not to interfere with the first user and thus achieves an extremely low rate. In fact, the curves for the second user for both BD and SO overlap.

#### 5.2.1.3 The Subspace-Based Grouping Algorithm

The BD and SO algorithms suffer from two major drawbacks: the dimensionality constraint and, as seen in the previous section, the difficulty in handling spatially correlated users.

[7] The Rician $K$-factor is defined as the ratio between the power of the LOS and the power of the NLOS. Alternatively, it can be expressed as the ratio of the power in the mean component of the channel to the power in the scattererd (varying) component [172, p. 20].

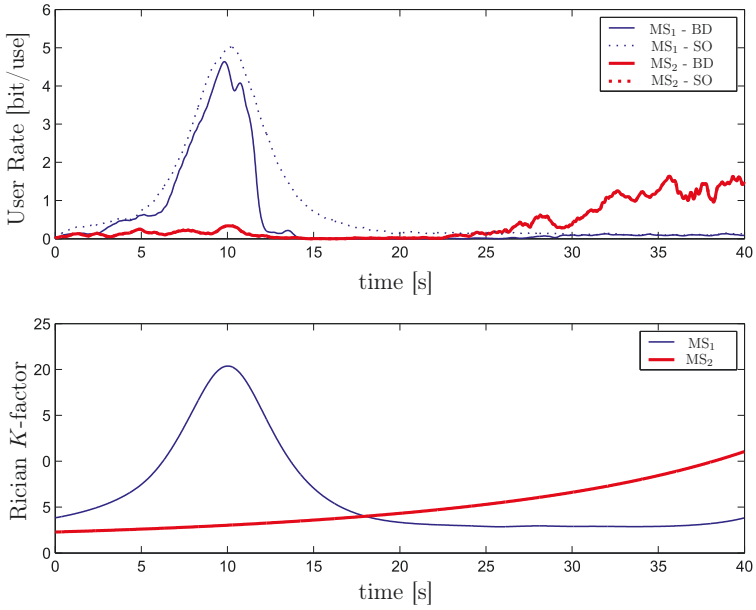


Fig. 5.15: User rates (top) and the Rician $K$-factor (below) plotted against time for the correlated scenario previously shown.

The dimensionality constraint forces the base station to have at least the same number of antennas as the sum of all antennas of the mobiles it intends to serve. Both problems can be efficiently solved by grouping the users in different sets, whereas each group will be treated in separate time slots. The resulting system will be a hybrid of Time-Division Multiple Access (TDMA) and SDMA. This solution requires an efficient algorithm which determines how the groups are formed. One criterion would be to consider the DOAs of the different users. Unfortunately this approach requires a greater effort since parameter estimation has to be performed. Furthermore, only certain kinds of antenna arrays support such a processing, the beam patterns of the antennas must be known, and a strong LOS must be present. Thus an antenna independent criterion is preferable.

The grouping algorithm here described works in the subspaces and therefore does not require any information on the antennas whatsoever.

The channel tensor $\boldsymbol{\mathcal{H}}_i$ describes the channel between the $i$-th user and the BS. For a given time snapshot, it is a matrix of dimensions $M_\mathrm{R} \times M_\mathrm{T}$. Let the columns of the matrix $\boldsymbol{V} \in \mathbb{C}^{M_\mathrm{T} \times M_\mathrm{U}}$ contain the strongest right singular vector of each of the $M_\mathrm{U}$ users. Each singular vector represents the best rank-1 approximation of the corresponding user's subspace. The more correlated the subspaces of users $i$ and $j$ are, the smaller will be the angle $\vartheta_{i,j}$ between their singular vectors.

The angle $\vartheta_{i,j}$ can be calculated as

$$\vartheta_{i,j} = \arccos(|\boldsymbol{V}(:,i)^H \cdot \boldsymbol{V}(:,j)|) = \arccos(|\upsilon_{i,j}|), \tag{5.26}$$

where $\boldsymbol{V}(:,i)$ denotes the $i$-th column of the matrix $\boldsymbol{V}$. Note that the singular vectors have

norm 1. Since the function arccos(·) is monotonic in the range of interest, we take $\upsilon_{i,j}$ as a measure of the spatial correlation between the users. If the $i$-th and $j$-th users are spatially uncorrelated, then $\upsilon_{i,j} = 0$ whereas if they are fully correlated, i.e., they span the same subspace, then $\upsilon_{i,j} = 1$. The absolute value of the Grammian of $\boldsymbol{V}$, namely $\boldsymbol{\Upsilon} = \text{abs}\left(\boldsymbol{V}^H \cdot \boldsymbol{V}\right)$ is a matrix whose upper and lower triangular part contains the absolute value of the indices $\upsilon_{i,j}$.

In the case of two groups, the following steps define the subspace-based grouping algorithm:

- *Step 1*: the most correlated pair of users is identified, determining the maximum in the upper triangular section of $\boldsymbol{\Upsilon}$. The two users are put in separate groups.
- *Step 2*: the users already assigned to a group are not considered in following steps.
- *Step 3*: among the remaining users the most correlated pair is identified. The users are assigned to different groups so that their correlation with the other users in the groups is minimized.
- *Step 4*: iteration, back to *Step 2* until all users have been allocated.

In case of more than two groups, for instance 3, the algorithm can be extended as follows.

- *Step 1*: the strongest pair is identified and the users are put in different groups.
- *Step 2*: among all remaining users the one having highest correlation with the first pair is determined and put in the remaining group.
- *Step 3*: the users already allocated are excluded from following steps.
- *Step 4*: among the remaining users the most correlated pair is identified. The users are assigned to different groups so that their correlation with the other users in the groups is minimized.
- *Step 5*. among all remaining users the one having highest correlation with the pair found in *Step 4* is determined and put in the remaining group.
- *Step 6*. iteration, back to *Step 3* until all users have been allocated.

The latter algorithm can be easily extended to cover more than 3 groups iterating *Step 2* and *5* as needed to cover all groups present.

Testing all possible combinations (in case of two groups) proved that our algorithm achieves the highest data rates possible.

Figure 5.16 shows an exemplary scenario generated with the IlmProp. A Base Station has a Uniform Circular Array (UCA) with 12 antennas. A total number of 6 users surround the BS, each one having 2 antennas, $\frac{\lambda}{2}$ spaced. The orientation of the mobiles' arrays is approximately orthogonal to their trajectory. All users but the sixth move only a few meters during the duration of the simulation. User 6, on the other hand, moves from a position very close to the first user to one which is close to the second. Potentially the BS could support all

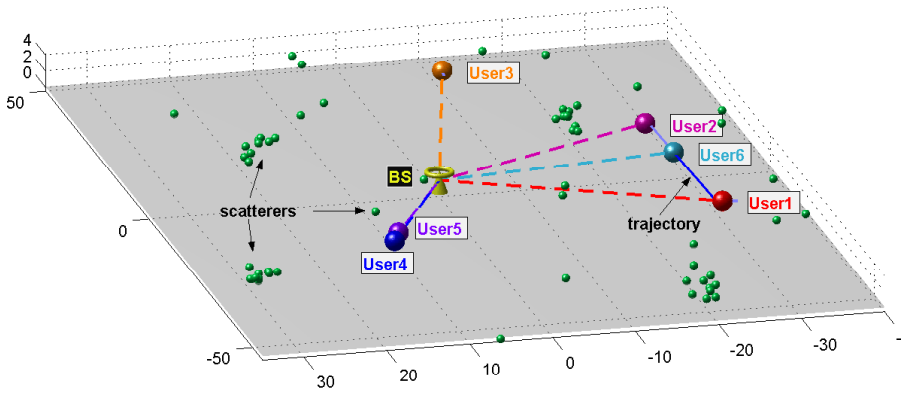


Fig. 5.16: A multi-user scenario generated with the IlmProp. The Line Of Sight (LOS) components are visible.

6 users at the same time. However, at some time snapshots some mobiles are very close one another, thus being strongly spatially correlated. These users are separated with difficulty by the beamforming algorithms investigated here. This issue can be avoided by grouping the users in two or more groups, allowing to put strongly correlated users into separate groups.

The narrowband channels for all users seen in Figure 5.16 have been calculated with the IlmProp at a frequency of 2 GHz with an average SNR of 20 dB for a total time of 2.8 seconds and 400 time snapshots. Assuming perfect channel knowledge at the transmitter, at each time snapshot the grouping algorithms have been employed. Subsequently, we apply the BD algorithm on each group, dividing for simplicity the available power equally among the users of the same group. This simplification is acceptable for this specific scenario since the mobiles have comparable path-losses, i.e., there is no near-far problem. The different groups are then multiplexed in time. The user rates are compared for different grouping strategies in Figure 5.17, which specifically shows the rates for 1, 2, 3 and 6 groups. Note that the curve for 6 groups corresponds to handling each user in a separate time slot. For this specific scenario, the best grouping strategy is two groups of three users each. In fact, with this configuration the BD is capable of separating the users while assuring no interference among them. With 3 groups of two users each, the BD has an even easier job in separating the users. However, the resulting user rates are lower due to the higher time multiplexing which decreases the length of each transmission time slot. When setting the spatial multiplexing to its maximum, i.e., with 1 group, in some cases it is impossible for the BD algorithm to assure high user rates. In fact, the sixth user is strongly correlated with the first at the beginning of the simulation, while it almost overlaps with the second in the final part. The BD algorithm inherently avoids interference among all users. Under this constraint it generates very inefficient modulation matrices for strongly correlated channels leading to low user rates, as already seen in the previous section. User 4 and 5 are strongly spatially correlated for the whole duration of the simulations. For this reason they always achieve low user rates. With two groups it is possible to separate these unfavorable pairs putting the users in separate groups. The gain achieved

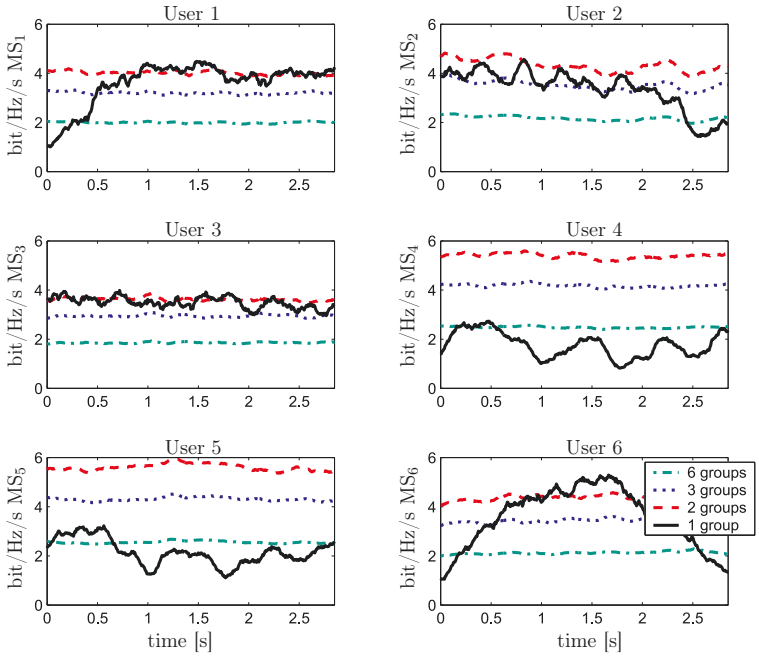


Fig. 5.17: User rates for the scenario seen in Figure 5.16 for different grouping strategies.

from the exploitation of the spatial diversity is clearly visible comparing the rates of the users when treated separately (6 groups) and when grouped in 2 or 3 groups.

The time variant IlmProp channels reveal that the grouping algorithm, when applied at each time snapshot, provides a very unstable solution, i.e., users jump from one group to another very frequently. In a real system this is of course undesirable because it would generate a great deal of overhead traffic. A simple solution consists in calculating the users' subspaces on the long term correlation matrices. The long term spatial correlation matrix at the transmitter for the $i$-th user at the $n$-th time snapshot is

$$\boldsymbol{R}_{\mathrm{T},i}^{(n)} = \rho \cdot \boldsymbol{R}_{\mathrm{T},i}^{(n-1)} + (1-\rho) \cdot \left(\boldsymbol{H}_i^{(n)}\right)^{\mathrm{H}} \cdot \boldsymbol{H}_i^{(n)}, \tag{5.27}$$

where the matrix $\boldsymbol{H}_i^{(n)} \in \mathbb{C}^{M_{\mathrm{R}} \times M_{\mathrm{T}}}$ describes the channel towards the $i$-th user at the $n$-th time snapshot and $\rho$ is a forgetting factor. From an EigenValue Decomposition (EVD) it is possible to extract the strongest eigenvector, i.e., the vector corresponding to the strongest eigenvalue. This vector represents the rank-1 approximation of the $i$-th user's subspace and can be fed to the grouping algorithm.

By setting a proper forgetting factor $\rho$, which depends on the time variance of the channels, it is possible to achieve the user rates seen in Figure 5.17 with extremely stable groups.

#### 5.2.1.4 Impact of the Channel Model

The IlmProp scenarios in Figures 5.16, 5.12, and 5.14 are examples on how the user can generate simple geometries which display specific traits for the spatial correlation, and its

evolution in time. However, the results given by the investigations performed on the IlmProp channels have to be taken carefully, as the IlmProp cannot determine how representative the scenarios are with respect to real environments.

The flexibility of the channel model allows us to reveal the limits of the two algorithms, namely the dimensionality of the antenna arrays and the difficulty in handling strongly spatially correlated users. The simple grouping algorithm described above has been tested on an IlmProp geometry, especially taking into consideration how the scenario evolves in time. This permits us to study the algorithms as they adapt to the different channel conditions. Our study reveals the advantages and drawbacks of these algorithms, helping in proposing solutions which allow us to implement these beamforming schemes in real applications.

### 5.2.2 The IlmProp and Scheduling Algorithms

In [16] we present a novel scheduling algorithm based on the one first published in [15] and then extended in [17].

The algorithm, called *ProSched*[8], is a low-complexity scheduling algorithm for wireless multi-user MIMO communication systems in which users are multiplexed via time-, frequency- and space-division multiple access schemes, TDMA, FDMA, and SDMA, respectively. The name "ProSched" was chosen because the scheduling algorithm is based on subspace projections.

In such systems, the transmission quality degrades considerably if users with spatially correlated channels are scheduled to be served at the same time and frequency. The ProSched approach works with both zero-forcing and non zero-forcing SDMA precoding schemes by deciding, for each time and frequency slot, which users are to be served in order to maximize the precoding performance. The number of users is not a fixed parameter of the algorithm (as often assumed for other schedulers present in the literature), but is also adjusted according to the channel conditions. While smaller SDMA groups allow us to transmit with higher average power per user, larger groups lead to higher multiplexing gains. The ProSched is based on a novel interpretation of the precoding process using orthogonal projections which permits us to estimate the precoding results of all user combinations of interest with significantly reduced complexity. Additionally, the possible user combinations are efficiently treated with the help of a tree-based sorting algorithm. The ProSched takes advantage of perfect channel state information, when available, or alternatively of second order channel statistics. The individual user Quality of Service (QoS) requirements can be considered in the decision making process.

To show the potential gain from proper spatial scheduling in simulations, the channel model must be able to reproduce spatial correlation between users. Therefore, we use the IlmProp. An area of 150 m × 120 m with buildings of up to 8 m height is modeled, in which up to 18 users move randomly at speeds of up to 70 km/h, as depicted in Figure 5.18. The users change their direction and speed by a limited amount after a random time interval. The

[8] International patent pending (WO/2007/033997).

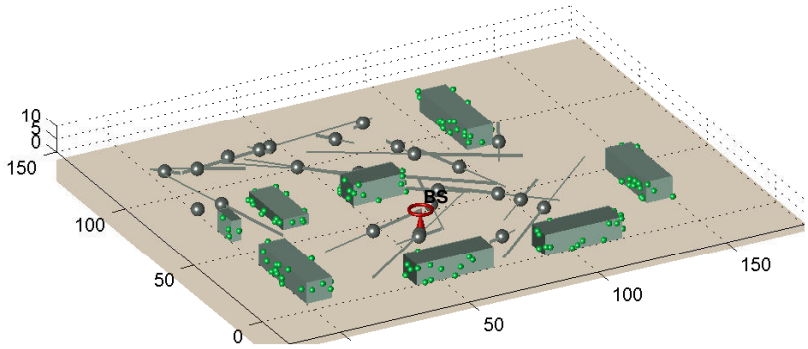


Fig. 5.18: An illustration of the geometry used to generate the channel with the IlmProp model.

BS mounts a UCA with 12 antennas while each mobile has 2 omnidirectional antennas, $\lambda/2$ spaced. The system operates at 2 GHz.

In Figures 5.19 we show 90 % outage rates in the frequency selective case using the ProSched algorithm extended to cope with multiple sub-carriers. The graphs show that ProSched greatly outperforms the Round Robin (RR) scheduler. Furthermore, it can be seen that a gain from spatial scheduling is possible in the entire simulated SNR range, whereas the biggest improvement can be achieved in the medium to high SNR range.

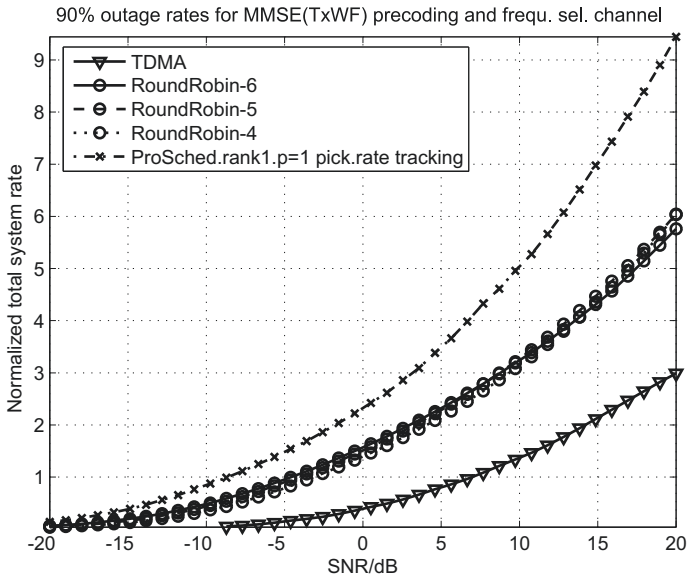


Fig. 5.19: Frequency selective case, MMSE (TxWF) [111], 12 users 24 OFDM sub-carriers: 90 % outage of the total system rate for a low complexity version of the scheduling algorithm compared to Round Robin and TDMA.

#### 5.2.2.1 Impact of the Channel Model

The ProSched algorithm serves the users optimally by grouping the ones which possess the smallest spatial correlation, as in this case it is possible to achieve higher SDMA gains. For this

reason, a channel which displays realistic spatial correlation is crucial to obtain meaningful results. Furthermore, to test the adaptive version of the algorithm it is needed that this correlation evolves realistically with time. In the IlmProp this is achieved very simply by letting the users move in the environment. In other channel models, such as the COST 259 or the 3GPP SCM, it would not be possible to model this.

### 5.2.3 The IlmProp to Evaluate Different Receiver Strategies

In this section we see how the IlmProp can be useful in evaluating different antenna configurations. The results of this section are published in [32] and [26]. As a practical example, we investigate different receiver strategies for a satellite to indoor broadcasting link. The transmitter is mounted on a GEostationary Orbit (GEO) satellite, whereas the receiver is fixed and is placed inside an office. We set the elevation of the satellite to 40°, assuming that the office is located in central Europe. In order to improve the link quality, we consider antenna arrays which can exploit both polarization diversity and spatial diversity.

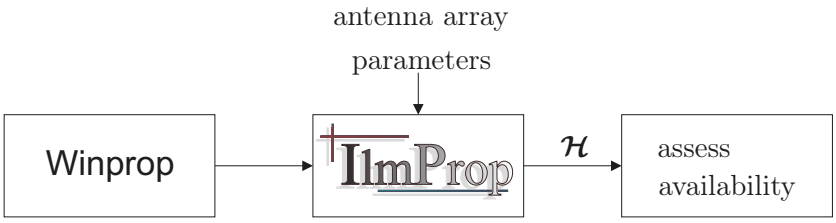


Fig. 5.20: IlmProp based framework to test different receiver strategies by means of the spatial availability.

Figure 5.20 shows the framework followed. For our analysis we use the Winprop, a simulation tool developed by AWE Communications [35]. The Winprop is a ray-tracer capable of predicting the path-loss for both indoor and outdoor environments.

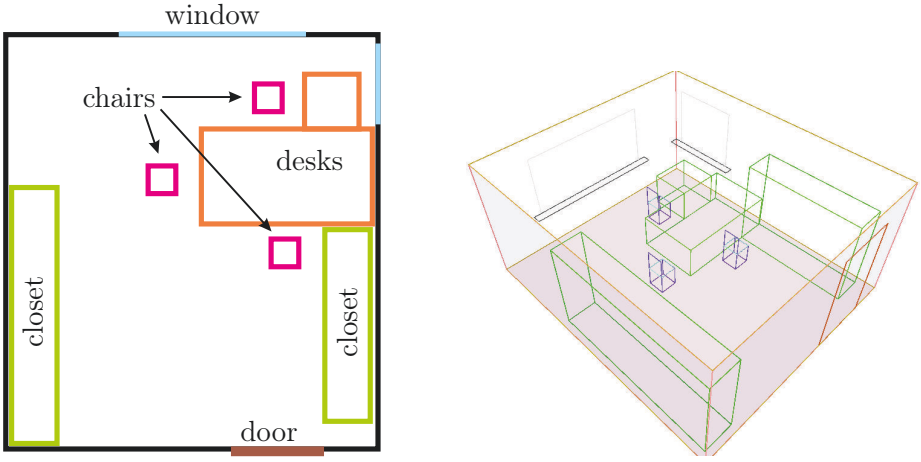


Fig. 5.21: Model of an office with the Winprop software [32, 26, 35].

Figure 5.21 shows the office modeled with the Winprop. For each receiver position within the room, the Winprop computes trajectories and path-strengths for all MPCs. The Winprop

is a software developed for system deployment, i.e., it is used by companies to determine which coverage a certain access point would obtain. With this tool, it is possible to decide where and how many base stations to deploy.

The output of the Winprop can be seen in Figure 5.22. The figure shows the predicted

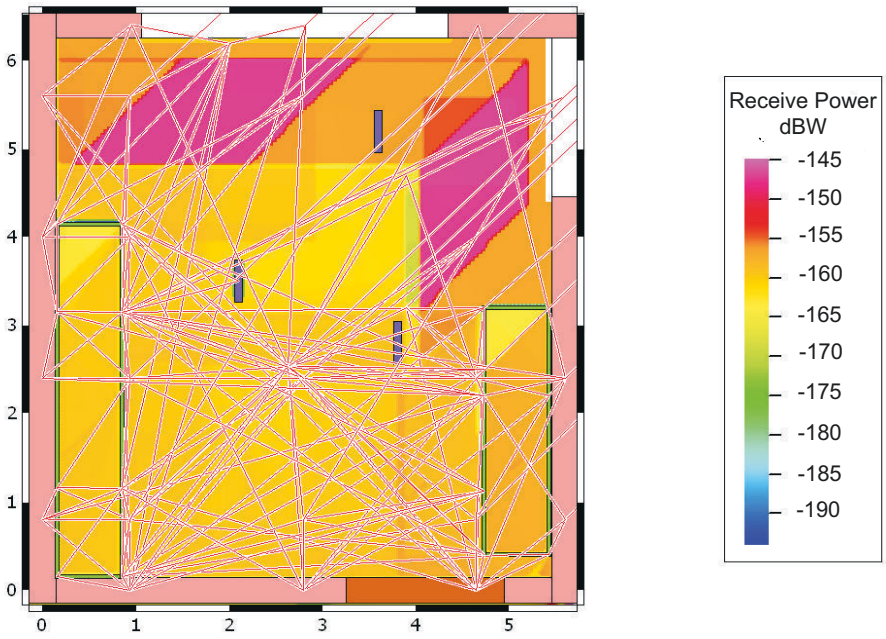


Fig. 5.22: Average receive power at 1 m height predicted with the Winprop [32, 26, 35].

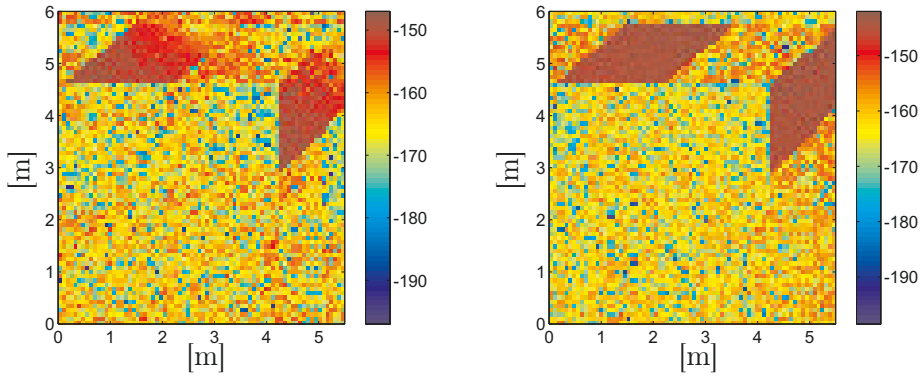


Fig. 5.23: Instantaneous receive power for a vertical dipole antenna (a) and a circularly polarized antenna (b). The values are given in dBW.

average receive power with a resolution of 8 cm at a height of 1 meter for an omnidirectional single antenna. The Winprop cannot cope with the distances required for a satellite link, so we modeled a transmitter 200 meters away from the office. The transmitter floats at a proper height to obtain the desired elevation. This distance is large enough so that the wavefronts can be assumed planar, and the only difference with a real satellite link is a smaller path-loss. The latter has been corrected in the IlmProp.

The paths' parameters are input to the IlmProp, with which we test different antenna arrays. The CIRs are computed for the following antennas:

- one vertically polarized dipole antenna
- one circularly polarized antenna
- two vertically polarized dipoles with different offsets
- two horizontally polarized dipoles with different offsets
- one vertically and one horizontally polarized dipole antennas placed at the same position

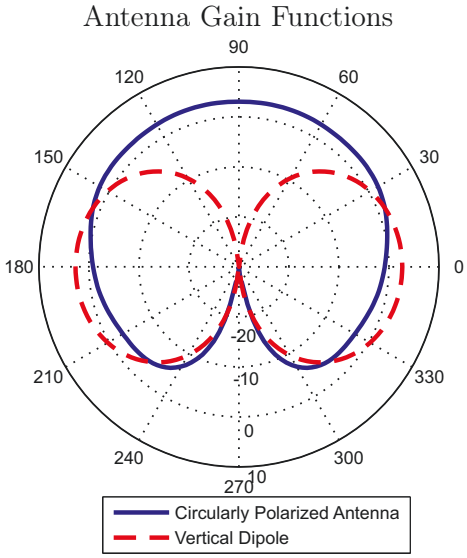


Fig. 5.24: Antenna gain function vs. elevation for a fixed azimuth. The radiation patterns are symmetric with respect to the vertical axis. The values are expressed in dBi.

The antenna gain functions[9] for the antennas considered are shown in Figure 5.24.

Figure 5.23 shows the instantaneous power computed with the IlmProp for a single vertical dipole (a) and for a single circularly polarized antenna (b). We can observe that the signal level changes rapidly in the NLOS regions, whereas it is stable near the windows, i.e., in a LOS regime. In particular, the circularly polarized antenna in the LOS benefits from a good reception as the satellite transmits with a circularly polarized wave. According to [159], in the NLOS the original polarization state is lost. Therefore, each MPC is modeled with a random polarization. The sum of MPCs is the origin of the spatial fading.

The performance of the different arrays are evaluated by means of the correlation coefficient and of the cumulative distribution function of the Fading Depth (FD). The correlation coefficient $\rho$ is defined as

$$\rho = \left| \frac{E\left[h_1 h_2^*\right]}{\sqrt{\left(E\left[|h_1|^2\right]\right)\left(E\left[|h_2|^2\right]\right)}} \right|, \tag{5.28}$$

where $h_1$ and $h_2$ are the channel coefficients for the first and second antenna, respectively. The FD at a certain receiver position, on the other hand, is defined as the difference between

[9] See Section 4.1.2

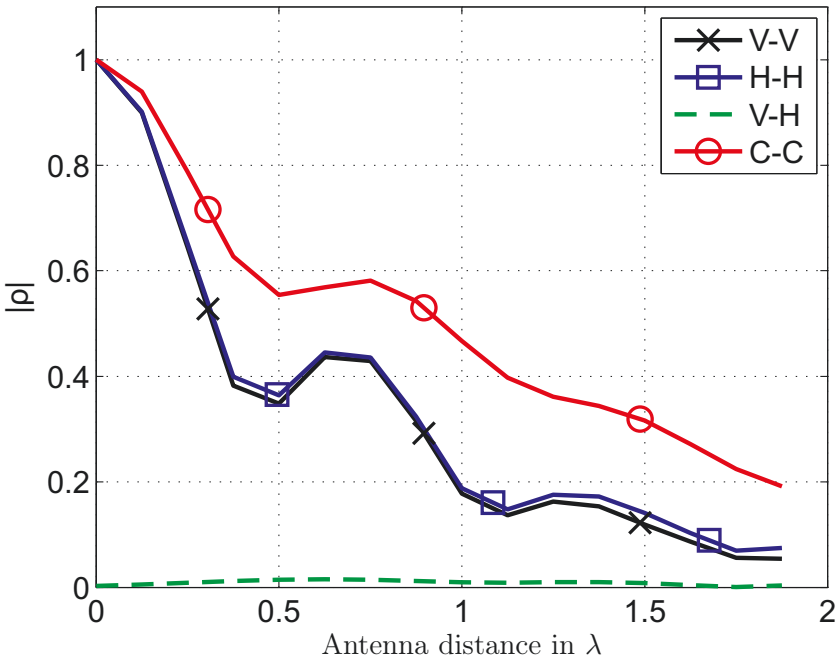


Fig. 5.25: Correlation coefficient for different antenna combinations.

the Carrier to Noise Ratio (CNR) outside the window, i.e., in a pure LOS regime, and the CNR one obtained in that point.

In Figure 5.25 we show the magnitude of the correlation coefficient for different distances of the antennas. The term 'V-V' denotes two vertically polarized dipole antennas, 'H-H' two horizontally polarized dipole antennas, while 'V-H' for one vertically and one horizontally polarized dipole antenna, and 'C-C' for correlation between two circularly polarized antennas. Due to the rich scattering environment, two antennas with an orthogonal polarization are fully uncorrelated even when co-located, indicating the possibility to exploit polarization diversity. To exploit spatial diversity with the same kind of antennas, on the other hand, it is necessary to displace the antennas by more than $\lambda/2$.

Figure 5.26 show the Cumulative Density Function (CDF) of the FD. We define *availability* as a situation in which the link margin is big enough to compensate the FD so that the CNR obtained is larger or equal to the CNR outside the window. Figure 5.26(a) shows that an availability of 30 % can be achieved with a link margin between 17 and 21 dB, while 80 % with 22 to 28 dB (depending on the receive antennas). Figure 5.26(b) shows the same curves magnified around higher values of availability. At 99 % availability, a significant difference in the performance can be observed. The 'V-H' outperforms the one antenna system 'V' by approximately 12.5 dB. In other words, the satellite would require 12.5 dB more transmit power to achieve the same availability with a one vertical dipole receiver with respect to a receiver with two antennas, one vertical and one horizontal.

For this investigation, both planar and spherical wave approximations were tested, leading to comparable results.

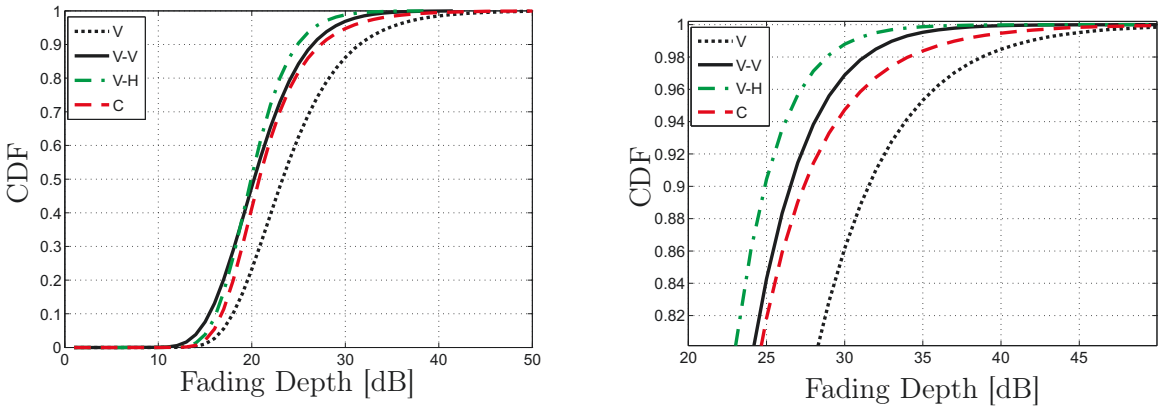


(a) Original (b) Zoomed

Fig. 5.26: Cumulative Density Function (CDF) of the Fading Depths (FDs) for different antenna configurations.

#### 5.2.3.1 Impact of the Channel Model

The IlmProp allows us to investigate different antenna configurations in the same environment. The accurate modeling of the radiation patterns and of the polarization states lets us investigate the impact of polarization diversity as well as spatial diversity. To obtain quantitative measures of the gains achieved by one strategy with respect to another, it is crucial to consider a deterministic scenario, in which all antenna arrays see the very same MPC. This is possible with the IlmProp, as all paths can be modeled explicitly in a deterministic fashion. The use of the ray-tracer Winprop to define the propagation paths assures that the channels are realistic.

### 5.2.4 The IlmProp to Evaluate the Performance of Antenna Arrays

The IlmProp can be particularly useful in evaluating the performance of antenna arrays in both theoretical environments as well as in realistic multi-user scenarios.

This section shows, as an example of this kind of investigation, the evaluation of a miniaturized antenna array developed in the Department for RF and Microwave Techniques at Ilmenau University of Technology. It was first presented in [220] and [219]. The array features three monopoles spaced by a quarter of the wavelength, and a passive Decoupling and Matching Network (DMN), which prevents gain reduction. The array operates at a center frequency of 1 GHz. At the same time, the DMN forms orthogonal radiation patterns, which divide the space into three different sections. To show the improvement due to the DMN, we compare the array with and without DMN on different IlmProp scenarios.

Figure 5.27 shows the antenna array. More details on the construction of the array and on its design can be found in [220, 219].

Figure 5.28 shows the antenna response function $a_\vartheta(\vartheta, \varphi)$ for the three antennas for the vertical polarization. The antenna response is introduced in Section 4.1.5. Figure 5.29 shows

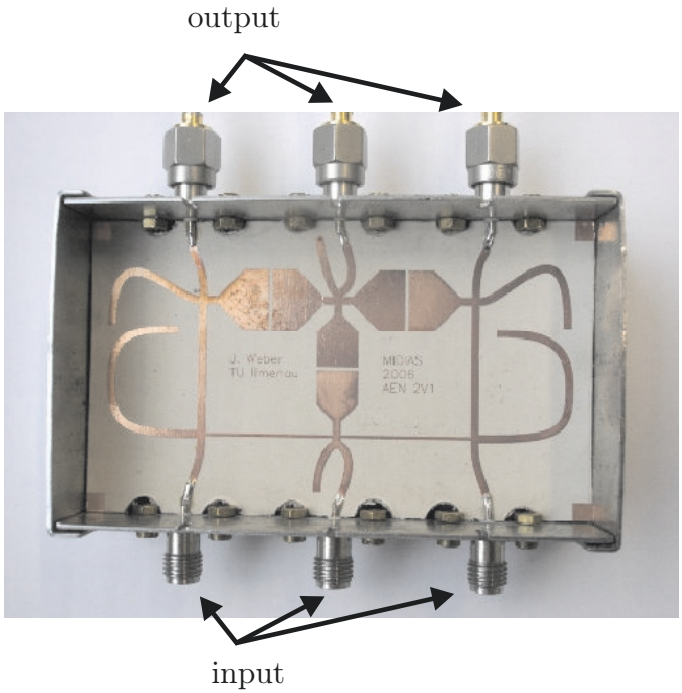


Fig. 5.27: The passive Decoupling and Matching Network (DMN). The output is fed to three dipole antennas, $\lambda/4$ spaced.

| antenna | $\xi$ | $g_{\max}$ | $d_{\max}$ | $g_{\max}$ [dB] | $d_{\max}$ [dB] |
|---|---|---|---|---|---|
| w/ DMN (a) | 0.64 | 4.6 | 7.1 | 6.6 | 8.5 |
| w/ DMN (b) | 0.64 | 3.7 | 5.7 | 5.6 | 7.6 |
| w/ DMN (c) | 0.65 | 4.8 | 7.4 | 6.8 | 8.7 |
| w/o DMN (a) | 0.63 | 2.3 | 3.6 | 3.5 | 5.5 |
| w/o DMN (b) | 0.52 | 2.0 | 3.8 | 3.0 | 5.8 |
| w/o DMN (c) | 0.65 | 2.4 | 3.7 | 3.8 | 5.7 |

Tab. 5.2: Antenna efficiency $\xi$, antenna gain $g_{\max}$, and antenna directivity $d_{\max}$ for the antennas of the arrays under study, with and without DMN.

the antenna responses for the horizontal polarization. Note that the antennas radiate significantly more in the vertical polarization.

Figures 5.30 and 5.31 show the antenna responses for the array without the DMN for the vertical and horizontal polarization, respectively.

Although the network introduces losses, the overall efficiency $\xi$ of the antenna system is improved, as the losses due to the high power mismatch are reduced. The antenna efficiency $\xi$, introduced in Section 4.1.2, is defined as the ratio of the radiated power to the power fed into the antenna port, thus accounting for the total losses of the antenna. To compute the efficiency we use the method presented in Section 4.4.4.5.

Table 5.2 shows the antenna efficiency $\xi$, antenna gain $g_{\max}$, and antenna directivity $d_{\max}$ for the elements of the arrays under study.

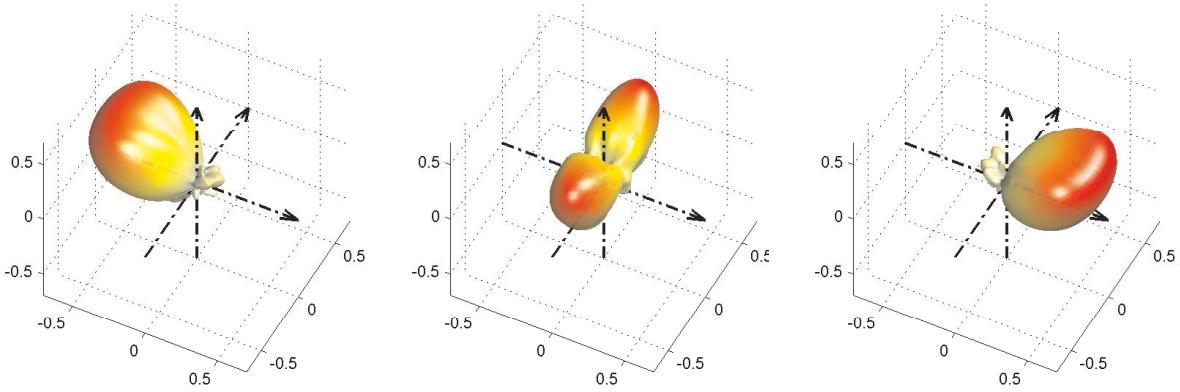


Fig. 5.28: Measured vertical antenna responses for the array with the passive Decoupling and Matching Network (DMN).

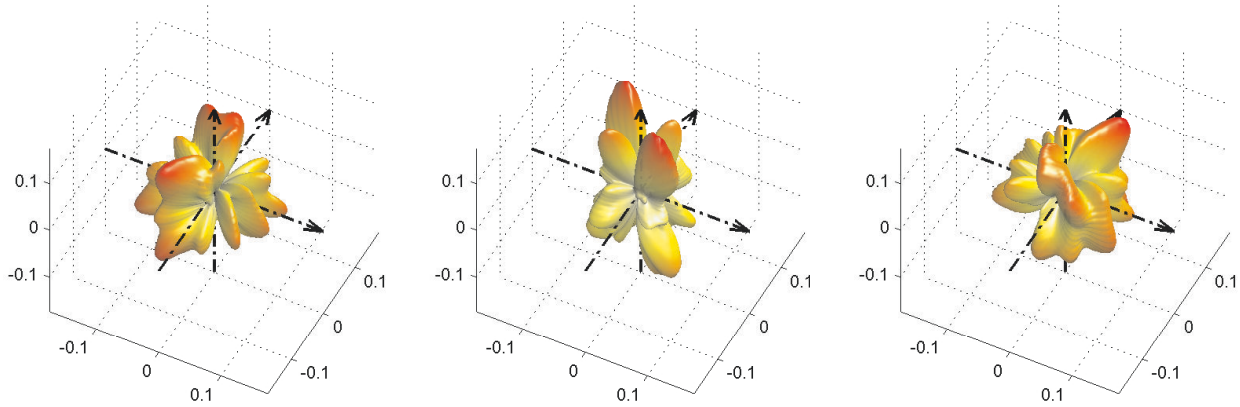


Fig. 5.29: Measured horizontal antenna responses for the array with the passive Decoupling and Matching Network (DMN).

First, we generate a scenario which mimics Jakes' assumptions for a Rayleigh channel [110]. All paths possess the same power. A large number of scatterers are placed on a sphere surrounding the array under test, as depicted in Figure 5.32. The scatterers provide a single bounce reflection and a random polarization status. In this environment rich of MPCs, we can compute the correlation coefficient $\rho_{i,j}$ as

$$\rho_{i,j} = \left| \frac{E\left[h_i h_j^*\right]}{\sqrt{\left(E\left[|h_i|^2\right]\right)\left(E\left[|h_j|^2\right]\right)}} \right|, \tag{5.29}$$

where $h_i$ and $h_j$ are the channel coefficients for the $i$-th and $j$-th antenna, respectively, and

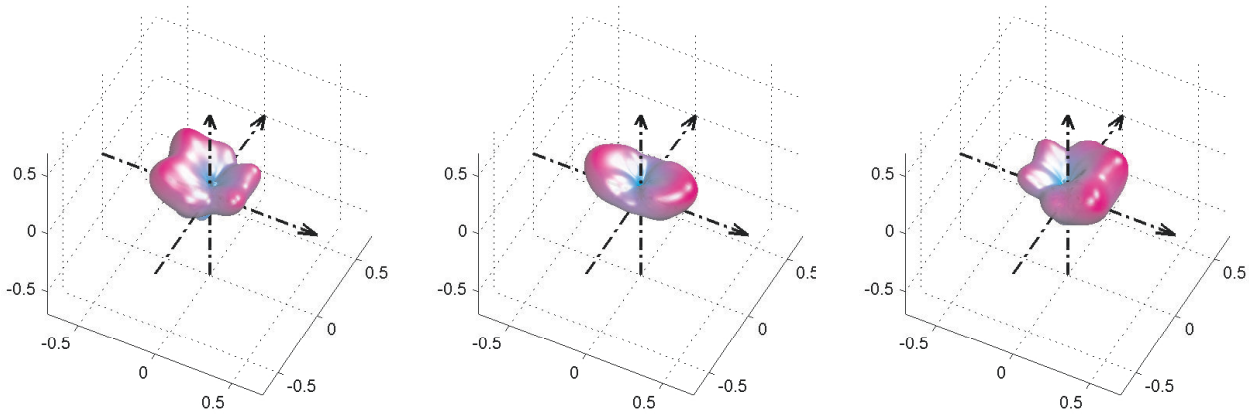


Fig. 5.30: Measured vertical antenna responses for the array without the passive Decoupling and Matching Network (DMN).

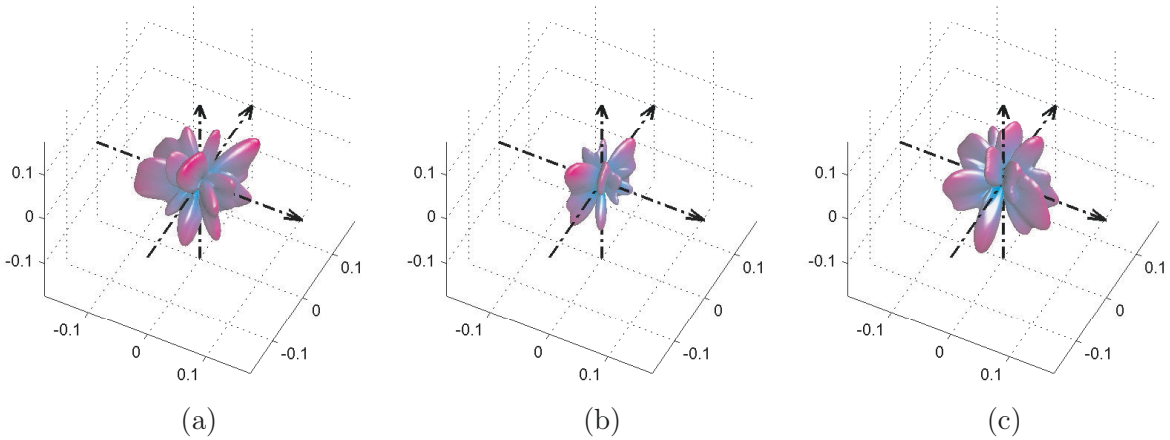


Fig. 5.31: Measured horizontal antenna responses for the array without the passive Decoupling and Matching Network (DMN).

the superscript $(\cdot)^*$ denotes complex conjugation. The average is performed across different realizations of the channels, obtained by moving the array. Table 5.3 lists the correlation coefficients for the proposed array with and without DMN.

The values for $\rho$ indicate that the use of the DMN effectively decorrelates the antennas by making the radiation patterns more orthogonal to each other, i.e., the energy is collected from different directions and, consequently, from different MPCs. Notice that the number of MPCs modeled influences the correlation factors in the table. Therefore, they should not be interpreted in absolute terms, but rather only relatively to each other. In fact, as the number of paths increases, the values of $\rho$ would decrease. Ideally, with an infinite number of MPCs,

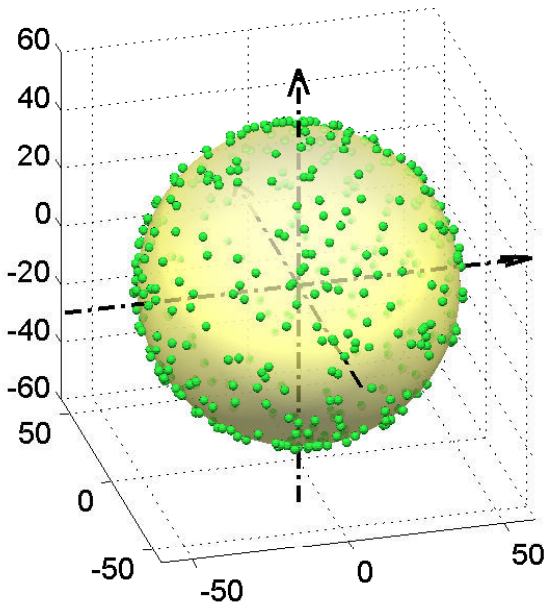


Fig. 5.32: Position of the scatterers in an IlmProp scenario approaching the conditions assumed by the Jakes model. The array under study is located in the origin while the transmitter is placed far from the sphere.

| Array | $\rho_{1,2}$ | $\rho_{2,3}$ | $\rho_{1,3}$ |
|---|---|---|---|
| 3-ULA w/ DMN | 0.13 | 0.11 | 0.08 |
| 3-ULA w/o DMN | 0.37 | 0.35 | 0.22 |

Tab. 5.3: Correlation coefficients for the antenna array with and without DMN.

the correlation coefficients of both arrays would equal zero.

In order to evaluate quantitatively the benefit offered by the proposed array with respect to the array without DMN, we compute the CDF of the capacity for the scenario mentioned above. To do so, we assume that the arrays are used as transmitters with a fixed available transmit power. The receiver employs one vertical dipole antenna only. Figure 5.33 shows the CDF curves. It can be observed that the array with the DMN provides higher capacities. The curve for the array with the DMN is shifted to the right due to the improved antenna efficiency, while it has a steeper slope due to the higher diversity. The latter is a direct consequence of the lower values of the correlation coefficients.

Figure 5.34 depicts a more realistic scenario. A fixed BS mounted at 10 meters height employs a UCA consisting of 16 vertical dipole antennas. Two cars (mounting the antenna arrays under study on their roofs) move on the trajectories shown in the figure. Several clusters provide the multi-path propagation, whereas two buildings introduce shadow fading. The MPCs coming from the clusters are rather powerful, so that the Rician $K$-factor ranges between 3 and 6 in the LOS regions.

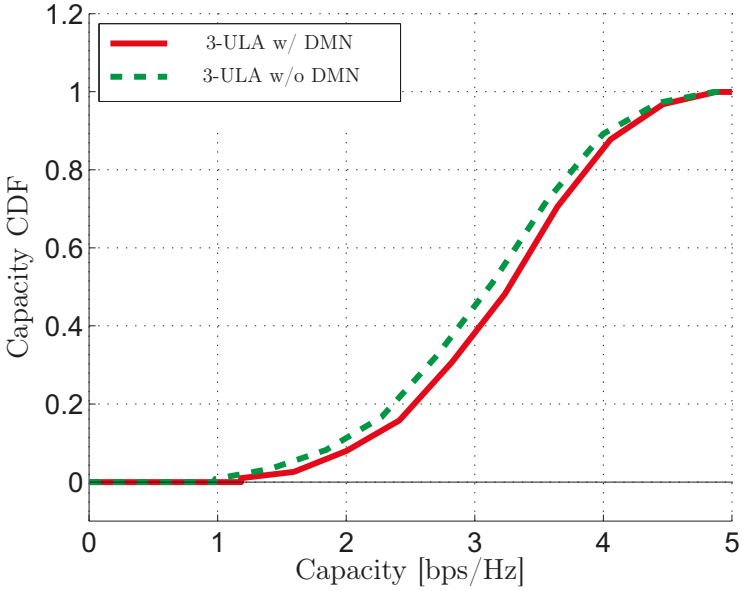


Fig. 5.33: Cumulative Density Function (CDF) of the capacity at an SNR of 10 dB for the antenna arrays under study.

We simulate the downlink by applying first the Block Diagonalization (BD) algorithm introduced in Appendix F. We send a single data stream to each MS, using strongest eigenmode transmission. Thanks to the BD scheme, the modulation vectors are chosen so that there will be no interference between the users. At the receiver we perform Maximum Ratio Combining (MRC), thus assuming that perfect CSI is known at both the Rx and Tx. An identical copy of the 3-ULA is mounted on each car. We first compute the channels for the version of the array with the DMN, and then without.

Figure 5.35 shows the user rates for the two MSs using the array with and without DMN. The plot shows only a representative time interval. It can be seen that for most of the time snapshots the array with DMN achieves higher user rates. However, in others, the array without DMN performs better. To investigate this more rigorously we compute the difference of the user rates and we plot its corresponding Cumulative Density Function (CDF) in Figure 5.35. Negative values of the abscissa represent time snapshots in which the array without DMN achieved a better rate. This happens in approximately 35% of the cases. The maximum gain over the array without DMN is 1.3 bps/Hz. In the remaining cases the proposed array performs better, reaching a gain up to 3 bps/Hz.

This simulation shows that in a case where the MPCs arrive from a few specific directions, on average the proposed array still performs better than the version without DMN. For the time snapshots in which this does not occur, the gain functions of the two arrays differ, and for specific directions of arrival one array has higher gains than the other. On average, however, the array with the DMN is capable of achieving better rates as it possesses higher diversity and orthogonal beam patterns.

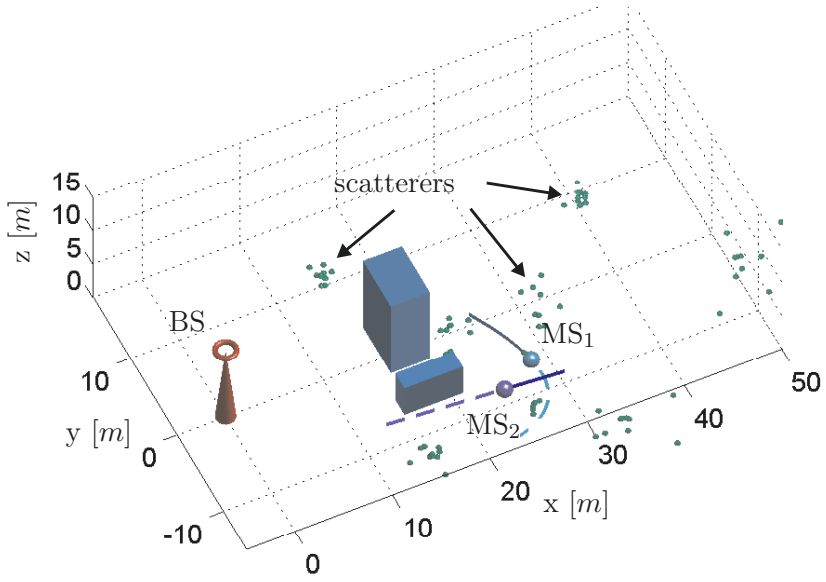


Fig. 5.34: Microcellular environment to test the 3-ULA with and without DMN Two buildings provide shadow fading. Several clusters of scatters are placed around the mobiles.

The better performance of the array with the DMN can be observed also in the Bit Error Rate (BER). Figure 5.37 shows the average BER curves for the microcellular scenario. As for the capacity curves we assume BD with strongest eigenmode transmission at the Tx, and MRC at the Rx. The transmission scheme assumed is BPSK. For a certain noise level which gives an average SNR $\bar{\gamma}$, we can compute the instantaneous SNR $\gamma(t)$ for each time snapshot t. Let the function $p_\gamma(\gamma)$ be the Probability Density Function (PDF) of the instantaneous SNR. We then compute the BER for each SNR $\gamma$, denoted by $p_e(\gamma)$, and obtain the average BER, namely $\bar{p}_e(\bar{\gamma})$, with the following integral

$$\bar{p}_e(\bar{\gamma}) = \int_{-\infty}^{\infty} p_e(\gamma) \cdot p_\gamma(\gamma)\, d\gamma. \tag{5.30}$$

The plots show that the array with the DMN achieves better BERs. In particular, the slope of the curves for the proposed array are steeper, indicating the higher diversity order.

#### 5.2.4.1 Impact of the Channel Model

By modeling the MPCs explicitly, the IlmProp allows us to model a scenario which approaches the assumptions taken by the theoretical model proposed by Jakes. In this case, we can assess quantitatively the gains provided by the proposed array with respect to the version without DMN. The gains are mostly due to the higher diversity order which characterizes the array. However, such a scenario is rather unrealistic, and therefore we use the IlmProp to model an environment in which these arrays might be actually used. We construct a microcellular

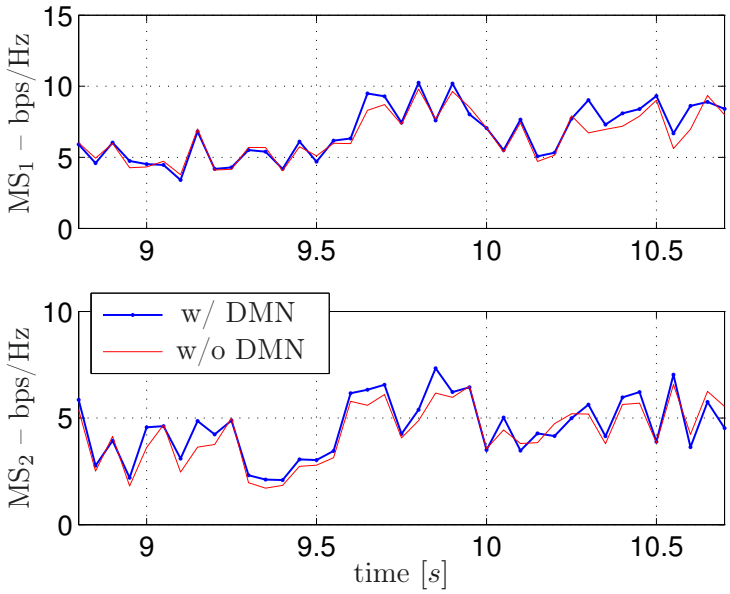


Fig. 5.35: User rates for the two users $MS_1$ and $MS_2$ mounting the array with and without DMN. The plot shows a representative time interval. The average SNR is 30 dB.

scenario in which the arrays are mounted on two MSs. The computation of the channels allow us to carry out several investigations, which confirm that the DMN improves the performance of the array.

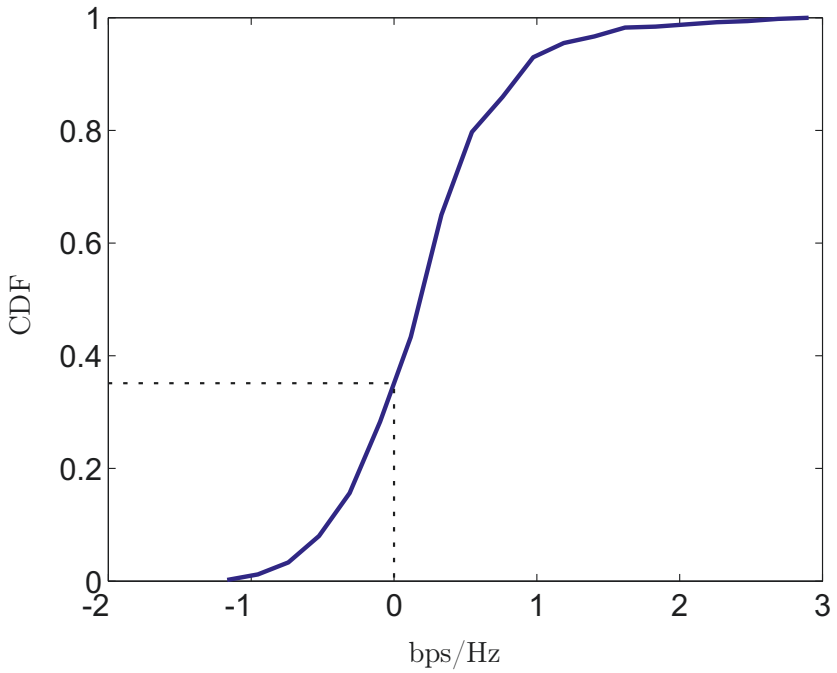


Fig. 5.36: Difference of the capacity obtained for the array with DMN and the one without. For approximately 65 % of the time snapshots the array with DMN achieves higher user rates. The average SNR is 30 dB.

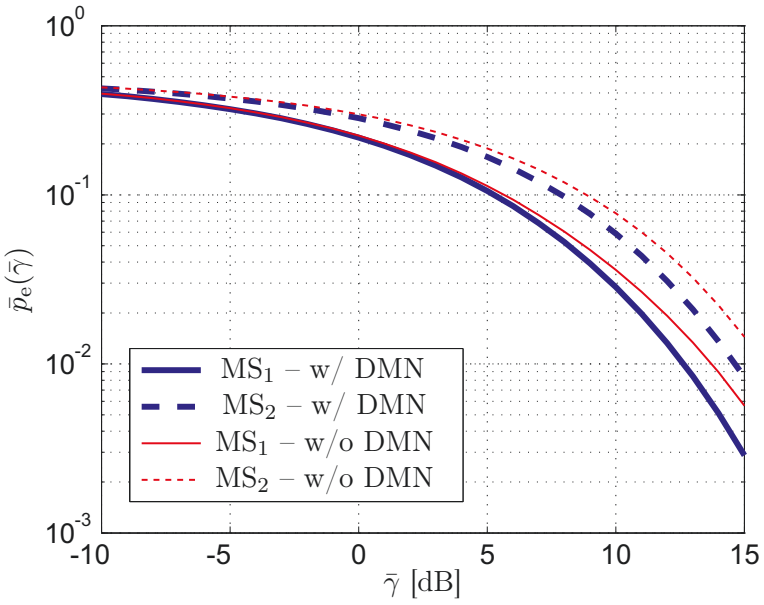


Fig. 5.37: Average Bit Error Rate (BER) vs. average $\bar{\gamma}$ for the microcellular scenario in Figure 5.34. We use BD with strongest eigenmode transmission and BPSK. At the receiver we assume MRC.

### 5.2.5 The IlmProp to Test Parameter Estimation Techniques

Validating high-resolution parameter estimation algorithms, such as [77, 208, 93, 27], is particularly difficult for several reasons. First, the data model assumed by the estimator does not necessarily fit the true propagation mechanism. In this case we speak of a *model mismatch*. Furthermore, assuming that the data model were exact, the algorithm can still suffer from a *model order mismatch*, i.e., estimating the wrong number of propagation paths.

One trivial solution is simply to assume no model mismatch and perfect model order estimation. By doing this, we can compare directly the parameters estimated with the exact ones for each path. Obviously, this approach is quite coarse, as it is unrealistic to believe that the order can be known exactly. While the errors due to the model mismatch are very difficult to characterize, the ones due to model order mismatch can be studied.

However, to do so, well-known error metrics like the mean-squared estimation error cannot be applied. Furthermore, the so-called *reconstruction error*, i.e., the difference between the measured and the (reconstructed) estimated MIMO channel matrix does not reflect the properties of the channel well. For this reason, in [5] and [4] the authors introduce a new metric, called the Environment Characterization Metric (ECM).

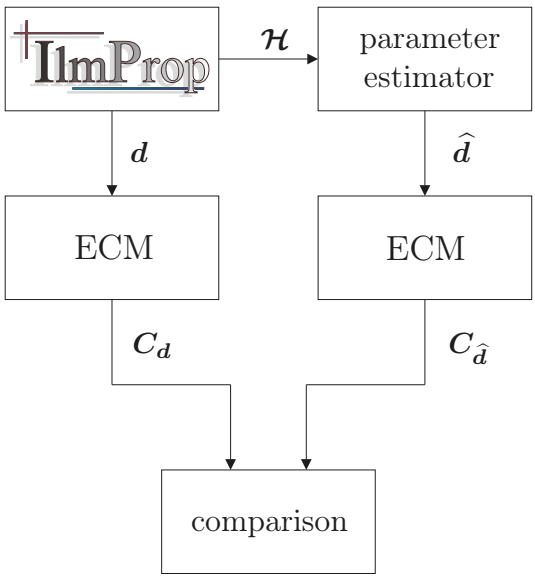


Fig. 5.38: IlmProp based framework to test the accuracy of a parameter estimator by means of the Environment Characterization Metric (ECM).

For testing the accuracy of the channel estimator we use the framework shown in Figure 5.38 for different environments generated with the IlmProp. The latter provides both the channel coefficients and the exact path parameters, denoted by $\boldsymbol{\mathcal{H}}$ and $\boldsymbol{d}$, respectively. The estimator analyzes $\boldsymbol{\mathcal{H}}$ to obtain the parameter estimates $\widehat{\boldsymbol{d}}$. The ECM is then computed for both exact and estimated parameters, obtaining $\boldsymbol{C_d}$ and $\boldsymbol{C_{\widehat{d}}}$, respectively. Finally, the latter can be compared to assess the accuracy of the estimator.

The ECM is computed for each time snapshot $t$ separately, and is computed as the co-

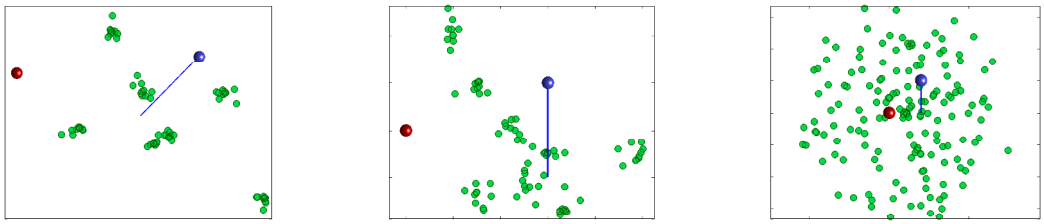

(a) (b) (c)

Fig. 5.39: Scenarios used for comparing the estimator performance: (a) few clustered paths, (b) larger clusters, (c) rich scattering

variance matrix of the vector containing the path parameters. The latter are first normalized so that they can range only between 0 and 1. The Singular Values (SVs) of the ECM can be interpreted as a "fingerprint" of the scenario. For more details on the ECM we refer the reader to the publications [5] and [4].

A practical example of the use of the ECM is given in the following. Figure 5.39 shows three scenarios modeled with the IlmProp. The scenarios feature: (a) well separated, dense clustered propagation paths with single-bounce scattering, (b) clustered propagation paths which are spread wider, (c) no clusters and double-bounce-only reflections. The channels have a bandwidth of 100 MHz, with 510 frequency bins. The MS employs a ULA with 15 sensors $0.45\lambda$ spaced and slightly directive radiation patterns. The BS employs a UCA with 15 sensors $0.4\lambda$ spaced and slightly directive beam patterns. Only vertical-to-vertical polarization is considered. No noise was added in all three scenarios.

For the clustered scenarios (a) and (b), only single-bounce scattering was assumed, whereas for the rich-scattering scenario (c) only double scattering paths occur.

The ISIS algorithm [77] was applied to the synthetic data generated by IlmProp for the different scenarios. Compared with the original Space Alternating Generalized Expectation-maximization (SAGE) algorithm [76], the ISIS algorithm exhibits a performance improvement in terms of convergence speed, detection ability of the weak paths, and computational effort [79]. The parameters estimated are DOA, DOD, TDOA, and polarization matrices of 40 paths for each individual snapshots.

Figure 5.40 shows the SVs in dB of the ECM for the three different scenarios. The values for the true paths are indicated by black darker lines, the estimated paths by red lighter lines, and the different SVs by different marker types.

To discuss the significance of the new metric, we first focus on the SVs of $\boldsymbol{C_d}$ only. In Figure 5.40(a) one can observe a large distance between the second and third SV, and between the 4th and 5th SV, where especially the last value of Scenario (a) changes strongly over time. Figure 5.40(b) shows also a large distance between the SVs. In Figure 5.40(c), the SVs are very close to each other and do not change significantly. The distance between the SVs of the ECM $\mathbf{C_d}$ provides information on the "compactness" of the paths in the environment.

To assess the performance of the parameter estimator, we now compare the singular values of $\mathbf{C}_{\boldsymbol{d}}$ with the ones from $\boldsymbol{C}_{\widehat{\boldsymbol{d}}}$.

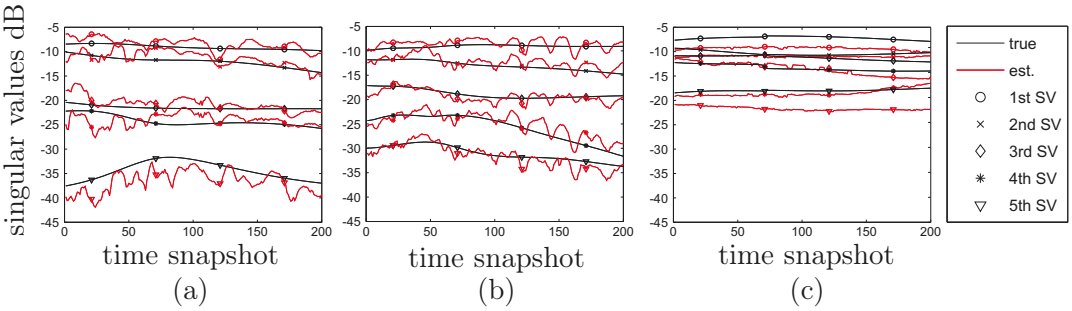


Fig. 5.40: Singular values of the Environment Characterization Metric (ECM) $\mathbf{C}_{\boldsymbol{\pi}}$ for the true and estimated parameters from the three scenarios.

For the first two environments with clustered propagation paths, one can observe that the general trend is the same, but the curves seem to vary around the correct value. The reason for this is the destructive/constructive interference of different paths at the Rx, which attenuates some clusters and amplifies others.

In the third (rich scattering) environment the SVs are typically underestimated, which indicates that the true propagation paths are spread wider than the estimated paths. In this instance, the parameter estimator suffers from the model order mismatch, a larger number of paths would be necessary to reflect the scenario correctly.

#### 5.2.5.1 Impact of the Channel Model

The investigation proposed in this section requires a ray-based channel model which gives the possibility to define the individual propagation paths explicitly. This is provided by the IlmProp, which, furthermore, allows the use of measured radiation patterns.

Notice that this analysis is not meant to validate the capability of the parameter estimator to estimate paths correctly. On the contrary, assuming that paths in real scenarios do appear in clusters, the investigation allows us to show the behavior of the estimator with respect to the cluster density.

If we wanted to validate the parameter estimator, it would be necessary to carry out a measurement campaign in a scenario also modeled in an accurate ray-tracer (see Section 3.3.2). Then, it would be possible to compare the paths obtained by the ray-tracer with the ones estimated. Alternatively, the localization algorithm described in Section 5.3.1 can be used for this aim, as shown in Sections 5.3.4 and 5.3.5.

### 5.2.6 The IlmProp to Investigate Subspace-Based Channel Models

Subspace-based models, such as the Weichselberger model proposed in [222] and [221], belong to the family of analytical models summarized in Section 3.2. This section introduces

the *correlation tensor-based channel model* proposed in [34]. This novel model extends the subspace-based model presented in [10] and [13]. In [60], a similar tensor-based channel model is introduced. The latter is however a straightforward tensor extension of the Weichselberger model, and therefore it assumes a Kronecker like structure of the eigenmodes. The tensor presented in [34] is more general, as it does not assume this. Tensor-based representations represent a significant contribution to the field of analytical channel modeling, as they extend it to more dimensions. In this work we merely describe the main idea behind the model, stressing how a geometry based channel model like the IlmProp is crucial in giving a physical interpretation to the model.

#### 5.2.6.1 The Basic Idea

According to equation (2.35), we represent the channel coefficients in form of the tensor

$$\boldsymbol{\mathcal{H}} \in \mathbb{C}^{M_\mathrm{R} \times M_\mathrm{T} \times M_\mathrm{f} \times M_\mathrm{t}}, \tag{5.31}$$

where $M_\mathrm{R}$ and $M_\mathrm{T}$ are the number of antennas at the transmitter and receiver, and $M_\mathrm{f}$ and $M_\mathrm{t}$ are the number of samples taken in frequency and time, respectively.

As in equation (2.93), we define the channel correlation tensor as

$$\boldsymbol{\mathcal{R}} = \mathrm{E}\left[\boldsymbol{\mathcal{H}}(t) \circ \boldsymbol{\mathcal{H}}(t)^*\right] \in \mathbb{C}^{M_\mathrm{R} \times M_\mathrm{T} \times M_\mathrm{f} \times M_\mathrm{t} \times M_\mathrm{R} \times M_\mathrm{T} \times M_\mathrm{f} \times M_\mathrm{t}}, \tag{5.32}$$

by using the tensor outer product defined in equation (D.13).

To calculate the correlation tensor numerically, we need to gather several realizations of the tensor $\boldsymbol{\mathcal{H}}$, in order to compute the expectation operator. This is in general not possible, as we measure the time variant, frequency selective MIMO channel only once. To solve this, we take one of the available dimensions to carry out the expectation. As the temporal dimension provides usually a large number of samples, we average over this dimension. Let the channel tensor $\boldsymbol{\mathcal{H}}(t)$ be defined as

$$\boldsymbol{\mathcal{H}}(t) \in \mathbb{C}^{M_\mathrm{R} \times M_\mathrm{T} \times M_f}, \tag{5.33}$$

so that it describes the frequency selective MIMO channel at time snapshot $t$. The six-dimensional correlation tensor can now be expressed as

$$\boldsymbol{\mathcal{R}} = \mathrm{E}\left[\boldsymbol{\mathcal{H}}(t) \circ \boldsymbol{\mathcal{H}}(t)^*\right] \in \mathbb{C}^{M_\mathrm{R} \times M_\mathrm{T} \times M_f \times M_\mathrm{R} \times M_\mathrm{T} \times M_f}. \tag{5.34}$$

and numerically computed as

$$\boldsymbol{\mathcal{R}} \approx \widehat{\boldsymbol{\mathcal{R}}} = \frac{1}{M_t} \sum_{k=1}^{M_t} \boldsymbol{\mathcal{H}}(t) \circ \boldsymbol{\mathcal{H}}(t)^* = \frac{1}{M_\mathrm{T}}\, \boldsymbol{\mathcal{H}} \bullet_4 \boldsymbol{\mathcal{H}}^*, \tag{5.35}$$

where $\bullet_4$ denotes the 4-mode inner product introduced in Section D.3.4.

In order to cope with time variant channels, we divide the channel into temporal windows of size $T_{\mathrm{W}}$, so that the channel within the $k$-th window, denoted by $\boldsymbol{\mathcal{H}}_k$, can be assumed stationary with respect to frequency and space along time. The window $\boldsymbol{\mathcal{H}}_k$ is depicted in Figure 5.41.

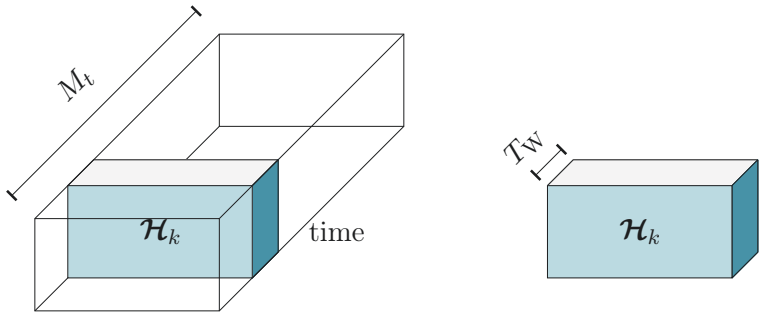


Fig. 5.41: Windowing in the time domain for the multi-dimensional channel $\boldsymbol{\mathcal{H}}$. Here we depict only 3 dimensions. Along time, the $k$-th window has size $T_{\mathrm{W}}$ whereas the channel tensor $\boldsymbol{\mathcal{H}}$ has size $M_t$.

The $k$-th window is described exhaustively by the 6-dimensional correlation tensor $\boldsymbol{\mathcal{R}}_k$, which we can estimate as

$$\boldsymbol{\mathcal{R}}_k \approx \widehat{\boldsymbol{\mathcal{R}}}_k = \frac{1}{T_{\mathrm{W}}} \cdot \boldsymbol{\mathcal{H}}_k \bullet_4 \boldsymbol{\mathcal{H}}_k^* \,. \tag{5.36}$$

In the following we omit the block index $k$ for simplicity. To get insight into the spatial structure of the channel, we decompose this correlation tensor via the following Higher Order Singular Value Decomposition (HOSVD)[10]

$$\widehat{\boldsymbol{\mathcal{R}}} = \boldsymbol{\mathcal{S}} \times_1 \boldsymbol{U}^{(1)} \times_2 \boldsymbol{U}^{(2)} \times_3 \boldsymbol{U}^{(3)} \times_4 \boldsymbol{U}^{(4)} \times_5 \boldsymbol{U}^{(5)} \times_6 \boldsymbol{U}^{(6)}.$$

Due to the symmetries displayed by the correlation tensor we can achieve

$$\begin{aligned} \boldsymbol{U}^{(4)} &= \boldsymbol{U}^{(1)*} \\ \boldsymbol{U}^{(5)} &= \boldsymbol{U}^{(2)*} \\ \boldsymbol{U}^{(6)} &= \boldsymbol{U}^{(3)*}, \end{aligned} \tag{5.37}$$

so that we can rewrite the HOSVD as

$$\widehat{\boldsymbol{\mathcal{R}}} = \boldsymbol{\mathcal{S}} \times_1 \boldsymbol{U}^{(1)} \times_2 \boldsymbol{U}^{(2)} \times_3 \boldsymbol{U}^{(3)} \times_4 \boldsymbol{U}^{(1)^*} \times_5 \boldsymbol{U}^{(2)^*} \times_6 \boldsymbol{U}^{(3)^*}. \tag{5.38}$$

The matrix $\boldsymbol{U}^{(n)}$ contains the left singular vectors of the $n$-th unfolding matrix $\widehat{\boldsymbol{\mathcal{R}}}_{(n)}$ of $\widehat{\boldsymbol{\mathcal{R}}}$. The core tensor $\boldsymbol{\mathcal{S}}$ can be calculated via the equation

$$\boldsymbol{\mathcal{S}} = \widehat{\boldsymbol{\mathcal{R}}} \times_1 \boldsymbol{U}^{(1)^{\mathrm{H}}} \times_2 \boldsymbol{U}^{(2)^{\mathrm{H}}} \times_3 \boldsymbol{U}^{(3)^{\mathrm{H}}} \times_4 \boldsymbol{U}^{(1)^{\mathrm{T}}} \times_5 \boldsymbol{U}^{(2)^{\mathrm{T}}} \times_6 \boldsymbol{U}^{(3)^{\mathrm{T}}}.$$

The proposed channel model consists in computing the correlation tensors for all windows,

[10] The Higher Order Singular Value Decomposition (HOSVD) is discussed in Section D.5.

as they describe exhaustively the correlation properties of the channel, seen as a temporal block stationary stochastic process.

In the following we give a brief description of two applications of the proposed channel model, namely the generation of new channel realizations and the subspace-based denoising of a channel measurement.

#### 5.2.6.2 Channel Synthesis

*Channel synthesis* indicates the procedure by which we can obtain new realizations of a channel described by a given correlation tensor $\boldsymbol{\mathcal{R}}$. Let $\tilde{\boldsymbol{\mathcal{H}}} \in \mathbb{C}^{M_\mathrm{R} \times M_\mathrm{T} \times M_f}$ denote the tensor containing a new random realization of the channel. It can be easily computed via a matrix–vector product as

$$\mathrm{vec}\left(\tilde{\boldsymbol{\mathcal{H}}}\right) = \boldsymbol{X} \cdot \boldsymbol{g} \in \mathbb{C}^{M_\mathrm{R} \cdot M_\mathrm{T} \cdot M_\mathrm{f} \times 1}, \tag{5.39}$$

where the filter matrix $\boldsymbol{X}$ has size $M_\mathrm{R} \cdot M_\mathrm{T} \cdot M_f \times M_\mathrm{R} \cdot M_\mathrm{T} \cdot M_f$, and the column vector $\boldsymbol{g} \in \mathbb{C}^{M_\mathrm{R} \cdot M_\mathrm{T} \cdot M_f \times 1}$ contains i.i.d. complex Gaussian white noise.

To obtain $\boldsymbol{X}$ we first introduce the correlation matrix $\boldsymbol{R} \in \mathbb{C}^{M_\mathrm{R} \cdot M_\mathrm{T} \cdot M_f \times M_\mathrm{R} \cdot M_\mathrm{T} \cdot M_f}$ which, according to equation (2.97), is defined as

$$\boldsymbol{R} = \mathrm{E}\left[\mathrm{vec}\left(\boldsymbol{\mathcal{H}}\right) \cdot \mathrm{vec}\left(\boldsymbol{\mathcal{H}}\right)^\mathrm{H}\right], \tag{5.40}$$

so that

$$\boldsymbol{\mathcal{R}}_{[7]}^\mathrm{T} = \boldsymbol{R}_{[3]}^\mathrm{T} = \mathrm{vec}\left\{\boldsymbol{\mathcal{R}}\right\} = \mathrm{vec}\left\{\boldsymbol{R}\right\}. \tag{5.41}$$

The subscript $(\cdot)_{[n]}$ indicates the $n$-th MATLAB-like unfolding introduced in Section D.2.2.

To obtain $\boldsymbol{X}$ we can simply substitute equation (5.39) in the expression of $\boldsymbol{R}$ as

$$\boldsymbol{R} = \mathrm{E}\left[\boldsymbol{X} \cdot \boldsymbol{g} \cdot \boldsymbol{g}^\mathrm{H} \cdot \boldsymbol{X}^\mathrm{H}\right] = \boldsymbol{X} \cdot \mathrm{E}\left[\boldsymbol{g} \cdot \boldsymbol{g}^\mathrm{H}\right] \cdot \boldsymbol{X}^\mathrm{H}, \tag{5.42}$$

and being

$$\mathrm{E}\left[\boldsymbol{g} \cdot \boldsymbol{g}^\mathrm{H}\right] = \boldsymbol{I}, \tag{5.43}$$

where $\boldsymbol{I}$ is an identity matrix of proper size, we have

$$\boldsymbol{R} = \boldsymbol{X} \cdot \boldsymbol{X}^\mathrm{H} \in \mathbb{C}^{M_\mathrm{R} \cdot M_\mathrm{T} \cdot M_\mathrm{f} \times M_\mathrm{R} \cdot M_\mathrm{T} \cdot M_\mathrm{f}} \tag{5.44}$$

This problem of matrix factorization can be solved by computing the SVD of $\boldsymbol{R}$ as follows

$$\boldsymbol{R} = \boldsymbol{U} \cdot \boldsymbol{\Sigma} \cdot \boldsymbol{U}^\mathrm{H}, \tag{5.45}$$

so that

$$\boldsymbol{X} = \boldsymbol{U} \cdot \boldsymbol{\Sigma}^{\frac{1}{2}}, \tag{5.46}$$

where the elements of the matrix $\boldsymbol{\Sigma}^{\frac{1}{2}}$ are equal to the square roots of the ones in the diagonal matrix $\boldsymbol{\Sigma}$. Notice that the matrix $\boldsymbol{X}$ is not unique, as we can multiply it from the right by a unitary matrix of proper size and still fulfill equation (5.44).

Alternatively, the filter $\boldsymbol{X}$ can be computed directly in tensor notation. We first carry out a HOSVD on the correlation tensor $\boldsymbol{\mathcal{R}}$ as follows

Using equations (D.37) and (5.41) we can write

$$(\boldsymbol{U}^* \otimes \boldsymbol{U}) \cdot \operatorname{vec}\{\boldsymbol{\Sigma}\} = \left(\boldsymbol{U}^{(3)*} \otimes \boldsymbol{U}^{(2)*} \otimes \boldsymbol{U}^{(1)*} \otimes \boldsymbol{U}^{(3)} \otimes \boldsymbol{U}^{(2)} \otimes \boldsymbol{U}^{(1)}\right) \cdot \operatorname{vec}\{\boldsymbol{\mathcal{S}}\}. \tag{5.47}$$

By applying the properties of the Kronecker product given in equations (B.1) and (B.2) we can write

$$\operatorname{vec}\left\{\boldsymbol{U} \cdot \boldsymbol{\Sigma} \cdot \boldsymbol{U}^{\mathrm{H}}\right\} = \operatorname{vec}\left\{\left(\boldsymbol{U}^{(N)} \otimes \cdots \otimes \boldsymbol{U}^{(1)}\right)^{\mathrm{H}} \cdot \tilde{\boldsymbol{S}} \cdot \left(\boldsymbol{U}^{(N)} \otimes \cdots \otimes \boldsymbol{U}^{(1)}\right)\right\}, \tag{5.48}$$

and now, by assuming that the arguments have the same size, we can set them equal. We then obtain

$$\boldsymbol{U} \cdot \boldsymbol{\Sigma} \cdot \boldsymbol{U}^{\mathrm{H}} = \left(\boldsymbol{U}^{(N)} \otimes \cdots \otimes \boldsymbol{U}^{(1)}\right)^{\mathrm{H}} \cdot \tilde{\boldsymbol{S}} \cdot \left(\boldsymbol{U}^{(N)} \otimes \cdots \otimes \boldsymbol{U}^{(1)}\right), \tag{5.49}$$

where the matrix $\tilde{\boldsymbol{S}}$, is introduced to simplify the notation. It is equal to

$$\tilde{\boldsymbol{S}} = \operatorname{vec}^{-1}_{[M_{\mathrm{R}} \cdot M_{\mathrm{T}} \cdot M_{\mathrm{f}} \times M_{\mathrm{R}} \cdot M_{\mathrm{T}} \cdot M_{\mathrm{f}}]}\{\operatorname{vec}\{\boldsymbol{\mathcal{S}}\}\} \in \mathbb{C}^{M_{\mathrm{R}} \cdot M_{\mathrm{T}} \cdot M_{\mathrm{f}} \times M_{\mathrm{R}} \cdot M_{\mathrm{T}} \cdot M_{\mathrm{f}}}. \tag{5.50}$$

The $\operatorname{vec}^{-1}_{[b \times c]}(\boldsymbol{a})$ is the *unvec operator*, which rearranges the elements of the column vector $\boldsymbol{a}$ into a matrix of size $b \times c$. Notice that $\tilde{\boldsymbol{S}}$ is obtained by simply rearranging the elements of the tensor $\boldsymbol{\mathcal{S}} \in \mathbb{C}^{I_1 \times \ldots \times I_N \times I_1 \times \ldots \times I_N}$ in form of a square matrix of same size as $\boldsymbol{R}$, namely $I_1 \ldots I_N \times I_1 \ldots I_N$.

Notice that the right term of equation (5.49) is not an Singular Value Decomposition (SVD), as the matrix $\tilde{\boldsymbol{S}}$ is not diagonal. Therefore, to obtain the filter matrix $\boldsymbol{X}$ we need to apply a second SVD on $\tilde{\boldsymbol{S}}$ as follows

$$\tilde{\boldsymbol{S}} = \boldsymbol{V} \cdot \tilde{\boldsymbol{\Sigma}} \cdot \boldsymbol{V}^{\mathrm{H}} \tag{5.51}$$

$$\boldsymbol{X} = \left(\boldsymbol{U}^{(3)} \otimes \boldsymbol{U}^{(2)} \otimes \boldsymbol{U}^{(1)}\right)^{\mathrm{H}} \cdot \boldsymbol{V} \cdot \tilde{\boldsymbol{\Sigma}}^{\frac{1}{2}}. \tag{5.52}$$

To prove this expression we substitute equation (5.51) into equation (5.49)

$$\boldsymbol{U} \cdot \boldsymbol{\Sigma} \cdot \boldsymbol{U}^{\mathrm{H}} = \left(\boldsymbol{U}^{(3)} \otimes \boldsymbol{U}^{(2)} \otimes \boldsymbol{U}^{(1)}\right)^{\mathrm{H}} \cdot \boldsymbol{V} \cdot \tilde{\boldsymbol{\Sigma}} \cdot \boldsymbol{V}^{\mathrm{H}} \cdot \left(\boldsymbol{U}^{(3)} \otimes \boldsymbol{U}^{(2)} \otimes \boldsymbol{U}^{(1)}\right). \tag{5.53}$$

The matrix resulting from the product of the terms $\left(\boldsymbol{U}^{(N)} \otimes \cdots \otimes \boldsymbol{U}^{(1)}\right)^{\mathrm{H}}$ and $\boldsymbol{V}$ is unitary.

Since the matrix $\tilde{\boldsymbol{\Sigma}}$ is diagonal, the right part of the equation is a SVD and therefore we have

$$\boldsymbol{U} = \left(\boldsymbol{U}^{(N)} \otimes \cdots \otimes \boldsymbol{U}^{(1)}\right)^{\mathrm{H}} \cdot \boldsymbol{V} \cdot \boldsymbol{\Phi} \tag{5.54}$$

$$\boldsymbol{\Sigma} = \tilde{\boldsymbol{\Sigma}}, \tag{5.55}$$

where the diagonal matrix $\boldsymbol{\Phi}$ contains only phase shifters which represent the ambiguity of the singular vectors. Notice that the computation of the filter matrix $\boldsymbol{X}$ in tensor notation does not require necessarily a lower computational cost.

#### 5.2.6.3 Denoising a Measured Channel

In order to reduce the noise in measured channels, we extend an idea proposed in [10]. For every window $k$, as defined above, we construct a tensor $\boldsymbol{\mathcal{Z}}(t)$, calculated for every time snapshot $t$, with the following equation

$$\boldsymbol{\mathcal{Z}}(t) = \boldsymbol{\mathcal{H}}(t) \times_1 \boldsymbol{U}^{(1)^{\mathrm{H}}} \times_2 \boldsymbol{U}^{(2)^{\mathrm{H}}} \times_3 \boldsymbol{U}^{(3)^{\mathrm{H}}}, \tag{5.56}$$

where the matrices $\boldsymbol{U}^{(n)}$ are computed from the time averaged correlation tensor $\widehat{\boldsymbol{\mathcal{R}}}$ given in (5.36). With the help of the tensor $\boldsymbol{\mathcal{Z}}(t)$, the channel can be reconstructed exactly via the synthesis equation

$$\boldsymbol{\mathcal{H}}(t) = \boldsymbol{\mathcal{Z}}(t) \times_1 \boldsymbol{U}^{(1)} \times_2 \boldsymbol{U}^{(2)} \times_3 \boldsymbol{U}^{(3)}. \tag{5.57}$$

Denoising the measurement tensor $\boldsymbol{\mathcal{H}}(t)$ is possible by simply considering only the first $L_n$ singular vectors of $\boldsymbol{U}^{(n)}$. In doing so, we assume that the omitted singular vectors span the noise space. Thus, we obtain the tensor $\boldsymbol{\mathcal{Z}}'(t) \in \mathbb{C}^{L_1 \times L_2 \times L_3}$ and

$$\boldsymbol{\mathcal{H}}_{\text{denoised}}(t) = \boldsymbol{\mathcal{Z}}'(t) \times_1 \boldsymbol{U}^{(1)}_{L_1} \times_2 \boldsymbol{U}^{(2)}_{L_2} \times_3 \boldsymbol{U}^{(3)}_{L_3}. \tag{5.58}$$

The latter represents the analogue of the well known low-rank approximation via the 2D SVD.

Figure 5.42 shows the reconstruction error for two IlmProp synthetic noisy channels, namely $\boldsymbol{\mathcal{H}}^{(a)}$ and $\boldsymbol{\mathcal{H}}^{(b)}$, and two denoising approaches. The channels correspond to the scenarios depicted in Figure 5.43. The second channel $\boldsymbol{\mathcal{H}}^{(b)}$, is richer in multi-path components than the first $\boldsymbol{\mathcal{H}}^{(a)}$. The reconstruction error is defined as the Euclidian distance between the noiseless channel and the reconstructed (denoised) channel. The thick lines represent the error obtained with the proposed tensor-based method. The thin lines show the reconstruction error achieved by applying a low–rank approximation directly on $\widehat{\boldsymbol{R}}$. We can observe that the tensor-based approach leads to a better subspace estimate, which translates into a lower reconstruction error.

#### 5.2.6.4 Physical Interpretation of the Eigenmodes

The IlmProp is particularly useful in deriving a physical interpretation for the eigenmodes. For the 2D approach this has been investigated in detail in [13]. With the help of an Ilm-

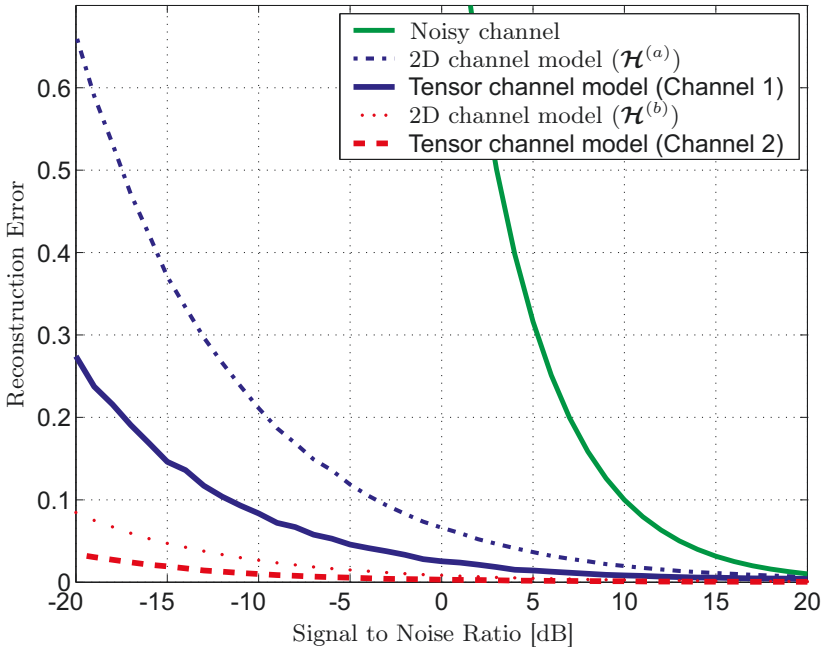


Fig. 5.42: Reconstruction error for two synthetic noisy channels: a rich multi–path channel $\mathcal{H}^{(a)}$; a 2–path channel $\mathcal{H}^{(b)}$. The tensor-based denoising outperforms the 2D approach for richer channels. The green curve represents the error for the noisy channels, i.e., the power of the noise.

Prop synthetic channel it was possible to show that the eigenmodes map the physical paths under specific conditions: when the number of paths is small enough, and the paths possess different powers, then different eigenmodes map different paths. We now carry out a similar investigation for the correlation tensor-based model described above.

Figure 5.44 shows an IlmProp scenario with a single user MIMO system. Both Rx and Tx mount a UCA with 6 vertical dipole antennas each. The Tx is connected to the Rx by 3 rays, marked with (a), (b), and (c). The paths originate from double, triple, and single bounce reflections through clusters of scatterers. The channel is computed for 15 frequency bins, spanning a bandwidth of 20 MHz at a center frequency of 5 GHz. The bandwidth and the spacing between the antennas have been chosen to avoid aliasing. The MS moves of a few meters with constant speed. Along the trajectory we take $M_t = 64$ samples, so that the channel tensor $\mathcal{H} \in \mathbb{C}^{M_\mathrm{R} \times M_\mathrm{T} \times M_t \times M_f}$ is

$$\mathcal{H} \in \mathbb{C}^{6 \times 6 \times 64 \times 15}. \tag{5.59}$$

Furthermore, we assume no channel estimation noise. The scattering coefficients and the position of the clusters have been chosen such that the three paths can be well resolved in delay time as well as in the angle domain. Figure 5.45 shows the power delay profile $P(\tau)$ as defined in Section 2.3.2.1 on page 35. Without loss of generality, we add a linear phase to the channels in order to subtract the propagation time of the first arrival. In this way, the shortest path (a) arrives at $\tau = 0$.

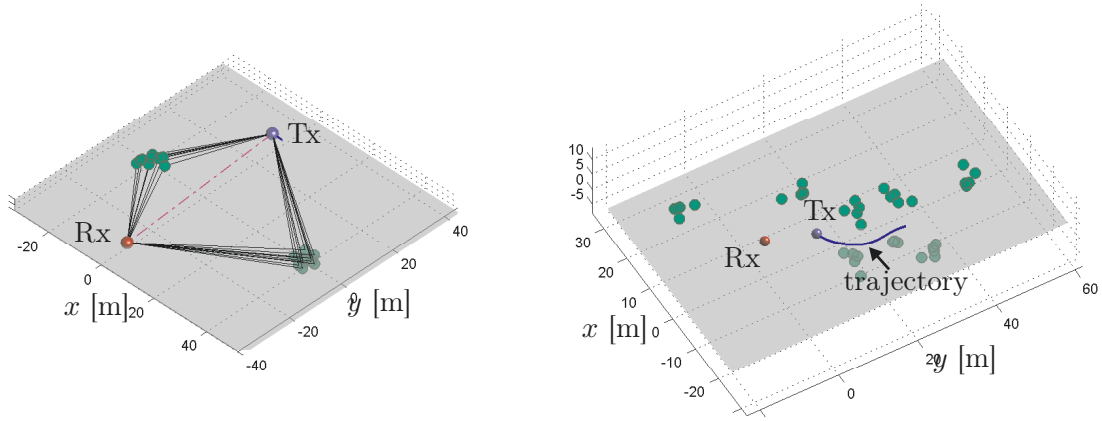


(a) (b)

Fig. 5.43: IlmProp scenarios to test the subspace-based denoising method. The second scenario (b) is richer in multi-path components than the first (a).

Figure 5.46 shows the joint power azimuthal profile[11] $P(\varphi_{\mathrm{T}}, \varphi_{\mathrm{R}})$, computed with the Bartlett method. The Bartlett method uses the array responses[12] to filter the full spatial correlation matrix $\boldsymbol{R}_{\mathrm{full}}$

$$P_{\mathrm{Bartlett}}(\varphi_{\mathrm{T}}, \varphi_{\mathrm{R}}) = \boldsymbol{a}_{\mathrm{e}}^{\mathrm{H}}(\varphi_{\mathrm{T}}, \varphi_{\mathrm{R}}) \cdot \boldsymbol{R}_{\mathrm{full}} \cdot \boldsymbol{a}_{\mathrm{e}}(\varphi_{\mathrm{T}}, \varphi_{\mathrm{R}}), \tag{5.60}$$

where $\boldsymbol{R}_{\mathrm{full}}$ is computed as in equation (3.4) and the vector $\boldsymbol{a}_{\mathrm{e}}(\varphi_{\mathrm{T}}, \varphi_{\mathrm{R}})$ is obtained as

$$\boldsymbol{a}_{\mathrm{e}}(\varphi_{\mathrm{T}}, \varphi_{\mathrm{R}}) = \boldsymbol{a}_{\theta,\mathrm{R}}(0, \varphi_{\mathrm{R}}) \otimes \boldsymbol{a}_{\theta,\mathrm{T}}(0, \varphi_{\mathrm{T}}). \tag{5.61}$$

The symbol $\otimes$ denotes the Kronecker product while the vector $\boldsymbol{a}_{\theta}(\varphi)$ is the antenna array response introduced in Section 4.1.5 for the vertical polarization, azimuth $\varphi$, and elevation $\theta = 0$. The subscripts $(\cdot)_{\mathrm{R}}$ and $(\cdot)_{\mathrm{T}}$ indicate the receiver and transmitter, respectively.

We now apply the correlation tensor-based model. As already mentioned, the MS moves only of a few meters and therefore we can consider the full data set as one temporal window of length $T_{\mathrm{W}} = M_t = 64$. The six-dimensional correlation tensor is computed with equation (5.36). By applying the HOSVD we obtain the singular values[13] depicted in Figure 5.47. The first set of singular values represents space at the Rx, the second one corresponds to space at the Tx, while the third is frequency. Due to the symmetries of the correlation tensor, the remaining 3 sets of singular values are identical, namely

$$\begin{aligned} \sigma^{(4)}_{m'_{\mathrm{R}}} &= \sigma^{(1)}_{m_{\mathrm{R}}}, && \text{for } m'_{\mathrm{R}} = m_{\mathrm{R}} = 1, 2, \ldots, 6 \\ \sigma^{(5)}_{m'_{\mathrm{T}}} &= \sigma^{(2)}_{m_{\mathrm{T}}}, && \text{for } m'_{\mathrm{T}} = m_{\mathrm{T}} = 1, 2, \ldots, 6 \\ \sigma^{(6)}_{f'} &= \sigma^{(3)}_{f}, && \text{for } f' = f = 1, 2, \ldots, 15. \end{aligned} \tag{5.62}$$

[11] The joint power azimuthal profile is defined in Section 2.3.2.6.
[12] Also referred to as array steering vectors.
[13] See Section D.5.2.1 on page 237 for more details on the singular values.

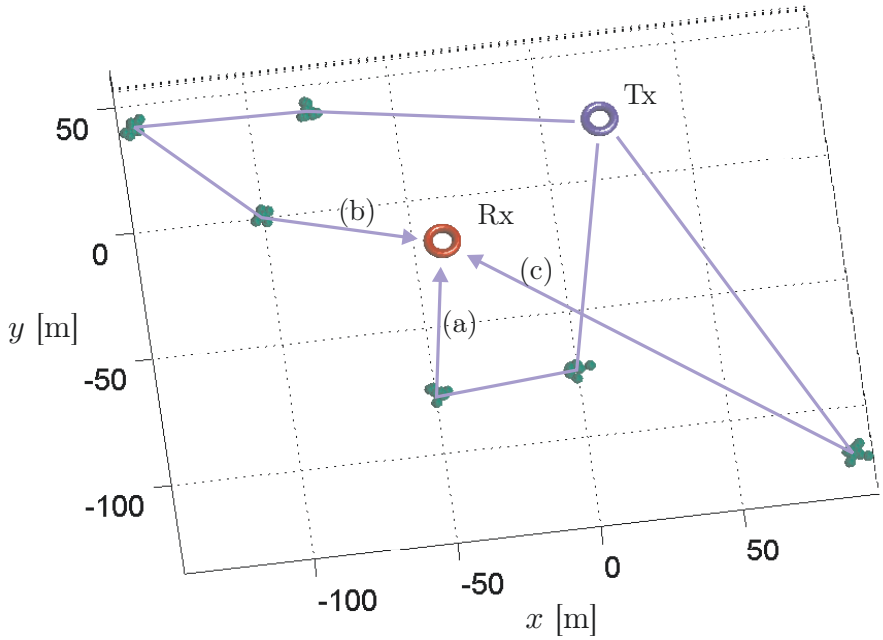


Fig. 5.44: IlmProp geometry to test the correlation tensor-based channel model. The Rx and Tx mount 6-UCAs. Three paths, namely (a), (b), and (c), connect the transmitter to the receiver.

Considering that we do not have any channel estimation noise, we would expect the $n$-ranks to be exactly 3 in all dimensions, as the channel is constructed by 3 paths only. This does not occur as the array response depends not only on the DOA but also on frequency, as already discussed in Section 5.2.5. For this reason, although at different frequencies the DOA stays the same, the antenna response spans a different subspace, so that the $n$-ranks are increased. This effect can be reduced by taking a smaller bandwidth. However, in doing so, the resolution in delay time would suffer, so that a trade-off needs to be considered.

By means of equation (5.56) we compute the tensor $\boldsymbol{\mathcal{Z}}(t)$. We now write the tensor channel $\boldsymbol{\mathcal{H}}(t) \in \mathbb{C}^{6\times6\times15}$ at the $t$-th time snapshot by means of the Tucker decomposition, given in Section D.5.3.2, as

$$\boldsymbol{\mathcal{H}}(t) = \sum_{m_\mathrm{R}=1}^{6} \sum_{m_\mathrm{T}=1}^{6} \sum_{f=1}^{15} \boldsymbol{\mathcal{Z}}(t)_{m_\mathrm{R},m_\mathrm{T},f} \cdot \boldsymbol{u}_{m_\mathrm{R}}^{(1)} \circ \boldsymbol{u}_{m_\mathrm{T}}^{(2)} \circ \boldsymbol{u}_{f}^{(3)}, \tag{5.63}$$

where $\boldsymbol{\mathcal{Z}}(t)_{m_\mathrm{R},m_\mathrm{T},f}$ is the $\{m_\mathrm{R}, m_\mathrm{T}, f\}$-th element of the tensor $\boldsymbol{\mathcal{Z}}(t)$ and the vectors $\boldsymbol{u}_{m_\mathrm{R}}^{(1)}$, $\boldsymbol{u}_{m_\mathrm{T}}^{(2)}$, and $\boldsymbol{u}_{f}^{(3)}$ are the $n$-mode singular vectors defined in Appendix D.5.2. As a straightforward extension to [10] and [13] we call the tensor $\boldsymbol{\mathcal{U}}^{\{m_\mathrm{R},m_\mathrm{T},f\}}$ the $\{m_\mathrm{R}, m_\mathrm{T}, f\}$-th eigenmode. It is defined as

$$\boldsymbol{\mathcal{U}}^{\{m_\mathrm{R},m_\mathrm{T},f\}} = \boldsymbol{u}_{m_\mathrm{R}}^{(1)} \circ \boldsymbol{u}_{m_\mathrm{T}}^{(2)} \circ \boldsymbol{u}_{f}^{(3)}, \tag{5.64}$$

so that the channel at any time snapshot $t$ can be constructed by the sum of the eigenmodes $\boldsymbol{\mathcal{U}}^{\{m_\mathrm{R},m_\mathrm{T},f\}}$ scaled by a proper weight specified in $\boldsymbol{\mathcal{Z}}(t)$.

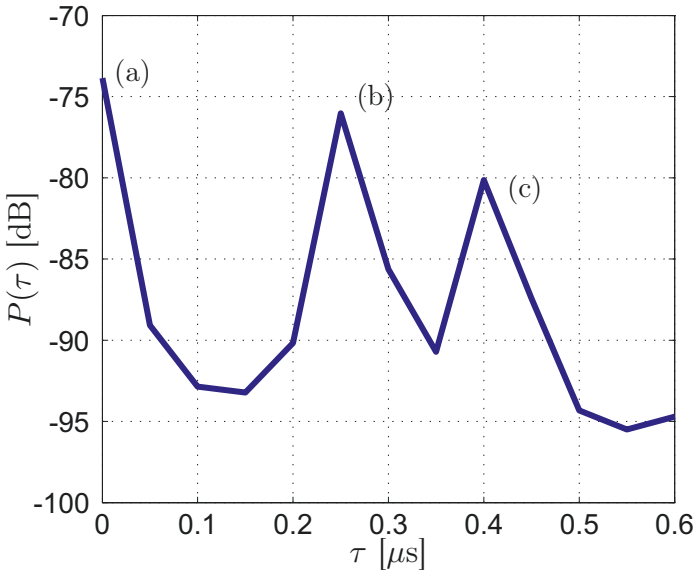


Fig. 5.45: Power delay profile $P(\tau)$ for the IlmProp scenario in Figure 5.44. The three peaks correspond to the paths marked with (a), (b), and (c).

In total there are $540 = 6 \cdot 6 \cdot 15$ eigenmodes. We now consider the three strongest, i.e., the ones which correspond to the weights having the largest average power. They are $\boldsymbol{\mathcal{U}}^{\{1,1,1\}}$, $\boldsymbol{\mathcal{U}}^{\{2,2,2\}}$, and $\boldsymbol{\mathcal{U}}^{\{3,3,3\}}$. We now proceed in giving a physical interpretation to the different eigenmodes. In order to visualize them, we reconstruct three channels by using only one eigenmode. The $k$-th channel, denoted by $\tilde{\boldsymbol{\mathcal{H}}}_k(t)$ is computed as

$$\tilde{\boldsymbol{\mathcal{H}}}_k(t) = \boldsymbol{\mathcal{Z}}(t)_{k,k,k} \cdot \boldsymbol{u}_k^{(1)} \circ \boldsymbol{u}_k^{(2)} \circ \boldsymbol{u}_k^{(3)} = \boldsymbol{\mathcal{Z}}(t)_{k,k,k} \cdot \boldsymbol{\mathcal{U}}^{\{k,k,k\}}. \tag{5.65}$$

For each channel we compute the power delay profile $\tilde{P}_k(\tau)$ and the joint power azimuthal profile $\tilde{P}_k(\varphi_{\mathrm{T}}, \varphi_{\mathrm{R}})$ as explained earlier. These functions are plotted in Figures 5.48 and 5.49. As a reference, in Figure 5.48 the dashed curve depicts the power delay profile $P_k(\tau)$ of the full channel.

From these figures it can be observed that each of the three strongest eigenmodes maps only one path. Notice that this occurs only under the strict conditions that the number of paths is small, that they can be well resolved in all domains, and that their powers differ by at least a few dBs. In fact, in a more realistic case with dozens of paths the eigenmodes would start mapping more than one path each. The way in which paths are mapped to eigenmodes is not determined directly by how similar their geometrical parameters are, but rather on how similar their corresponding subspaces are.

#### 5.2.6.5 Impact of the Channel Model

A ray-based channel model like the IlmProp is particularly interesting in testing a multi-dimensional channel model like the one proposed based on the correlation tensor. In fact, the

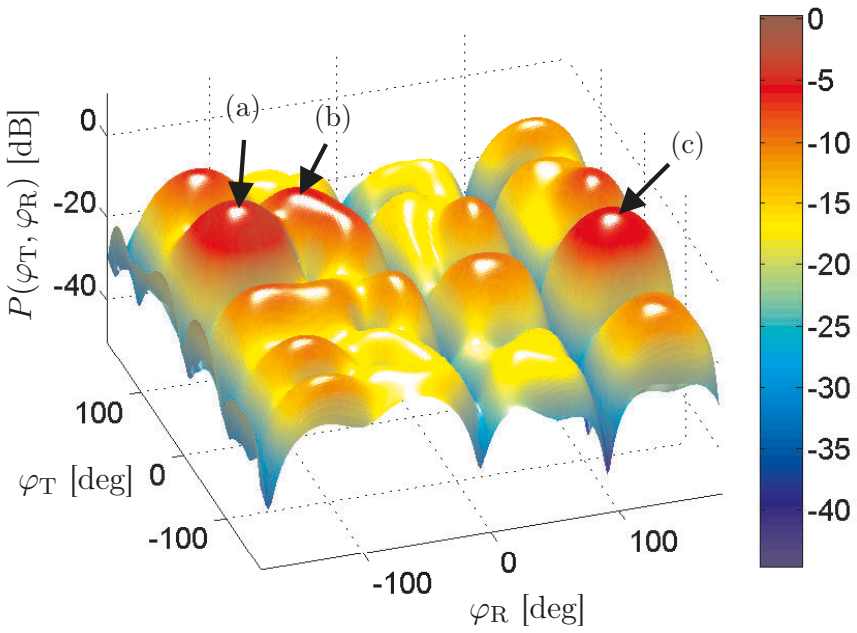


Fig. 5.46: Joint power azimuthal profile $P(\varphi_T, \varphi_R)$ for the IlmProp scenario in Figure 5.44. The peaks corresponding to the paths are marked with (a), (b), and (c). The function is computed with the Bartlett method, which provides a rather coarse resolution. In fact, the third path has a similar power to one of the side lobes of the first path.

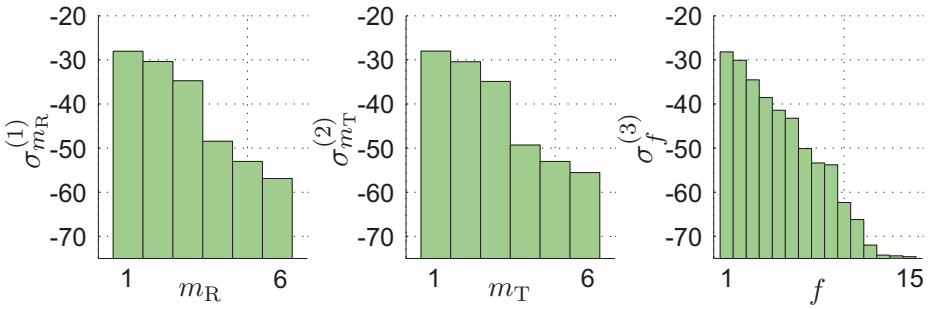


Fig. 5.47: Singular values from the HOSVD of the correlation tensor.

possibility to control explicitly the paths allows us to assess the noise reduction capabilities of the model with respect to scenarios with different richness in multi-path. The IlmProp is also useful in deriving a physical interpretation of the tensor eigenmodes. Nonetheless, the IlmProp bounds us to obey the laws of the GTD, which we could easily break if we set the paths' parameters directly. For instance, for one path we could assign values to the DOA, DOD, and TDOA independently and from those compute a channel, even though no path with such values could exist physically. The non intuitive way in which paths are mapped to eigenmodes can be investigated with specific scenarios built with the IlmProp, in order to gain a deeper understanding of the physical interpretation of the channel's eigenstructure.

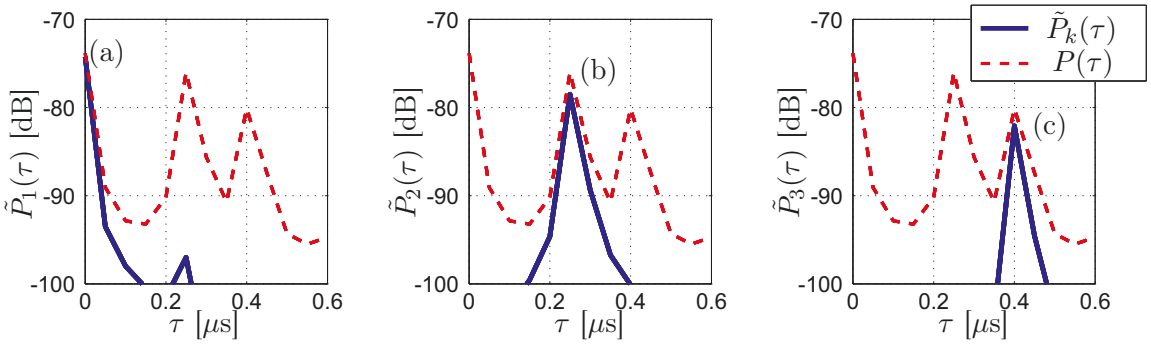


Fig. 5.48: Power delay profiles for the three channels reconstructed using the three strongest eigenmodes separately. Each eigenmode maps one path only.

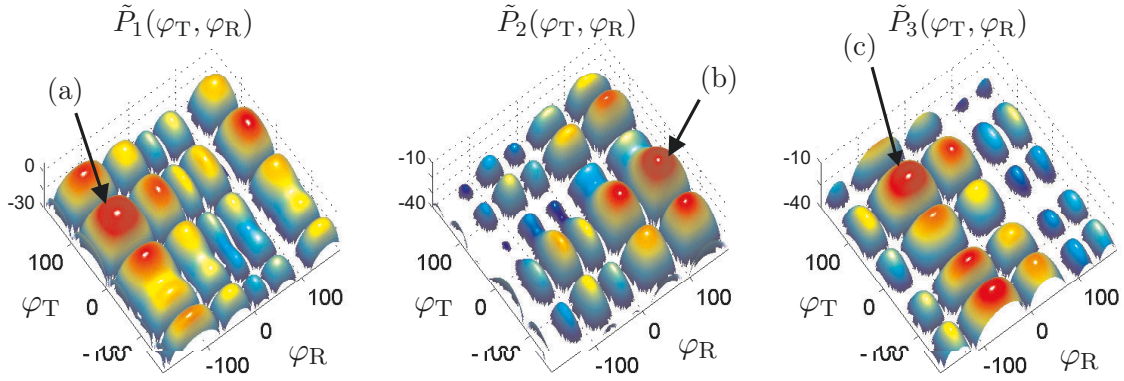


Fig. 5.49: Joint power azimuthal profiles for the three channels reconstructed using the three strongest eigenmodes separately. Each eigenmode maps one path only.

### 5.2.7 Other IlmProp-Based Investigations

The IlmProp has been applied to other investigations.

In [21] and [20], the authors test a spatial multiplexing scheme for a multi-hop scenario modeled with the IlmProp.

In [18], a three users scenario is constructed with the IlmProp. Two users move on very similar trajectories, remaining spatially correlated with one another for the total time of the simulation. This creates a difficult environment for spatial multiplexing techniques such as BD, introduced in Appendix F and discussed in Section 5.2.1. Two other SDMA schemes have been tested on this scenario, namely Successive Optimization Tomlinson-Harashima precoding (SO THP) [111] and Successive MMSE (SMMSE) [196]. Simulation results show that SMMSE provides the best BER performance regardless of the number of receive antennas per user. The complexity of this technique is also reasonable which makes it a potential candidate for the implementation in future wireless systems. It outperforms other linear techniques (such as BD) and even non-linear techniques like SO THP.

In [19], the authors propose a subspace-based method to estimate the Rician $K$-factor

from measurements. To test this algorithm, besides considering channel measurements, also synthetic channels were processed. The latter were generated with an early implementation of the IlmProp.

In [2], an automatic cluster tracking algorithm is presented. To validate it the algorithm has been applied on IlmProp channels. The time variance introduced by a moving MS makes DOAs, DODs, and TDOAs vary at each time snapshot in accordance with the geometry. This is ideal to test such an algorithm. In [3], the algorithm has been successfully tested on channel measurements as well.

In [229], Xiao and Burr present an extended definition of the CMD proposed in [101] and use it to compare different channel models to a channel measurement. The models considered were the IlmProp, a 3GPP SCM-based extension [230], and the WINNER SCM, discussed in Section 3.4.4. With respect to the extended CMD, the results show a good agreement with the measurement, so that

> *"the IlmProp channel model can well reflect the multi-path structure of the time variant channels, and is capable of predicting the short-term time variation of the frequency selective channels in outdoor scenarios mainly including single-bounce reflections."* [229]

In [25] the authors test a novel subspace-based channel prediction framework on synthetic IlmProp channels. The explicit modeling of the MPCs eases the generation of channels which exhibit a desired spatial richness. In this case a car to bridge scenario has been modeled. The MPCs become increasingly significant with respect to the LOS as the MS approaches the bridge on which the BS is mounted. In fact, near the bridge there are several IOs, while far from it the propagation is dominated by two paths only, namely the LOS and the ground reflection, which has been modeled according to the laws of physics. The IlmProp-based results confirm the experimental ones in [232], in which the authors analyze a similar car two bridge channel measurement.

## 5.3 Measurement-based Applications

In Section 5.2, we present numerous non measurement-based applications of the IlmProp. In these cases, the main advantage is that the high flexibility of the IlmProp allows the user to model with little effort various scenarios whose channels display specific desired features. On the other hand, since the user is asked to define the geometry, the IlmProp cannot assure that the synthetic channels are realistic or representative.

Another possibility, which guarantees a high realism of the synthetic channels, is to construct an IlmProp scenario based on the estimates obtained from high-resolution parameter estimation techniques, such as ESPRIT or SAGE. To do so, we follow and extend the Measurement-Based Parametric Channel Model (MBPCM) concept, first proposed by Thomä *et al.* in [209].

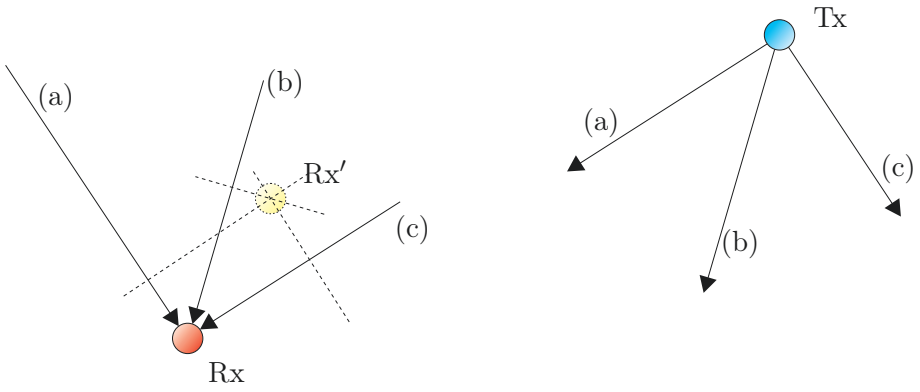


Fig. 5.50: Original MBPCM concept. Via high-resolution parameter estimation techniques we obtain an antenna independent description of the propagation. In this example, three paths are identified. With this knowledge, we can estimate the channel at the position Rx′ for arbitrary antenna arrays.

Figure 5.50 shows the basic idea of the MBPCM. We first obtain an antenna independent description of the propagation by means of a high-resolution parameter estimator. In the figure, as an example, we depict 3 paths, denoted by (a), (b), and (c). The parameter estimator provides a path-strength, a DOA, a DOD, and a TDOA for each path. With this knowledge, we can compute the channel for two arbitrary antenna arrays at the positions Rx and Tx, respectively. By assuming planar wavefronts, we can also predict the channel at the receiver position Rx′, by simply considering proper phase shifts due to the different propagation lengths. Of course, the validity of the method decreases as the reconstruction point Rx′ is chosen further away from Rx. This is due to the planar wavefront approximation which becomes more coarse with distance, as already discussed on page 24. Of course, for even larger distances, the propagation conditions might change, so that a new channel measurement is indispensable. Following the same idea, we can modify other parameters and obtain realistic synthetic channels, for instance

- substitute the arrays employed for the measurement with an application-oriented one
- modify the carrier frequency
- increase the bandwidth
- increase the density of the frequency sampling
- introduce obstacles
- modify the position and orientation of the MS

The impact of this approach has become significant, as larger arrays are being used for channel sounding. In fact, arrays which comprise many sensors distributed on spheres or cylinders allow us to observe propagation paths all around the array with a high angular resolution. On the other hand, due to their cost and size, these arrays are not suited for a practical system, which probably will mount no more than 8 directional antennas at the BS, and 2 or 4 at the MS. For this reason, the MBPCM concept is particularly attractive, as it allows us to use antenna arrays most suited for the measurements during the channel

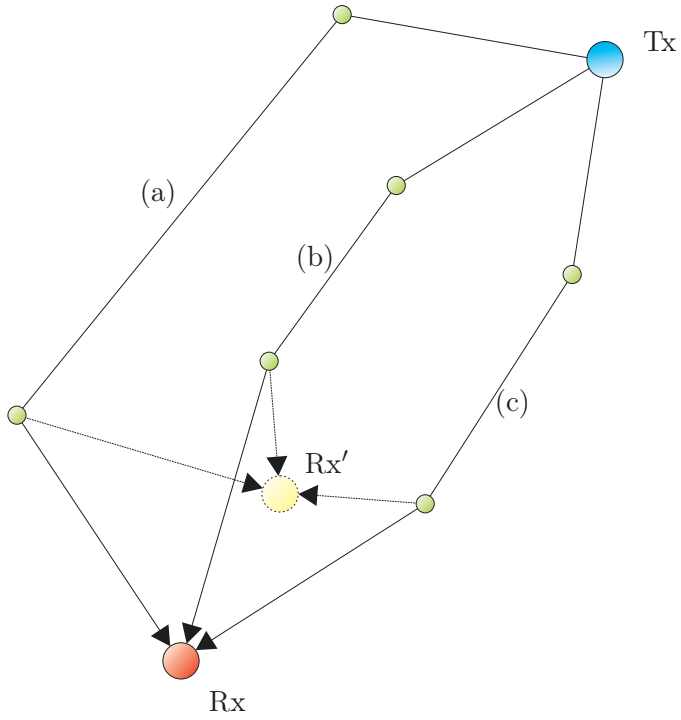


Fig. 5.51: Extended MBPCM concept. Via a localization algorithm we estimate the position of the IOs, denoted by small green dots. With this knowledge we can estimate more accurately the channel at the position Rx′ for arbitrary antenna arrays.

sounding campaigns and, in a post-processing step, evaluate the performance of other arrays which are more appropriate for a practical use.

Notice that the method proposed in [209] treats the receiver and transmitter separately, and does not require the knowledge on how the path propagated from the Tx to the Rx, but merely on the DOD from which it left the transmitter and on the DOA at which it reached the receiver.

In order to increase the accuracy of the MBPCM reconstruction, we estimate also the path trajectory by identifying the two IOs nearest to the Tx and Rx, respectively.

Figure 5.51 depicts the IlmProp-based MBPCM scheme. Assuming that we can estimate the position of the IOs, marked with green dots, we can compute the channel for the position Rx′ more precisely by considering new DOAs, DODs, and TDOAs.

Notice that the two methods provide identical results when we reconstruct the channel in the position where it was measured, namely Rx.

The scatterers localization algorithm leads to other applications. It yields a powerful visualization tool for the parameter estimates, leading to interesting physical interpretations of the propagation. At the same time, it provides validation for the measurement campaign and the parameter estimator.

Figure 5.52 shows the steps required for the MBPCM in conjunction with the use of the IlmProp. The multi-dimensional channel $\boldsymbol{\mathcal{H}}_{\text{meas}}$, gathered from a channel sounding campaign,

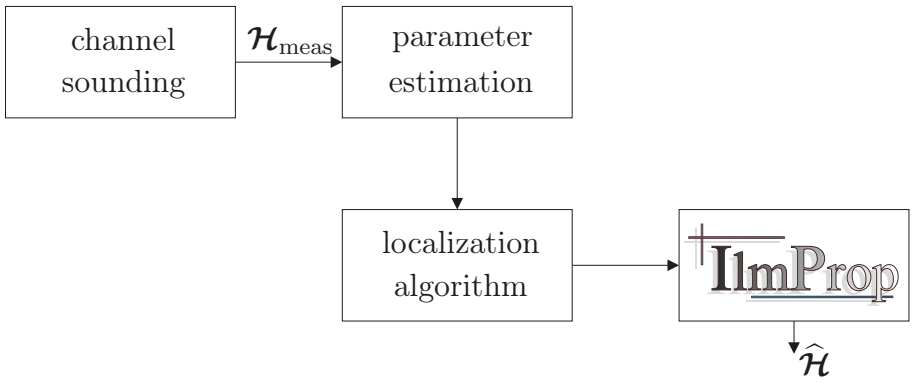


Fig. 5.52: Schematics of the Measurement-Base Parametric Channel Modeling.

is processed by a parameter estimation technique, which identifies the paths parameters mentioned above.

The latter are fed into the IO localization algorithm which outputs the parameters describing the geometry used by the IlmProp. The obtained geometry is effectively an antenna independent description of the scenario. At this point we can substitute the antenna array used for the measurement with some other antenna which is more suited for a practical application. The IlmProp can then compute new synthetic CIRs denoted by $\widehat{\mathcal{H}}$, anywhere in the vicinity of the measured position. The synthetic channel will mimic the real channel which would have been measured with this antenna.

The following section introduces the localization algorithm.

Sections 5.3.3 and 5.3.4 show examples of the first step of the localization algorithm, on a synthetic scenario and on two-dimensional (2D) channel measurement, respectively. Section 5.3.5 deals with a 3D measurement on which the full IlmProp-based MBPCM concept has been tested.

### 5.3.1 The Localization Algorithm

The localization algorithm comprises two steps

- probability map inversion
- scatterers identification.

The first step, the *probability map inversion*, requires the parameter estimates as well as accurate information on the position and orientation of the antenna arrays. The result of this step is a 3D Probability Density Function (PDF) which expresses the probability of an IO of being in a certain position in space. The second step, the *scatterers identification*, determines the position and scattering coefficient of the scatterers, practically generating the parameters which define an IlmProp geometry.

The first step is dealt in the following section, while the second in Section 5.3.1.2. Section 5.3.1.3 deals with a clustering phase which can precede the localization algorithm.

#### 5.3.1.1 The Probability Map Inversion

The probability map inversion step, as mentioned above, is based on the assumption that the position and orientation of the transmit and receive arrays are known. We assume that the parameter estimator delivers paths characterized by a Time Delay Of Arrival (TDOA) $\tau$, a Direction Of Departure (DOD) $\varphi_{\mathrm{T}}$, $\theta_{\mathrm{T}}$, in azimuth and elevation, respectively, as well as by a Direction Of Arrival (DOA) $\varphi_{\mathrm{R}}$, $\theta_{\mathrm{R}}$. All propagation paths are modeled as double bounces, so that two scatterers $S_{\mathrm{T}}$ and $S_{\mathrm{R}}$, or points of interaction, need to be found for each path. First, let us consider one path only and assume that its parameters are known exactly. As Figure 5.53 shows, the path starts at the transmitter (Tx), is reflected or diffracted by $S_{\mathrm{T}}$ towards $S_{\mathrm{R}}$, and from there it reaches the receiver (Rx). The Tx and Rx arrays, and the two scatterers form a trapezoid-like geometry in 3D space.

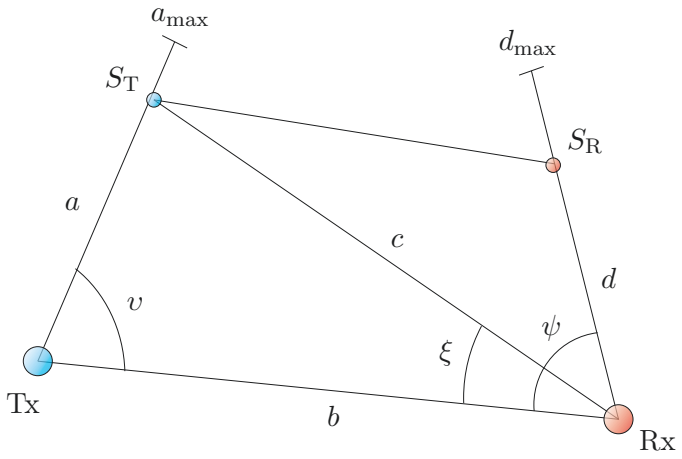


Fig. 5.53: Modeling of a double reflection path.

The scatterer $S_{\mathrm{T}}$ is bound to lie on a semi-line, with origin at the Tx, and in the direction defined by the DOD. Similarly, $S_{\mathrm{R}}$ must lie on a semi-line originating at the Rx, directed as the DOA. The total path length $L$ is however bound to be equal to the product of the velocity of light and the TDOA $\tau$. On these semi-lines we want to localize $S_{\mathrm{T}}$ and $S_{\mathrm{R}}$.

Let $a$ define the distance between the Tx and $S_{\mathrm{T}}$ for one specific time snapshot. Then, the problem of finding the location of $S_{\mathrm{T}}$ and $S_{\mathrm{R}}$ in 3D space is equivalent to a one-dimensional (1D) problem, namely finding $a$. The total length constraint limits the distance $a$ to a certain value $a_{\max}$, so that $0 \leq a \leq a_{\max}$. Similarly, the distance $d$ between the Rx and $S_{\mathrm{R}}$ is $0 \leq d \leq d_{\max}$. The values of $a_{\max}$ and $d_{\max}$ can be computed as

$$\begin{aligned} a_{\max} &= \frac{L^2 - b^2}{2L - 2b \cdot \cos(\nu)} \\ d_{\max} &= \frac{L^2 - b^2}{2L - 2b \cdot \cos(\psi)} \end{aligned} \tag{5.66}$$

Note that once $a$ is known, the position of $S_{\mathrm{R}}$ can be uniquely found by determining $d$ as

$$d = \frac{1}{2} \cdot \frac{(L-a)^2 - c^2}{L - a - c \cdot \cos(\xi)}, \tag{5.67}$$

where,

$$c = \sqrt{a^2 + b^2 - 2\ a\ b \cdot \cos(\upsilon)}. \tag{5.68}$$

The geometrical interpretation of the variables $b$, $c$, $\xi$, $\upsilon$, and $\psi$ can be deduced from Figure 5.53.

In order to determine $a$, we assume that $S_{\mathrm{T}}$ and $S_{\mathrm{R}}$ do not move in space with time, while the Tx does. At a different time snapshot, the location of the Tx will be different, and the new semi-line on which $S_{\mathrm{T}}$ has to lie will be different as well. Assuming perfect parameter estimation, the two semi-lines leaving the Tx at the two different time instants will evidently meet in $S_{\mathrm{T}}$, thus allowing us to find its location. Note that if the path were in reality a single reflection or even a Line of Sight (LOS), we could still model it with a double interaction. In the former case we would find overlapping $S_{\mathrm{T}}$ and $S_{\mathrm{R}}$, while in the latter we would find $S_{\mathrm{T}}$ and $S_{\mathrm{R}}$ lying on the Tx and Rx, respectively.

Let us now consider a realistic scenario, in which the path parameters are obtained by a high resolution parameter estimation technique performed on measurements, and thus affected by errors. In order to localize the interacting objects we follow a classic Bayesian formulation of inversion theory [203, 170].

Let $\boldsymbol{m}$ and $\boldsymbol{d}$ be the model and data vectors, respectively, so that $\boldsymbol{m}$ contains the parameters of the model which we want to estimate and $\boldsymbol{d}$ contains the noiseless observations. In our case, the vector $\boldsymbol{m}$ contains the coordinates in $x$, $y$, and $z$ of $S_{\mathrm{T}}$ and $S_{\mathrm{R}}$, while $\boldsymbol{d}$ contains the TDOA, DOA, and DOD of the corresponding path. When treating the elements of $\boldsymbol{m}$ and $\boldsymbol{d}$ as random variables we can write

$$p\left(\boldsymbol{m}|\boldsymbol{d}\right) = \frac{p\left(\boldsymbol{d}|\boldsymbol{m}\right) p\left(\boldsymbol{m}\right)}{p\left(\boldsymbol{d}\right)}, \tag{5.69}$$

where $p\left(\boldsymbol{m}|\boldsymbol{d}\right)$ is the conditional PDF of $\boldsymbol{m}$ given $\boldsymbol{d}$, $p\left(\boldsymbol{d}|\boldsymbol{m}\right)$ is the conditional PDF of $\boldsymbol{d}$ given $\boldsymbol{m}$, and $p\left(\boldsymbol{m}\right)$ is the marginal PDF of $\boldsymbol{m}$ independent of $\boldsymbol{d}$, as $p\left(\boldsymbol{d}\right)$ is for $\boldsymbol{d}$. The function $p\left(\boldsymbol{m}\right)$ contains the *a priori* information on the model space, which in our case can be the fact that the scatterers have higher probability of being in certain areas, or that they cannot be in other regions (for example inside buildings). The function $p\left(\boldsymbol{m}|\boldsymbol{d}\right)$ is said to be the *a posteriori* PDF of $\boldsymbol{m}$ because it contains the probability of the location of the scatterer by considering the observations. In case of noiseless observations and complete observability, $p\left(\boldsymbol{d}|\boldsymbol{m}\right)$ will be a Dirac $\delta$ in the location of the scatterer. We now observe that $p\left(\boldsymbol{d}\right)$ is a constant with respect to $\boldsymbol{m}$, and we substitute the noisy observations $\boldsymbol{d}^{\mathrm{obs}}$ into $\boldsymbol{d}$ in equation (5.69), and we obtain

$$p\left(\boldsymbol{m}|\boldsymbol{d}^{\mathrm{obs}}\right) \sim p\left(\boldsymbol{d}^{\mathrm{obs}}|\boldsymbol{m}\right) p\left(\boldsymbol{m}\right), \tag{5.70}$$

where the symbol $\sim$ indicates proportionality.

The general solution to the inversion problem consist in obtaining the PDF $p\left(\boldsymbol{m}|\boldsymbol{d}^{\text{obs}}\right)$ since it gives us the probability of $\boldsymbol{m}$ considering the observations, the a priori information, and the statistical distribution of the errors committed both in the measurements and in the theory. The latter is caused by an inaccurate description of the physical processes by which the model parameters $\boldsymbol{m}$ are mapped to the data $\boldsymbol{d}$ (usually referred to as *forward problem*).

In order to obtain specific values for $\boldsymbol{m}$ (instead of a density function), we can either maximize $p\left(\boldsymbol{m}|\boldsymbol{d}^{\text{obs}}\right)$ and obtain the *Maximum A Posteriori* (MAP) estimates, or maximize $p\left(\boldsymbol{d}^{\text{obs}}|\boldsymbol{m}\right)$ to obtain the *Maximum Likelihood* (ML) estimates. The former obviously differs by considering the *a priori* information on the model space. The function $p\left(\boldsymbol{d}^{\text{obs}}|\boldsymbol{m}\right)$ is known as the *likelihood function* because it gives a measure of how good the model parameters $\boldsymbol{m}$ fit the data $\boldsymbol{d}^{\text{obs}}$.

Deriving the statistical properties of the errors is not trivial and simplifications are required. As commonly done, we model them with zero mean Gaussian distributions, so that the observed parameters, namely the TDOA, the DOA, and the DOD are affected by independent zero mean Gaussian noise. Let the corresponding noise variances be $\sigma^2_{\text{TDOA}}$, $\sigma^2_{\text{DOA}}$, and $\sigma^2_{\text{DOD}}$, respectively. For the latter, the estimation noise variance is assumed to be symmetrical with respect to the exact direction.

Furthermore, we assume the a priori probability $p\left(\boldsymbol{m}\right)$ constant in the whole model space.

Given the assumptions mentioned above, we can write the a posteriori PDF at an arbitrary point in space $\boldsymbol{P} = [x, y, z]^{\text{T}}$ as

$$p\left(\boldsymbol{m}|\boldsymbol{d}^{\text{obs}}\right) = \chi\left(\boldsymbol{P}|\tau_{k,t}, \varphi_{\text{T},k,t}, \theta_{\text{R},k,t}\right), \tag{5.71}$$

where $\tau_{k,t}$, $\varphi_{\text{R},k,t}$, and $\theta_{\text{R},k,t}$ are the TDOA and DOA (azimuth and elevation) for the $k$-th path at time instant $t$. The function $\chi$ is derived by simple geometrical considerations. It is a modified bi-variate Gaussian distribution, and looks like a pencil beam, as depicted in Figure 5.54.

For convenience, we describe it in an alternative coordinate system defined by the variables $\rho$ and $\omega$, as depicted in Figure 5.55. The variable $\rho$ is equal to the distance between the array and $\boldsymbol{P}$, whereas $\omega$ is the angle between the segment Tx-$\boldsymbol{P}$ and the line defined by the DOD. Although it is defined in the 3D space, we do not need a third variable due to its axial symmetry. We then refer to it as Pencil-Beam Probability Density Function (PeBPDF) $\chi(\rho, \omega|k, t)$, where we omit the parameters $\tau$, $\varphi$ and $\theta$ for simplicity.

The PeBPDF for the $k$-th path at time instant $t$, $\chi(\rho, \omega|k, t)$ is defined as

$$\chi(\rho, \omega|k, t) = \gamma \cdot \begin{cases} \mathrm{e}^{-\frac{\omega^2}{\sigma^2_{\text{DOD}}}} & 0 \leq \rho \leq a_{\max} \\ \mathrm{e}^{-\frac{\omega^2}{\sigma^2_{\text{DOD}}}} \cdot \mathrm{e}^{-\frac{(\rho - a_{\max})^2}{\sigma^2_{\rho}}} & \rho > a_{\max}, \end{cases} \tag{5.72}$$

where $\gamma$ is a factor to render the volume integral of the PeBPDF equal to 1. A derivation of the factor $\gamma$ is given in Appendix A.1.

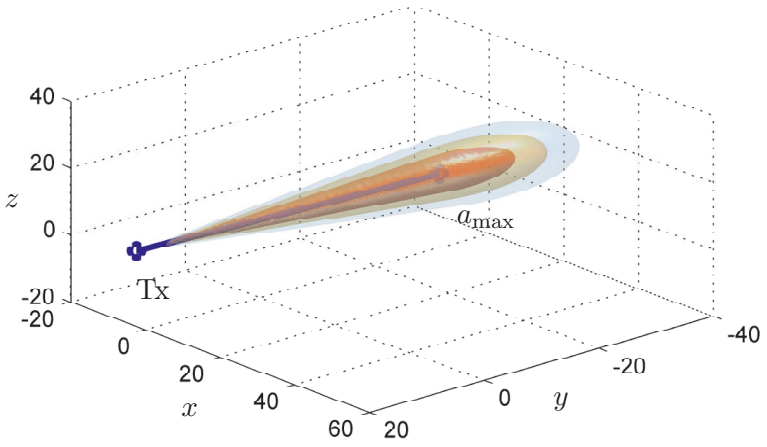


Fig. 5.54: Pencil-Beam Probability Density Function (PeBPDF). The surf plots represent the values $\{-3,\ -6,\ -10\}$ dB of the distribution.

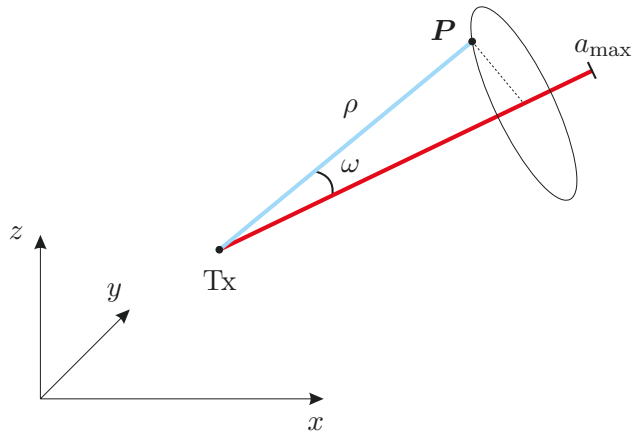


Fig. 5.55: Relationship between the Cartesian coordinates $x$, $y$, and $z$ and $\rho$, $\omega$ for a point in space $\boldsymbol{P}$ in case of an error on the angle symmetric with respect to the exact path.

For $\rho \leq a_{\max}$ we have equal probability along $\rho$, and a Gaussian distribution along angle, representing the error made by the parameter estimator. For $\rho > a_{\max}$ we have a bi-variate Gaussian so that we can also consider the error made on the TDOA. The variance $\sigma_\rho^2$ is the variance of the error on the path length. Therefore, we have: $\sigma_\rho^2 = c^2 \cdot \sigma_{\text{TDOA}}^2$, where $c$ is the speed of light. Note that the PeBPDF can be easily computed for Cartesian coordinates by means of simple coordinate transformation rules.

When the antenna array used for the channel sounding does not show the proper symmetries, i.e., we cannot assume that the error on the angle is symmetric with respect to the exact path, we need to consider a more complicated model. Let us now assume that the error of the estimator has variances $\sigma_\varphi^2$ and $\sigma_\theta^2$ for the azimuth and elevation, respectively.

The formula for the PeBPDF assumes a more complicated expression

$$\chi(\rho,\omega|k,t) = \kappa \cdot \begin{cases} \mathrm{e}^{-\frac{\Delta\theta^2}{\sigma_\theta^2}}\,\mathrm{e}^{-\frac{\Delta\varphi^2}{\sigma_\varphi^2}} & 0 \le \rho \le a_{\max} \\ \mathrm{e}^{-\frac{\Delta\theta^2}{\sigma_\theta^2}}\,\mathrm{e}^{-\frac{\Delta\varphi^2}{\sigma_\varphi^2}}\,\mathrm{e}^{-\frac{(\rho-a_{\max})^2}{\sigma_\rho^2}} & \rho > a_{\max}, \end{cases} \tag{5.73}$$

where the PeBPDF is expressed in the coordinate system defined by $\rho$, $\Delta\theta$, and $\Delta\varphi$, so that

$$\begin{aligned} \Delta\theta &= \theta_P - \theta_{\mathrm{T}} \\ \Delta\varphi &= \varphi_P - \varphi_{\mathrm{T}} \end{aligned} \tag{5.74}$$

and the variables $\varphi_P$, $\varphi_{\mathrm{T}}$, $\theta_P$, and $\theta_{\mathrm{T}}$ are indicated in Figure 5.56. The factor $\kappa$, similarly

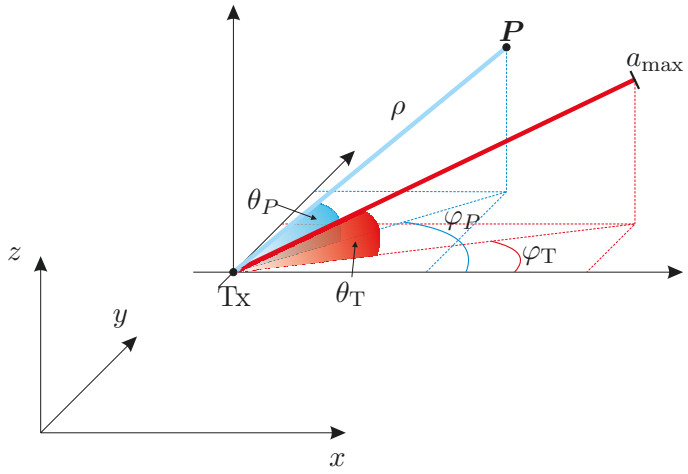


Fig. 5.56: Relationship between the Cartesian coordinates $x$, $y$, and $z$ and $\Delta\varphi = \varphi_P - \varphi_{\mathrm{T}}$, $\Delta\theta = \theta_P - \theta_{\mathrm{T}}$ for a point in space $\boldsymbol{P}$ in case of an error with different variances in azimuth and elevation.

to $\gamma$ in equation (5.72), is a computed so that the volume integral of the PeBPDF equals 1. The computation of the factor $\kappa$ is not trivial and is explained in detail in Appendix A.2 on page 212.

In a practical case, the estimates for the DOA, DOD, TDOA, are given by the parameter estimator. However, to compute the PeBPDF in equation (5.72) or (5.73) the variances of the estimates are also needed. This issue is addressed in Section 5.3.2.

The PeBPDF expresses the a posteriori probability of one scatterer only at one particular time instant. We now compute the total PDF $p_{\mathrm{map}}(x,y,z)$, which we refer to as the *probability map*. It expresses the probability for a scatterer to be in a specific point in space $\boldsymbol{P} = [x,y,z]^{\mathrm{T}}$, considering all $K$ paths for both Tx and Rx, and for all time snapshots $M_t$. It is defined as

$$p_{\mathrm{map}}(\boldsymbol{P}) = \frac{1}{2 \cdot K \cdot T} \sum_{t=1}^{M_t} \sum_{k=1}^{K} \cdot \left( p_{\mathrm{R}}(\boldsymbol{P}|k,t) + p_{\mathrm{T}}(\boldsymbol{P}|k,t) \right), \tag{5.75}$$

where $p_{\mathrm{R}}(\boldsymbol{P}|k,t)$ and $p_{\mathrm{T}}(\boldsymbol{P}|k,t)$ are the PeBPDFs from equation (5.72) or (5.73) expressed in

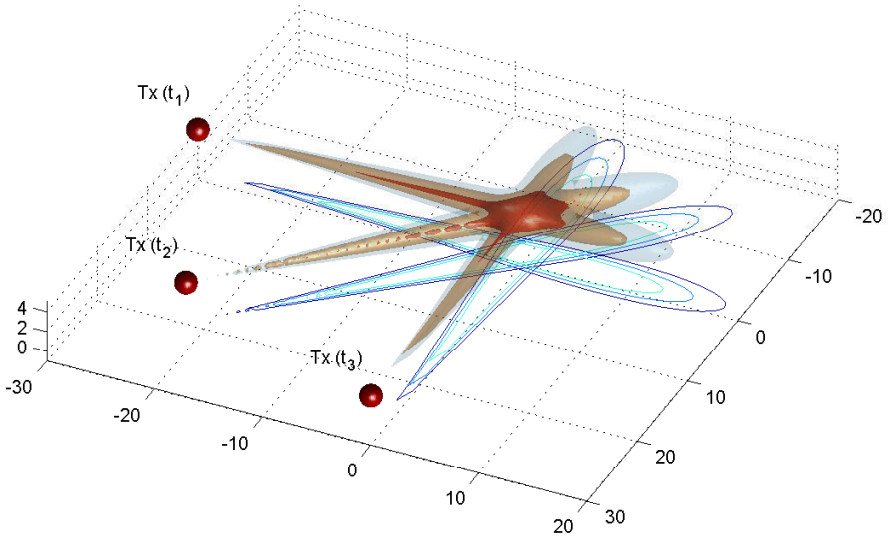


Fig. 5.57: Probability map for one scatterer and three separate time snapshots. Higher probability is focused at the spatial location of the IO. The contour plots show the individual PeBPDF.

Cartesian coordinates for the $k$-th path seen at the Rx and Tx, respectively. The probability map is simply an average of the different PDFs. If the mobile moves around a cluster, as depicted in Figure 5.57, the different pencil beams will overlap only around the location of the scatterer. The movement is essential, because if a scatterer is seen always from the same perspective, the probability map will not focus anywhere. For this reason, it can be convenient to compute the probability map considering solely the information coming from the mobile side only.

Once the probability map $p_{\text{map}}(x, y, z)$ has been computed, it can be directly used to give a physical interpretation to the propagation paths extracted by the parameter estimation technique. To do so, we can verify whether real objects are located at the coordinates where the probability focused. A practical example of this is given in Section 5.3.3 for a synthetic scenario meant as a validation set up, and in Sections 5.3.4 and 5.3.4 for measurements.

The ***masking phenomenon*** occurs when we deal with a large number of paths. A scatterer "illuminated" by many paths will have a higher probability than one corresponding to a few, although the latter might be much better resolvable. This concept is illustrated in Figure 5.58. Six paths are identified, one for each of the six time snapshots considered. Two of them illuminate the first scatterer $S_1$, whereas the remaining ones point towards $S_2$. Due to this, $S_2$ is resolved with higher probability than $S_1$, even if we assume that all six paths are characterized by the same estimation error. Because of the masking phenomenon we cannot look at the values of the probability map on an absolute scale, but we should rather consider the local maxima and the shapes built by it, as discussed in Section 5.3.3. Examples of the masking phenomenon can be observed in Figures 5.70 and 5.71 in Section 5.3.5, where we

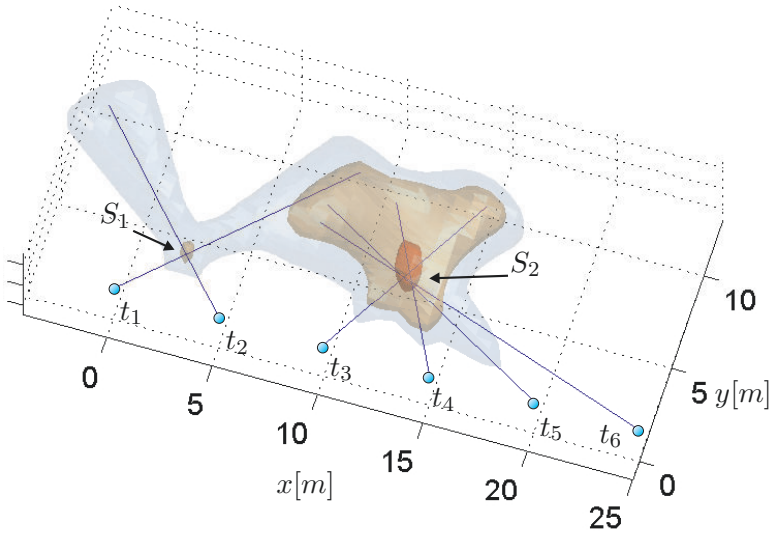


Fig. 5.58: Figure illustrating the *masking phenomenon*. The surfaces represent the $p_{\text{map}}$ for values $\{-10,\ -6,\ -1\}$ in dB. The first scatterer $S_1$ is resolved with higher probability than $S_2$. This is due the fact that $S_2$ is illuminated by more paths. One path is identified in each of the six time snapshots, i.e., positions of the MS.

analyze a 3D full polarimetric measurement.

#### 5.3.1.2 Scatterers Identification

Once the probability map $p_{\text{map}}(x, y, z)$ has been computed as explained in the previous section, we proceed in determining the exact position of the IOs for each path. To do so we consider for each path the segments Tx-$a_{\max}$ and Rx-$d_{\max}$ and we choose the parameter $a \in [0, a_{\max}]$ and consequently the position of $S_{\text{T}}$ and $S_{\text{R}}$ so that the probability is maximized. This idea is visualized in Figure 5.59. The scattering coefficient matrices $\boldsymbol{\rho} \in \mathbb{C}^{2\times 2}$ introduced in Section 5.1.1 are determined according to the path-strength estimated and the corresponding path-loss. In fact, if $\tau_p$ and $\boldsymbol{\gamma}_p \in \mathbb{C}^{2\times 2}$ are the TDOA and the polarimetric path-strengths computed by the parameter estimator for the $p$-th path, and $\boldsymbol{\rho}_{p,\text{T}}$, $\boldsymbol{\rho}_{p,\text{T}}$ are the scattering coefficient matrices for $S_{\text{T}}$ and $S_{\text{R}}$, respectively, we have that

$$\boldsymbol{\gamma}_p = \boldsymbol{\rho}_{p,\text{T}} \odot \boldsymbol{\rho}_{p,\text{T}} \cdot \frac{1}{4\pi f \tau_p} \in \mathbb{C}^{2\times 2}, \tag{5.76}$$

where $f$ denotes the frequency, $c$ the velocity of light, and $\odot$ is the Schur element-wise product.

Notice that the resulting geometry will match exactly the parameter estimates, meaning that the obtained path, for the measured positions of the Tx and Rx, will exhibit DOAs, DODs and TDOAs identical to the ones estimated.

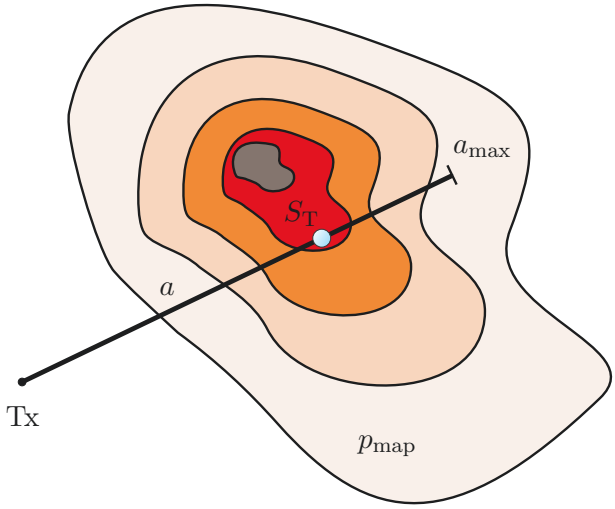


Fig. 5.59: Schematics of the IO identification algorithm. The scatterer $S_{\mathrm{T}}$ is placed according to the probability map $p_{\mathrm{map}}$.

When the IlmProp geometry has been obtained, we can proceed in computing new synthetic channels for different antennas and at different positions of the arrays. This is applied and validated in Section 5.3.5.

#### 5.3.1.3 The Clustering Phase

In order to improve the localization accuracy and reduce the algorithm's computational complexity, it is possible to pre-process the parameter estimates to identify *clusters*. To do so we use an automatic clustering framework introduced in [62, 63], which consists of three major components: (i) a metric to calculate distances in the multi-dimensional parameter space, (ii) a clustering algorithm, which agglomerates paths in a given data set to clusters, (iii) a cluster validation algorithm determining the correct number of clusters. The clustering algorithm is based on an algorithm called *KMeans*, but was extended to joint clustering in the multi-dimensional parameter domain (normalizing delays and angles) and to take power into account.

The result of this framework is for each data set a number of *cluster centroids*, i.e., center positions of each cluster in the parameter domain, as well as spreads for angles and delays. In the examples shown in Sections 5.3.3 and 5.3.4 we demonstrate that clustering does not change the directional properties of the channel, moreover it can improve the localization of the scatterers.

### 5.3.2 Variances of the Estimates: the CRLB

In order to apply the localization algorithm explained in Section 5.3.1, we need the variances of the estimator with respect to the DOA, DOD, and TDOA. This is in general a very complicated task. In the case of the data model used by the IlmProp, which is the same

applied by the RIMAX algorithm [180, 208], there exist an efficient method to compute the Cramér-Rao Lower Bound (CRLB). It is not credible that an estimator reaches the CRLB – nonetheless by setting the variances to this bound we still capture the main behavior of the estimator, i.e., the estimates of a path will be affected by larger errors when the path is weak or is close to other paths.

In the following we present the main idea behind the computation of the deterministic CRLB [201].

Let the vector $\boldsymbol{d} \in \mathbb{C}^{L\times 1}$ contain the $L = 7K$ exact parameters of $K$ paths, and $\widehat{\boldsymbol{d}} \in \mathbb{C}^{L\times 1}$ its noisy estimates. The $k$-th path is described by its TDOA $\tau_k$, DOA (as azimuth and elevation) $\varphi_{\mathrm{R},k}$, $\theta_{\mathrm{R},k}$, DOD $\varphi_{\mathrm{T},k}$, $\theta_{\mathrm{T},k}$, as well as by a complex path-strength, expressed by its real and imaginary part $\gamma_{\mathrm{Re},k}$ and $\gamma_{\mathrm{Im},k}$, respectively. As we consider only one complex path-strength we are implicitly assuming that we do not consider polarization. The parameters are arranged as follows

$$\begin{aligned}\boldsymbol{d} = [&\tau_{1\ldots K}\ ,\ \varphi_{\mathrm{R},1\ldots K}\ ,\ \theta_{\mathrm{R},1\ldots K}\ ,\ \varphi_{\mathrm{T},1\ldots K}\ ,\\ &\theta_{\mathrm{T},1\ldots K}\ ,\ \gamma_{\mathrm{Re},1\ldots K}\ ,\ \gamma_{\mathrm{Im},1\ldots K}]^{\mathrm{T}}\ ,\end{aligned} \tag{5.77}$$

so that the vector $\boldsymbol{d}$ has length $L = 7 \cdot K$.

By taking an unbiased efficient estimator we set

$$\mathrm{E}\left\{\left(\boldsymbol{d} - \widehat{\boldsymbol{d}}\right) \cdot \left(\boldsymbol{d} - \widehat{\boldsymbol{d}}\right)^{\mathrm{T}}\right\} \equiv \boldsymbol{C}, \tag{5.78}$$

where $\boldsymbol{C} \in \mathbb{C}^{L\times L}$ is the CRLB matrix. Notice that the CRLB is an asymptotic bound, so that an unbiased efficient estimator reaches the bound only for SNR$\rightarrow \infty$. Usually, unbiased estimators have a variance close to the bound for large intervals of the SNR. However, for lower regions the estimator variance might diverge from it significantly. Several publications (such as [80, 151, 44]) have investigated this problem, known as the "SNR threshold phenomenon", and other bounds have been proposed. However, we do not address this issue here, as it is outside the scope of this work. In the following, we assume to work at an SNR region where the estimator indeed reaches the CRLB or where the variances are at least proportional to it.

At time snapshot $t$, the parameter estimator receives a noisy observation of the channel in the form of a 3D ($M_{\mathrm{R}} \times M_{\mathrm{T}} \times M_f$) tensor $\boldsymbol{\mathcal{H}}^{\mathrm{obs}}$, where $M_{\mathrm{R}}$, and $M_{\mathrm{T}}$ are the number of receive and transmit antennas, respectively, and $M_f$ is the number of frequency bins. The channel realization $\boldsymbol{\mathcal{H}}^{\mathrm{obs}}$ is a result of a known tensor valued function $\boldsymbol{\mathcal{S}}(\cdot) : \mathbb{R}^{L\times 1} \rightarrow \mathbb{C}^{M_{\mathrm{R}}\times M_{\mathrm{T}}\times M_f}$ which maps the $L$ real-valued parameters contained in $\boldsymbol{d}$ to the $M_{\mathrm{R}}\times M_{\mathrm{T}}\times M_f$ values contained in the observation $\boldsymbol{\mathcal{H}}^{\mathrm{obs}}$, plus a noise term, as in

$$\boldsymbol{\mathcal{H}}^{\mathrm{obs}} = \boldsymbol{\mathcal{S}}(\boldsymbol{d}) + \boldsymbol{\mathcal{N}}, \tag{5.79}$$

where the tensor $\boldsymbol{\mathcal{N}}$ contains i.i.d. ZMCSCG noise. Notice that we omit to denote the dependency on time for simplicity.

The function $\boldsymbol{\mathcal{S}}(\boldsymbol{d})$ in practice maps the model parameters contained in $\boldsymbol{d}$ to the observations.

We now write equation 5.79 in vector form by means of the vec$\{\cdot\}$ operator, introduced in Appendix D.2.2. The equivalent vector valued function $\boldsymbol{s}(\cdot) : \mathbb{R}^{L\times 1} \rightarrow \mathbb{C}^{M_{\mathrm{R}}\cdot M_{\mathrm{T}}\cdot M_f\times 1}$ is simply defined as

$$\boldsymbol{s}(\cdot) = \mathrm{vec}\left\{\boldsymbol{\mathcal{S}}(\cdot)\right\}, \tag{5.80}$$

so that we can write

$$\boldsymbol{h}^{\mathrm{obs}} = \boldsymbol{s}(\boldsymbol{d}) + \boldsymbol{n}, \tag{5.81}$$

where

$$\boldsymbol{h}^{\mathrm{obs}} \doteq \mathrm{vec}\left\{\boldsymbol{\mathcal{H}}^{\mathrm{obs}}\right\} \in \mathbb{C}^{M_{\mathrm{R}}\cdot M_{\mathrm{T}}\cdot M_f\times 1} \tag{5.82}$$

$$\boldsymbol{n} \doteq \mathrm{vec}\left\{\boldsymbol{\mathcal{N}}\right\} \in \mathbb{C}^{M_{\mathrm{R}}\cdot M_{\mathrm{T}}\cdot M_f\times 1}. \tag{5.83}$$

In order to determine the CRLB matrix we need first to compute the Fisher Information Matrix (FIM) $\boldsymbol{F}(\boldsymbol{d})$ by means of the Jacobian $\boldsymbol{J}(\boldsymbol{d})$.

The Jacobian $\boldsymbol{J}(\boldsymbol{d})$ is the matrix valued function containing the first order partial derivatives of the data model $\boldsymbol{s}(\boldsymbol{d})$ with respect to $\boldsymbol{d}$ as

$$\boldsymbol{J}(\boldsymbol{d}) = \frac{\partial}{\partial \boldsymbol{d}^{\mathrm{T}}}\boldsymbol{s}(\boldsymbol{d}) \in \mathbb{C}^{M_{\mathrm{R}}\cdot M_{\mathrm{T}}\cdot M_f\times L}. \tag{5.84}$$

Then, the Fisher Information Matrix $\boldsymbol{F}(\boldsymbol{d})$ can be computed as

$$\boldsymbol{F}(\boldsymbol{d}) = \frac{2}{\sigma_n^2}\,\Re\left\{\boldsymbol{J}^{\mathrm{H}}(\boldsymbol{d})\cdot\boldsymbol{J}(\boldsymbol{d})\right\} \in \mathbb{C}^{L\times L}, \tag{5.85}$$

where we assume that the noise correlation square matrix of size $(M_{\mathrm{R}}\cdot M_{\mathrm{T}}\cdot M_f)^2$ is equal to $\sigma_n^2\boldsymbol{I}$, and $\Re\{\cdot\}$ extracts the real part from its argument. Notice that the variance of the noise, namely $\sigma_n^2$, is an unknown parameter as well, and therefore should be included to the vector $\boldsymbol{d}$. However, it is decoupled from the other parameters and therefore does not influence the computation of the CRLB matrix.

The $L$ values on the diagonal of the FIM tell us how "informative" the channel observation is with respect to each of the $L$ parameters. The off-diagonal elements, on the other hand, account for the mutual information between the parameters.

The CRLB matrix $\boldsymbol{C}(\boldsymbol{d})$ can be easily computed from the FIM $\boldsymbol{F}(\boldsymbol{d})$ as

$$\boldsymbol{C}(\boldsymbol{d}) = \boldsymbol{F}^{-1}(\boldsymbol{d}), \tag{5.86}$$

so that the $i$-th element of the diagonal of $\boldsymbol{C}(\boldsymbol{d})$ is the variance of the noisy estimate of the $i$-th element of $\boldsymbol{d}$.

Richter, in [180], proposes a method to compute the *numerical* values for the CRLB matrix in an efficient and numerically stable way. It is based on Kathri-Rao products [119] and can

include the EADFs of the antenna arrays. The numerical stability is obtained by properly normalizing the parameters in the vector $\boldsymbol{d}$. In fact, as they are, they have very different ranges. Namely, the delays are in the order of $10^{-7}$ while the angles are values around 1. Without the normalization, the FIM becomes badly conditioned and the inversion is carried out with high errors.

### 5.3.3 3D Probability Map Computation on a Synthetic Scenario

This section reviews an investigation published in [7], carried out to assess the validity of our approach. We model a cluster-based propagation environment with the help of the IlmProp. A scenario with 7 fixed clusters is generated. Each cluster consists of 6 to 8 scatterers. To simulate unrealistic paths estimates, artefacts of an estimator used in practice, we add 6 paths for each of the 41 time snapshots. These outlyers are characterized by randomly varying TDOA, DOA, and DOD, and are meant to test the robustness of the algorithm.

Figure 5.60 shows the scheme followed for the simulations. The parameter estimation phase is simplified by taking the exact parameters $\boldsymbol{d}$ characterizing the paths and adding white Gaussian noise. The variance of the noise added to each parameter for each path at each time snapshot is set to be equal to the Cramér-Rao Lower Bound (CRLB), computed as explained in the Section 5.3.2. Therefore, we assume an unbiased efficient estimator operating at high SNR regions.

For the numerical computation we assume a $2 \cdot 16 \times 16$ MIMO system, where the base station (Rx) employs a 16-ULA, while the mobile (Tx) uses a cross ULA oriented as describe above. All antennas are assumed omnidirectional. The parameter estimator receives for every time snapshot $F = 345$ frequency bins spanning a bandwidth of 120 MHz. Once the CRLB variances have been computed for the parameters of all paths at all time instants, we generate white Gaussian noise accordingly.

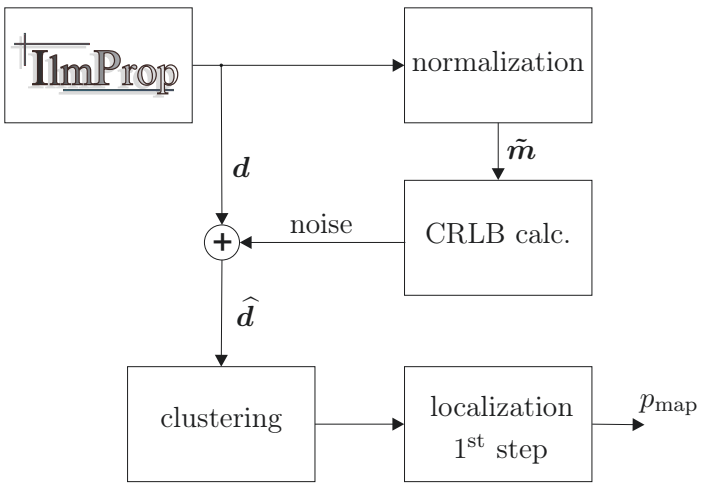


Fig. 5.60: Scheme of the simulations carried out to validate the first step of the localization algorithm.

An alternative possibility to assess the variances introduced by the estimator would be to actually carry out the parameter estimation on the synthetic channel matrices computed by the IlmProp, as one would do on real channel measurements. This approach has been followed for a SAGE-like parameter estimator in [5].

#### 5.3.3.1 The Clustering and Probability Map Inversion Phases

The noisy estimates $\widehat{\boldsymbol{d}}$ are then fed to the automatic clustering algorithm proposed in [62, 63]. The algorithm returns TDOA, DOA, and DOD of each centroid for each time snapshot. This information is passed to the localization algorithm, which computes the 3D probability map $p_{\text{map}}$. The map is then superimposed on the interacting objects constituting the clusters to verify their correct localization, as depicted in Figure 5.61. The transmitter moves along the trajectory indicated, while the receiver (not shown) is fixed. The probability map is computed for the transmit side only. Most clusters are correctly localized. The accuracy depends on the variety of points of view from which the transmitter sees the clusters. As already mentioned, the clustering phase is not necessarily needed.

The parameters coming from the parameter estimation phase could be fed directly to the localization algorithm, so that instead of clusters, we would localize the individual components which constitute the clusters. The results from this approach are shown in Figure 5.62. However, this method requires a much larger computational complexity with no or little gain in accuracy. Note that the centroids can describe the environment completely with respect to the localization problem.

The outlyers deteriorate the accuracy of neither method. In fact, when we use the clustering phase these paths are automatically pruned because they do not belong to any cluster. In case of using the parameter estimates directly, the PDFs of the outlyers are eliminated by averaging over different time instants if they are uncorrelated.

Another improvement can be obtained by localizing the centroids of different paths separately. The tracking algorithm proposed in [2] allows us to identify the centroids and, at the same time, track their evolution in time. This permits us to compute the probability map for each centroid separately, thus reducing the computational complexity of the localization phase even further.

The results shown in Figures 5.62 and 5.61 show that when the assumptions are met, the probability map inversion step delivers a PDF which concentrates around the real position of the IOs. The accuracy depends on the variety of points of view from which the transmitter sees the scatterers.

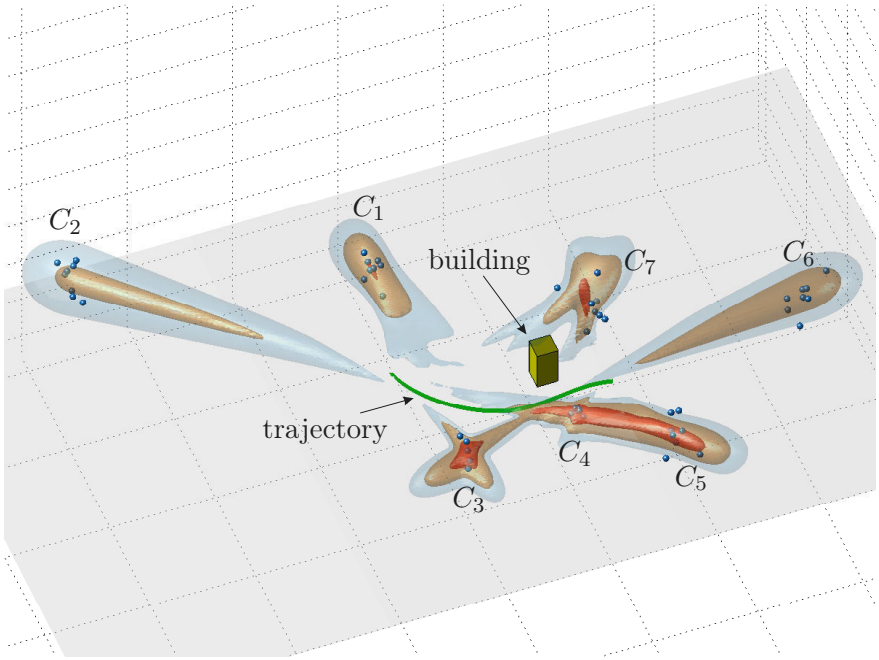


Fig. 5.61: Probability map (obtained from the clustered estimates) superimposed on the real locations of scattering clusters for an IlmProp scenario. The probability focuses on the exact locations with different degrees of accuracy. The surfaces represent the values $\{-12,\ -8.5,\ -4.5\}$ dB with respect to the maximum of the PDF.

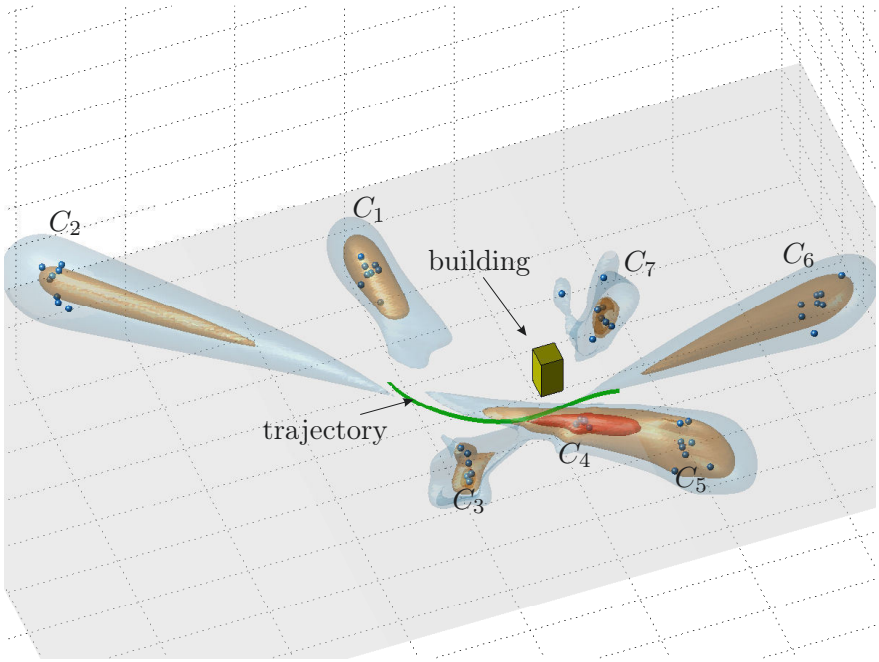


Fig. 5.62: Probability map (obtained from the un-clustered estimates) superimposed on the real locations of scattering clusters for an IlmProp scenario. The surfaces correspond to the values $\{-12,\ -8.5,\ -4.5\}$ dB with respect to the maximum of the PDF.

### 5.3.4 2D Probability Map Computation on Measurements

To test the applicability of our methods, in [6], we consider high-resolution parameter estimates derived from measured channels. The latter were gathered in a sounding campaign [104, 211], carried out in the vicinity of a small square in the town center of Ilmenau, Germany. Most houses surrounding the streets and the square are 3 stories high with massive stone walls. The channels were measured with a multi-dimensional MEDAV RUSK MIMO channel sounder [155] employing a 8 element dual polarized ULA at the fixed receiver and a 16 element UCA at the mobile transmitter. The high-resolution parameter estimator used was the RIMAX [180, 208], which is a modified maximum likelihood estimator.

Figure 5.63 shows the trajectories of the mobile transmitter for five different measurement runs. The UCA and the transmitter of the channel sounder was mounted on a trolley which was pulled by hand at constant speed. The sounder measured 385 frequency bins across a bandwidth of 120 MHz at 5.2 GHz, with a sampling time interval between 9 and 20 ms, depending on the measurement run. This made the maximum Doppler shift resolvable 55 and 25 Hz, respectively, corresponding to a radial speeds of approximately 10 and 5 km/h. The receiver (ULA) was mounted in one corner of the square (see Figure 5.63) facing the fountain which is depicted as a circle in Figure 5.63. Both azimuth and elevation information could be estimated at the Tx side only, and therefore the localization has been carried out in

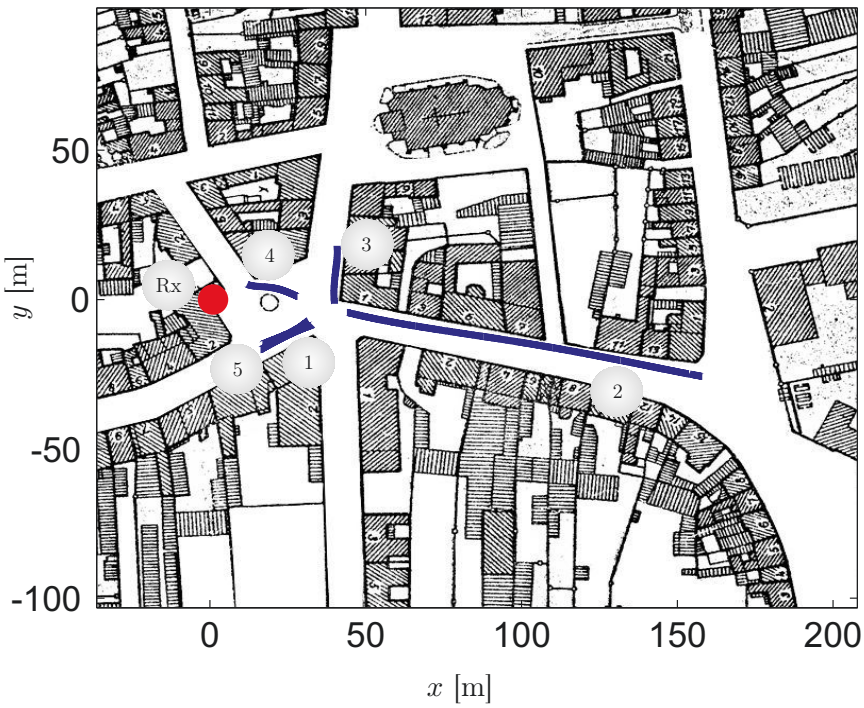


Fig. 5.63: City map of the town center of Ilmenau, Germany. Five measurement runs are indicated in blue, whereas the position of the fixed receiver is red. The square and most streets are closed to traffic.

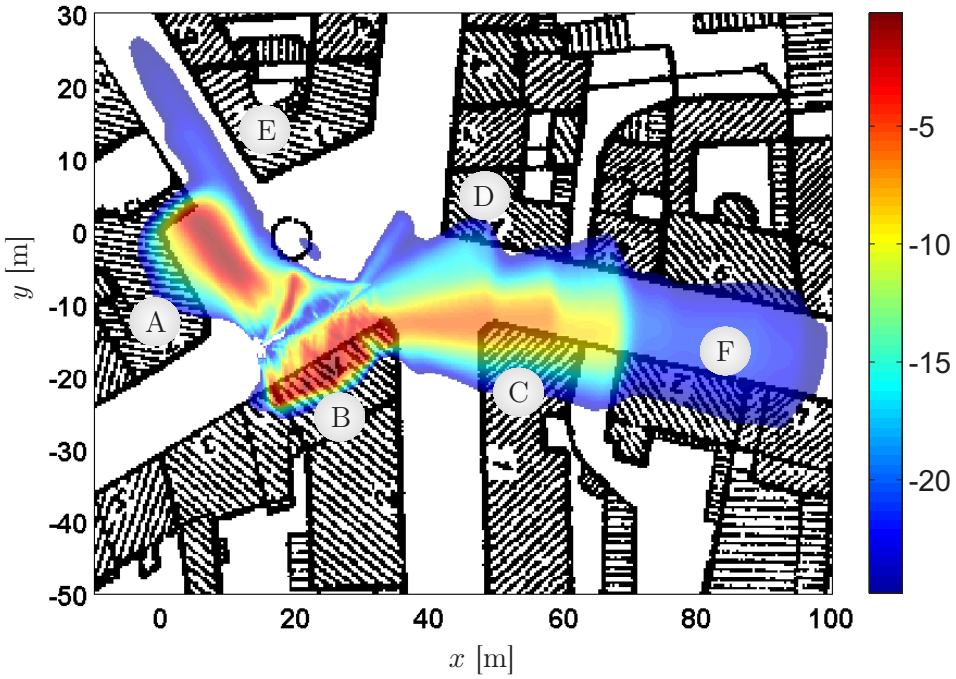


Fig. 5.64: Probability map $p_{\text{map}}(x, y)$ computed for the transmitter only for the first measurement run. The values are given in dB.

2 dimension only, i.e., on the azimuthal plane.

In order to estimate the variances $\sigma_{\text{TDOA}}$, $\sigma_{\text{DOD}}$, and $\sigma_{\text{DOA}}$ for each path at each time instant we first compute the deterministic CRLB as shown in Section 5.3.2. Higher variances broaden the PeBPDFs, while lower ones make them more narrow. Although the CRLB is a very optimistic estimate of the estimates' variances, it represents a good relative metric for the reliability of the paths. For instance, the CRLB will be large for paths which can be hardly separated because they lie too close to other paths in the parameter space. The same will happen for weak paths. Experiments have shown that taking standard deviations even 6 times larger than the ones obtained by the CRLB computation leads to very similar results, so that even though the absolute values of the probability change, their relative variation has the same trend. In other words, the probability will focus in certain areas in the same way. On the contrary, setting the variances $\sigma_{\text{TDOA}}$, $\sigma_{\text{DOD}}$, and $\sigma_{\text{DOA}}$ to some fixed value has the effect of impairing the localization because it suppresses the information about the reliability of the estimates.

Figure 5.64 shows the probability map $p_{\text{map}}(x, y)$ for the first measurement run. Since the receiver did not move, we use only $p_{\text{T}}(x, y|k, t)$ for its computation. From this measurement run alone it is possible to see a concentration of probability around the receiver, below the fountain, and in correspondence of the north wall of building B. The highly focused maximum below the fountain is in correspondence of a trailer parked in the restricted area. There are some beams directed towards the corner of building C. However, there are too few paths with mostly the same point of view to obtain a concentration of probability. The shape of the

street along the east side of building E is very well recognizable by the $p_{\text{map}}(x, y)$ function.

Assuming that the interacting objects did not move during all measurement runs, it is possible to combine different measurements. The resulting probability map, which is the mean of the $p_{\text{map}}$ functions for the five different runs, is depicted in Figure 5.65. Most probability is focused around the receiver. This is because the paths corresponding to the LOS localize a scatterer in the position of the receiver. In most of the 2800 time snapshots measured the mobile was in a pure LOS regime. This leads to a very large number of spatially correlated paths, i.e., all pointing in one direction, making the absolute value of the probability in that point very high. The range plotted is quite large, approximately 30 dB, so that the small local maxima would be visible. This has the effect of making the absolute maximum (corresponding the scatterer in the Rx position) appear very broad.

It can be observed that in general the shape of the streets has been very well represented, meaning that there is little probability focused inside buildings. Parts of the walls of the B and D buildings, as well as the corners of building C and E, contributed significantly to the propagation. In particular, at the corner of building C there is a metal traffic sign which presumably has diffracted the signal. The local maximum at the bottom left corner of building E almost disappears in the tails of the absolute maximum. Besides the already mentioned trailer, there are several other local maxima visible along the street F. The latter are probably metal signs from several shops, as well as street lights mounted on metal masts.

Unfortunately during the measurement campaign the position and orientation of the transmitter was assessed with poor accuracy. In order to improve the precision, in LOS regimes, we used the TDOA, DOD and DOA estimates to improve the accuracy of the position and orientation of the transmitter. Assuming known the position and orientation of the receiver, to each {TDOA, DOD, DOA} corresponds uniquely a position and an orientation of the transmitter. In order to average over the estimation errors we perform linear regressions thus obtaining the optimum estimate for the mobile trajectory in a least square sense.

By comparing the position of the local maxima with the objects physically present in the environment we estimate an accuracy of a few meters. We believe that with more precise information about the position and orientation of the arrays, as well as full 3D DOD DOA information, we would obtain a much higher resolution.

We now consider the pre-processing step explained in the section on page 182, in which clusters are automatically identified in the parameter space. The output of this phase is a number of centroids for each time snapshot characterized by a DOD, DOA, TDOA, and strength. Furthermore, for each cluster a delay spread and a spread in angle at the Rx and Tx sides are also provided. This information is processed in the first phase of the localization algorithm in the same manner as described in Section 5.3.1.1. The resulting probability map is depicted in Figure 5.63.

It can be seen that most objects are reproduced by the localization with a clustering pre-processing phase. The computational complexity of the localization step is significantly

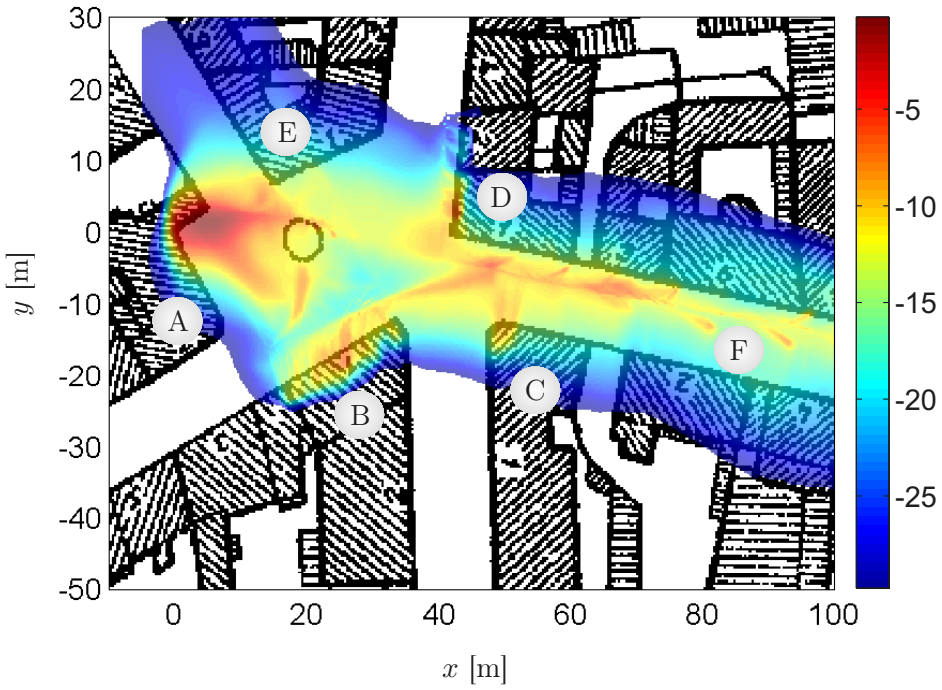


Fig. 5.65: Probability map $p_{\text{map}}(x, y)$ computed for the transmitter only for all measurement runs. The values are given in dB.

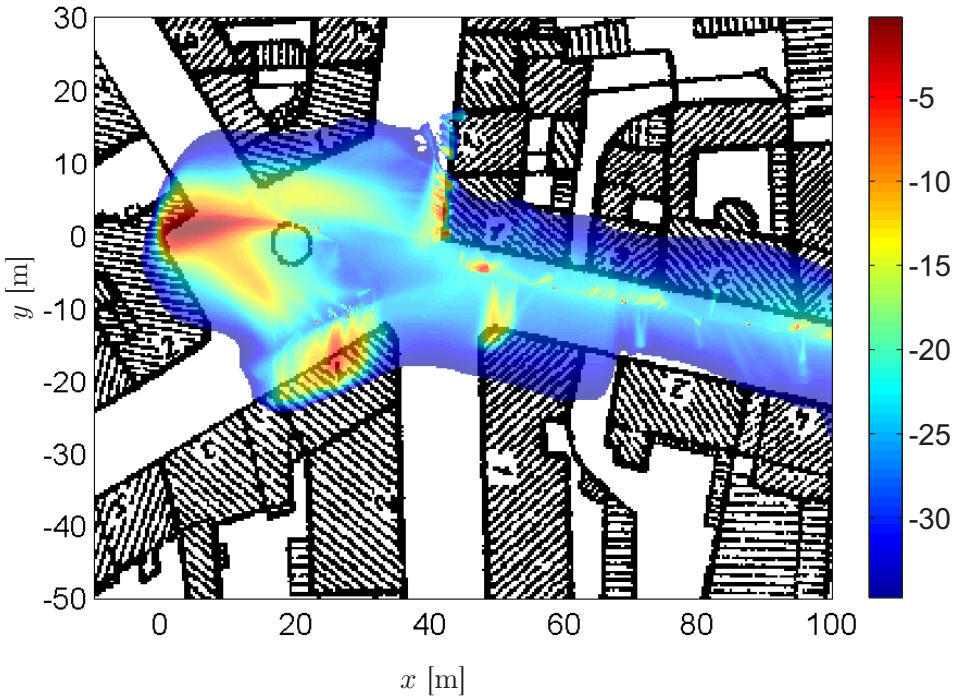


Fig. 5.66: Probability map $p_{\text{map}}(x, y)$ computed for the transmitter only for all measurement runs after the automatic clustering algorithm. The values are given in dB.

reduced since the number of centroids is in general much smaller than the original number of paths.

The results shown in Figure 5.66 also indicate that the clusters which were recognized in the parameter space also exist as clusters in space. This result was anticipated, as the idea on clusters itself comes from the fact that we expect IOs which are close in space to give birth to paths which share similar parameters. Nonetheless, the localization method presented here gives more evidence to sustain this approach.

### 5.3.5 3D Probability Map Computation on Measurements

This section, outcome of a joint work with Markus Landmann, shows the results of the localization algorithm introduced in Section 5.3.1 applied on a full polarimetric MIMO channel measurement. The latter has been carried out recently in Tokyo[14]. The measurement campaign, together with interesting results on the polarization behavior of both discrete and diffuse multi-path components, have been published in [140].

#### 5.3.5.1 General Description of the Measurements

The configuration of the measurement system is summarized in Table 5.4, while the MS trajectory is plotted on the city map in Figure 5.67. For this measurement the transmitter part of the sounder was kept fixed while the receiver was moving. In the following they will be denoted by BS and MS, respectively. Notice that we denote with MS the mobile receiver and with BS the fixed transmitter. Well calibrated antenna arrays (manufactured by IRK Dresden [36]) were employed at both link-ends. They allowed to estimate the Cross-Polarization Ratio (XPR) of the specular components up to $\pm$ 40 dB. The XPR is defined as the power ratio of the co-polarization and the cross-polarization. It is therefore a measure of the behavior of the channel with respect to the polarization. For instance, an XPR equal to infinity means that the environment does not modify the polarization status of the waves. An XPR of 0, on the other hand, signifies that the channel converts all power sent on one polarization into the orthogonal one. The Cross-Polarization Discrimination (XPD), on the contrary, measures the discrimination capabilities of an antenna. In fact, because of the coupling, the antenna itself introduces some cross-talk between polarizations. For this reason, the XPR can be estimated only up to $\pm$ 40 dB, as the reference horn antenna used in the calibration possesses an XPD of 40 dB. For the DMC, the maximum resolvable XPR of the channel is limited by the XPD of the antenna array elements, given in Table 5.4.

The high-resolution parameter estimation step was particularly expensive in terms of processing time, as 10 high-end PCs were employed for three whole weeks. The estimator

[14] The authors would like to thank the National Institute of Information and Communications Technology (NICT) and FUJITSU for the support and provision of the measurement equipment. Furthermore, we would like to thank the members of the Takada Laboratory of Tokyo Institute of Technology for the support during the measurements and Markus Landmann, for the carrying out the parameter-estimation step and for his valuable support in analyzing the parameters estimates.

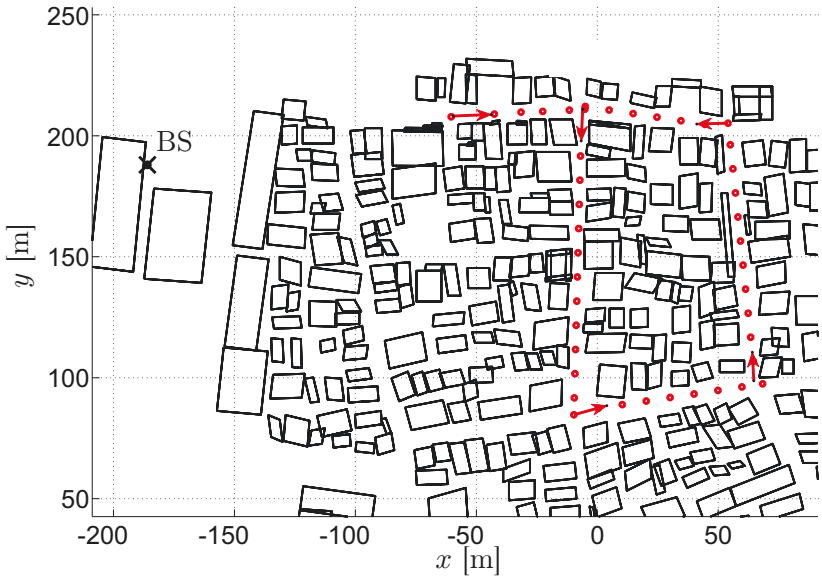


Fig. 5.67: City map of the Tokyo measurement. The trajectory of the MS as well as the position of the fixed BS is depicted.

used was the already mentioned RIMAX algorithm [180, 208], a modified iterative maximum likelihood estimator.

Of particular notice is the impressive number of MIMO channel coefficients recorded, namely 1536. They result from the 8 antennas at the BS, 48 antennas at the MS, and 2 polarizations at both sides. This led to a very precise full polarimetric DOA, DOD estimation, which included azimuth and elevation at both sides.

As mentioned in Section 5.3.1, the position and orientation of the antenna arrays is of crucial importance. For the MS this information is obtained by measuring the start and end points of a measurement run by means of a LASER distometer. The positions in between are computed assuming that the MS was pulled at constant velocity. The orientations of the arrays is far more critical than the their positions, as a small error is reflected in large ones in the IO localization. For the measurement presented here, the orientation has been assessed via LASER pointers for the start and end points only, whereas the orientation during the measurement run was interpolated. Notice that each measurement run was about 10 m long, so that the position and orientation can be considered fairly accurate.

A total of 1028 time snapshots has been considered. On average, for each snapshot a total of 60 paths has been identified, for a total of 60789 paths. For each path, 9 parameters have been estimated, namely DOA, DOD, TDOA, and path-strength. The path-strength comprises four complex factors, whereas the DOA and DOD consist of two angles each, so that an impressive total of 790.257 real valued parameters have been estimated.

| | |
|---|---|
| MIMO Channel Sounder | RUSK Fujitsu [155] |
| Tx power at the antenna | ca. 2.8 W |
| Carrier frequency / wavelength | 4.5 GHz / 6.67 cm |
| Measurement bandwidth | 120 MHz |
| Maximum multi-path delay | 3.2 $\mu$s chosen according to the environment |
| Number of multiplexed Tx/Rx ports | 16 Tx / 96 Rx |
| Total number of MIMO channels | 1536 |
| Measurement time of one snapshot | 10 ms |
| Time between 2 snapshots | 1.5 s |
| Tx/Rx synchronization | Rubidium reference |
| Base Station (Tx side) | 4 × 2 elements Polarimetric Uniform Rectangular Patch Array (PURPA) |
| Mobile Station (Rx Side) | 24 × 2 elements Stacked Polarimetric Uniform Circular Patch Array (SPUCPA) |
| XPD Tx/Rx Array | 13–15 dB / 10–14 dB |
| BS height | 35 m |
| MS height | 1.6 m |
| buildings height around the MS | 2-3 floors, residential area |
| length of the measurement route | 490 m |

Tab. 5.4: Set-up for the Tokyo measurements analyzed with the localization algorithm.

#### 5.3.5.2 The Probability Map Inversion Step

The information provided by the RIMAX has been processed by the localization algorithm introduced in Section 5.3.1 so that the results of the first phase, namely the probability map $p_{\text{map}}(x, y, z)$, are depicted in Figure 5.68 to 5.71. For the computation we considered both sides, namely the Rx and the Tx, and processed the path parameters directly, i.e., without the automatic clustering. Since the arrays showed different behavior in azimuth and elevation, we use the asymmetric PeBPDF given in equation (5.73). The variances of the estimator have been set to the CRLB computed as explained in Section 5.3.2. The iso-surfaces plotted in the figures represent the probability map at the values $\{-30,\ -23,\ -18,\ -15\}$ dB with respect to the maximum of the PDF.

In Figure 5.68, the surfaces represent the points of $p_{\text{map}}$ which assume a value of -30 dB with respect to the maximum. The position of the receiver, and the trajectory of the mobile are visible. As mentioned on page 180, while evaluating the probability map, the masking phenomenon makes it impossible to interpret the absolute value of $p_{\text{map}}(x, y, z)$. On the other hand, we need to look for the shapes drawn by probability in search for local maxima. At this level of the probability it is possible to distinguish the shape of a few streets, marked with (a). These streets disappear for higher values of the probability, in Figure 5.69, indicating that only a few paths were directed towards those directions (with respect to the overall amount of paths estimated). In this figure, plotted for $p_{\text{map}}(x, y, z) = -23$ dB, we can recognize a higher concentration of probability around the trajectory of the MS as well as at the access of

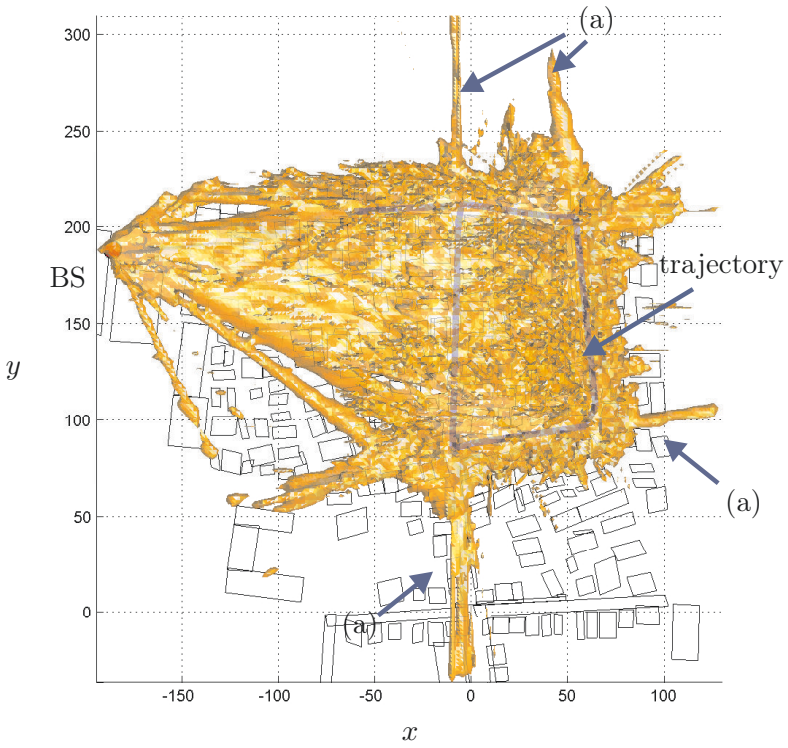


Fig. 5.68: Visualization of the 3D probability map. The iso-surface is plotted for a $p_{\text{map}} = -30$ dB. It is possible to distinguish the shape of a few streets, marked with (a).

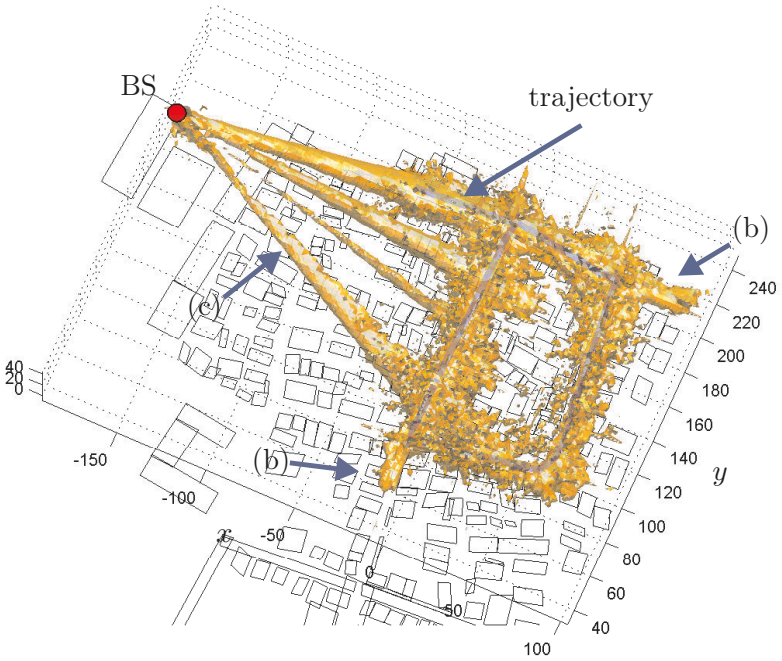


Fig. 5.69: Visualization of the 3D probability map. The iso-surface is plotted for a $p_{\text{map}} = -23$ dB. Higher probability concentrates around the trajectory of the MS as well as at the access of two roads, marked with (b). Presumably, LOS paths or obstructed LOS can be also seen, (c), due to the masking phenomenon.

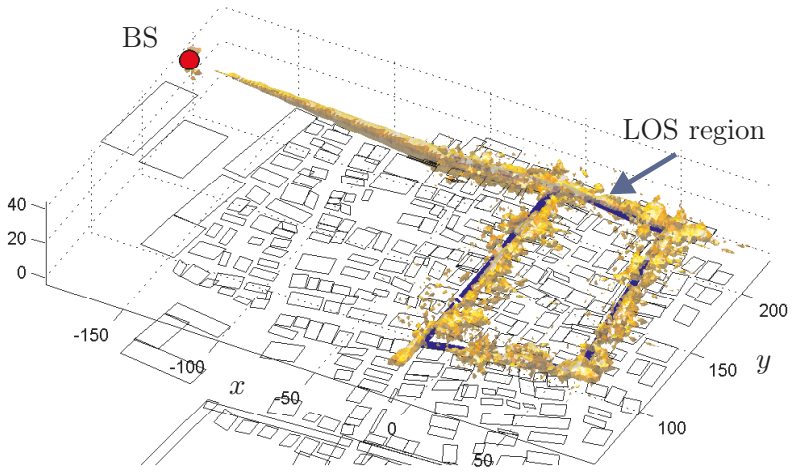


Fig. 5.70: Visualization of the 3D probability map. The iso-surface is plotted for a $p_{\text{map}} = -18$ dB. The strong LOS region is marked. Many LOS paths cause the beam-like cone connecting the BS to the LOS region (masking phenomenon).

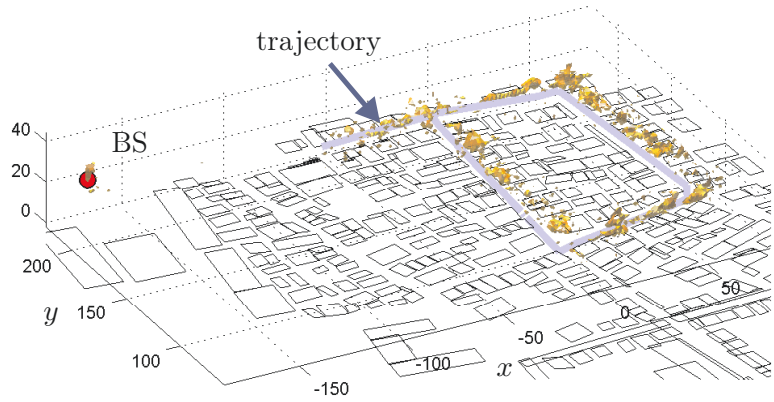


Fig. 5.71: Visualization of the 3D probability map. The iso-surface is plotted for a $p_{\text{map}} = -15$ dB. The objects localized with highest probability are the ones in the vicinity of the MS' trajectory.

two roads, marked with (b). The beams marked with (c) running from the BS towards four different points at the trajectory are due to the masking phenomenon, discussed on page 180. In fact, the presence of a LOS or simply the preferred way used by the EM wave to access the street along which the MS was moving gave origin to many paths directed towards those points, leading to higher probability between those points and the BS. In fact they are the result of several PeBPDFs oriented in the very same direction.

Figure 5.70 shows the probability map for -18 dB. Several clusters appear in the vicinity of the trajectory. the strong LOS component experienced on the street leading to the rectangle

causes the focussing of probability from the BS towards this area. Notice that also around the BS there is a local maximum of probability. It is the result of the PeBPDFs corresponding to the LOS originating from the MS. The accuracy of this localization over more than 200 meters distance proves the high care taken in the measurement campaign in recording the position and orientation of the MS. In the last figure of the $p_{\text{map}}$, Figure 5.70 we plot the surfaces for a value of -15 dB. At this level, only the maximum over the BS and a few clusters remain.

Even though the masking phenomenon complicates the evaluation of the results, the visualization proposed in the figures above mentioned represents a useful tool in validating the whole processing chain as well as in giving a physical interpretation to the propagation. A particularly interesting aspect of this method is that we can visualize in one picture more than one measurement run, as already emphasized in Section 5.3.4.

An interesting investigation which we leave to future work consists in applying the probability map inversion step with respect to different polarizations. The estimator delivers four path weights for each path. By selecting only those paths with significant power for each of the four possible polarization pairs, namely v $\rightarrow$ v, v $\rightarrow$ h, h $\rightarrow$ v, and h $\rightarrow$ h, we can compute four probability maps. By comparing the maps, it will be possible to distinguish the objects which reflected energy conserving the polarization status from those which introduced cross-talk.

#### 5.3.5.3 The Scatterers Identification Step

Once the probability map has been computed, we proceed in the second phase of the localization algorithm: the scatterers identification. Following the method introduced in Section 5.3.1.2, for each path we decide the position of the scatterer near the transmitter, namely $S_{\text{T}}$, by placing it where the probability is highest and according to the DOD. The position of the scatterer near the receiver, $S_{\text{R}}$, is uniquely determined by the geometry, as given in equation (5.67). The position of the scatterers is shown in Figure 5.72. Magnifications are depicted in Figures 5.73 and 5.74. The red (darker) dots mark the position of the scatterers at the MS side, whereas the blue (lighter) ones the scatterers at the BS side. As the magnification in Figure 5.73 shows, the scatterers at the MS are all very close to the mobile trajectory, and represent local scatterers around it. The scatters at the BS, on the other hand, can be observed both near the mobile trajectory as well as far away from it. This is the case of the clouds of scatterers marked with (d) and (e) in Figure 5.72. The positions assumed by the scatterers marked with (d) correspond to two buildings, also depicted in Figure 5.74. The IO clouds marked with (e) in Figure 5.72 correspond to the street crossing of the nearby streets around the mobile trajectory. Presumably, the waves traveled from the BS to the crossings where they are scattered by objects which have a clear view towards the MS.

Other considerations can be made when considering the parameters $a$ and $a_{\max}$ defined in Section 5.3.1 and depicted in Figure 5.53. Figure 5.75 shows the CDFs of these parameters.

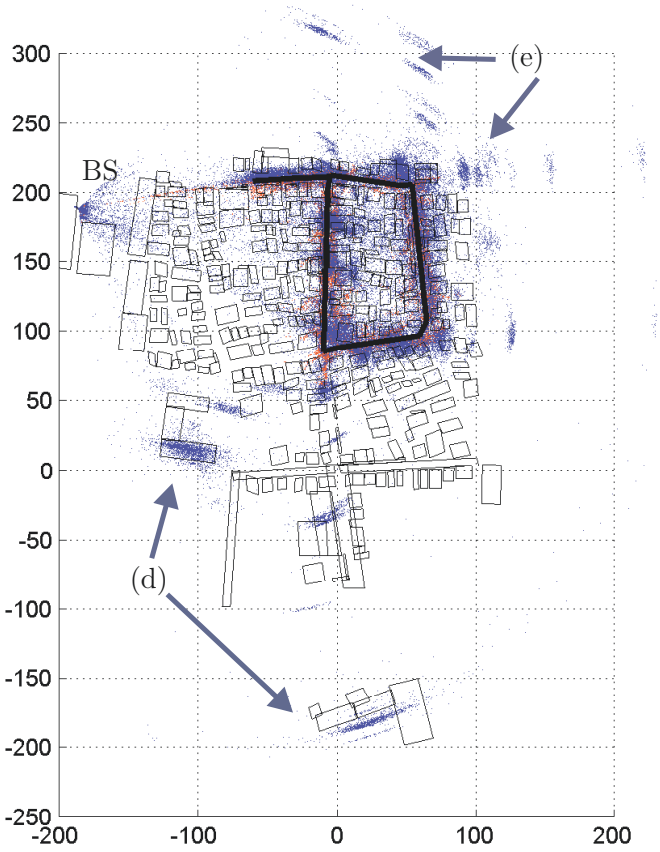


Fig. 5.72: Position of the IOs identified with the localization algorithm. The blue (lighter) dots are the scatterers for the BS side, while the red (darker) ones are at the MS. The clouds of scatterers marked with (d) represent two buildings which reflected large portions of power because of their favorable orientation and of the reflective materials of their facades. The clouds marked with (e) are street crossings.

The closest scatterer is at 3.1 m, while the furthest away is at 261 m. The parameter $a_{\max}$ gives the length of the segment on which the scatterer $S_{\mathrm{T}}$ must lie. Plot (b) shows that the minimum length is 7.9 m, and that slightly less than 10 % of the segments have a length larger than 10 m. In fact, the longest segments has $a_{\max} = 455$ m.

Fig. 5.73: Magnified view of Figure 5.72. The line indicates the trajectory of the MS. The red (darker) dots indicate the scatters seen by the BS, while the blue (lighter) ones the IOs at the mobile.


Fig. 5.74: Magnified view of the far scatterers from Figure 5.72. The buildings marked with (d) are particularly well resolved by the localization algorithm.

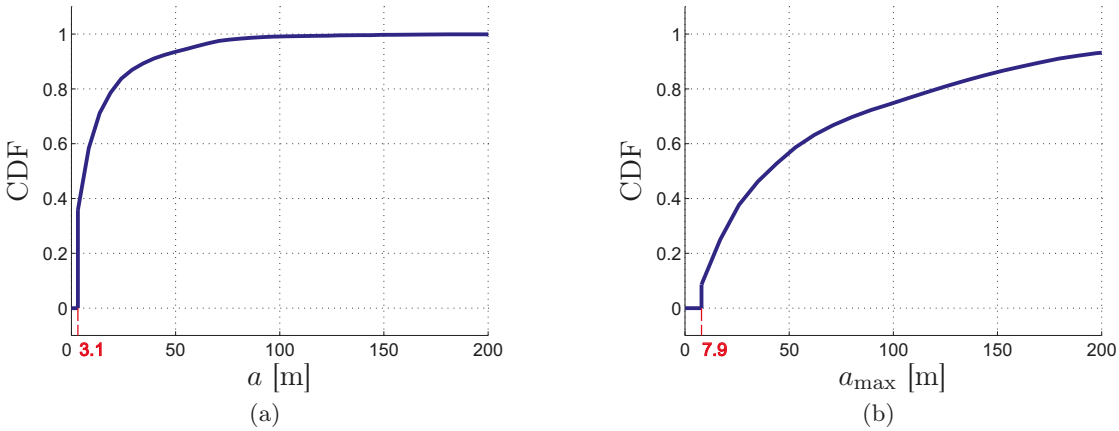


Fig. 5.75: Cumulative Density Function (CDF) of the parameters $a$ and $a_{\max}$ defined as in Figure 5.53. The term $a$ is the distance between the MS and the identified scatterer, while $a_{\max}$ denotes the maximum distance from the MS at which the IO could have been.

#### 5.3.5.4 Channel Reconstruction at Different MS Positions

One of the biggest advantages of the MBPCM concept [209], is the possibility to obtain channels for antenna arrays different than the ones used in the channel sounding campaign. However, in order to validate this approach we would need two sets of channel measurements, i.e., one on which to perform the parameter estimation followed by the localization algorithm, and one with a second antenna array. In this way we could compare the reconstructed channel with the measured one. To perform such a measurement goes beyond the aims of this thesis, and is left to future work . In order to test the MBPCM concept in combination with the localization algorithm, we limit ourselves in testing the MBPCM for synthetic radiation patterns at different locations. We use the information obtained for a certain position of the MS to estimate the channel coefficients for a different one. In order to assess the accuracy of the method, we reconstruct the channels exclusively for positions which were actually measured. Let $\mathcal{I}_t$ denote the IlmProp geometry obtained with the proposed localization algorithm for the time snapshot $t$. The geometry comprises all the information about the paths. For each path we have a DOA, DOD, TDOA, and four complex path weights, for a full polarimetric double directional description of the channel. Let further $\boldsymbol{\mathcal{H}}(t,\mathcal{I}_t)$ be the channel reconstructed for the position at time snapshot $t$ with the geometrical information contained in $\mathcal{I}_t$. The reconstruction is carried out with the system equation given in (5.8) assuming planar wavefronts. As already mentioned, when computing the channel in this way, the exact position of the scatterers is not relevant, as only the DOA, DOD, and TDOA matter. However, when we move the MS in some other position, then these parameters change depending on the position of the corresponding IOs. In order to test that the localization of the IOs can improve the channel reconstruction in this case, we compare three approaches

- standard MBPCM [209]
- IlmProp-based MBPCM
- constant channel approach.

We now consider two time snapshots, $t$ and $t'$, and the corresponding geometries $\mathcal{I}_t$ and $\mathcal{I}_{t'}$, as depicted in Figure 5.76. The scatterers defined by $\mathcal{I}_t$ are denoted by red circles, whereas the ones for $\mathcal{I}'_t$ are denoted by yellow squares. According to the high-resolution parameter estimates, the best approximation of the real measured channel at time snapshot $t'$ is $\boldsymbol{\mathcal{H}}(t',\mathcal{I}_{t'})$, which we therefore take as reference. In the figure, $\boldsymbol{\mathcal{H}}(t',\mathcal{I}_{t'})$ consists of the paths (a), (b), and (c).

Figure 5.77 illustrates the standard and the IlmProp-based MBPCM methods. The standard MBPCM method in Plot (a) consists in using the DOA, DOD, and TDOA estimated at the time snapshot $t$ for all paths and simply compute the new phase shifts due to the displacement, assuming planar wavefronts. We denote the channel obtained in this way as $\widehat{\boldsymbol{\mathcal{H}}}_{\text{standard}}(t',\mathcal{I}_t)$. Plot (b), on the other hand, shows the IlmProp-based MBPCM approach. According to the position of the scatterers localized for the time snapshot $t$ we compute for each path the new DOA, DOD, and TDOA for the position of the MS at time $t'$. The channel

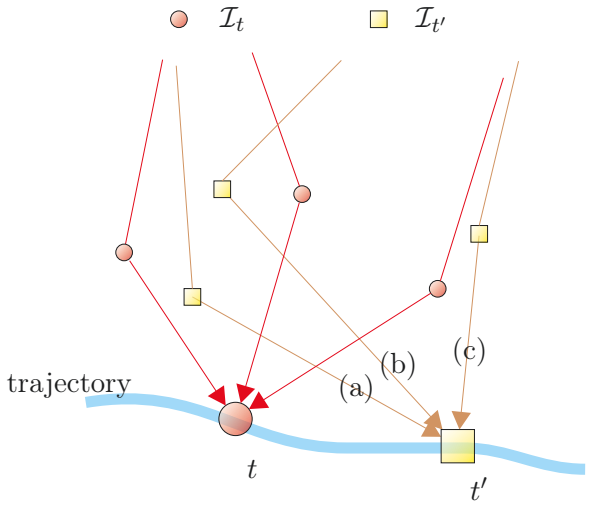


Fig. 5.76: For two time snapshots, namely $t$ and $t'$ the corresponding IlmProp geometries are denoted by $\mathcal{I}_t$ and $\mathcal{I}'_t$. The channel at time $t'$ consists of three paths, namely (a), (b), and (c).

computed with this approach is denoted by $\widehat{\boldsymbol{\mathcal{H}}}_{\text{IlmProp}}(t', \mathcal{I}_t)$. The constant channel approach, on the other hand, consists in assuming that the channel at time $t'$ is identical to the one at time $t$. The estimated channel, denoted by $\widehat{\boldsymbol{\mathcal{H}}}_{\text{constant}}(t', \mathcal{I}_t)$ is then equal to $\boldsymbol{\mathcal{H}}(t, \mathcal{I}_t)$. All channels are computed employing one omnidirectional antenna at each link-end, and computing the four polarimetric channels separately, namely the vertical to vertical component $\widehat{\boldsymbol{\mathcal{H}}}_{\text{v}\to\text{v}}$, the vertical to horizontal $\widehat{\boldsymbol{\mathcal{H}}}_{\text{v}\to\text{h}}$, and the other two, namely $\widehat{\boldsymbol{\mathcal{H}}}_{\text{h}\to\text{v}}$ and $\widehat{\boldsymbol{\mathcal{H}}}_{\text{h}\to\text{h}}$. The channels were computed for the center frequency $f = 4.5$ GHz.

To assess the accuracy of the different methods we compute the Normalized Squared Error (NSE) between the estimated channel $\widehat{\boldsymbol{\mathcal{H}}}(t', \mathcal{I}_t)$ and the reference one $\boldsymbol{\mathcal{H}}(t', \mathcal{I}_{t'})$ considering

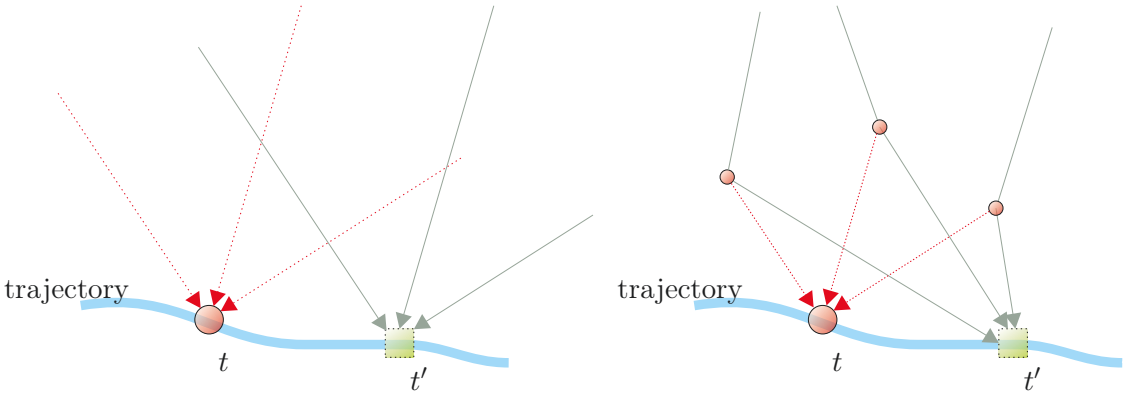


(a) Standard MBPCM approach

(b) IlmProp-based MBPCM approach

Fig. 5.77: Test-bed to validate the MBPCM concept. The standard approach uses the same DOA, DOD, and TDOA estimated at time $t$ to compute the channel at $t'$. The IlmProp-based approach recomputes these parameters according to the position of the scatterers localized at time $t$. At the fixed BS the methods coincide.

the time snapshots $t$ and $t'$. Considering one polarization only, the channels at time $t'$ are scalars. Nevertheless we denote them with the tensor notation $\boldsymbol{\mathcal{H}}$, as the formulas in the following can be applied to multi-dimensional channels as well, for instance, considering more frequency bins or antenna arrays. Omitting the dependency on polarization for simplicity, the Normalized Squared Error (NSE) is expressed as follows

$$\mathrm{NSE}(t,t') = \frac{\mathrm{abs}\left(\mathrm{abs}\left(\widehat{\boldsymbol{\mathcal{H}}}(t',\mathcal{I}_t)\right) - \mathrm{abs}\left(\boldsymbol{\mathcal{H}}(t',\mathcal{I}_{t'})\right)\right)^2}{P}, \tag{5.87}$$

where $P$ is the average power of the reference channel considering all time snapshots. The abs(.) operator computes the absolute value, in this case of scalars.

The reconstruction error will presumably depend on the distance between the positions of the MS at times $t$ and $t'$, which we denote with $d(t,t')$. For this reason, we consider all possible pairs of measurement points and compute the NSE$(t,t')$ as explained above. We then compute the Normalized Mean Squared Error denoted by NMSE$(d)$ by averaging the NSE$(t,t')$ for the time instants $t$ and $t'$ which have a distance $d = d(t,t')$

$$\mathrm{NMSE}(d) = \mathrm{E}\left[\mathrm{NSE}(t,t')\right], \quad \text{for } \forall\ t,t' : d(t,t') = d. \tag{5.88}$$

In a similar fashion we compute the variance of the NSE with the expression

$$\sigma^2_{\mathrm{NSE}}(d) = \mathrm{E}\left[\mathrm{NSE}^2(t,t')\right] - \mathrm{E}\left[\mathrm{NSE}(t,t')\right]^2, \quad \text{for } \forall\ t,t' : d(t,t') = d. \tag{5.89}$$

To compute numerically the expectation operators in equations (5.88) and (5.89), we average over all possible pairs of measurement points with a distance $d(t,t') \in \left[d-\lambda \quad d+\lambda\right]$.

Figure 5.78 shows the NSE versus distance $d(t,t')$ for all pairs $\{t,t'\}$ considered. The Normalized Mean Squared Error (NMSE) computed as in equation (5.88) is plotted in Figure 5.79, whereas the variance is depicted in Figure 5.80.

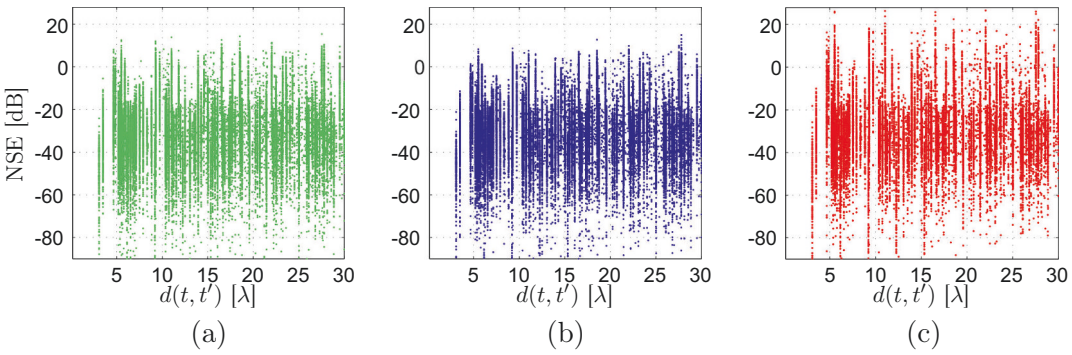


Fig. 5.78: NSE vs. distance for all possible pairs in the Tokyo channel measurement under study. The NSE is the normalized squared error of the reconstructed channel, computed with three different approaches: (a) standard MBPCM, (b) IlmProp-based MBPCM, and (c) constant channel approach.

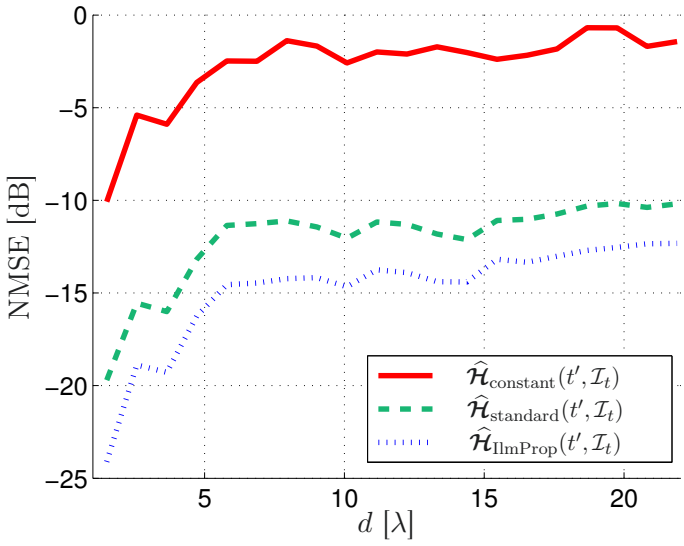


Fig. 5.79: NMSE vs. distance. The NSE is the normalized squared error of the reconstructed channel, computed with three different approaches: standard MBPCM, IlmProp-based MBPCM, and constant channel approach. The average is carried out considering all pairs of measured points.

Notice that the shortest distance which we can observe is approximately $2.5\,\lambda$, which corresponds to 20 cm. This is already quite a large displacement in that the propagation conditions might have changed considerably.

Nonetheless, Figure 5.79 shows good results for the proposed IlmProp-based MBPCM reconstruction. In fact, with the localization algorithm we are able to achieve a better accuracy in the channel estimation with a gain between 2 and 4 dB with respect to the NMSE of the standard method. Larger gains are achieved for shorter distances. Also the variance in Figure 5.80 indicates a better performance of the IlmProp-based approach.

We can observe that the NMSE increases rapidly until $5\,\lambda$, from where it increases much slower. The variance in Figure 5.80 shows a similar trend, especially for the standard MBPCM approach. This behavior can be attributed to the fact that within $5\,\lambda$ we can still predict the fast-fading. The reconstruction error increases rapidly as we move away from the original point where we estimated the geometry since the fast-fading affects the channel already within fractions of the wavelength. For distances larger than $5\,\lambda$, on the other hand, we can at most estimate the shadow-fading. As this affects the channel only within several wavelengths, the error grows much slower with distance.

These investigations prove the correctness and practical applicability of the proposed algorithms. However, for future work, it is of particular interest to study the performance of the MBPCM in the range between 0 and $2.5\,\lambda$, interval for which we could not evaluate the methods, as adequate measurements were not available.

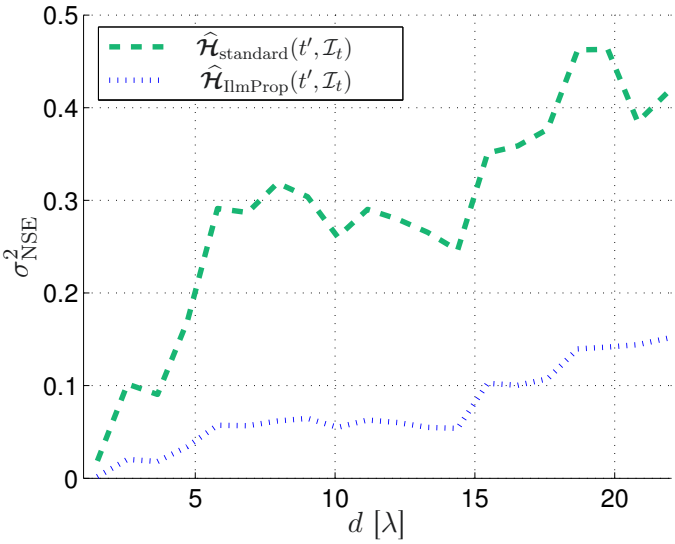


Fig. 5.80: Variance of the NSE vs. distance. The NSE is the normalized squared error of the reconstructed channel, computed with two different approaches: standard MBPCM and IlmProp-based MBPCM. The variance for the constant channel approach (not shown) is much higher. The average is carried out considering all pairs of measured points.

## 5.4 The IlmProp Project

The success of a channel model, measured by how many researchers are using it, depends not only on its intrinsic scientific value, but also on several other factors. A simple model makes it automatically easier to understand. In this case, more compact ways to describe it can be formulated, permitting an easier dissemination of the key ideas. The availability of public code is another factor which favors the diffusion of a channel model in the scientific community. When channel models are included in important standards, they are immediately accepted and broadly employed. Last but not least, the number of renowned researchers who already applied it, as well as the reputation of the people who developed it represent one of the major causes of a channel model's fate.

For these reasons, the most well known channel models currently used are the ones developed within large research projects. In fact, a large number of researchers participated to the development of such models. Furthermore, since the projects themselves are very visible, these models soon became largely popular. In a sort of virtuous cycle, the more researchers publish papers and journals based on these models, the more people are likely to use them, as they provide a sort of benchmark test-beds. In the interest of making the IlmProp a useful tool for the entire research community, at the beginning of 2006 we published part of the code on the Internet under the page `http://www.tu-ilmenau.de/ilmprop`. Since then, close to 50 people from numerous different institutions downloaded the MATLAB® implementation. In this number fall several students researching for their master theses, as well as senior researchers simply looking for a geometry-based channel model for frequency selective time

variant multi-user MIMO systems. The IlmProp became a project on which many people worked. Obviously, the biggest interest came from the Communications Research Lab where this work was written. Several graduate, undergraduate, and Ph.D. students worked on the development of the IlmProp, or simply became users. At the same time, we initiated several cooperations with different research centers and universities, most of which lead to successful publications.

# 6. CONCLUDING REMARKS

Due to the multi-path nature of the radio link, geometry-based channel models represent an ideal solution to represent the most relevant attributes of the channels.

When we investigate signal processing algorithms which are sensible to correlation in frequency, time, space, and between users, available directional channel models are incapable of representing realistically these features as they do not model their temporal evolution. Other models based on deterministic approaches involve a significant modeling effort in terms of computational complexity and, most importantly, in terms of the time needed to gather and input the geometrical information describing the environment.

The IlmProp is a flexible geometry-based channel modeling framework which copes with time variant frequency selective multi-user MIMO systems. It represents a trade-off between directional channel models and ray-tracers. The IlmProp allows multiple users to coexist in the same environment and models the Multi-Path Components (MPCs) explicitly by means of point-like Interacting Objects (IOs) placed in the three-dimensional space.

For geometry-based channel models it is crucial to model accurately and efficiently the far-field antenna radiation patterns. We have dealt in detail with this topic, proposing a novel descriptor based on the Discrete Vector Spherical Fourier Transform (DVSFT). This method allows us to describe the radiation patterns with higher accuracy than other known methods, as the DVSFT represents the natural Fourier domain for spherical problems. The proposed method leads to several novel applications, most of which are particularly beneficial in the antenna calibration stage, i.e., when the antenna radiation patterns are measured. We can filter the measurement noise in an optimal way and measure on sampling grids which comprise less points yet capturing the same information. When the DVSFT coefficients have been computed, we can express the radiation pattern in angular domain on any arbitrary coordinate system without loss of information. This is particular interesting as the antenna calibration step can be optimized regardless of the representation which will be used later for the application.

By modeling in detail the polarimetric radiation patterns, we can compare and evaluate different antenna arrays and array configurations under realistic conditions.

The IlmProp can be also used to improve the so-called Measurement-Based Parametric Channel Model (MBPCM) concept. The latter allows us to obtain realistic synthetic channels for antenna arrays, mobile trajectories, and frequency bandwidths other than the ones used during the measurement. This is possible thanks to an antenna independent double directional channel description. The proposed novel automatic localization algorithm, allows us

to estimate the complete trajectory of the propagation paths from high-resolution parameter estimates. With the knowledge of the position of the scatterers we can improve the MBPCM concept by exploiting the more accurate information on the paths' trajectories.

Moreover, the localization algorithm gives a powerful visualization tool to validate the channel measurements and the parameter estimator, as well as to gain a deeper understanding of the propagation conditions of the environment under study. This is possible thanks to a probability density function which expresses the probability that an IO is located at a certain position in three-dimensional space.

The localization algorithm and the improved MBPCM concept have been tested on synthetic and measured scenarios. The results show the correctness and applicability of the methods.

# Appendices

## Appendix A

# PROOFS AND DERIVATIONS

## A.1 Normalization Factor for the Symmetric PeBPDF

The integral over the whole model space of the Pencil Beam Pencil-Beam Probability Density Function (PeBPDF) defined in equation (5.72), must be equal to 1

$$\int_z \int_y \int_x \chi(x, y, z)\ \mathrm{d}x\ \mathrm{d}y\ \mathrm{d}z = 1. \tag{A.1}$$

Here we omit the variables $k$ and $t$ for simplicity. This integral can be expressed in the coordinate system used in equation (5.72) as

$$\int_\psi \int_\omega \int_\rho \chi(\rho, \omega, \psi)\ \Upsilon\ \mathrm{d}\rho\ \mathrm{d}\omega\ \mathrm{d}\psi = 1, \tag{A.2}$$

where the coordinate $\psi$ is the rotation with respect to the axis of symmetry of the PDF and $\Upsilon$ is the determinant of the Jacobian of the coordinate transformations as defined by the "Change of Variables Theorem" [113]. Without loss of generality we take a PeBPDF aligned on the $x$ axis, so that the two coordinate systems, namely $\{x, y, z\}$ and $\{\rho, \omega, \psi\}$ relate to each other as shown in Figure A.1. The coordinate transformations are

$$\begin{aligned} x &= \rho\ \cos(\omega) \\ y &= \rho\ \sin(\omega)\ \cos(\psi) \\ z &= \rho\ \sin(\omega)\ \sin(\psi), \end{aligned} \tag{A.3}$$

and $\Upsilon$ is

$$\Upsilon = \left| \frac{\partial(x, y, z)}{\partial(\rho, \omega, \psi)} \right| = \rho^2\ \sin(\omega). \tag{A.4}$$

Equation (A.2) can be cut into two parts as follows

$$\begin{aligned} \int_{-\pi}^{\pi} \int_{-\pi}^{\pi} \int_{a_{\max}}^{\infty} \gamma \cdot \mathrm{e}^{-\frac{\omega^2}{\sigma_\omega^2}} \cdot \mathrm{e}^{-\frac{(\rho - a_{\max})^2}{\sigma_\rho^2}}\ \Upsilon\ \mathrm{d}\rho\ \mathrm{d}\omega\ \mathrm{d}\psi + \\ + \int_{-\pi}^{\pi} \int_{-\pi}^{\pi} \int_{0}^{a_{\max}} \gamma \cdot \mathrm{e}^{-\frac{\omega^2}{\sigma_\omega^2}}\ \Upsilon\ \mathrm{d}\rho\ \mathrm{d}\omega\ \mathrm{d}\psi = 1. \end{aligned} \tag{A.5}$$

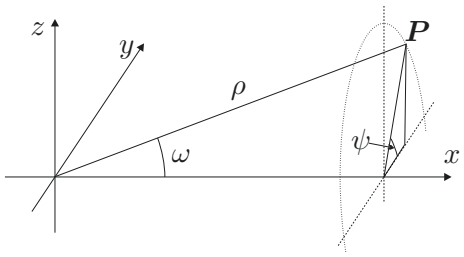


Fig. A.1: Relationship between the Cartesian coordinates $x$, $y$, and $z$ and $\rho$, $\omega$, and $\psi$, for a point in space $\boldsymbol{P}$.

Then, the factor $\gamma$ is computed by solving equation (A.5) with respect to $\gamma$

$$\begin{aligned} \gamma &= \frac{1}{\nu_1 + \nu_2} \\ \nu_1 &= \frac{\sqrt{\pi}}{2}\, a_{\max}^2\, \sigma_{\mathrm{DOA}} \cdot \operatorname{erf}\left(\frac{\pi}{\sigma_{\mathrm{DOA}}}\right) \\ \nu_2 &= \pi\, \sigma_\rho\, \sigma_{\mathrm{DOA}} \cdot \operatorname{erf}\left(\frac{\pi}{\sigma_{\mathrm{DOA}}}\right) \left(\pi a_{\max} + \sqrt{\pi}\sigma_\rho\right), \end{aligned} \tag{A.6}$$

where the error function $\operatorname{erf}(\alpha)$ is defined as

$$\operatorname{erf}(\alpha) = \frac{2}{\sqrt{\pi}} \int_0^\alpha \mathrm{e}^{-g^2} \mathrm{d}g. \tag{A.7}$$

## A.2 Normalization Factor for the Asymmetric PeBPDF

The integral over the whole model space of the Pencil Beam Pencil-Beam Probability Density Function (PeBPDF) defined in equation (5.73), must be equal to 1

$$\int_z \int_y \int_x \chi(x, y, z)\ \mathrm{d}x\ \mathrm{d}y\ \mathrm{d}z = 1. \tag{A.8}$$

Here we omit the variables $k$ and $t$ for simplicity. This integral can be expressed in the coordinate system shown in Figure A.2 as

$$\int_\psi \int_\omega \int_\rho \chi(\rho, \Delta\theta, \Delta\varphi)\ \Upsilon\ \mathrm{d}\rho\ \mathrm{d}\Delta\theta\ \mathrm{d}\Delta\varphi = 1, \tag{A.9}$$

where the segment of the PeBPDF runs from $\boldsymbol{A}$ to $\boldsymbol{B}$ and we compute in the general point $\boldsymbol{P}$. The term $\Upsilon$ is the determinant of the Jacobian of the coordinate transformations as defined by the "Change of Variables Theorem" [113].

Without loss of generality we can take the point $\boldsymbol{A}$ in the origin and $\varphi_{\mathrm{T}} = 0$, as depicted in Figure A.3.

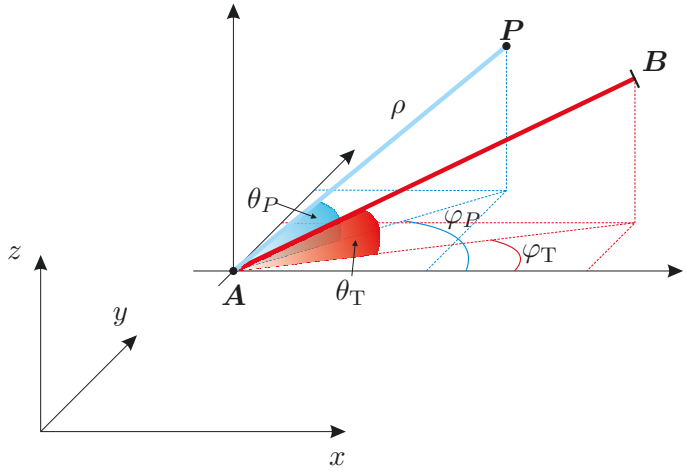


Fig. A.2: Relationship between the Cartesian coordinates $x$, $y$, and $z$ and $\Delta\varphi = \varphi_P - \varphi_\mathrm{T}$, $\Delta\theta = \theta_P - \theta_\mathrm{T}$ for a point in space $\boldsymbol{P}$ in case of an error with different variances in azimuth and elevation.

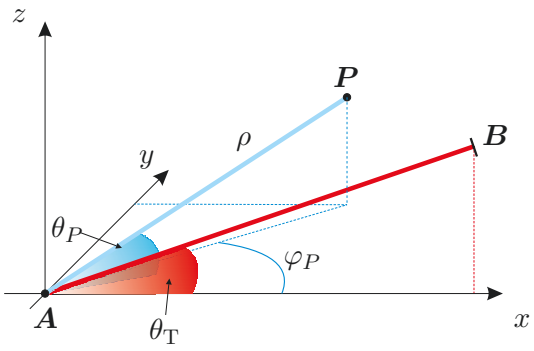


Fig. A.3: Relationship between the Cartesian coordinates $x$, $y$, and $z$ and $\Delta\varphi = \varphi_P$, $\Delta\theta = \theta_P - \theta_\mathrm{T}$ for a point in space $\boldsymbol{P}$ in case of an error with different variances in azimuth and elevation.

The coordinate transformations are

$$\begin{aligned} x &= \rho\ \cos(\Delta\theta + \theta_T)\ \cos(\Delta\varphi) \\ y &= \rho\ \cos(\Delta\theta + \theta_T)\ \sin(\Delta\varphi) \\ z &= \rho\ \sin(\Delta\theta + \theta_T), \end{aligned} \tag{A.10}$$

and $\Upsilon$ is

$$\Upsilon = \left| \frac{\partial(x, y, z)}{\partial(\rho, \Delta\theta, \Delta\varphi)} \right| = \rho^2\ \sin(\Delta\theta). \tag{A.11}$$

Equation (A.9) can be cut into two parts as follows

$$\int_{-\pi}^{\pi}\int_{-\frac{\pi}{2}}^{\frac{\pi}{2}}\int_{a_{\max}}^{\infty} \kappa \cdot \mathrm{e}^{-\frac{\Delta\theta^2}{\sigma_\theta^2}} \mathrm{e}^{-\frac{\Delta\varphi^2}{\sigma_\varphi^2}} \mathrm{e}^{-\frac{(\rho-a_{\max})^2}{\sigma_\rho^2}} \ \Upsilon \ \mathrm{d}\rho \ \mathrm{d}\Delta\vartheta \ \mathrm{d}\Delta\varphi + \\ + \int_{-\pi}^{\pi}\int_{-\frac{\pi}{2}}^{\frac{\pi}{2}}\int_{0}^{a_{\max}} \kappa \cdot \mathrm{e}^{-\frac{\Delta\theta^2}{\sigma_\theta^2}} \mathrm{e}^{-\frac{\Delta\varphi^2}{\sigma_\varphi^2}} \ \Upsilon \ \mathrm{d}\rho \ \mathrm{d}\Delta\vartheta \ \mathrm{d}\Delta\varphi = 1. \tag{A.12}$$

Then, the factor $\kappa$ is computed by solving equation (A.12) with respect to $\kappa$

$$\begin{aligned} \kappa &= \frac{24\, e^{\sigma_\theta^2/4}}{\kappa_1\, \kappa_2\, \kappa_3} \\ \kappa_1 &= \pi\, \sigma_\theta\, \sigma_\varphi\, \mathrm{erf}(\pi/\sigma_\varphi)\, \cos(\theta_P) \\ \kappa_2 &= \Re\left\{\mathrm{erf}\left(\frac{\pi - j.2\theta_P}{2\sigma_\theta}\right) + \mathrm{erf}\left(\frac{\pi + j.2\theta_P}{2\sigma_\theta}\right)\right\} \\ \kappa_3 &= 4\, a_{\max}^3 + 6\, a_{\max}^2 \sqrt{\pi}\sigma_\rho + 12\, a_{\max}\sigma_\rho^2 + 3\sqrt{\pi}\sigma_\rho^3 \cos(\theta_P) \end{aligned} \tag{A.13}$$

where the error function $\mathrm{erf}(\alpha)$ is defined as

$$\mathrm{erf}(\alpha) = \frac{2}{\sqrt{\pi}} \int_0^{\alpha} \mathrm{e}^{-g^2} \mathrm{d}g. \tag{A.14}$$

Notice that equation (A.13) requires that we compute the erf function of a complex argument. In general, we would need to define a curve on the complex plane on which to compute the integral in equation (A.14). However, the integrated functions are complex analytical functions and we can therefore solve the integral by means of their Taylor series without specifying any curve in the complex plane. This can be carried out with the approximation given in [103, p. 299] as

$$\Re\left\{\mathrm{erf}(\alpha + j\beta)\right\} \simeq \mathrm{erf}(\alpha) + \frac{\mathrm{e}^{-\alpha^2}}{2\pi\alpha}\left(1 - \cos(2\alpha\beta)\right) + \frac{2}{\pi}\mathrm{e}^{-\alpha^2} \sum_{n=1}^{32} \frac{\mathrm{e}^{-n^2/4}}{n^2 + 4\alpha^2} f_n(\alpha, \beta),$$

where

$$f_n(\alpha, \beta) = 2\alpha - 2\alpha \cosh(n\beta) \cdot \cos(2\alpha\beta) + n \sinh(n\beta) \cdot \sin(2\alpha\beta).$$

Appendix B

# MATHEMATICAL OPERATORS AND THEIR PROPERTIES

This appendix deals with several mathematical operators and their properties.

## B.1 The Kronecker Product

Let the symbol $\otimes$ represent the Kronecker product. Then, according to [52], the following property holds:

$$(\boldsymbol{A} \otimes \boldsymbol{B}) \otimes \boldsymbol{C} = \boldsymbol{A} \otimes (\boldsymbol{B} \otimes \boldsymbol{C}) \tag{B.1}$$

$$\mathrm{vec}(\boldsymbol{A} \cdot \boldsymbol{B} \cdot \boldsymbol{C}) = (\boldsymbol{C}^{\mathrm{T}} \otimes \boldsymbol{A}) \cdot \mathrm{vec}(\boldsymbol{B}) \tag{B.2}$$

## B.2 The Cross Product

The cross product between the vectors $\boldsymbol{a}$ and $\boldsymbol{b}$ is denoted as

$$\boldsymbol{c} = \boldsymbol{a} \times \boldsymbol{b}.$$

The resulting vector $\boldsymbol{c}$ is defined as the vector which is perpendicular to both $\boldsymbol{a}$ and $\boldsymbol{b}$ with a magnitude equal to the area of the parallelogram they span, i.e.,

$$\|\boldsymbol{c}\| = \|\boldsymbol{a}\| \, \|\boldsymbol{b}\| \sin(\theta).$$

The angle $\theta$ and the direction of $\boldsymbol{c}$ are displayed in Figure B.1.

## B.3 The Kronecker Delta Symbol

The Kronecker delta symbol, denoted by $\delta_{m,n}$, is defined as

$$\delta_{m,n} = \begin{cases} 1 & \text{for } m = n \\ 0 & \text{otherwise.} \end{cases} \tag{B.3}$$

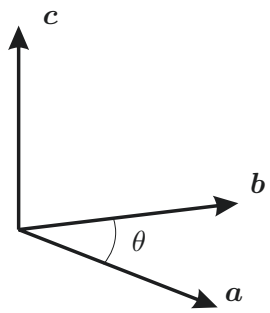


Fig. B.1: Visualization of the cross product $\boldsymbol{c} = \boldsymbol{a} \times \boldsymbol{b}$

The variables $m$ and $n$ can be defined in any domain.

Appendix C

# QUADRATURES ON THE SPHERE

The non trivial problem of approximating a continuous integral numerically is known in science as *quadrature* or *cubature* [71, pp. 561–615]. In Section C.1 we state the general problem for integrals of univariate functions. In Section C.2 we introduce three different types of quadratures on the sphere. The latter are essential for applying the Discrete Vector Spherical Fourier Transform (DVSFT) on measured radiation patterns (see Section 4.4.3).

## C.1 The Quadrature Problem for Univariate Functions

A continuous definite integral is approximated as follows

$$\int_I f(x)\,\mathrm{d}x \approx \sum_{i=0}^{N} f(x_i)\,w_i \ , \tag{C.1}$$

where the value of the function $f(x)$ is known at the $N+1$ values $x_i$, which we call the *quadrature points*. The term $w(x_i)$ represents the *quadrature weights*. The integration interval is denoted by $I$. The quadrature problem consists in finding optimal quadrature points and their corresponding quadrature weights.

Following the approach given in [71], we now require the approximation in equation (C.1) to be exact on the interval $I = [a, b]$ for monomials $x^m$ of degree $m = 0,\ 1,\ 2,\ \ldots,\ M$, so that $M \geq N$

$$\int_I x^m\,\mathrm{d}x \ \stackrel{!}{=}\ \sum_{i=0}^{N} x_i^m\,w_i \ . \tag{C.2}$$

We can now solve analytically the integral in (C.2) as

$$\int_a^b x^m\,\mathrm{d}x = \frac{1}{m+1}\left(b^{m+1} - a^{m+1}\right), \tag{C.3}$$

which leads to the following

$$\sum_{i=0}^{N} x_i^m\,w_i = \frac{1}{m+1}\left(b^{m+1} - a^{m+1}\right) \ , \quad m = 0, 1, \ldots, M \ . \tag{C.4}$$

By solving equation (C.4) we obtain the quadrature points $x_i$ and weights $w_i$ which allow us to compute exactly the desired integral up to degree $M$ numerically. The quadrature which possesses the minimum number of points is the Gaussian quadrature, which, as proved in [162], is capable of integrating polynomials up to degree $M = 2N + 1$. In the literature there exist several quadrature rules, such as the Newton-Cotes quadrature, the MacLaurin quadrature rules, the Euler-Maclaurin quadrature rules, and the Chebyshev quadrature [162].

## C.2 Quadratures for the 2-Sphere

When dealing with functions on the unit sphere $\mathcal{S}^2$ (also referred to as the 2-sphere), the problem given in equation (C.1) changes to

$$\int_{\mathcal{S}^2} f(\vartheta, \varphi)\, \mathrm{d}\Omega \approx \sum_{i=0}^{N-1} f(\vartheta_i, \varphi_i)\, w_i \ , \tag{C.5}$$

where the function $f$ is known at the quadrature points given by $\vartheta_i$ and $\varphi_i$, and $w_i$ are the quadrature weights. The quadrature points can be organized in a regular lattice. In this case we can rewrite equation (C.5) as two sums, one for the co-elevation $\vartheta$ and one for azimuth $\varphi$

$$\int_{\mathcal{S}^2} f(\vartheta, \varphi)\, \mathrm{d}\Omega \approx \sum_{u=0}^{N_u-1} w_u \sum_{v=0}^{N_v-1} w_v\, f(\vartheta_u, \varphi_v) = \sum_{v=0}^{N_v-1} w_v \sum_{u=0}^{N_u-1} w_u\, f(\vartheta_u, \varphi_v). \tag{C.6}$$

The weights can be computed separately along $\vartheta$ and $\varphi$ and do not depend on each other. This makes it possible to use two simpler univariate quadrature formulas separately for the two variables.

### C.2.1 Quadratures for Spherical Harmonics

In this work we use quadratures for integrating Vector Spherical Harmonics (VSHs) (see Section 4.4.2) on the 2-sphere. The VSHs can be separated in $\vartheta$ and $\varphi$, as evident in equation (4.41). In this section we introduce two quadratures which take advantage of this fact, namely the *Chebyshev* and *Gauss-Legendre* quadratures, and a third quadrature, proposed by *Lebedev*.

#### C.2.1.1 Chebyshev Quadrature

The Chebyshev quadrature rule [195] requires a uniform sampling in both co-elevation $\vartheta$ and azimuth $\varphi$. Due to its simplicity, this sampling grid is used frequently, e.g., in antenna radiation pattern measurements. Let $\mathscr{G}_{\mathrm{Ch}}^{(M)}$ define the grid points of the Chebyshev grid of

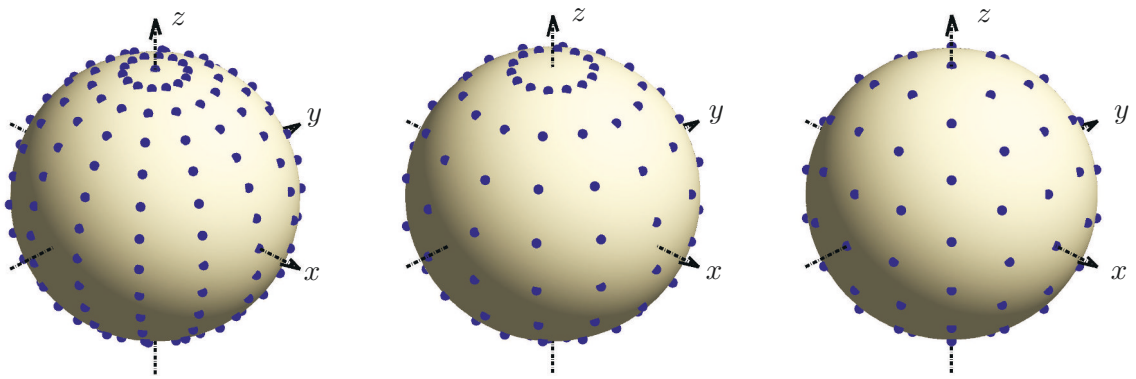


(a) Chebyshev (b) Gauss-Legendre (c) Lebedev

Fig. C.1: Quadrature grids on the sphere.

order $M$, i.e., to integrate polynomials exactly up to degree $M$, as follows

$$\mathscr{G}_{\mathrm{Ch}}^{(M)} = \Bigg\{ (\vartheta_u, \varphi_v) \;:\; \vartheta_u = \frac{\pi u}{M-1};\; \varphi_v = \frac{2\pi v}{M-1}; \\ u, v \in \mathbb{Z};\; u \in [0,\; M-1];\; v \in \left[ -\frac{M-1}{2}, \frac{M-1}{2} \right) \Bigg\} \;, \tag{C.7}$$

where $M$ can only assume odd values. This grid is named Chebyshev since the cosine of the sampling points in co-elevation $\cos(\vartheta_u)$ are the zeros of the Chebyshev polynomial of order $M$. The total number of samples is $N_{\mathrm{Ch}} = M \times (M-1)$, with sampling intervals $\Delta\vartheta = \frac{\pi}{M-1}$ and $\Delta\varphi = \frac{2\pi}{M-1}$. Thus, when integrating VSHs, we can correctly compute the spherical modes[1] $m$ between $-\frac{M-1}{2}$ and $\frac{M-1}{2}$. Figure C.1(a) shows the Chebyshev grid of order $M = 15$ ($N_{\mathrm{Ch}} = 210$). The quadrature weights are calculated as

$$w_{u,\mathrm{Ch}}^{(M)} = \varepsilon_u^{(M-1)} \frac{4\pi}{M-1} \sum_{s=0}^{(M-1)/2} \varepsilon_u^{((M-1)/2)} \frac{2}{1-4s^2} \cos\left( \frac{us\,2\pi}{M-1} \right) \;, \tag{C.8}$$

$$w_{v,\mathrm{Ch}}^{(M)} = \frac{1}{M-1} \;, \tag{C.9}$$

where

$$\varepsilon_u^{(M)} = \begin{cases} 0.5 & \text{for } u = 0, M \\ 1 & \text{for } u = 1, 2, \ldots, M-1 \;. \end{cases} \tag{C.10}$$

Note that the weights $w_{v,\mathrm{Ch}}^{(M)}$ are equal for all azimuths. The quadrature problem given in (C.6) can be solved as

$$\int_{\mathcal{S}^2} f(\vartheta, \varphi)\, \mathrm{d}\Omega \approx \sum_{u=0}^{M} w_{u,\mathrm{Ch}}^{(M)} \sum_{v=-(M-1)/2}^{(M-3)/2} w_{v,\mathrm{Ch}}^{(M)}\, f(\vartheta_u, \varphi_v) \;, \tag{C.11}$$

[1] See Section 4.4.2 .

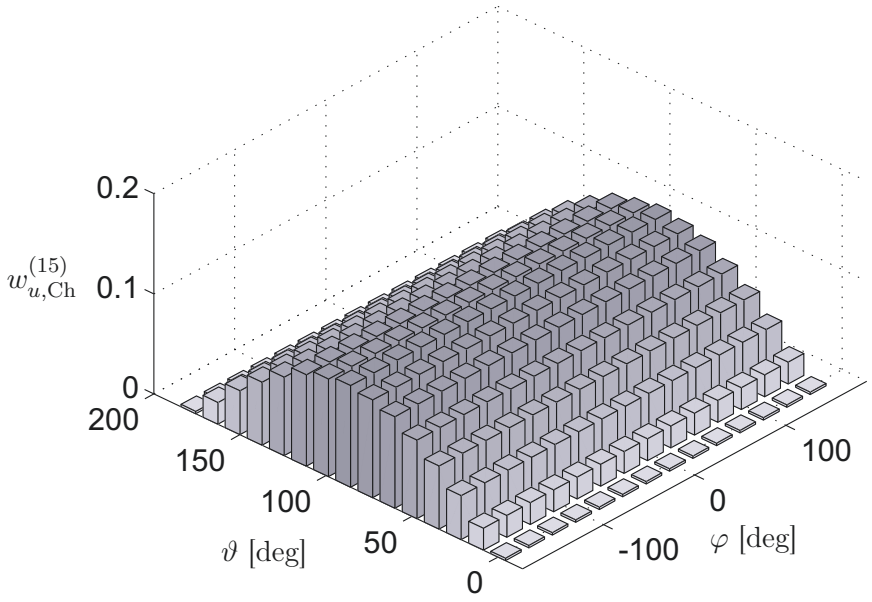


Fig. C.2: Chebyshev weights along azimuth $\varphi$ and co-elevation $\vartheta$ for $M = 15$.

where $\{\vartheta_u, \varphi_v\} \in \mathscr{G}^{(M)}_{\mathrm{Ch}}$. Using (C.9), the above equation simplifies to

$$\int_{\mathcal{S}^2} f(\vartheta, \varphi)\, \mathrm{d}\Omega \approx \frac{1}{M-1} \sum_{u=0}^{M} w^{(M)}_{u,\mathrm{Ch}} \sum_{v=-(M-1)/2}^{(M-3)/2} f(\vartheta_u, \varphi_v)\ . \tag{C.12}$$

The weights $w^{(M)}_{u,\mathrm{Ch}}$ along azimuth and co-elevation are depicted in Figure C.2 for $M = 15$, i.e., for 15 samples in $\vartheta$ and 13 in $\varphi$.

#### C.2.1.2 Gauss-Legendre Quadrature

The Gauss-Legendre quadrature [195] requires the function to be sampled at the zeros of the Legendre polynomials of order $(M+1)/2$ in elevation and uniformly in azimuth. Let $\mathscr{G}^{(M)}_{\mathrm{GL}}$ define the grid points of the Gauss-Legendre grid of order $M$ as

$$\mathscr{G}^{(M)}_{\mathrm{GL}} = \Bigg\{ (\vartheta_u, \varphi_v) \ :\ \vartheta_u = \arccos\left(z_u^{\left(\frac{M-1}{2}\right)}\right);\ \varphi_v = \frac{2\pi v}{M-1}; \\ u, v \in \mathbb{Z};\ u \in \left[0, \frac{M-1}{2}\right];\ v \in \left[-\frac{M-1}{2}, \frac{M-1}{2}\right) \Bigg\}\ , \tag{C.13}$$

where $z^{(i)}_u$ are the zeros of the Legendre polynomial of order $i+1$. The order $M$ is the maximum degree of the polynomials integrated exactly and can only posses odd integer values. The total number of samples is $N_{\mathrm{GL}} = \frac{M+1}{2} \times (M-1)$. The sampling interval in $\varphi$ is the same as for the Chebyshev quadrature, $\Delta\varphi = \frac{2\pi}{M-1}$, thus, we can compute the spherical modes $m$ of the

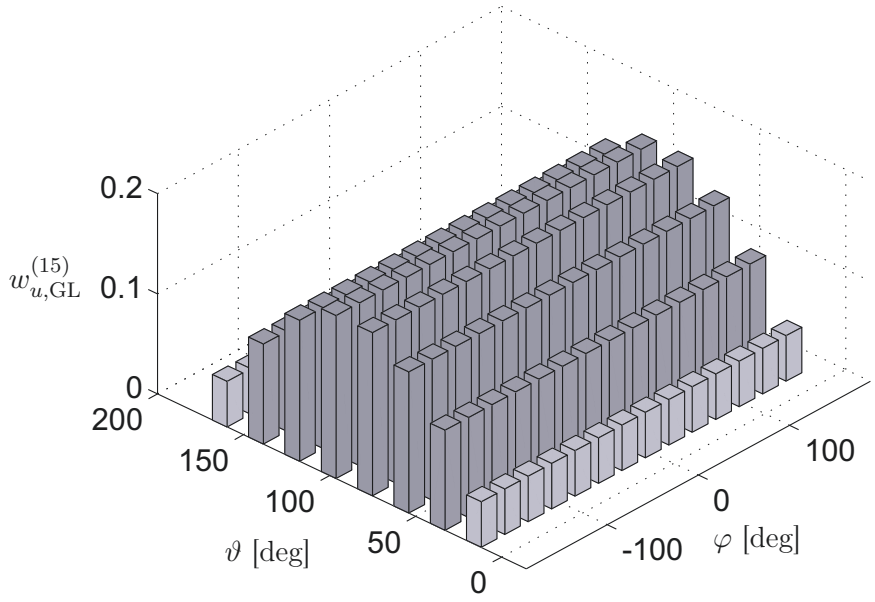


Fig. C.3: Gauss-Legendre weights along azimuth $\varphi$ and co-elevation $\vartheta$ for $M = 15$.

VSHs[2] between $-\frac{M-1}{2}$ and $\frac{M-1}{2}$ correctly[3]). Note that the Gauss-Legendre grid does not incorporate any sample at the poles. Figure C.1(b) shows the Gauss-Legendre grid of order $M = 15$ ($N_{\mathrm{GL}} = 112$). The quadrature weights along the longitudes $w^{(M)}_{u,\mathrm{GL}}$ can be computed with the well-known Gaussian quadrature rule [71], while the weights along the latitudes are the same as for the Chebyshev quadrature, i.e.,

$$w^{(M)}_{v,\mathrm{GL}} = \frac{1}{M-1} \,. \tag{C.14}$$

Finally, the quadrature problem (C.6) can be solved using the Gauss-Legendre quadrature as

$$\int_{\mathcal{S}^2} f(\vartheta,\varphi)\,\mathrm{d}\Omega \approx \sum_{u=0}^{(M-1)/2} w^{(M)}_{u,\mathrm{GL}} \sum_{v=-(M-1)/2}^{(M-3)/2} w^{(M)}_{v,\mathrm{GL}}\, f(\vartheta_u,\varphi_v) \,, \tag{C.15}$$

where $(\vartheta_u,\varphi_v) \in \mathscr{G}^{(M)}_{\mathrm{GL}}$. Using (C.14), we can simplify (C.15) to

$$\int_{\mathcal{S}^2} f(\vartheta,\varphi)\,\mathrm{d}\Omega \approx \frac{1}{M-1} \sum_{u=0}^{(M-1)/2} w^{(M)}_{u,\mathrm{GL}} \sum_{v=-(M-1)/2}^{(M-3)/2} f(\vartheta_u,\varphi_v) \,. \tag{C.16}$$

Figure C.3 shows the weights of the Gaussian quadrature along co-elevation for quadrature order $M = 15$, i.e., 8 sampling points in $\vartheta$ and 14 in $\varphi$.

[2] See Section 4.4.2.
[3] When VSHs are integrated, we have a standard Fourier transform along azimuth.

Tab. C.1: Comparison of the Chebyshev, Gauss-Legendre, and Lebedev quadratures

| $M$ | $L$ | $N_{\mathrm{Ch}}$ | $N_{\mathrm{GL}}$ | $N_{\mathrm{Lb}}$ |
|---|---|---|---|---|
| 5 | 10 | 20 | 12 | 14 |
| 15 | 30 | 210 | 112 | 68 |
| 31 | 62 | 930 | 480 | 350 |
| 59 | 118 | 3422 | 1740 | 1202 |
| 131 | 262 | 17030 | 8580 | 5810 |

#### C.2.1.3 Lebedev Quadrature

If we do not force the quadrature points to lie on a lattice separable in $\vartheta$ and $\varphi$, one intuitive grid would be a uniform sampling on the sphere, meaning that each point has the same distance to its nearest neighbors. Euclid, in 300 BC, has shown that there exist only five of such grids, usually called *Platonic bodies*. The platonic body with the largest number of vertices is the dodecahedron [225], which, as the name suggests, possesses 20 vertices. This number is unfortunately too low to obtain an exhaustive description of a radiation pattern. The Lebedev grid [142, 143, 144, 147, 145, 146] approaches an ideal uniform distribution of samples by choosing points symmetrically to an octahedron. Figure C.1(c) shows the Lebedev grid with $N_{\mathrm{Lb}} = 86$ points ($M = 15$). The variables $\vartheta$ and $\varphi$ cannot be treated separately, but rather only as pairs $\{\vartheta_u, \varphi_u\}$. Finding the quadrature weights for this grid is rather complicated and no general formula can be given. There exists a Fortran code [228] which generates Lebedev grids and the corresponding weights up to order $M = 131$. The Lebedev grids only exist for orders $M$ between 3 and 31 in increments of 2 and between 35 and 131 in increments of 6 [218]. The order $M$ is the maximum degree of the polynomials which are integrated exactly. The number of points of the Lebedev grid can be approximated with

$$N_{\mathrm{Lb}} \approx \frac{(M+1)^2}{3} \,. \tag{C.17}$$

We denote the set of grid points of the Lebedev grid of order $M$ with $\mathscr{G}_{\mathrm{Lb}}^{(M)}$, and the corresponding weights with $w_{s,\mathrm{Lb}}^{(M)}$. The quadrature problem (C.5) can be written as

$$\int_{\mathcal{S}^2} f(\vartheta,\varphi)\,\mathrm{d}\Omega \approx \sum_{s=0}^{N_{\mathrm{Lb}}-1} f(\vartheta_s,\varphi_s)\, w_{s,\mathrm{Lb}}^{(M)} \,, \tag{C.18}$$

where $\{\vartheta_s, \varphi_s\} \in \mathscr{G}_{\mathrm{Lb}}^{(M)}$. Figure C.4 shows the Lebedev weights for a grid of order $M = 15$ over azimuth $\varphi$ and co-elevation $\vartheta$. It can be seen that the weights differ only slightly (not as much as with the Chebyshev or Gauss-Legendre quadratures). This is expected, given the almost equal support areas of the sampling points on the sphere. If there existed larger platonic bodies, given the symmetries displayed, we would expect equal weights for all points.

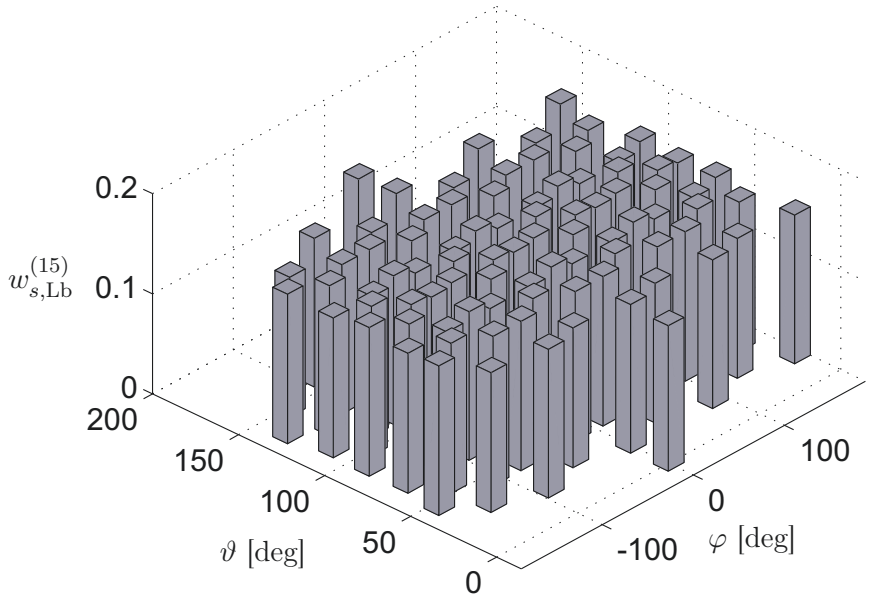


Fig. C.4: Lebedev weights along azimuth $\varphi$ and co-elevation $\vartheta$ for $M = 15$.

#### C.2.1.4 Comparison of the Different Quadratures

When the quadratures here introduced are used to integrate VSHs, as discussed in Section 4.4.3, for a grid order $M$ we can cope with VSHs with level $l \leq L$, where $L = 2M$. Table C.1 shows the number of required sampling points for the three quadratures with respect to selected grid orders $M$, which is the maximum degree of the polynomials integrated exactly. On page 225, a complete version of Table C.1 is given, with all orders $M$ between 3 and 131 for which the Lebedev grid exists. The relationship between the number of sampling points for different quadratures for any given order $M$ can be approximated as

$$N_{\mathrm{Ch}} \approx 2N_{\mathrm{GL}} \approx 3N_{\mathrm{Lb}}. \tag{C.19}$$

The simplest grid for measurements is the Chebyshev grid, since sampling both angles uniformly enables very accurate positioning of the measurement probe with a step motor. Additionally, due to the uniform sampling, it permits the application of 2-D FFT based techniques (see Section 4.3) for analyzing and storing the sampled data. However, it is the most inefficient quadrature grid with respect to the required number of samples if spherical integration has to be performed.

The Gauss-Legendre grid is the optimal solution if both angles should be separable since the Gauss quadrature along elevation is optimal[4] [71]. It needs approximately half the points of the Chebyshev quadrature, but the sampled data can be stored in a matrix and processed

[4] With *optimal* we mean that it is impossible to exactly compute integrals of polynomials up to a degree $M$ with less sampling points than the ones required for the Gauss quadrature.

separately on $\vartheta$ and $\varphi$. However, more sampling points on the sphere than with the Lebedev grid are required.

The Lebedev quadrature is the only truly bivariate quadrature. The weights are given explicitly for each sampling point on the sphere and cannot be separated into weights along azimuth and weights along elevation. This results in less sampling points than the other grids, which is the major advantage. However, processing both angles separately has a significantly lower computational complexity than processing them jointly (see (C.5) and (C.6) in comparison). Therefore, although there are less sampling points, solving integrals on the sphere using the Lebedev quadrature might have a higher computational complexity than using one of the other quadratures.

| $M$ | $L$ | $N_{\mathrm{Ch}}$ | $N_{\mathrm{GL}}$ | $N_{\mathrm{Lb}}$ | $N_{\mathrm{GL}}/N_{\mathrm{Ch}}$ | $N_{\mathrm{Lb}}/N_{\mathrm{Ch}}$ | $N_{\mathrm{Lb}}/N_{\mathrm{GL}}$ |
|---|---|---|---|---|---|---|---|
| 3 | 1 | 6 | 4 | 6 | 66.67% | 100.00% | 150.00% |
| 5 | 2 | 20 | 12 | 14 | 60.00% | 70.00% | 116.67% |
| 7 | 3 | 42 | 24 | 26 | 57.14% | 61.90% | 108.33% |
| 9 | 4 | 72 | 40 | 38 | 55.56% | 52.78% | 95.00% |
| 11 | 5 | 110 | 60 | 50 | 54.55% | 45.45% | 83.33% |
| 13 | 6 | 156 | 84 | 74 | 53.85% | 47.44% | 88.10% |
| 15 | 7 | 210 | 112 | 86 | 53.33% | 40.95% | 76.79% |
| 17 | 8 | 272 | 144 | 110 | 52.94% | 40.44% | 76.39% |
| 19 | 9 | 342 | 180 | 146 | 52.63% | 42.69% | 81.11% |
| 21 | 10 | 420 | 220 | 170 | 52.38% | 40.48% | 77.27% |
| 23 | 11 | 506 | 264 | 194 | 52.17% | 38.34% | 73.48% |
| 25 | 12 | 600 | 312 | 230 | 52.00% | 38.33% | 73.72% |
| 27 | 13 | 702 | 364 | 266 | 51.85% | 37.89% | 73.08% |
| 29 | 14 | 812 | 420 | 302 | 51.72% | 37.19% | 71.90% |
| 31 | 15 | 930 | 480 | 350 | 51.61% | 37.63% | 72.92% |
| 35 | 17 | 1190 | 612 | 434 | 51.43% | 36.47% | 70.92% |
| 41 | 20 | 1640 | 840 | 590 | 51.22% | 35.98% | 70.24% |
| 47 | 23 | 2162 | 1104 | 770 | 51.06% | 35.62% | 69.75% |
| 53 | 26 | 2756 | 1404 | 974 | 50.94% | 35.34% | 69.37% |
| 59 | 29 | 3422 | 1740 | 1202 | 50.85% | 35.13% | 69.08% |
| 65 | 32 | 4160 | 2112 | 1454 | 50.77% | 34.95% | 68.84% |
| 71 | 35 | 4970 | 2520 | 1730 | 50.70% | 34.81% | 68.65% |
| 77 | 38 | 5852 | 2964 | 2030 | 50.65% | 34.69% | 68.49% |
| 83 | 41 | 6806 | 3444 | 2354 | 50.60% | 34.59% | 68.35% |
| 89 | 44 | 7832 | 3960 | 2702 | 50.56% | 34.50% | 68.23% |
| 95 | 47 | 8930 | 4512 | 3074 | 50.53% | 34.42% | 68.13% |
| 101 | 50 | 10100 | 5100 | 3470 | 50.50% | 34.36% | 68.04% |
| 107 | 53 | 11342 | 5724 | 3890 | 50.47% | 34.30% | 67.96% |
| 113 | 56 | 12656 | 6384 | 4334 | 50.44% | 34.24% | 67.89% |
| 119 | 59 | 14042 | 7080 | 4802 | 50.42% | 34.20% | 67.82% |
| 125 | 62 | 15500 | 7812 | 5294 | 50.40% | 34.15% | 67.77% |
| 131 | 65 | 17030 | 8580 | 5810 | 50.38% | 34.12% | 67.72% |

Appendix D

# TENSOR CALCULUS

This chapter introduces the notation and some basics properties of tensors. The theory presented here is mostly based on didactic papers by de Lathauwer *et al.* [65, 66, 67].

Table D.1 summarizes the notation used to distinguish between scalars, vectors, matrices, and tensors

| Symbols | Description |
|---|---|
| $a,\ b,\ c$ | scalar |
| $\boldsymbol{a},\ \boldsymbol{b},\ \boldsymbol{c}$ | column vector |
| $\boldsymbol{A},\ \boldsymbol{B},\ \boldsymbol{C}$ | matrix |
| $\boldsymbol{\mathcal{A}},\ \boldsymbol{\mathcal{B}},\ \boldsymbol{\mathcal{C}}$ | tensors |
| $(\boldsymbol{\mathcal{A}})_{i_1,i_2,\ldots,i_N}$ | element of a tensor |

Tab. D.1: Notation used in this chapter.

Vectors and matrices are denoted by lower and upper case boldface letters, respectively, whereas tensors are denoted by boldface calligraphic upper case letters.

## D.1 The $n$–mode Vectors

In the matrix case we distinguish between row and column vectors. Their straightforward extension to tensors is given by the $n$–mode vectors of a $N$-th order tensor $\boldsymbol{\mathcal{A}} \in \mathbb{C}^{I_1 \times I_2 \times \cdots \times I_N}$, where $I_n$ is the size in the $n$-th dimension.

They are defined as the $I_n$-dimensional vectors obtained from $\boldsymbol{\mathcal{A}}$ by varying the index $i_n$ and keeping the other indices fixed. In Figure D.1, this is shown for a three-dimensional (3D) tensor. Please note that in general there are $\prod_{i=1}^{N} I_i$ such vectors. In the two-dimensional (2D) case the column vectors are equal to the 1-mode vectors, and the row vectors are equal to the 2-mode vectors.

**Definition D.1.1.** Assume a $N$-th order tensor $\boldsymbol{\mathcal{A}} = \{a_{i_1,i_2,\ldots,i_N}\} \in \mathbb{C}^{I_1 \times I_2 \times \cdots \times I_N}$. The $n$–mode vectors $\{\boldsymbol{a}_n\}$, each of dimension $I_n$, are built by varying the index $i_n$ of $\{a_{i_1,i_2,\ldots,i_n,\ldots,i_N}\}$ while keeping the other indices fixed.

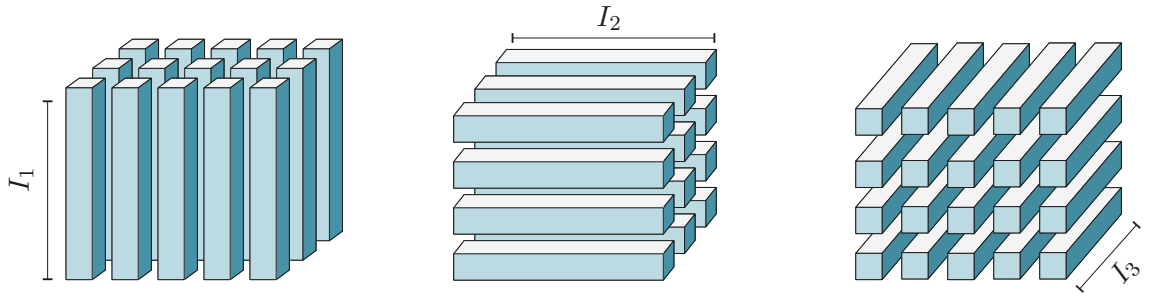


Fig. D.1: For a 3D tensor of size $I_1 \times I_2 \times I_3$ the plots show: (a) 1-mode vectors, (b) 2-mode vectors, and (c) 3-mode vectors.

## D.2 Matrix Representations

As we discuss in the following sections, it is useful to define 2D matrix representations of an arbitrary $N$-th order tensor $\boldsymbol{\mathcal{A}}$. We refer to these representations as *matrix unfoldings*. To create such an unfolding, we stack all $n$-mode vectors of a $N$-th order tensor one after the other. This procedure is shown in Figure D.2 for a 3D tensor. Clearly there are $N$ different matrix unfoldings. Note that the exact ordering of the stacked $n$-mode vectors is irrelevant for the properties presented in this chapter.

**Definition D.2.1.** Assume a $N$-th order tensor $\boldsymbol{\mathcal{A}} \in \mathbb{C}^{I_1 \times I_2 \times \cdots \times I_N}$. Then the $n$-th unfolding $\boldsymbol{\mathcal{A}}_{(n)}$ is the matrix, consisting of all $n$-mode vectors $\{\boldsymbol{a}_n\}$, and

$$\boldsymbol{\mathcal{A}}_{(n)} \in \mathbb{C}^{I_n \times \prod_{\substack{i=1 \\ i \neq n}}^{N} I_i}$$

Their ordering for the computation of the Higher Order Singular Value Decomposition (HOSVD) is irrelevant.

A special case is represented by the $(N+1)$-th unfolding. In this case the index which is kept fix is $i_{N+1}$ which can only be equal to 1, as this dimension is singleton. All elements of the tensor are then stacked in a row vector of size $1 \times I_1 \cdot \ldots \cdot I_N$.

As mentioned above, the ordering of the $n$-mode vectors is irrelevant for the computation of the HOSVD (dealt in Section D.5.2). Nonetheless, for other representations a precise definition of the unfoldings is necessary. We now introduce two unfoldings. The first one is by de Lathauwer *et al.* [65, 66, 67], whereas the second is new.

### D.2.1 The de Lathauwer Unfolding

Assume a tensor $\boldsymbol{\mathcal{A}} = \{a_{i_1,i_2,\ldots i_N}\} \in \mathbb{C}^{I_1 \times \cdots \times I_N}$. The unfolding is defined as

$$\boldsymbol{\mathcal{A}}_{(n)} = \{a_{j,k}\} \in \mathbb{C}^{I_n \times (I_1 \cdots I_{n-1} I_{n+1} \cdots I_N)}, \tag{D.1}$$

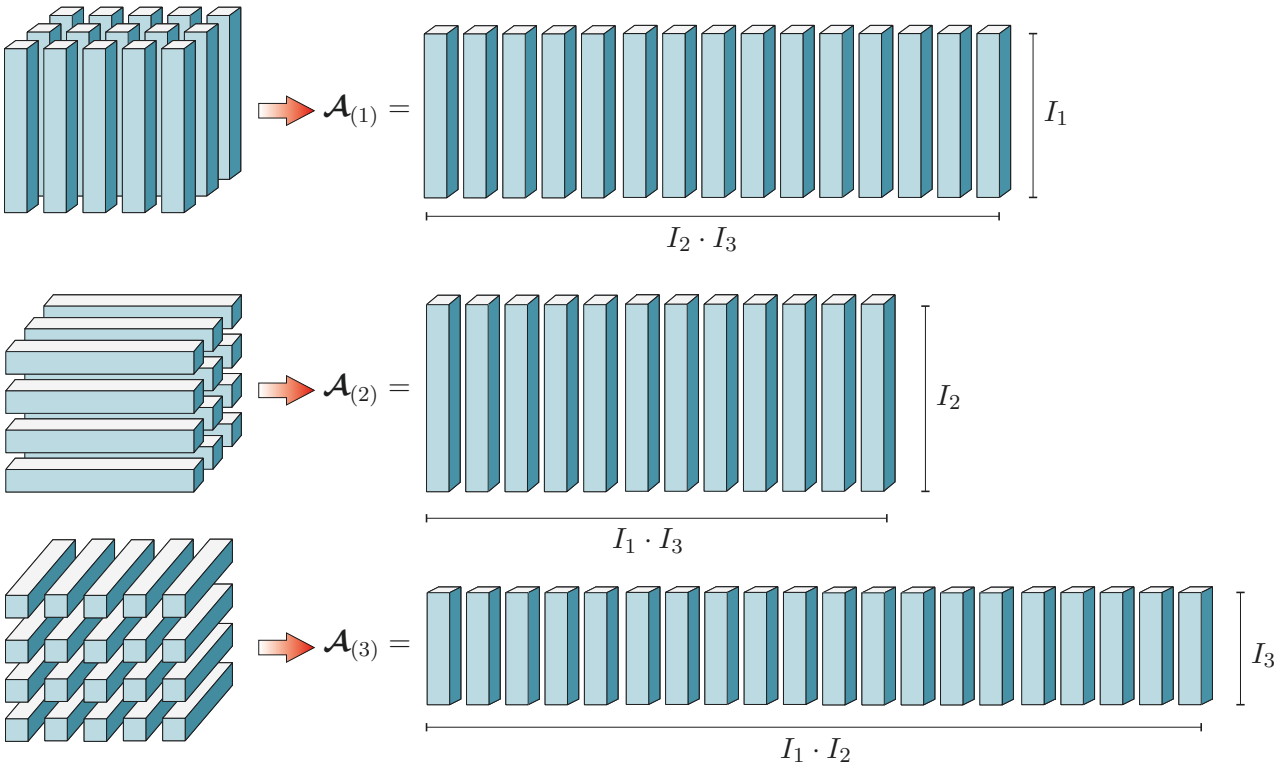


Fig. D.2: Matrix unfoldings of a 3D tensor.

where

$$\begin{aligned} j &= i_n \\ k &= 1 + \sum_{l=n+1}^{N} (i_L - 1) \prod_{q=1}^{n-1} I_q \prod_{p=l+1}^{N} I_p + \sum_{l=1}^{n-1} \prod_{q=l+1}^{n-1} I_q. \end{aligned} \tag{D.2}$$

The indices vary in the following cyclic order

$$i_{n-1}, i_{n-2}, \ldots, i_1, i_N, i_{N-1}, \ldots, i_{n+1}. \tag{D.3}$$

### D.2.2 The MATLAB-like Unfolding

This unfolding, apparently unknown in the literature is very similar to the one proposed by de Lathauwer. The main difference is that it is more intuitive and it is consistent with the MATLAB® command `reshape`. It is denoted by

$$\mathcal{A}_{[n]} \in \mathbb{C}^{I_n \times \prod_{\substack{i=1 \\ i \neq n}}^{N} I_i},$$

and it is defined as

$$\mathcal{A}_{[n]} = \{a_{j,k}\} \in \mathbb{C}^{I_n \times (I_1 I_2 \cdots I_{n-1} I_{n+1} I_{n+2} \cdots I_N)},$$

with $j = i_n$ and

$$k = 1 + \sum_{l=1, l\neq n}^{N} (i_L - 1) \cdot \prod_{q=1, q\neq n}^{l-1} I_q \, .$$

This definition assures that the indices of the $n$–mode vectors vary faster in the following ascending order

$$i_1, i_2, \ldots, i_{n-1}, i_{n+2}, \ldots, i_N \, . \tag{D.4}$$

This ordering becomes particularly important for our later derivations. The $N+1$ unfolding, as mentioned above, is a row vector of size $1 \times I_1 \cdot \ldots \cdot I_N$. Interestingly, we have that

$$\boldsymbol{\mathcal{A}}^{\mathrm{T}}_{[N+1]} = \mathrm{vec}\,\{\boldsymbol{\mathcal{A}}\}\,, \tag{D.5}$$

where $\mathrm{vec}\,\{\cdot\}$ is the so-called *vector operator*, which is implemented in MATLAB® with the simple command

```
A(:),
```
(D.6)

where `A` is the multi-dimensional array containing the elements of the tensor $\boldsymbol{\mathcal{A}}$.

**Definition D.2.2.** Assume a $N$-th order tensor $\boldsymbol{\mathcal{A}} \in \mathbb{C}^{I_1 \times I_2 \times \cdots \times I_N}$. Then the $n$-th unfolding $\boldsymbol{\mathcal{A}}_{(n)}$ is the matrix, consisting of all $n$-mode vectors $\{\boldsymbol{a}_n\}$, and

$$\boldsymbol{\mathcal{A}}_{(n)} \in \mathbb{C}^{I_n \times \prod_{\substack{i=1 \\ i\neq n}}^{N} I_i}$$

Their ordering is irrelevant.

## D.3 Tensor Operators

In the following we will define all operations that will be necessary for dealing with tensors. Notice that the multiplication of a tensor with a scalar, as well as the addition and subtraction of tensors with the same size have to be carried out element-wise, analogously to the vector and matrix case.

### D.3.1 The Concatenation Operator

While matrices can be either stacked on top of each other, or side by side, with $N$-th order tensors we have more degrees of freedom. We denote the concatenation operator introduced in [27] with the symbol $\smile_n$, so that given two $N$-th order tensors $\boldsymbol{\mathcal{A}}$ and $\boldsymbol{\mathcal{B}}$ we have

$$\boldsymbol{\mathcal{C}} = \boldsymbol{\mathcal{A}} \smile_n \boldsymbol{\mathcal{B}}, \tag{D.7}$$

so that $\boldsymbol{\mathcal{C}}$ is the result of the concatenation of $\boldsymbol{\mathcal{A}}$ and $\boldsymbol{\mathcal{B}}$ along the $n$-th dimension. Obviously $\boldsymbol{\mathcal{A}}$ and $\boldsymbol{\mathcal{B}}$ need to have the same size along all dimensions but the $n$-th.

### D.3.2 The Scalar Product

The scalar product of two vectors can be extended in a straightforward way to the scalar product of two tensors $\boldsymbol{\mathcal{A}}$ and $\boldsymbol{\mathcal{B}}$. Please note that both tensors must have the same size.

**Definition D.3.1.** Assume two $N$-th order tensors $\boldsymbol{\mathcal{A}} = \{a_{i_1,i_2,\ldots,i_N}\}$ and $\boldsymbol{\mathcal{B}} = \{b_{i_1,i_2,\ldots,i_N}\}$ of same size $\mathbb{C}^{I_1 \times I_2 \times \cdots \times I_N}$. Then the scalar product $\langle \boldsymbol{\mathcal{A}}, \boldsymbol{\mathcal{B}} \rangle$ is defined as

$$\langle \boldsymbol{\mathcal{A}}, \boldsymbol{\mathcal{B}} \rangle = \sum_{i_1=1}^{I_1} \sum_{i_2=1}^{I_2} \cdots \sum_{i_N=1}^{I_N} a_{i_1,i_2,\ldots,i_N} \cdot b^*_{i_1,i_2,\ldots,i_N}. \tag{D.8}$$

### D.3.3 The n-mode Product

The calculation of the $n$-mode product of a tensor $\boldsymbol{\mathcal{A}}$ and a matrix $\boldsymbol{U}$ is carried out by multiplying every $n$-mode vector of $\boldsymbol{\mathcal{A}}$ with this matrix. Therefore, we could also interpret this product as a coordinate transformation for the $n$-mode vectors. Obviously, the number of columns of $\boldsymbol{U}$ must equal the size of $\boldsymbol{\mathcal{A}}$ along dimension $n$, namely $I_n$. This multiplication will be denoted by the $\times_n$ symbol.

**Definition D.3.2.** Assume a tensor $\boldsymbol{\mathcal{A}} = \{a_{i_1,i_2,\ldots,i_N}\} \in \mathbb{C}^{I_1 \times I_2 \times \cdots \times I_N}$ and a matrix $\boldsymbol{U} \in \mathbb{C}^{J_n \times I_n}$. Then the $n$-mode product, denoted by $\boldsymbol{\mathcal{A}} \times_n \boldsymbol{U}$, is a $(I_1 \times I_2 \times \cdots \times I_{n-1} \times J_n \times I_{n+1} \times \cdots \times I_N)$ tensor, whose entries are given by

$$(\boldsymbol{\mathcal{A}} \times_n \boldsymbol{U})_{i_1,\ldots,i_{n-1},j_n,i_{n+1},\ldots,i_N} = \sum_{i_n=1}^{I_n} a_{i_1,\ldots,i_n,\ldots,i_N} \cdot u_{j_n,i_n}, \tag{D.9}$$

for all possible values of the indices.

Equation (D.9) can be greatly simplified using the following matrix unfolding

$$\boldsymbol{\mathcal{A}}_{(n)} = \boldsymbol{U} \cdot \boldsymbol{\mathcal{B}}_{(n)}. \tag{D.10}$$

To calculate $\boldsymbol{\mathcal{A}} = \boldsymbol{\mathcal{B}} \times_n \boldsymbol{U}$ we simply build the $n$-th unfolding of $\boldsymbol{\mathcal{B}}$, and multiply it from the left with the matrix $\boldsymbol{U}$. The result will be the $n$-th unfolding matrix of $\boldsymbol{\mathcal{A}}$. Figure D.3 depicts the equation $\boldsymbol{\mathcal{A}} = \boldsymbol{\mathcal{B}} \times_1 \boldsymbol{U}^{(1)} \times_2 \boldsymbol{U}^{(2)} \times_3 \boldsymbol{U}^{(3)}$.

In the following we present some important properties of the $n$-mode product.

**Property D.3.3.** *Given the tensor* $\boldsymbol{\mathcal{A}} \in \mathbb{C}^{I_1 \times \cdots \times I_N}$ *and the matrices* $\boldsymbol{F} \in \mathbb{C}^{J_n \times I_n}$, *and* $\boldsymbol{G} \in \mathbb{C}^{J_m \times I_m}$ *with* $(m \neq n)$, *we have*

$$(\boldsymbol{\mathcal{A}} \times_n \boldsymbol{F}) \times_m \boldsymbol{G} = (\boldsymbol{\mathcal{A}} \times_m \boldsymbol{G}) \times_n \boldsymbol{F} = \boldsymbol{\mathcal{A}} \times_n \boldsymbol{F} \times_m \boldsymbol{G}. \tag{D.11}$$

**Property D.3.4.** *Given the tensor* $\boldsymbol{\mathcal{A}} \in \mathbb{C}^{I_1 \times \cdots \times I_N}$ *and the matrices* $\boldsymbol{F} \in \mathbb{C}^{J_n \times I_n}$, *and* $\boldsymbol{G} \in \mathbb{C}^{K_n \times J_n}$, *we have*

$$(\boldsymbol{\mathcal{A}} \times_n \boldsymbol{F}) \times_n \boldsymbol{G} = \boldsymbol{\mathcal{A}} \times_n (\boldsymbol{G} \cdot \boldsymbol{F}). \tag{D.12}$$

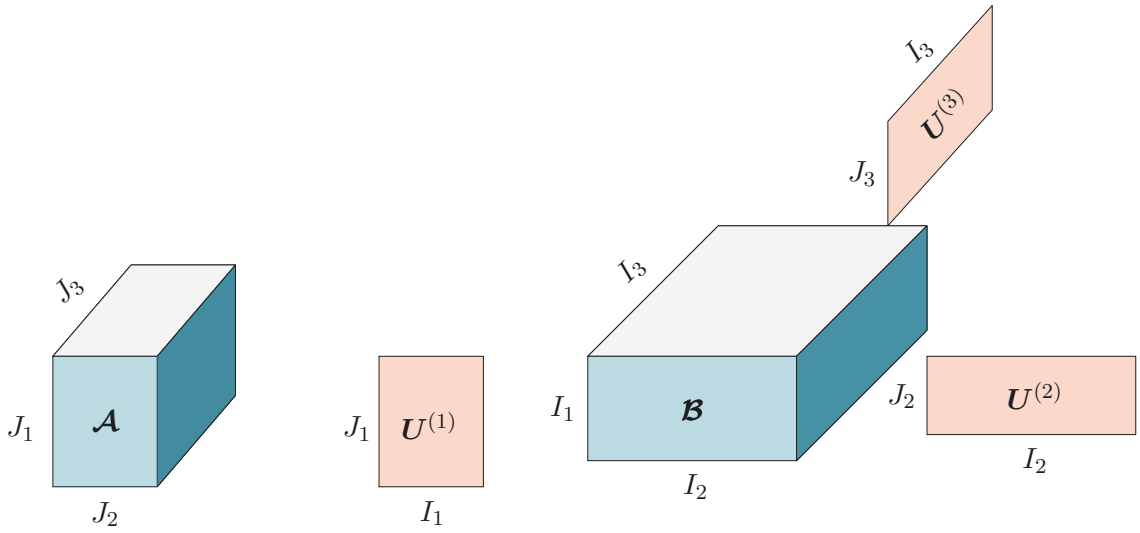


Fig. D.3: Visualization of the equation $\boldsymbol{\mathcal{A}} = \boldsymbol{\mathcal{B}} \times_1 \boldsymbol{U}^{(1)} \times_2 \boldsymbol{U}^{(2)} \times_3 \boldsymbol{U}^{(3)}$ for tensors of order 3.

#### D.3.3.1 Tensor Outer Product

The outer product (sometimes just called tensor product) $\boldsymbol{\mathcal{A}} = \boldsymbol{\mathcal{B}} \circ \boldsymbol{\mathcal{C}}$ of two tensors is very similar to the Kronecker product. In fact, it generates all possible combinations of pairwise element-products. However, the result is reshaped into a new tensor of order $M = N + K$ where $N$ and $K$ are the orders of $\boldsymbol{\mathcal{B}}$ and $\boldsymbol{\mathcal{C}}$, respectively. Mathematically, the outer product is defined as follows

**Definition D.3.5.** Assume a $N$-th order tensor $\boldsymbol{\mathcal{A}} = \{a_{i_1,i_2,\ldots,i_N}\} \in \mathbb{C}^{I_1 \times \cdots \times I_N}$ and $\boldsymbol{\mathcal{B}} = \{b_{j_1,j_2,\ldots,j_K}\} \in \mathbb{C}^{J_1 \times J_2 \times \cdots \times J_K}$. Then, the outer product of $\boldsymbol{\mathcal{A}}$ and $\boldsymbol{\mathcal{B}}$, denoted as $(\boldsymbol{\mathcal{A}} \circ \boldsymbol{\mathcal{B}})$ is a $N + K$ dimensional tensor, of size $I_1 \times \ldots \times I_N \times J_1 \times \ldots \times J_K$, defined as

$$(\boldsymbol{\mathcal{A}} \circ \boldsymbol{\mathcal{B}})_{i_1,\ldots,i_N,j_1,\ldots,j_K} = a_{i_1,\ldots,i_N} \cdot b_{j_1,\ldots,j_K}, \tag{D.13}$$

for all possible values of the indices.

Please note that the outer product between two vectors $\boldsymbol{u}$ and $\boldsymbol{v}$ gives a matrix, that can also be expressed in terms of a matrix multiplication $\boldsymbol{u} \circ \boldsymbol{v} = \boldsymbol{u} \cdot \boldsymbol{v}^{\mathrm{T}}$. In the following we introduce some properties of the outer product.

**Property D.3.6.** *Assume three tensors $\boldsymbol{\mathcal{A}}$, $\boldsymbol{\mathcal{B}}$, and $\boldsymbol{\mathcal{C}}$ of arbitrary size and dimension. Then the associative law holds*

$$(\boldsymbol{\mathcal{A}} \circ \boldsymbol{\mathcal{B}}) \circ \boldsymbol{\mathcal{C}} = \boldsymbol{\mathcal{A}} \circ (\boldsymbol{\mathcal{B}} \circ \boldsymbol{\mathcal{C}}) = \boldsymbol{\mathcal{A}} \circ \boldsymbol{\mathcal{B}} \circ \boldsymbol{\mathcal{C}}. \tag{D.14}$$

**Property D.3.7.** *Assume a tensor $\boldsymbol{\mathcal{A}}$ of arbitrary size and dimension, and two tensors $\boldsymbol{\mathcal{B}}$ and $\boldsymbol{\mathcal{C}}$ of the same arbitrary size and dimension. Then the distributive law holds*

$$\boldsymbol{\mathcal{A}} \circ (\boldsymbol{\mathcal{B}} + \boldsymbol{\mathcal{C}}) = \boldsymbol{\mathcal{A}} \circ \boldsymbol{\mathcal{B}} + \boldsymbol{\mathcal{A}} \circ \boldsymbol{\mathcal{C}}. \tag{D.15}$$

### D.3.4 The n-mode Tensor Inner Product

The $n$-mode inner product between the tensors $\boldsymbol{\mathcal{B}}$ and $\boldsymbol{\mathcal{C}}$ denoted by the symbol $\bullet_n$ operates like an outer product followed by a summation along the $n$-th dimension. The resulting tensor $\boldsymbol{\mathcal{A}} = \boldsymbol{\mathcal{B}} \bullet_n \boldsymbol{\mathcal{C}}$ has order $N + K - 2$ where $N$ and $K$ are the orders of $\boldsymbol{\mathcal{B}}$ and $\boldsymbol{\mathcal{C}}$, respectively.

**Definition D.3.8.** Assume a $N$-th order tensor $\boldsymbol{\mathcal{A}} = \{a_{i_1,\ldots,i_N}\} \in \mathbb{C}^{I_1 \times \cdots \times I_N}$ and a $K$-th order tensor $\boldsymbol{\mathcal{B}} = \{b_{j_1,\ldots,j_K}\} \in \mathbb{C}^{J_1 \times \cdots \times J_K}$. Then, the $n$-mode inner product denoted as $(\boldsymbol{\mathcal{A}} \bullet_n \boldsymbol{\mathcal{B}})$ is a tensor of dimension $N + K - 2$ defined as

$$(\boldsymbol{\mathcal{A}} \bullet_n \boldsymbol{\mathcal{B}})_{i_1,\ldots,i_{n-1},i_{n+1}\ldots,i_N,j_1,\ldots,j_{n-1},j_{n+1}\ldots,j_K} = \sum_{l=1}^{L} a_{i_1,\ldots,i_{n-1},l,i_{n+1}\ldots,i_N} \cdot b_{j_1,\ldots,j_{n-1},l,j_{n+1}\ldots,j_K}, \tag{D.16}$$

for all possible values of the indices, and under the condition that $I_n = J_n = L$.

A simpler interpretation of the $\bullet_n$ operator is given in the following. Assume a $N$-th order tensor $\boldsymbol{\mathcal{A}} = \{a_{i_1,i_2,\ldots,i_N}\} \in \mathbb{C}^{I_1 \times I_2 \times \cdots \times I_N}$ and a $K$-th order tensor $\boldsymbol{\mathcal{B}} = \{b_{j_1,j_2,\ldots,j_K}\} \in \mathbb{C}^{J_1 \times J_2 \times \cdots \times J_K}$. Let $\boldsymbol{\mathcal{A}}_{i_p=l}$ denote the $(N-1)$-th dimensional subtensor of $\boldsymbol{\mathcal{A}}$, obtained by keeping the index along the dimension $p$ fixed to $l$ with $l \in 1 \ldots I_p$. The tensor $\boldsymbol{\mathcal{B}}_{i_p=l}$ is defined in an analogous way. Then, the $n$-mode inner product $(\boldsymbol{\mathcal{A}} \bullet_n \boldsymbol{\mathcal{B}})$ can be written as

$$(\boldsymbol{\mathcal{A}} \bullet_p \boldsymbol{\mathcal{B}}) = \sum_{l=1}^{L} \boldsymbol{\mathcal{C}}^{(l)} \tag{D.17}$$

$$\boldsymbol{\mathcal{C}}^{(l)} = \boldsymbol{\mathcal{A}}_{i_p=l} \circ \boldsymbol{\mathcal{B}}_{i_p=l}, \tag{D.18}$$

with the condition that $I_p = J_p = L$.

An example of this interpretation is given in Figure D.4.

## D.4 Properties of Tensors

Now we deal with the generalization of some elementary properties that are well-known in the matrix and vector case. In particular, we discuss two different definitions for the rank of a tensor.

### D.4.1 The Higher Order Norm of a Tensor

The higher order norm of a tensor is obtained by squaring the magnitude of all its elements, followed by a sum.

**Definition D.4.1.** Assume a tensor $\boldsymbol{\mathcal{A}}$ of arbitrary size and order. Then the higher order norm of $\boldsymbol{\mathcal{A}}$ is given by

$$\|\boldsymbol{\mathcal{A}}\|_{\mathrm{H}} = \sqrt{\langle \boldsymbol{\mathcal{A}}, \boldsymbol{\mathcal{A}} \rangle}. \tag{D.19}$$

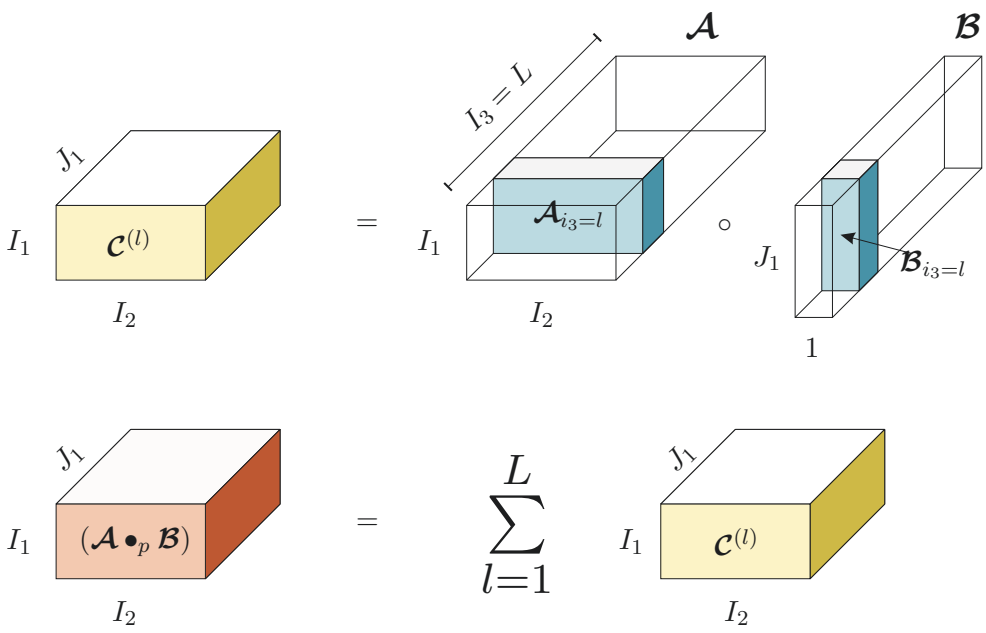


Fig. D.4: Visual representation of the $n$-mode inner product $\mathcal{A} \bullet_3 \mathcal{B}$. The subtensors $\mathcal{A}_{i_3=l}$ and $\mathcal{B}_{i_3=l}$ have size $I_1 \times I_2$ and $J_1 \times 1$, respectively.

The higher order norm of a tensor $\mathcal{A}$ is equal to the Frobenius norm of any of its unfoldings, so that

$$\|\mathcal{A}\|_{\mathrm{H}} = \|\mathcal{A}_{(n)}\|_{\mathrm{F}}, \quad \text{for } n = 1, 2, \ldots, N, \tag{D.20}$$

where $N$ is the order of the tensor.

#### D.4.1.1 Orthogonality of Tensors

This property is the straightforward extension of the orthogonality property for vectors or matrices.

**Definition D.4.2.** Assume two tensors $\mathcal{A}$ and $\mathcal{B}$ of same arbitrary size and order. Then $\mathcal{A}$ and $\mathcal{B}$ are orthogonal if their scalar product is zero.

$$\mathcal{A} \perp \mathcal{B} \iff \langle \mathcal{A}, \mathcal{B} \rangle = 0. \tag{D.21}$$

### D.4.2 n-ranks of Tensors

We first define the $n$-ranks of a tensor, which are a direct generalization of the column and row rank of matrices.

**Definition D.4.3.** The $n$-rank of a tensor $\mathcal{A} \in \mathbb{C}^{I_1 \times I_2 \times \cdots \times I_N}$, denoted by $\mathrm{rank}_n(\mathcal{A})$ is the dimension of the vector space spanned by the $n$-mode vectors (or as an alternative definition, the number of linear independent $n$-mode vectors) of $\mathcal{A}$. Therefore, we have

$$\mathrm{rank}_n(\mathcal{A}) = \mathrm{rank}\left(\mathcal{A}_{(n)}\right). \tag{D.22}$$

Note that in the matrix case, we have $\text{rank}_1 = \text{rank}_2$ .

### D.4.3 Rank of tensors

If we look at the matrix singular value decomposition, it follows that it can also be written as a sum of rank-1 terms. The generalization of this idea brings us to the definition of a tensor rank. To do so, we first define a *rank-1 tensor*

**Definition D.4.4.** A $N$-th order tensor $\boldsymbol{\mathcal{A}}$ has rank 1, when it equals the outer product of $N$ vectors $\boldsymbol{u}^{(1)}, \boldsymbol{u}^{(2)}, \ldots, \boldsymbol{u}^{(N)}$:

$$\boldsymbol{\mathcal{A}} = \boldsymbol{u}^{(1)} \circ \boldsymbol{u}^{(2)} \circ \cdots \circ \boldsymbol{u}^{(N)}. \tag{D.23}$$

This definition leads us directly to the definition of the rank of a tensor.

**Definition D.4.5.** The rank of an arbitrary $N$-th order tensor $\boldsymbol{\mathcal{A}}$, denoted as $\text{rank}(\boldsymbol{\mathcal{A}})$, is the minimal number of rank-1 tensors that yields A in a linear combination.

Note that there is no connection between the rank of a tensor and its $n$-ranks. We can merely state that $\text{rank}_n(\boldsymbol{\mathcal{A}}) \leq \text{rank}(\boldsymbol{\mathcal{A}})$. Let us now verify these definitions on a simple example taken from [65].

Consider the tensor $\boldsymbol{\mathcal{A}} \in \mathbb{R}^{2\times 2\times 2}$ defined by

$$\begin{cases} a_{2,1,1} = a_{1,2,1} = a_{1,1,2} = 1 \\ a_{1,1,1} = a_{2,2,2} = a_{1,2,2} = a_{2,1,2} = a_{2,2,1} = 0 \end{cases} \tag{D.24}$$

The 1-rank, 2-rank and 3-rank are all equal to 2. The rank however, equals 3 since

$$\boldsymbol{\mathcal{A}} = \boldsymbol{x}_2 \circ \boldsymbol{y}_1 \circ \boldsymbol{z}_1 + \boldsymbol{x}_1 \circ \boldsymbol{y}_2 \circ \boldsymbol{z}_1 + \boldsymbol{x}_1 \circ \boldsymbol{y}_1 \circ \boldsymbol{z}_2$$

In which

$$\boldsymbol{x}_1 = \boldsymbol{y}_1 = \boldsymbol{z}_1 = \begin{pmatrix} 1 \\ 0 \end{pmatrix} \qquad \boldsymbol{x}_2 = \boldsymbol{y}_2 = \boldsymbol{z}_2 = \begin{pmatrix} 0 \\ 1 \end{pmatrix}$$

is a decomposition in a minimal linear combination of rank-1 tensors.

## D.5 Higher Order Singular Value Decomposition (HOSVD)

We now introduce the Higher Order Singular Value Decomposition HOSVD. There are two approaches to define such a decomposition. In the following subsection we concentrate on the generalization based on the $n$-ranks of a tensor. The other form, based on the tensor rank, the so-called canonical decomposition, is briefly discussed in D.5.5. The papers from Comon *et al.* give more details on the HOSVD [58, 57, 56, 154]. First of all let us express the 2D Singular Value Decomposition (SVD) in tensor notation.

### D.5.1 Matrix Singular Value Decomposition in Tensor Notation

The well known Singular Value Decomposition (SVD) [87] of a matrix $\boldsymbol{F} \in \mathbb{C}^{I_1 \times I_2}$ is

$$\boldsymbol{F} = \boldsymbol{U} \cdot \boldsymbol{S} \cdot \boldsymbol{V}^H,$$

where $\boldsymbol{U} \in \mathbb{C}^{I_1 \times I_1}$ and $\boldsymbol{V} \in \mathbb{C}^{I_2 \times I_2}$ are unitary matrices, and $\boldsymbol{S}$ is a pseudo-diagonal matrix. The latter equation can be expressed in tensor notation as

$$\boldsymbol{F} = \boldsymbol{S} \times_1 \boldsymbol{U}^{(1)} \times_2 \boldsymbol{U}^{(2)},$$

where

$$\begin{aligned} \boldsymbol{U}^{(1)} &= \boldsymbol{U} \\ \boldsymbol{U}^{(2)} &= \boldsymbol{V}^*. \end{aligned}$$

Note that the columns of $\boldsymbol{U}^{(1)}$, also known as the 1-mode singular vectors, provide an orthogonal basis for the column space of $\boldsymbol{F}$, which we also refer to as 1-mode vector space. Similarly, the columns of $\boldsymbol{U}^{(2)} = \boldsymbol{V}^{(2)^*}$, or 2-mode singular vectors, provide an orthogonal basis for the row space of $\boldsymbol{F}$, i.e., the 2-mode vector space.

### D.5.2 Higher Order Singular Value Decomposition

The extension to higher orders is stated in the following

**Theorem D.5.1.** *Any $N$-th order complex tensor $\boldsymbol{\mathcal{A}} \in \mathbb{C}^{I_1 \times \cdots \times I_N}$ can be decomposed in the form*

$$\boldsymbol{\mathcal{A}} = \boldsymbol{\mathcal{S}} \times_1 \boldsymbol{U}^{(1)} \times_2 \boldsymbol{U}^{(2)} \cdots \times_N \boldsymbol{U}^{(N)}, \tag{D.25}$$

*where $\boldsymbol{U}^{(n)} \in \mathbb{C}^{I_n \times I_n}$ is a unitary matrix $\forall$ $n$, and the so-called* core tensor *$\boldsymbol{\mathcal{S}}$ is a tensor of same size as $\boldsymbol{\mathcal{A}}$. The columns of the matrix $\boldsymbol{U}^{(n)}$ are the $n$-mode singular vectors, so that*

$$\boldsymbol{U}^{(n)} = \begin{bmatrix} \boldsymbol{u}_1^{(n)} & \boldsymbol{u}_2^{(n)} & \dots & \boldsymbol{u}_{I_n}^{(n)}, \end{bmatrix}$$

*where $\boldsymbol{u}_i^{(n)}$ is the $i$-th $n$-mode singular vector.*

Figure D.5 shows an exemplary HOSVD for a 3D tensor.

Notice that unlike to the matrix case, the core tensor $\boldsymbol{\mathcal{S}}$ is in general a tensor filled with non-zero elements. However, it possesses the following properties

**Property D.5.2.** *A core tensor $\boldsymbol{\mathcal{S}}$ from a HOSVD possesses the property of* all-orthogonality*, i.e., two arbitrary subtensors of $\boldsymbol{\mathcal{S}}$ along one arbitrary dimension are orthogonal. Therefore, for all possible values of $n$, $\alpha$ and $\beta$*

$$\langle \boldsymbol{\mathcal{S}}_{i_n=\alpha}, \boldsymbol{\mathcal{S}}_{i_n=\beta} \rangle = 0, \quad \forall\ \alpha \neq \beta. \tag{D.26}$$

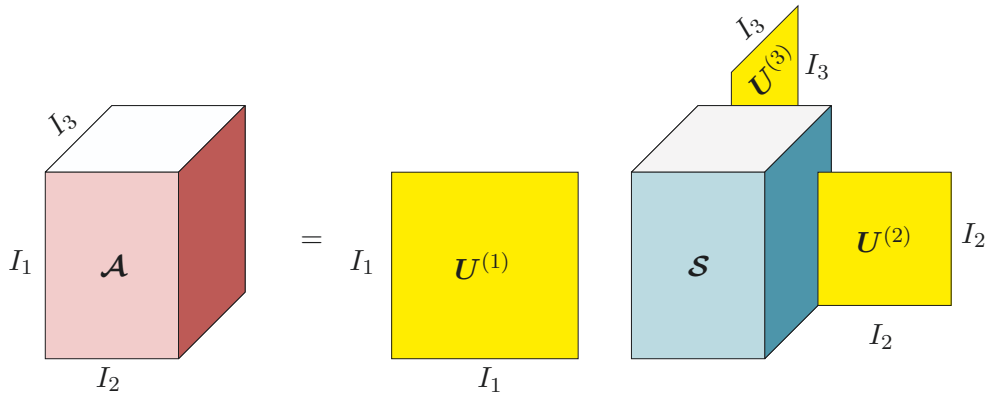


Fig. D.5: Visualization of the HOSVD for a 3D tensor.

**Property D.5.3.** *A core tensor $\mathcal{S}$ from a HOSVD possesses the* ordering *property, which implies that the norms of all subtensors along one arbitrary dimension are ordered in the following way*

$$\|\mathcal{S}_{i_n=1}\|_{\mathrm{H}} \geq \|\mathcal{S}_{i_n=2}\|_{\mathrm{H}} \geq \cdots \geq \|\mathcal{S}_{i_n=I_n}\|_{\mathrm{H}}, \quad \forall\ n = 1 \ldots N. \tag{D.27}$$

### D.5.2.1 The n-mode Singular Values

To obtain the $i$-th $n$-mode singular value $\sigma_i^{(n)}$, we need to compute the higher order norm of the subtensors $\mathcal{S}_{i_n=i}$. Therefore, in the $n$-th direction there are $I_n$ $n$-mode singular values, which we store in the column vector $\boldsymbol{\sigma}^{(n)}$ as

$$\boldsymbol{\sigma}^{(n)} = \begin{bmatrix} \sigma_1^{(n)} & \sigma_2^{(n)} & \ldots & \sigma_{I_n}^{(n)} \end{bmatrix}^{\mathrm{T}}$$

Figure D.6 illustrate graphically the $n$-mode singular values for a 3D tensor. By fixing the

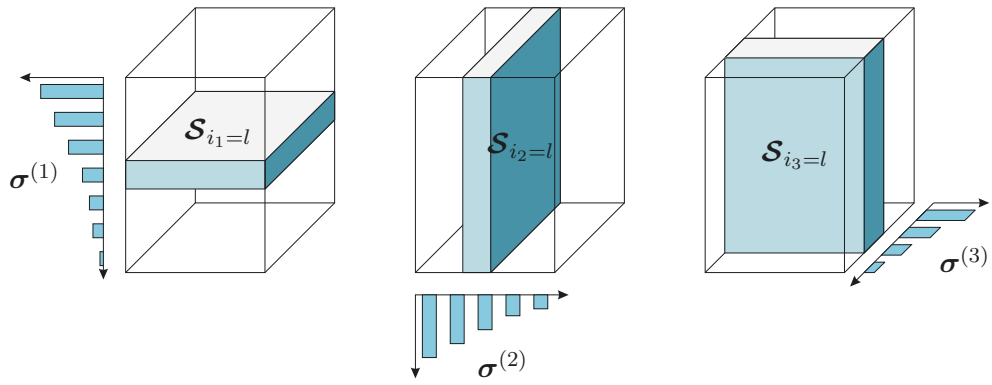


Fig. D.6: Visualization of the $n$-mode singular values for a 3D core tensor.

first index $i_1 = l$ we obtain the subtensor $\mathcal{S}_{i_1=l}$, whose higher order norm gives $\sigma_l^{(1)}$, i.e., the $l$-th element of the vector $\boldsymbol{\sigma}^{(1)}$. As Property (D.5.3) indicates, the $n$-mode singular values are sorted, as also visible in Figure D.6.

#### D.5.2.2 Computing the HOSVD

To compute the higher order singular value decomposition of the tensor $\boldsymbol{\mathcal{A}}$, we first need the unitary matrix $\boldsymbol{U}^{(n)}$ of equation D.25 $\forall\ n$, which can be calculated from the $n$-th unfolding $\boldsymbol{\mathcal{A}}_{(n)}$ via a matrix Singular Value Decomposition (SVD) as

$$\boldsymbol{\mathcal{A}}_{(n)} = \boldsymbol{U}^{(n)} \cdot \boldsymbol{\Sigma^{(n)}} \cdot \boldsymbol{V}^{(n)^{\mathrm{H}}}. \tag{D.28}$$

When the unitary matrices for $n = 1,\ 2,\ \ldots,\ N$, are known, we can compute the core tensor $\boldsymbol{\mathcal{S}}$ as follows

$$\begin{aligned}
\boldsymbol{\mathcal{A}} &= \boldsymbol{\mathcal{S}} \times_1 \boldsymbol{U}^{(1)} \times_2 \cdots \times_N \boldsymbol{U}^{(N)} \\
\boldsymbol{\mathcal{A}} \times_1 \boldsymbol{U}^{(1)^{\mathrm{H}}} \times_2 \cdots \times_N \boldsymbol{U}^{(N)^{\mathrm{H}}} &= \boldsymbol{\mathcal{S}} \times_1 \boldsymbol{U}^{(1)} \times_2 \cdots \times_N \boldsymbol{U}^{(N)} \times_1 \boldsymbol{U}^{(1)^{\mathrm{H}}} \times_2 \cdots \times_N \boldsymbol{U}^{(N)^{\mathrm{H}}} \\
\boldsymbol{\mathcal{A}} \times_1 \boldsymbol{U}^{(1)^{\mathrm{H}}} \times_2 \cdots \times_N \boldsymbol{U}^{(N)^{\mathrm{H}}} &= \boldsymbol{\mathcal{S}} \times_1 \left(\boldsymbol{U}^{(1)} \cdot \boldsymbol{U}^{(1)^{\mathrm{H}}}\right) \times_2 \cdots \times_N \left(\boldsymbol{U}^{(N)} \cdot \boldsymbol{U}^{(N)^{\mathrm{H}}}\right),
\end{aligned}$$

and since $\left(\boldsymbol{U}^{(1)} \cdot \boldsymbol{U}^{(1)^{\mathrm{H}}}\right) = \boldsymbol{I}$, we have

$$\boldsymbol{\mathcal{S}} = \boldsymbol{\mathcal{A}} \times_1 \boldsymbol{U}^{(1)^{\mathrm{H}}} \times_2 \boldsymbol{U}^{(2)^{\mathrm{H}}} \cdots \times_N \boldsymbol{U}^{(N)^{\mathrm{H}}}. \tag{D.29}$$

### D.5.3 Alternative Representations

#### D.5.3.1 The Kronecker Representation of the HOSVD

As discussed in D.3.3, it is possible to write the $n$-mode product in terms of matrix operations. With the help of the Kronecker product, denoted by the symbol $\otimes$, we write equation (D.25) in terms of matrix operations by using the de Lathauwer unfolding defined in Section D.2.1, so that

$$\boldsymbol{\mathcal{A}}_{(n)} = \boldsymbol{U}^{(n)} \cdot \boldsymbol{\mathcal{S}}_{(n)} \cdot \left(\boldsymbol{U}^{(n+1)} \otimes \cdots \otimes \boldsymbol{U}^{(N)} \otimes \boldsymbol{U}^{(1)} \otimes \cdots \otimes \boldsymbol{U}^{(n-1)}\right)^{\mathrm{T}}. \tag{D.30}$$

To prove this, let $\boldsymbol{\Sigma}^{(n)} \in \mathbb{R}^{I_n \times I_n}$ be a diagonal matrix of singular values

$$\boldsymbol{\Sigma}^{(n)} = \mathrm{diag}\left(\sigma_1^{(n)}, \sigma_2^{(n)}, \ldots, \sigma_{In}^{(n)}\right), \tag{D.31}$$

and $\boldsymbol{V}^{(n)} \in \mathbb{C}^{(I_{n+1}\cdots I_N \cdot I_1 \cdots I_{n-1}) \times I_n}$, where

$$\boldsymbol{V}^{(n)^{\mathrm{H}}} = \tilde{\boldsymbol{\mathcal{S}}}_{(n)} \cdot \left(\boldsymbol{U}^{(n+1)} \otimes \boldsymbol{U}^{(n+2)} \otimes \cdots \otimes \boldsymbol{U}^{(N)} \otimes \boldsymbol{U}^{(1)} \otimes \boldsymbol{U}^{(2)} \otimes \cdots \otimes \boldsymbol{U}^{(n-1)}\right)^{\mathrm{T}}. \tag{D.32}$$

The matrix $\tilde{\boldsymbol{\mathcal{S}}}_{(n)}$ is a normalized version of $\boldsymbol{\mathcal{S}}_{(n)}$, so that its rows have unit norm. This normalization can expressed as

$$\boldsymbol{\mathcal{S}}_{(n)} = \boldsymbol{\Sigma}^{(n)} \cdot \tilde{\boldsymbol{\mathcal{S}}}_{(n)}. \tag{D.33}$$

In order to substitute $\boldsymbol{V}^{(n)}$ and $\boldsymbol{\Sigma}^{(n)}$ in equation (D.30), we write it as

$$\begin{aligned}\boldsymbol{\mathcal{A}}_{(n)} &= \boldsymbol{U}^{(n)} \cdot \boldsymbol{\mathcal{S}}_{(n)} \cdot \left(\boldsymbol{U}^{(n+1)} \otimes \boldsymbol{U}^{(n+2)} \otimes \cdots \otimes \boldsymbol{U}^{(N)} \otimes \boldsymbol{U}^{(1)} \otimes \boldsymbol{U}^{(2)} \otimes \cdots \otimes \boldsymbol{U}^{(n-1)}\right)^{\mathrm{T}} \\ &= \boldsymbol{U}^{(n)} \cdot \boldsymbol{\Sigma}^{(n)} \cdot \tilde{\boldsymbol{\mathcal{S}}}_{(n)} \cdot \left(\boldsymbol{U}^{(n+1)} \otimes \boldsymbol{U}^{(n+2)} \otimes \cdots \otimes \boldsymbol{U}^{(N)} \otimes \boldsymbol{U}^{(1)} \otimes \boldsymbol{U}^{(2)} \otimes \cdots \otimes \boldsymbol{U}^{(n-1)}\right)^{\mathrm{T}},\end{aligned}$$

so that it appears clear that

$$\boldsymbol{\mathcal{A}}_{(n)} = \boldsymbol{U}^{(n)} \cdot \boldsymbol{\Sigma}^{(\boldsymbol{n})} \cdot \boldsymbol{V}^{(n)^{\mathrm{H}}}. \tag{D.34}$$

As stated before, the basis matrices $\boldsymbol{U}^{(n)}$ in the HOSVD can be calculated from the left singular matrices of the matrix unfoldings $\boldsymbol{\mathcal{A}}_{(n)}$. This equation represents a strong link between the matrix SVD and the HOSVD, which implies that many properties of the SVD have clear counterparts in the multi-dimensional HOSVD.

Equation (D.30) can be rewritten when using the MATLAB-like unfolding defined in Section D.2.2 as

$$\boldsymbol{\mathcal{A}}_{[n]} = \boldsymbol{U}^{(n)} \cdot \boldsymbol{\mathcal{S}}_{[n]} \cdot \left(\boldsymbol{U}^{(n-1)} \otimes \cdots \otimes \boldsymbol{U}^{(1)} \otimes \boldsymbol{U}^{(N)} \otimes \cdots \otimes \boldsymbol{U}^{(n+1)}\right)^{\mathrm{T}}. \tag{D.35}$$

This expression can be simplified further for the special case represented by the $N+1$ unfolding as follows

$$\boldsymbol{\mathcal{A}}_{[N+1]} = \boldsymbol{\mathcal{S}}_{[N+1]} \cdot \left(\boldsymbol{U}^{(N)} \otimes \boldsymbol{U}^{(N-1)} \otimes \cdots \otimes \boldsymbol{U}^{(1)}\right)^{\mathrm{T}} \in \mathbb{C}^{1 \times I_1 \cdot \ldots \cdot I_N}, \tag{D.36}$$

since the $N+1$-th unitary matrix $\boldsymbol{U}^{(N+1)}$ is equal to 1. Expressed with respect to the vec operator, we have

$$\mathrm{vec}\,\{\boldsymbol{A}\} = \left(\boldsymbol{U}^{(N)} \otimes \boldsymbol{U}^{(N-1)} \otimes \cdots \otimes \boldsymbol{U}^{(1)}\right) \cdot \mathrm{vec}\,\{\boldsymbol{S}\} \in \mathbb{C}^{I_1 \cdot \ldots \cdot I_N \times 1}. \tag{D.37}$$

#### D.5.3.2 The Tucker Decomposition

The HOSVD leads also to a decomposition that is very similar to the canonical decomposition discussed in Section D.5.5, and which is referred to as the *triadic decomposition*, or *Tucker decomposition*. For the tensor $\boldsymbol{\mathcal{A}}$ it is defined as

$$\boldsymbol{\mathcal{A}} = \sum_{i_1=1}^{I_1} \sum_{i_2=1}^{I_2} \cdots \sum_{i_N=1}^{I_N} s_{i_1,i_2,\ldots,i_N} \cdot \boldsymbol{u}_{i_1}^{(1)} \circ \boldsymbol{u}_{i_2}^{(2)} \circ \cdots \circ \boldsymbol{u}_{i_N}^{(N)}, \tag{D.38}$$

where the coefficients $i_{i_1,i_2,\ldots,i_N}$ are the entries of the ordered core tensor $\boldsymbol{\mathcal{S}}$. This equation describes the tensor $\boldsymbol{\mathcal{A}}$ as a linear combination of orthogonal rank-1 tensors. The orthogonality of the rank-1 tensors follows from the orthogonality of the $n$-mode singular vectors. Figure D.7 depicts the Tucker decomposition for a 3D tensor.

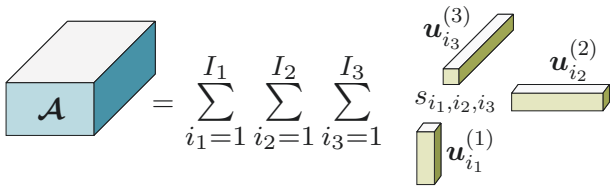


Fig. D.7: Visualization of the triadic decomposition of $\boldsymbol{\mathcal{A}}$.

Unfortunately, equation (D.7) does not give the minimal number of rank-1 tensors which combined, give back the original tensor $\boldsymbol{\mathcal{A}}$.

### D.5.4 Properties of the HOSVD

As mentioned above, many properties of the matrix SVD have very clear higher-order counterparts. In this subsection we list the most important.

**Property D.5.4.** *The n-mode singular values are uniquely defined. When the n-mode singular values are different, then the n-mode singular vectors are determined up to a multiplication with an unit phase factor.*

This property ensures the uniqueness of the HOSVD, similarly to the matrix SVD case.

**Property D.5.5.** *Let the HOSVD of $\boldsymbol{\mathcal{A}}$ be given as in Theorem D.5.1. Then the following equation holds*

$$\|\boldsymbol{\mathcal{A}}\|_{\mathrm{H}}^2 = \sum_{i=1}^{\mathrm{rank}_1(\boldsymbol{\mathcal{A}})} \left(\sigma_i^{(1)}\right)^2 = \cdots = \sum_{i=1}^{\mathrm{rank}_N(\boldsymbol{\mathcal{A}})} \left(\sigma_i^{(N)}\right)^2 = \|\boldsymbol{\mathcal{S}}\|_{\mathrm{H}}^2. \tag{D.39}$$

In multilinear algebra, as well as in matrix algebra, the Frobenius-norm is unitarily invariant. As a consequence, the fact that the squared Frobenius-norm of a matrix equals the sum of its squared singular values can be generalized. The proof of this property follows directly from the connection between the HOSVD and the matrix SVD described by equation (D.28).

We now introduce the following

**Definition D.5.6.** The $n$-mode *oriented energy* of a $N$-th order tensor $\boldsymbol{\mathcal{A}} \in \mathbb{C}^{I_1 \times I_2 \times \cdots \times I_N}$ in direction of a unit-norm vector $\boldsymbol{x}$, denoted by $OE(\boldsymbol{x}, \boldsymbol{\mathcal{A}})$, is the oriented energy of the set of $n$-mode vectors

$$OE(\boldsymbol{x}, \boldsymbol{\mathcal{A}}) = \|\boldsymbol{x}^{\mathrm{H}} \cdot \boldsymbol{\mathcal{A}}_{(n)}\|_{\mathrm{F}}^2. \tag{D.40}$$

Here, the concept of oriented energy of a given matrix, is directly generalized to the multidimensional case. This principle builds the basis for signal separation algorithms. Now, the following property holds.

**Property D.5.7.** *The directions for which the n-mode oriented energy reaches a maximum are given by the n-mode singular vectors. The energy values in these directions are given by the corresponding n-mode singular values.*

Due to the ordering assumption of the HOSVD, this implies that the $n$-mode oriented energy of a tensor $\boldsymbol{\mathcal{A}}$ reaches the global maximum along the direction $\boldsymbol{u}_1^{(n)}$.

**Property D.5.8.** *Let the HOSVD of $\boldsymbol{\mathcal{A}}$ be given as in Theorem D.5.1 and the tensor $\widehat{\boldsymbol{\mathcal{A}}}$ be defined by setting the smallest $n$-mode singular values $\sigma^{(n)}_{\widehat{S}_n+1}, \sigma^{(n)}_{\widehat{S}_n+2}, \ldots, \sigma^{(n)}_{I_n}$, and the corresponding parts of $\boldsymbol{\mathcal{S}}$ to zero for given values of $\widehat{S}_n : \forall\, n$. Then we have*

$$\|\boldsymbol{\mathcal{A}} - \widehat{\boldsymbol{\mathcal{A}}}\|_{\mathrm{H}}^2 \leq \sum_{i_1=\widehat{S}_n+1}^{I_1} \sigma_{i_1}^{(1)^2} + \sum_{i_2=\widehat{S}_n+1}^{I_2} \sigma_{i_2}^{(2)^2} + \cdots + \sum_{i_1=\widehat{S}_N+1}^{I_N} \sigma_{i_N}^{(N)^2}. \tag{D.41}$$

This property gives the multi-dimensional extension of the lower rank approximation in the matrix case. However, $\widehat{\boldsymbol{\mathcal{A}}}$ is not the best $n$-rank $\widehat{S}_n$ approximation of $\boldsymbol{\mathcal{A}}$ in a least mean square sense. An optimum approximation can be found by the higher order orthogonal iteration method, as presented in [65]. Nevertheless, in practical cases $\widehat{\boldsymbol{\mathcal{A}}}$ can still be considered a good approximation of $\boldsymbol{\mathcal{A}}$, as discussed in Section 5.2.6.

Figure D.8 gives a visual representation for a 3D tensor. The $n$-mode singular values which are set to zero are marked in red. The corresponding non-zero subtensor is marked in color, as well as the significant $n$-mode singular vector.

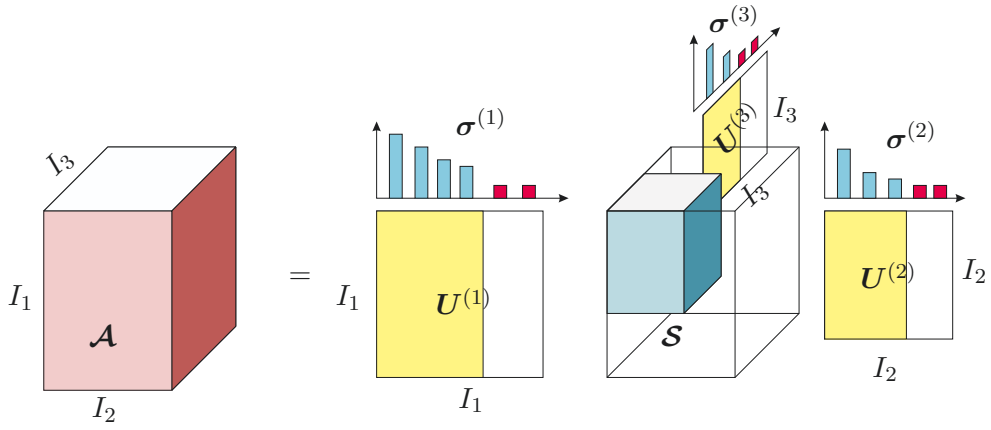


Fig. D.8: Visualization of the low rank approximation for a 3D tensor. The $n$-mode singular values which are set to zero are marked in red. The corresponding non-zero subtensor is marked in color, as well as the significant $n$-mode singular vectors.

**Property D.5.9.** *Let the HOSVD of $\boldsymbol{\mathcal{A}}$ and $\boldsymbol{\mathcal{B}}$ be given as above. Then the outer product $(\boldsymbol{\mathcal{A}} \circ \boldsymbol{\mathcal{B}})$ can be decomposed as*

$$\begin{aligned}(\boldsymbol{\mathcal{A}} \circ \boldsymbol{\mathcal{B}}) &= \left(\boldsymbol{\mathcal{S}}_A \times_1 \boldsymbol{U}^{(1)} \times_2 \cdots \times_N \boldsymbol{U}^{(N)}\right) \circ \left(\boldsymbol{\mathcal{S}}_B \times_1 \boldsymbol{V}^{(1)} \times_2 \cdots \times_M \boldsymbol{V}^{(M)}\right) \\ &= (\boldsymbol{\mathcal{S}}_A \circ \boldsymbol{\mathcal{S}}_B) \times_1 \boldsymbol{U}^{(1)} \cdots \times_N \boldsymbol{U}^{(N)} \times_{N+1} \boldsymbol{V}^{(1)} \times_{N+2} \cdots \times_{N+M} \boldsymbol{V}^{(N+M)}.\end{aligned} \tag{D.42}$$

**Property D.5.10.** *Let the HOSVD of $\boldsymbol{\mathcal{A}}$ be given as above. Then the complex conjugate of $\boldsymbol{\mathcal{A}}$ can be denoted as*

$$\boldsymbol{\mathcal{A}}^* = \boldsymbol{\mathcal{S}}^* \times_1 \boldsymbol{U}^{(1)^*} \times_2 \cdots \times_N \boldsymbol{U}^{(N)^*}. \tag{D.43}$$

### D.5.5 Canonical Decomposition

A major difference between the matrix SVD and the tensor HOSVD is that the latter does not provide exact information on the rank of a tensor. For this reason, we introduce the *CANonical DECOMPosition* (in short CANDECOMP), also called *PARAllel FACtors model* (PARAFAC), which decomposes a tensor $\boldsymbol{\mathcal{A}} \in \mathbb{C}^{I_1 \times I_2 \times \cdots \times I_N}$ in rank($\boldsymbol{\mathcal{A}}$) rank-1 tensors. It is defined as

$$\boldsymbol{\mathcal{A}} = \sum_{r=1}^{\operatorname{rank}(\boldsymbol{\mathcal{A}})} \lambda_r \cdot \left( \boldsymbol{u}_r^{(1)} \circ \boldsymbol{u}_r^{(2)} \circ \cdots \circ \boldsymbol{u}_r^{(N)} \right). \tag{D.44}$$

Unfortunately its computation is much more challenging than the HOSVD.

Appendix E

# COORDINATE SYSTEMS

This appendix introduces the coordinate systems used throughout this work, namely, the Cartesian, polar, and helicity coordinate systems. Further information about them can be found in [216].

## E.1 Cartesian Coordinate System

Let $x$, $y$ and $z$ be the Cartesian coordinates of a point in space identified by the vector $\boldsymbol{r}$, as depicted in Figure E.1. Let further the Cartesian basis vectors be denoted by $\boldsymbol{e}_x$, $\boldsymbol{e}_y$, and $\boldsymbol{e}_z$. The vector $\boldsymbol{r}$ can then be expressed as

$$\boldsymbol{r} = x\ \boldsymbol{e}_x + y\ \boldsymbol{e}_y + z\ \boldsymbol{e}_z. \tag{E.1}$$

The basis vectors $\boldsymbol{e}_x$, $\boldsymbol{e}_y$, and $\boldsymbol{e}_z$ form a real orthonormal basis

$$\begin{array}{ccccccc} \boldsymbol{e}_x^{\mathrm{T}}\boldsymbol{e}_y & = & \boldsymbol{e}_x^{\mathrm{T}}\boldsymbol{e}_z & = & \boldsymbol{e}_y^{\mathrm{T}}\boldsymbol{e}_z & = & 0 \\ \boldsymbol{e}_x^{\mathrm{T}}\boldsymbol{e}_x & = & \boldsymbol{e}_y^{\mathrm{T}}\boldsymbol{e}_y & = & \boldsymbol{e}_z^{\mathrm{T}}\boldsymbol{e}_z & = & 1\ . \end{array} \tag{E.2}$$

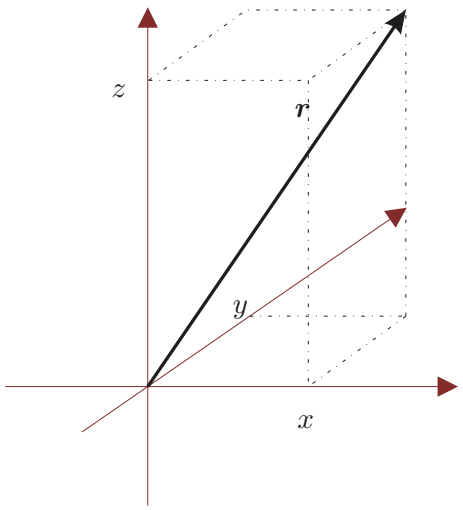


Fig. E.1: Cartesian coordinate system. The vector $\boldsymbol{r}$ is expressed in terms of its coordinates $x$, $y$ and $z$.

Throughout this work we assume the right-handed Cartesian coordinate system, which has the following properties

$$\boldsymbol{e}_x \times \boldsymbol{e}_y = \boldsymbol{e}_z \ , \qquad \boldsymbol{e}_y \times \boldsymbol{e}_z = \boldsymbol{e}_x \ , \qquad \boldsymbol{e}_z \times \boldsymbol{e}_x = \boldsymbol{e}_y \ . \tag{E.3}$$

## E.2 Polar Coordinate System

A point in a polar coordinate system[1] defined by the vector $\boldsymbol{r}$, is determined by the real numbers $r$, $\theta$, $\varphi$, where $r$ is the length of the vector $\boldsymbol{r}$, $\theta$ is the elevation, and $\varphi$ is the azimuth. Alternatively to elevation, in many fields researchers prefer to use co-elevation, which we denote with the symbol $\vartheta$. Figure E.2 shows graphically $r$, $\theta$, $\vartheta$, and $\varphi$.

The angles $\vartheta$ and $\varphi$ are called the *polar angles* of the position vector $\boldsymbol{r}$.

The relations between Cartesian and polar coordinates are given by

$$\begin{aligned} x &= r\sin\vartheta\cos\varphi \ , \quad & r &= \sqrt{x^2+y^2+z^2} \ , & 0 &\le r \le \infty \ , \\ y &= r\sin\vartheta\cos\varphi \ , \quad & \vartheta &= \arccos\frac{z}{\sqrt{x^2+y^2+z^2}} \ , & 0 &\le \vartheta \le \pi \ , \\ z &= r\cos\vartheta \ , & \varphi &= \operatorname{atan2}(x,y) \ , & -\pi &\le \varphi \le \pi \ , \end{aligned} \tag{E.4}$$

where the function atan2 is the four-quadrant arctan function defined as

$$\operatorname{atan2}(x,y) = \begin{cases} \arctan\frac{y}{x} & \text{for } x > 0 \\ \arctan\frac{y}{x} + \pi & \text{for } x < 0,\ y \ge 0 \\ \arctan\frac{y}{x} - \pi & \text{for } x < 0,\ y < 0 \\ \frac{\pi}{2} & \text{for } x = 0,\ y > 0 \\ -\frac{\pi}{2} & \text{for } x = 0,\ y < 0 \end{cases} . \tag{E.5}$$

Notice that one might take $[0,\ 2\pi]$ instead of $[-\pi, \pi]$ for the range in which the azimuth $\varphi$ can vary. Since the azimuth is periodic with modulo $2\pi$ this is equivalent.

Let $\boldsymbol{e}_r$, $\boldsymbol{e}_\theta$, and $\boldsymbol{e}_\varphi$ be the unit norm polar basis vectors. They are shown in Figure E.3.

The polar basis vectors form a real orthonormal basis

$$\begin{aligned} \boldsymbol{e}_r^{\mathrm{T}}\boldsymbol{e}_\vartheta &= \boldsymbol{e}_r^{\mathrm{T}}\boldsymbol{e}_\varphi &= \boldsymbol{e}_\vartheta^{\mathrm{T}}\boldsymbol{e}_\varphi &= 0 \ , \\ \boldsymbol{e}_r^{\mathrm{T}}\boldsymbol{e}_r &= \boldsymbol{e}_\vartheta^{\mathrm{T}}\boldsymbol{e}_\vartheta &= \boldsymbol{e}_\varphi^{\mathrm{T}}\boldsymbol{e}_\varphi &= 1 \ , \end{aligned} \tag{E.6}$$

which is right-handed

$$\boldsymbol{e}_r \times \boldsymbol{e}_\vartheta = \boldsymbol{e}_\varphi \ , \qquad \boldsymbol{e}_\vartheta \times \boldsymbol{e}_\varphi = \boldsymbol{e}_r \ , \qquad \boldsymbol{e}_\varphi \times \boldsymbol{e}_r = \boldsymbol{e}_\vartheta \ . \tag{E.7}$$

[1] Note that the polar coordinate system is often called "spherical".

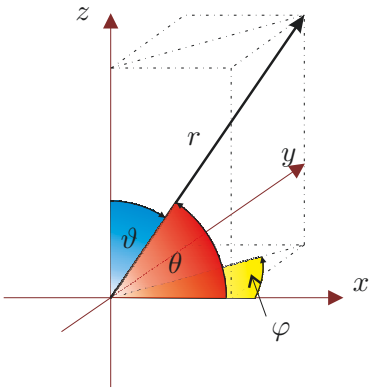


Fig. E.2: The diagram shows the polar coordinates, i.e., azimuth $\varphi \in [0,\ 2\pi]$, elevation $\theta \in [-\frac{\pi}{2}, \frac{\pi}{2}]$, co-elevation $\vartheta \in [0, \pi]$, and radius $r \in [0, \infty)$. The arrows indicate positive angles.

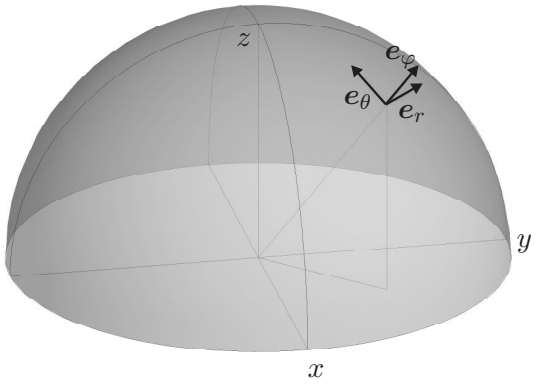


Fig. E.3: The polar basis vectors $\boldsymbol{e}_r$, $\boldsymbol{e}_\theta$, and $\boldsymbol{e}_\varphi$.

In contrast to the Cartesian basis vectors, the polar basis vectors depend on the angles $\vartheta$, $\varphi$, i.e., on the position on the sphere. This has to be taken into account when evaluating the derivatives

$$\begin{aligned}
&\frac{\partial}{\partial r}\boldsymbol{e}_r = 0\ , && \frac{\partial}{\partial r}\boldsymbol{e}_\vartheta = 0\ , && \frac{\partial}{\partial r}\boldsymbol{e}_\varphi = 0\ , \\
&\frac{\partial}{\partial \vartheta}\boldsymbol{e}_r = \boldsymbol{e}_\vartheta\ , && \frac{\partial}{\partial \vartheta}\boldsymbol{e}_\vartheta = -\boldsymbol{e}_r\ , && \frac{\partial}{\partial \vartheta}\boldsymbol{e}_\varphi = 0\ , \\
&\frac{\partial}{\partial \varphi}\boldsymbol{e}_r = \boldsymbol{e}_\varphi \sin\vartheta\ , && \frac{\partial}{\partial \varphi}\boldsymbol{e}_\vartheta = \boldsymbol{e}_\varphi \cos\vartheta\ , && \frac{\partial}{\partial \varphi}\boldsymbol{e}_\varphi = -\boldsymbol{e}_r \sin\vartheta - \boldsymbol{e}_\vartheta \cos\vartheta\ .
\end{aligned} \tag{E.8}$$

## E.3 Helicity Coordinate System

From the polar basis vectors the complex *helicity basis vectors* can be constructed by

$$\boldsymbol{e}_+ = -\frac{1}{\sqrt{2}}\left(\boldsymbol{e}_\vartheta + j\boldsymbol{e}_\varphi\right)\ , \qquad \boldsymbol{e}_0 = \boldsymbol{e}_r\ , \qquad \boldsymbol{e}_- = \frac{1}{\sqrt{2}}\left(\boldsymbol{e}_\vartheta - j\boldsymbol{e}_\varphi\right)\ . \tag{E.9}$$

They form a complex orthonormal basis

$$\begin{array}{rclcrcl} \boldsymbol{e}_+^{\mathrm{H}}\boldsymbol{e}_0 & = & \boldsymbol{e}_+^{\mathrm{H}}\boldsymbol{e}_- & = & \boldsymbol{e}_0^{\mathrm{H}}\boldsymbol{e}_- & = & 0\ , \\ \boldsymbol{e}_+^{\mathrm{H}}\boldsymbol{e}_+ & = & \boldsymbol{e}_0^{\mathrm{H}}\boldsymbol{e}_0 & = & \boldsymbol{e}_+^{\mathrm{H}}\boldsymbol{e}_+ & = & 1\ . \end{array} \tag{E.10}$$

The vector products between the helicity basis vectors can be written as

$$\boldsymbol{e}_+ \times \boldsymbol{e}_0 = j\boldsymbol{e}_+\ , \qquad \boldsymbol{e}_0 \times \boldsymbol{e}_- = j\boldsymbol{e}_-\ , \qquad \boldsymbol{e}_+ \times \boldsymbol{e}_- = j\boldsymbol{e}_0\ . \tag{E.11}$$

The polar basis vectors can be computed from the helicity basis vectors as follows

$$\boldsymbol{e}_r = \boldsymbol{e}_0\ , \qquad \boldsymbol{e}_\vartheta = \frac{1}{\sqrt{2}}\left(\boldsymbol{e}_- - \boldsymbol{e}_+\right)\ , \qquad \boldsymbol{e}_\varphi = \frac{j}{\sqrt{2}}\left(\boldsymbol{e}_- + \boldsymbol{e}_+\right)\ . \tag{E.12}$$

## Appendix F

# THE BD AND THE SO ALGORITHMS

In Section 5.2.1 we compare the throughput achieved by employing two recently developed algorithms for transmit beamforming in multi-user MIMO systems. These algorithms are briefly reviewed in this appendix and can be found in [193, 194]. Both algorithms aim to maximize the overall capacity subject to zero multi-user interference constraints.

In the downlink of a multi-user MIMO system the received vector $\boldsymbol{x}_i$ at the $i$-th mobile at a certain instant in time can be calculated as

$$\boldsymbol{x}_i = \boldsymbol{H}_i \boldsymbol{M}_i \boldsymbol{d}_i + \boldsymbol{n}_i, \tag{F.1}$$

where $\boldsymbol{H}_i$ is the flat-fading channel matrix for the $i$-th user, $\boldsymbol{M}_i \in \mathbb{C}^{M_\mathrm{T} \times S_i}$ is its modulation matrix, which performs the beamforming, and $\boldsymbol{d}_i$ is a data vector of arbitrary dimension $S_i$, which then represents the number of parallel data streams sent to the $i$-th user [179]. The noise vector $\boldsymbol{n}_i$ contains i.i.d. complex Gaussian random numbers with variance $\sigma_n^2$. The channel matrix $\boldsymbol{H}_i$ has dimension $M_{\mathrm{R,i}} \times M_\mathrm{T}$, where $M_\mathrm{T}$ and $M_{\mathrm{R,i}}$ are the antennas at the base station and at the $i$-th mobile, respectively.

The goal of the Block Diagonalization (BD) and of the Successive Optimization (SO) algorithms is to find the modulation matrices for all users served by the base station.

The *Block-Diagonalization* is a generalization of the channel inversion which suppresses completely all interference among the users, although allowing interference among the different data streams directed to the same user. This means that potentially the BS station can send up to $M_{\mathrm{R,i}}$ parallel data streams to the $i$-th user, which will use its $M_{\mathrm{R,i}}$ antennas to separate them. On the other hand the $i$-th user will not receive any interference from the data streams sent to other mobiles. The diagonalization of the channel occurs then only in blocks, each block belonging to one user only. In case of $S_i \geq 2$ the remaining equalization steps are left to the $i$-th user.

The columns of the modulation matrix $\boldsymbol{M}_i$ are the beamforming vectors towards the $i$-th user. The matrix $\tilde{\boldsymbol{H}}_i$, containing all channels but the $i$-th, is defined as

$$\tilde{\boldsymbol{H}}_i = [\boldsymbol{H}_1^T \quad \dots \quad \boldsymbol{H}_{i-1}^T \quad \boldsymbol{H}_{i+1}^T \quad \dots \quad \boldsymbol{H}_{M_\mathrm{U}}^T]^\mathrm{T}, \tag{F.2}$$

where $M_\mathrm{U}$ is the total number of users. In order to fulfill the zero-interference constraint

the columns of $\boldsymbol{M}_i$ must lie in the null space of $\tilde{\boldsymbol{H}}_i$. The BD algorithm constructs the $i$-th modulation matrix taking the strongest eigenvectors from the $i$-th channel subspace projected into the null space of $\tilde{\boldsymbol{H}}_i$. The total power allocated for the $i$-th user is assigned to the different eigenbranches via the water-filling strategy.

*The Successive Optimization* algorithm, on the other hand, follows a slightly different philosophy. The modulation matrix for the $i$-th user is chosen so that no interference is given to the user $1, \ldots, i-1$, while optimizing the transmit power to compensate for the interference received from these very users.

The detailed description of these algorithms can be found in [193, 194].

The user rate $r_i$ for the $i$-th user can be calculated as

$$r_i = \log_2 \left| \boldsymbol{I} + \frac{P}{M_{\mathrm{T}}} \boldsymbol{H}_i \boldsymbol{M}_i (\boldsymbol{R}_{nn})^{-1} \boldsymbol{M}_i^{\mathrm{H}} \boldsymbol{H}_i^{\mathrm{H}} \right| \tag{F.3}$$

where the superscript $(\cdot)^{\mathrm{H}}$ denotes the Hermitian transpose. The correlation matrix of the noise $\boldsymbol{R}_{nn}$ is simply $\sigma_n^2 \boldsymbol{I}$ for the BD, as the other users do not interfere. For the SO algorithm, however, the noise correlation matrix must consider the interference generated by the user $1, \ldots, i-1$ and thus becomes

$$\boldsymbol{R}_{nn} = \sigma_n^2 \boldsymbol{I} + \sum_{j=1}^{i-1} \boldsymbol{M}_j^{\mathrm{H}} \boldsymbol{H}_i^{\mathrm{H}} \boldsymbol{H}_i \boldsymbol{M}_j. \tag{F.4}$$

The Signal to Noise Ratio (SNR) is defined as $\mathrm{SNR} = \frac{P}{\sigma_n^2}$ where $P$, the total power available at the base station, is set to $M_{\mathrm{T}}$.

Notice that in [16] we describe a new derivation for the BD algorithm based on projection matrices.

# GLOSSARY OF ACRONYMS, SYMBOLS AND NOTATION

## Acronyms

| | |
|---|---|
| **1D** | one-dimensional |
| **2D** | two-dimensional |
| **3D** | three-dimensional |
| **AAS** | Antenna Array System |
| **ANS** | ANtenna System |
| **BD** | Block Diagonalization |
| **BER** | Bit Error Rate |
| **BS** | Base Station |
| **CDF** | Cumulative Density Function |
| **CG** | Computer Graphics |
| **CIR** | Channel Impulse Response |
| **CMD** | Correlation Matrix Distance |
| **CNR** | Carrier to Noise Ratio |
| **CRLB** | Cramér-Rao Lower Bound |
| **CSI** | Channel State Information |
| **DC** | Direct Current |
| **DCM** | Directional Channel Model |
| **DFT** | Discrete Fourier Transform |
| **DMC** | Diffuse Multi-path Component |
| **DMN** | Decoupling and Matching Network |
| **DOA** | Direction Of Arrival |
| **DOD** | Direction Of Departure |
| **DVSFT** | Discrete Vector Spherical Fourier Transform |
| **EADF** | Effective Aperture Distribution Function |
| **ECM** | Environment Characterization Metric |
| **EM** | ElectroMagnetic |
| **EVD** | EigenValue Decomposition |
| **FD** | Fading Depth |
| **FFT** | Fast Fourier Transform |
| **FIM** | Fisher Information Matrix |
| **FS** | Fourier Series |
| **GEO** | GEostationary Orbit |
| **GLS** | GLobal System |
| **GO** | Geometric Optics |
| **GTD** | Geometrical Theory of Diffraction |
| **HOSVD** | Higher Order Singular Value Decomposition |
| **IDFT** | Inverse Discrete Fourier Transform |
| **IDVSFT** | Inverse Discrete Vector Spherical Fourier Transform |
| **IFFT** | Inverse Fast Fourier Transform |

| | |
|---|---|
| **IO** | Interacting Object |
| **IVSFT** | Inverse Vector Spherical Fourier Transform |
| **LOS** | Line Of Sight |
| **LPS** | Level Power Spectrum |
| **LTI** | Linear Time Invariant |
| **MBPCM** | Measurement-Based Parametric Channel Model |
| **MIMO** | Multiple Input Multiple Output |
| **MISO** | Multiple Input Single Output |
| **MPC** | Multi-Path Component |
| **MRC** | Maximum Ratio Combining |
| **MS** | Mobile Station |
| **MSE** | Mean Squared Error |
| **NLOS** | Non Line Of Sight |
| **NMSE** | Normalized Mean Squared Error |
| **NSE** | Normalized Squared Error |
| **PDF** | Probability Density Function |
| **PeBPDF** | Pencil-Beam Probability Density Function |
| **PULPA** | Polarimetric Uniform Linear Patch Array |
| **QoS** | Quality of Service |
| **RMS** | Root Mean Square |
| **RMSE** | Root Mean Squared Error |
| **RR** | Round Robin |
| **SAGE** | Space Alternating Generalized Expectation-maximization |
| **SDMA** | Space-Division Multiple Access |
| **SF** | Spreading Function |
| **SFT** | Spherical Fourier Transform |
| **SH** | Spherical Harmonicfor scalar functions |
| **SIMO** | Single Input Multiple Output |
| **SISO** | Single Input Single Output |
| **SME** | Spherical Mode Expansion |
| **SMMSE** | Successive MMSE |
| **SNR** | Signal to Noise Ratio |
| **SO** | Successive Optimization |
| **SO THP** | Successive Optimization Tomlinson-Harashima precoding |
| **SPUCPA** | Stacked Polarimetric Uniform Circular Patch Array |
| **SV** | Singular Value |
| **SVD** | Singular Value Decomposition |
| **SWE** | Spherical Wave Expansion, synonym for the SME |
| **TDOA** | Time Delay Of Arrival |
| **TDMA** | Time-Division Multiple Access |
| **UCA** | Uniform Circular Array |
| **ULA** | Uniform Linear Array |
| **URA** | Uniform Rectangular Array |
| **URPA** | Uniform Rectangular Patch Array |
| **VSFT** | Vector Spherical Fourier Transform |
| **VSH** | Vector Spherical Harmonic |
| **WSOS** | Wide Sense Omni-Stationary |
| **WSS** | Wide Sense Stationary |
| **XPD** | Cross-Polarization Discrimination |
| **XPR** | Cross-Polarization Ratio |
| **ZDSC** | Zero Delay Spread Cluster |
| **ZF** | Zero Forcing |
| **ZMCSCG** | Zero Mean Circular Symmetric Complex Gaussian |

## Symbols and Notation

| | |
|---|---|
| $a,\ b,\ c$ | scalars |
| $\boldsymbol{a},\ \boldsymbol{b},\ \boldsymbol{c}$ | column vectors |
| $\boldsymbol{A},\ \boldsymbol{B},\ \boldsymbol{C}$ | matrices |
| $\boldsymbol{\mathcal{A}},\ \boldsymbol{\mathcal{B}},\ \boldsymbol{\mathcal{C}}$ | tensors |
| $h,\ \boldsymbol{h},\ \boldsymbol{H},\ \boldsymbol{\mathcal{H}}$ | channel coefficient, vector, matrix, and tensor, respectively |
| $\boldsymbol{R},\ \boldsymbol{R}$ | correlation matrix and tensor, respectively |
| $t$ | time |
| $f$ | frequency |
| $\tau$ | delay time |
| $\nu$ | Doppler frequency |
| $\lambda$ | wavelength |
| $\vartheta$ | elevation, where $-\frac{\pi}{2} \leq \theta \leq \frac{\pi}{2}$; $\vartheta = \frac{\pi}{2}$ is the north pole |
| $\vartheta$ | co-elevation, where $0 \leq \vartheta \leq \pi$; $\vartheta = 0$ is the north pole |
| $\varphi$ | azimuth, $\varphi = 0$ is the $x$-axis; positive values are towards the $y$ axis |
| $M_t,\ M_f$ | sampling points in time and frequency, respectively |
| $M_{\mathrm{R}},\ M_{\mathrm{T}}$ | number of antenna at the receiver and transmitter, respectively |
| $M_{\mathrm{U}}$ | number of users |
| $M_{\boldsymbol{P}}$ | number of Multi-Path Components (MPCs) |
| $\boldsymbol{I}$ | Identity matrix |
| $\delta_{ab}$ | Kronecker $\delta$-symbol, $\delta_{ab} = \begin{cases} 1 & \text{if } b = a \\ 0 & \text{if } b \neq a \end{cases}$ |
| $\delta(x)$ | Dirac $\delta$-function, $\delta(x) = \begin{cases} \infty & \text{if } x = 0 \\ 0 & \text{if } x \neq 0 \end{cases}$, $\int_{-\infty}^{\infty} \delta(x)\mathrm{d}x = 1$ |
| $\boldsymbol{b}(\vartheta, \varphi)$ | antenna polarimetric radiation pattern |
| $\boldsymbol{A}(\vartheta, \varphi)$ | polarimetric array response |
| $d(\vartheta, \varphi)$ | antenna directivity function |
| $g(\vartheta, \varphi)$ | antenna gain function |
| $\xi$ | antenna efficiency $\left(= \frac{g(\vartheta,\varphi)}{d(\vartheta,\varphi)}\right)$ |

### Symbols specific to Chapter 2

| | |
|---|---|
| $\Omega$ | a direction in the 3D space defined by the azimuth elevation pair $\{\varphi,\ \theta\}$ |
| $\Omega_{\mathrm{R}}$ | Direction Of Arrival (DOA) |
| $\Omega_{\mathrm{T}}$ | Direction Of Departure (DOD) |
| $\boldsymbol{\Omega}_{\mathrm{R}}$ | unit vector representing the DOA, so that $-\boldsymbol{\Omega}_{\mathrm{R}}$ points towards the direction $\Omega_{\mathrm{R}}$ (see Figure 2.11) |
| $\boldsymbol{\Omega}_{\mathrm{T}}$ | unit vector representing the DOD, so that $\boldsymbol{\Omega}_{\mathrm{T}}$ points towards the direction $\Omega_{\mathrm{R}}$ (see Figure 2.11) |
| $\boldsymbol{p}_{\mathrm{O}}$ | origin of the coordinate system. Also referred to as the *origin of phases*, it is equal to $\boldsymbol{0} = [0,\ 0,\ 0]^{\mathrm{T}}$ |
| $\boldsymbol{p}_{\mathrm{T}}$ | position vector of the transmitter w.r.t. $\boldsymbol{p}_{\mathrm{O}}$ |
| $\boldsymbol{p}_{\mathrm{R}}$ | position vector of the receiver w.r.t. $\boldsymbol{p}_{\mathrm{O}}$ |

| | |
|---|---|
| $\boldsymbol{q}_{\mathrm{T}}$ | normalized position vector of the transmitter w.r.t. $\boldsymbol{p}_{\mathrm{O}}$ |
| $\boldsymbol{q}_{\mathrm{R}}$ | normalized position vector of the receiver w.r.t. $\boldsymbol{p}_{\mathrm{O}}$ |
| $h(\cdots)$ | channel function. The arguments define in which domains it is represented |
| $R(\cdots)$ | correlation function. The arguments define in which domains it is represented |
| $P(\cdot)$ | power profile. The argument defines the domain in which it is represented |
| $\tilde{P}(\cdot)$ | normalized power profile. The argument defines the domain in which it is represented |
| $\rho(\cdot)$ | autocorrelation function. The argument defines the domain in which it is represented |
| $P_{\mathrm{m}}$ | total received average power |
| $\mu_{\cdot}$ | mean value |
| $\sigma_{\cdot}^2$ | variance |
| $\Delta f_{\mathrm{coe}}$ | coherence bandwidth |
| $\Delta t_{\mathrm{coe}}$ | coherence time |
| $\boldsymbol{\Delta q}_{\mathrm{coe}}$ | coherence distance |
| $\sigma_\tau(\tau)$ | RMS delay spread |
| $\sigma_\nu(\nu)$ | RMS Doppler spread |
| $\sigma_\Omega(\Omega)$ | RMS angle spread |

### Symbols specific to Chapter 4

| | |
|---|---|
| $\mathrm{d}\Omega$ | solid angle element ($= \sin\vartheta\,\mathrm{d}\vartheta\,\mathrm{d}\varphi$) |
| $\mathcal{S}^2$ | 2-sphere, the sphere with unit radius |
| $c$ | speed of light (in vacuum $\approx 3 \cdot 10^8$ m/s) |
| $k$ | wave number ($= 2\pi/\lambda$), sometimes called phase constant |
| $\omega$ | angular frequency ($= 2\pi f = k\,c$) |
| $r$ | radius |
| $Y_{lm}(\vartheta, \varphi)$ | scalar Spherical Harmonics of level (order) $l$ and mode $m$, where $l = 0, 1, 2, \ldots$ and $m \leq \lvert l \rvert$ |
| $\boldsymbol{Y}_{lm}^{(\nu)}(\vartheta, \varphi)$ | Vector Spherical Harmonics of component $\nu$, level (order) $l$, and mode $m$, where $\nu = 0, 1$; $l = 0, 1, 2, \ldots$; and $m \leq \lvert l \rvert$ |
| $B_{lm}^{(\nu)}$ | expansion coefficients in the series of Vector Spherical Harmonics (VSHs) $\boldsymbol{Y}_{lm}^{(\nu)}(\vartheta, \varphi)$ of the antenna radiation pattern $\boldsymbol{b}(\vartheta, \varphi)$. |
| $\Gamma_l^{(\nu)}$ | Level Power Spectrum (LPS), component $\nu$, level $l$ (see (4.60)). It is the mean power over the modes of $B_{lm}^{(\nu)}$. |
| $L$ | Bandlimit of VSFT spectrum, thus, $B_{lm}^{(\nu)} = 0$ for $l > L$ |
| $D_{mm'}^{l}(\alpha, \beta, \gamma)$ | Wigner $D$-function |
| $G_l^{(\nu)}$ | spherical Wiener filter, component $\nu$ in level $l$ (constant for all modes $m$, see Section 4.4.4.4) |

### Symbols specific to Chapter 5

| | |
|---|---|
| $p$ | path number |
| $\gamma_p$ | path weight |
| $d_p$ | path lenght |
| $\omega_p$ | boolean variable set to 0 if the $p$-th path is obstructed |
| $\rho_i$ | scattering coefficient for the $i$-th Interacting Object (IO) |
| $\boldsymbol{\rho}_i$ | scattering coefficient matrix (includes polarization) |
| $\boldsymbol{M}$ | precoding matrix |
| $\boldsymbol{m}$ | vector containing the model parameters, i.e., the positions of the IOs |
| $\boldsymbol{d}$ | vector containing the high-resolution parameter estimates |
| $\boldsymbol{C}(\boldsymbol{d})$ | Cramér-Rao Lower Bound (CRLB) matrix |
| $d(t, t')$ | distance between the measurement points at time instants $t$ and $t'$ |

# BIBLIOGRAPHY

## Own Publications and Technical Documents

[1] D. Baum, J. Hansen, G. Del Galdo, M. Milojevic, J. Salo, and P. Kyösti, "An interim channel model for beyond-3G systems - extending the 3GPP Spatial Channel Model (SCM)," in *IEEE Vehicular Technology Conference, VTC Spring*, Stockholm, Sweden, May 2005.

[2] N. Czink and G. Del Galdo, "Validating a novel automatic cluster tracking algorithm on synthetic IlmProp time-variant MIMO channels," in *TD(05)105 - COST 273 Post-Project Meeting*, Lisbon, Portugal, Nov. 2005.

[3] N. Czink, G. Del Galdo, and C. Mecklenbräuker, "A novel automatic cluster tracking algorithm," in *17th Int. Symp. on Personal, Indoor, and Mobile Radio Communications (PIMRC)*, Helsinki, Finland, Sept. 2006.

[4] N. Czink, G. Del Galdo, X. Yin, E. Bonek, and J. Ylitalo, "A novel environment characterization metric for clustered MIMO channels used to validate a SAGE parameter estimator," *Wireless Personal Communications*, 2007, submitted for publication.

[5] N. Czink, G. Del Galdo, X. Yin, and C. Mecklenbräuker, "A novel environment characterisation metric for clustered MIMO channels used to validate a SAGE parameter estimator," in *IST Mobile Summit 2006*, Mykonos, Greece, June 2006.

[6] G. Del Galdo, V. Algeier, N. Czink, and M. Haardt, "Spatial localization of scattering objects from high-resolution parameter estimates," in *NEWCOM-ACORN Workshop*, Vienna, Austria, Sept. 2006.

[7] G. Del Galdo, N. Czink, and M. Haardt, "Cluster spatial localization from high-resolution parameter estimation," in *IEEE/ITG Workshop on Smart Antennas (WSA)*, Reisensburg Castle near Ulm, Germany, Mar. 2006.

[8] G. Del Galdo and M. Haardt, "IlmProp: a flexible geometry-based simulation environment for multiuser MIMO communications," in *COST 273 Temporary Document, No. TD(03)188*, Prague, Czech Republic, Sept. 2003.

[9] G. Del Galdo and M. Haardt, "Comparison of zero-forcing methods for downlink spatial multiplexing in realistic multi-user MIMO channels," in *IEEE Vehicular Technology Conference, VTC Spring*, Milan, Italy, May 2004.

[10] G. Del Galdo, M. Haardt, and M. Milojevic, "A subspace-based channel model for frequency selective time variant MIMO channels," in *15th Int. Symp. on Personal, Indoor, and Mobile Radio Communications (PIMRC)*, Barcelona, Spain, Sept. 2004.

[11] G. Del Galdo, J. Lotze, M. Haardt, and C. Schneider, "Advanced geometry-based modeling for MIMO scenarios in comparsion with real measurements," in *48th International Scientific Colloquium (IWK)*, Ilmenau, Germany, Sept. 2003.

[12] G. Del Galdo, J. Lotze, M. Landmann, and M. Haardt, "Modelling and manipulation of polarimetric antenna beam patterns via spherical harmonics," in *14th European Signal Processing Conference (EUSIPCO)*, Florence, Italy, Sept. 2006.

[13] G. Del Galdo, M. Milojevic, M. Haardt, and M. Hennhöfer, "Efficient channel modelling for frequency selective MIMO channels," in *WSA Workshop on Smart Antennas*, Munich, Germany, Mar. 2004.

[14] G. Del Galdo, C. Schneider, and M. Haardt, "Geometry-based channel modeling in MIMO scenarios in comparison with channel sounder measurements," *Advances in Radio Science - Kleinheubacher Berichte*, 2003.

[15] M. Fuchs, G. Del Galdo, and M. Haardt, "A novel tree-based scheduling algorithm for the downlink of multi-user MIMO systems with ZF beamforming," in *IEEE Int. Conf. Acoust., Speech, and Signal Processing (ICASSP)*, Philadelphia, PA, USA, Mar. 2005.

[16] ——, "Low complexity space-time-frequency scheduling for MIMO systems with SDMA," *accepted for publication in IEEE Transactions on Vehicular Technology*, Oct. 2006.

[17] M. Fuchs, G. Del Galdo, and M. Haardt, "Low complexity spatial scheduling ProSched for MIMO systems with multiple base stations and a central controller," in *IEEE/ITG Workshop on Smart Antennas (WSA)*, Reisensburg Castle near Ulm, Germany, Mar. 2006.

[18] M. Haardt, V. Stankovic, and G. Del Galdo, "Efficient multi-user MIMO downlink precoding and scheduling," in *Proc. IEEE Int. Workshop on Computational Advances in Multi-Sensor Adaptive Processing (CAMSAP 2005)*, Puerto Vallarta, Mexico, Dec. 2005, keynote presentation.

[19] M. Hennhöfer, G. Del Galdo, and M. Haardt, "Analysis of MIMO channel measurements," in *13th IFAC Symposium of System Identification*, Rotterdam, The Neatherlands, Aug. 2003.

[20] ——, "Increasing the throughput in wireless multi-hop systems via spatial multiplexing," in *10th WWRF Meeting*, New York, NY, US, Oct. 2003.

[21] M. Hennhöfer, M. Haardt, and G. Del Galdo, "Increasing the throughput in wireless multi-hop networks by using spatial multiplexing," in *IEEE Vehicular Technology Conference, VTC Spring*, Milan, Italy, May 2004.

[22] M. Landmann and G. Del Galdo, "Efficient antenna description for MIMO channel modelling and estimation," in *European Microwave Week*, Amsterdam, The Netherlands, Oct. 2004.

[23] J. Lotze, G. Del Galdo, and M. Haardt, "Estimation of reflection coefficients for the IlmProp channel modeling environment using path loss models," in *51st International Scientific Colloquium (IWK)*, Ilmenau, Germany, Sept. 2006.

[24] J. Meinilä, T. Jämsä, P. Kyösti, D. Laselva, H. El-Sallabi, J. Salo, G. Del Galdo, and M. Milojevic, "D5.1: A set of channel and propagation models for early link and system level simulations," WINNER, Tech. Rep., 2005, available at http://www.ist-winner.org.

[25] M. Milojevic, G. Del Galdo, and M. Haardt, "Subspace-based framework for the prediction of MIMO OFDM channels," in *11-th International OFDM Workshop (InOWo 2006)*, Hamburg, Germany, Aug. 2006.

[26] M. Milojevic, G. Del Galdo, N. Song, M. Haardt, and A. Heuberger, "Spatio-temporal availability in satellite-to-indoor broadcasting," in *European Microwave Week*, Munich, Germany, Oct. 2007.

[27] F. Römer, M. Haardt, and G. Del Galdo, "Higher order SVD based subspace estimation to improve multi-dimensional parameter estimation algorithms," in *40th Asilomar Conf. on Signals, Systems, and Computers*, Pacific Grove, CA, US, Nov. 2006.

[28] J. Salo, G. Del Galdo, J. Salmi, P. Kyösti, M. Milojevic, D. Laselva, and C. Schneider, "MATLAB implementation of the 3GPP spatial channel," in *COST 273 Meeting, TD(05)030*, Bologna, Italy, Jan. 2005.

[29] ——, "MATLAB implementation of the 3GPP Spatial Channel Model (3GPP TR 25.996)," On-line, Jan. 2005, available at http://www.tkk.fi/Units/Radio/scm/.

[30] A. Schlesinger, G. Del Galdo, B. Albrecht, and S. Husung, "Holographic sound field analysis with a scalable spherical microphone-array," in *122nd Audio Engineering Society (AES) Conference*, Vienna, Austria, May 2007, accepted for publication.

[31] A. Schlesinger, G. Del Galdo, B. Albrecht, S. Husung, J. Lotze, H.-P. Schade, and M. Haardt, "Holographische modalanalyse mit skalierbarem kugelarray," in *33rd German Annual Conference on Acoustics, DAGA*, Stuttgart, Germany, Mar. 2007.

[32] N. Song, G. Del Galdo, M. Milojevic, M. Haardt, and A. Heuberger, "Spatial availability in satellite-to-indoor broadcasting communications," in *7th Workshop Digital Broadcasting*, Erlangen, Germany, Sept. 2006.

[33] J. Weber, G. Del Galdo, C. Volmer, M. Haardt, and M. A. Hein, "MIMO capability of a miniaturised antenna array with a decoupling and matching network," in *WSA Workshop on Smart Antennas*, Vienna, Austria, Feb. 2007.

[34] M. Weis, G. Del Galdo, and M. Haardt, "A correlation tensor-based model for time variant frequency selective MIMO channels," in *WSA Workshop on Smart Antennas*, Vienna, Austria, Feb. 2007.

## References by Other Authors

[35] "http://www.awe-communications.com."

[36] "http://www.irk-dresden.de."

[37] "IEEE standard definitions of terms for antennas (IEEE std 145-1983)," Tech. Rep.

[38] "D2.7 assessment of advanced beamforming and MIMO technologies," WINNER, Tech. Rep., 2005, available at http://www.ist-winner.org.

[39] G. T. 25.996, "3rd generation partnership project; technical specification group radio access network; spatial channel model for MIMO simulations (release 6)," v6.1.0.

[40] D. S. Ahluwalia, R. M. Lewis, and J. Boersma, "Uniform asymptotic theory of diffraction by a plane screen," *SIAM Journ. Appl. Math.*, vol. 16, no. 4, pp. 783–807, 1968.

[41] R. J. Allard and D. H. Werner, "The model-based parameter estimation of antenna radiation patterns using windowed interpolation and spherical harmonics," vol. 51, no. 8, pp. 1891–1906, Aug. 2003.

[42] J. B. Andersen, "Antenna arrays in mobile communications: gain, diversity, and channel capacity." *IEEE Antennas and Propagation Magazine*, pp. 12–16, Apr. 2000.

[43] J. B. Andersen, J. dum Nielsen, G. Bauch, and M. Herdin, "The large office environment-measurement and modeling of the wideband radio channel," in *The 17th Annual IEEE International Symposium on Personal Indoor and Mobile Radio Communications, 2006*, 2006.

[44] L. Atallah, J. P. Barbot, and P. Larzabal, "From the Chapman-Robbins bound towards the barankin bound in the threshold behaviour prediction," *IEE Electronic letters*, vol. 40, no. 4, pp. 279–280, Feb. 2004.

[45] D. Baum, J. Salo, M. Milojevic, P. Kyösti, and J. Hansen, "MATLAB implementation of the Spatial Channel Model Extended," On-line, Jan. 2005, available at http://www.tkk.fi/Units/Radio/scm/.

[46] D. S. Baum, H. El-Sallabi, T. Jämsä, J. Meinilä, P. Kyösti, X. Zhao, D. Laselva, J.-P. Nuutinen, L. Hentilä, P. Vainikainen, J. Kivinen, L. Vuokko, P. Zetterberg, M. Bengtsson, K. Yu, N. Jaldén, T. Rautiainen, K. Kalliola, M. Milojevic, C. Schneider, and J. Hansen, "D5.4: Final report on link level and system level channel models," WINNER, Tech. Rep. IST-2003-507581, 2005, available at http://www.ist-winner.org.

[47] P. A. Bello, "Characterization of randomly time-variant linear channels," *IEEE Trans. Comm. Syst.*, vol. CS-11, pp. 360–393, Dec. 1963.

[48] J. A. R. Blais and M. A. Soofi, "Spherical harmonic transforms using quadratures and least squares," in *Computational Science, ICCS 2006*, Part III, Lecture Notes in Computer Science, LNCS 3993, V. N. Alexandrov, G. D. van Albada, P. M. A. Sloot, and J. J. Dongarra, Eds. Springer-Verlag, 2006, pp. 48–55.

[49] H. Bölcskei, Ed., *Space-Time Wireless Systems – From Array Processing to MIMO Communications*. Cambridge Univ. Press, 2006.

[50] T. N. Bondar', G. I. Kolomiitseva, and O. A. Saiutina, "Spherical harmonic models of secular variations of the geomagnetic field for three overlapping periods: 1920-1986, 1938-1986, and 1958-1986," *Geomagnetizm i Aeronomiia*, vol. 29, pp. 835–839, Oct. 1989.

[51] C. A. Brau, *Modern Problems in Classical Electrodynamics*. Oxford University Press, 2004.

[52] J. B. Brewer, "Kronecker products and matrix calculus in system theory," *IEEE Trans. on Circuits and Systems*, vol. 25, no. 9, pp. 772–281, Sept. 1978.

[53] D. M. Brink and G. R. Satchler, *Angular Momentum*, 2nd ed. London: Oxford University Press, 1968.

[54] D. Chizhik, F. Rashid-Farrokhi, J. Ling, and A. Lozano, "Effects of antenna separation on the capacity of BLAST in correlated channels," *Commun. Lett.*, vol. 4, pp. 337–339, Nov. 2000.

[55] C. Chuah, J. M. Kahn, and D. Tse, "Capacity of multi-antenna array systems in indoor wireless environment," *IEEE Global Telecommunications Conference, Sydney, Australia, 1998*, vol. 5, pp. 1894–1899, 1998.

[56] P. Comon, "Tensor decompositions, state of the art and applications," *IMA Conf. mathematics in Signal Processing, Warwick, UK*, 2000.

[57] ——, "Tensor diagonalization, a useful tool in signal processing," *10th IFAC SYID Symp., vol. 1, pp 77–88, Copenhagen, Denmark*, 2001.

[58] P. Comon, B. Mourrain, L.-H. Lim, and G. H. Golub, "Genericity and rank deficency of higher order symmetric tensors," *IEEE Int. Conf. Acoust. Speech Signal Proc. (ICASSP)*, 2006.

[59] L. M. Correia, Ed., *COST259 Final Report: Wireless Flexible Personalized Communications*. J. Wiley, NY, 2001.

[60] N. Costa and S. Haykin, "A novel wideband MIMO channel model and McMaster's wideband MIMO SDR," *Asilomar Conf. on Signals, Systems, and Computers*, Nov. 2006., to be published.

[61] P. A. Cox, *Introduction to Quantum Theory and Atomic Structure*. New York: Oxford University Press, 1996.

[62] N. Czink and P. Cera, "A novel framework for clustering parametric MIMO channel data including MPC powers," in *COST 273 Post-Project Meeting*, Lisbon, Portugal, Nov. 2005.

[63] N. Czink, P. Cera, J. Salo, E. Bonek, J.-P. Nuutinen, and J. Ylitalo, "A framework for automatic clustering of parametric MIMO channel data including path powers," in *IEEE Vehicular Technology Conference 2006 Fall*, 2006.

[64] E. Damosso and L. M. Correia, Eds., *Digital Mobile Radio Towards Future Generation Systems – COST 231 Final Report*. Brussels, Belgium: COST Office, 1999, ch. 4 Propagation Prediction Models, pp. 115–208. [Online]. Available: http://www.lx.it.pt/cost231/final_report.htm

[65] L. de Lathauwer, B. de Moor, and J. Vandewalle, "A multilinear singular value decomposition," *SIAM J. Matrix Anal. Appl.*, vol. 21, no. 4, p. 1253Ű1278, 2000.

[66] ——, "On the best rank-1 and rank-$(r_1, r_2, \ldots, r_n)$ approximation of higher-order tensors," *SIAM J. Matrix Anal. Appl.*, vol. 21, no. 4, pp. 1324–1342, 2000.

[67] L. de Lathauwer and J. Vandewalle, "Dimensionality reduction in higher-order signal processing and rank - $(r_1, r_2, \ldots, r_n)$ reduction in multilinear algebra," *Linear Algebra and its applications*, vol. 391, pp. 31–55, 2004.

[68] *Stochastic Climate Models*, lecture notes, Department of Atmospheric Sciences, Texas A&M University, Texas, USA, 2003, lecture: Atmo631: Climate Modeling, ch. 7. [Online]. Available: http://www.met.tamu.edu/class/atmo631/CMCh7.pdf (Accessed: 26-Apr-06)

[69] V. Devanathan, *Angular Momentum Techniques in Quantum Mechanics*, ser. Fundamental Theories of Physics, A. van der Merve, Ed. Dordrecht, Boston, London: Kluwer Academic Publishers, 2002, vol. 108.

[70] S. Drabowitch, A. Papiernik, H. D. Griffiths, J. Encinas, and B. L. Smith, *Modern Antennas*. Chapman & Hill, 1998.

[71] G. Engeln-Müllges, K. Niederdrenk, and R. Wodicka, *Numerik-Algorithmen – Verfahren, Beispiele, Anwendungen*. Berlin, Heidelberg: Springer–Verlag, 2005.

[72] V. Erceg, L. Schumacher, P. Kyritsi, A. Molisch, D. S. Baum, and A. Y. G. et al., "TGn channel models," *IEEE 802.11-03/940r2*, Jan. 2004.

[73] R. Ertel, P. Cardieri, K. Sowerby, T. Rappaport, and J. Reed, "Overview of spatial channel models for antenna array communication systems," *IEEE Pers. Commun. Mag.*, vol. 5, pp. 10–22, Feb. 1998.

[74] M. Failli, Ed., *Digital land mobile radio communications COST 207*. Tech. Rep., European Commission, 1989.

[75] B. H. Fleury, "First- and second-order characterization of direction dispersion and space selectivity in the radio channel," *IEEE Trans. of Inf. Theory*, vol. 46, no. 6, pp. 2027–2043, Sept. 2000.

[76] B. H. Fleury, D. Dahlhaus, R. Heddergott, and M. Tschudin, "Wideband angle of arrival estimation using the sage algorithm," *in Proc. IEEE Fourth Int. Symp. Spread Spectrum Techniques and Applications (ISSSTA'96), Mainz, Germany*, pp. 29–85, Sept. 1996.

[77] B. H. Fleury, X. Yin, P. Jourdan, and A. Stucki, "High-resolution channel parameter estimation for communication systems equipped with antenna arrays," *Proc. 13th IFAC Symposium on System Identification (SYSID 2003), Rotterdam, The Netherlands*, no. ISC-379, 2003.

[78] B. H. Fleury, X. Yin, and A. Kocian, "Impact of the propagation conditions on the properties of MIMO channels," *International Conference on Electromagnetics in Advanced Applications, ICEAA'03, Torino, Italy*, pp. 783–786, Sept. 2003.

[79] B. H. Fleury, X. Yin, K. G. Rohbrandt, P. Jourdan, and A. Stucki, "Performance of a high-resolution scheme for joint estimation of delay and bidirection dispersion in the radio channel," *Proc. IEEE Vehicular Technology Conference, VTC 2002 Spring*, vol. 1, pp. 522–526, May 2002.

[80] P. Forster, P. Larzabal, and E. Boyer, "Threshold performance analysis of maximum likelihood DOA estimations," *IEEE Transactions on Signal Processing*, vol. 52, Nov. 2004.

[81] G. J. Foschini and M. J. Gans, "On limits of wireless communications in a fading environment," *Wireless Personal Communications*, vol. 6, pp. 331–335, 1998.

[82] H. T. Friis, "A note on a simple transmission formula," *Proc. of the IRE*, vol. 41, pp. 254–256, May 1946.

[83] T. Fügen, J. Maurer, T. Kayser, and W. Wiesbeck, "Verification of 3D ray-tracing with measurements in urban macrocellular environments," in *IEEE/ITG Workshop on Smart Antennas (WSA)*, Reisensburg Castle near Ulm, Germany, Mar. 2006.

[84] D. Gesbert, H. Bolcskei, D. Gore, and A. Paulraj, "MIMO wireless channels: Capacity and performance prediction," *IEEE Globecom 2000, San Francisco, CA, Nov. 27-Dec. 1*, vol. 2, pp. 1083–1088, 2000.

[85] I. I. Gikhman and A. V. Skorohod, *The Theory of Stochastic Processes I.* Springer, 1974.

[86] A. Goldsmith, *Wireless Communications.* Cambridge University Press, 2006.

[87] G. H. Golub and C. F. van Loan, *Matrix Computations.* Johns Hopkins University Press, 1996.

[88] K. M. Górski, B. D. Wandelt, E. Hivon, F. K. Hansen, and A. J. Banday, *The HEALPix Primer*, Jet Propulsion Laboratory, California Institute of Technology, Pasadena, California, Aug. 2005, revision 2.0. [Online]. Available: http://healpix.jpl.nasa.gov/pdf/intro.pdf (Accessed: 23-Oct-06)

[89] W. C. Graustein, *Introduction to Higher Geometry.* Macmillan, New York, 1930.

[90] M. Gustafsson and S. Nordebo, "On the spectral efficiency of a sphere," Lund Institute of Technology, Lund, Sweden, Tech. Rep., Dec. 2004. [Online]. Available: http://www.es.lth.se/teorel/Publications/TEAT-7000-series/TEAT-7127.pdf (Accessed: 05-Oct-06)

[91] ——, "Bandwidth, Q factor, and resonance models of antennas," *Progress In Electromagnetics Research (PIER)*, vol. 62, pp. 1–20, 2006.

[92] ——, "Characterization of MIMO antennas using spherical vector waves," vol. 54, no. 9, Sept. 2006.

[93] M. Haardt and J. A. Nossek, "Unitary ESPRIT: How to obtain increased estimation accuracy with a reduced computational burden," *IEEE Transactions on Signal Processing*, vol. 43, pp. 1232–1242, 1995.

[94] ——, "Simultaneous Schur decomposition of several non-symmetric matrices to achieve automatic pairing in multidimensional harmonic retrieval problems," *IEEE Trans. Signal Processing*, vol. 46, pp. 161–169, Jan. 1998.

[95] M. Haardt, R. S. Thomä, and A. Richter, "Multidimensional high-resolution parameter estimation with applications to channel sounding," *High-Resolution and Robust Signal Processing, Marcel Dekker*, 2003.

[96] J. E. Hansen, *Spherical Near-Field Antenna Measurements*, ser. IEE Electromagnetic Waves Series. London, U.K.: Peter Peregrinus Ltd., 1988, no. 26.

[97] W. W. Hansen, "A new type of expansion in radiation problems," *Physical Review*, vol. 47, pp. 139–143, Jan. 1935.

[98] R. F. Harrington, *Time-Harmonic Electromagnetic Fields*, ser. Electrical and Electronic Engineering Series. New York: McGraw-Hill, 1961.

[99] R. Hedergott, U. P. Bernhard, and B. H. Fleury, "Stochastic radio channel model for advanced indoor mobile communication systems," in *Personal Indoor and Mobile Radio Communications (PIMRC)*, Helsinki, Finland, Sept. 2004.

[100] M. H. A. J. Herben, M. Jevrosimovic, Y. L. C. de Jong, M. R. J. A. E. Kwakkernaat, E. F. T. Martijn, J. R. S. Oliviera, P. Pajovic, R. H. van Poppel, and S. Savov, "Deliverable D2.3: Channel modelling for UMTS: Characterisation of outdoor- and outdoor-to-indoor propagation," Radio@hand project, Tech. Rep., 2005. [Online]. Available: http://www.brabantbreedband.nl (Accessed: 01-Mar-06)

[101] M. Herdin and E. Bonek, "A MIMO correlation matrix based metric for characterizing non-stationarity," in *IST Mobile Summit 2006*, 2006.

[102] J. G. Hocking and G. S. Young, *Topology*. Dover Publications, 1988.

[103] L. H. Hodges and A. V. Astin, *Handbook of Mathematical Functions With Formulas, Graphs, and Mathematical Tables, tenth edition*, M. Abramowitz and I. A. Stegun, Eds. National Bureau of Standards, Applied Mathematics Series - 55, 1972.

[104] A. Hong, R. Thomä, and W. Zirwas, "Considerations on the relationship between path loss and spatial characteristics based on MIMO measurements," in *IEEE/ITG Workshop on Smart Antennas (WSA)*, Reisensburg Castle near Ulm, Germany, Mar. 2006.

[105] A. Hottinen, O. Tirkkonen, and R. Wichman, *Multi-antenna Transceiver Techniques for 3G and Beyond*. New York, NY, USA: John Wiley & Sons, 2003.

[106] T. Hult, A. Mohammed, and S. Nordebo, "Active suppression of electromagnetic fields using a MIMO antenna system," *17th International Conference on Applied Electromagnetics and Communications (ICEC03)*, 2003.

[107] J. T. Hviid, J. B. Andersen, J.Toftgard, and J.Bojer, "Terrain-based propagation model for rural area - an integral equation approach," *IEEE Transactions on Antennas and Propagation*, vol. 43, no. 1, pp. 41–46, Jan. 1995.

[108] IEEE 802.11-03/940r2, "IEEE P802.11 Wireless LANs, TGn Channel Models," Tech. Rep., 2004.

[109] J. D. Jackson, *Klassische Elektrodynamik*, 3rd ed. Berlin, New York: Walter de Gruyter, 2002.

[110] W. C. Jakes, Ed., *Microwave Mobile Communications*. Piscataway, NJ: IEEE Press, 1974.

[111] M. Joham, J. Brehmer, and W. Utschick, "MMSE approaches to multiuser spatio-temporal Tomlinson-Harashima precoding," in *Proc. 5th International ITG Conference on Source and Channel Coding (ITG SCC'04)*, Jan. 2004, pp. 387–394.

[112] Y. L. C. Jong de and M. H. A. J. Herben, "Experimental verification of ray-tracing based propagation prediction models for urban microcellular environments," *in Proceedings of IEEE Vehicular Technology Conference (VTC)*, vol. 3, pp. 1434–1438, Sept. 1999.

[113] W. Kaplan, *Advanced Calculus*. Addison Wesley Publishing Company, 1991.

[114] R. Kattenbach, "Statistical modeling of small-scale fading in directional radio channels," *IEEE Journal on Selected Areas in Communications*, vol. 20, no. 3, pp. 584–592, Apr. 2002.

[115] M. Kazhdan, T. Funkhouser, and S. Rusinkiewicz, "Rotation invariant spherical harmonic representation of 3d shape descriptors," in *Eurographics Symposium on Geometry Processing*, L. Kobbelt, P. Schröder, and H. Hoppe, Eds., 2003. [Online]. Available: http://www.cs.jhu.edu/~misha/MyPapers/SGP03.pdf (Accessed: 07-Aug-06)

[116] J. Keiner and D. Potts, "Fast evaluation of quadrature formulae on the sphere," 2006, Universität zu Lübeck, Preprint 2006-6. [Online]. Available: http://www-user.tu-chemnitz.de/~potts/paper/quadraturS2.pdf (Accessed: 12-Jun-06)

[117] J. B. Keller, "Geometrical theory of diffraction," *Journ. Opt. Soc. Am.*, vol. 52, no. 2, pp. 116–130, 1962.

[118] J. P. Kermoal, L. Schumacher, K. I. Pedersen, and P. E. Mogensen, "A stochastic MIMO radio channel model with experimental validation," *IEEE Journal on Selected Areas in Communications*, vol. 20, no. 6, pp. 1211–1226, Aug. 2002.

[119] C. G. Khatri and C. R. Rao, *Solutions to some functional equations and their applications to characterization of probability distributions.* Sankhya Se. A, 30: 167-180, 1968.

[120] A. Y. Khinchin, "Uspekhi mat. nauk," *Russian Mathematical Surveys, (in Russian)*, vol. 5, pp. 42–51, 1938. [Online]. Available: http://math.ras.ru/UMN (Accessed: 01-Mar-06)

[121] R. W. P. King, *Fundamental Electromagnetic Theory.* Dover: New York, 1963.

[122] A. Klein, W. Mohr, R. Thomas, P. Weber, and B. Wirth, "Direction-of-arrival of partial waves in wideband mobile radiochannels for intelligent antenna concepts," in *Vehicular Technology Conference, Atlanta, GA*, 1996.

[123] O. Klemp, G. Armbrecht, and H. Eul, "Analytic modelling of polarization diversity performance for frequency-independent planar mulitarm antennas," in *10th ITG-IEEE Workshop on Smart Antennas 2006*, Ulm, Germany, 13-14 March 2006.

[124] O. Klemp and H. Eul, "Analytical approach for mimo performance and electromagnetic coupling in linear dipole arrays," in *2nd IEEE International Symposium on Wireless Communication Systems*, Siena, Italy, 5-7 September 2005.

[125] ——, "Radiation pattern analysis of antenna systems for mimo- and diversity configurations," *Advances in Radio Science*, no. 3, pp. 157Ű–165, 2005.

[126] O. Klemp, S. K. Hampel, and H. Eul, "Study of mimo capacity for linear dipole arrangements using spherical mode expansions," in *14th IST Mobile & Wireless Communications Summit*, Dresden, Germany, 19-23 June 2005.

[127] P. Koivisto, "Demonstration of reflection error reduction in antenna radiation patterns using spherical wave expansion," *Microwave and Optical Technology Letters*, vol. 43, no. 4, pp. 280–284, Nov. 2004.

[128] P. K. Koivisto, "Analytical solution for characteristic modal power distribution and truncation limit for spherical wave expansion of antenna radiation pattern," *Journal of Electromagnetic Waves and Applications*, vol. 16, no. 9, pp. 1307–1328, 2002.

[129] ——, "Reduction of errors in antenna radiation patterns using optimally truncated spherical wave expansion," *Progress in Electromagnetic Research (PIER)*, vol. 47, pp. 313–333, 2004. [Online]. Available: http://ceta.mit.edu/pier/pier47/15.0312031.Koivisto.pdf (Accessed: 18-May-06)

[130] P. K. Koivisto and J. C.-E. Sten, "On the influence of incomplete radiation pattern data on the accuaracy of a spherical wave expansion," *Progress in Electromagnetic Research (PIER)*, vol. 52, pp. 185–204, 2005. [Online]. Available: http://ceta.mit.edu/pier/pier52/09.0408092.Koivisto.S.pdf (Accessed: 3-Aug-06)

[131] P. J. Kostelec and D. N. Rockmorey, "FFTs on the rotation group," Santa Fe Institute, Working Paper Series 03-11-060, 2003. [Online]. Available: http://www.santafe.edu/research/publications/workingpapers/03-11-060.pdf (Accessed: 3-Aug-06)

[132] R. G. Kouyoumjian and P. H. Pathak, "A uniform asymptotic theory of diffraction for an edge in a perfectly conducting surface," *Proc. IEEE*, vol. 62, no. 11, pp. 1448–1462, 1974.

[133] H. Krim and M. Viberg, "Two decades of array signal processing research: the parametric approach," *IEEE Signal Processing Magazine*, vol. 13, pp. 67–94, July 1996.

[134] A. Kuchar, J.-P. Rossi, and E. Bonek, "Directional macro-cell channel characterization from urban measurements," *IEEE Trans. On Antennas and Propagation*, vol. vol. 48, no. no. 2, pp. 137–146, 2000.

[135] L. D. Landau and E. M. Lifshitz, *Quantum Mechanics - Non-Relativistic Theory*, 3rd ed., ser. Course of Theoretical Physics. Oxford, New York, Beijing: Pergamon Press, 1977, vol. 3.

[136] M. Landmann, "Antenna array modelling, evaluation and design in the context of high resolution parameter estimation and experimental channel modelling," Ph.D. dissertation, Technische Universität Ilmenau, 2007, to appear in the Fall.

[137] M. Landmann, A. Richter, and R. Thomä, "Performance evaluation of real antenna arrays for high-resolution DOA estimation in channel sounding - part 1: Channel parameter resolution limits," in *COST 273 Temporary Document, Prague, Czech Republic, No. TD(03)199, September*, 2003.

[138] M. Landmann, A. Richter, and R. S. Thomä, "DOA resolution limits in MIMO channel sounding," *2004 International Symposium on Antennas and Propagation and USNC/URSI National Radio Science Meeting, Monterey, CA*, June 2004.

[139] ——, "Performance evaluation of antenna arrays for high-resolution DOA estimation in channel sounding," *International Symposium on Antennas and Propagation, Sendai, Japan*, Aug. 2004.

[140] M. Landmann, K. Sivasondhivat, J.-I. Takada, I. Ichirou, and R. S. Thomä, "Polarisation behaviour of discrete multipath and diffuse scattering in urban environments at 4.5 GHz," *EURASIP Journal on Wireless Communications and Networking, Special Issue*, 2006.

[141] M. Landmann and J. Takada, "On the plane wave assumption in indoor channel modelling," in *IEICE Society Conference*, Sapporo, Japan, Sept. 2005, p. 1.

[142] V. I. Lebedev, "Values of the nodes and weights of ninth to seventeenth order gauss-markov quadrature formulae invariant under the octahedron group with inversion," *Computational Mathematics and Mathematical Physics*, vol. 15, pp. 44–51, 1975.

[143] ——, "Quadratures on a sphere," *Zh. výchisl. Mar. mat. Fiz.*, vol. 16, no. 2, pp. 293–306, 1976.

[144] ——, "Spherical quadrature formulas exact to orders 25–29," *Siberian Mathematical Journal*, vol. 18, pp. 99–107, 1977.

[145] ——, "A quadrature formula for the sphere of 59th algebraic order of accuracy," *Russian Acad. Sci. Dokl. Math.*, vol. 50, pp. 283–286, 1995.

[146] V. I. Lebedev and D. N. Laikov, "A quadrature formula for the sphere of the 131st algebraic order of accuaracy," *Doklady Mathematics*, vol. 59, no. 3, pp. 477–481, 1999.

[147] V. I. Lebedev and A. L. Skorokhodov, "Quadrature formulas of orders 41, 47, and 53 for the sphere," *Russian Acad. Sci. Dokl. Math.*, vol. 45, pp. 587–592, 1992.

[148] S. W. Lee and G. A. Deschamps, "A uniform asymptotic theory of diffraction of edge diffraction," *IEEE Trans. Ant, Prop.*, vol. AP-24, no. 1, pp. 25–34, 1976.

[149] J. Lotze, "Efficient polarimetric antenna radiation pattern modeling," Master's thesis, Technische Universität Ilmenau, 2006.

[150] E. F. T. Martijn, M. H. A. J. Herben, P. F. M. Smulders, M. Jevrosimovic, and S. Savov, "Deliverable D2.1: State of the art channel models," Radio@hand project, Tech. Rep., 2002. [Online]. Available: http://www.brabantbreedband.nl

[151] R. J. McAulay and L. P. Seidman, "A useful form of the Barankin lower bound and its application to ppm threshold analysis," *IEEE Jorunal IT*, vol. 15, pp. 273–279, Mar. 1969.

[152] D. A. McNamara, C. W. I. Pistorius, and J. A. G. Malherbe, *Introduction to the Uniform Geometrical Theory of Diffraction.* Boston: Artech House, 1990.

[153] D. P. McNamara, M. Beach, and P. N. Fletcher, "Spatial correlation in indoor MIMO channels," *in Proceedings of Personal Indoor and Mobile Radio Communications (PIMRC), Lisbon, Portugal, 2002*, vol. 1, pp. 290–294, 2002.

[154] J. McWhirter and I. Proudler, Eds., *Mathematics in Signal Processing V.* Oxford University Press, 2001.

[155] MEDAV GmbH D-91080 Uttenreuth, "More information on the RUSK MIMO channel sounder can be found at http://www.channelsounder.de."

[156] J. Meyer and G. W. Elko, "A highly scalable spherical microphone array based on an orthonormal decomposition of the soundfield," in *IEEE International Conference on Acoustics, Speech, and Signal Processing (ICASSP '02)*, vol. 2, Orlando, USA, May 2002, pp. 1781–1784.

[157] P. E. Mogensen, K. I. Pedersen, F. Frederiksen, B. Fleury, P. Espensen, L. Olesen, and S. Leth-Larsen, "TSUNAMI-II final report," *ACTS-TSUNAMI, Brussels, Belgium*, Sept. 1998.

[158] A. Molisch, *Wireless Communications.* John Wiley & Sons, Oct. 2005.

[159] B. G. Molnár, I. Frigyes, Z. Bodnár, Z. Herczku, Z. Kormányos, J. Bérces, I. Papp, and L. Juhász, "A detailed experimental study of the LEO satellite to indoor channel characteristics," *International Journal of Wireless Information Networks*, Apr. 1999.

[160] P. M. Morse and H. Feshbach, *Methods of Theoretical Physics, Part II: Chapters 9 to 13.* New York, Toronto, London: McGraw–Hill, 1953.

[161] A. L. Moustakas, "Communication through a diffusive medium: Coherence and capacity," *Science*, vol. 287, pp. 287–290, Jan. 2000.

[162] K. Niederdrenk and H. Yserentant, *Funktionen einer Veränderlichen : analytische und numerische Behandlung*, ser. Rechnerorientierte Ingenieurinformatik. Brauenschweig, Wiesbaden: Vieweg, 1987.

[163] S. Nordebo and M. Gustafsson, "Statistical signal analysis for the inverse source problem of electromagnetics," vol. 54, no. 6, pp. 2357–2361, June 2006.

[164] S. Nordebo, M. Gustafsson, and J. Lundbäck, "Fundamental limitations for DOA and polarization estimation with applications in array signal processing," vol. 54, no. 10, pp. 4055–4061, Oct. 2006.

[165] S. Nordebo, M. Gustafsson, and K. Persson, "Sensitivity analysis for antenna near-field imaging," Lund Institute of Technology, Lund, Sweden, Tech. Rep., Oct. 2005. [Online]. Available: http://www.es.lth.se/teorel/Publications/TEAT-7000-series/TEAT-7139.pdf (Accessed: 05-Oct-06)

[166] C. Oestges, H. Özcelik, and E. Bonek, "On the practical use of analytical MIMO channel models," in *2005 IEEE Antennas and Propagation Society International Symposium*, Washington, USA, July 2005, pp. 406–409.

[167] H. Özcelik, M. Herdin, W. Weichselberger, J. Wallace, and E. Bonek, "Deficiencies of the 'Kroneckerť MIMO radio channel model," *Electronics Letters*, no. 39(16), pp. 1209–1210, 2003.

[168] A. Papoulis and S. U. Pillai, *Probability, Random Variables and Stochastic Processes.* McGraw-Hill, Inc., 1987.

[169] A. Paraboni, *Antenne.* McGraw-Hill Libri Italia s.r.l., 1999.

[170] R. L. Parker, *Geophysical Inverse Theory.* Princeton University Press, 1994.

[171] C. R. Paul, K. W. Whites, and S. A. Nasar, *Introduction to Electromagnetic Fields, third edition.* McGraw-Hill, Inc., 1998.

[172] A. Paulraj, R. Nabar, and D. Gore, *Introduction to space-time wireless communications.* Cambridge: Cambridge University Press, 2003.

[173] K. I. Pedersen, J. B. Andersen, J. P. Kermoal, and P. Modensen, "A stochastic multiple-input-multiple-output radio channel model for evaluation of space-time coding algorithms," *in IEEE VTC 2000, Boston, MA, Sept. 24-28*, pp. 893–897, 2000.

[174] T. Pedersen and B. H. Fleury, "A realistic radio channel model based on stochastic propagation graphs," in *Proceedings 5th MATHMOD Vienna – 5th Vienna Symposium on Mathematical Modelling*, vol. 1,2, Feb. 2006, p. 324, ISBN 3–901608–30–3.

[175] ——, "Radio channel modelling using stochastic propagation graphs," 2007, accepted for publication at the ICC2007 conference.

[176] D. Potts, "Schnelle Fourier-Transformationen für nicht äquidistante Daten und Anwendungen," Habilitationsschrift, Universität zu Lübeck, Technisch-Naturwissenschaftliche Fakultät, Lübeck, March 2003.

[177] J. G. Proakis, *Digital Communications.* University Press (Belfast), Ltd.: McGraw-Hill, Inc., 1995.

[178] J. G. Proakis and D. G. Manolakis, *Digital Signal Processing.* Prentice–Hall, International, Inc, 1996.

[179] W. Qiu, H. Tröger, and M. Meurer, "Joint transmission (JT) in multi-user MIMO transmission systems," *in COST 273 TD(02)008, EURO-COST*, 2002.

[180] A. Richter, "Estimation of radio channel parameters: Models and algorithms," Ph.D. dissertation, Technische Universität Ilmenau, 2005.

[181] A. Richter, M. Landman, and R. S. Thomä, "A gradient based method for maximum likelihood channel parameter estimation from multidimensional channel sounding measurement," *XXVII URSI General Assembly, Maastricht, NL*, Aug. 2002.

[182] A. Richter, M. Landmann, and R. S. Thomä, "A flexible algorithm for channel parameter estimation from channel sounding measurements," *COST 273 Temporary Document TD(04)045, Athens, Greece*, Jan. 2004.

[183] A. Richter, J. Salmi, and V. Koivunen, "On distributed scattering in radio channels and its contribution to MIMO channel capacity," in *in Proc 1st European Conference on Antennas and Propagation (EuCAP 2006)*, Nice, France, Nov. 2006, best Paper Award.

[184] E. Roeckner, G. Bäuml, L. Bonaventura, R. Brokopf, M. Esch, M. Giorgetta, S. Hagemann, I. Kirchner, L. Kornblueh, E. Manzini, A. Rhodin, U. Schlese, U. Schulzweida, and A. Tompkins, "The atmospheric general circulation model ECHAM5, part I," Max Planck Institute for Meteorology, Hamburg, Report, Nov. 2003, report No. 349. [Online]. Available: http://edoc.mpg.de/175329 (Accessed: 21-Sep-06)

[185] Y. A. Rozanov, *Stationary random processes.* Holden Day, 1967, translated from Russian.

[186] W. C. Sabine, *Collected Papers on Acoustics.* Los Altos, US: Peninsula Publishing,, 1993.

[187] A. A. M. Saleh and R. A. Valenzuela, "A statistical model for indoor multipath propagation," *IEEE J.Selected Areas Comm.*, vol. 5, pp. 128–137, Feb. 1987.

[188] T. K. Sarkar, Z. Ji, K. Kim, A. Medour, and M. Salazar-Palma, "A survey of various propagation models for mobile communication," vol. 45, no. 3, pp. 51–82, June 2003.

[189] A. M. Sayeed, "Deconstructing multiantenna fading channels," *IEEE Trans. Signal Process.*, vol. 50, no. 10, pp. 2563–2579, Oct. 2002.

[190] R. D. Schafer, *An Introduction to Nonassociative Algebras.* New York: Dover, 1996.

[191] D.-S. Shiu, *Wireless Communications using Dual Antenna Arrays*. Kluwer Academic Publishers, 2000.

[192] D.-S. Shiu, G. J. Foschini, M. J. Gans, and J. M. Kahn, "Fading correlation and its effects on the capacity of multielement antenna systems," *IEEE Trans. on Comm.*, vol. 48, no. 3, pp. 502–513, Mar. 2000.

[193] Q. Spencer and M. Haardt, "Capacity and downlink transmission algorithms for a multi-user MIMO channel," in *Proc. 36th Asilomar Conf. on Signals, Systems, and Computers*, Pacific Grove, CA, Nov. 2002.

[194] Q. H. Spencer, A. L. Swindlehurst, and M. Haardt, "Zero-forcing methods for downlink spatial multiplexing in multiuser MIMO channels," *IEEE Transactions on Signal Processing*, vol. 52, Feb. 2004.

[195] F. Sprengel, "Can we use the known fast spherical fourier transform in numerical meteorology?" *GMD Report*, vol. 142, July 2001. [Online]. Available: http://www.gmd.de/endofservice/publications/report/0142/Text.pdf (Accessed: 3-Jul-06)

[196] V. Stankovic and M. Haardt, "Multi-user MIMO downlink precoding for users with multiple antennas," in *Proc. of the 12-th Meeting of the Wireless World Research Forum (WWRF), Toronto, ON, Canada*, Nov. 2004.

[197] M. Stein and G. Weiss, *Introduction to Fourier Analysis on Euclidean Spaces*. Princeton University Press, 1971.

[198] M. Steinbauer, "The radio propagation channel - a non-directional, directional, and double-directional point-of-view," Ph.D. dissertation, Vienna University of Technology, Vienna, Austria, 2001.

[199] M. Steinbauer, D. Hampicke, G. Sommerkorn, A. Molisch, R. Thomä, and E. Bonek, "Array measurement of the double-directional mobile radio channel," in *51st Vehicular Technology Conference (VTC2000-Spring)*, Tokyo, Japan, May 2000.

[200] M. Steinbauer, A. Molisch, and E. Bonek, "The double-directional radio channel," *IEEE Antennas and Propagation Magazine*, vol. vol. 43, no. no. 4, pp. 51–63, 2001.

[201] P. Stoica and A. Nehorai, "MUSIC, maximum likelihood, and Cramer-Rao bound," *IEEE Transactions on Acoustics, Speech, and Signal Processing*, vol. 37, pp. 720–741, 1989.

[202] J. A. Stratton, *Electromagnetic Theory*. New York and London: McGraw-Hill, 1941.

[203] A. Tarantola, *Inverse Problem Theory and Methods for Model Parameter Estimation*. Society for Industrial and Applied Mathematic, 2004. [Online]. Available: http://www.ipgp.jussieu.fr/~tarantola/

[204] V. Tarokh, A. Naguib, N. Seshadri, and A. R. Calderbank, "Space-time codes for high data rate wireless communication: performance criteria in the presence of channel estimation errors, mobility, and multiple-paths." *IEEE Trans. on Comm.*, vol. 47, pp. 199–207, 1998.

[205] V. Tarokh, N. Seshadri, and A. R. Calderbank, "Space-time codes for high data rate wireless communication: performance criterion and code construction," *IEEE Trans. of Inf. Theory*, vol. 44, pp. 744–765, 1998.

[206] I. E. Teletar, "Capacity of multi-antenna gaussian channels," *European Transactions on Telecommunications*, vol. 10, no. 6, pp. 585–595, Nov./Dec. 1999, published in October, 1995 as a Technical Memorandum. Bell Laboratories.

[207] H. Teutsch and W. Kellermann, "Eigen-beam processing for direction-of-arrival estimation using spherical apertures," in *Joint Workshop for Hands-Free Speech Communication and Microphone Arrays (HSCMA)*, Piscataway, USA, Mar. 2005.

[208] R. Thomä, M. Landmann, and A. Richter, "RIMAX – a maximum likelihood framework for parameter estimation in multidimensional channel sounding," *2004 Intl. Symp. on Antennas and Propagation, Sendai, JP*, 2004.

[209] R. S. Thomä, D. Hampicke, M. Landmann, A. Richter, and G. Sommerkorn, "Measurement-based parametric channel modelling (MBPCM)," *ICEAA, Torino*, Sept. 2003.

[210] R. S. Thomä, D. Hampicke, A. Richter, G. Sommerkorn, A. Schneider, and U. Trautwein, "Identification of time-variant directional mobile radio channels," *9th Virginia Tech Symp. Wireless Personal Communications, Blacksburg, VA*, pp. 11–22, June 1999.

[211] U. Trautwein, M. Landmann, G. Sommerkorn, and R.Thomä, "System-oriented measurement and analysis of MIMO channels," in *COST 273 Meeting, TD(05)063*, Bologna, Italy, Jan. 2005.

[212] http://www.propsim.net, "Elektrobit Oy, Automaatiotie 1 (PL 45), 90461 Oulunsalo, Finland," Tech. Rep.

[213] R. A. Valenzuela, "Ray tracing prediction of indoor radio propagation," *in Proceedings of Personal Indoor and Mobile Radio Communications (PIMRC), The Hague, The Netherlands*, pp. 140–143, 1994.

[214] G. A. J. van Dooren, "A deterministic approach to the modelling of electromagnetic wave propagation in urban environments," PhD thesis, University of Eindhoven, The Netherlands, 1994.

[215] H. L. Van Trees, *Detection, Estimation, and Modulation Theory, Part IV, Optimum Array Processing.* Wiley, Apr. 2002.

[216] D. A. Varshalovich, A. N. Moskalev, and V. K. Khersonskii, *Quantum Theory of Angular Momentum.* Singapore: World Scientific Publishing Co Pte Ltd., 1988.

[217] R. Vaughan and J. B. Andersen, *Channels, propagation and antennas for mobile communications*, ser. IEE electromagnetic waves series, vol. 50. London: The Institution of Electrical Engineers (IEE), 2003.

[218] X.-G. Wang and T. Carrington, Jr., "Using lebedev grids, sine spherical harmonics, and monomer contracted basis functions to calculate bending energy levels of HF trimer," *Journal of Theoretical and Computational Chemistry*, vol. 2, no. 4, pp. 599–608, 2003.

[219] J. Weber, C. Volmer, K. Blau, R. Stephan, and M. A. Hein, "Implementation of a miniaturised antenna array with predefined orthogonal radiation patterns," in *Proc. 1th European Conf. on Antennas and Prop., EUCAP'06*, Nice, France, Nov. 2006.

[220] ——, "Miniaturised antenna arrays using decoupling networks with realisitic elements," vol. 54, no. 6, June 2006, pp. 2733–2740.

[221] W. Weichselberger, "Spatial structure of multiple antenna radio channels – a signal processing viewpoint," Ph.D. dissertation, Technische Universität Wien, Vienna, Austria, 2003.

[222] W. Weichselberger, M. Herdin, H. Özcelik, and E. Bonek, "A stochastic MIMO channel model with joint correlation of both link ends," *IEEE Trans. on Wireless Comm.*, vol. 5, no. 1, pp. 90–100, Jan. 2006.

[223] E. W. Weisstein. (2004, Jan.) Generalized Fourier Series. From: *MathWorld* – A Wolfram Web Ressource. [Online]. Available: http://mathworld.wolfram.com/GeneralizedFourierSeries.html (Accessed: 11-Sep-06)

[224] ——. (2006, Feb.) Parseval's Theorem. From: *MathWorld* – A Wolfram Web Ressource. [Online]. Available: http://mathworld.wolfram.com/ParsevalsTheorem.html (Accessed: 12-Nov-06)

[225] ——. (2006, Jan.) Platonic Solid. From: *MathWorld* – A Wolfram Web Ressource. [Online]. Available: http://mathworld.wolfram.com/PlatonicSolid.html (Accessed: 03-Nov-06)

[226] E. T. Whittaker and G. Robinson, *The Calculus of Observations: A Treatise on Numerical Mathematics*. New York: Dover Publications, 1967.

[227] J. Winter, U. Martin, A. Molisch, R. Kattenbach, I. Gaspard, M. Steinbauer, and M. Grigat, "Description of the modelling method," *METAMORP Public Report C-2/1, Deutsche Telekom, Darmstadt, Germany*, Feb. 1999.

[228] C. v. Wuellen and D. Laikov. (2000) A FORTRAN code to generate Lebedev grids up to order $l = 131$. Computational Chemistry List, ltd. [Online]. Available: http://server.ccl.net/cca/software/SOURCES/FORTRAN/Lebedev-Laikov-Grids/index.shtml (Accessed: 10-May-06)

[229] H. Xiao and A. Burr, "An extended correlation matrix distance metric used to evaluate the short-term time variation of wideband channels predicted by different MIMO channel models," in *NEWCOM-ACORN Workshop*, Vienna, Austria, Sept. 2006.

[230] ——, "A time-variant wideband spatial channel model based on the 3GPP mode montréal," in *Proc. IEEE Vehicular Technology Conference, VTC Fall, Montréal, Quebec, Canada*, 2006.

[231] H. Xu, D. Chizhik, H. Huang, and R. Valenzuela, "A generalized spaceŰtime multiple-input multiple-output (MIMO) channel model," *IEEE Trans. on Wir. Comm.*, vol. 3, no. 3, pp. 966–975, May 2004.

[232] D. Yacoub, C. Schneider, S. Warzügel, W. Teich, R. Thomä, and J. Lindner, "Capacity of measured MIMO channels in dependence of array element spacing and distance between antennas," in *IEEE/ITG Workshop on Smart Antennas (WSA)*, Reisensburg Castle near Ulm, Germany, Mar. 2006.

[233] B. T. T. Yeo, "Computing spherical transform and convolution on the 2-sphere," MIT - Computer Science and Artificial Intelligence Laboratory, Cambridge, USA, Tech. Rep., May 2005. [Online]. Available: http://people.csail.mit.edu/ythomas/6869.pdf (Accessed: 20-Mar-06)

[234] K. Yu, M. Bengtsson, B. Ottersten, D. McNamara, P. Karlsson, and M. Beach., "A wideband statistical model for NLOS indoor MIMO channels." in *Proc. IEEE Vehicular Technology Conference, VTC Spring*, vol. 1, Birmingham, AL, US, May 2002, pp. 370–374.

[235] K. Yu and B. Ottersten, "Models for MIMO Propagation Channels, A Review," *Special Issue on Adaptive Antennas and MIMO Systems, Wiley Journal on Wireless Communications and Mobile Computing*, vol. 2, no. 7, pp. 653–666, Nov. 2002.

[236] T. Zwick, C. Fischer, D. Didascalon, and W. Wiesbeck, "A stochastic spatial channel model based on wave-propagation modeling," *IEEE Journal on Select. Areas in Comm.*, vol. 18, no. 1, pp. 6–15, Jan. 2000.

# INDEX